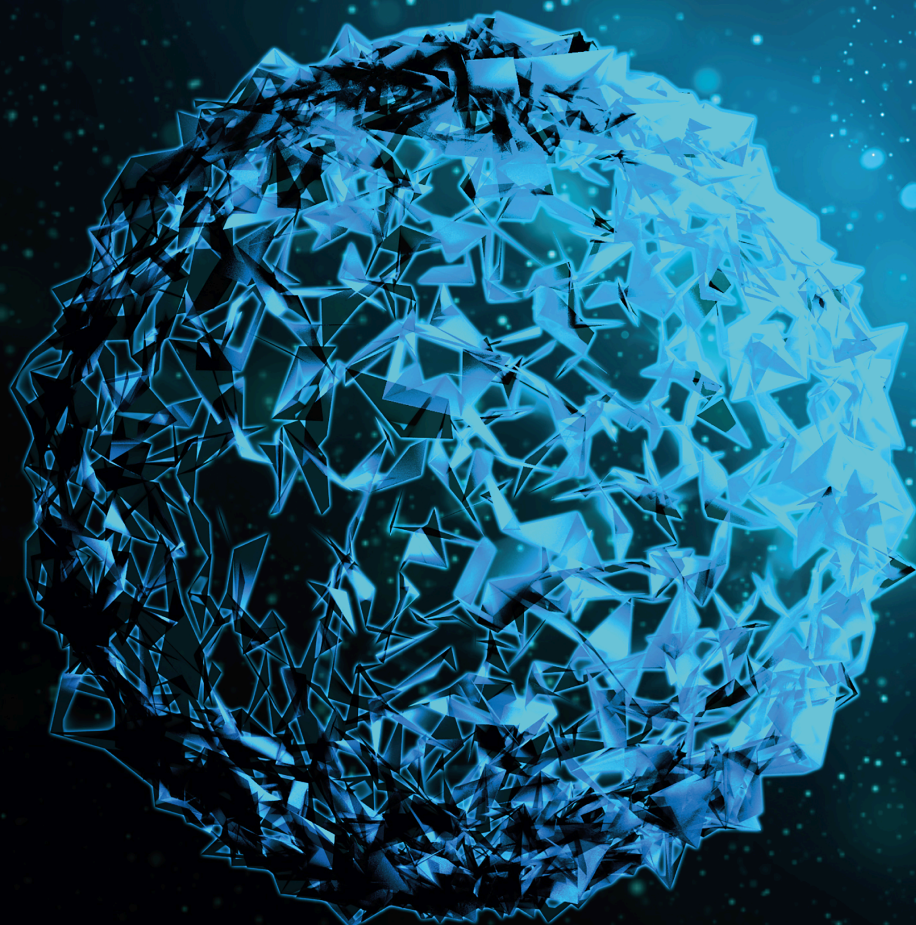# Network Pharmacology and Molecular Docking for Drug Discovery 2022

Lead Guest Editor: Chunpeng Wan
Guest Editors: Muhammad Farrukh Nisar, Oscar Herrera Calderon, and Rupesh Kumar Gautam

Network Pharmacology and Molecular Docking for Drug Discovery 2022

Network Pharmacology and Molecular Docking for Drug Discovery 2022

Lead Guest Editor: Chunpeng Wan
Guest Editors: Muhammad Farrukh Nisar, Oscar Herrera Calderon, and Rupesh Kumar Gautam

Contents

Retraction

Retracted: Network Pharmacology-Integrated Molecular Docking Reveals the Expected Anticancer Mechanism of *Picrorhizae Rhizoma* Extract

BioMed Research International

This article has been retracted by Hindawi following an investigation undertaken by the publisher [1]. This investigation has uncovered evidence of one or more of the following indicators of systematic manipulation of the publication process:

(1) Discrepancies in scope

(2) Discrepancies in the description of the research reported

(3) Discrepancies between the availability of data and the research described

(4) Inappropriate citations

(5) Incoherent, meaningless and/or irrelevant content included in the article

(6) Manipulated or compromised peer review

The presence of these indicators undermines our confidence in the integrity of the article's content and we cannot, therefore, vouch for its reliability. Please note that this notice is intended solely to alert readers that the content of this article is unreliable. We have not investigated whether authors were aware of or involved in the systematic manipulation of the publication process.

Wiley and Hindawi regrets that the usual quality checks did not identify these issues before publication and have since put additional measures in place to safeguard research integrity.

We wish to credit our own Research Integrity and Research Publishing teams and anonymous and named external researchers and research integrity experts for contributing to this investigation.

The corresponding author, as the representative of all authors, has been given the opportunity to register their agreement or disagreement to this retraction. We have kept a record of any response received.

References

[1] X. Hu, S. Zhao, Y. Cai et al., "Network Pharmacology-Integrated Molecular Docking Reveals the Expected Anticancer Mechanism of *Picrorhizae Rhizoma* Extract," *BioMed Research International*, vol. 2022, Article ID 3268773, 16 pages, 2022.

Retraction

Retracted: Multifunctional Drug-Loaded Phase-Change Nanoparticles Inhibit the Epithelial-Mesenchymal Transition of Hepatocellular Carcinoma by Affecting the Activity of Activated Hepatic Stellate Cells

BioMed Research International

This article has been retracted by Hindawi following an investigation undertaken by the publisher [1]. This investigation has uncovered evidence of one or more of the following indicators of systematic manipulation of the publication process:

(1) Discrepancies in scope

(2) Discrepancies in the description of the research reported

(3) Discrepancies between the availability of data and the research described

(4) Inappropriate citations

(5) Incoherent, meaningless and/or irrelevant content included in the article

(6) Manipulated or compromised peer review

The presence of these indicators undermines our confidence in the integrity of the article's content and we cannot, therefore, vouch for its reliability. Please note that this notice is intended solely to alert readers that the content of this article is unreliable. We have not investigated whether authors were aware of or involved in the systematic manipulation of the publication process.

Wiley and Hindawi regrets that the usual quality checks did not identify these issues before publication and have since put additional measures in place to safeguard research integrity.

We wish to credit our own Research Integrity and Research Publishing teams and anonymous and named external researchers and research integrity experts for contributing to this investigation.

The corresponding author, as the representative of all authors, has been given the opportunity to register their agreement or disagreement to this retraction. We have kept a record of any response received.

References

[1] X. Zou, T. Li, Y. Mao et al., "Multifunctional Drug-Loaded Phase-Change Nanoparticles Inhibit the Epithelial-Mesenchymal Transition of Hepatocellular Carcinoma by Affecting the Activity of Activated Hepatic Stellate Cells," *BioMed Research International*, vol. 2022, Article ID 6441179, 18 pages, 2022.

Retraction

Retracted: MSN@IL-4 Sustainingly Mediates Macrophagocyte M2 Polarization and Relieves Osteoblast Damage via NF-κB Pathway-Associated Apoptosis

BioMed Research International

This article has been retracted by Hindawi following an investigation undertaken by the publisher [1]. This investigation has uncovered evidence of one or more of the following indicators of systematic manipulation of the publication process:

(1) Discrepancies in scope

(2) Discrepancies in the description of the research reported

(3) Discrepancies between the availability of data and the research described

(4) Inappropriate citations

(5) Incoherent, meaningless and/or irrelevant content included in the article

(6) Manipulated or compromised peer review

The presence of these indicators undermines our confidence in the integrity of the article's content and we cannot, therefore, vouch for its reliability. Please note that this notice is intended solely to alert readers that the content of this article is unreliable. We have not investigated whether authors were aware of or involved in the systematic manipulation of the publication process.

Wiley and Hindawi regrets that the usual quality checks did not identify these issues before publication and have since put additional measures in place to safeguard research integrity.

We wish to credit our own Research Integrity and Research Publishing teams and anonymous and named external researchers and research integrity experts for contributing to this investigation.

The corresponding author, as the representative of all authors, has been given the opportunity to register their agreement or disagreement to this retraction. We have kept a record of any response received.

References

[1] C. Shi, F. Yuan, Z. Li et al., "MSN@IL-4 Sustainingly Mediates Macrophagocyte M2 Polarization and Relieves Osteoblast Damage via NF-κB Pathway-Associated Apoptosis," *BioMed Research International*, vol. 2022, Article ID 2898729, 10 pages, 2022.

Retraction

Retracted: PRP from Personal Blood Relieves Joint Fluid-Inducing Synovial Injury through NF-κB Pathway and Mitochondrial Apoptosis in Human Synovial Fibroblast Cells

BioMed Research International

This article has been retracted by Hindawi following an investigation undertaken by the publisher [1]. This investigation has uncovered evidence of one or more of the following indicators of systematic manipulation of the publication process:

(1) Discrepancies in scope

(2) Discrepancies in the description of the research reported

(3) Discrepancies between the availability of data and the research described

(4) Inappropriate citations

(5) Incoherent, meaningless and/or irrelevant content included in the article

(6) Peer-review manipulation

The presence of these indicators undermines our confidence in the integrity of the article's content and we cannot, therefore, vouch for its reliability. Please note that this notice is intended solely to alert readers that the content of this article is unreliable. We have not investigated whether authors were aware of or involved in the systematic manipulation of the publication process.

In addition, our investigation has also shown that one or more of the following human-subject reporting requirements has not been met in this article: ethical approval by an Institutional Review Board (IRB) committee or equivalent, patient/participant consent to participate, and/or agreement to publish patient/participant details (where relevant).

Wiley and Hindawi regrets that the usual quality checks did not identify these issues before publication and have since put additional measures in place to safeguard research integrity.

We wish to credit our own Research Integrity and Research Publishing teams and anonymous and named external researchers and research integrity experts for contributing to this investigation.

The corresponding author, as the representative of all authors, has been given the opportunity to register their agreement or disagreement to this retraction. We have kept a record of any response received.

References

[1] L. Xie, W. Lin, L. Zhu et al., "PRP from Personal Blood Relieves Joint Fluid-Inducing Synovial Injury through NF-κB Pathway and Mitochondrial Apoptosis in Human Synovial Fibroblast Cells," *BioMed Research International*, vol. 2022, Article ID 4496949, 10 pages, 2022.

Research Article

Antiangiogenic Potential of Troxerutin and Chitosan Loaded Troxerutin on Chorioallantoic Membrane Model

Gowtham Kumar Subbaraj [iD],[1] Harini Elangovan [iD],[1] Prema Chandramouli [iD],[1] Santhosh Kumar Yasam [iD],[1] Kirubhanand Chandrasekaran [iD],[2] Langeswaran Kulanthaivel [iD],[3] Sangavi Pandi [iD],[3] and Senthilkumar Subramanian [iD][4]

[1]Faculty of Allied Health Sciences, Chettinad Hospital and Research Institute, Chettinad Academy of Research and Education (Deemed to be University), Kelambakkam, 603 103 Tamil Nadu, India
[2]Department of Anatomy, All India Institute of Medical Sciences (AIIMS), Nagpur, Maharashtra, India
[3]Cancer Genetics & Molecular Biology Laboratory, Department of Biotechnology, Science Campus, Alagappa University, Karaikudi, Tamil Nadu 630003, India
[4]School of Medicine, College of Medicine and Health Science, Jigjiga University, Ethiopia

Correspondence should be addressed to Senthilkumar Subramanian; senthilkumarsubramanian@jju.edu.et

Angiogenesis is crucial to the development of cancer because it allows the transport of oxygen, nutrients, and growth factors as well as the spread of tumors to distant organs. Inhibitors of angiogenesis prevent the formation of blood vessels that allow tumor cells to shrink, rather than promote tumor growth. Chitosan acts as a carrier for many drugs, since the compound has various properties such as biodegradable, less toxicity, more stable, simple, easy to prepare, and biocompatible. The aim of the current study was to evaluate the efficacy of chitosan nanoparticles encapsulated with troxerutin (Chi-Trox NPs) against angiogenesis and cancer *in ova* chick chorioallantoic membrane (CAM) model. Chi-Trox NPs were synthesized using a nanoprecipitation method and were characterized by various analyses. 24 hours' fertilized eggs (6 eggs/group) were treated with native Trox and Chi-Trox NPs for 5 days. The antiangiogenic activity was evaluated by morphometric, histopathological, immunohistochemical (CD104 and vimentin), and mRNA expression of MMP and FGF2 using RT-PCR. The anticancer activity was evaluated by histopathological, immunohistochmical (CD44), and mRNA expression of FGF2 and MMP. The synthesized chitosan NPs were successfully encapsulated with troxerutin, and the loading efficiency of chitosan NPs was found to be $86.4 \pm 0.12\%$ and $13.2 \pm 0.16\%$ respectively. Morphometric analysis of Chi-Trox NPs showed a considerable decrease in the number of blood vessels compared with control and native Trox. The histopathological observation of CAM confirmed that Chi-Trox NPs induce a significant reduction in inflammatory cells and the thickness of blood capillaries compared to control and native Trox. The immunohistochemical evaluation of CAM revealed Chi-Trox decreased CD104, vimentin and CD44 protein levels were compared with control and native Trox. Furthermore, the mRNA expression levels of FGF2 and MMP were significantly downregulated compared to their native forms. From the obtained results, Chi-Trox NPs possess significant inhibition of angiogenesis and can be used as therapeutic agents for cancer in the future.

1. Introduction

Angiogenesis is the process by which new blood vessels are generated from preexisting vessels in the early stages of vasculogenesis [1]. The process of angiogenesis plays a critical role in cancer growth, as solid tumors require blood supply to grow. A tumor can actually cause angiogenesis by emitting chemical signals that stimulate it. The newly formed blood vessels take oxygen and nutrients, allowing the tumors to grow and invade, thereby enabling the cancerous cells to spread throughout the body [2]. Proangiogenic and antiangiogenic factors control the growth of new blood vessels.

Fibroblast growth factor (FGF) and vascular endothelial growth factor (VEGF) are proangiogenesis agents, while endostatin and TGF are antiangiogenesis agents [3, 4]. Flavonoids are secondary plant compounds that are frequently present in fruits, vegetables, and certain drinks. Flavonoids are known to have a broad range of health promoting effects [5]. As of now, flavonoids and their subordinates have been studied for their effectiveness in inhibiting the growth of cancerous cells and regulating vascular growth [6]. A significant challenge to cancer management is the cost-effectiveness of the current treatments. This burden causes immense economic hardship for societies around the world. Thus, the use of natural substances such as flavonoids for the prevention as well as the treatment of cancer can be considered an alternative therapeutic strategy [7].

Troxerutin, commonly known as vitamin P4, is a derivative of the bioflavonoid rutin, which can be found in tea, coffee, cereal grains, and a variety of vegetables and fruits [8]. Because of its high water solubility, troxerutin has been found to be readily absorbed by the gastrointestinal system and to produce protective effects without being cytotoxic [9]. This naturally occurring troxerutin has a number of biological functions, such as fighting cancer, reducing inflammation, fighting free radicals, and fighting diabetes.

Chitosan is a type of polymer that provides excellent protection and may be utilized for the delivery of active substances [10]. The encapsulation of flavonoids with chitosan nanoparticles has only been briefly studied in the past [11–13]. Compared to bulk chitosan, chitosan nanoparticles are used more frequently in biological applications because of their physicochemical properties, which include size, surface area, cationic nature, active functional groups, high permeability towards biological membranes, nontoxicity to humans, cost-effectiveness, higher encapsulation efficiency and/or through blending with other components, and broad biological activities. Chitosan nanoparticles have been employed in the distribution of active components due to their capacity to provide protection and stability. They offer defense against oxidation and enzymatic degradation as well as breakdown or damage brought on by exposure to oxygen, light, heat, and pressure [14, 15]. In the past few years, the chick chorioallantoic membrane (CAM) assay has emerged as the best tumor model among others, which provides a suitable and powerful system to assess the ability of nanoparticles to deliver anticancer drugs [16]. The CAM is formed during the development of the avian allantois and chorion. In a short period of time, this structure expands, creating a rich vascular network that functions as an interface for gas and waste exchange [17]. The CAM assay is preferable over other *in vivo* or *in vitro* models because it is highly sensitive and cost-effective. The aim of the present study was to prepare and characterize chitosan nanoparticles encapsulated with troxerutin and examine their antiangiogenic and anticancer efficacy in a CAM model.

2. Materials and Methods

Troxerutin (CAS-7085-55-4) was purchased from Cayman chemicals, USA. Chitosan (CAS-448869) was purchased from Sigma Aldrich, USA. Ethanol (64-17-5) was purchased from Changshu Chemicals Co., Ltd., China. Fertilized eggs were purchased from Tamil Nadu Veterinary and Animal Sciences University, Chennai, India. Anti-vimentin (SKU: AM074GP), CD34 (AN779GP) antibodies were purchased from BioGeneX, USA. Primers used were as follows: FGF2 (Forward: 5′CCTG GCACTGAATGTGCAAC3′; Reverse: 5′AACCCTCATTA AAGGGCAGACA3′) and MMP (Forward: 5′GTTACCACA GCGGGGTTTCT3′; Reverse: 5′TTTCAGATGGAAAACC AAGATGGA3′); c-DNA synthesis kit (6110A) were purchased from Takara, USA. TRIzol reagent (15596026) was obtained from Invitrogen, USA. All other compounds employed in the experiment were of an analytical grade.

2.1. Docking Studies

2.1.1. Sequences and Homologous Analysis.
The amino acid sequences are extracted from the primary database UniProt. To identify the homologous structure of the protein BlastP search was performed against the protein data bank [18]. From this search, evolutionary and functional relationships between protein sequences were analyzed.

2.1.2. Exploration of Physicochemical Properties.
Physicochemical properties were analyzed using the ProtParam tool [19]. This tool computationally predicts the total number of amino acids, molecular weight, iso-electric point, gravy, negatively charged amino acid, and positively charged amino acid present in the protein.

2.1.3. Protein Structure Modeling.
From the blast result, protein structure will be predicted by homology modeling or template-based modeling. High identity and query coverage lead to homology modeling. Homology modeling was constructed using the prime module in Schrodinger (Prime, Schrodinger, LLC, New York, NY, USA, 2021). Low identity and query coverage protein lead to template-based protein structure prediction. Template-based protein modeled using LOMETS server [20]. A three-dimensional protein structure was refined using galaxy web [21].

2.1.4. Protein Structural Validation.
Three-dimensional modeled protein validated in SAVES server. The stereo chemical property of the targeted protein was analyzed using PROCHECK tool [22]. The quality of protein was checked in the Ramachandran plot. The Ramachandran plot helps to determine the quality of protein using amino acid present in the protein structure. The Ramachandran plot favored region was represented by red color. Additional allowed region was represented by yellow color. White region in the plot shows the disallowed region present in the protein structure.

2.1.5. Target Preparation and Ligand Preparation.
Targeted protein was prepared in the protein preparation wizard in Schrodinger software (Impact, Schrodinger, LLC, New York, NY, USA, 2021). Targeted protein was prepared for further studies. Protein preparation includes removal of water molecules from the structure, add hydrogen atoms, and optimize the hydrogen bond using PROPKA minimization. This step

helps to remove atomic clashes. During protein preparation protein structure was simulated using OPLS_2005 force field. The potential ligand molecules were in the LigPrep tool. LigPrep tool was embedded in the Schrodinger software (LigPrep, Schrodinger, LLC, New York, NY, USA, 2021). This tool helps to generate the accurate ligand with its appropriate ionization states and energy ring conformation. LigPrep OPLS_2005 force field was used to generate ligand molecules. Using LigPrep, we can remove improper ligand molecules.

2.1.6. Active Site and Receptor Grid Generation. An active site is essential for inhibitor action of small molecules. A ligand molecule binds in the active site of the protein. The active site pocket of the protein was predicted by sitemap module present in the Schrodinger module (SiteMap, Schrodinger, LLC, New York, NY, USA, 2021). The active site was predicted based on the physical descriptor of the protein such as site volume and size of the site. A sitemap helps to identify the best using site score. Receptor grid generation using the glide module in Schrodinger (Receptor Grid Generation, Schrodinger, LLC, New York, NY, USA, 2021). Receptor grid generation plays a vital role in validation of specific receptor molecules. This process is essential to validate the target.

2.2. Molecular Docking. Molecular docking approach is employed to predict the binding interaction between the protein and ligand. Molecular docking was performed in glide ligand docking in the Schrodinger suite (Glide, Schrodinger, LLC, New York, NY, USA, 2021). The best compound was identified based on docking score. Glide extra precision scoring function is a novel scoring function to estimate the binding affinities. The top lead molecules were determined based on docking score.

2.3. Synthesis of Chitosan Nanoparticles Encapsulated with Troxerutin (Chi-Trox NPs). Briefly, 100 mg of chitosan was weighed and added to the solution containing acetic acid and water (1 : 100 ratio). The solution was kept in magnetic stirrer at 200 rpm until chitosan was dissolved completely. To this solution, 0.1% Trox in ethanol was added and kept in magnetic stirrer at 200 rpm for overnight. To this, 10 ml sodium tri polyphosphate (STPP) was added with a final concentration of 0.35 g in 100 ml of distilled water. The solution was centrifuged at 10000 rpm for 10 minutes, and pellet was washed 3 times with distilled water. Finally Chi-Trox NPs were collected by dissolving the pellet in distilled water.

2.4. Characterization. A Malvern zeta sizer was used to quantify the particle size distributions of Trox and Chi-Trox NPs using dynamic light scattering (DLS). In order to evaluate the distribution of particle size of the drugs, 100 μl of the Trox and Chi-Trox NPs were dissolved in 900 μl of milliQ water. The surface morphology, size, and distribution of Trox and Chi-Trox nanoparticles were analyzed using scanning electron microscopy (SEM). Sonication was used to create a diluted sample that was well distributed. After that, the samples were dried and coated with a gold layer (sputter coating), visualized using a Qunta 200 SEM. Using

Table 1: Physiochemical properties of CD104 and vimentin.

Properties	CD104	Vimentin
Number of amino acids	118	84
Molecular weight (Da)	12	10
Theoretical pI	5.89	4.54
Total number of negatively charged residue (Asp+Glu)	12	22
Total number of positively charged residue (Arg+Lys)	10	16
Number of atoms	1774	1461
Aliphatic index	76.69	91.86
Grand average of hydropathicity (GRAVY)	-0.520	-1.047

Fourier transform infrared (FT-IR) spectroscopy with attenuated total reflection (ATR), the molecular vibrations of chitosan, Trox, and synthesized Chi-Trox NPs were examined. To study the spectra, a sufficient amount of material were deposited on the crystal surface, and peak values in the range of 500 cm^{-1} to 4000 cm^{-1} (Model BRUKER-ALPHA, Germany) were recorded using the OPUS program.

2.5. Drug Release Kinetic Assay. To study the drug release kinetics of synthesized Chi-Trox NPs, dialysis membrane method was used. The Trox and Chi-Trox NPs were suspended in distilled water. In 100 ml of phosphate buffer saline (PBS), the dialysis membrane was submerged. A magnetic stirrer was used to agitate the beaker at a speed of 250 rpm. An appropriate quantity of sample was removed from the beaker at specified time intervals (replaced with fresh PBS medium). UV-Vis spectrophotometer was used to analyze the samples at 480 nm.

2.6. Antiangiogenic Activity of Chi-Trox NPs on Chick Chorioallantoic Membrane (CAM). During day 1, the eggs were wiped with ethanol, a small window (2 cm in diameter) was drilled on the egg shell, and 3 ml of albumin was removed using a 21 gauge needle. On day 3, under sterile conditions, a sterile disc was placed on top of the developing CAM. The discs were loaded with a 10 μmol concentration of Trox and Chi-Trox NPs. The present work was grouped as follows: group I served as the control without any treatment. Group II received a 10 μmol concentration of Trox. Group III received 10 μmol concentrations of Chi-Trox NPs. After treatment with the appropriate drugs, the window on the egg was closed with sterile tape. The eggs were incubated at 37°C with a relative humidity (RH) of 50–60% until day 5. At the end of the 5th day, the egg windows were opened and the CAM membranes were photographed. The morphometric analysis of the Trox and Chi-Trox NPs was analyzed using the ImageJ software. The CAM membranes were collected and fixed in 10% formalin and stored at -20°C for further studies such as mRNA expression.

2.7. Anticancer Activity of Chi-Trox NPs on CAM. Freshly fertilized chicken eggs were incubated at a temperature of 37°C and a humidity of 50–60%. On the third day of embryo development, eggs were cleaned with ethanol, 3 ml of
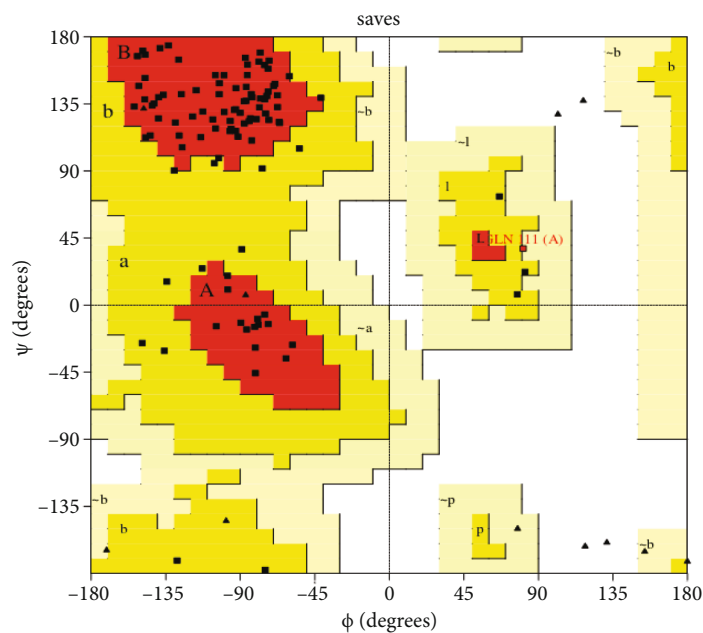
FIGURE 1: Ramachandran plot for cluster of differentiation 104 (CD104) protein.
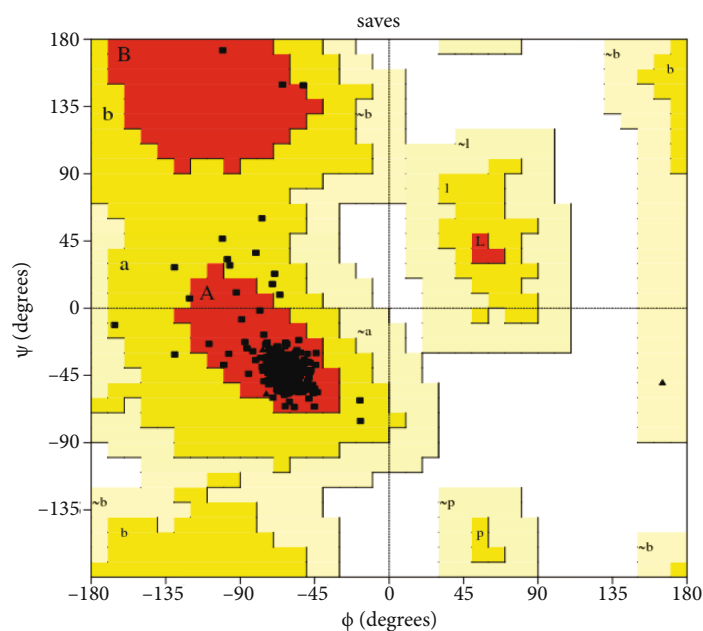
FIGURE 2: Ramachandran plot for vimentin protein.

albumin was extracted through a tiny window on top of the CAM, and then eggs were parafilm-sealed. The egg window was opened on day 10, a filter disc was inserted inside, and 2×10^6 HeLa cancer cells were transplanted into the disc. The window was then closed with parafilm. On day 14, egg windows were opened, $10\,\mu$mol concentrations of Chi-Trox NPs and Trox were placed onto filter discs, and windows were sealed with parafilm. After three days of treatment, egg windows were opened, and tumor development on CAM tissues were collected and preserved in 10% formalin for further research.

2.8. Histopathological Examination of CAM. A 10% formalin fixative solution was flooded over the CAM area treated with Trox and Chi-Trox NPs. Using scissors and forceps, about $1\,cm^2$ of membrane surrounding the treated area was carefully removed and dehydrated in various alcohol grades (50%, 70%, 90%, and absolute) followed by embedding in paraffin wax. A rotary microtome (Weswicox, Japan) was used to take vertical tissue sections ($6\,\mu$m). Before staining with hematoxylin and eosin, sections were treated with alcohol in progressive sequence of absolute, 90%, 70%, and 50% and cleaned with xylene. Qualitative assessment was
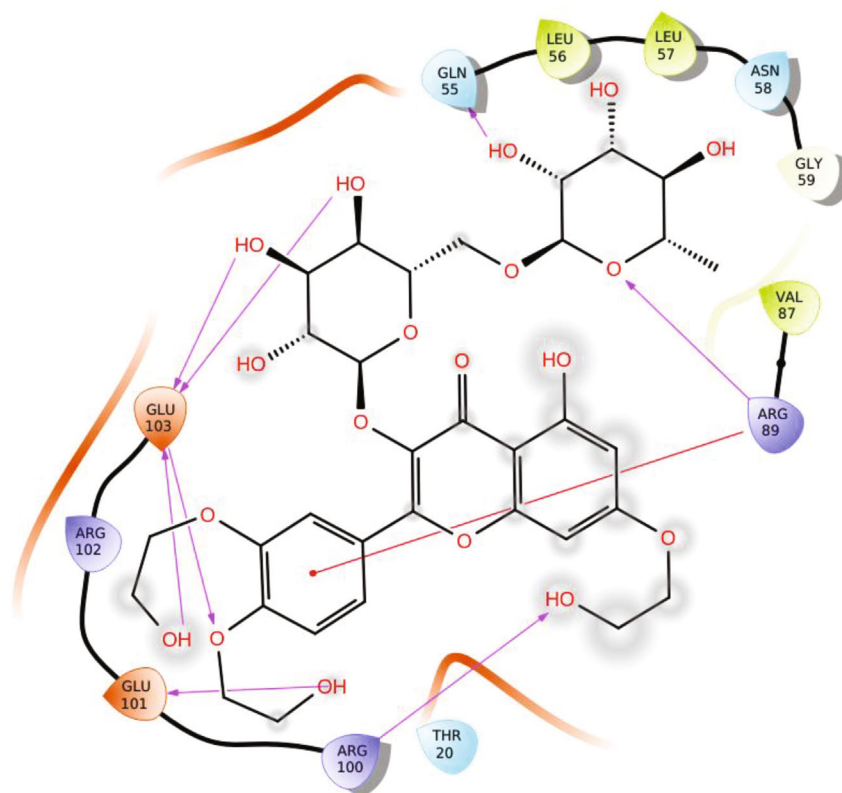
FIGURE 3: Interaction between troxerutin and CD104 protein.
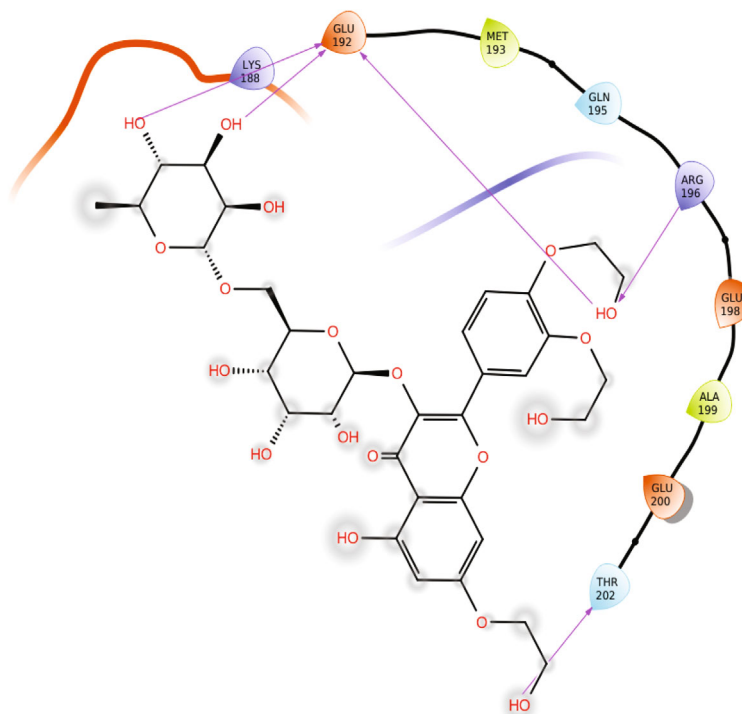
FIGURE 4: Interaction between troxerutin and vimentin protein.

TABLE 2: Docking analysis of CD104 and vimentin with troxerutin.

S. no.	Docking complexes	Docking score (Kcal/Mol)	Interacting residues with distance
1.	CD104_Toxerutin	-6.208	Gln_55 (2.17 Å), Arg_89 (2.58 Å), Arg_100 (2.87 Å), Glu 101 (1.84 Å) and 103 (1.98 Å, 2.26 Å, 1.85 Å, and 2.31 Å)
2.	Vimentin_Troxerutin	-6.411	Glu_192 (1.73 Å, 1.73 Å, and 2.11 Å), Arg _196 (2.44 Å), Thr_202 (2.05 Å)
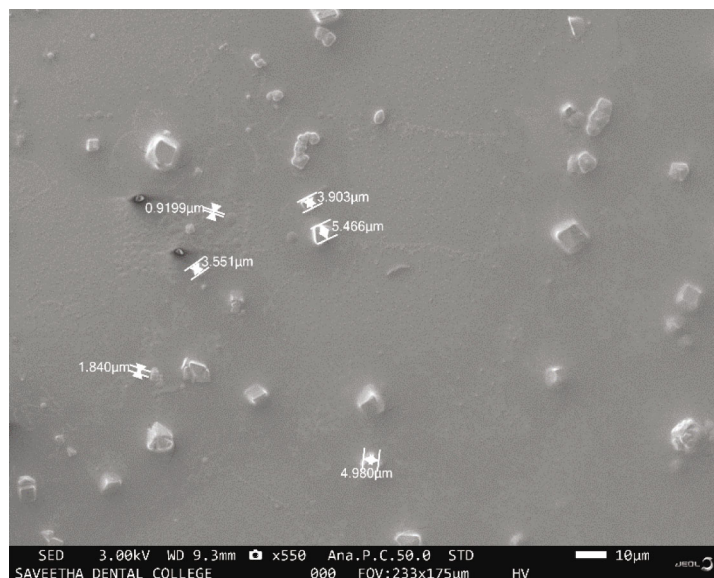
(a)
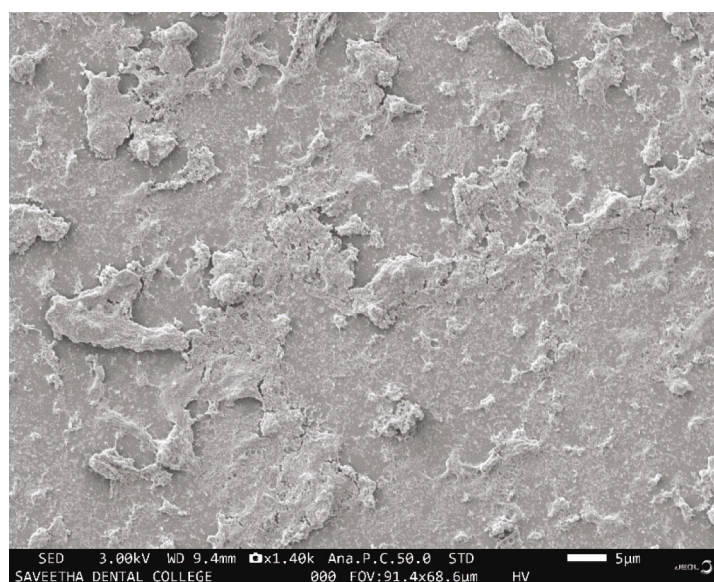
(b)

FIGURE 5: SEM results of (a) troxerutin and (b) Chi-Trox NPs.

conducted through the use of a light microscope at a magnification of 40x after mounting with digital picture exchange, and the pictures were captured using light microscope attached with a Nikon camera at 10x.

2.9. Immunohistochemistry Examination of CAM. A sterile container was used to collect the CAM membranes, and it was fixed in a 10% formalin solution. For 2 h, CAM paraffin slices (6 μm) were incubated at 60°C on a heat plate. A xylene and ethanol solution was applied to dewaxed membrane sections followed by PBS wash. A heat plate was used for antigen retrieval at 37°C for 10 min, and 1% protease (Sigma-Aldrich, USA) was added. In order to reduce the amount of endogenous peroxidase activity in the sections,

Size Distribution by Intensity

(a)

Size Distribution by Intensity

(b)
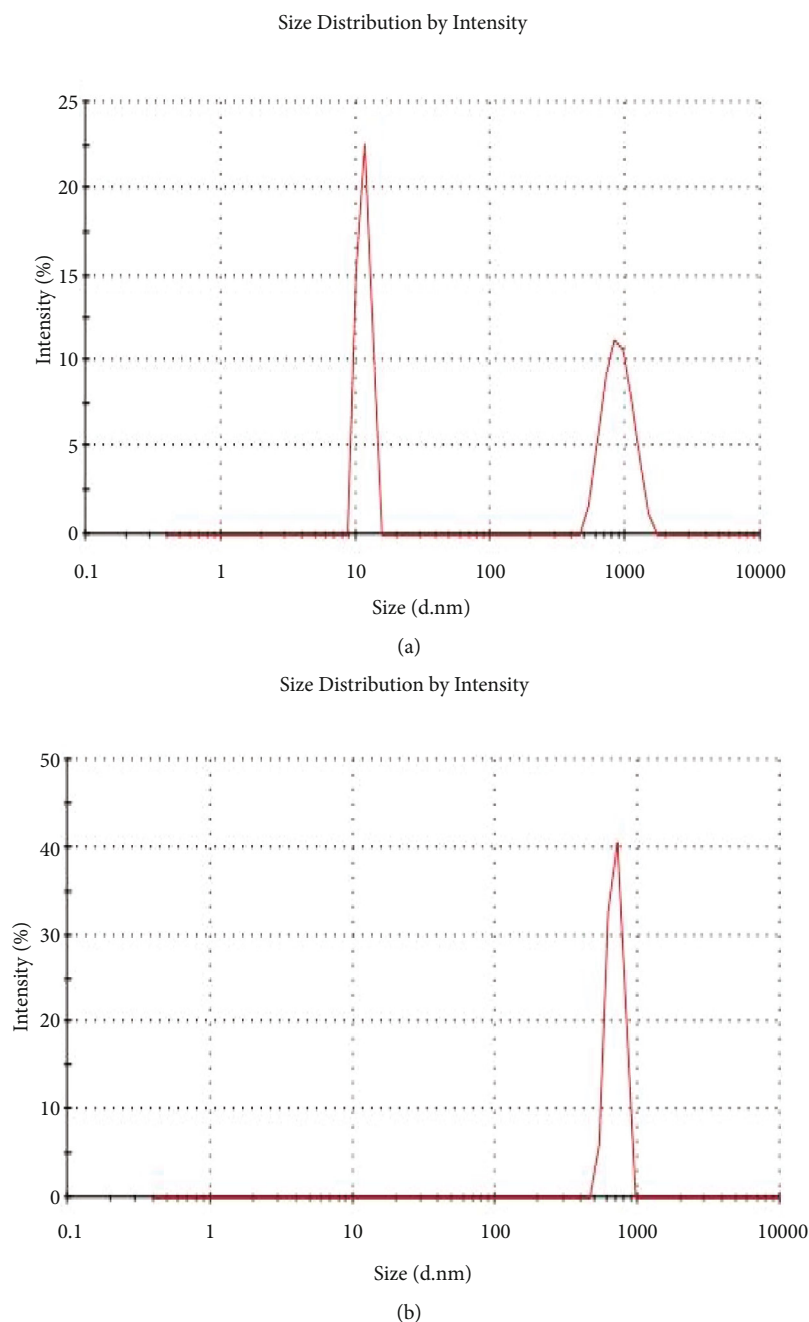
Figure 6: DLS results of (a) troxerutin and (b) Chi-Trox NPs.

0.3% hydrogen peroxide was used. The samples were then blocked with goat serum for 30 min prior to incubating overnight at 4°C with polyclonal anti-vimentin antibodies (1 : 500), anti-CD34 antibodies (1 : 500), and anti-CD44 antibodies (1 : 500). After this, the sections of membrane were incubated for 1 h at room temperature with goat secondary antibody (anti-mouse 1 : 500 (Dako, USA), followed by peroxidase-HRP conjugated at 1 : 500 (Dako). Diaminobenzidine/H_2O_2 substrate (Sigma-Aldrich, USA) was used to detect the immune reactivity. To counterstain the sections, 10% hematoxylin was applied and the sections were dehydrated and mounted in Pertex (Medite Medizintechnik, Germany).

2.10. Gene Expression Analysis by Real-Time PCR. TRIzol kit method was used to isolate the total RNA from the CAM. The isolated RNA was transcribed into cDNA using Takara kit method. All the primers sequences used in the current study were tabulated in Table 1. β-Actin was considered a reference gene. The RT-PCR assay was performed to amplify the gene of interest with SYBR green master mix (Takara, Japan). The following cycles were programmed during the amplification; initial denaturation at 95°C for 5 min followed by 40 cycles of 95°C for 30 s, 59–60°C for 30 s, and 72°C for 30 s.

2.11. Statistical Analysis. The analysis was carried out in triplicate, and all statistical data were presented as the mean ±

(a)

(b)
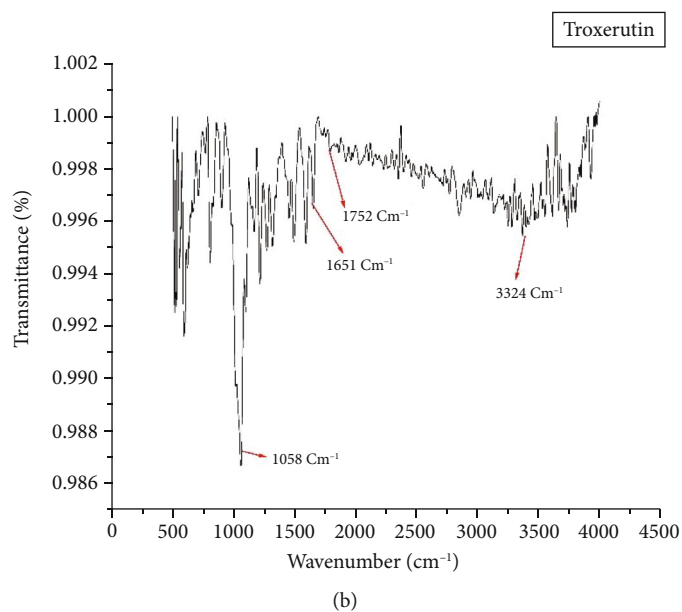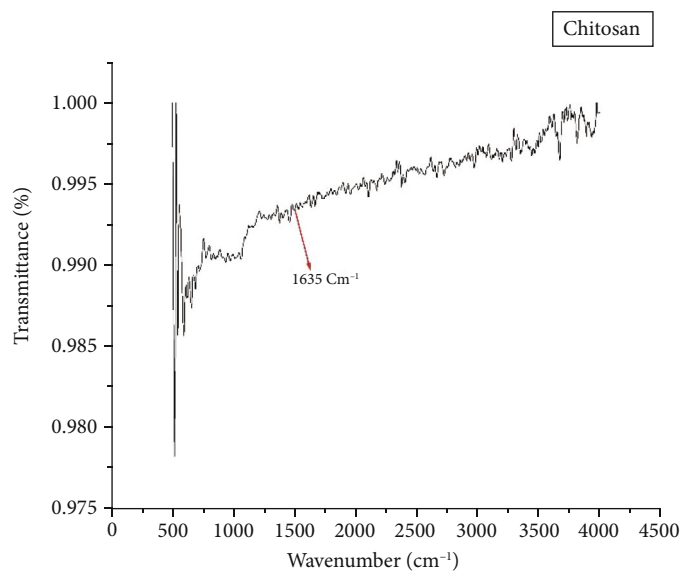
Figure 7: Continued.

Chi–Trox

(c)
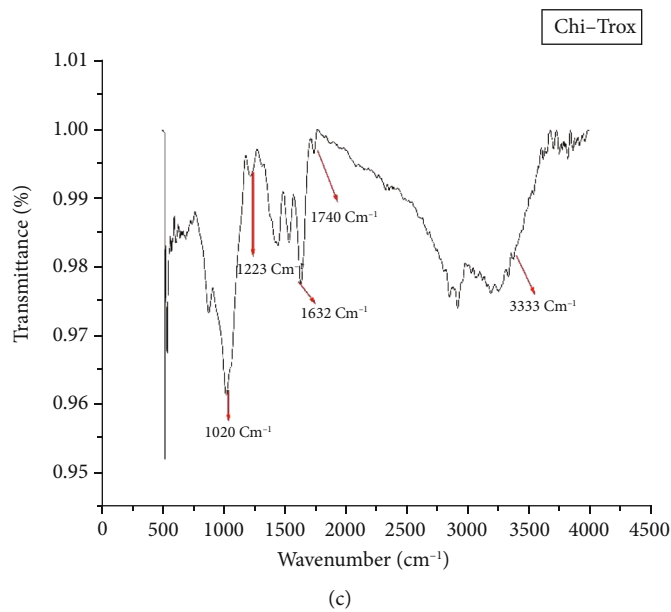
Figure 7: FT-IR results of (a) chitosan, (b) troxerutin, and (c) Chi-Trox NPs.

standard deviation. GraphPad Prism version 9 was used to do one-way analysis of variance (ANOVA) and Duncan's multiple range tests to determine significant differences between mean values. The $p < 0.05$ values were deemed statistically significant.

3. Results and Discussion

3.1. Sequence Analysis

3.1.1. Cluster of Differentiation 104 (CD104) Protein Modeling.
Cluster of differentiation 104 (CD104) was retrieved from the Protein Data Bank (PDB ID 2YRZ). A three-dimensional structure of CD104 prepared in the protein preparation wizard embedded in the Schrodinger suite. In this process, we remove water molecules present in protein structure. Structure optimization includes optimization of hydrogen bond. Minimization restrained using OPLS_2005 force field. CD104 protein stereo chemical quality was analyzed using pro check in SAVES server. Ramachandran plot red color represents the most favored region is 84.4%. The yellow color region represent additional allowed region is 14.6%. The ramachandran plot for CD104 is shown in Figure 1.

(1) Cluster of Differentiation 104 (CD104) Protein Modeling.

3.1.2. Vimentin Protein Modeling.
Vimentin protein was retrieved from RCSB Protein Data Bank (PDB ID: 1GK4). The protein structure was imported using protein preparation wizard in the Schrodinger suite. Protein structure was preprocessed including assign bond order and replace hydrogen atoms, conversion of selenomethionines to methionines. Optimization of hydrogen bond was done; then, the structure was minimized using OPLS_2005 force field. The stereo chemical quality of a vimentin protein structure was

analyzed using PROCHECK in SAVES server. Analysis was based on overall structure geometry as well as residue-by-residue geometry. Using PROCHECK, the Ramachandran plot was analyzed. The Ramachandran plot shows the most favored region is 96.7% and additional allowed region is 3.3%. The Ramachandran plot for vimentin protein was shown in Figure 2.

3.1.3. Physicochemical Analysis.
Physical and chemical properties of the protein were predicted in the expasy ProtParam tools. ProtParam tool predicts the number of amino acid, molecular weight, isoelectric point, total number of negatively charged residue, total number of positively charged residue, total number of atoms and their composition, aliphatic index, and grand average of hydropathicity (GRAVY). GRAVY value below zero indicates the hydrophilic nature of the protein. Hence, all the proteins (CD104 and vimentin) are hydrophilic in nature. Aliphatic index defined as the relative volume occupied by aliphatic amino acid side chain such as alanine, valine, and leucine. High aliphatic index (above 66.5) shows thermally stable over a wide temperature range. All these protein has a high aliphatic index, and these are protein thermally stable. Physicochemical properties of proteins were shown in Table 1.

3.2. Molecular Docking Studies

3.2.1. Binding Poses of CD104 with Troxerutin.
In glide docking protocol, troxerutin and cd104 were docked using glide ligand docking module in Schrodinger packages. Interacting residues between troxerutin and CD104 are Gln 55, Arg 89, Glu 103, and Glu101. Hydroxyl group of the ligand interacts with Gln 55 and forms hydrogen bonds with bond length of 2.17 Å. Arginine 89 interacts with ligand hydroxyl group forms hydrogen bond with distance 2.58 Å and pi-cation. Glutamic acid 103 interacts with ligand and forms 4

(a)

(b)
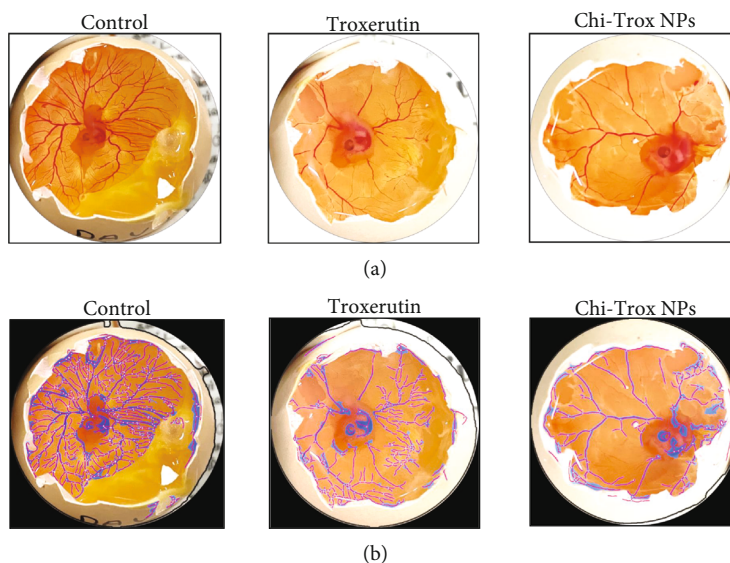
FIGURE 8: Chorioallantoic membrane *in ova* photographs showing vascular plexus after the incubation with control and treated groups (Trox and Trox-Chi NPs). (a) The photographs were taken after the treatment, incubation day-5. (b) Morphometric analysis of CAM treated with Trox and Chi-Trox NPs.
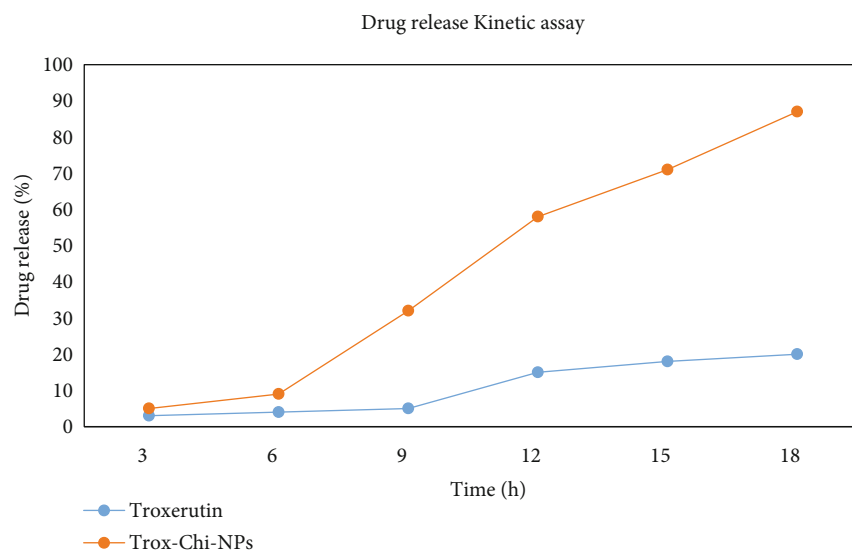
FIGURE 9: Drug release kinetic assay of Chi-Trox NPs.

hydrogen bond interactions between the protein and ligand. Bond distance between the amino acid Glu 103 and ligand are 1.98 Å, 2.26 Å, 1.85 Å, and 2.31 Å. Interaction between protein and ligand molecules shows good binding affinity. Docking score was found to be -6.208 Kcal/Mol. Interactions between CD104 and troxerutin were shown in Figure 3.

3.2.2. Binding Poses of Vimentin with Troxerutin. Vimentin protein was docked with troxerutin compound. Interacting residues are Glu192, Arg 196, and Thr 202. Glutamic acid residue at the position of 192 interacting with troxerutin forms 3 hydrogen bonds. Bond distance between protein and troxerutin is 1.73 Å, 1.73 Å, and 2.11 Å. Amino acid arginine residue at the position of 196 interacts with

hydroxyl group of the troxerutin and form hydrogen bond with bond length of 2.44 Å. Thr 202 interacts with the ligand molecule forms hydrogen bond with distance of 2.05 Å. Docking score between vimentin and troxerutin was found to be -6.411. Interaction between troxerutin and vimentin protein was shown in Figure 4. Molecular docking interaction between proteins (CD104 and vimentin) and troxerutin was shown in Table 2.

3.3. Drug Encapsulation. Encapsulation and drug loading efficiency of chitosan NPs were $86.4 \pm 0.12\%$ and $13.2\% \pm 0.16\%$. Chitosan NPs show maximum encapsulation efficiency; after that, there is no change in encapsulation efficiency due to the polymer dispersion saturation.

TABLE 3: Morphometric analysis of Trox and Chi-Trox NPs in chick embryo chorioallantoic membrane (CAM) using ImageJ software.

Group	Blood vessel density (mean ± SD)	Total vessel network (mean ± SD)	Total branching points (mean ± SD)	Total nets (mean ± SD)
Control	26.66 ± 1.52	34648 ± 818.51	94 ± 3.51	31 ± 2
Trox 10 μmol	20.46 ± 0.55[a*]	30223 ± 1664.1[a*]	62 ± 1.52[a*]	24 ± 2[a*]
Chi-Trox 10 μmol	14.76 ± 1.72[b*c*]	18898 ± 989[b*c*]	31 ± 2[b*c*]	11.66 ± 1.52[b*c*]

Comparison made between control and Trox, Control and Chi-Trox NPs, and Trox and Chi-Trox NPs. SD: standard deviation; statistical analysis was done by using student t-test; [a*]significant difference of Trox compared with the control ($p < 0.05$), [b*]significant difference of Chi-Trox NPs compared with the control ($p < 0.05$); and [c*]significant difference of Chi-Trox NPs compared with Trox ($p < 0.05$).

(a)　　　　(b)　　　　(c)
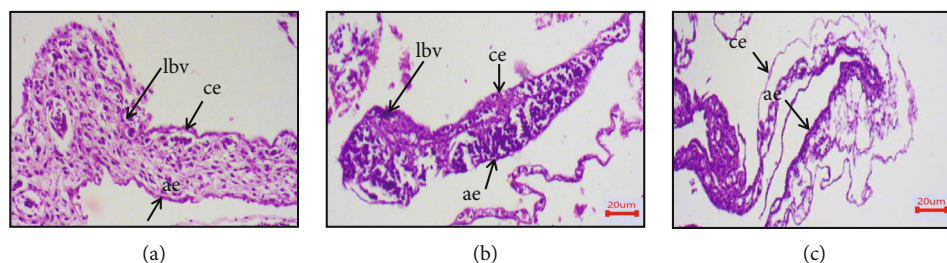
FIGURE 10: Histological examinations of Chi-Trox NPs on CAM morphology: (a) control, (b) Trox, and (c) Chi-Trox NPs. lbv: large blood vessel; ae: allantoic epithelium; ce: chorionic epithelium.

(a)　　　　(b)

(c)
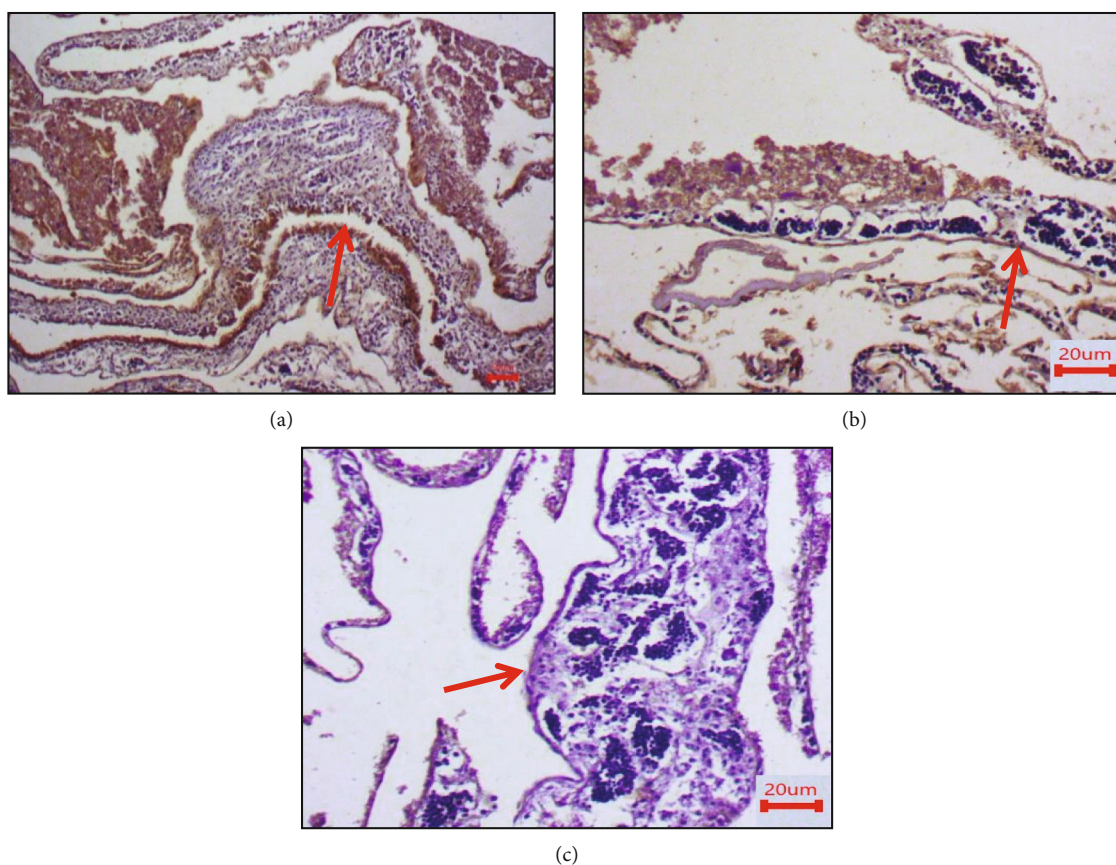
FIGURE 11: Immunohistostaining of CD104 in chick embryo chorioallantoic membranes (CAM): (a) control, (b) Trox, and (c) Chi-Trox.

3.4. Particle Size Measurement. Size and polydispersity index (PDI) are crucial assessments for the characterization of nanoparticles, since they affect crucial characteristics such as loading and the stability of the substance within nanopar-ticles. It is well known that the smaller the particle size, the larger the exposed surface area, which results in a quicker release of encapsulated therapeutics. Smaller particles also have a higher risk of aggregation during storage, making it

(a)

(b)

(c)
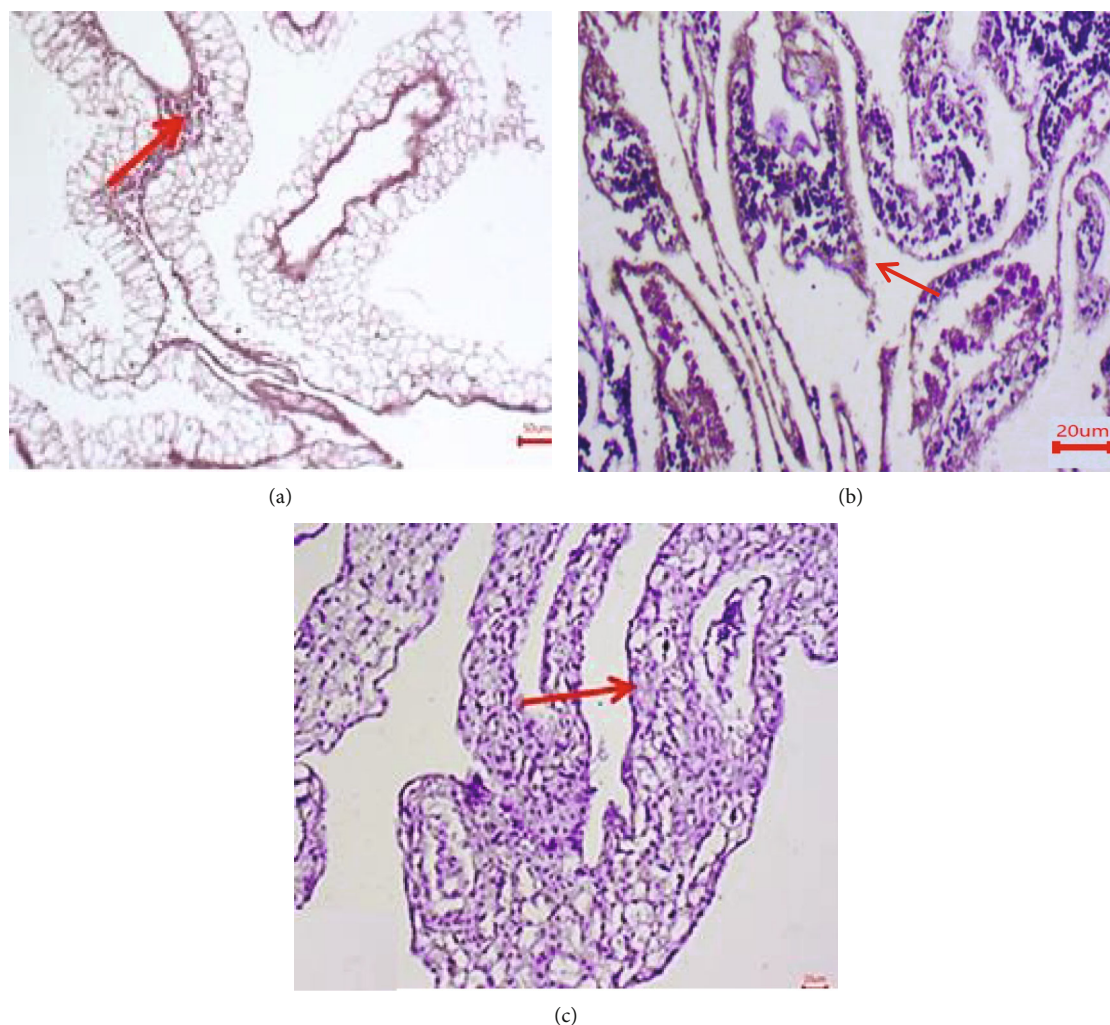
Figure 12: Immunohistostaining of vimentin in chick embryo chorioallantoic membranes (CAM): (a) control, (b) Trox, and (c) Chi-Trox. Red arrow shows expression of vimentin.

crucial to design nanoparticles with a low PDI in order to maintain optimum stability through a more precise control of particle size. Notably, the repeatability of characteristics such as stability and release is closely related to a low PDI, as a large PDI indicates that the size distributions of the sample are not uniform. In the present study, the average particle size of Trox and Chi-Trox NPs were analyzed by the DLS as shown in Figure 5. The size of Trox and Chi-Trox NPs were found to be 896 d·nm and 692 d·nm, respectively, with a PDI of 0.885 and 0.355 (Figure 6). Results are in agreement with the previous studies reported by Luque-Alcaraz et al. [23], Ilk et al. [24], Li et al. [25] which were observed to have similar kind of results with chitosan encapsulated flavonoids.

3.5. FT-IR Analysis.
FT-IR studies were carried out to confirm the similarity between Trox and Chi-Trox NPs (Figure 7). The FT-IR spectra of Trox showed peaks at $1058\,cm^{-1}$ (C-O stretching), $1651\,cm^{-1}$ (C=C stretching), $1752\,cm^{-1}$ (C=O stretching), and $3324\,cm^{-1}$ (O-H stretch-

ing). The FT-IR spectra of Chi-Trox showed peaks at $1020\,cm^{-1}$ (C-N stretching), $1632\,cm^{-1}$ (N-H stretching), $1740\,cm^{-1}$ (C=O stretching), and $3333\,cm^{-1}$ (O-H stretching). The presence of absorption band at $1223\,cm^{-1}$ corresponding to P=O stretch indicates the interaction between phosphate groups of STPP and Chi-Trox NPs. No characteristic peaks of troxerutin were observed in the spectra, which may be indicative the presence of troxerutin was encapsulated with chitosan NPs, and this interaction was possibly occurred by hydrogen bonds or hydrophobic interactions. Similar kind of results were observed in previous studies reported by Hao et al. [26] and Kumar et al. [27].

3.6. SEM Analysis.
Particle size and morphological studies of the Trox and synthesized Chi-Trox NPs were carried out using SEM (Figure 8). The microscopic image of Trox showed that the size was ranging $4\,\mu m$ with square shape. The microscopic images of Chi-Trox NPs were showed spherical shape morphology, with size ranging 500 nm. This happened because of high thermodynamic and shape

stability of Chi-Trox NPs. Chi-Trox NPs have an agglomerated appearance due to ionic interactions between the drug, cross-linker, and polymer [28, 29].

3.7. Drug Release Kinetic Assay. The drug release profile of Chi-Trox NPs was analyzed, and it was compared with the native Trox (Figure 9). The Trox drug was released 6% in 3 hours whereas Chi-Trox NPs also released 6%. But after 9 hours, Chi-Trox NPs were released 31% in sustained manner and reached 85% after 18 hours whereas Trox released only 8% in 9 hours and 20% only in 18 hours. From the results, it was inferred that Chi-Trox NPs were releases more than native Trox. Similar types of results were observed in the previous studies in which chitosan encapsulated nanoparticles were released faster and sustained manner than the native forms [30–32].

3.8. Morphometric Analysis of CAM. The CAM assay provides *in vivo* evidence of angiogenesis. The CAM treated with Chi-Trox NPs (10 μmol) showed significant decrease in the blood vessel density, total blood vessel network, total blood vessel branch points, and total blood vessel nets ($p < 0.05$) compared to the control and Trox (shown in Figure 8 and Table 3) The present study results were consistent with the previous reports [33, 34].

3.9. Histopathology Examination of CAM (Antiangiogenesis). Using hematoxylin and eosin-stained sections of the CAM-treated area, we evaluated the morphological changes of the CAM to validate the antiangiogenic potential of Trox and Chi-Trox NPs (shown in Figure 10). The control CAM (without treatment) showed normal shape blood vessels and thick chorionic and allantoic epithelial layers. Large blood vessels were observed at the stromal area. In addition to this, congested small blood capillaries and protienaceous fluid was observed on surroundings of large blood vessels. The CAM treated with Trox showed irregular appearance of blood vessels at the thin chorionic and allantoic epithelial layer. Less number of large blood vessels were seen at stromal area compared the control. In addition to this, few small blood capillaries were seen around the large blood vessels. The CAM treated with Chi-Trox NPs showed comparatively thin chorionic and allantoic epithelial layer with diminished stromal area. Large blood vessels were not seen. Furthermore, very few small blood vessels were found compared to control and Trox indicates inhibition of sprouting. The results were inagreement with previously published articles [35, 36].

3.10. Immunohistochemistry Examination of CAM (Antiangiogenesis). In the present study, we attempted to detect the expression levels of CD104 and vimentin on CAM using IHC (Figures 11 and 12). The results showed that CD104 was highly expressed in control CAM (without treatment) compared with and Trox and Chi-Trox NPs. The results of vimentin also showed high expression levels in the control group compared to Trox and Chi-Trox NPs. The results of this investigation indicated that Chi-Trox NPs could inhibit angiogenesis in CAM. These results were in agreement with the previously reported studies. van Beij-
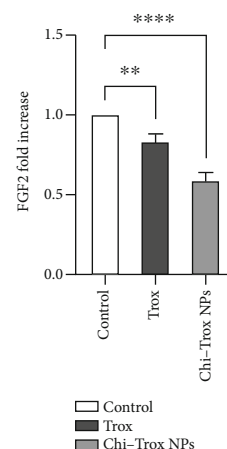
FIGURE 13: Effects of Trox and Chi-Trox NPs on the expression of FGF2 in chick chorioallantoic membrane. Comparison made between control and Trox, control and Chi-Trox NPs. Trox: troxerutin; Chi-Trox NPs: chitosan nanoparticles encapsulated with troxerutin; SD: standard deviation. The statistical analysis was done by using ANOVA and Tukey's post hoc test. *significant difference compared with control ($p < 0.05$); **significant difference compared with the control ($p < 0.01$); ***significant difference compared with the control ($p < 0.001$); and ****significant difference compared with the control ($p < 0.0001$).
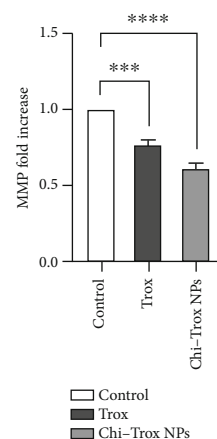
FIGURE 14: Effects of Trox and Chi-Trox NPs on the expression of MMP in chick chorioallantoic membrane. Comparison made between control and Trox and control and Chi-Trox NPs; Trox: troxerutin; Chi-Trox NPs: chitosan nanoparticles encapsulated with troxerutin; SD: standard deviation. The statistical analysis was done by using ANOVA and Tukey's post hoc test. *Significant difference compared with the control ($p < 0.05$); **significant difference compared with the control ($p < 0.01$); ***significant difference compared with the control ($p < 0.001$); ****significant difference compared with the control ($p < 0.0001$).

num et al. [37] reported the expression of vimentin antibody in CAM. The results revealed that vimentin expression in endothelial cells of CAM was reduced which resulted in the inhibition of angiogenesis. Nayak et al. [38]

(a)

(b)
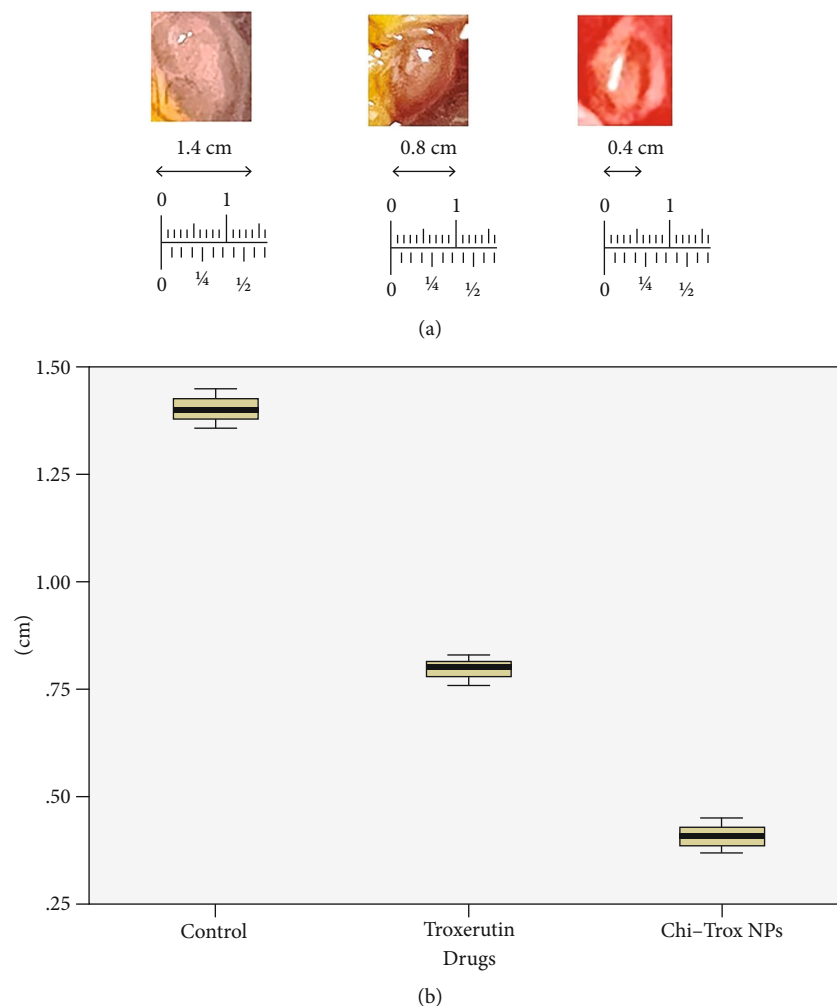
FIGURE 15: (a) Inhibition of growth in HeLA cells in the CAM by Trox and Chi-Trox NPs. (b) Quantification of A498 cell tumor size after treatment with Trox and Chi-Trox NPs using box plot.

demonstrated the expression levels of vimentin in oral submucous fibrosis using IHC analysis. Chen and Wang [39] studied the prognostic value of vimentin in metastatic renal cell carcinoma (mRCC) using IHC. They revealed that expression of vimentin is associated with immunosuppression in mRCC and that the immunosuppressive status might be linked to the presence of programmed cell death ligand-1 (PDL-1) or programmed cell death protien-1 (PD-1) among those mRCCs. Liu et al. [40] demonstrated the expression of CD104 using IHC in prostate cancer, and results revealed that CD104 may play a key role as a biomarker in the prostate cancer.

3.11. mRNA Expression on CAM (Antiangiogenesis). In the present investigation, the mRNA expression levels of MMP and FGF2 in tissues isolated from CAM in the control and treatment groups were analyzed by RT-PCR. Compared with control and Trox, the CAM treated with Chi-Trox NPs showed significant suppression in MMP and FGF2 mRNA expressions ($p < 0.05$) (Figures 13 and 14). Previously, few studies were reported on the mRNA

expression profiling of MMP and FGF2 using RT-PCR. Hong et al. [41] demonstrated the mRNA expression of MMP-2 and MMP-9 in 3T3-L1 adipocyte cell lines. The results revealed that MMP-2 and MMP-9 levels were significantly decreased after treatment with quercetin compared with the control. Webb et al. [42] reported the mRNA expression of MMP-2 and MMP-9 in retinoblastoma cell lines. The results demonstrated that downregulation of MMP-2 and MMP-9 decreases the cell migration and angiogenesis. Bae et al. [43] demonstrated that the mRNA expression of MMP-2 and MMP-9 in HT1080 human fibro sarcoma cells was significantly downregulated after treatment with *L. tetragonum* plant extract. Wu et al. [44] demonstrated that FGF2 mRNA expression in HUVEC cell lines was significantly downregulated after treatment with formononetin.

3.12. Anticancer Activity on CAM. The cellular and morphological changes of CAM tumor sections were analyzed using macroscopic and histopathology (shown in Figures 15 and 16). The quantification of tumor size was evaluated and
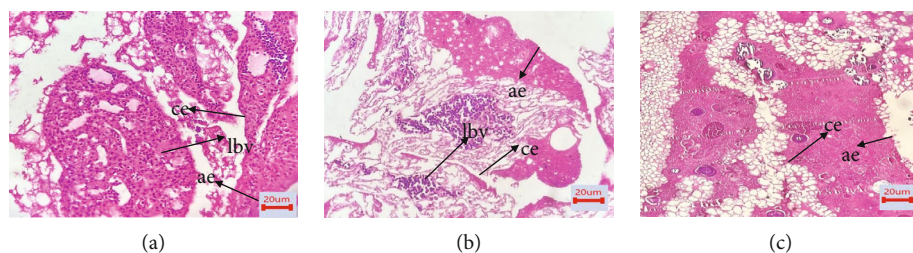
FIGURE 16: Histological examinations of Chi-Trox NPs on CAM morphology: (a) control, (b) Trox, and (c) Chi-Trox NPs. lbv: large blood vessel; ae: allantoic epithelium; ce: chorionic epithelium.

(a)

(b)

(c)
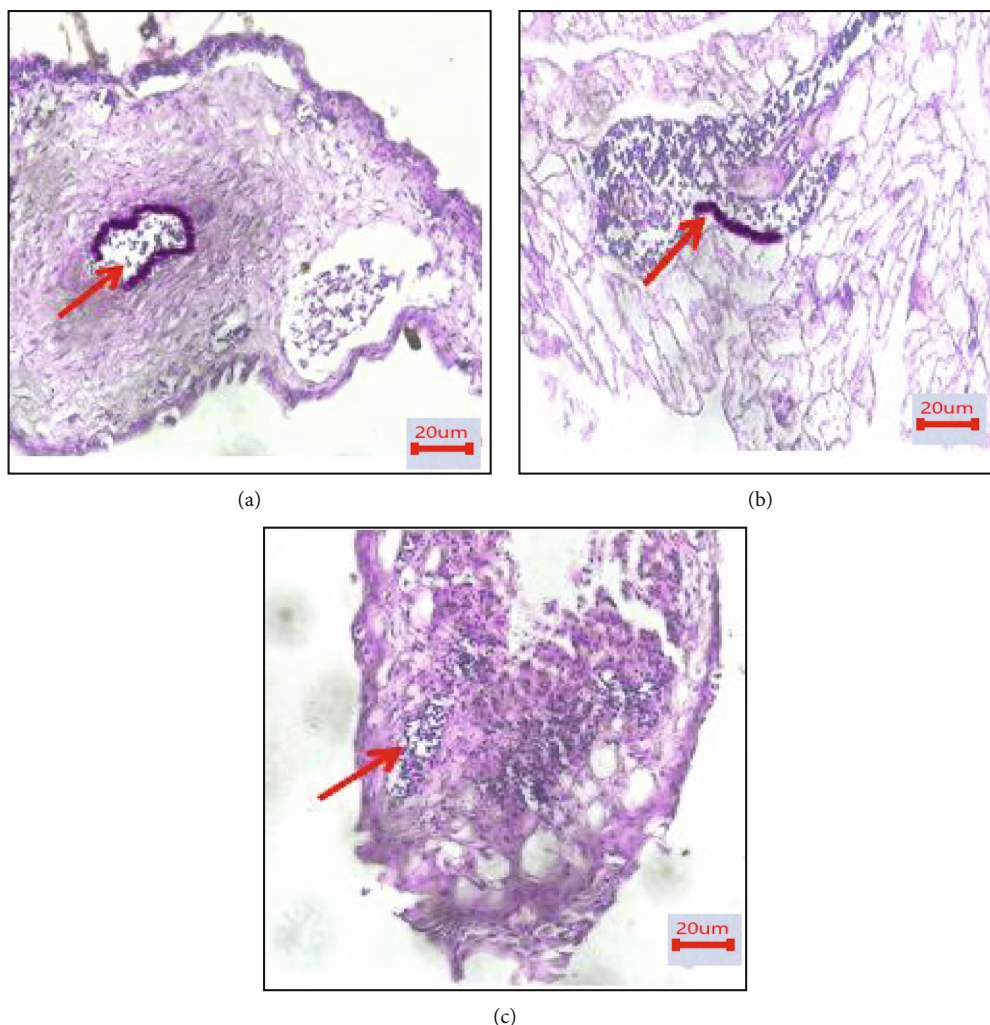
FIGURE 17: Immunohistostaining of CD44 in chick embryo chorioallantoic membranes (CAM): (a) control, (b) Trox, and (c) Chi-Trox.

compared with the control. The results revealed that tumor size was significantly decreased upon treatment with Trox and Chi-Trox NPs ($p < 0.01$). The results demonstrated that control CAM (without treatment) showed a thick stratum, and more number of large blood vessels was observed between the allantoic and chorionic epithelial layer. Irregular appearance of blood vessels was observed at the subepithelium connective tissue. The CAM treated with Trox showed decrease in the blood cell formation with thin stratum. Few large blood vessels were seen compared to the control. The CAM treated with Chi-Trox NPs showed thin stratum, and large blood vessels were not seen compared to the control and Trox indicates the suppression of tumor. The immunohistochemical analysis showed high expression levels of CD44 compared to Trox and Chi-Trox NPs (Figure 17). The mRNA expression levels of FGF2 and MMP-9 on CAM treated with Chi-Trox NPs were significantly downregulated compared to the control and Trox (Figures 18 and 19). Similar type of results were observed in previous studies reported by Vu et al. [45] and Slekiene et al. [46].
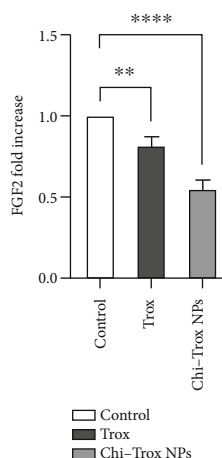
FIGURE 18: Anticancer effects of Trox and Chi-Trox NPs on the expression of FGF2 in chick chorioallantoic membrane. Comparison made between control and Trox and control and Chi-Trox NPs; Trox: troxerutin; Chi-Trox NPs: chitosan nanoparticles encapsulated with troxerutin; SD: standard deviation. The statistical analysis was done by using ANOVA and Tukey's post hoc test. *Significant difference compared with the control ($p < 0.05$); **significant difference compared with the control ($p < 0.01$); ***significant difference compared with the control ($p < 0.001$); ****significant difference compared with the control ($p < 0.0001$).
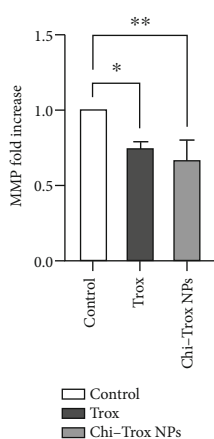
FIGURE 19: Anticancer effects of Trox and Chi-Trox NPs on the expression of MMP in chick chorioallantoic membrane. Comparison made between control and Trox and control and Chi-Trox NPs. Trox: troxerutin; Chi-Trox NPs: chitosan nanoparticles encapsulated with troxerutin; SD: standard deviation. The statistical analysis was done by using ANOVA and Tukey's post hoc test. *Significant difference compared with the control ($p < 0.05$); **significant difference compared with the control ($p < 0.01$); ***significant difference compared with the control ($p < 0.001$); ****significant difference compared with the control ($p < 0.0001$).

4. Conclusion

The chitosan nanoparticles were successfully encapsulated with troxerutin and characterized by various analyses such as DLS, FT-IR, and SEM. The *in vitro* drug release kinetic assay confirmed that Chi-Trox NPs released sustained manner compared with Trox. The Chi-Trox NPs have more anti-angiogenic potential than Trox by decreasing the blood vessel formation. Histopathology results showed decrease in the blood vessels formation supports the antiangiogenic ability. The immunohistochemical results showed low expression levels of CD104 and vimentin on endothelial cells (ECs) of CAM indicate inhibition of blood vessels. Furthermore, the mRNA expression levels of angiogenesis markers such as FGF2 and MMP were downregulated indicates its antiangiogenic activity. The anticancer activity results revealed suppression of tumor by inhibiting the blood vessel formation. The immunohistochemical results revealed low expression levels of CD44. Furthermore, the mRNA expression of FGF2 and MMP were downregulated indicates the anticancer activity. Altogether our findings suggest that Chi-Trox NPs could be a useful angiogenic inhibitor and can be more effectively used in future especially for the treatment of cancer.

Abbreviations

Trox:	Troxerutin
Chi-Trox NPs:	Chitosan encapsulated troxerutin nanoparticles
CAM:	Chick chorioallantoic membrane
IHC:	Immunohistochemistry
VEGF:	Vascular endothelial growth factor
MMP:	Matrix metalloproteinase
FGF2:	Fibroblast growth factor-2
DLS:	Dynamic light scattering
SEM:	Scanning electron microscope
FT-IR:	Fourier-transform infrared.

Data Availability

All data used to support the findings of this study are available from the corresponding author upon request.

Conflicts of Interest

The authors declare that they have no competing interests.

Authors' Contributions

GKS, HE, PC, SKY, LK, and SS have designed the study and executed the work. KC and SP helped to revise the manuscript. Harini Elangovan, Prema Chandramouli, Santhosh Kumar Yasam, Kirubhanand Chandrasekaran, and Langeswaran Kulanthaivel equally contributed to this work, and they are equal first authors.

Acknowledgments

References

[1] G. Eelen, L. Treps, X. Li, and P. Carmeliet, "Basic and therapeutic aspects of angiogenesis updated," *Circulation Research*, vol. 127, no. 2, pp. 310–329, 2020.

[2] M. S. O'Reilly, T. Boehm, Y. Shing et al., "Endostatin: an endogenous inhibitor of angiogenesis and tumor growth," *Cell*, vol. 88, no. 2, pp. 277–285, 1997.

[3] J. M. Curry, T. D. Eubank, R. D. Roberts et al., "M-CSF signals through the MAPK/ERK pathway via Sp1 to induce VEGF production and induces angiogenesis in vivo," *PLoS One*, vol. 3, no. 10, article e3405, 2008.

[4] Z. Abdolmaleki, H. A. Arab, S. Amanpour, and S. Muhammadnejad, "Anti-angiogenic effects of ethanolic extract of *Artemisia sieberi* compared to its active substance, artemisinin," *Revista Brasileira de Farmacognosia*, vol. 26, no. 3, pp. 326–333, 2016.

[5] A. N. Panche, A. D. Diwan, and S. R. Chandra, "Flavonoids: an overview," *Journal of Nutritional Science*, vol. 5, p. e47, 2016.

[6] Y. Fu, W. Liu, and O. P. Soladoye, "Towards innovative food processing of flavonoid compounds: insights into stability and bioactivity," *LWT*, vol. 150, article 111968, 2021.

[7] S. Kumar and A. K. Pandey, "Chemistry and biological activities of flavonoids: an overview," *The Scientific World Journal*, vol. 2013, Article ID 162750, 16 pages, 2013.

[8] Z. Ahmadi, R. Mohammadinejad, S. Roomiani, E. G. Afshar, and M. Ashrafizadeh, "Biological and therapeutic effects of troxerutin: molecular signaling pathways come into view," *Journal of Pharmaco Puncture*, vol. 24, no. 1, pp. 1–13, 2021.

[9] Q. Shan, J. Zhuang, G. Zheng et al., "Troxerutin reduces kidney damage against BDE-47-induced apoptosis via inhibiting NOX2 activity and increasing Nrf2 activity," *Oxidative Medicine and Cellular Longevity*, vol. 2017, Article ID 6034692, 12 pages, 2017.

[10] L. M. Lazer, B. Sadhasivam, K. Palaniyandi et al., "Chitosan-based nano-formulation enhances the anticancer efficacy of hesperetin," *International Journal of Biological Macromolecules*, vol. 107, no. Part B, pp. 1988–1998, 2018.

[11] S. Narayan, "Chitosan-Based Nanoformulation as Carriers of Small Molecules for Tissue Regeneration," in *Functional Chitosan*, S. Jana and S. Jana, Eds., Springer, Singapore, 2019.

[12] W. S. Vedakumari, N. Ayaz, A. S. Karthick, R. Senthil, and T. P. Sastry, "Quercetin impregnated chitosan–fibrin composite scaffolds as potential wound dressing materials—fabrication, characterization and in vivo analysis," *European Journal of Pharmaceutical Sciences*, vol. 15, no. 97, pp. 106–112, 2017.

[13] A. Anitha, V. G. Deepagan, V. D. Rani, D. Menon, S. V. Nair, and R. Jayakumar, "Preparation, characterization, *in vitro* drug release and biological studies of curcumin loaded dextran sulphate -chitosan nanoparticles," *Carbohydrate Polymers*, vol. 84, no. 3, pp. 1158–1164, 2011.

[14] A. R. Bilia, C. Guccione, B. Isacchi, C. Righeschi, F. Firenzuoli, and M. C. Bergonzi, "Essential oils loaded in nanosystems: a developing strategy for a successful therapeutic approach," *Evidence-based Complementary and Alternative Medicine*, vol. 2014, Article ID 651593, 14 pages, 2014.

[15] Z. A. Raza, S. Khalil, A. Ayub, and I. M. Banat, "Recent developments in chitosan encapsulation of various active ingredients for multifunctional applications," *Carbohydrate Research*, vol. 492, article 108004, 2020.

[16] F. D. Victorelli, V. M. de Oliveira Cardoso, N. N. Ferreira et al., "Chick embryo chorioallantoic membrane as a suitable *in vivo* model to evaluate drug delivery systems for cancer treatment: A review," *European Journal of Pharmaceutics and Biopharmaceutics*, vol. 153, no. 153, pp. 273–284, 2020.

[17] P. Nowak-Sliwinska, T. Segura, and M. L. Iruela-Arispe, "The chicken chorioallantoic membrane model in biology, medicine and bioengineering," *Angiogenesis*, vol. 17, no. 4, pp. 779–804, 2014.

[18] S. F. Altschul, W. Gish, W. Miller, E. W. Myers, and D. J. Lipman, "*Basic local alignment search tool*," *Molecular Biology*, vol. 215, no. 3, pp. 403–410, 1990.

[19] E. Gasteiger, C. Hoogland, A. Gattiker et al., "Protein Identification and Analysis Tools on the ExPASy Server," in *The Proteomics Protocols Handbook. Springer Protocols Handbooks*, J. M. Walker, Ed., Humana Press, 2005.

[20] W. Zheng, Q. Wuyun, X. Zhou, Y. Li, P. Freddolino, and Y. Zhang, "LOMETS3: integrating deep learning and profile alignment for advanced protein template recognition and function annotation," *Nucleic Acids Research*, vol. 50, no. W1, pp. W454–W464, 2022.

[21] J. Ko, H. Park, L. Heo, and C. Seok, "GalaxyWEB server for protein structure prediction and refinement," *Nucleic Acids Research*, vol. 40, no. W1, p. W294, 2012.

[22] R. A. Laskowski, M. W. MacArthur, D. S. Moss, and J. M. Thornton, "PROCHECK: a program to check the stereochemical quality of protein structures," *Journal of Applied Crystallography*, vol. 26, no. 2, pp. 283–291, 1993.

[23] A. G. Luque-Alcaraz, J. Lizardi, F. M. Goycoolea et al., "Characterization and antiproliferative activity of nobiletin-loaded chitosan nanoparticles," *Journal of Nanomaterials*, vol. 2012, Article ID 100, 7 pages, 2012.

[24] S. Ilk, N. Saglam, and M. Özgen, "Kaempferol loaded lecithin/chitosan nanoparticles: preparation, characterization, and their potential applications as a sustainable antifungal agent," *Artificial Cells, Nanomedicine, and Biotechnology*, vol. 45, no. 5, pp. 907–916, 2017.

[25] F. Li, Y. Shi, J. Liang, and L. Zhao, "Curcumin-loaded chitosan nanoparticles promote diabetic wound healing via attenuating inflammation in a diabetic rat model," *Journal of Biomaterials Applications*, vol. 34, no. 4, pp. 476–486, 2019.

[26] J. Hao, B. Guo, S. Yu et al., "Encapsulation of the flavonoid quercetin with chitosan-coated nano-liposomes," *LWT- Food Science and Technology*, vol. 1, no. 8, pp. 37–44, 2017.

[27] S. P. Kumar, K. Birundha, K. Kaveri, and K. R. Devi, "Antioxidant studies of chitosan nanoparticles containing naringenin and their cytotoxicity effects in lung cancer cells," *International Journal of Biological Macromolecules*, vol. 78, pp. 87–95, 2015.

[28] V. Arulmozhi, K. Pandian, and S. Mirunalini, "Ellagic acid encapsulated chitosan nanoparticles for drug delivery system in human oral cancer cell line (KB)," *Colloids and Surfaces B: Biointerfaces*, vol. 110, pp. 313–320, 2013.

[29] M. Yusefi, H. Y. Chan, S. Y. Teow et al., "5-fluorouracil encapsulated chitosan-cellulose fiber bionanocomposites: synthesis,

characterization and in vitro analysis towards colorectal cancer cells," *Nano Materials*, vol. 11, no. 7, p. 1691, 2021.

[30] R. K. Das, N. Kasoju, and U. Bora, "Encapsulation of curcumin in alginate-chitosan-pluronic composite nanoparticles for delivery to cancer cells," *Nanomedicine: Nanotechnology, Biology and Medicine*, vol. 6, no. 1, pp. 53–60, 2010.

[31] C. Onyebuchi and D. Kavaz, "Chitosan and N, N, N-trimethyl chitosan nanoparticle encapsulation of *Ocimum Gratissimum* essential oil: optimised synthesis, in vitro release and bioactivity," *International Journal of Nanomedicine*, vol. 14, pp. 7707–7727, 2019.

[32] R. S. Nair, A. Morris, N. Billa, and C. O. Leong, "An evaluation of curcumin-encapsulated chitosan nanoparticles for transdermal delivery," *AAPS PharmSciTech*, vol. 20, no. 2, pp. 1–3, 2019.

[33] F. Rahmani, E. Karimi, and E. Oskoueian, "Synthesis and characterisation of chitosan-encapsulated genistein: its antiproliferative and anti-angiogenic activities," *Journal of Microencapsulation*, vol. 37, no. 4, pp. 305–313, 2020.

[34] R. Sanatkar, G. Rahimi Kalateh Shah Mohammad, E. Karimi, E. Oskoueian, and R. Hendra, "Evaluation of daidzein-loaded chitosan microcapsules for the colon cancer drug delivery: synthesis, characterization and release behaviour," *Polymer Bulletin*, vol. 79, no. 9, pp. 7391–7395, 2022.

[35] R. Manjunathan and M. Ragunathan, "In ovo administration of human recombinant leptin shows dose dependent angiogenic effect on chicken chorioallantoic membrane," *Biological Research*, vol. 48, no. 1, p. 29, 2015.

[36] G. Bessa, P. R. Melo-Reis, L. A. Araújo et al., "Angiogenic activity of latex from Euphorbia tirucalliLinnaeus 1753 (Plantae, Euphorbiaceae)," *Brazilian Journal of Biology*, vol. 75, no. 3, pp. 752–758, 2015.

[37] J. R. van Beijnum, E. J. Huijbers, K. van Loon et al., "Extracellular vimentin mimics VEGF and is a target for anti-angiogenic immunotherapy," *Nature Communications*, vol. 13, pp. 1–20, 2022.

[38] M. T. Nayak, A. Singh, R. S. Desai, and S. S. Vanaki, "Immunohistochemical analysis of vimentin in oral submucous fibrosis," *Journal of Cancer Epidemiology*, vol. 2013, Article ID 549041, 6 pages, 2013.

[39] X. Chen and H. Wang, "Prognostic value of vimentin is associated with immunosuppression in metastatic renal cell carcinoma," *Frontiers in Oncology*, vol. 10, p. 1181, 2020.

[40] A. Y. Liu, M. P. Roudier, and L. D. True, "Heterogeneity in primary and metastatic prostate cancer as defined by cell surface CD profile," *The American Journal of Pathology*, vol. 165, no. 5, pp. 1543–1556, 2004.

[41] S. Y. Hong, A. W. Ha, and W. Kim, "Effects of quercetin on cell differentiation and adipogenesis in 3T3-L1 adipocytes," *Nutrition Research and Practice*, vol. 15, no. 4, pp. 444–455, 2021.

[42] A. H. Webb, B. T. Gao, Z. K. Goldsmith et al., "Inhibition of MMP-2 and MMP-9 decreases cellular migration, and angiogenesis in in vitro models of retinoblastoma," *BMC Cancer*, vol. 17, p. 434, 2017.

[43] M. J. Bae, F. Karadeniz, J. H. Oh et al., "MMP-Inhibitory Effects of Flavonoid Glycosides from Edible Medicinal Halophyte *Limonium tetragonum*," *Evidence-based Complementary and Alternative Medicine*, vol. 2017, Article ID 6750274, 8 pages, 2017.

[44] X. Y. Wu, H. Xu, Z. F. Wu et al., "Formononetin, a novel FGFR2 inhibitor, potently inhibits angiogenesis and tumor growth in preclinical models," *Oncotarget*, vol. 6, no. 42, p. 44563, 2015.

[45] B. T. Vu, S. A. Shahin, J. Croissant et al., "Chick chorioallantoic membrane assay as an *in vivo* model to study the effect of nanoparticle-based anticancer drugs in ovarian cancer," *Scientific Reports*, vol. 8, no. 1, p. 8524, 2018.

[46] L. Slekiene, D. Stakisaitis, I. Balnyte, and A. Valanciute, "Sodium valproate inhibits small cell lung cancer tumor growth on the chicken embryo chorioallantoic membrane and reduces the p53 and EZH2 expression," *Dose-Response*, vol. 16, no. 2, article 1559325818772486, 2018.

Research Article

Investigation on the Mechanisms of *Zanthoxylum bungeanum* for Treating Diabetes Mellitus Based on Network Pharmacology, Molecular Docking, and Experiment Verification

Yuanshe Huang,[1] Zhaomiao Gong ,[2] Chen Yan ,[3] Ke Zheng,[4] Lidan Zhang,[5] Jing Li,[1] E. Liang,[1] Lai Zhang ,[1] and Jingxin Mao [2,5]

[1]*Anshun University, Guizhou Anshun 561000, China*
[2]*Chongqing Medical and Pharmaceutical College, Chongqing 400030, China*
[3]*An Shun City People's Hospital, Guizhou Anshun 561000, China*
[4]*Department of Endocrine and Breast Surgery, The First Affiliated Hospital of Chongqing Medical University, No. 1 Youyi Road, Yuzhong District, Chongqing 400016, China*
[5]*College of Pharmaceutical Sciences, Southwest University, Chongqing 400715, China*

Correspondence should be addressed to Lai Zhang; 975575681@qq.com and Jingxin Mao; maomao1985@email.swu.edu.cn

Objective. The aim of the study was to explore the potential mechanism of *Zanthoxylum bungeanum* in the treatment of diabetes mellitus (DM) using network pharmacology. *Methods*. The DrugBank database and TCMSP platform were used to search for the main chemical components and their targets of *Zanthoxylum bungeanum*, and the genes related to diabetes mellitus were obtained from the genecards database. Import the data into the Venny 2.1.0 platform for intersection analysis to obtain the *Zanthoxylum bungeanum*-DM-gene dataset. The protein-protein interaction (PPI) analysis of *Zanthoxylum bungeanum*-DM gene was performed using the String data platform, and the visualization and network topology analysis were performed using Cytoscape 3.8.2. The KEGG pathway enrichment and biological process of GO enrichment analysis were carried out using the David platform. The active ingredients and key targets of *Zanthoxylum bungeanum* were molecularly docked to verify their biological activities by using Discovery Studio 2019 software. *Zanthoxylum bungeanum* was extracted and isolated by ethanol and dichloromethane. HepG2 cells were cultured, and cell viability assay was utilized to choose the suitable concentration of *Zanthoxylum bungeanum* extract (ZBE). The western blot assay was used for measuring the expression of AKT1, IL6, HSP90AA1, FOS, and JUN proteins in HepG2 cells. *Results*. A total of 5 main compounds, 339 targets, and 16656 disease genes were obtained and retrieved, respectively. A total of 187 common genes were screened, and 20 core genes were finally obtained after further screening. The antidiabetic active ingredients of *Zanthoxylum bungeanum* are kokusaginin, skimmianin, diosmetin, beta-sitosterol, and quercetin, respectively. The main targets for its antidiabetic effect are AKT1, IL6, HSP90AA1, FOS, and JUN, respectively. GO enrichment analysis revealed that the biological process of *Zanthoxylum bungeanum* and DM is related to a positive regulation of gene expression, positive regulation of transcription, positive regulation of transcription from RNA polymerase II promoter, response to drug, positive regulation of apoptotic process, and positive regulation of cell proliferation, etc. KEGG enrichment analysis revealed that common biological pathways mainly including the phospholipase D signaling pathway, MAPK signaling pathway, beta-alanine metabolism, estrogen signaling pathway, PPAR signaling pathway, and TNF signaling pathway. Molecular docking results showed that AKT1 with beta-sitosterol and quercetin, IL-6 with diosmetin and skimmianin, HSP90AA1 with diosmetin and quercetin, FOS with beta-sitosterol and quercetin, and JUN with beta-sitosterol and diosmetin have relatively strong binding activity, respectively. Experiment verification results showed that DM could be significantly improved by downregulating the expression of AKT1, IL6, HSP90AA1, FOS, and JUN proteins after being treated at concentrations of 20 μmol/L and 40 μmol/L of ZBE. *Conclusion*. The active components of *Zanthoxylum bungeanum* mainly including kokusaginin, skimmianin, diosmetin, beta-sitosterol, and quercetin. The therapeutic effect of *Zanthoxylum bungeanum* on DM may be achieved by downregulating core target genes including AKT1, IL6, HSP90AA1, FOS, and JUN, respectively. *Zanthoxylum bungeanum* is an effective drug in treatment of DM related to the above targets.

1. Introduction

Diabetes mellitus (DM) is one of the most serious endocrine disorders and noncommunicable diseases that threaten human health worldwide, mainly manifested as carbohydrate, fat, and protein metabolism disorders; the prevalence rate is increasing globally [1]. According to the International Diabetes Federation (IDF) global diabetes map in 2019, the number of diabetic patients was about 116.4 million people. Based on the IDF forecast, the number of diabetic patients in the world will reach 700 million in 2045, with more than 4 million people dying of diabetes and its complications, DM has become a very serious global health crisis [2]. According to research, DM is becoming a serious problem that threatens global health [3]. However, our current understanding of the cause and optimal treatment of this disease is not fully elaborated. The current drug treatment cannot control the continuous development of hyperglycemia well and even cause adverse reactions such as hypoglycemia, which will make patients bear further economic burdens. What is even more terrifying is the macrovascular and microvascular caused by hyperglycemia and hyperlipidemia. As well as damage to the heart, brain, and kidneys, the region's health system and economy are under enormous pressure [4]. Therefore, there is an urgent need to develop optimal and effective treatments and conduct in-depth research on the prevention and treatment of DM [5].

Zanthoxylum bungeanum is widely distributed in China, mainly in Sichuan, Guizhou, Gansu, Shaanxi, Chongqing, and other provinces. Zanthoxylum bungeanum is a traditional Chinese medicine (TCM) with a long history of edible and medicinal use [6]. It is rich in resources and has great development and utilization value. The 2020 edition of "Chinese Pharmacopoeia" recorded that Zanthoxylum bungeanum is warm in nature, pungent in taste, and returns to the spleen, stomach, and kidney meridians, and has the effects of warming and relieving pain, killing insects and relieving itching. The medicinal parts are the dried and ripe peel of the Rutaceae plant green pepper (Zanthoxylum schinifolium Sieb.et Zucc.) or Chinese Zanthoxylum bungeanum (Zantohxylum bungeanum Maxin.) [7]. The peel of Zanthoxylum bungeanum is rich in chemical components, mainly including volatile oils, alkaloids, amides, flavonoids, lignin, coumarin, triterpenoids, and other compounds [8]. The pharmacological activities of Zanthoxylum bungeanum are manifested in analgesia, anti-inflammatory, antioxidant, antibacterial, and antiobesity [9]. In recent years, many studies have been revealed that the extract of Zanthoxylum bungeanum exhibits the antidiabetic effect [10, 11].

Due to the complex components of TCM that takes a lot of manpower, material resources and time to study the molecular mechanism of TCM through animal experiments or cell experiments. In recent years, many scholars have studied the chemical constituents and pharmacological effects of Zanthoxylum bungeanum, but few studies have combined the chemical constituents and network pharmacology of Zanthoxylum bungeanum. With the development of bioinformatics and network pharmacology, technologies and methods based on biological data integration provide a convenient way to clarify the complex mechanism of action of TCM [12]. In the present study, the network pharmacology method was used to explore the mechanism of Zanthoxylum bungeanum in the treatment of DM. With the help of various public databases to obtain the effective active components of Zanthoxylum bungeanum and related antidiabetic targets, predict the antidiabetic targets of Zanthoxylum bungeanum, and conduct enrichment analysis for the relevant targets. We use Discovery Studio 2019 software for molecular docking to study the binding ability between receptors and small drug molecules and provide a reference for its in-depth research and clinical application. This study combined network pharmacology and molecular docking verification to explore the antidiabetic mechanism of Zanthoxylum bungeanum.

2. Materials and Methods

2.1. Collection of Active Components and Targets of Zanthoxylum bungeanum.
All the chemical components of Zanthoxylum bungeanum were collected through the Traditional Chinese Medicine Systems Pharmacology Database and Analysis Platform (TCMSP), the threshold of oral bioavailability (OB) was ≥30%, and molecular weight (WM) was <500; the compounds were screened based on the drug-likeness (DL) threshold ≥ 0.18. After screening the main chemical components of Zanthoxylum bungeanum, the targets of active ingredients of Zanthoxylum bungeanum were screened out through the TCMSP analysis platform and DrugBank database.

2.2. Screening of Diabetes Mellitus Disease Targets.
The GeneCards database provides comprehensive, user-friendly information on all annotated and predicted human genes. The DisGeNET database containing one of the largest publicly available collections of genes and variants associated with human diseases. Using the human GeneCards database (https://www.genecards.org/) and DisGeNET database (https://www.disgenet.org/) to search with "diabetes" OR "diabetes mellitus" OR "DM" to obtain diabetes disease targets, respectively. The Venny 2.1.0 online mapping tool (https://bioinfogp.cnb.csic.es/tools/venny/index.html) was used to match the targets related to the active components of Zanthoxylum bungeanum obtained in Section 2.1 and the diabetes disease targets for mapping, draw a Venn diagram, and delete the duplicate targets to obtain the potential therapeutic targets of the active components of Zanthoxylum bungeanum.

2.3. Construction of Drug-Active Ingredient-Target Gene-Disease Network.
The target genes corresponding to the active components of Zanthoxylum bungeanum obtained in Section 2.1, and the diabetes-related target genes screened in Section 2.2 were matched and mapped. The common genes of the two obtained were used as the key targets of Zanthoxylum bungeanum in the treatment of DM. The Cytoscape 3.8.2 software was applied to builds the relationship network of "drug-active ingredient-target gene-disease" and uses the "Analyze network" function in the

TABLE 1: General information of active ingredients of *Zanthoxylum bungeanum*.

Mol ID	Molecule name	MW	OB (%)	DL	HL
MOL013271	Kokusaginin	259.28	66.68	0.2	-3.19
MOL002663	Skimmianin	259.28	40.14	0.2	-2.43
MOL002881	Diosmetin	300.28	31.14	0.27	16.34
MOL000358	Beta-sitosterol	414.79	36.91	0.75	5.36
MOL000098	Quercetin	302.25	46.43	0.28	14.4

software to perform topological analysis on the above network to clarify the mechanism of *Zanthoxylum bungeanum* in the treatment of DM.

2.4. Construction of Protein-Protein Interaction (PPI) Network of Diabetes Targets.

The String database (https://cn.string-db.org/) was used to search for known and predicted PPI. Input the common targets of *Zanthoxylum bungeanum* and DM into the String database, select the study species as human ("Homosapiens"), set the confidence to be >0.4, hide disconnected nodes in the network, and use the downloaded.tsv file in String with R 4.0.4 language software is processed, and the PPI diagram is drawn according to the degree value (degree); the top 20 PPI core gene targets are finally obtained.

2.5. Gene Ontology (GO), Kyoto Encyclopedia of Genes, and Genomes (KEGG) Functional Enrichment Analysis.

Based on the David database (https://david.ncifcrf.gov/), GO functional annotation and KEGG pathway enrichment analyses were performed on the intersection target genes of *Zanthoxylum bungeanum* and DM. The species was limited to "Human," and the enriched entries with q values (that is, corrected P values) less than 0.05 were retained and sorted according to the size of the q values. The R 4.0.4 language software was applied to the obtained genes for GO and KEGG enrichment analyses and visualization. The GO analysis selects the top 10 enrichment results for display, and the KEGG analysis selects the top 20 enrichment results for display, respectively.

2.6. Component-Target Molecular Docking.

The 2D structure of the active ingredient compound of *Zanthoxylum bungeanum* under item "1.1" was downloaded from the PubChem database (https://pubchem.ncbi.nlm.nih.gov/) and saved in "sdf" format as a small molecule ligand. We download the 3D structure of the protein corresponding to the core target from the RSCBPDB database (https://www.rcsb.org/) and save it in pdb format as a protein receptor. We use Discovery Studio 2019 software to process small molecule ligands, remove original ligands and water molecules, and add hydrogen atoms to the protein receptors to preprocess and find active pockets and then mix the core target protein receptors. Molecular docking with protein ligands [13] was done. The binding activity was evaluated by libdock score; the larger the libdock score, the better the binding activity and the more stable the docking. The Discovery Studio 2019 software was used to draw the binding mode diagram between the core target protein receptor and the small mol-
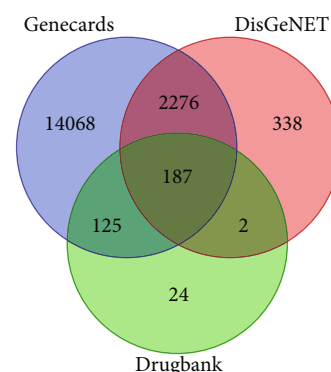
FIGURE 1: Venn diagram of the common target gene screening of *Zanthoxylum bungeanum* and diabetes.

ecule ligand of the active ingredient of *Zanthoxylum bungeanum*, which was displayed in 3D and 2D structures, respectively.

2.7. Experiment Verification

2.7.1. Reagents and Equipment.

Fetal bovine serum and high sugar DMEM were purchased from Gibco Company. Trypsin, CCK8 kit, BCA protein concentration determination kit, rabbit anti-AKT1, IL6, HSP90AA1, FOS, and JUN were all purchased from Cell Signaling Technology and Beyotime Biotechnology, respectively. CO_2 constant temperature incubator (Thermo Company), microplate reader (Tecan, Switzerland), electrophoresis apparatus (S1000, Biorad), electric blast drying oven (DHG-9070A, Shanghai Yiheng), gel imaging analysis system (Tanon-4600, Tianneng Technology), and SW-CJ-1FD/2FD ultra clean workbench (Jiangsu Suzhou Purification Equipment Factory) were used for the experiment.

2.7.2. Material, Extraction, and Isolation.

Zanthoxylum bungeanum (5 kg) was purchased from Jiangjin District, Chongqing, China, in May 2021. It was identified by Vice Professor Guowei Wang, College of Pharmacy, Southwest University of China. The voucher specimen (no. 20210015) has been deposited in the Herbarium of Anshun University. After being dried, *Zanthoxylum bungeanum* was extracted three times with 95% ethanol. The extract was evaporated to obtain a residue (0.5 kg), suspended in water, and fractionated with dichloromethane to obtain a *Zanthoxylum bungeanum* dichloromethane extract (ZBE, 54 g).

(a)

(b)
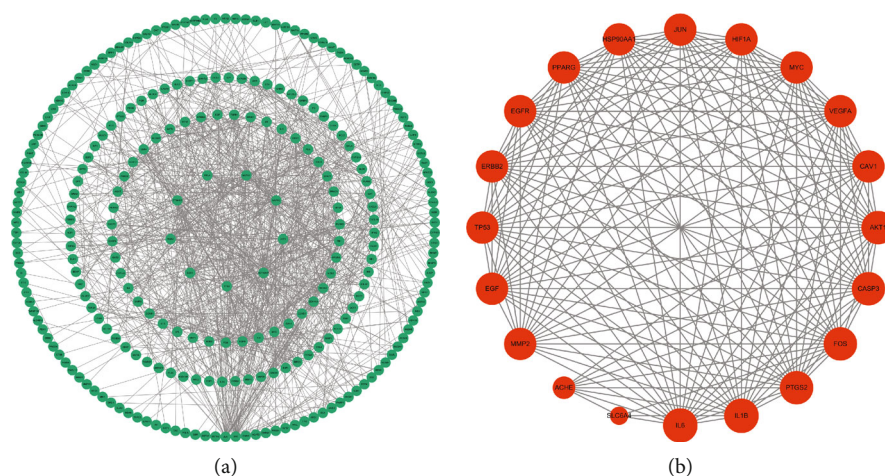
FIGURE 2: Construction of PPI network on *Zanthoxylum bungeanum* in the treatment of diabetes. (a) PPI visualization network diagram of 187 targets. (b) PPI visualization network diagram of 20 core targets.

TABLE 2: Topological parameters of core target genes in the intersection genes of *Zanthoxylum bungeanum* and diabetes.

Core target gene	Betweenness centrality	Closeness centrality	Degree	Score
JUN	0.10115515	0.40967742	45	929.6329377
HSP90AA1	0.05450466	0.39379845	40	1040.573485
AKT1	0.13233367	0.41983471	40	1933.09329
FOS	0.01853274	0.36285714	28	1026.474052
IL6	0.01959522	0.34002677	23	1484.812682

2.7.3. Cell Experiment

(1) Cell Culture. Human hepatoma cell line HepG2 was purchased from the cell bank of Chinese Academy of Sciences. The frozen cells were quickly thawed, added to the culture medium, and centrifuged for 3 min; then, the supernatant was discarded, the cells were transferred to the culture bottle, and the prepared complete culture medium (10% fetal bovine serum, 1% penicillin streptomycin mixture, 89% high sugar DMEM) was added, and the cells were cultured in a 37°C, 5% CO_2 incubator. When the cells in the culture bottle fuse to 80%~90%, they can be digested with trypsin and transferred to a new culture bottle.

(2) Cell Grouping and Treatment. Cell modeling was as follows: 38.5 mg of palmitic acid was dissolved in 1.5 mL of anhydrous ethanol to obtain a palmitic acid master batch at a concentration of 100 mmol/L. 0.5 mL of the master batch was diluted with high-sugar DMEM containing 1% BSA to obtain 10 mL of 5 mmol/L palmitic acid solution. After filtration and debacterization, the cells were incubated for 24 h with DMEM containing 35 mmol/L glucose to obtain 0.25 mmol/L of the modeling agent.

Grouping and drug administration was as follows: the control group (Ctrl) was given culture medium, the model group (Mod) and ZBE group were incubated in the incubator for 24 h after the intervention of the modeling agent by

discarding the old medium and adding DMEM and ZBE extract with different concentration at 5, 10, 20, 40, and 80 μmol/L, respectively.

(3) Cytotoxicity and Cell Viability Assay. The HepG2 cells were inoculated in 96-well plates at a density of 5×10^4 cells/well in a volume of 100 μL. After 24 h of cell culture, the cells were given a mold-making agent intervention for 24 h. The old solution was discarded, and the experimental groups were given different concentrations (5, 10, 20, 40, and 80 μmol/L) of ZBE extract diluted in DMEM. After 24 h of administration, the medium was replaced with new medium; 10 μL of CCK8 assay solution was added to each well, incubated in the incubator for 30 min, shaken, and mixed; and the optical density value (OD value) was read at a wavelength of 450 nm on an enzyme marker to calculate the cell growth rate.

(4) Western Blot Assay. The western blot method was used for AKT1, IL6, HSP90AA1, FOS, and JUN protein expressions in HepG2 cells. The HepG2 cells were inoculated in 6-well plates at a density of 2×10^5 cells/well. After successful modeling, ZBE was added at 20 μmol/L (low) and 40 μmol/L (high), respectively, for 24 h. RIPA lysis solution was added to each well for 220 μL, and the cells were lysed on ice for 10 min and scraped off and transferred to an EP tube, and the cells were repeatedly blown and broken in a
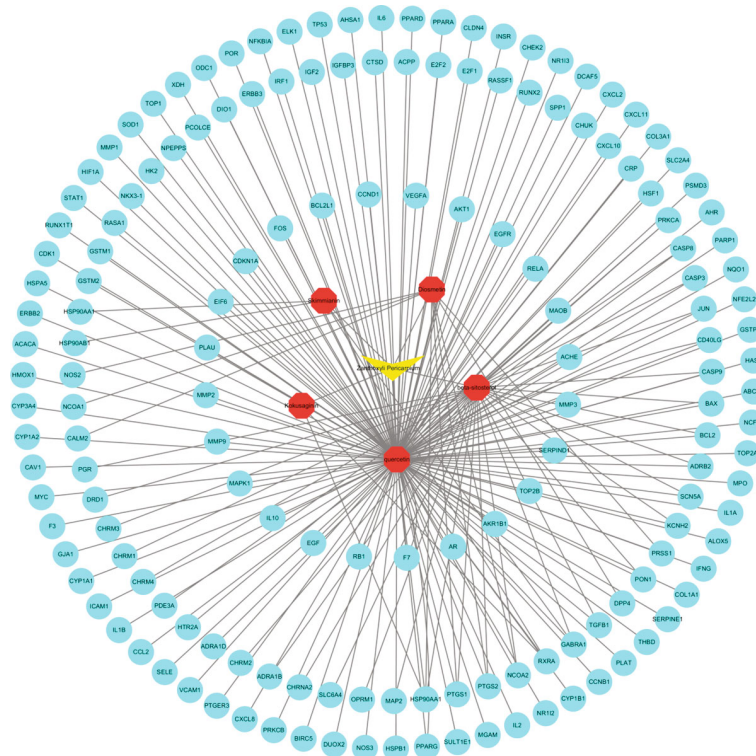
FIGURE 3: Construction of "drug-compound-intersection target" interaction network.
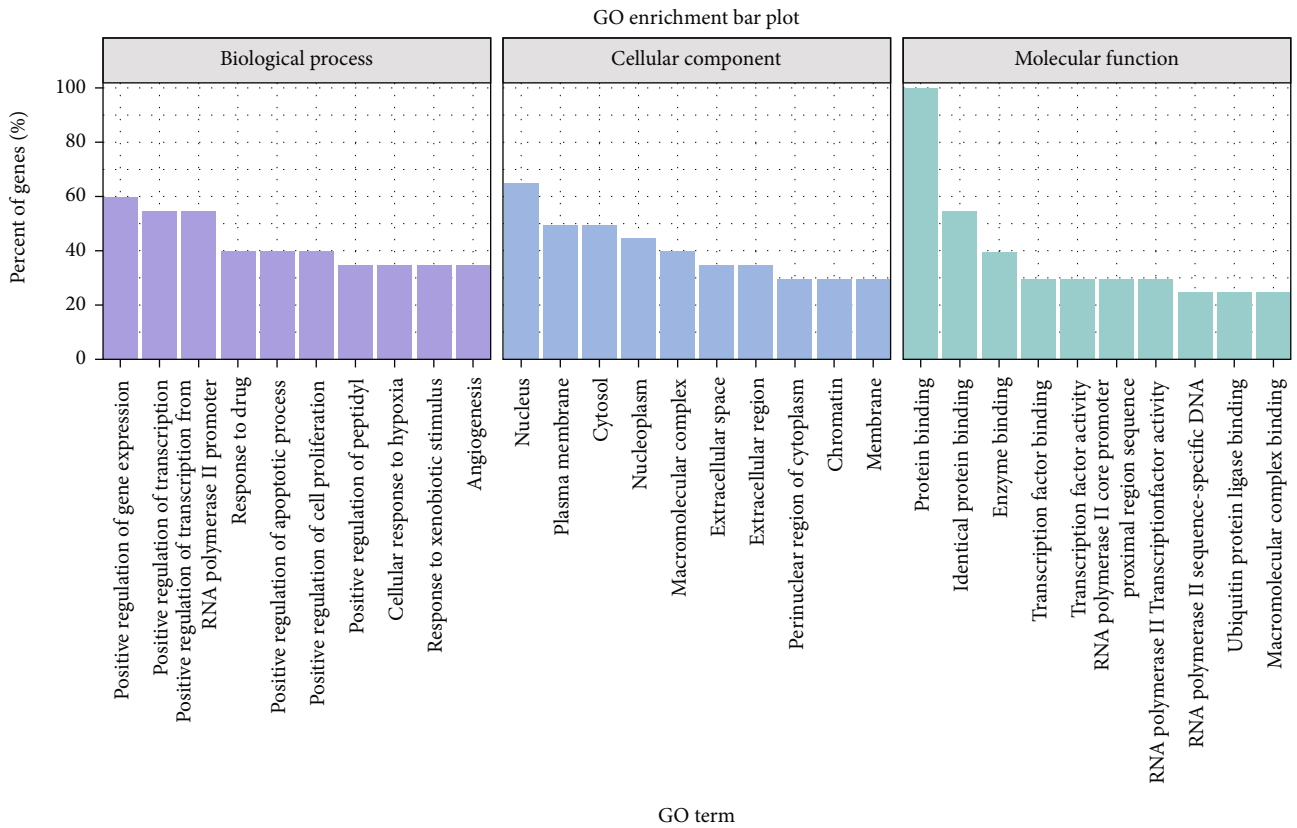
FIGURE 4: Bar diagram of GO functional enrichment analysis.
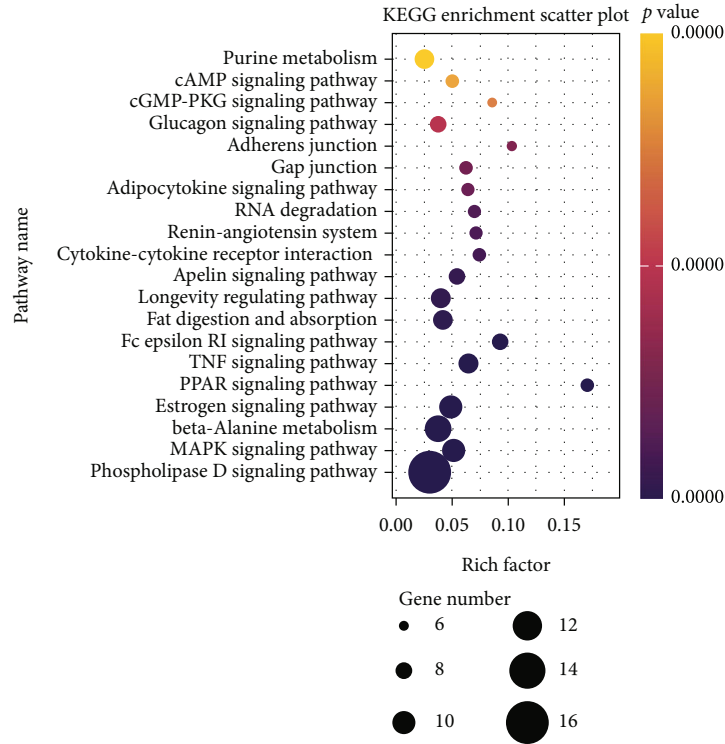
FIGURE 5: Bubble diagram of KEGG pathway enrichment analysis.
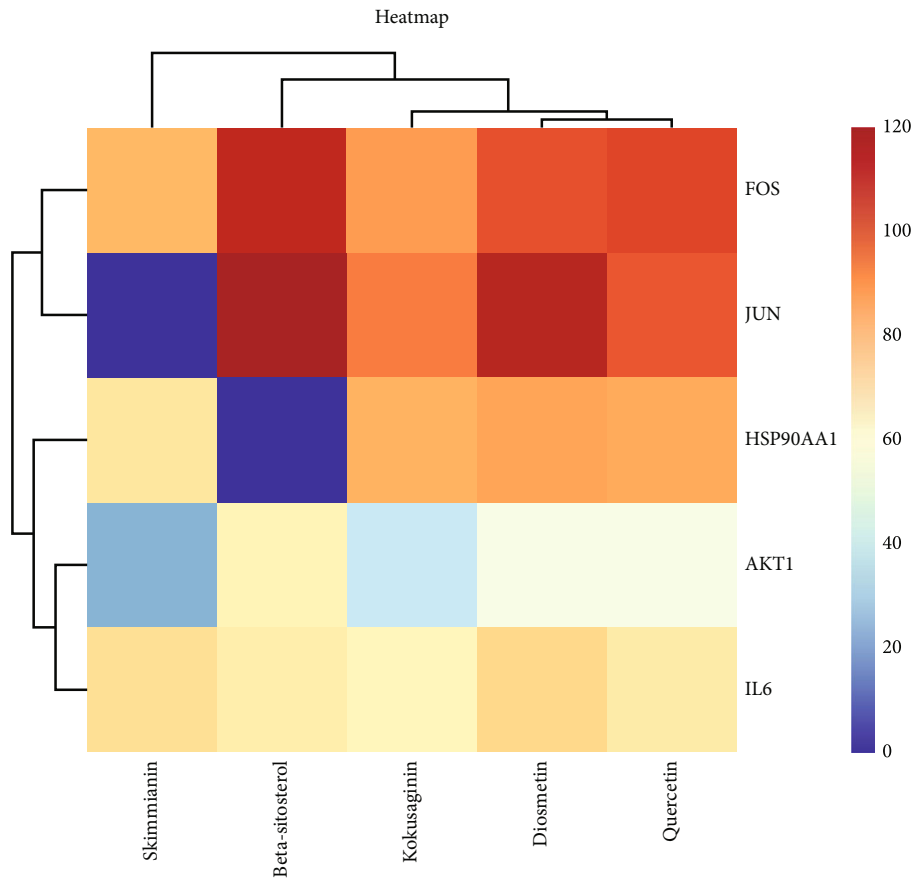
FIGURE 6: Heatmap of main active ingredients of *Zanthoxylum bungeanum* with 5 core target genes.

cell crusher and continued to be lysed on ice for 10 min. The supernatant was extracted, and the protein concentration of each group was determined using the BCA kit, diluted and leveled using 5× protein loading buffer, and denatured in boiling water. The protein sample volume of 40 μg per well was added to the precast gel, and electrophoresis buffer was added for electrophoresis (110 V, 80 min). The proteins were transferred to the PVDF membrane, blocked with 5% BSA for 1 h. The primary antibody (1 : 1000) was added overnight; the membrane was washed three times with TBST and incubated with goat anti-rabbit secondary antibody (1 : 1000) for 1 h. The membrane was washed three times with TBST and washed in ECL luminescent solution for color development and photographed, and the grayscale values of the bands were counted.

(5) Statistical Analysis. Statistical analysis was carried out using SPSS 20.0 software. The statistical significance of the differences was measured between groups by ANOVA, and all the data were statistically analyzed by mean ± S.D. $P < 0.05$ was considered statistically significant, and $P < 0.01$ was considered to be significantly different.

3. Results

3.1. Screening of Active Components of Zanthoxylum bungeanum. Taking OB, WM value, and DL properties as screening criteria, qualified compounds were screened from the TCMSP database. A total of 5 active components of Zanthoxylum bungeanum met the screening criteria, including kokusaginin, skimmianin, diosmetin, beta-sitosterol, and quercetin, respectively (Table 1).

3.2. Acquisition of Diabetes Target Extraction and Intersection Target. Antidiabetes-related targets were obtained from GeneCards and DrugBank databases. A total of 339 drug component targets and 16656 antidiabetes-related targets were combined and intersected to obtain 312 Zanthoxylum bungeanum targets for the treatment of diabetes. The Venn diagram was drawn, as shown in Figure 1.

3.3. Construction of PPI Network and Screening of Core Targets. A total of 312 common targets were imported into the string database. After removing duplicate and unverifiable targets, 187 targets remained to build the PPI network (Figure 2(a)). We import the obtained PPI network data into Cytoscape 3.8.2 software, analyze the network topology parameters, select the degree value greater than the median, and obtain 20 core targets (Figure 2(b), Table 2).

3.4. Construction of "Drug-Compound-Intersection Target" Interaction Network. By comparing the degree values of each component in the "drug-compound -intersection target" network, the top 5 active components were selected including kokusaginin, skimmianin, diosmetin, beta-sitosterol, and quercetin, which could interact with 2, 4, 9, 31, and 145 target proteins, respectively. The top 5 target proteins were AKT1, IL6, HSP90AA1, FOS, and JUN (Figure 3).

TABLE 3: The results of molecular docking.

Compound	Target	PDB	Libdock score
Kokusaginin	AKT1	1 h10	40.36
Skimmianin	AKT1	1 h10	26.46
Diosmetin	AKT1	1 h10	56.65
Beta-sitosterol	AKT1	1 h10	67.85
Quercetin	AKT1	1 h10	56.04
Kokusaginin	IL6	1alu	66.33
Skimmianin	IL6	1alu	77.02
Diosmetin	IL6	1alu	79.18
Beta-sitosterol	IL6	1alu	70.68
Quercetin	IL6	1alu	71.44
Kokusaginin	HSP90AA1	1byq	88.68
Skimmianin	HSP90AA1	1byq	73.36
Diosmetin	HSP90AA1	1byq	91.09
Beta-sitosterol	HSP90AA1	1byq	0
Quercetin	HSP90AA1	1byq	89.96
Kokusaginin	FOS	1a02	93.34
Skimmianin	FOS	1a02	87.24
Diosmetin	FOS	1a02	105.47
Beta-sitosterol	FOS	1a02	118.17
Quercetin	FOS	1a02	107.43
Kokusaginin	JUN	1jnm	98.24
Skimmianin	JUN	1jnm	0
Diosmetin	JUN	1jnm	120.99
Beta-sitosterol	JUN	1jnm	125.09
Quercetin	JUN	1jnm	104.87

3.5. GO Analysis Results of the Intersection Targets of Zanthoxylum bungeanum in the Treatment of DM. The R 4.0.4 software was used to conduct GO enrichment analysis on the 187 intersection targets of Zanthoxylum bungeanum in the treatment of DM. A total of 215 biological process items, 29 cell cellular items, and 39 molecular function items were obtained (all the results satisfy $P < 0.05$ and $Q < 0.05$), and the top 10 entries by Q-Value were visualized separately (Figure 4). The results of GO analysis showed that the biological pathways of Zanthoxylum bungeanum-diabetic disease intersection targets mainly including positive regulation of gene expression, positive regulation of transcription, positive regulation of transcription from RNA polymerase II promoter, response to drug, positive regulation of apoptotic process, positive regulation of cell proliferation, positive regulation of peptidyl, cellular response to hypoxia, response to xenobiotic stimulus, angiogenesis, nucleus, plasma membrane, cytosol, nucleoplasm, macromolecular complex, extracellular space, extracellular region, perinuclear region of cytoplasm, chromatin, membrane, protein binding, identical protein binding, enzyme binding, transcription factor binding, transcription factor activity, RNA polymerase II core promoter proximal region sequence, RNA polymerase II transcription factor activity, RNA polymerase II sequence-specific DNA, ubiquitin protein ligase binding, and macromolecular complex binding.

(a)

(b)

(c)

(d)

(e)
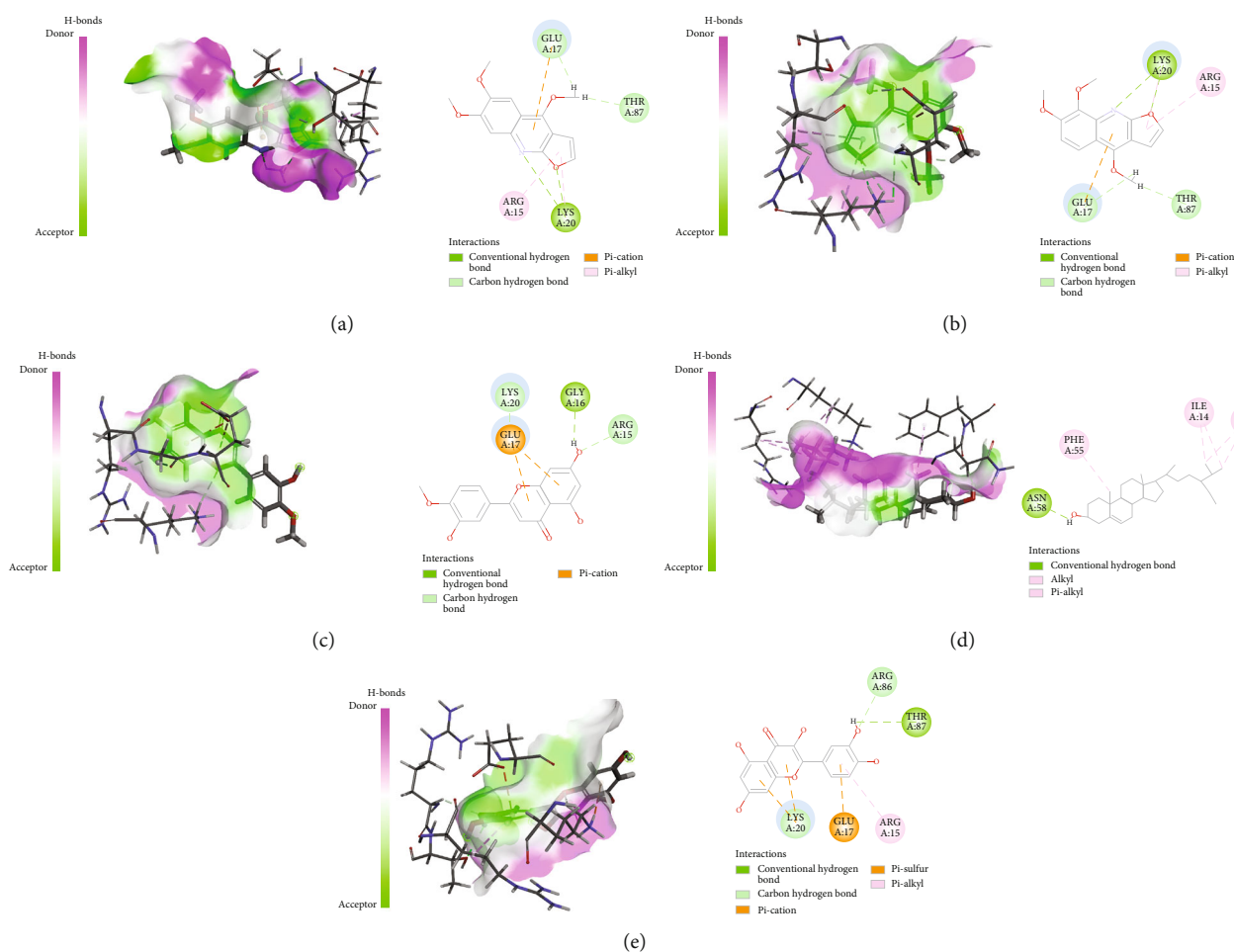
FIGURE 7: Molecular docking of AKT1 with 5 main ingredients: (a) kokusaginin, (b) skimmianin, (c) diosmetin, (d) beta-sitosterol, and (e) quercetin, respectively.

3.6. KEGG Metabolic Pathway Enrichment Analysis Results. The KEGG pathway enrichment analysis of 187 intersection targets of *Zanthoxylum bungeanum* in the treatment of DM showed that there were 99 signaling pathways involved in the treatment of DM by *Zanthoxylum bungeanum* with a P value of less than 0.05, mainly enriched in the phospholipase D signaling pathway, MAPK signaling pathway, beta-alanine metabolism, estrogen signaling pathway, PPAR signaling pathway, TNF signaling pathway, fc epsilon RI signaling pathway, fat digestion and absorption, longevity regulating pathway, apelin signaling pathway, cytokine-cytokine receptor interaction, renin-angiotensin system, RNA degradation, adipocytokine signaling pathway, gap junction, adherens junction, glucagon signaling pathway, cGMP-PKG signaling pathway, and cAMP signaling pathway and purine metabolism. We take 20 pathways with significant differences and visualized them as bubble charts (Figure 5). The P value represents the significance of the enriched target. The smaller the P value, the redder the color, and vice versa. It reflects that the same target of TCM may participate in different biological processes, and the purpose of treating diseases can be achieved by improving biological processes.

3.7. Results of Molecular Docking. Active ingredients and targets with high connectivity were screened out according to network pharmacology and analyzed using Discovery Studio 2019 software. The docking results of the 5 core targets and the corresponding active ingredients of TCM showed that kokusaginin, skimmianin, diosmetin, beta-sitosterol, and quercetin were main compounds of *Zanthoxylum bungeanum*. The libdock scores were higher than other components, suggesting that it is more likely to be the key drug active molecule of *Zanthoxylum bungeanum* in the treatment of DM (Figure 6, Table 3). Among them, beta-sitosterol (67.85) and quercetin (56.04) had the strong binding ability with AKT1 (Figure 7); diosmetin (79.18) and skimmianin (77.02) had the strong binding ability with IL-6 (Figure 8); diosmetin (91.09) and quercetin (107.43) had the strong binding ability with HSP90AA1 (Figure 9); beta-sitosterol (118.17) and quercetin (107.4) had the strong binding ability with FOS (Figure 10); beta-sitosterol (125.09) and diosmetin (120.99) had the strong binding ability with JUN (Figure 11). In addition, kokusaginin, skimmianin, diosmetin, beta-sitosterol, and quercetin form a hydrogen bond with the active site LYS-A: 20 (Figure 7(a)), LYS-A: 20 (Figure 7(b)), GLY-A: 16 (Figure 7(c)), ASN-A: 54

(a)

(b)

(c)

(d)

(e)
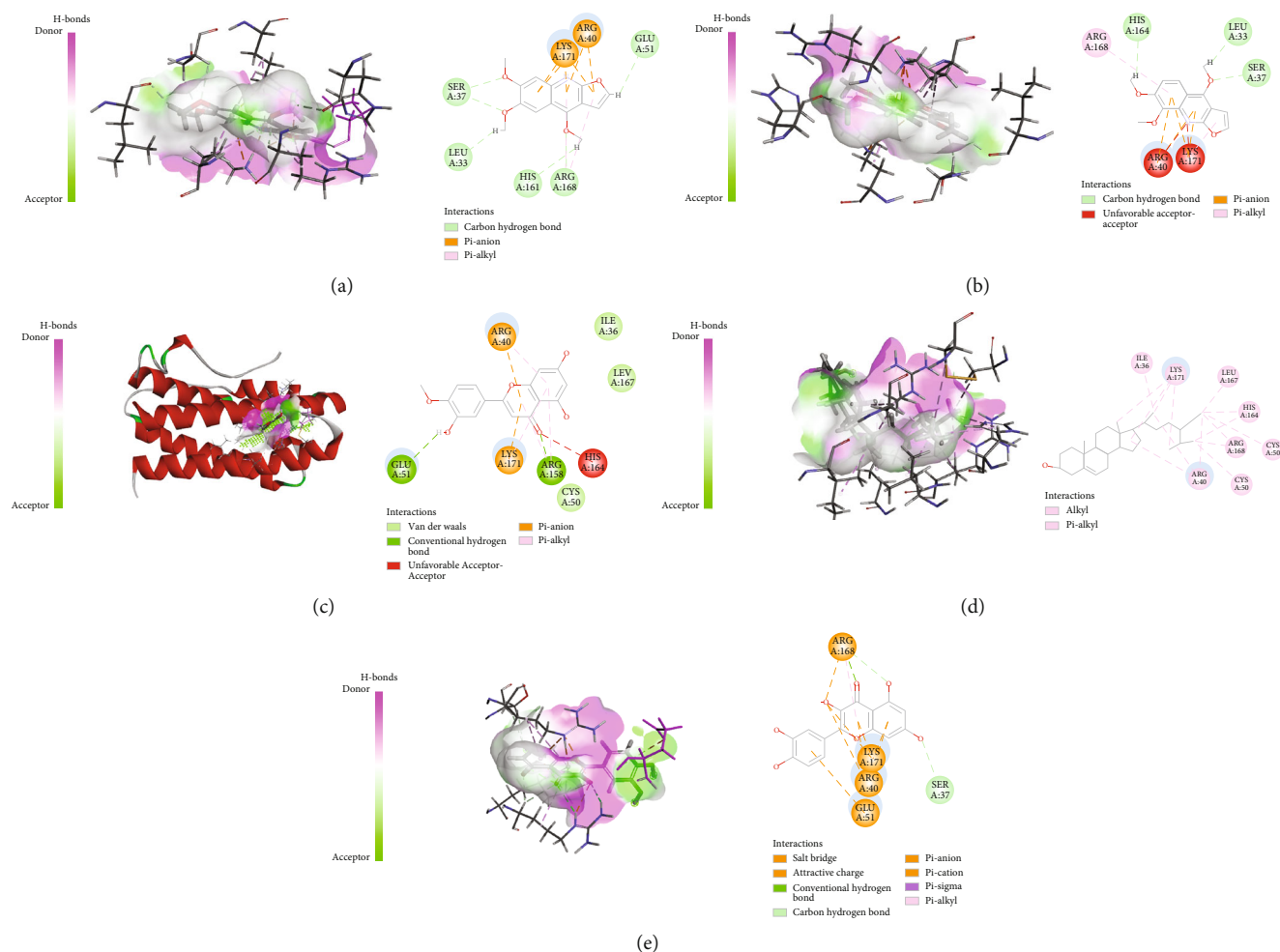
FIGURE 8: Molecular docking of IL-6 with 5 main ingredients: (a) kokusaginin, (b) skimmianin, (c) diosmetin, (d) beta-sitosterol, and (e) quercetin, respectively.

(Figure 7(d)), and THR-A: 87 (Figure 7(d)) of the protein encoded by the AKT1 gene, respectively. Diosmetin forms a hydrogen bond with the active site GLU-A: 51 and ARG-A: 168 of the protein encoded by the AKT1 gene (Figure 8(c)). Kokusaginin, skimmianin, diosmetin, and quercetin forms a hydrogen bond with the active site GLY-A: 97 (Figure 9(a)), ASN-A: 51 (Figure 9(b)), ASN-A: 106 and SER-A: 52 (Figure 9(c)), ASN-A: 51, and LEU-A: 48 (Figure 9(d)), of the protein encoded by the HSP90AA1 gene, respectively. Kokusaginin, skimmianin, diosmetin, and quercetin forms a hydrogen bond with the active site ARG-F: 146 (Figure 10(a)), ARG-F: 143 and DA-B: 5005 (Figure 10(b)), DC-B: 5003 (Figure 10(c)), and ARG-F: 143 (Figure 10(e)) of the protein encoded by FOS gene, respectively. Skimmianin and quercetin form a hydrogen bond with the active site DA-B: 5005 (Figure 11(b)), DC-B: 5002, and ARG-F: 143 (Figure 11(d)) of the protein encoded by the JUN gene, respectively.

3.8. Results of Cell Cytotoxicity/Viability Test.
The cell cytotoxicity/viability test results showed that the concentration of ZBE between 5 μmol/L and 80 μmol/L has no toxicity to HepG2 cells. In addition, it was revealed that no significantly inhibit the proliferation of HepG2 cells when concentration of ZBE at 5 μmol/L to 40 μmol/L. Furthermore, ZBE exhibits the relatively stable effect on DM at concentration of 20 μmol/L and 40 μmol/L, respectively (Figure 12). Therefore, the 20 μmol/L and 40 μmol/L of ZBE were chosen for next step experiment.

3.9. Effects of ZBE on the Expression of AKT1, IL6, HSP90AA1, FOS, and JUN Proteins in HepG2 Cells.
Compared with the control group, the expression of AKT1, IL6, HSP90AA1, FOS, and JUN proteins in the model group was upregulated ($P < 0.01$). Compared with the model group, the protein expression in the low-concentration group ($P < 0.05$, $P < 0.01$) and the high-concentration group ($P < 0.01$) of ZBE significantly decreased. The results showed that DM could be significantly improved by downregulating the expression of related proteins (AKT1, IL6, HSP90AA1, FOS, and JUN) after being treated with different concentrations (20 μmol/L and 40 μmol/L) of ZBE (Figure 13).

(a)

(b)

(c)

(d)
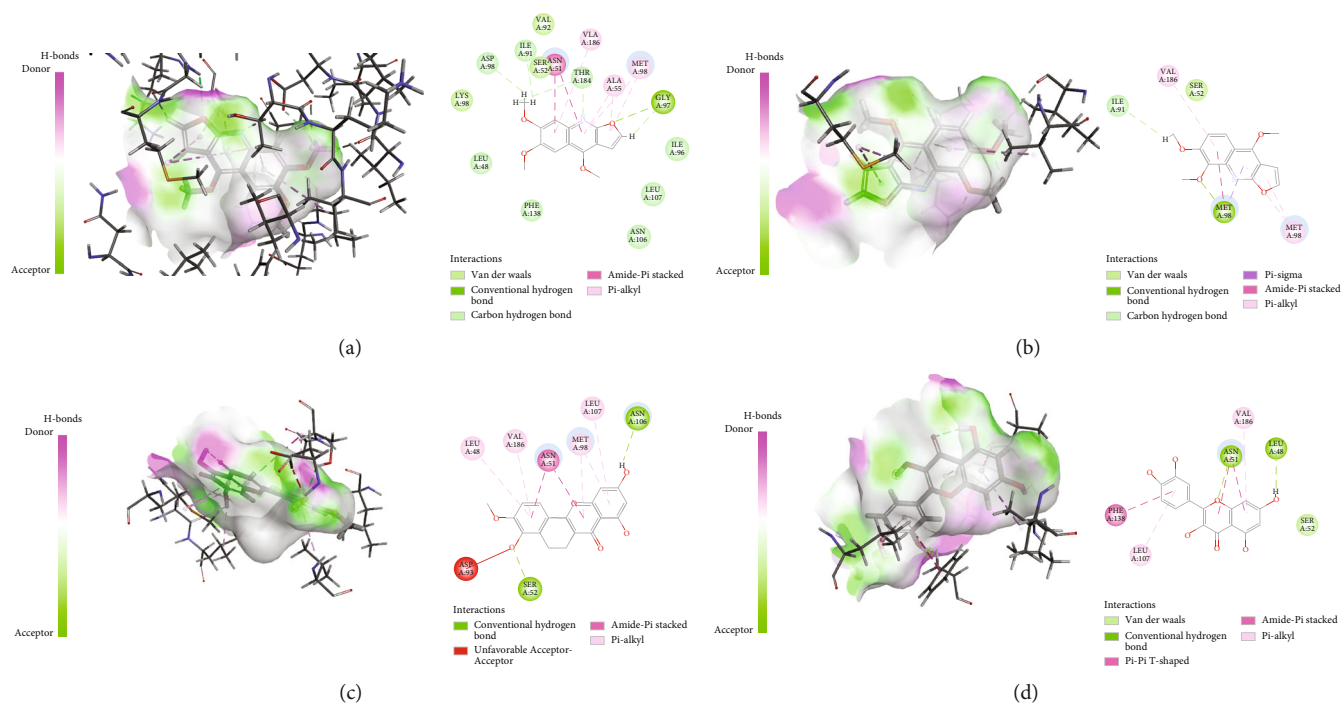
FIGURE 9: Molecular docking of HSP90AA1 with 5 main ingredients: (a) kokusaginin, (b) skimmianin, (c) diosmetin, and (d) quercetin, respectively.

4. Discussion and Conclusion

There are few studies on the treatment of diabetes-related diseases with *Zanthoxylum bungeanum* extract, and the active components, targets, and mechanisms of *Zanthoxylum bungeanum* in the treatment of DM are not completely clear. In recent years, some researchers have used network pharmacology methods and carried out systems biology, biological network construction and analysis methods to evaluate the pharmacological effects of TCM, to clarify the effective active components of TCM and potential disease targets, and then to explore the molecular mechanism of TCM to exert its efficacy [14].

In the present study, the method of network pharmacology was used to analyze and explore the active components, key targets, and signaling pathways of *Zanthoxylum bungeanum* in the treatment of DM. It was found that there were 5 active components in *Zanthoxylum bungeanum* that acted on 187 targets related to DM. The main targets to play the role of antidiabetes action are AKT1, IL6, HSP90AA1, FOS, and JUN. Using R 4.0.4 language software package and bioconductor bioinformatics software package, GO analysis and KEGG analysis were performed on the potential DM targets of *Zanthoxylum bungeanum*. The results showed that the common biological process of *Zanthoxylum bungeanum* and DM is related to positive regulation of gene expression, positive regulation of transcription, positive regulation of transcription from RNA polymerase II promoter, response to drug, positive regulation of apoptotic process, positive regulation of cell proliferation, etc. The mechanism of action of *Zanthoxylum bungeanum* in the treatment of DM involves multiple pathways including positive regulation of gene expression, positive regulation of transcription, positive regulation of transcription from RNA polymerase II promoter, response to drug, and positive regulation of apoptotic process, etc.

The main active components of *Zanthoxylum bungeanum* were kokusaginin, skimmianin, diosmetin, beta-sitosterol, and quercetin, respectively, of top 5 analyzed by network pharmacology. It was reported that kokusaginin as an anti-multidrug resistance agent in chemotherapy for breast carcinoma which is closed with AKT pathway [13]. In addition, it was reported that kokusaginine's potential as a good inhibitor against hepatitis C virus and type 2 diabetes [15, 16]. It was revealed that skimmianin treatment suppressed the transcription of TNF-a and IL-6 genes, highlighting the downregulation of cytokine production and subsequent production of PGE2, inhibited NO production, indicating its anti-inflammatory effect [17]. A previous study showed that diosmetin protects against renal injury in streptozotocin- (STZ-) induced diabetic nephropathy mice by modulating the AKT/NF-κB/iNOS signaling pathway [18]. It was also found that diosmetin ameliorate type 2 diabetic mellitus by upregulating *Corynebacterium glutamicum* to regulate IRS/PI3K/AKT-mediated glucose metabolism disorder in mice [19]. Beta-sitosterol is a plant sterol which has the similar chemical structure like cholesterol [20]. Previous findings indicated that beta-sitosterol improves glycemic control through activation of IR in the adipose tissue of high-fat and sucrose-induced type-2 diabetic rats [21]. Quercetin is a polyphenol which has been shown in vitro as well as in a few animal models to have several
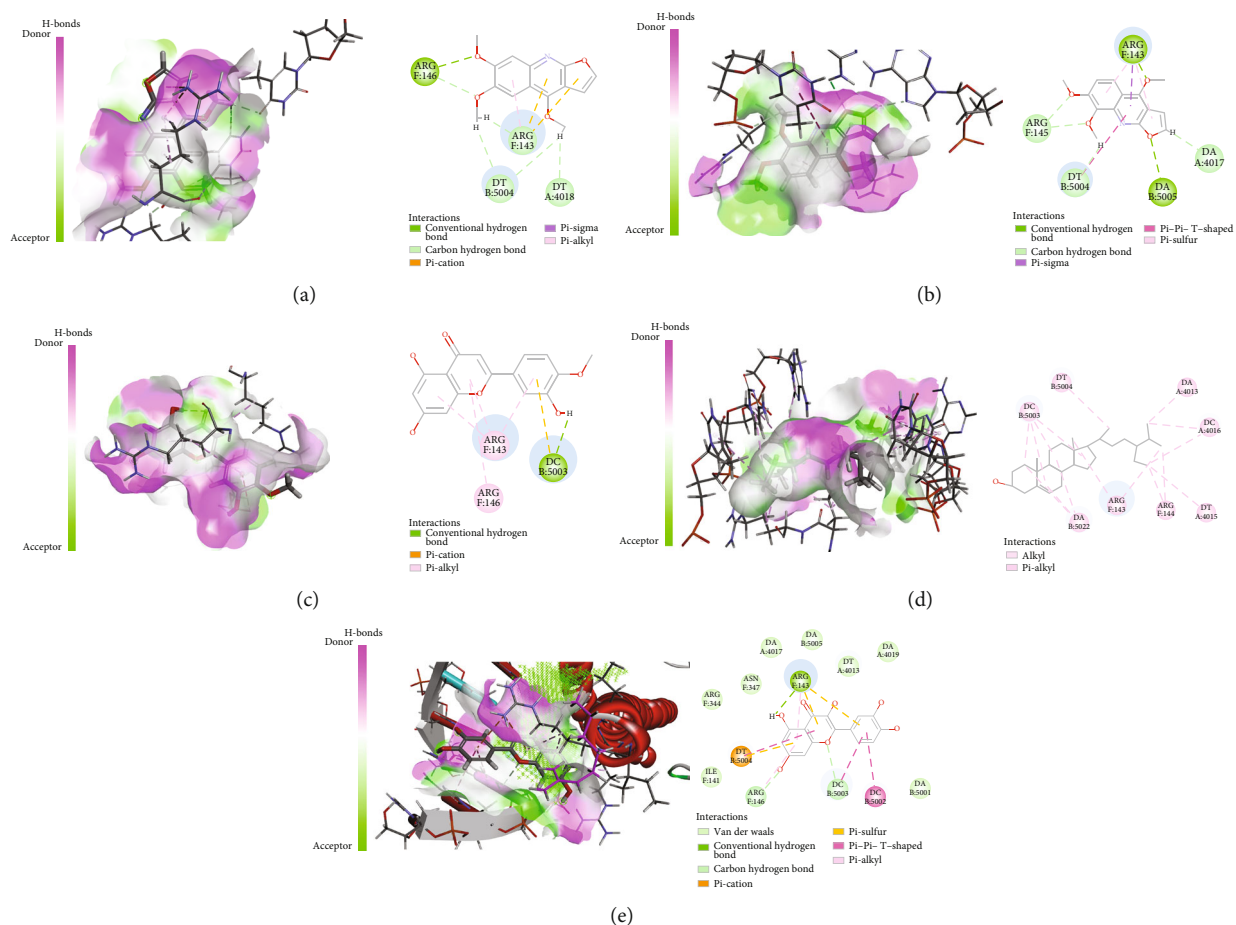
FIGURE 10: Molecular docking of FOS with 5 main ingredients: (a) kokusaginin, (b) skimmianin, (c) diosmetin, (d) beta-sitosterol, and (e) quercetin, respectively.
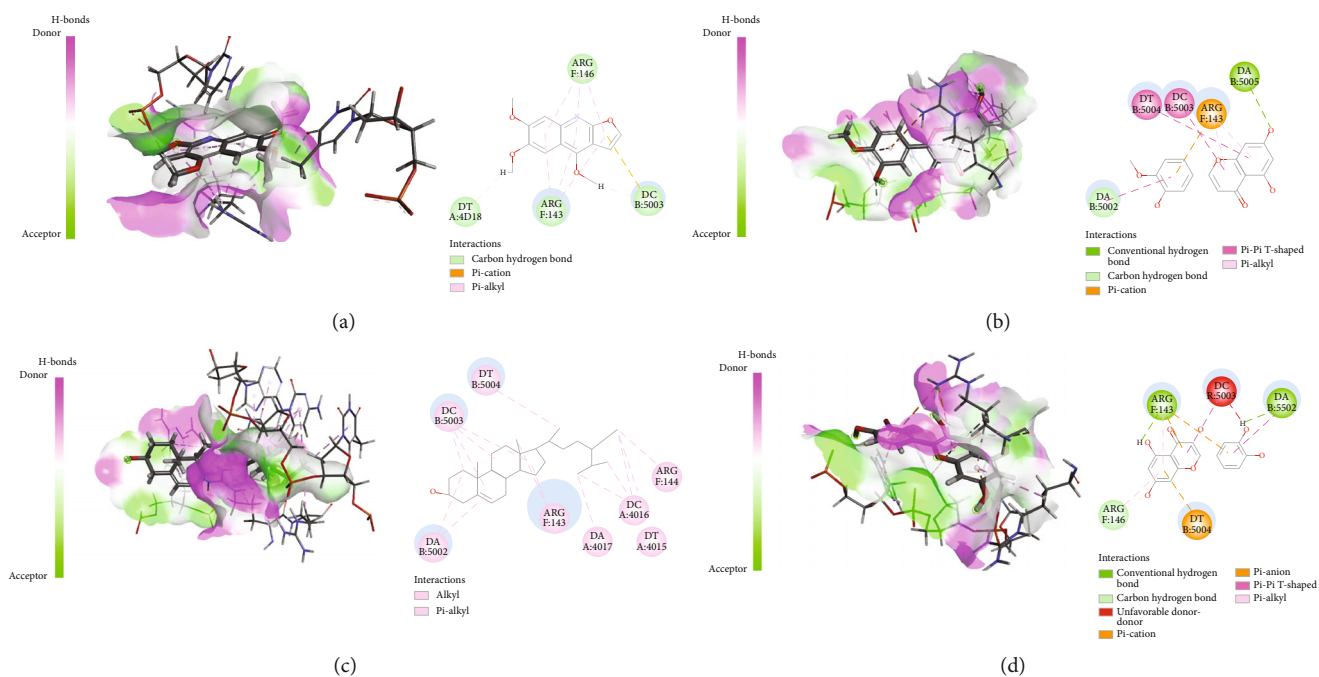
FIGURE 11: Molecular docking of JUN with 5 main ingredients: (a) kokusaginin, (b) diosmetin, (c) beta-sitosterol, and (d) quercetin, respectively.
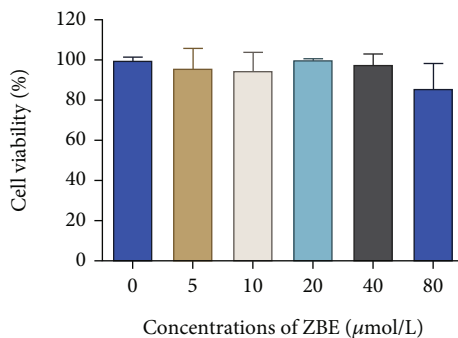
FIGURE 12: Effects of different concentrations of ZBE on HepG2 cell cytotoxicity/viability.

(a)   (b)
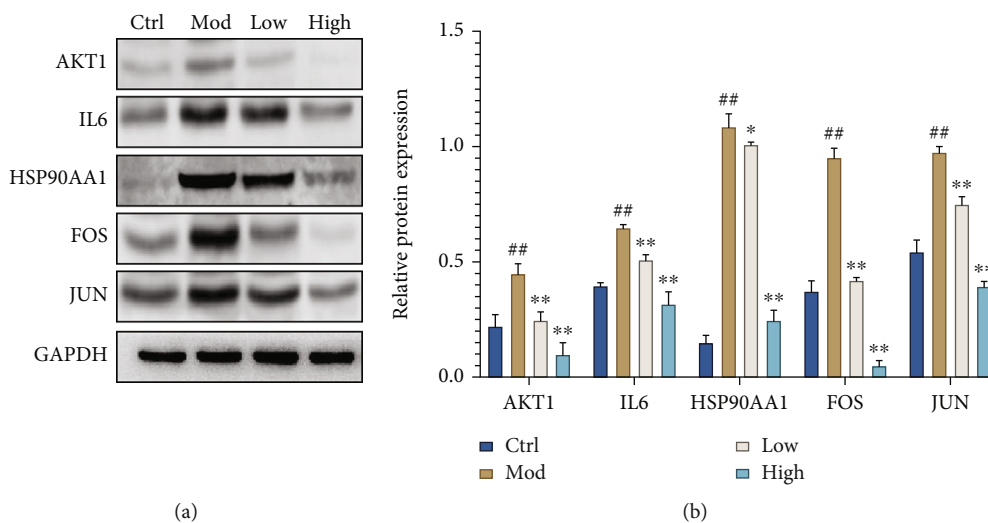
FIGURE 13: Effect of ZBE on expressions of AKT, P-AKT, FOXO1, P-FOXO1, and JNK proteins in HepG2 cells. The data represent the mean $\pm$ SD ($n = 6$). **$P < 0.05$ and **$P < 0.01$ vs. the control group; #$P < 0.05$ and ##$P < 0.01$ vs. the model group.

potential anti-inflammatory as well as anticarcinogenic applications. It was revealed that quercetin exhibits anti-inflammatory properties in relation to obesity and type 2 diabetic mellitus [22]. Furthermore, it has been demonstrated that quercetin could be used to successfully prevent some of the clinical complications of diabetes [23]. A previous study also showed that quercetin intake was inversely related to the prevalence of type 2 diabetic mellitus in the Chinese population, suggesting a protective effect of quercetin in the development of type 2 diabetic mellitus [24]. Above all, all the active components of *Zanthoxylum bungeanum* exhibits various effects in the treatment of DM especially diosmetin, quercetin, and beta-sitosterol which is similar with our prediction.

AKT1 is one of 3 closely related serine/threonine protein kinases (AKT1, AKT2, and AKT3) known as AKT kinases, and it regulates many processes, including metabolism, proliferation, cell survival, growth, and angiogenesis. AKT is an important target kinase downstream of PI3K. PIP3 can bind to AKT, transfer AKT from the cytoplasm to the cell membrane, and phosphorylate Ser473 and Thr308 to fully activate AKT, thereby initiating the PI3K/AKT signaling pathway [25]. It was reported that the PI3K-AKT signaling

pathway may inhibit the gluconeogenesis pathway and reduce the output of glucose, thereby exerting a hypoglycemic effect in db/db mice [26]. Previous studies have reported that *Zanthoxylum bungeanum* extract may play a hypoglycemic effect by downregulating PGC-1α in the liver [27]. Inflammation is closely related to the occurrence and development of diabetes. IL-6, as an important cytokine in inflammatory response, has a high content in the serum of patients with diabetes [28]. The *Zanthoxylum bungeanum* extract has an anti-inflammatory effect by inhibiting the release of TNF-α and IL-6 [29]. It is speculated that *Zanthoxylum bungeanum* may play a hypoglycemic effect by inhibiting the inflammatory response. The pathways involved in HSP90AA1 include BH4 synthesis, recycling, recovery, and regulation, eNOS activation, and VEGFR2-mediated vascular permeability [30], consistent with the pathways involved in the treatment of diabetes by *Zanthoxylum bungeanum*. As a class of nuclear protein transcription factors, FOS proteins play an important role in regulating cell growth, division, proliferation, and programmed death [31]. It was reported that the reduced expression of the immediate early gene FOS as an indicator of pain transmission supports the diabetes-induced loss of sensation in this

type 1 model of diabetes [32]. C-JUN protein is one of the activating protein-1 (AP-1) transcription complexes and is the most transcriptionally active transcription factor in the AP-1 complex. C-JUN protein expression and activation can be stimulated, thereby regulating biological processes such as cell proliferation and apoptosis [33]. The inflammatory kinase JNK is proposed to be a key player, as whole-body JNK1-null mice protects against obesity-induced insulin resistance. This presents a potential therapeutic target (JUN) to restore insulin sensitivity and preserve β-cell function [34].

Taken together, the active components of *Zanthoxylum bungeanum* mainly including kokusaginin, skimmianin, diosmetin, beta-sitosterol, and quercetin. The findings indicated that AKT1, IL6, HSP90AA1, FOS, and JUN are the most likely targets for *Zanthoxylum bungeanum* on treating DM. Experiment verification results revealed that DM could be significantly improved by downregulating the expression of AKT1, IL6, HSP90AA1, FOS, and JUN proteins after administrated 20 μmol/L and 40 μmol/L of ZBE. *Zanthoxylum bungeanum* is an effective drug in treatment of DM related to above core targets. The present study preliminarily clarifies that *Zanthoxylum bungeanum* may treat DM through multitargets and multipathways, which provides a new idea and points out a new direction for further experimental research and clinical application.

Data Availability

All data included or relevant to the study are available upon request by contact with the corresponding author.

Conflicts of Interest

All authors declare that there have not any commercial or associative interest that represents competing interests in connection with the work submitted.

Authors' Contributions

Jingxin Mao and Lai Zhang conceived and designed the research. Yuanshe Huang, Zhaomiao Gong, Jingxin Mao, Chen Yan, Ke Zheng, and E Liang carried out the analysis and wrote the paper in the study. Jingxin Mao, Lidan Zhang, and E Liang finished the drawing and manuscript revision work. Yuanshe Huang and Zhaomiao Gong contributed equally to this work.

Acknowledgments

References

[1] R. Williams, S. Karuranga, B. Malanda et al., "Global and regional estimates and projections of diabetes-related health expenditure: results from the International Diabetes Federation Diabetes Atlas, 9th edition," *Diabetes Research and Clinical Practice*, vol. 162, article 108072, 2020.

[2] P. Saeedi, I. Petersohn, P. Salpea et al., "Global and regional diabetes prevalence estimates for 2019 and projections for 2030 and 2045: results from the International Diabetes Federation Diabetes Atlas, 9th edition," *Diabetes Research and Clinical Practice*, vol. 157, article 107843, 2019.

[3] G. Roglic, "WHO global report on diabetes: a summary," *International Journal of Noncommunicable Diseases*, vol. 1, no. 1, p. 3, 2016.

[4] R. Krishnamoorthi, S. Joshi, H. Z. Almarzouki et al., "A novel diabetes healthcare disease prediction framework using machine learning techniques," *Engineering*, vol. 2022, Article ID 1684017, 10 pages, 2022.

[5] J. McSharry, M. Byrne, B. Casey et al., "Behaviour change in diabetes: behavioural science advancements to support the use of theory," *Diabetic Medicine*, vol. 37, no. 3, pp. 455–463, 2020.

[6] M. Zhang, J. Wang, L. Zhu et al., "Zanthoxylum bungeanum Maxim.(Rutaceae): a systematic review of its traditional uses, botany, phytochemistry, pharmacology, pharmacokinetics, and toxicology," *International Journal of Molecular Sciences*, vol. 18, no. 10, p. 2172, 2017.

[7] P. C. Chinese, *Pharmacopoeia of the People's Republic of China*, China Medical Science Press, Beijing, China, 2020.

[8] Z. Nooreen, S. Tandon, N. P. Yadav, P. Kumar, T. D. Xuan, and A. Ahmad, "Zanthoxylum: a review of its traditional uses, naturally occurring constituents and pharmacological properties," *Current Organic Chemistry*, vol. 23, no. 12, pp. 1307–1341, 2019.

[9] L. Chen, M. B. Hu, Z. Y. Chen, G. Wang, Q. Su, and Y. J. Liu, "Preparation, structural characterization and neuroprotective effects of polysaccharides from the pericarp of _Zanthoxylum bungeanum_ Maxim against H_2O_2-induced oxidative damage in PC12 cells," *South African Journal of Botany*, vol. 142, pp. 165–174, 2021.

[10] X. Wei, B. Yang, G. Chen et al., "Zanthoxylumalkylamides improve amino acid metabolism in type 2 diabetes mellitus rats," *Journal of Food Biochemistry*, vol. 44, no. 10, article e13441, 2020.

[11] Y. Zhang, M. Wang, H. Dong, X. Yu, and J. Zhang, "Anti-hypoglycemic and hepatocyte-protective effects of hyperoside from Zanthoxylum bungeanum leaves in mice with high-carbohydrate/high-fat diet and alloxan-induced diabetes," *International Journal of Molecular Medicine*, vol. 41, no. 1, pp. 77–86, 2018.

[12] Z. Zhou, B. Chen, S. Chen et al., "Applications of network pharmacology in traditional Chinese medicine research," *Evidence-based Complementary and Alternative Medicine*, vol. 2020, Article ID 1646905, 7 pages, 2020.

[13] H. Chen, S. Li, S. Wang, W. Li, N. Bao, and W. Ai, "The inhibitory effect of kokusaginine on the growth of human breast cancer cells and MDR-resistant cells is mediated by the inhibition of tubulin assembly," *Bioorganic & Medicinal Chemistry Letters*, vol. 28, no. 14, pp. 2490–2492, 2018.

[14] W. Zhou and Y. Wang, "A network-based analysis of the types of coronary artery disease from traditional Chinese medicine perspective: potential for therapeutics and drug discovery," *Journal of Ethnopharmacology*, vol. 151, no. 1, pp. 66–77, 2014.

[15] T. S. Wahyuni, A. Widyawaruyanti, M. I. Lusida et al., "Inhibition of hepatitis C virus replication by chalepin and pseudane IX isolated from _Ruta angustifolia_ leaves," *Fitoterapia*, vol. 99, pp. 276–283, 2014.

[16] J. S. M. Richardson, N. Aminudin, and S. N. Abd Malek, "Chalepin: a compound from Ruta angustifolia L. Pers exhibits cell cycle arrest at S phase, suppresses nuclear factor-kappa B (NF-κB) pathway, signal transducer and activation of transcription 3 (STAT3) phosphorylation and extrinsic apoptotic pathway in non-small cell lung cancer carcinoma (A549)," *Pharmacognosy Magazine*, vol. 13, Suppl 3, pp. S489–S498, 2017.

[17] M. Ratheesh, G. Sindhu, and A. Helen, "Anti-inflammatory effect of quinoline alkaloid skimmianine isolated from Ruta graveolens L," *Inflammation Research*, vol. 62, no. 4, pp. 367–376, 2013.

[18] Y. Jiang, J. Liu, Z. Zhou, K. Liu, and C. Liu, "Diosmetin attenuates Akt signaling pathway by modulating nuclear factor kappa-light-chain-enhancer of activated B cells (NF-κB)/inducible nitric oxide synthase (iNOS) in streptozotocin (STZ)-induced diabetic nephropathy mice," *Medical Science Monitor: International Medical Journal of Experimental and Clinical Research*, vol. 24, pp. 7007–7014, 2018.

[19] X. Gong, L. Xiong, C. Bi, and B. Zhang, "Diosmetin ameliorate type 2 diabetic mellitus by up-regulating _Corynebacterium glutamicum_ to regulate IRS/PI3K/AKT-mediated glucose metabolism disorder in KK-Ay mice," *Phytomedicine*, vol. 87, article 153582, 2021.

[20] R. Ponnulakshmi, B. Shyamaladevi, P. Vijayalakshmi, and J. Selvaraj, "In silico and in vivo analysis to identify the antidiabetic activity of beta sitosterol in adipose tissue of high fat diet and sucrose induced type-2 diabetic experimental rats," *Toxicology Mechanisms and Methods*, vol. 29, no. 4, pp. 276–290, 2019.

[21] S. Babu, M. Krishnan, P. Rajagopal et al., "Beta-sitosterol attenuates insulin resistance in adipose tissue via IRS-1/Akt mediated insulin signaling in high fat diet and sucrose induced type-2 diabetic rats," *European Journal of Pharmacology*, vol. 873, article 173004, 2020.

[22] S. Chen, H. Jiang, X. Wu, and J. Fang, "Therapeutic effects of quercetin on inflammation, obesity, and type 2 diabetes," *Mediators of Inflammation*, vol. 2016, Article ID 9340637, 5 pages, 2016.

[23] G. J. Shi, Y. Li, Q. H. Cao et al., "In vitro and in vivo evidence that quercetin protects against diabetes and its complications: a systematic review of the literature," *Biomedicine & Pharmacotherapy*, vol. 109, pp. 1085–1099, 2019.

[24] Z. Yao, Y. Gu, Q. Zhang et al., "Estimated daily quercetin intake and association with the prevalence of type 2 diabetes mellitus in Chinese adults," *European Journal of Nutrition*, vol. 58, no. 2, pp. 819–830, 2019.

[25] T. F. Franke, S. I. Yang, T. O. Chan et al., "The protein kinase encoded by the _Akt_ proto-oncogene is a target of the PDGF-activated phosphatidylinositol 3-kinase," *Cell*, vol. 81, no. 5, pp. 727–736, 1995.

[26] Y. Gao, M. Zhang, R. Zhang, L. You, T. Li, and R. H. Liu, "Whole grain brown rice extrudate ameliorates the symptoms of diabetes by activating the IRS1/PI3K/AKT insulin pathway in db/db mice," *Journal of Agricultural and Food Chemistry*, vol. 67, no. 42, pp. 11657–11664, 2019.

[27] X. Li, Y. Zhang, S. Wang et al., "A review on the potential use of natural products in overweight and obesity," *Phytotherapy Research*, vol. 36, no. 5, pp. 1990–2015, 2022.

[28] J. C. Pickup, G. D. Chusney, S. M. Thomas, and D. Burt, "Plasma interleukin-6, tumour necrosis factor α and blood cytokine production in type 2 diabetes," *Life Sciences*, vol. 67, no. 3, pp. 291–300, 2000.

[29] J. Hou, J. Wang, J. Meng et al., "_Zanthoxylum bungeanum_ seed oil attenuates LPS-induced BEAS-2B cell activation and inflammation by inhibiting the TLR4/MyD88/NF- _κ_ B signaling pathway," *Evidence-based Complementary and Alternative Medicine*, vol. 2021, Article ID 2073296, 13 pages, 2021.

[30] A. Oliveros-Díaz, J. Olivero-Verbel, Y. Pájaro-González, and F. Díaz-Castillo, "Molecular human targets of bioactive alkaloid-type compounds from Tabernaemontana cymose Jacq," *Molecules*, vol. 26, no. 12, p. 3765, 2021.

[31] E. Shaulian and M. Karin, "AP-1 in cell proliferation and survival," *Oncogene*, vol. 20, no. 19, pp. 2390–2400, 2001.

[32] M. S. Johnson, J. M. Ryals, and D. E. Wright, "Diabetes-induced chemogenic hypoalgesia is paralleled by attenuated stimulus- induced Fos expression in the spinal cord of diabetic mice," *The Journal of Pain*, vol. 8, no. 8, pp. 637–649, 2007.

[33] S. Ogawa, J. Lozach, K. Jepsen et al., "A nuclear receptor corepressor transcriptional checkpoint controlling activator protein 1-dependent gene networks required for macrophage activation," *Proceedings of the National Academy of Sciences*, vol. 101, no. 40, pp. 14461–14466, 2004.

[34] J. H. M. Yung and A. Giacca, "Role of c-Jun N-terminal kinase (JNK) in obesity and type 2 diabetes," *Cell*, vol. 9, no. 3, p. 706, 2020.

Research Article

Huoxiang Zhengqi Oral Liquid Attenuates LPS-Induced Acute Lung Injury by Modulating Short-Chain Fatty Acid Levels and TLR4/NF-κB p65 Pathway

Ruying Tang ,[1] **Jianjun Zhang** ,[2] **Rui Zhang** ,[2] **Xinyu Li,**[3] **Ruilin Lv,**[1] **Haipeng Nan,**[1] **Jinlian Liu,**[2] **Zhongpeng Zhao,**[3] **Wei He,**[3] **and Linyuan Wang** [1]

[1]*School of Chinese Materia Medica, Beijing University of Chinese Medicine, Beijing, China*
[2]*School of Traditional Chinese Medicine, Beijing University of Chinese Medicine, Beijing, China*
[3]*School of Basic Medical Sciences, Anhui Medical University, Hefei, China*

Correspondence should be addressed to Linyuan Wang; wangly@bucm.edu.cn

Huoxiang Zhengqi Oral Liquid (HZOL) is a classic Chinese patent medicine used in China for more than 1,000 years in treating gastrointestinal and respiratory diseases. Clinically applied HZOL in early respiratory disease stages can reduce the proportion of lung infection patients that progress to severe acute lung injury (ALI). However, few pharmacological studies evaluated its level of protection against ALI. We explored mechanisms of HZOL against ALI by employing network pharmacology, molecular docking, and rat experiments. Firstly, network pharmacology prediction and published biological evaluation of active ingredients of HZOL suggested that HZOL exerted the protective effect in treating ALI mainly in the areas of regulation of cell adhesion, immune response, and inflammatory response and closely related to the NF-κB pathway. Secondly, molecular docking results demonstrated that imperatorin and isoimperatorin combined well with targets in the NF-κB pathway. Finally, ALI rats induced by lipopolysaccharides (LPS) were used to validate prediction after pretreatment with HZOL for 2 weeks. Results confirmed that lung and colon injury occurred in ALI rats. Furthermore, HZOL exerts anti-inflammatory effects on LPS-induced ALI and gut injury by repairing lung and colon pathology, reducing and alleviating pulmonary edema, inhibiting abnormal enhancement of thymus and spleen index, modulating hematologic indices, and increasing levels of total short-chain fatty acids (SCFAs) in the cecum. Additionally, abnormal accumulation of inflammatory cytokines IL-6, IL-1β, TNF-α, and IFN-γ in serum and bronchoalveolar lavage fluid was significantly reduced after pretreating with HZOL. Furthermore, HZOL downregulated the expression of TLR4, CD14, and MyD88 and phosphorylation of NF-κB p65 in lung tissue. Altogether, HZOL was found to exert an anti-inflammatory effect regulation by increasing levels of SCFAs, inhibiting the accumulation of inflammatory cytokines, and attenuating the activation of the TLR4/NF-κB p65 pathway. Our study provided experimental evidences for the application of HZOL in preventing and treating ALI.

1. Introduction

Acute lung injury (ALI) has the pathophysiological characteristic of morphologic and functional lung abnormalities caused by the destruction of pulmonary capillaries and alveolar epithelia, resulting in severe inflammation in the lung [1, 2]. Acute lung injury (ALI), with the high mortality rate of 40%, is usually caused by various pathogenic factors, such as pathogenic microorganism infections. ALI is characterized by acute respiratory distress syndrome and refractory hypoxemia, accompanied by gastrointestinal dysfunction [3]. At the earliest stage of ALI, cytokine upregulation—represented by eradication or containment of invading microbes—and lung permeability increase, along with recruitment of inflammatory cells, followed by further aggravation if the ALI goes untreated [4]. As a result, lung

inflammation and vascular hyperpermeability continue to worsen, often leading to acute respiratory distress syndrome (ARDS). Evidences from experimental studies have proved that through intraperitoneal injection, lipopolysaccharides (LPS) can induce not only acute lung injury but also intestinal injury [5]. Importantly, in the pathological state of LPS-induced inflammation and immune disorders in the ALI animal model, not only was an accumulation of inflammatory cytokine observed in the lung, but also short-chain fatty acid (SCFA) disbalance occurred in the cecum, demonstrating a close association in the lung-gut axis of ALI [6]. ALI can increase intestinal bacterial load, while it can decrease total SCFAs and individual SCFAs (acetic, propionic, butyric, valeric, and isobutyric acids) in the cecum [7]. Commonly, most SCFAs are produced in the cecum and proximal colon, which provides energy and nutrients for the microbiota. Especially, SCFAs are representative metabolites of the microbiota and are also associated with the lung and gut damage. It is an effective strategy to treat ALI from the lung-gut axis by inhibiting lung inflammation and modulating gut injury.

Clinically, aspirin, salbutamol, and ketoconazole are commonly used as anti-inflammatory drugs which have some side effects; finding the treatments for ALI safely and effectively is meaningful [8]. In recent years, the prevention and treatment of ALI with TCM formulas have increasingly indicated the advantages of using TCM theory. Of note, significant positive effects have been achieved using Traditional Chinese Medicine (TCM) in treating ALI. Huoxiang Zhengqi Oral Liquid (HZOL) is the adjuvant preventive treatment of pulmonary inflammation in China [9]. HZOL is typically used in treating gastrointestinal and pulmonary diseases as it confers a number of pharmacological benefits, including antibacterial, analgesic, and antiviral effects, along with regulation of gastrointestinal function [10]. It is often used in the clinical treatment of functional dyspepsia, diarrhea, acute gastroenteritis, gastrointestinal cold, and other diseases. It can be used not only to regulate gastrointestinal diseases including irritable bowel syndrome, vomiting, and diarrhea but also to treat influenza-like lung diseases resulting from wind chill or heat dampness, in line with the TCM theory [11].

Modern studies have revealed that the active ingredients of HZOL and its pharmacological experiments have demonstrated that these ingredients exhibit antiulcerative, antibacterial, anti-inflammatory, and antiviral effects [12–15]. HZOL is used clinically in China for over 1,000 years in treating gastrointestinal-type colds on account of its anti-inflammatory properties and positive effects on immunological regulation. The main manifestations of gastrointestinal-type cold refer to influenza with gastrointestinal symptoms, which are caused by wind, cold, heat, and dampness invading the muscle surface and digestive systems according to the theory of TCM. HZOL exerts anti-inflammatory effect and immune regulation in gastrointestinal diseases in previous studies [16, 17]. However, detailed mechanisms of HZOL as an agent in lung disease remain unclear. Researches have verified that the active ingredients of HZOL exert anti-inflammatory, antibacterial, and immunomodulatory effects, which are effective in the treatment of ALI.

Therefore, the therapeutic effect and mechanism of HZOL in treating ALI were performed in this study.

At present, network pharmacology can be used to theoretically analyze multiple compounds and targets to predict the therapeutic mechanisms of action of TCMs in relation to treating diseases based on different databases [18]. An increasing number of studies on TCM formulations use network pharmacology to explore their pharmacodynamic mechanism [19, 20]. Furthermore, molecular docking was an auxiliary validation of network pharmacology. Therefore, we employed network pharmacology to identify putative targets and candidate pathways of HZOL against ALI. Then, molecular docking was employed to verify interaction between active components and pathway target proteins to further explore the molecular mechanism of network pharmacology prediction results. Finally, we validated the mechanism of HZOL in ALI model rats induced by LPS according to the predicted results and measured the content levels of SCFAs in the cecum. In summary, mechanisms of HZOL in treating ALI and gut injury were performed. Figure 1 shows the study procedures.

2. Materials and Methods

2.1. Network Pharmacology and Molecular Docking. In accordance with the study conducted by [21], we performed a network pharmacological analysis of Huoxiang Zhengqi Oral Liquid (HZOL). Firstly, we collected information about the eight published active ingredients of HZOL—honokiol, magnolol, hesperidin, liquiritin, naringin, thymol, imperatorin, and isoimperatorin—from the PubChem database [12, 15]. Next, DrugBank, BATMEN-TCM, and Swiss Target databases were used to collect potential targets. Then, the OMIM and DisGeNET databases were used to research ALI targets using the keyword "Acute Lung Injury." All of these targets were normalized in UniProt. Then, common targets were acquired using a tool to calculate and draw custom Venn diagrams. Next, a common target PPI network was constructed and the top five hub genes were obtained. GO and KEGG analyses were performed by the DAVID online database; then, "functional annotation clustering" was selected to export the data and screen the key pathway. Finally, molecular docking was done to predict the interaction of ingredient ligands and target receptors. The crystal structures of targets in the predicted key pathway were downloaded from the RCSB PDB database, while the structures of eight published active ingredients of HZOL were obtained from the TCMSP database. Then, we used the AutoDock 4.2.6 software to remove ligands, structure water molecules, and add polar hydrogen atoms and charges to the protein crystal structures before docking. Finally, the Discovery Studio software was used to evaluate the interaction between the targets and the active ingredients.

2.2. Preparation of Drugs. HZOL was purchased from the Taiji Group Chongqing Fuling Pharmaceutical Co., Ltd. Production of HZOL following the Chinese Pharmacopeia 2015 (Approved number, Z50020409; Lot number, 20071956). Quality of HZOL was able to ascertain both stability and
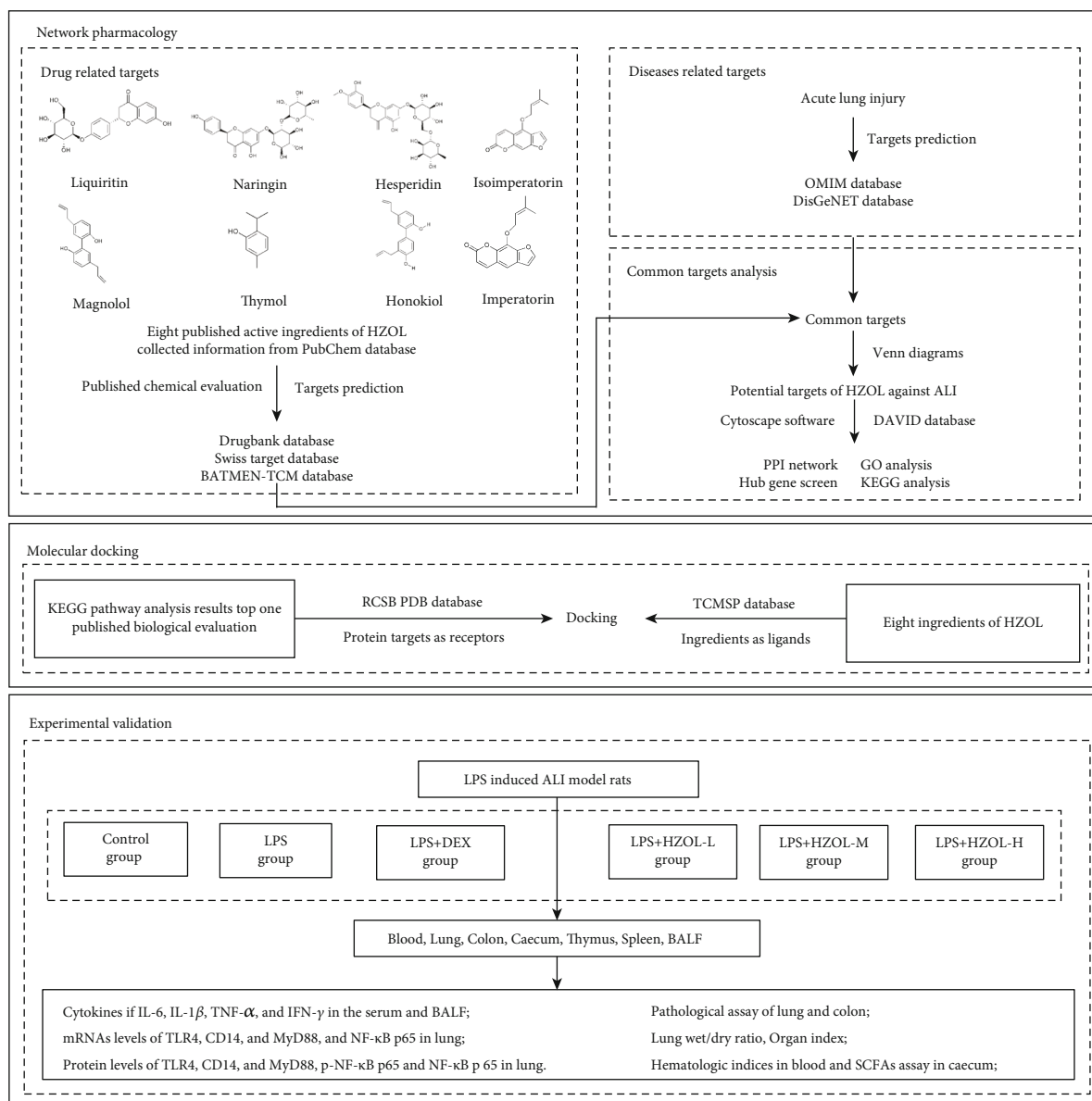
Figure 1: Procedures in this study.

controllability. Introduction of HZOL was follows: firstly, prescription of HZOL consists of ten herbs including Atractylodis Rhizoma 80 g, Magnoliae Officinalis Cortex 80 g, Poria 120 g, Pinelliae Rhizoma 80 g, Citri Reticulatae Pericarpium 80 g, Angelicae Dahuricae Radix 120 g, Arecae Pericarpium 120 g, Licorice extract 10 g, Patchouli oil 0.8 mL, and volatile oil in Perillae Folium 0.4 mL. Secondly, HZOL was standardised prepared following the method of the criteria of the Chinese Pharmacopeia 2015 as previous study described [10]. Thirdly, content determination of HZOL was controlled with magnolol, honokiol, and hesperidin. In a nutshell, per milliliter of HZOL contained magnolol and honokiol no less than 0.30 mg and hesperidin no less than 0.10 mg.

2.3. Animals and Treatment. Healthy male Wistar rats weighing 180–200 g (12 weeks, permit number SCXK, Beijing, 2016-0002) were purchased from SPF (Beijing) Bio-

technology Co., Ltd. (Beijing, China) and kept in standard cages with standard laboratory animal feed and water. The rats were housed at a constant temperature of $22 \pm 2°C$ and a relative humidity of $55 \pm 5\%$, with 12 h day/night cycles. The use of rats and the experimental protocols were reviewed and approved by the Institutional Animal Care and Use Committee at Beijing University of Chinese Medicine (No. BUCM-4-2020100907-4029).

A total of 60 rats were randomly divided into six groups ($n = 10$), and the used dose administration was as follows: a control group (control), lipopolysaccharide group (LPS), LPS+dexamethasone group (LPS+DEX), LPS+HZOL low-dose group (LPS+HZOL-L), LPS+HZOL middle-dose group (LPS+HZOL-M), and LPS+HZOL high-dose group (LPS+HZOL-H). The daily dose of HZOL for human adults is 0.33 mL/kg (clinical dose is 20 mL/one day/60 kg body weight of one person), and the equivalent dose in rat is 10-

fold that of adults in previous reported research (3.33 mL/ kg/d, 10-fold of the clinical dose) [10]. The rats except the control group were administered a single dose of LPS (5 mg/kg, Escherichia coli 055: B5 L2880, Sigma, USA) intraperitoneally according to a previous study [22]. The rats in the LPS+HZOL groups received an oral administration of the agents for 2 weeks before LPS injection at different doses (LPS+HZOL-L, 1.67 mL/kg, 5-fold of the clinical dose; LPS +HZOL-M, 3.33 mL/kg, 10-fold of the clinical dose; and LPS+HZOL-H, 6.67 mL/kg, 20-fold of the clinical dose) following a previous study [10], while DEX (5 mg/kg) was administrated via stomach perfusion for six days before the LPS treatments [18, 23]. The dosage was adjusted according to the body weight of rats. After 6 h LPS administration, the animals were anaesthetized with 20% urethane (5 mL/kg) by intraperitoneal injection and related biological samples were collected.

2.4. Pathological Assay and Pathology Scores. We obtained partial sections of lung tissues and colon tissues. We routinely fixed the tissue with 4% paraformaldehyde and then gradient dehydration. The samples were cut, embedded in paraffin, bleached, and stained in hematoxylin and eosin (H&E). The score of lung injury and colon injury was performed by other investigators who were blinded to the study. For the lung injury, scoring principles were as follows: (1) alveolar congestion, (2) hemorrhage, (3) infiltration of neutrophils in the airspace or vessel wall, and (4) thickness of the alveolar wall formation. Each lung injury item was scored as follows: no damage or minimal damage = 0, mild damage = 1, moderate damage = 2, severe damage = 3, and diffuse injury = 4. Then, the lung injury was scored according to previous study and all scores were added up to obtain a total score [23, 24]. Besides, the total histological score for colon injury ranges from 0 to 8 according to previous study as follows: epithelium: normal morphology = 0, loss of goblet cells = 1, loss of goblet cells in large areas = 2, loss of crypts = 3, and loss of crypts in large areas =4; infiltration: no infiltrate = 0, infiltrate around crypts = 1, infiltrate into the lamina muscularis mucosae = 2, extensive infiltration into the lamina muscularis mucosae and thickening of the mucosa = 3, and infiltration of the submucosal layer = 4 [25].

2.5. Lung Wet/Dry Ratio and Organ Index. In accordance with the reported study, we calculated lung wet/dry ratio = wet weight/dry weight [23]. In addition, the whole body and absolute thymus and spleen weights were recorded, and the organ index was calculated as organ index = absolute organ weight/body weight.

2.6. Hematologic Index Assay. Using a Mindray automatic animal blood cell analyzer (BC-2800 VET, Shenzhen, China), part of the whole blood was collected in an EDTA-treated blood collection tube for the determination of white blood cell (WBC) count, granulocyte concentration (GRAN%), basophil concentration (BASO%), eosinophil concentration (EOS%), lymphocyte concentration (LYM%), and blood platelet count (PLT).

TABLE 1: Primers for RT-qPCR.

Primer name	Sequence (5′ to 3′)
TLR4	
Forward	CCAGGTGTGAAATTGAGACAATTG
Reverse	AAGCTGTCCAATATGGAAACCC
CD14	
Forward	CGGGTTCCTACTCAGATTCTATTCG
Reverse	CGAGCCAGGTATCCGTTGTT
MyD88	
Forward	AAGGTGTCGTCGCATGGTG
Reverse	TTGGTGCAAGGGGTTGGTATAGT
NF-κB p65	
Forward	ACCTGTTCCAAAGAGCACCCA
Reverse	GGTCTGTGAACACTCCTGGGTC
GAPDH	
Forward	CTGGAGAAACCTGCCAAGTATG
Reverse	GGTGGAAGAATGGGAGTTGCT

2.7. Enzyme-Linked Immunosorbent Assay (ELISA). The serum samples were obtained through separation from anterior blood samples. Besides, the bronchoalveolar lavage fluid (BALF) was collected from the left lung by bronchial intubation. Normal saline with a total volume of 3 mL was instilled and retrieved three times. Finally, the cytokines interleukin-6 (IL-6), interleukin-1β (IL-1β), tumor necrosis factor-α (TNF-α), and interferon-γ (IFN-γ) in the serum and BALF samples were measured using commercially available ELISA kits (Ray Biotech. Inc., USA; ProteinTech®, Chicago, IL, USA).

2.8. Real-Time Quantitative Polymerase Chain Reaction (RT-qPCR) Analysis. Levels of Toll-like receptor 4 (TLR4), cluster of differentiation 14 (CD14), myeloid differentiation factor 88 (MyD88), and nuclear factor-kappa B (NF-κB p65) mRNAs were identified by RT-qPCR. Lung tissues were dissociated with TRIzol reagent, and total RNA was determined. Then, RNA of each sample was utilized to synthesize the first-strand cDNA. Table 1 shows the sequences for primers. Next, the cDNA was amplified. $2^{-\Delta\Delta Ct}$ method was used for quantification.

2.9. Western Blot Analysis. The concentration of total proteins in lung tissues was tested using a BCA kit. Next, 40 μg of protein samples was dissolved in an equal volume of loading buffer and was then separated by 10% SDS-PAGE and transferred onto PVDF membranes. After blocking with TBST containing 5% nonfat milk for 1 h at room temperature, the membranes were incubated with primary antibodies at 4°C overnight. The primary antibodies used were TLR4, CD14, MyD88, p-NF-κB p65, NF-κB p65, and GAPDH, respectively (Proteintech Group, Rosemont, IL, USA; Cell Signaling Technology, Beverly, MA, USA). Next, the membranes were washed in TBST and incubated with secondary antibodies for 1.5 h at room temperature. Finally, the signals of the target proteins were detected, and target

TABLE 2: Information of the 8 active ingredients of HZOL.

Compound	Molecular formula	PubChem CID	Molecule ID	OB (%)	DL
Honokiol	$C_{18}H_{18}O_2$	72303	MOL005955	60.67	0.15
Magnolol	$C_{18}H_{18}O_2$	72300	MOL000210	69.19	0.15
Hesperidin	$C_{28}H_{34}O_{15}$	10621	MOL007930	13.33	0.67
Liquiritin	$C_{21}H_{22}O_9$	503737	MOL004903	65.69	0.74
Naringin	$C_{27}H_{32}O_{14}$	442428	MOL005812	6.92	0.78
Thymol	$C_{10}H_{14}O$	6989	MOL002042	41.47	0.03
Imperatorin	$C_{16}H_{14}O_4$	10212	MOL001941	34.55	0.22
Isoimperatorin	$C_{16}H_{14}O_4$	68081	MOL001942	45.46	0.23

(a)

(b)

(c)
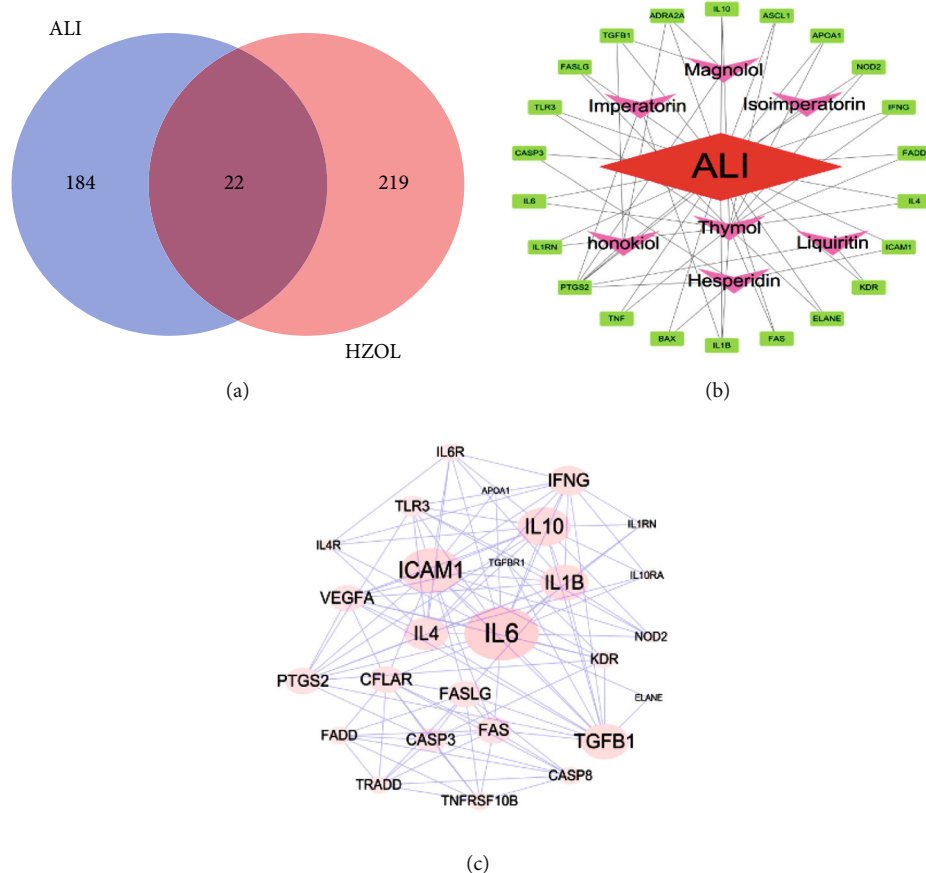
FIGURE 2: Common target network analysis and identification of hub genes of HZOL for ALI. (a) Common targets of HZOL and ALI. (b) Common target-active ingredient-disease network. (c) PPI network of twenty-two common targets with 22 nodes and 214 edges.

bands were exposed by chemiluminescence and quantified using ImageJ software.

2.10. Measurement of SCFAs in Cecum Contents. SCFAs were tested using GC-MS analysis according to the protocol used in a previous study [6]. The conditions of Thermo TRACE 1310-ISQ LT were coupled with a GC column of Agilent HP-INNOWAX and the MS conditions of electron impact ionization (EI) source, single ion mode (SIM) scanning mode, and 70 eV electron energy.

2.11. Statistical Analysis. All experimental data were expressed as the means ± SD. Statistical analysis was carried out using SPSS 20.0 software in a one-way analysis of variance (ANOVA) followed by the least significant difference (LSD) post hoc test for comparison of multiple groups. P value < 0.05 was considered statistically significant.

3. Results

3.1. Common Targets, Hub Genes, GO, and KEGG Analysis of HZOL in Treating ALI. Information of identified eight active ingredients of HZOL is shown in Table 2, while as shown in Figure 2(a), after normalizing in UniProt, 241 gene symbols of HZOL and 206 gene symbols of ALI were

(a)

(b)

FIGURE 3: Continued.

(c)

(d)
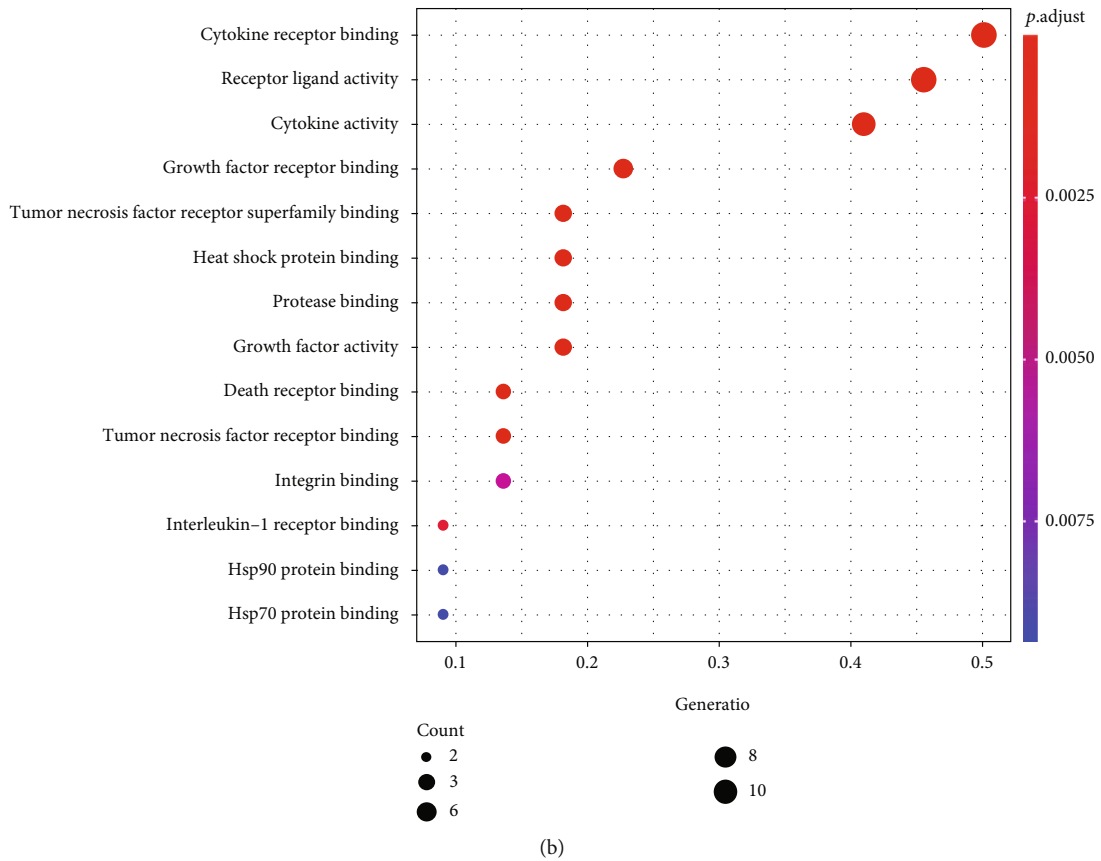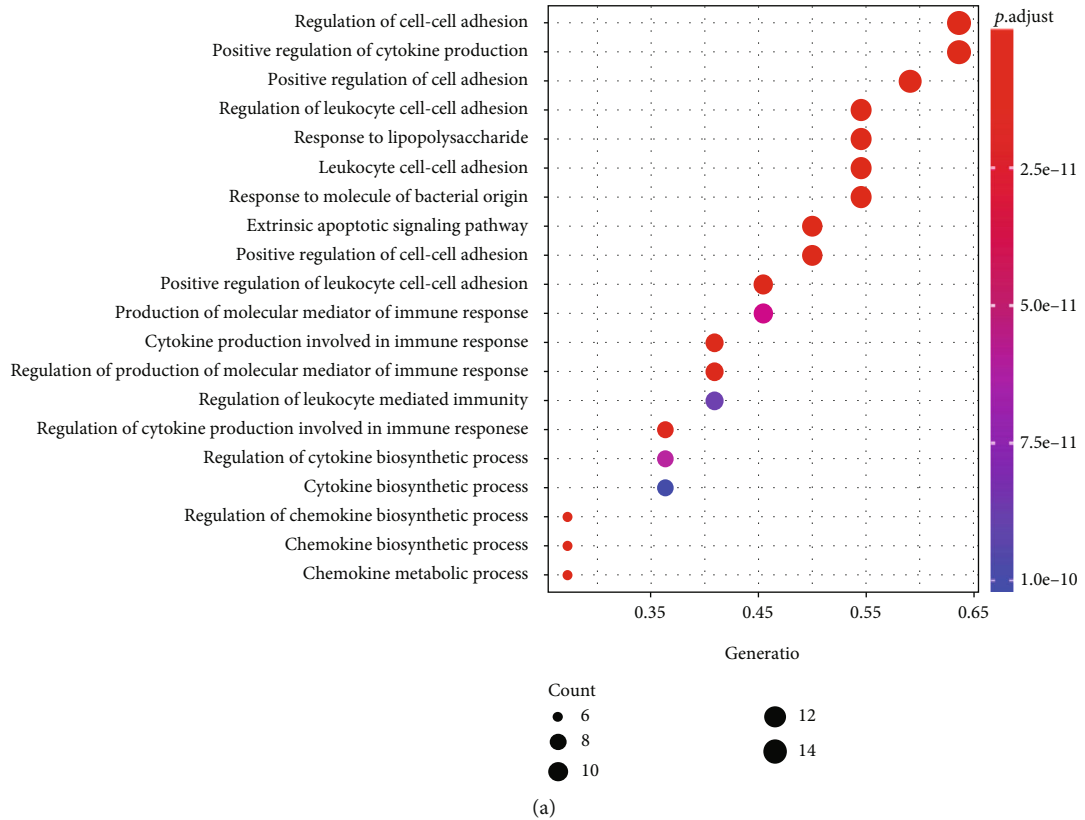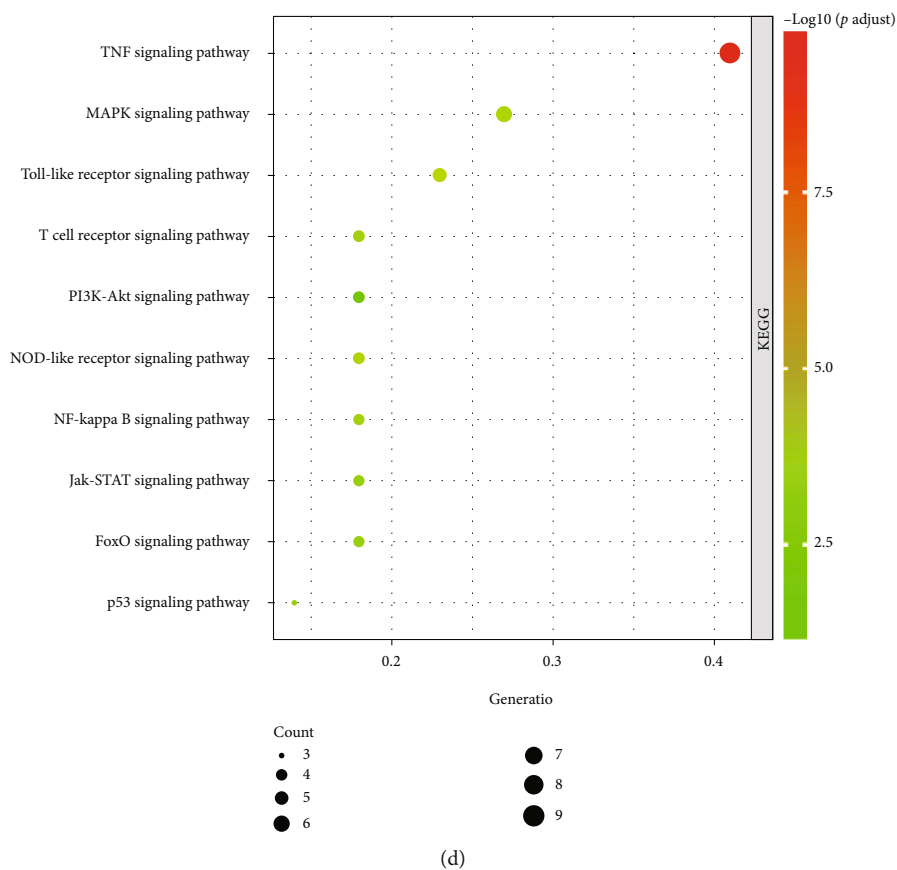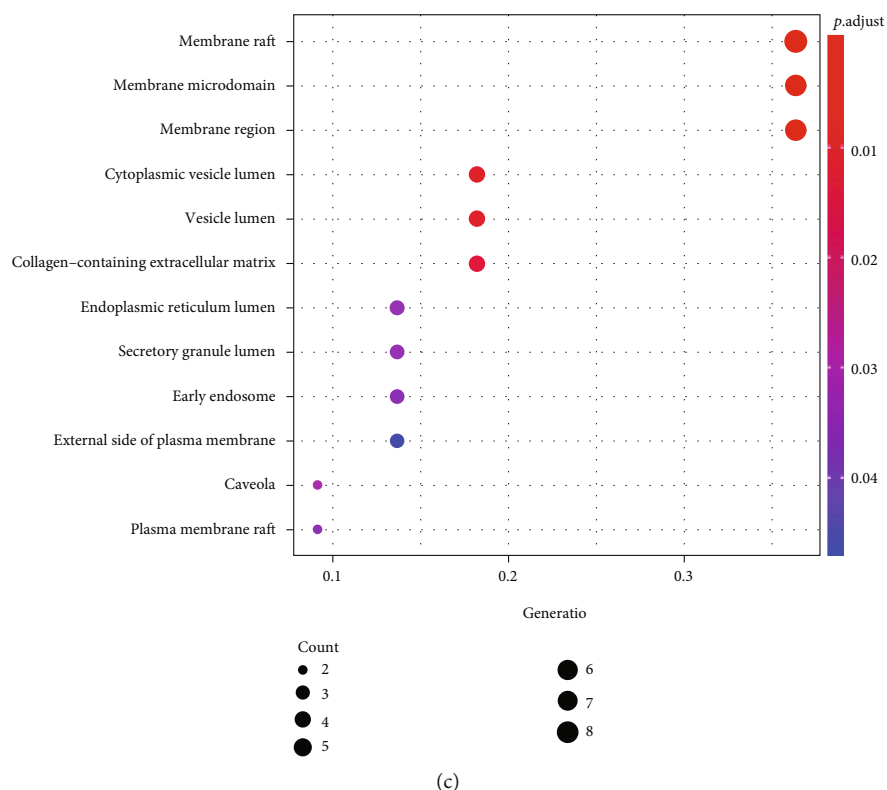
FIGURE 3: GO and KEGG analyses of twenty-two common target-related genes. (a) Top 20 biological processes (BPs). (b) Top 14 molecular functions (MFs). (c) Top 12 cellular components (CCs). (d) Top 10 KEGG signaling pathways.

TABLE 3: Detailed information of top 1 cluster of functional annotation clustering results.

Category	Term	P value	Genes	Fold enrichment
	Annotation cluster 1, enrichment score: 5.5093			
GOTERM_BP_DIRECT	GO:0045429: positive regulation of nitric oxide biosynthetic process	1.71E-09	IL6, IFNG, IL1B, PTGS2, TNF, ICAM1	106.5032
GOTERM_BP_DIRECT	GO:0042346: positive regulation of NF-kappa B import into the nucleus	2.21E-06	IL1B, PTGS2, TNF, TLR3	145.3853
GOTERM_BP_DIRECT	GO:0031622: positive regulation of fever generation	1.49E-05	IL1B, PTGS2, TNF	457.9636
KEGG_PATHWAY	hsa04064: NF-kappa B signaling pathway	0.001636	IL1B, PTGS2, TNF, ICAM1	15.81379

TABLE 4: Efficacy evaluation of the 8 active ingredients of HZOL for ALI/ARDS or inflammatory.

Compound	Therapeutic effects	Mechanisms	References
Honokiol	Honokiol inhibited lung inflammatory injury in ARDS mice induced by LPS	Inhibited Sirt3/AMPK pathway	[27]
	Honokiol inhibited inflammatory response in human monocyte-derived dendritic cells	Inhibited NF-κB and MAPK pathways	[28]
	Honokiol has anti-inflammatory bioactivities in ALI mice induced by LPS	Inhibited NF-κB pathway	[29]
Magnolol	Magnolol reducing inflammatory response and oxidative stress in sepsis mice	Inhibited HMGB1/TLR4/NF-κB pathway	[30]
	Magnolol inhibits LPS-induced inflammatory response in RAW264.7 cells	Inhibited NF-κB and MAPK pathways	[31]
Hesperidin	Hesperidin has anti-inflammatory effect in a systematic review and meta-analysis of randomized controlled clinical trials	Moderated VCAM-1 levels	[32]
	Hesperidin has anti-inflammatory effect in ALI rat induced by A virus (H1N1)	Inhibited MAPK pathways	[33]
Liquiritin	Liquiritin has anti-inflammatory effect in ALI mice induced by LPS	Inhibited NF-κB pathway, TRPV1, and TRPA1	[34]
Naringin	Naringin anti-inflammation in peritoneal macrophage cells and sepsis mice	Inhibited NF-κB activation	[35]
	Naringin has anti-inflammatory effect in ALI mice induced by LPS	Inhibited NF-κB pathway	[36]
Thymol	Thymol anti-inflammatory effects in LPS-induced RAW264.7 cells	NF-κB and MAPK pathways	[37]
	Thymol has anti-inflammatory effects in porcine intestinal epithelial cells	Reduce ROS and proinflammatory cytokine expression	[38]
Imperatorin	Imperatorin has antibacterial, anti-inflammatory, and antioxidant effects in LPS-induced macrophage-like RAW264.7 cells	Binds to TLR4 coreceptor and activates the Nrf2 pathway	[39]
	Imperatorin antibacterial and anti-inflammatory in RAW 264.7 macrophages	Inhibited NF-κB and MAPK activation	[40]
	Imperatorin has anti-inflammatory effect in ALI mice induced by LPS	Inhibited the p-IκB, JNK, ERK, and p38/MAPK	[41]
Isoimperatorin	Isoimperatorin as a potential TLR4 antagonist inhibited inflammatory responses induced by LPS in a mouse model	Inhibited LPS-TLR4/MD-2-NF-kappa B pathway	[42]
	Isoimperatorin has anti-influenza and anti-inflammatory effects in in vitro experiments	Inhibited NA-mediated progeny virus release	[43]

obtained, and 22 common targets were obtained after the process of taking the intersection. The active ingredient-common target-disease network is shown in Figure 2(b). In Figure 2(c), the results of a PPI network of twenty-two common targets showed that the top five hub genes were IL-6,

IL-10, ICAM-1, IL-1β, and IL-4. As shown in Figures 3(a)–3(d), the fundamental mechanisms of HZOL on ALI were screened, including 1541 BPs, 12 CCs, 14 MFs, and 82 significant pathways (P value ≤ 0.05). Furthermore, the results shown in Figure 3 suggested that HZOL

TLR4-imperatorin

Interactions
- 🟩 Van der waals
- 🟩 Conventional hydrogen bond
- ⬜ Carbon hydrogen bond
- 🟧 Pi-cation
- 🟪 A1ky1
- 🟪 Pi-A1ky1

(a)

CD14-imperatorin

Interactions
- 🟩 Van der waals
- 🟩 Conventional hydrogen bond
- ⬜ Carbon hydrogen bond
- 🟧 Pi-cation
- 🟪 A1ky1
- 🟪 Pi-A1ky1

(b)

MyD88-isoimperatorin

Interactions
- 🟩 Van der waals
- 🟩 Conventional hydrogen bond
- ⬜ Carbon hydrogen bond
- 🟧 Pi-cation
- 🟪 A1ky1
- 🟪 Pi-A1ky1

(c)

NF-κB p65-isoimperatorin

Interactions
- 🟩 Van der waals
- 🟩 Conventional hydrogen bond
- ⬜ Carbon hydrogen bond
- 🟧 Pi-cation
- 🟪 A1ky1
- 🟪 Pi-A1ky1

(d)

Figure 4: Continued.

(e)

FIGURE 4: Molecular docking results of active ingredients and TLR4/NF-κB p65 signaling pathway-related targets. (a) TLR4, with PDB ID 2Z62; (b) CD14, with PDB ID 4GLP; (c) MyD88, with PDB ID 4DOM; (d) NF-κB p65, with PDB ID 6YPY; (e) docking results of binding energy between ligands and receptors.

treating ALI mainly involved cell adhesion, immune response, inflammatory response, and signal transduction. In Figure 3(d), key signaling pathways were closely related to the TNF signaling pathway, MAPK signaling pathway, Toll-like receptor signaling pathway, NOD-like receptor signaling pathway, NF-kappa B signaling pathway, etc.

3.2. Potential Mechanisms of HZOL Treating ALI by Network Pharmacological Analysis. The functional annotation clustering results involved eight clusters. Information relating to the top 1 cluster, with an enrichment score of 5.51, is provided in Table 3. This finding indicated that the NF-κB pathway (hsa04064) was the key mechanism. Functional annotation clustering analysis results have shown that the NF-κB pathway (hsa04064) was the potential pathway of HZOL in treating ALI in the top 1 cluster. Combining with the top 10 key signaling pathways of KEGG enrichment results above by overlapping, the NF-κB pathway was screened out as the potential mechanisms of HZOL in treating ALI. Network pharmacological results prove that the NF-κB signaling pathway was the potential anti-inflammatory pathway of HZOL in treating ALI.

Furthermore, we explored the published efficacy evaluation of the eight active ingredients of HZOL regarding their mechanism of action in ALI/ARDS or inflammation. The published research results in Table 4 have shown that the 8 main active components of HZOL including honokiol, magnolol, hesperidin, liquiritin, naringin, thymol, imperatorin, and isoimperatorin performed an anti-inflammatory and immune regulation function, and their experimental results

showed that the mechanisms were mainly revealed in inhibiting the NF-κB pathway, MAPK pathway, and TLR4 receptor to restrain the inflammatory responses. Previous studies have reported that LPS can bind to a receptor complex consisting of TLR4 and CD14, and then, NF-κB protein can be activated via a myeloid differentiation factor MyD88-dependent pathway, eventually leading to the production of NF-κB-induced proinflammatory cytokines [26]. According to our network pharmacological prediction of the NF-κB signaling pathway and the biological published effect mechanisms involving the NF-κB signaling pathway and TLR4 receptor, targets in the TLR4/NF-κB p65 pathway involving TLR4, CD14, MyD88, and NF-κB p65 were selected as the key targets in our study to observe the treatment of HZOL in ALI. All the raw data of the network pharmacology analysis results are shown in Supplementary Material (1).

3.3. Molecular Docking Analysis between Active Ingredients and Core Proteins. It is known that the lower the binding energy, the stronger the binding pattern between the ligands and the receptors. Results showed that imperatorin bound well to TLR4, CD14, and NF-κB p65 (Figures 4(a), 4(b), and 4(d)) with the lowest value of the binding energy, while isoimperatorin bound well to MyD88 (Figure 4(c)) with the minimum binding energy. Moreover, their binding patterns mainly involved hydrogen bonding and hydrophobic interactions. The molecular docking results of the binding energy between ligands and receptors are shown in Figure 4(e). These results suggested that eight compounds especially

(a)

(b)

(c)

(d)

(e)
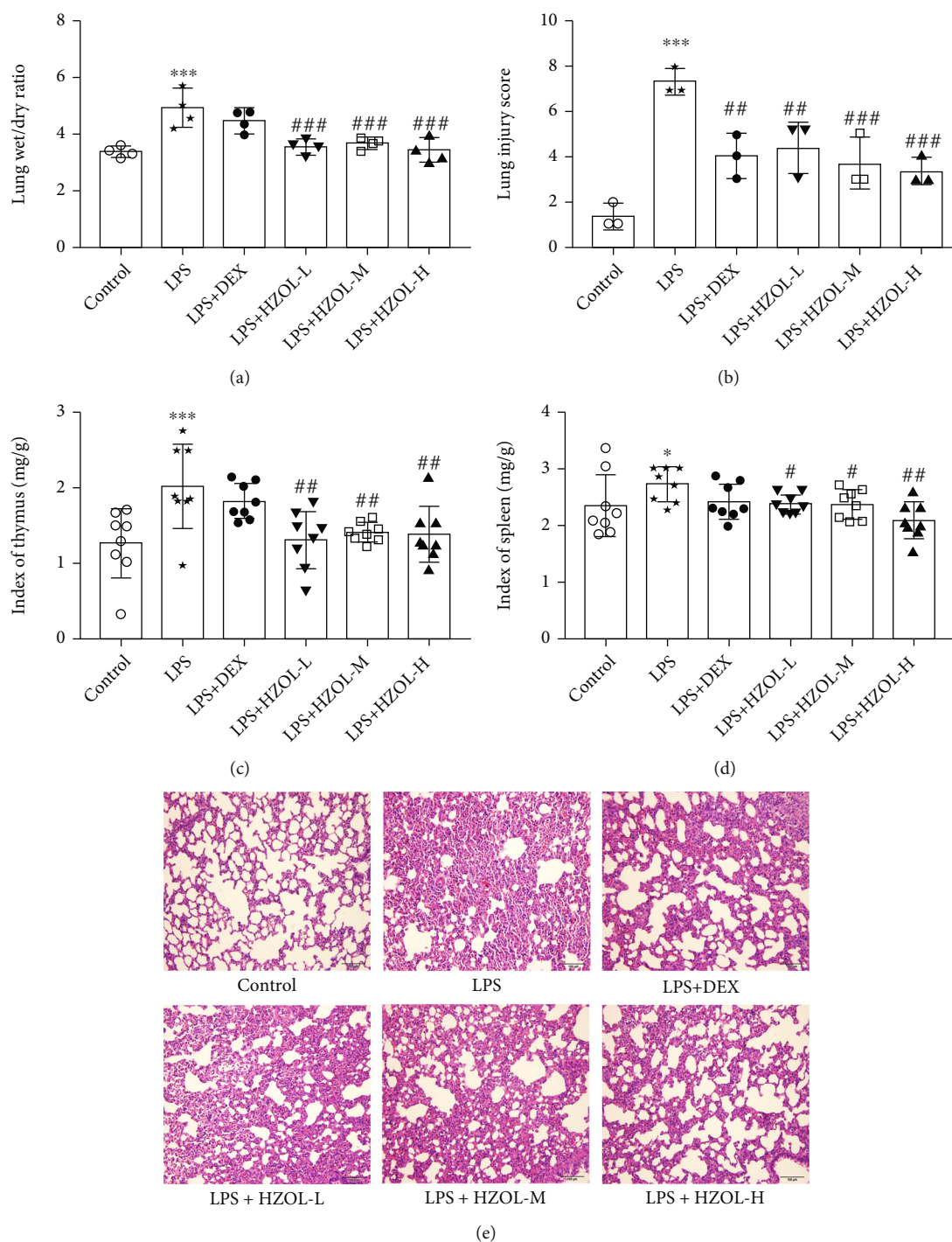
Figure 5: Lung wet/dry ratio, organ index, and pathohistological evaluations of lung tissues. (a) Lung wet/dry ratio ($n = 4$). (b) Lung injury score ($n = 3$). (c) Thymus index ($n = 8$). (d) Spleen index ($n = 8$). (e) H&E staining of lung tissues in control, lipopolysaccharide (LPS, 5 mg/kg), LPS+dexamethasone (DEX, 30 μg/kg), LPS+HZOL-L (1.67 mL/kg), LPS+HZOL-M (3.33 mL/kg), and LPS+HZOL-H (6.67 mL/kg) groups ($n = 3$). Mean ± SD. $^*P < 0.05$ and $^{***}P < 0.001$ vs. the control group. $^\#P < 0.05$, $^{\#\#}P < 0.01$, and $^{\#\#\#}P < 0.001$ vs. the LPS group.

imperatorin and isoimperatorin could combine well with the targets in the NF-κB inflammation pathway preliminary verifying the prediction results of network pharmacology.

3.4. HZOL Ameliorated Lung Edema and Lung Pathological Injury and Inhibited the Enhancement of Thymus and Spleen Indexes Induced by LPS. As the results show in Figures 5(a)

and 5(b), the wet/dry ratio and lung injury score were remarkably elevated after LPS stimulation of the lung. Conversely, they were distinctly attenuated by HZOL. In addition, the organ indexes of the thymus and spleen were calculated to assess the state of the host immune capability. In Figures 5(c) and 5(d), thymus and spleen indexes increased in model rats, while these results were reversed by treating with HZOL in

(a)

(b)

(c)

(d)

(e)

(f)
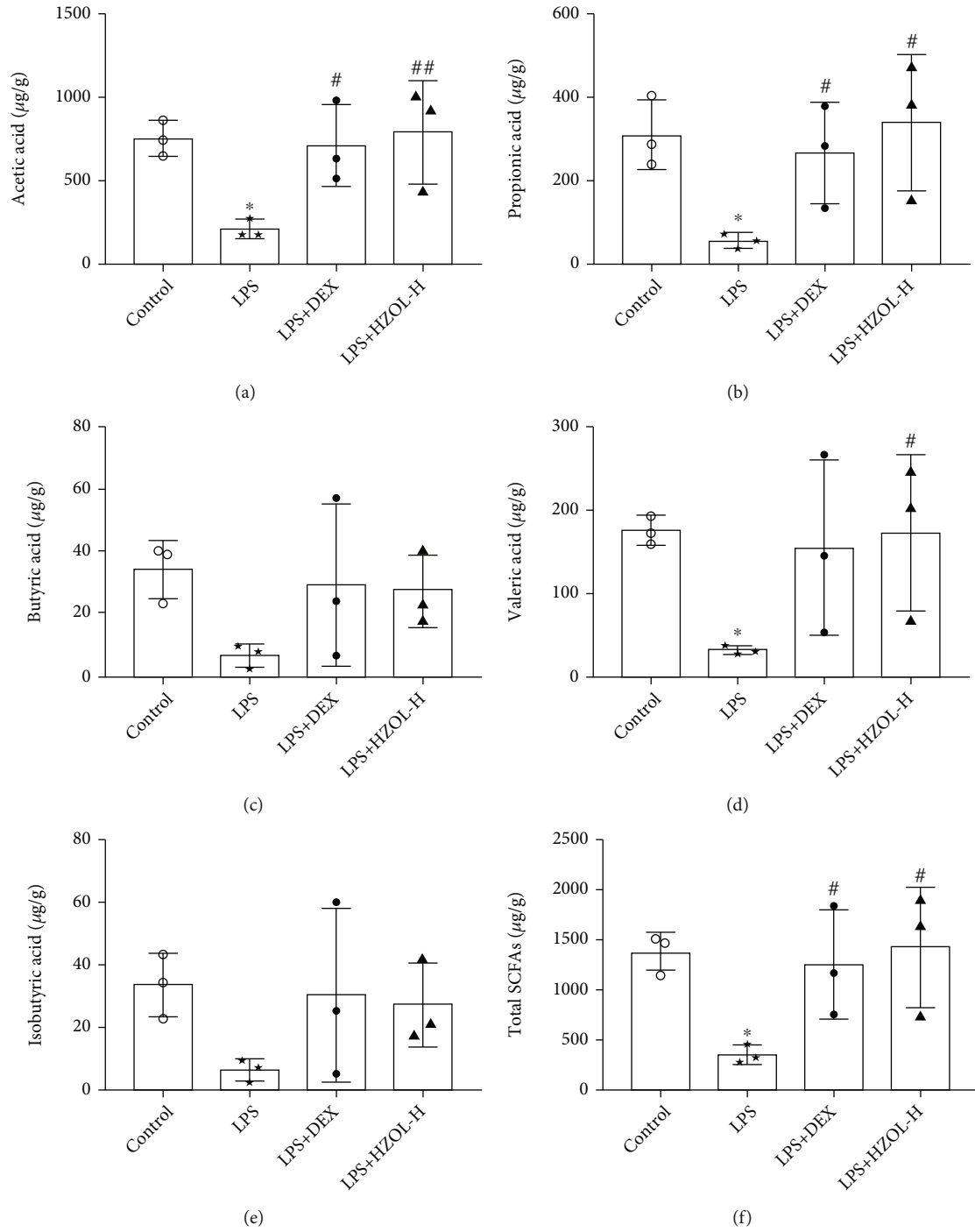
Figure 6: Continued.

(g)

(h)
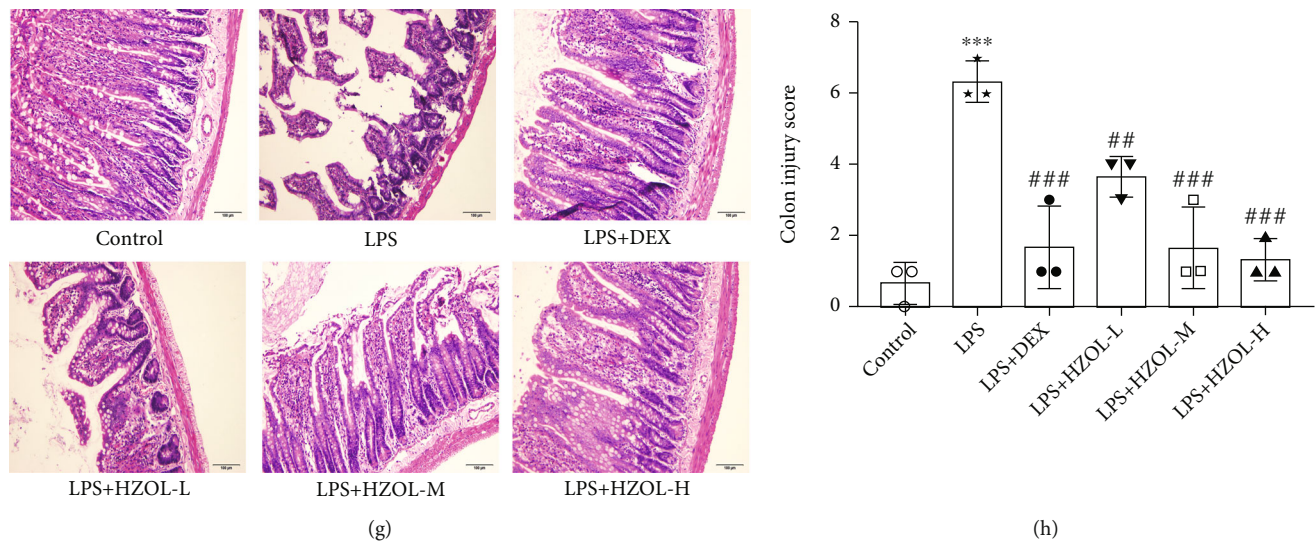
Figure 6: Analytical parameters for GC-MS method of SCFAs in cecum contents and pathohistological evaluation of colon tissues. (a) Acetic acids. (b) Propionic acids. (c) Butyric acids. (d) Valeric acids. (e) Isobutyric acids. (f) Total SCFAs. (g) H&E staining of colon tissues. (h) Colon injury score. Mean ± SD ($n = 3$). $^*P < 0.05$ and $^{***}P < 0.001$ vs. the control group. $^\#P < 0.05$, $^{\#\#}P < 0.01$, and $^{\#\#\#}P < 0.001$ vs. the LPS group.

different doses. However, the organ protection of the DEX group was inferior to HZOL in lung edema, and abnormal increases in the indexes of the thymus and spleen were observed—changes induced by LPS. Furthermore, in the LPS group in Figure 5(e), the alveolar structure was disordered and the alveolar wall was not complete. In contrast, the HZOL group and the DEX group showed that the continuity of alveolar structure and the incompleteness of the alveolar wall were improved, and the infiltration of inflammatory cells and interstitial cells was decreased with different doses of HZOL.

3.5. HZOL Alleviated Colonic Pathological Injury and Modulated Short-Chain Fatty Acids Induced by LPS.
The results in Figures 6(a)–6(f) showed that total SCFAs and individual SCFAs (acetic, propionic, butyric, valeric, and isobutyric acids) in the cecum were reduced in LPS rats. After pretreatment with DEX and HZOL, total SCFAs and individual SCFAs in the cecum were significantly increased. In addition, pathohistological evaluations and colon injury score of colon tissues were performed, as shown in Figures 6(g) and 6(h). Colonic histopathology results revealed that in the control group, the colonic mucosa was intact and smooth, and the glandular layer was clear. However, in the LPS model group, the colonic mucosal epithelium was eroded, the crypt structure of the glands was destroyed, the goblet cells were lost, and inflammatory cells were infiltrated. After pretreatment with HZOL, the colonic mucosal damage was significantly alleviated, the crypts of glands were arranged in order, the epithelial structure was complete, and the inflammatory cell infiltration was reduced. Besides, HZOL attenuated the severity degree of colon injury score. These results demonstrated that HZOL has protective effects on LPS-induced gut injury.

3.6. HZOL Improving Hematologic Indices.
We next explored the pathological changes of related organs and the physiological and pathological changes in the circulation sys-

tem, and we assessed the alteration in blood cells from the rats' plasma. In our results in Figures 7(a)–7(f), the data showed that WBCs, GRAN%, BASO%, and EOSIN% were increased, while the PLT and LYM% were decreased in plasma—changes induced by LPS. Notably, DEX and HZOL in different doses reverted the hematologic indices markedly by reducing the WBC count, GRAN%, BASO%, and EOSIN% and increasing the PLT and LYM%.

3.7. HZOL Alleviated Inflammatory Responses Induced by LPS.
The serum and bronchoalveolar lavage fluid concentrations of IL-6, IL-1β, TNF-α, and IFN-γ were evaluated to assess the anti-inflammatory activity of HZOL in this research. The results are shown in Figures 8(a)–8(h). LPS significantly increased the production of IL-6, IL-1β, TNF-α, and IFN-γ, while the HZOL and DEX groups inhibited these cytokines in the rats' serum and BALF.

3.8. Effects of HZOL Pretreatment on TLR4/NF-κB p65 Signaling Pathway.
The mRNA levels in the LPS group involving TLR4, CD14, MyD88, and NF-κB p65 were significantly upregulated, respectively. In contrast, they were significantly downregulated by DEX and HZOL in different doses in Figures 9(a)–9(d). However, the results shown in Figures 9(f)–9(j) of our study indicated that HZOL only affected the protein expression level of p-NF-κB p65, but not the expression level of total NF-κB p65. Besides, in Figures 9(e)–9(j), upregulating protein levels of TLR4, CD14, MyD88, and p-NF-κB p65/NF-κB p65 ratio induced by LPS were significantly downregulated, respectively, after treating with HZOL or DEX. These observational findings demonstrated that expressions of TLR4, CD14, MyD88, and p-NF-κB p65 on the TLR4/NF-κB p65 signaling pathway in ALI mice were downregulated after pretreatment with HZOL. The mechanism is shown in Figure 10. All the

(a)

(b)

(c)

(d)

(e)

(f)
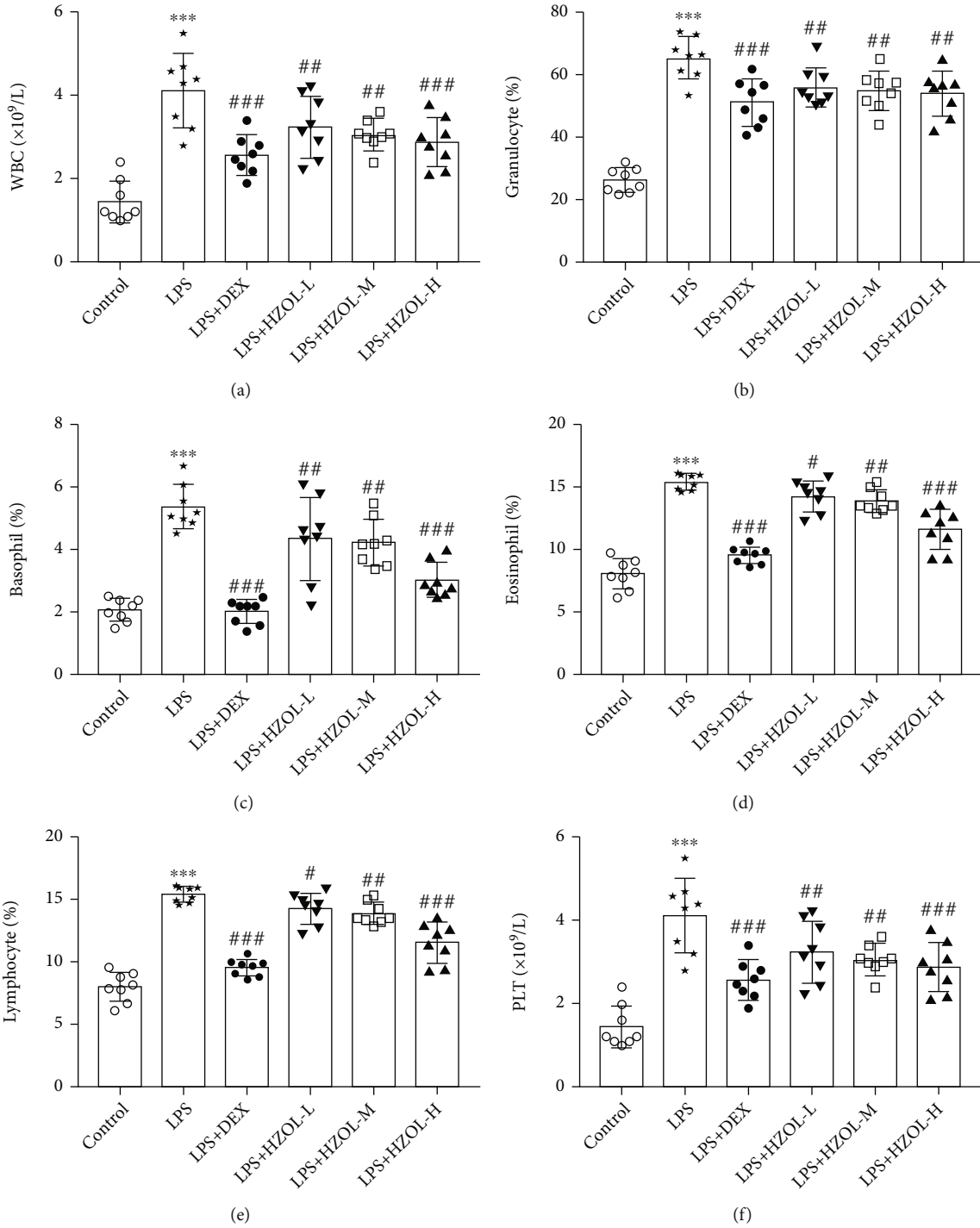
Figure 7: Hematologic indices of (a) white blood cells (WBC), (b) granulocyte percentage (GRAN%), (c) basophil percentage (BASO%), (d) eosinophil percentage (EOSIN%), (e) lymphocyte percentage (LYM%), and (f) blood platelets (PLT) on plasma of rats. Mean $\pm$ SD ($n = 8$). *** $P < 0.001$ vs. the control group. # $P < 0.05$, ## $P < 0.01$, and ### $P < 0.001$ vs. the LPS group.

raw data of the experimental validation results are shown in Supplementary Material (2).

4. Discussion

Lipopolysaccharides (LPS) can cause a bacterial type of pneumonia, which can eventually lead to the onset of ALI.

ALI can be induced by different diseases and pathological states, such as trauma, pneumonia, sepsis, and endotoxemia [44]. Besides, studies demonstrated that ALI induced by LPS can release proinflammatory cytokines in the lung and lead to immune dysfunction, indicating that LPS can be used to establish animal models of ALI that exhibit similar clinical characteristics to ALI [45–47]. LPS-induced ALI is

(a)

(b)

(c)

(d)

(e)

(f)
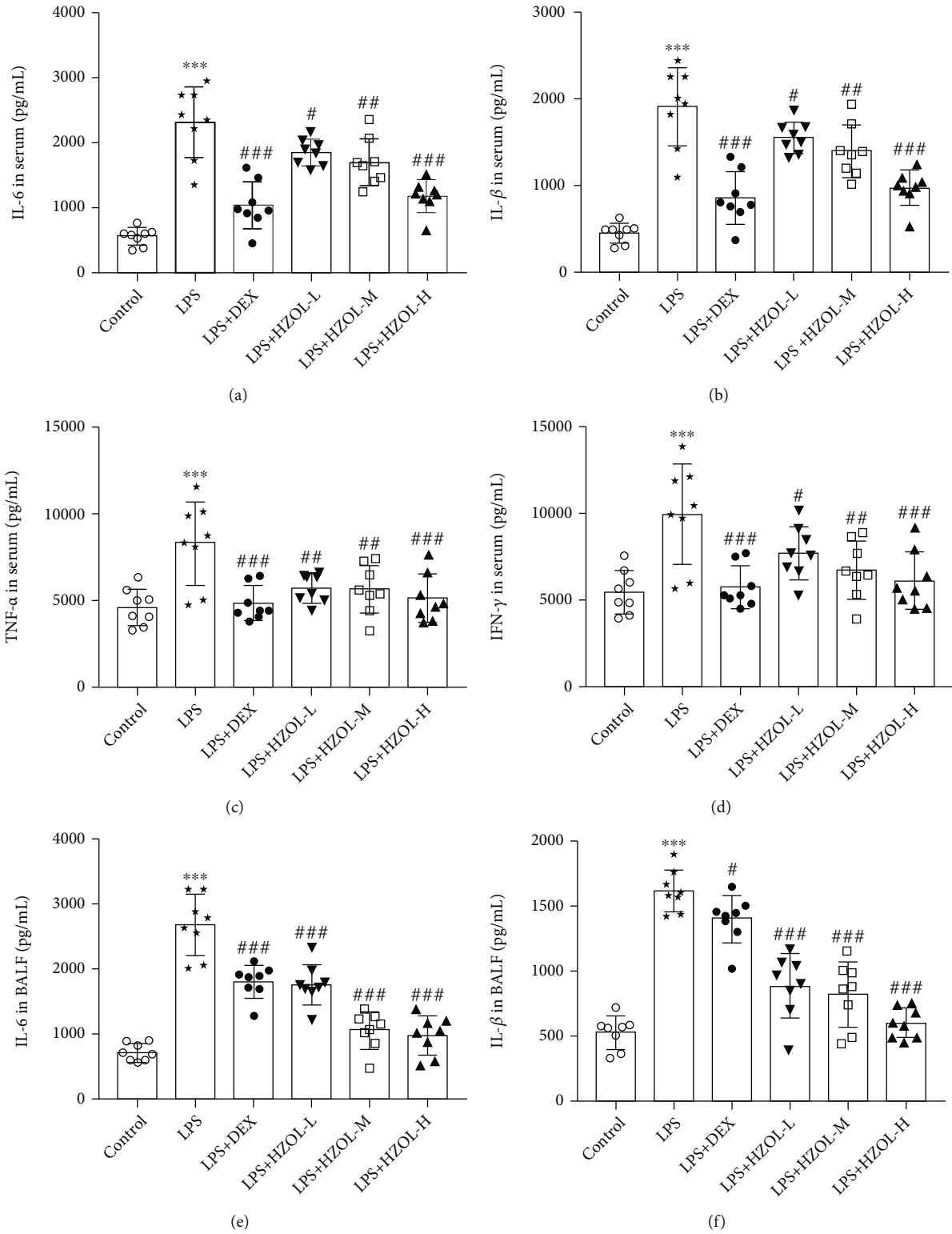
Figure 8: Continued.

(g)

(h)
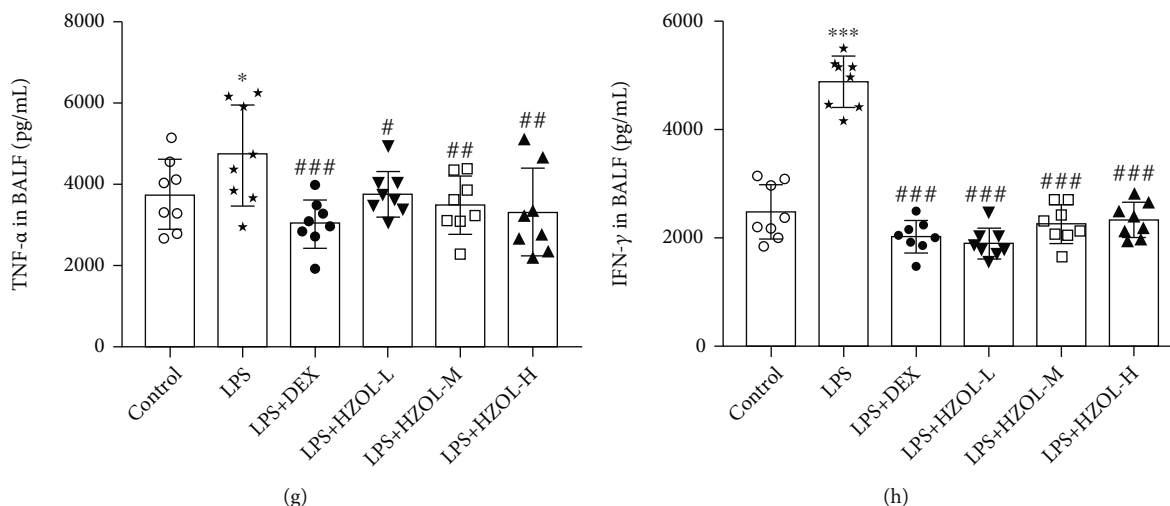
FIGURE 8: IL-6, IL-1β, TNF-α, and INF-γ concentrations in serum and BALF. The concentrations of (a) IL-6, (b) IL-1β, (c) TNF-α, and (d) INF-γ in serum and (e) IL-6, (f) IL-1β, (g) TNF-α, and (h) INF-γ in BALF were measured by ELISA kits. Mean $\pm$ SD ($n = 8$). $^{*}P < 0.05$ and $^{***}P < 0.001$ vs. the control group. $^{\#}P < 0.05$, $^{\#\#}P < 0.01$, and $^{\#\#\#}P < 0.001$ vs. the LPS group.

administered in three ways mainly. The first one to induce ALI directly is the intranasal perfusion or intratracheal instillation, but the course of disease rapidly develops from ALI to ARDS and causes respiratory failure and death finally [48]. The second one of ALI is induced by the caudal vein injection, which is suitable to study the early pathogenesis of ALI in a short time, but the operation is difficult and the success rate is relatively low [49]. The third one is intraperitoneal injection which is a common and easy method to induce the sepsis causing systemic inflammatory changes and then simulating secondary lung damage to establish ALI [50]. Moreover, colon barrier dysfunction, acute colon injury, and disturbance of microbiota appearance can be induced by LPS according to previous reported researches [51]. Therefore, anti-inflammatory on regulation of lung and colon injury is an effective strategy for the treatment of ALI rats induced by LPS. In our study, intraperitoneal injection method was used to induce ALI and we observed the inflammatory changes in the lung as well as in the gut as results.

Microbiome metabolite SCFAs can promote antimicrobial and anti-inflammatory pathways, participating in inflammation response in the lung and gut [52]. SCFAs are the important contributors in the modulation of gut-lung dysfunction. In a previous study of a mouse model either in pneumonia exposure high-dose propionate or in lung ischemia reperfusion injury, once lung inflammation occurred, SCFAs were produced in the gut which can enter the lungs through blood circulation, then activating the lung immunity, increasing the content of SCFAs in the lung, inhibiting the production of proinflammatory factors, and thus modulating lung immune responses to inhibit inflammation finally [53]. Moreover, once inflammation is triggered by LPS, the number of WBCs in rats increases significantly to help the host resist bacterial invasion. Besides, the recruitment of neutrophils, eosinophils, and basophils is essential to the host for killing bacteria; the GRAN%, EOSIN%, and BASO% contributed in regulating the inflam-

matory response [54]. In addition, the LYM% may reflect the immune status, and blood platelets enhance the stress elasticity of the host and accelerate the reconstruction rate of injured pulmonary vessels [55]. LPS may also cause extensive damage to organs, including the immune-related thymus and spleen, leading to immune dysfunction [22]. Consistently, the results of our in vivo experiments demonstrated that pretreatment with HZOL could alleviate pulmonary edema, downregulating the lung wet/dry ratio, improving the lung pathological assay, inhibiting LPS-induced abnormal enhancement of the immune-related thymus and spleen, and maintaining the balance in blood parameters by reducing the WBC, GRAN%, BASO%, and EOSIN%, while increasing the PLT and LYM%. It appears that HZOL can also repair colon damage and regulate immune disorders by increasing the levels of all SCFAs and individual SCFAs (acetic, propionic, butyric, valeric, and isobutyric acids) in the cecum during the stress of LPS-induced ALI. Our results suggested that HZOL exerts anti-inflammatory effects on LPS-induced ALI.

In the mechanism prediction of action relating to the therapeutic effect of HZOL in ALI, network pharmacology results suggested that the NF-κB pathway was the principal pathway. Besides, published literature demonstrated that the NF-κB pathway and TLR4 receptor were closely linked to cytokine production and crucial in regulating inflammatory responses, which are also related to the development of ALI [23]. Previous studies have reported that LPS can bind to a receptor complex consisting of TLR4 and CD14, and then, NF-κB protein can be activated via a myeloid differentiation factor MyD88-dependent pathway, eventually leading to the production of NF-κB-induced proinflammatory cytokines [26]. In addition, molecular docking results suggested that eight ingredients of HZOL especially imperatorin and isoimperatorin combine well with the targets in the NF-κB inflammation pathway of TLR4, CD14, MyD88, and NF-κB p65, preliminary verifying the prediction results of network pharmacology. Furthermore, the inflammatory
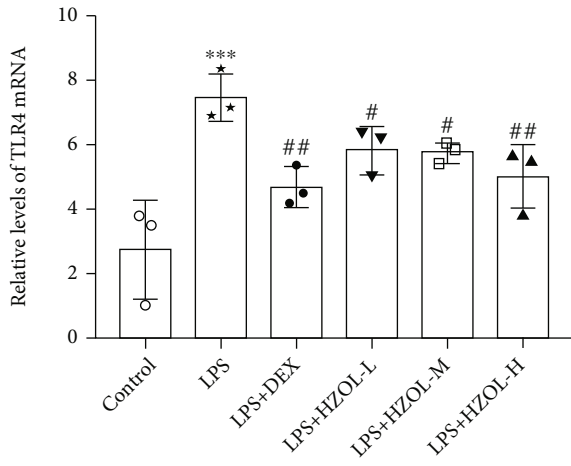
(a)
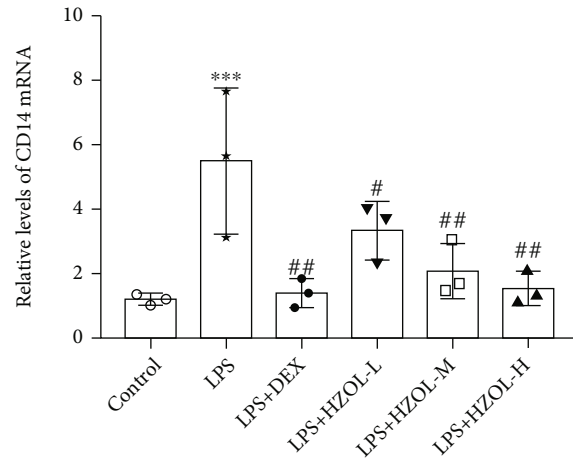
(b)
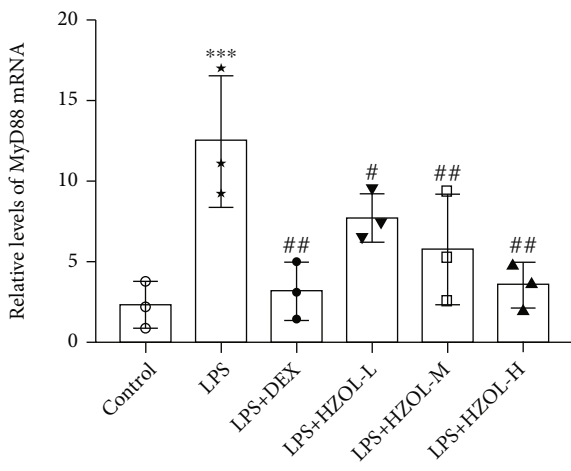
(c)
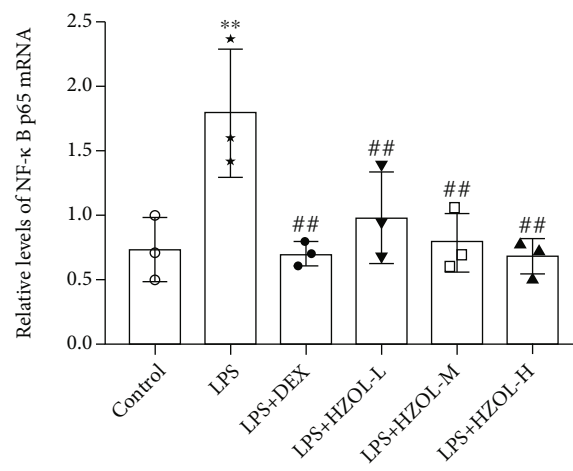
(d)
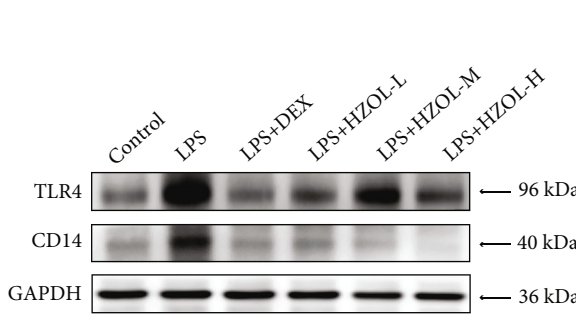
(e)
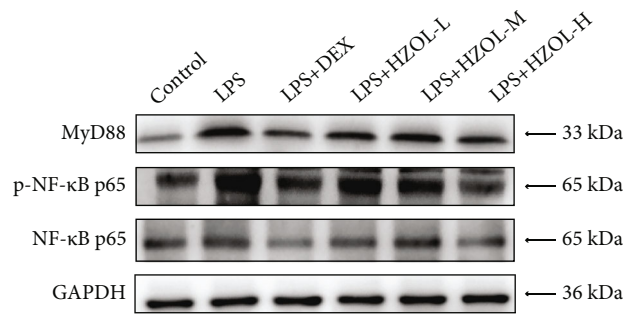
(f)

Figure 9: Continued.

(g)

(h)

(i)

(j)
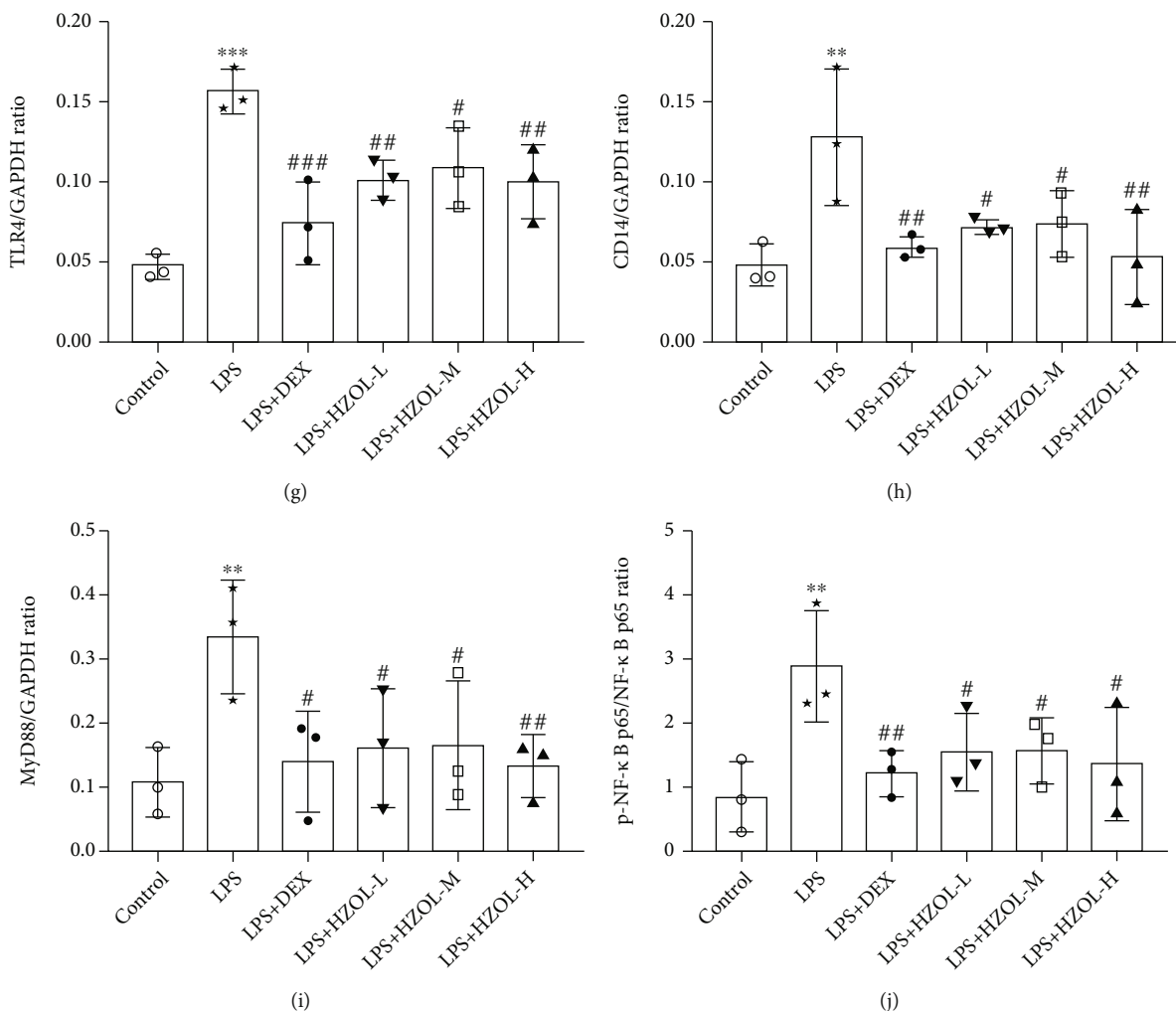
Figure 9: HZOL treatment effect on the expression of TLR4, CD14, MyD88, p-NF-κB p65, and NF-κB p65. Expression of mRNA of (a) TLR4, (b) CD14, (c) MyD88, and (d) NF-κB p65 in lung tissue was detected by RT-qPCR, while the protein expression of (e, g) TLR4, (e, h) CD14, (f, i) MyD88, and (f, j) p-NF-κB p65/NF-κB p65 ratio in lung tissue was detected by western blotting. Mean $\pm$ SD ($n = 3$). $^{**}P < 0.01$ and $^{***}P < 0.001$ vs. the control group. $^{#}P < 0.05$, $^{##}P < 0.01$, and $^{###}P < 0.001$ vs. the LPS group.

response of the host is caused by IL-6, IL-1β, TNF-α, and IFN-γ, along with constant stimulation of excessive LPS, triggering an inflammatory storm that ultimately leads to the onset of ALI [56, 57]. According to our network pharmacological prediction results and related ALI pharmacological literature reports, we explored the effect of HZOL on the TLR4/NF-κB p65 pathway in an ALI mouse model. Through a pharmacological experiment involving an LPS-induced ALI rat model, our results suggested that uncontrolled prolongation of inflammatory responses was remarkably inhibited by HZOL through downregulation IL-6, IL-1β, TNF-α, and IFN-γ in serum and the bronchoalveolar lavage fluid. Moreover, HZOL downregulated the protein expression and the mRNA levels of TLR4, CD14, MyD88, p-NF-κB p65, and NF-κB p65 in ALI model rats. Our theoretical prediction and in vivo experimental verification are consistent with those of previous animal studies, indicating that the TLR4/NF-κB pathway is closely related to LPS-induced reactions [58–60]. Results indicated that the protective effect of

HZOL against ALI was mainly involved with the TLR4/NF-κB p65 inflammatory pathway.

HZOL increased the levels of SCFAs, inhibiting the accumulation of inflammatory cytokines and attenuating the expressions of TLR4, CD14, MyD88, p-NF-κB p65, and NF-κB p65 of the TLR4/NF-κB p65 inflammatory pathway in our LPS-induced lung and gut injury model. Briefly, pretreatment with HZOL contributes to protective effect against LPS-induced ALI and gut injury. Mechanisms involved may lead to increased immune function and reduced inflammatory responses by increasing SCFA levels and inhibiting activation of the TLR4/NF-κB p65 pathway. Although HZOL has been used for many centuries in humans, little is known about its pharmacological role in lung disease. Our study explored the therapeutic effect and mechanism of its antipneumonia effect. Finally, our study contributed to the pharmacology of HZOL in relation to its application in the treatment of ALI. This study provided experimental evidence regarding the role of HZOL in preventing and treating
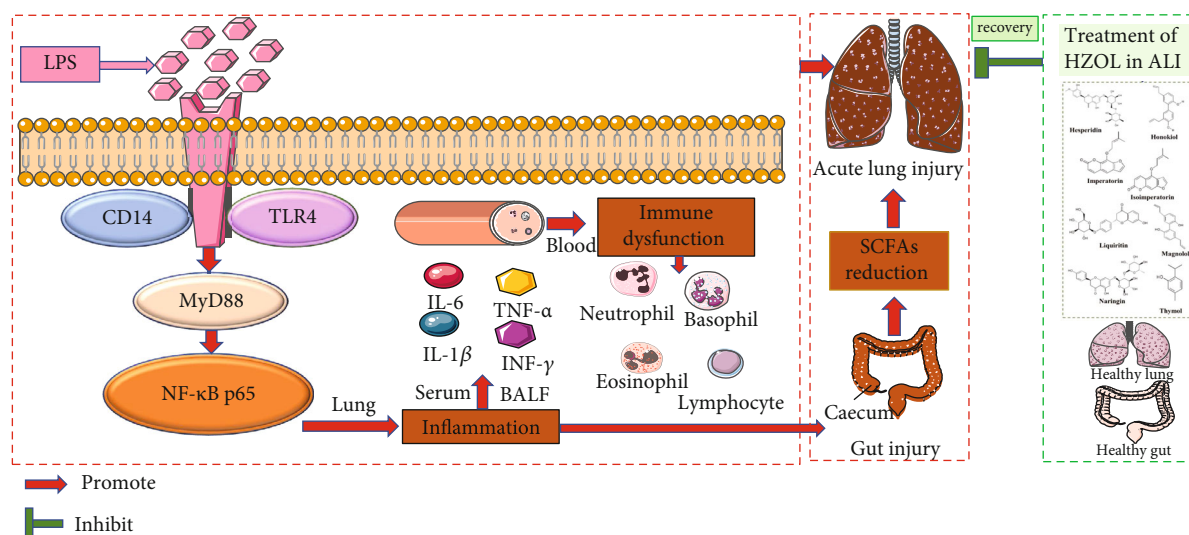
FIGURE 10: Schematic diagram of the TLR4/NF-κB p65 signaling pathways related to the anti-inflammatory effects of HZOL on LPS-induced ALI.

acute lung injury and gut injury. Future research should focus on the lung-gut axis to demonstrate the anti-inflammatory of the lung-protective qualities of HZOL in order to encourage a broader application of HZOL in clinical settings.

5. Conclusions

In summary, HZOL plays an important anti-inflammatory and immune regulation role in the lung-gut axis by balancing the levels of SCFAs in the cecum, reducing the accumulation of inflammatory cytokines, downregulating inflammatory signaling pathways, relieving pulmonary edema, and repairing damage to colon tissue in the LPS-induced ALI rat model. HZOL can reverse LPS-induced changes relating to the inflammatory cytokines and immune dysfunction and attenuating the expressions of TLR4, CD14, MyD88, NF-κB p65, and p-NF-κB p65 of the TLR4/NF-κB p65 pathway. Our study provided evidences for the practical application of HZOL in the treatment of ALI to encourage a broader application of HZOL in clinical settings. Furthermore, our study further suggests that the therapeutic effects and mechanisms of HZOL in preventing and treating ALI and gut injury may also have other clinical applications.

Data Availability

The raw data supporting the conclusions of this article are included in the paper.

Conflicts of Interest

The authors declare that there are no conflicts of interest regarding the publication of this article.

Authors' Contributions

All authors approved the submitted version.

Acknowledgments

Supplementary Materials

Supplementary Material (1): all the data of network pharmacology analysis. Supplementary Material (2): all the data of experimental validation results. (Supplementary Materials)

References

[1] S. D. Oliveira, M. Castellon, J. W. Chen et al., "LPS-induced acute lung inflammation, Cav-1 degradation, and eNOS uncoupling is associated with endothelial dysfunction and pulmonary vascular remodeling," American Journal of Respiratory and Critical Care Medicine, vol. 193, 2016.

[2] Y. Li, X. Huang, S. Huang et al., "Central role of myeloid MCPIP1 in protecting against LPS-induced inflammation and lung injury," Signal Transduction and Targeted Therapy, vol. 2, no. 1, p. 15, 2017.

[3] D. Shah, P. das, S. Acharya et al., "Small immunomodulatory molecules as potential therapeutics in experimental murine models of acute lung injury (ALI)/acute respiratory distress syndrome (ARDS)," International Journal of Molecular Sciences, vol. 22, no. 5, 2021.

[4] B. Q. Wang, M. Shi, J. P. Zhang et al., "Knockdown of TFPI-anchored endothelial cells exacerbates lipopolysaccharide-induced acute lung injury via NF-κB signaling pathway," Shock, vol. 51, no. 2, pp. 235–246, 2019.

[5] M. F. Doursout, H. Horton, L. Hoang et al., "Lactoferrin moderates LPS-induced hypotensive response and gut injury in rats," International Immunopharmacology, vol. 15, no. 2, pp. 227–231, 2013.

[6] S. Shao, D. Wang, W. Zheng et al., "A unique polysaccharide from _Hericium erinaceus_ mycelium ameliorates acetic acid-induced ulcerative colitis rats by modulating the composition of the gut microbiota, short chain fatty acids levels and

GPR41/43 respectors," *International Immunopharmacology*, vol. 71, pp. 411–422, 2019.

[7] L. Li, W. W. Fu, R. T. Wu et al., "Protective effect of _Ganoderma atrum_ polysaccharides in acute lung injury rats and its metabolomics," *International Journal of Biological Macromolecules*, vol. 142, pp. 693–704, 2020.

[8] Z. H. Ding, R. X. Zhong, Y. N. Yang et al., "Systems pharmacology reveals the mechanism of activity of Ge-Gen-Qin-Lian decoction against LPS-induced acute lung injury: a novel strategy for exploring active components and effective mechanism of TCM formulae," *Pharmacological Research*, vol. 156, article 104759, 2020.

[9] M. Xiao, J. Tian, Y. Zhou et al., "Efficacy of Huoxiang Zhengqi dropping pills and Lianhua Qingwen granules in treatment of COVID-19: a randomized controlled trial," *Pharmacological Research*, vol. 161, article 105126, 2020.

[10] Y. Liu, W. Liu, Q. X. Peng, J. L. Peng, L. Z. Yu, and J. L. Hu, "Protective effect of Huoxiang Zhengqi oral liquid on intestinal mucosal mechanical barrier of rats with postinfectious irritable bowel syndrome induced by acetic acid," *Evidence-Based Complementary and Alternative Medicine*, vol. 2014, Article ID 218383, 10 pages, 2014.

[11] W. Zhuang, Z. Fan, Y. Chu et al., "Chinese patent medicines in the treatment of coronavirus disease 2019 (COVID-19) in China," *Frontiers in Pharmacology*, vol. 11, p. 1066, 2020.

[12] K. Li, J. Yuan, and W. Su, "Determination of liquiritin, naringin, hesperidin, thymol, imperatorin, honokiol, isoimperatorin, and magnolol in the traditional Chinese medicinal preparation Huoxiang-zhengqi liquid using high-performance liquid chromatography," *Yakugaku Zasshi*, vol. 126, no. 11, pp. 1185–1190, 2006.

[13] Y. N. Ni, L. S. Zhang, J. Churchill, and S. Kokot, "Application of high performance liquid chromatography for the profiling of complex chemical mixtures with the aid of chemometrics," *Talanta*, vol. 72, no. 4, pp. 1533–1539, 2007.

[14] H. Z. Guo, X. M. Pang, W. Q. Zhang, W. Y. Jiang, and X. C. Pang, "Dissolution determination of five components in Huoxiang Zhengqi tablets using partitioned dispersive liquid-liquid microextraction combined with HPLC-UV," *Analytical Methods*, vol. 5, no. 11, pp. 2674–2678, 2013.

[15] Z. H. Shi, Z. M. Li, L. N. Qiu, M. H. Sun, D. Zhang, and H. Y. Zhang, "Sugaring-out assisted liquid/liquid extraction coupled with HPLC for the analysis of honokiol and magnolol in traditional Chinese herbal formula Huoxiang-Zhengqi oral liquid," *Journal of Liquid Chromatography & Related Technologies*, vol. 38, no. 6, pp. 722–728, 2015.

[16] Y. H. He, H. Y. Zhao, Z. L. Liu et al., "Effects of huoxiangzhengqi liquid on enteric mucosal immune responses in mice with Bacillus dysenteriae and Salmonella typhimurium induced diarrhea," *World Journal of Gastroenterology: WJG*, vol. 12, no. 45, pp. 7346–7349, 2006.

[17] C. Xie, X. F. Wang, X. J. Qi, L. L. Lu, and H. C. Chan, "Effect of Huoxiang-zhengqi liquid on HCO(3)(-) secretion by intact porcine distal airway epithelium," *Sheng Li Xue Bao*, vol. 60, no. 1, pp. 90–96, 2008.

[18] D. He, Q. Li, G. L. Du, J. J. Sun, G. F. Meng, and S. L. Chen, "Research on the mechanism of Guizhi to treat nephrotic syndrome based on network pharmacology and molecular docking technology," *BioMed Research International*, vol. 2021, Article ID 8141075, 13 pages, 2021.

[19] B. R. Zhang, W. C. Dan, G. L. Zhang, and X. M. Wang, "Molecular mechanism of Gleditsiae Spina for the treatment of high-

grade serous ovarian cancer based on network pharmacology and pharmacological experiments," *BioMed Research International*, vol. 2022, Article ID 5988310, 15 pages, 2022.

[20] Y. Huang, S. S. Gao, Z. H. Gong, W. J. Li, J. J. Sun, and M. J. Sun, "Mechanism of Sanhua decoction in the treatment of ischemic stroke based on network pharmacology methods and experimental verification," *BioMed Research International*, vol. 2022, Article ID 7759402, 20 pages, 2022.

[21] X. H. Li, H. Tang, Q. Tang, and W. Chen, "Decoding the mechanism of Huanglian Jiedu decoction in treating pneumonia based on network pharmacology and molecular docking," *Frontiers in Cell and Developmental Biology*, vol. 9, article 638366, 2021.

[22] G. Deng, H. He, Z. Chen et al., "Lianqinjiedu decoction attenuates LPS-induced inflammation and acute lung injury in rats via TLR4/NF-κB pathway," *Biomed Pharmacother*, vol. 96, pp. 148–152, 2017.

[23] L. Y. Peng, H. T. Shi, M. Yuan et al., "Madecassoside protects against LPS-induced acute lung injury via inhibiting TLR4/NF-κB activation and blood-air barrier permeability," *FPHAR*, vol. 11, p. 807, 2020.

[24] Y. J. Chen, J. J. Dong, J. Liu et al., "Network pharmacology-based investigation of protective mechanism of Aster tataricus on lipopolysaccharide-induced acute lung injury," *International Journal of Molecular Sciences*, vol. 20, no. 3, 2019.

[25] L. Chen, X. L. Zhong, W. Y. Cao et al., "JQ1 as a BRD4 inhibitor blocks inflammatory pyroptosis-related acute colon injury induced by LPS," *Frontiers in Immunology*, vol. 12, article 609319, 2021.

[26] C. Q. Xu, G. Chen, W. W. Yang et al., "Hyaluronan ameliorates LPS-induced acute lung injury in mice via Toll-like receptor (TLR) 4-dependent signaling pathways," *International Immunopharmacology*, vol. 28, no. 2, pp. 1050–1058, 2015.

[27] L. Chen, W. Li, D. Qi, L. Lu, Z. Zhang, and D. Wang, "Honokiol protects pulmonary microvascular endothelial barrier against lipopolysaccharide-induced ARDS partially via the Sirt3/AMPK signaling axis," *Life Sciences*, vol. 210, pp. 86–95, 2018.

[28] C. Y. Li, L. K. Chao, S. C. Wang et al., "Honokiol inhibits LPS-induced maturation and inflammatory response of human monocyte-derived dendritic cells," *Journal of Cellular Physiology*, vol. 226, no. 9, pp. 2338–2349, 2011.

[29] L. K. Chao, P. C. Liao, C. L. Ho et al., "Anti-inflammatory bioactivities of honokiol through inhibition of protein kinase C, mitogen-activated protein kinase, and the NF-kappaB pathway to reduce LPS-induced TNFalpha and NO expression," *Journal of Agricultural and Food Chemistry*, vol. 58, no. 6, pp. 3472–3478, 2010.

[30] J. P. Ma, B. Tang, S. J. Zheng, and Z. Y. Zhu, "Magnolol mitigates lung injury in sepsis mice by reducing inflammatory response and oxidative stress and regulating HMGB1/TLR4/NF-kappa B signaling pathway," *Latin American Journal of Pharmacy*, vol. 38, no. 12, pp. 2530–2536, 2019.

[31] Y. Fu, B. Liu, N. Zhang et al., "Magnolol inhibits lipopolysaccharide-induced inflammatory response by interfering with TLR4 mediated NF-κB and MAPKs signaling pathways," *Journal of Ethnopharmacology*, vol. 145, no. 1, pp. 193–199, 2013.

[32] E. Lorzadeh, N. Ramezani-Jolfaie, M. Mohammadi, Y. Khoshbakht, and A. Salehi-Abargouei, "The effect of hesperidin supplementation on inflammatory markers in human adults: a systematic review and meta-analysis of randomized

controlled clinical trials," *Chemico-Biological Interactions*, vol. 307, pp. 8–15, 2019.

[33] Z. Ding, G. Sun, and Z. Zhu, "Hesperidin attenuates influenza A virus (H1N1) induced lung injury in rats through its anti-inflammatory effect," *Antiviral Therapy*, vol. 23, no. 7, pp. 611–615, 2018.

[34] Z. Liu, P. Wang, S. Lu et al., "Liquiritin, a novel inhibitor of TRPV1 and TRPA1, protects against LPS-induced acute lung injury," *Cell Calcium*, vol. 88, article 102198, 2020.

[35] M. Gil, Y. K. Kim, S. B. Hong, and K. J. Lee, "Naringin decreases TNF-α and HMGB1 release from LPS-stimulated macrophages and improves survival in a CLP-induced sepsis mice," *PLoS One*, vol. 11, no. 10, article e0164186, 2016.

[36] Y. Liu, H. Wu, Y. C. Nie, J. L. Chen, W. W. Su, and P. B. Li, "Naringin attenuates acute lung injury in LPS-treated mice by inhibiting NF-κB pathway," *International Immunopharmacology*, vol. 11, no. 10, pp. 1606–1612, 2011.

[37] J. Chen, D. L. Li, L. N. Xie et al., "Synergistic anti-inflammatory effects of silibinin and thymol combination on LPS-induced RAW264.7 cells by inhibition of NF-κB and MAPK activation," *Phytomedicine*, vol. 78, article 153309, 2020.

[38] F. A. Omonijo, S. Liu, Q. Hui et al., "Thymol improves barrier function and attenuates inflammatory responses in porcine intestinal epithelial cells during lipopolysaccharide (LPS)-induced inflammation," *Journal of Agricultural and Food Chemistry*, vol. 67, no. 2, pp. 615–624, 2019.

[39] M. H. Huang, Y. H. Lin, P. C. Lyu et al., "Imperatorin interferes with LPS binding to the TLR4 co-receptor and activates the Nrf2 antioxidative pathway in RAW264.7 murine macrophage cells," *Antioxidants*, vol. 10, no. 3, 2021.

[40] W. Guo, J. Sun, L. Jiang et al., "Imperatorin attenuates LPS-induced inflammation by suppressing NF-κB and MAPKs activation in RAW 264.7 macrophages," *Inflammation*, vol. 35, no. 6, pp. 1764–1772, 2012.

[41] J. J. Sun, G. F. Chi, L. W. Soromou et al., "Corrigendum to "Preventive effect of imperatorin on acute lung injury induced by lipopolysaccharide in mice" [Int. Immunopharmacol. 14 (2012) 369-374]," *International Immunopharmacology*, vol. 16, no. 1, pp. 122–122, 2013.

[42] G. R. Chen, Y. N. Liu, Y. B. Xu, M. B. Zhang, S. Guo, and G. Zhang, "Isoimperatorin exerts anti-inflammatory activity by targeting the LPS-TLR4/MD-2-NF-kappa B pathway," *European Journal of Inflammation*, vol. 19, article 20587392211000573, 2021.

[43] Y. N. Lai, T. T. Han, S. F. Zhan, Y. Jiang, X. H. Liu, and G. Li, "Antiviral activity of isoimperatorin against influenza A virus in vitro and its inhibition of neuraminidase," *Frontiers in Pharmacology*, vol. 12, article 657826, 2021.

[44] V. Baradaran Rahimi, H. Rakhshandeh, F. Raucci et al., "Anti-inflammatory and anti-oxidant activity of Portulaca oleracea extract on LPS-induced rat lung injury," *Molecules*, vol. 24, no. 1, p. 139, 2019.

[45] P. Karki and A. Birukova, "Socs1 protection against LPS-induced lung injury and inflammation is dependent on microtubule stability," *American Journal of Respiratory and Critical Care Medicine*, vol. 201, 2020.

[46] S. R. Kim, H. J. Kim, Y. C. Lee, and S. H. Kim, "NLRP3 inflammasome conjugates with mitochondria in LPS-induced acute lung injury," *European Respiratory Journal*, vol. 56, 2020.

[47] X. Zhan, R. Cui, X. Geng et al., "LPS-induced mitochondrial DNA synthesis and release facilitate RAD50-dependent acute lung injury," *Signal Transduction and Targeted Therapy*, vol. 6, no. 1, p. 103, 2021.

[48] G. Tian, C. Li, Y. Zhai et al., "GC-MS based metabolomic profiling of lung tissue couple with network pharmacology revealed the possible protection mechanism of Pudilan Xiaoyan Oral Liquid in LPS-induced lung injury of mice," *Biomedicine & Pharmacotherapy*, vol. 124, article 109833, 2020.

[49] X. Li, C. Shan, Z. Wu, H. Yu, A. Yang, and B. Tan, "Emodin alleviated pulmonary inflammation in rats with LPS-induced acute lung injury through inhibiting the mTOR/HIF-1α/VEGF signaling pathway," *Inflammation Research*, vol. 69, no. 4, pp. 365–373, 2020.

[50] H. Zhang, J. Sha, X. Feng et al., "Dexmedetomidine ameliorates LPS induced acute lung injury via GSK-3β/STAT3-NF-κB signaling pathway in rats," *International Immunopharmacology*, vol. 74, article 105717, 2019.

[51] L. Gu, N. Li, J. Gong, Q. Li, W. Zhu, and J. Li, "Berberine ameliorates intestinal epithelial tight-junction damage and downregulates myosin light chain kinase pathways in a mouse model of endotoxinemia," *Journal of Infectious Diseases*, vol. 203, no. 11, pp. 1602–1612, 2011.

[52] A. Mohammed, H. K. Alghetaa, J. H. Zhou, S. Chatterjee, P. Nagarkatti, and M. Nagarkatti, "Protective effects of Δ9-tetrahydrocannabinol against enterotoxin-induced acute respiratory distress syndrome are mediated by modulation of microbiota," *British Journal of Pharmacology*, vol. 177, no. 22, pp. 5078–5095, 2020.

[53] X. Tian, J. Hellman, A. R. Horswill, H. A. Crosby, K. P. Francis, and A. Prakash, "Elevated gut microbiome-derived propionate levels are associated with reduced sterile lung inflammation and bacterial immunity in mice," *Frontiers in Microbiology*, vol. 10, p. 159, 2019.

[54] H. C. Suh, T. Benoukraf, P. Shyamsunder et al., "LPS independent activation of the pro-inflammatory receptor Trem1 by C/EBPε in granulocytes," *Scientific Reports*, vol. 7, no. 1, article 46440, 2017.

[55] Y. Zhong, X. Zhang, X. Hu, and Y. Li, "Effects of repeated lipopolysaccharide treatment on growth performance, immune organ index, and blood parameters of Sprague-Dawley rats," *Journal of Veterinary Research*, vol. 62, no. 3, pp. 341–346, 2018.

[56] C. Li, P. Yang, Y. Sun et al., "IL-17 response mediates acute lung injury induced by the 2009 pandemic influenza A (H1N1) virus," *Cell Research*, vol. 22, no. 3, pp. 528–538, 2012.

[57] X. Li, R. Huang, K. Liu et al., "Fucoxanthin attenuates LPS-induced acute lung injury via inhibition of the TLR4/MyD88 signaling axis," *Aging*, vol. 13, no. 2, pp. 2655–2667, 2021.

[58] L. Feng, N. Yang, C. Li et al., "Pudilan xiaoyan oral liquid alleviates LPS-induced respiratory injury through decreasing nitroxidative stress and blocking TLR4 activation along with NF-κB phosphorylation in mice," *Journal of Ethnopharmacology*, vol. 214, pp. 292–300, 2018.

[59] G. Feng, B. Sun, H. X. Liu, Q. H. Liu, L. Zhao, and T. L. Wang, "EphA2 antagonism alleviates LPS-induced acute lung injury via Nrf2/HO-1, TLR4/MyD88 and RhoA/ROCK pathways," *International Immunopharmacology*, vol. 72, pp. 176–185, 2019.

[60] K. Wang, H. Zhang, J. Zhang, E. Jia, and G. Zhu, "Prediction of immune factors and signaling pathways in lung injury induced by LPS based on network analysis," *Saudi Journal of Biological Sciences*, vol. 26, no. 8, pp. 2068–2073, 2019.

Hindawi

Research Article

The Effect of *Citrus aurantium* on Non-Small-Cell Lung Cancer: A Research Based on Network and Experimental Pharmacology

Liangliang Yao [ID],[1] **Xuan Zhang,**[2] **Chaoming Huang,**[2] **Yi Cai** [ID],[2]
and Chunpeng (Craig) Wan [ID][3]

[1]*Affiliated Hospital of Jiangxi University of Chinese Medicine, Nanchang 330006, China*
[2]*Guangzhou Municipal and Guangdong Provincial Key Laboratory of Molecular Target & Clinical Pharmacology, The NMPA and State Key Laboratory of Respiratory Disease, School of Pharmaceutical Sciences and the Fifth Affiliated Hospital, Guangzhou Medical University, Guangzhou 511436, China*
[3]*College of Agronomy, Jiangxi Agricultural University, Jiangxi Key Laboratory for Post-Harvest Technology and Nondestructive Testing of Fruits & Vegetables, Nanchang 330045, China*

Correspondence should be addressed to Yi Cai; yicaisysu@163.com and Chunpeng (Craig) Wan; chunpengwan@jxau.edu.cn

Purpose. To screen the main active components of *Citrus aurantium* through a network pharmacology approach, construct a component-disease target network, explore its molecular mechanism for the treatment of non-small-cell lung cancer (NSCLC), and validate it experimentally. *Methods.* The active ingredients in *Citrus aurantium* and the targets of *Citrus aurantium* and NSCLC were collected through the Traditional Chinese Medicine Systematic Pharmacology Database and Analysis Platform (TCMSP), GeneCards, and OMIM databases. The protein interaction network was constructed using the STRING database, and the component-disease relationship network graph was analyzed using Cytoscape 3.9.1. The Metascape database can be used for GO and KEGG enrichment analyses. The Kaplan-Meier plotter was applied for overall survival analysis of key targets of *Citrus aurantium* in the treatment of NSCLC. Real-time PCR (RT-PCR) and Western blotting were used to determine the mRNA and protein levels of key targets of *Citrus aurantium* for the treatment of NSCLC. *Results.* Five active ingredients of *Citrus aurantium* were screened, and 54 potential targets for the treatment of NSCLC were found, of which the key ingredient was nobiletin and the key targets are TP53, CXCL8, ESR1, PPAR-α, and MMP9. GO and KEGG enrichment analyses indicated that the mechanism of nobiletin in treating NSCLC may be related to the regulation of cancer signaling pathway, phosphatidylinositol-3 kinase (PI3K)/protein kinase B (Akt) signaling pathway, lipid and atherosclerosis signaling pathway, and neurodegenerative signaling pathway. The experimental results showed that nobiletin could inhibit the proliferation of NSCLC cells and upregulate the levels of P53 and PPAR-α and suppress the expression of MMP9 ($P < 0.05$). *Conclusion.* *Citrus aurantium* can participate in the treatment of NSCLC through multiple targets and pathways.

1. Introduction

Currently, lung cancer remains one of the most common cancers and has a very high mortality rate, accounting for approximately 18% of all cancer-related deaths [1]. According to the histological classification, lung cancer is divided into small-cell lung cancer (SCLC, 15% of all lung cancers) and non-small-cell lung cancer (NSCLS, 85% of all lung cancers) [2]. The process of NSCLC development is complex and diverse, involving multiple signaling pathways, such as PI3K/Akt signaling pathway, human matrix metalloproteinase 9 (MMP9), cell cycle protein-dependent kinase 1 (CDK1), and Wnt/β-catenin signaling pathway [3–6]. According to recent research results, the treatment of NSCLC is mainly based on Western medicine,

including surgery, chemotherapy, radiotherapy, targeted therapy, and immunotherapy [7, 8]. However, these treatments are often accompanied by undesirable consequences such as susceptibility to recurrence and metastasis, poor prognosis, and high costs [9]. In addition, many targeted drugs used to treat NSCLC (e.g., EGFR-TKI and ALK-TKI), although they can prolong the survival of patients with advanced disease, the resistance of these drugs limits their long-term efficacy [10, 11]. Studies have shown that Chinese medicine can be very helpful in the adjuvant treatment or prognosis of NSCLC, reducing the adverse effects of EGFR-TKIs, improving disease-free survival (DFS), and having better tolerability [12, 13].

Aurantii Fructus, also known as ZhiQiao, is the dried unripe fruit of *Citrus aurantium* L. and its cultivated variants and is a traditional Chinese medicine. According to previous studies, *Citrus aurantium* has several potential pharmacological effects, such as promotion of intestinal motility [14], antidepressant effects [15, 16], antikidney stones [17], and antihepatotoxicity [18]. In addition, studies have shown that *Citrus aurantium* also has potential therapeutic effects on cardiovascular disease and cancer [19]. Weifuchun tablet is a proprietary Chinese medicine containing three Chinese herbs, namely, red ginseng, Isodon amethystoides, and *Citrus aurantium*, to relieve precancerous lesions of gastric cancer by regulating intestinal microbial balance and treating atrophy and intestinal metaplasia (IM) [20]. The above studies show that *Citrus aurantium* is a good anticancer herbal medicine, but the therapeutic effect and mechanism of action of *Citrus aurantium* on NSCLC have not been reported yet and deserve further study.

In this study, the protein interaction network between the active ingredients of *Citrus aurantium*, drug targets, and NSCLC-related disease genes was constructed through a network pharmacology approach to predict the potential targets and related pathways of *Citrus aurantium* for the treatment of NSCLC, which was then validated by cellular and molecular experiments, thus providing a theoretical basis for further clinical studies.

2. Materials and Methods

2.1. Collection of Active Ingredients and Targets of Citrus aurantium. The active ingredients of *Citrus aurantium* were obtained by searching "Zhiqiao" using the Traditional Chinese Medicine System Pharmacology Database and Analysis Platform (TCMSP) according to our previous study [21]. Then, we screened the list of ingredients with the criteria of oral bioavailability (OB) $\geq 30\%$ and drug-likeness (DL) ≥ 0.18. Similarly, in the TCMSP database, the targets of active ingredients were screened in the list of relevant targets and a database of active ingredients and targets of *Citrus aurantium* was created. The target names were corrected using UniProt (https://www.uniprot.org/).

2.2. Collection of Disease Targets. Two online human-related gene databases, GeneCards (https://www.genecards.org/) and OMIM (https://omim.org/), were searched using the keyword "non-small-cell lung cancer" to obtain the NSCLC-related genes. The genes from the two databases were then integrated to create a database of NSCLC disease targets.

2.3. Venn Diagram of Genes Associated with Citrus aurantium and NSCLC. The target genes of *Citrus aurantium* and the target genes of NSCLC were uploaded on the Venny 2.1.0 online platform to map the Venn diagram and obtain the crossover genes of *Citrus aurantium* and NSCLC, i.e., the drug-disease cointeraction target genes.

2.4. Construction and Analysis of Protein Interaction Network. The information related to *Citrus aurantium* active ingredient and NSCLC target genes was imported into the network visualization software Cytoscape 3.9.1 (https://cytoscape3.9.1.org//) to construct a network diagram of the *Citrus aurantium* active ingredient-NSCLC target gene relationship. The data were analyzed using the CentiScaPe2.2 plug-in in Cytoscape 3.9.1 to calculate the nodes of each active ingredient in the network.

2.5. GO and KEGG Enrichment Analyses. The crossover genes of *Citrus aurantium* and NSCLC were entered into the STRING database (https://string-db.org/), and "Homo sapiens" was selected to map the protein interaction network. Subsequently, data analysis was performed using the CentiScaPe2.2 plug-in in Cytoscape 3.9.1 to screen for key targets in *Citrus aurantium* and NSCLC. Then, the crossover genes were entered into the Metascape database, "Homo sapiens" was selected, GO and KEGG enrichment analyses were performed, the data obtained from the analyses were stored, *P* values were calculated, and the relevant data were entered into the online platform Weishengxin (https://www.bioinformatics.com.cn/) to plot bubble plots.

2.6. Kaplan-Meier Analysis. The Kaplan-Meier plotter (https://kmplot.com/analysis/) was able to assess the impact of 54,000 genes on survival rates for 21 cancer types. Among them, the largest dataset includes breast, ovarian, lung, and gastric cancers [22]. In this study, it was used to assess the prognostic value of nobiletin-key target mRNA expression in NSCLC. Each of the 12 key targets was uploaded to the database to obtain a Kaplan-Meier survival plot, where the number of risks is shown below the main plot. When $P < 0.05$, it indicates that the results are significantly different. In this study, the threshold value with the best performance was used as the cutoff value, and "array quality control" was selected as "no filtered array quality."

2.7. Drugs and Reagents. Dulbecco's modified Eagle medium (DMEM), fetal bovine serum (FBS), 0.25% trypsin-EDTA, and penicillin-streptomycin solution were purchased from Gibco (Logan, Utah, USA). Real-time PCR kits were purchased from Takara Co., Ltd. (Dalian, China). Rabbit anti-p53 and β-tubulin antibodies were purchased from CST Inc. (Boston, MA, USA). Chemiluminescent substrates were purchased from Pierce (Rockford, IL, USA).

2.8. *Cell Culture.* A549 cells were added to DMEM medium (Gibco) with 10% fetal bovine serum (FBS), 100 U/mL penicillin, and 100 U/mL streptomycin and maintained at 37°C, 95% air, and 5% CO_2 in a humid environment. When the cells reached 80% to 90% fusion, the cells were digested with trypsin-EDTA (0.25%, Sigma), followed by passaging culture.

2.9. *CCK-8 Analysis.* Cell viability was assayed using Cell Counting Kit-8 (CCK-8). NSCLC cells in logarithmic growth phase were inoculated at 5×10^3 per well into 96-well microplates and cultured for 24 h. Then, NSCLC cells were treated with different concentrations of nobiletin (0, 10, 20, and 40 μM) for 12, 24, and 48 h. CCK-8 solution (10 mL) was added to each well and incubated for another 1 h. Finally, the absorbance of each well was measured at 450 nm by a multivolume spectrophotometer system (USA, BioTek Instruments Inc.).

2.10. *Clone Formation Test.* NSCLC cells (1×10^3 cells/well) in logarithmic growth phase were inoculated in 6-well culture plates and incubated at 37°C for 48 h. The cells were fixed with 4% paraformaldehyde (Solaibo, Beijing, China) for 10 min and stained with crystal violet (Sigma-Aldrich, China) for 30 min, and colonies containing more than 10 cells were observed under a microscope.

2.11. *Real-Time PCR.* Total RNA was extracted from cultured cells using TRIzol reagent (Invitrogen). mRNA was subsequently quantified, and cDNA was synthesized by reverse transcription, and mRNA levels of target genes were measured using a Bio-Rad quantitative PCR instrument. The specific primers used for RT-PCR are shown in Table 1, and GAPDH was used as an endogenous control. To ensure the validity and accuracy of the data, all reactions were performed three times.

2.12. *Western Blotting.* Total protein was extracted from the cells using RIPA lysis buffer, and the extracted protein was then quantified using the BCA protein quantification kit according to the manufacturer's instructions. Subsequently, equivalent proteins were separated on 10% SDS-PAGE, then transferred to poly(vinylidene fluoride) (PVDF) membranes and blocked against nonspecific antibodies; primary antibodies were added, incubated for 1-2 h at room temperature, and then incubated with secondary antibodies for 1 h at room temperature; and target protein expression was detected by chemiluminescence, and the bands were analyzed in grayscale by the ImageJ software.

2.13. *Statistical Analysis.* All data were expressed as mean ± standard deviation, and statistical analysis was performed using the SPSS 13.0 statistical software. One-way analysis of variance (ANOVA) was used for comparison of means between multiple groups. Differences were considered statistically significant at $P < 0.05$.

TABLE 1: Characteristics of active ingredients in *Citrus aurantium*.

No.	Mol ID	Molecule name	Molecular weight	OB (%)	DL
1	MOL013381	Marmin	332.43	38.23	0.31
2	MOL002341	Hesperetin	302.3	70.31	0.27
3	MOL000358	Beta-sitosterol	414.79	36.91	0.75
4	MOL004328	Naringenin	272.27	59.29	0.21
5	MOL005828	Nobiletin	402.43	61.67	0.52

OB: oral bioavailability; DL: drug-likeness.

3. Results

3.1. *Establishment of a Database of Active Ingredients and Targets of Citrus aurantium.* Through the TCMSP database, 17 active ingredients of *Citrus aurantium* were available, and the list of ingredients was screened by oral bioavailability (OB) ≥ 30% and adult drug similarity (DL) ≥ 0.18, and finally, five highly active ingredients were obtained (Table 1).

Similarly, 124 relevant targets for five highly active ingredients were available in the TCMSP database. Target names were corrected and deduplicated using UniProt to finally obtain 80 relevant target genes for *Citrus aurantium*. Based on GeneCards and OMIM databases, a total of 6177 target genes related to NSCLC were obtained. The Venn diagram of *Citrus aurantium* and NSCLC was drawn using the Venny 2.1.0 online platform, and 54 crossover genes were obtained by analysis (Table 2 and Figure 1(a)).

3.2. *Protein Interaction Network Analysis.* The protein interaction network graph of *Citrus aurantium* with NSCLC can be obtained by entering the crossover genes into the STRING online platform and hiding the free nodes outside the network (Figure 1(b)). After analysis, there are 52 nodes and 195 edges with an average node number of 7.22. In the network diagram, network nodes represent proteins, edges represent protein-protein associations, and different color edges indicate different meanings: light blue indicates from selected databases, purple indicates experimentally determined, and these two are known; green indicates gene neighborhood, red indicates gene fusion, and dark blue indicates gene cooccurrence, and these three are predicted; there are also yellow that indicates text mining, black indicates coexpression, and white indicates protein homology. The protein interaction network map was imported into Cytoscape 3.9.1, and the data were analyzed using the CentiScaPe2.2 plug-in, and 12 key targets (Figure 1(c)) were obtained after filtering based on the mediator centrality (BC), closeness centrality (CC), and degree centrality (DC) parameters. As can be seen from the figure, the top seven genes with node degree values are TP53, CAT, ESR1, MMP9, CXCL8, MAPK14, and PPAR-α, indicating that these genes are in key positions in the protein interaction network.

3.3. *Construction and Analysis of Drug Component-Disease Target Networks.* The information related to the active ingredients of *Citrus aurantium* and the crossover genes between

TABLE 2: 54 potential target genes of *Citrus aurantium* therapy for NSCLC.

No.	Target	Symbol	UniProt ID
1	Prostaglandin G/H synthase 1	PTGS1	P23219
2	Prostaglandin G/H synthase 2	PTGES3	Q15185
3	Heat shock protein HSP 90	HSPB1	P04792
4	Phosphatidylinositol-4,5-bisphosphate 3-kinase catalytic subunit, gamma isoform	PIK3CG	P48736
5	mRNA of PKA catalytic subunit C-alpha	AKAP13	Q12802
6	Nuclear receptor coactivator 1/nuclear receptor coactivator 2	BUD23	O43709
7	Progesterone receptor	NR3C2	P08235
8	Muscarinic acetylcholine receptor M3	CHRM3	P20309
9	Muscarinic acetylcholine receptor M1	CHRM1	P11229
10	CGMP-inhibited $3',5'$-cyclic phosphodiesterase A	PDE3A	Q14432
11	Muscarinic acetylcholine receptor M2	CHRM2	P08172
12	Neuronal acetylcholine receptor subunit alpha-2	CHRNA3	P32297
13	Mu-type opioid receptor	OPRM1	P35372
14	Cytochrome P450-cam	FGFR4	P22455
15	Apoptosis regulator Bcl-2/apoptosis regulator BAX	BCL2L1	Q07817
16	Caspase-9	CASP9	P55211
17	Transcription factor AP-1	ESR1	P03372
18	Caspase-8	CARD8	Q9Y2G2
19	Transforming growth factor beta-1	LYN	P07948
20	Serum paraoxonase/arylesterase 1	PON1	P27169
21	Microtubule-associated protein 2	MAP4	P27816
22	Transcription factor p65	CDK9	P50750
23	RAC-alpha serine/threonine-protein kinase	BCR	P11274
24	Mitogen-activated protein kinase 1/mitogen-activated protein kinase 3	MAPK14	Q16539
25	Bcl2 antagonist of cell death	MAPK8	P45983
26	Catalase	CAT	P04040
27	Peroxisome proliferator-activated receptor gamma	PPARA	Q07869
28	Apolipoprotein B-100	APOB	P04114
29	Phospholipase B1, membrane-associated	SNCA	P37840
30	3-Hydroxy-3-methylglutaryl-coenzyme A reductase	HMGCR	P04035
31	Cytochrome P450 19A1	CYP19A1	P11511
32	Glutathione S-transferase P	GSTP1	P09211
33	UDP-glucuronosyltransferase 1-1	UGT1A1	P22309
34	Glutathione reductase, mitochondrial	GSTO1	P78417
35	Adiponectin	ADIPOQ	Q15848
36	Aldo-keto reductase family 1 member C1	AKR1C2	P52895
37	Liver carboxylesterase 1	CES1	P23141
38	Nitric oxide synthase, inducible	NOS2	P35228
39	Thrombin	CXCL8	P10145
40	Androgen receptor	PKN1	Q16512
41	Coagulation factor Xa/coagulation factor VII	F2RL1	P55085
42	mRNA of protein-tyrosine phosphatase, nonreceptor type 1	PTPN22	Q9Y2R2
43	DNA topoisomerase II	DHX9	Q08211
44	Estrogen receptor beta	PDGFRB	P09619
45	Dipeptidyl peptidase IV	DPP4	P27487
46	Serine/threonine-protein kinase Chk1	CDK1	P06493
47	Trypsin-1	PRSS1	P07477
48	Calcium-activated potassium channel subunit alpha 1	KCNMA1	Q12791

No.	Target	Symbol	UniProt ID
49	Glycogen synthase kinase-3 beta	GSK3B	P49841
50	Matrix metalloproteinase-9	MMP9	P14780
51	Cellular tumor antigen p53	TP53	P04637
52	Cytosolic phospholipase A2	ANXA3	P12429
53	Scavenger receptor cysteine-rich type 1 protein M130	CD163	Q86VB7
54	Ephrin type-B receptor 2	MMP2	P08253

(a)

(b)

(c)
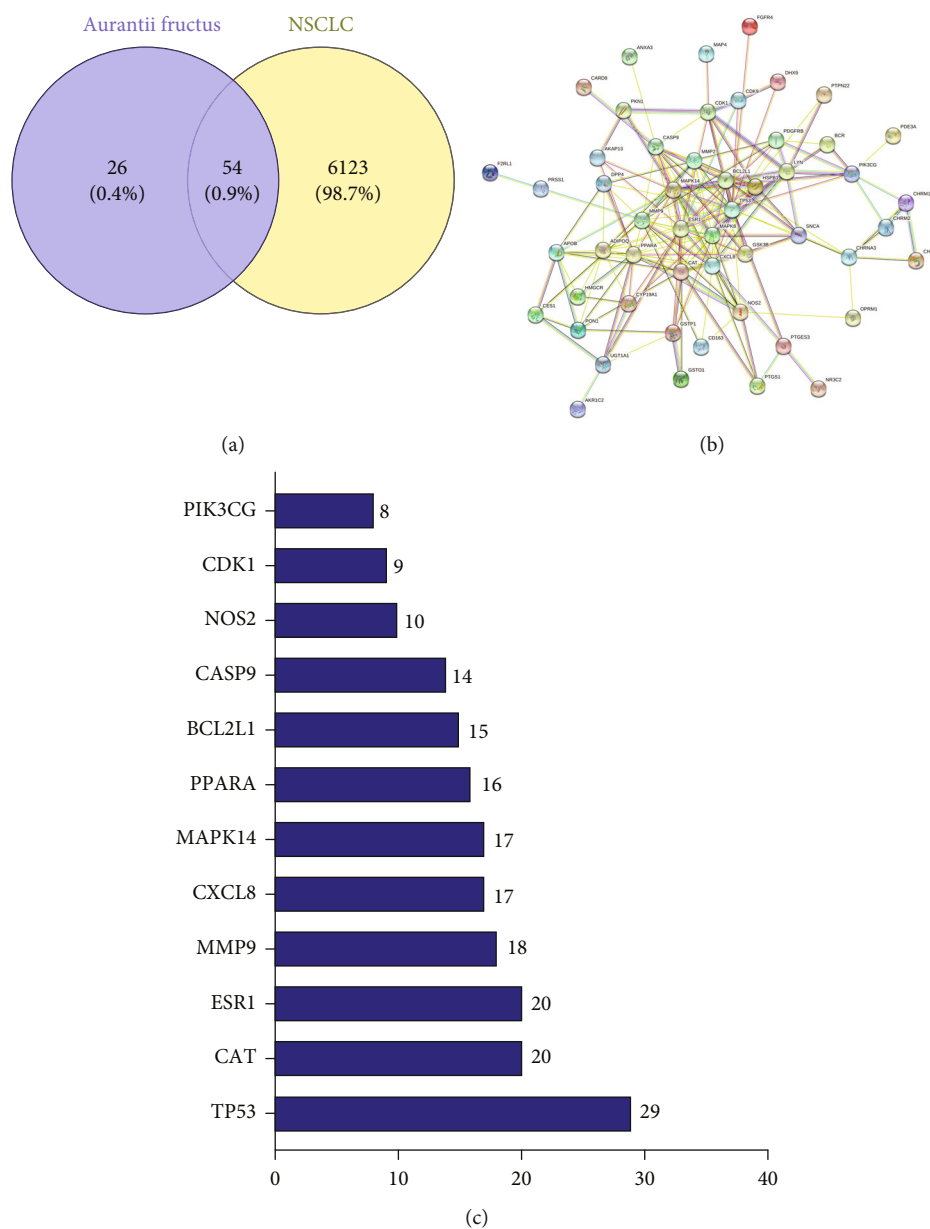
FIGURE 1: Network diagram of potential target genes and PPI of *Citrus aurantium* for the treatment of NSCLC. (a) Venny results of potential target genes of *Citrus aurantium* for the treatment of NSCLC. (b) PPI network diagram of 51 target genes. (c) Key targets of *Citrus aurantium*-NSCLC.
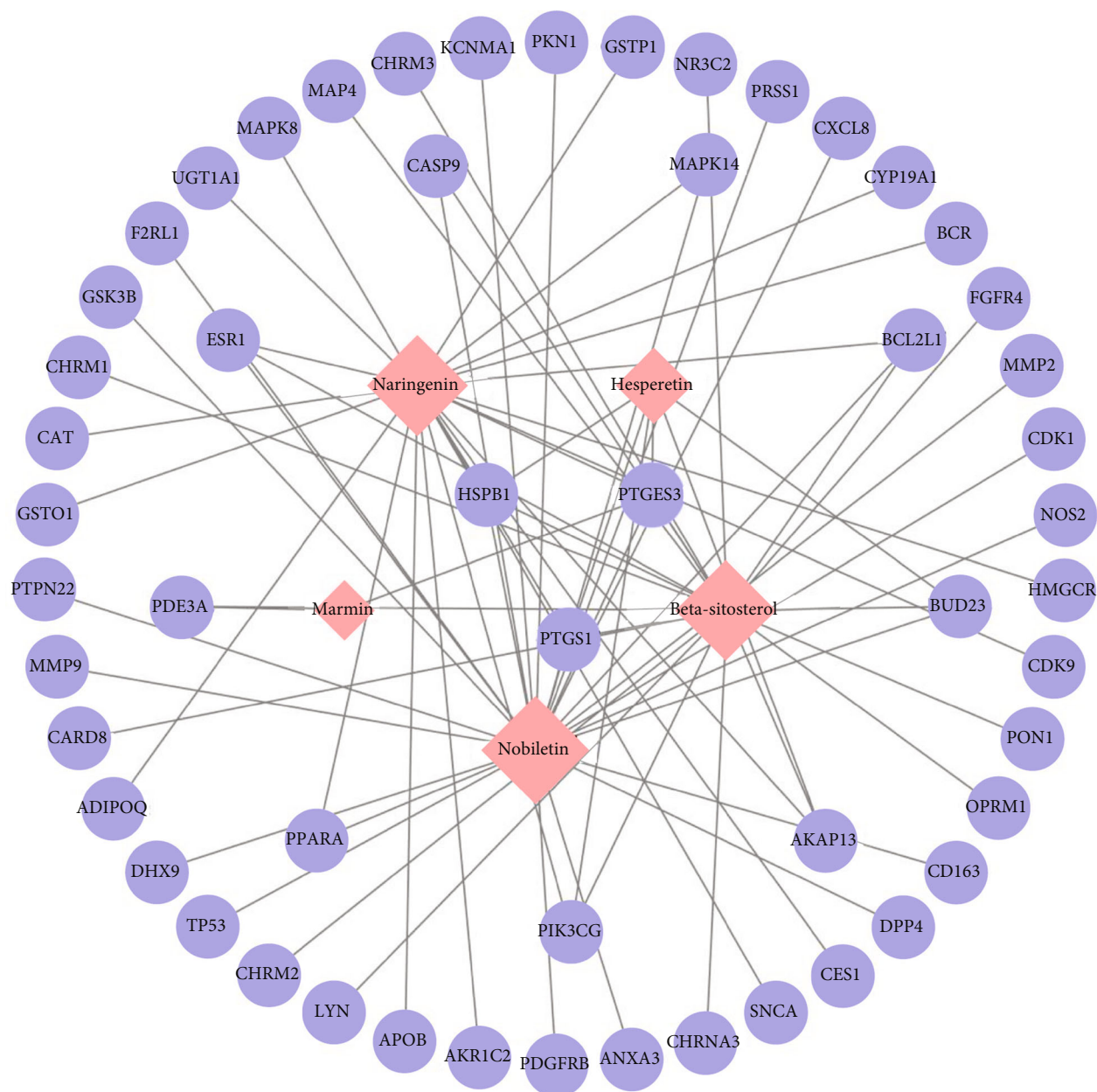
Figure 2: *Citrus aurantium*-NSCLC potential target gene network.

Table 3: The list of key active components in *Citrus aurantium* dependent on the centrality of a node.

No.	Molecule name	Degree	Closeness unDir	Betweenness unDir
1	Hesperetin	6	0.006329114	36.36140351
2	Beta-sitosterol	21	0.0078125	1319.583584
3	Naringenin	23	0.008064516	1510.188889
4	Nobiletin	26	0.008474576	1761.830409
5	Marmin	2	0.006024096	10.03571429

Citrus aurantium and NSCLC was imported into Cytoscape 3.9.1 to construct a *Citrus aurantium* component-NSCLC target network map (Figure 2). Using one of the analyses, CentiScaPe2.2, the key component of *Citrus aurantium* for the treatment of NSCLC was finally obtained as nobiletin based on the mesocentricity (BC), closeness centrality

(a)

(b)

FIGURE 3: Continued.

Go- Molecular function

(c)

KEGG- Pathway analysis

(d)
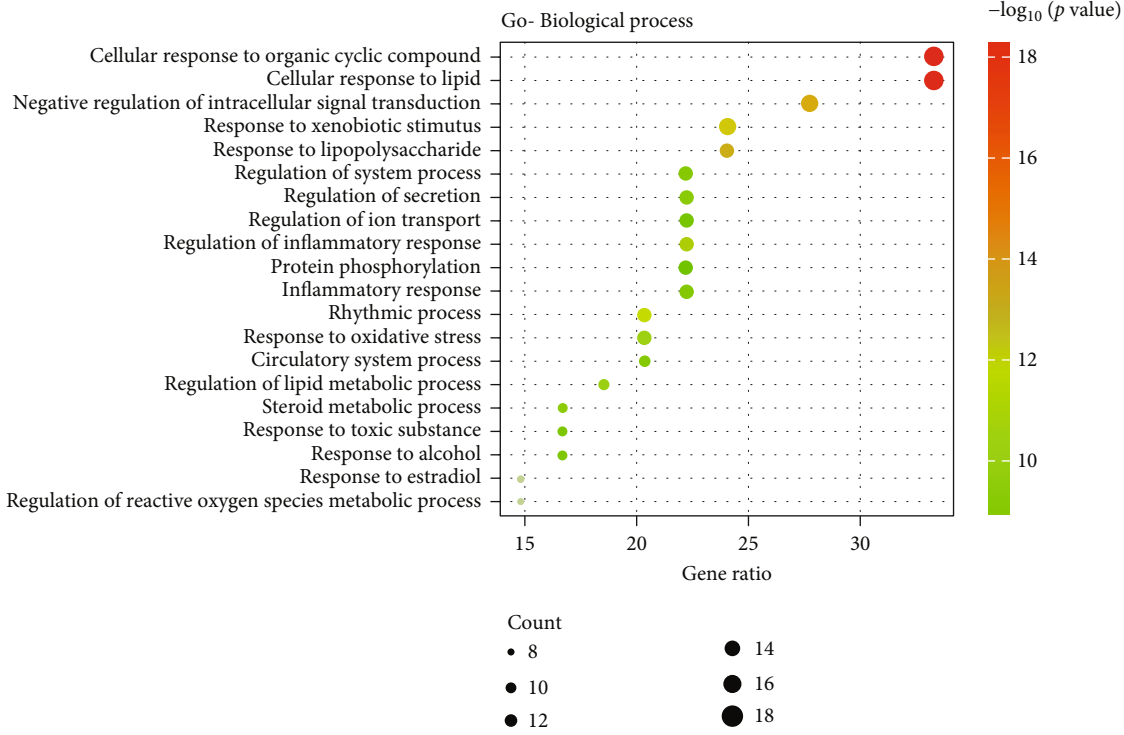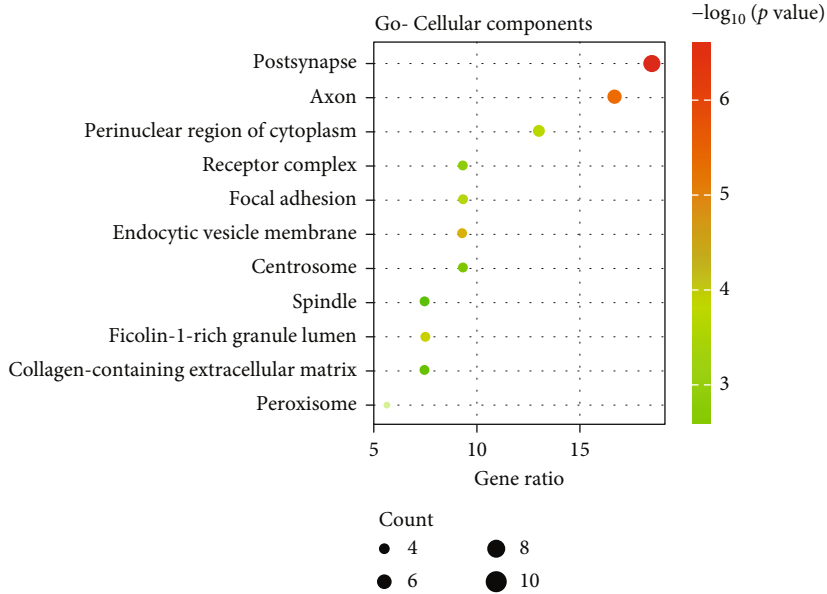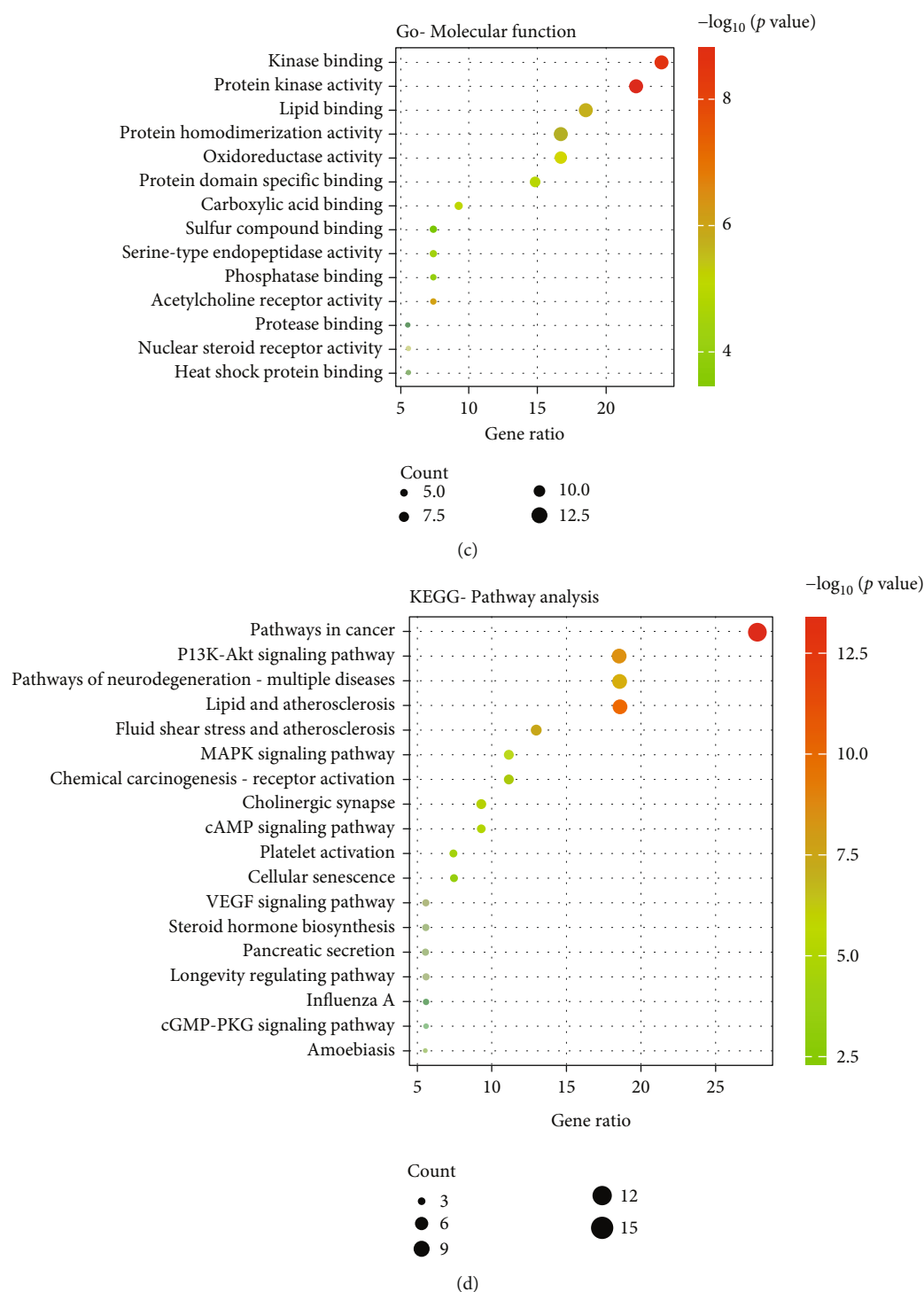
Figure 3: GO and KEGG analyses of potential target genes of *Citrus aurantium* in NSCLC. GO analysis of biological processes (a), molecular functions (b), and cellular components (c) of potential target genes of *Citrus aurantium* in NSCLC. (d) KEGG enrichment analysis of potential target gene signaling pathway of *Citrus aurantium* in NSCLC.

(CC), and degree centrality (DC) parameters. The results showed that nobiletin was higher than the other four components, suggesting that nobiletin in *Citrus aurantium* is a key component in the treatment of NSCLC (Table 3).

3.4. GO and KEGG Enrichment Analyses. The *Citrus aurantium*-NSCLC crossover genes were entered into the Metas-

cape database for GO and KEGG enrichment analyses. Based on $P < 0.01$, a minimum number of 3, and enrichment factor > 1.5, GO analysis yielded 20 biological processes, 14 molecular functions, and 11 cellular compositions that are component targets of *Citrus aurantium* for the treatment of NSCLC (Figures 3(a)–3(c)). The results showed that cellular responses to organic cyclic compounds

FIGURE 4: Continued.

(e)

(f)

(g)

(h)
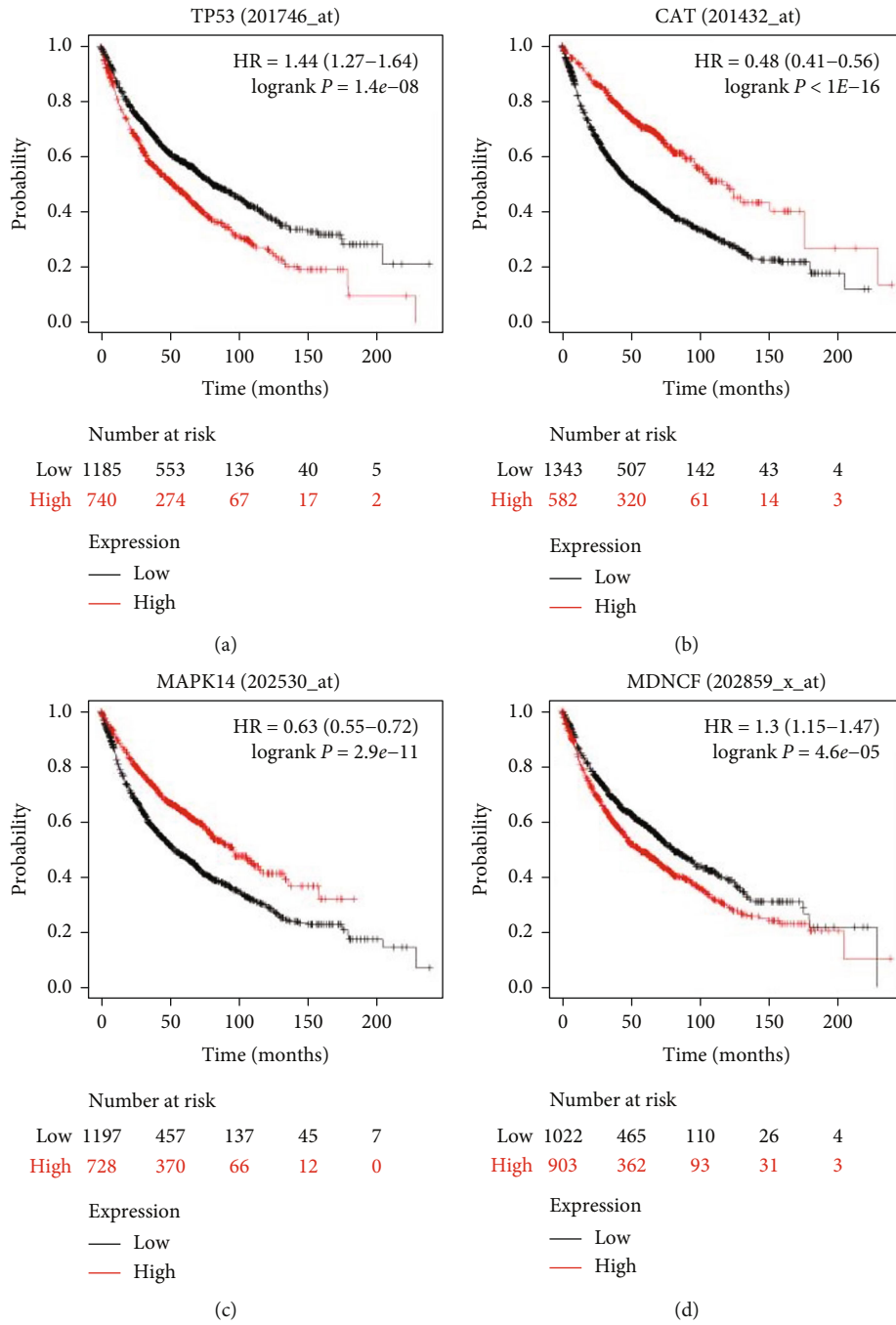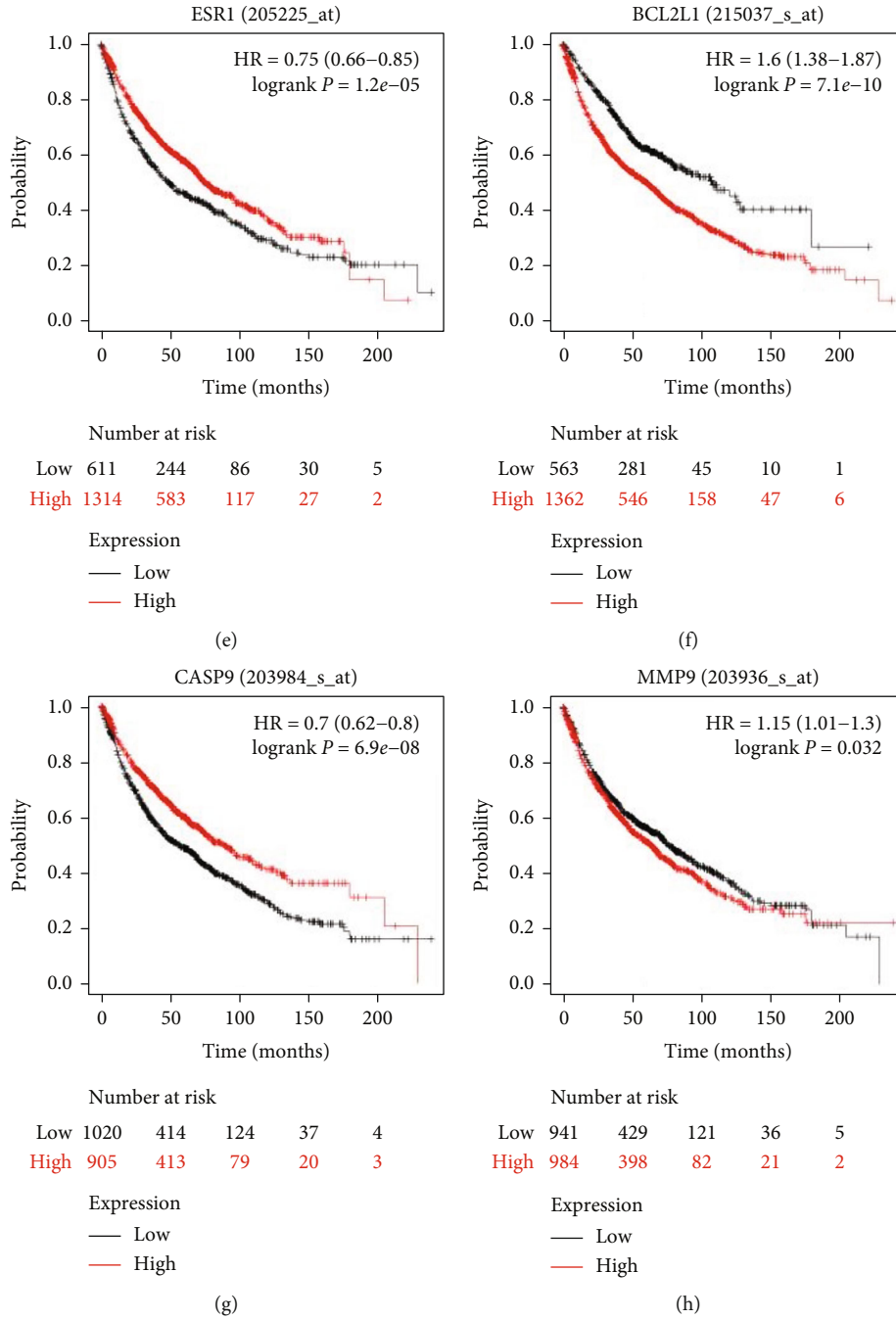
FIGURE 4: Continued.
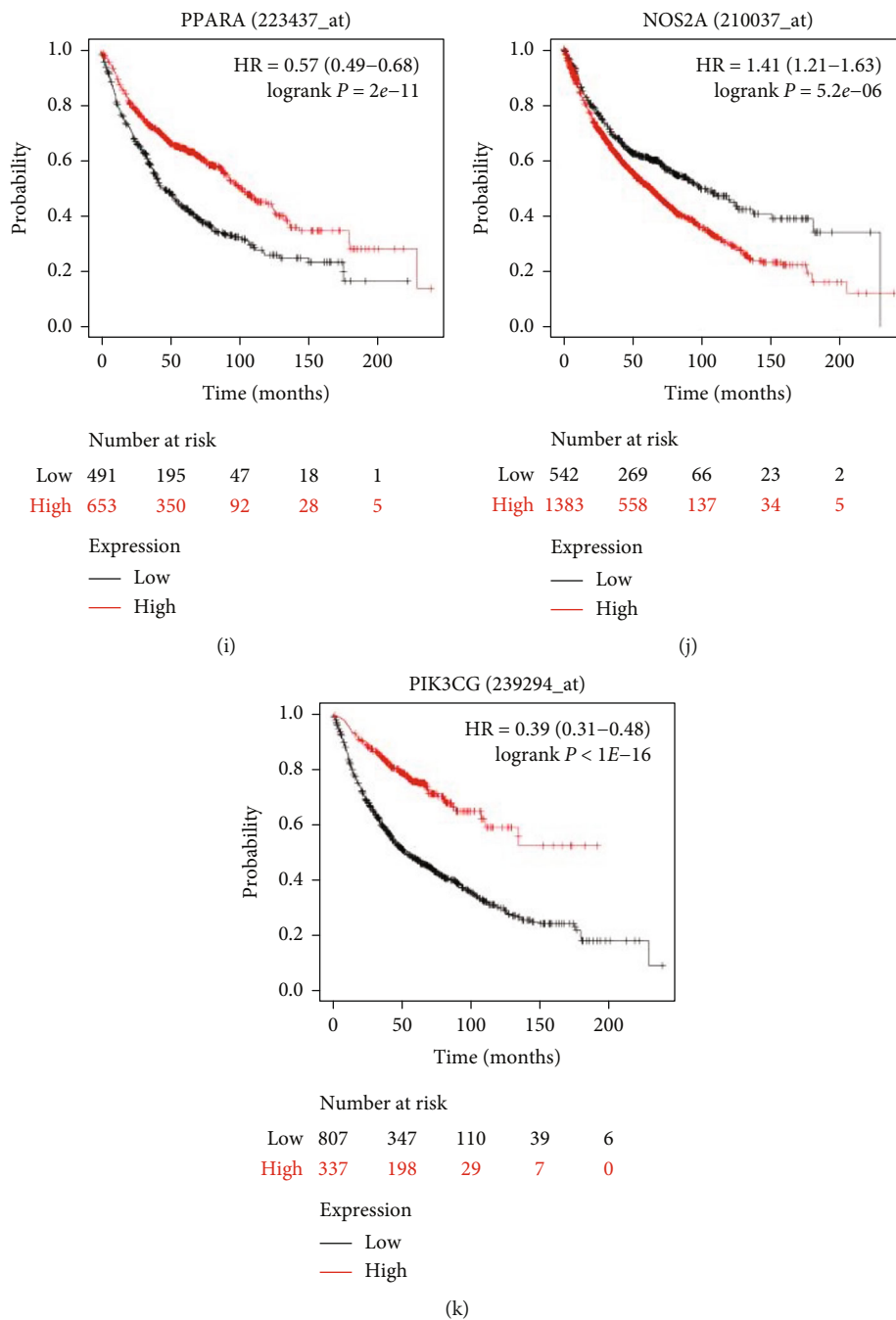
FIGURE 4: Prognostic characteristics of 12 key targets in nobiletin-NSLC. Overall survival (OS) survival curves for key targets were plotted using the Kaplan-Meier plotter database ($P < 0.05$, $n = 2437$). (a) TP53; (b) CAT; (c) MAPK14; (d) MDCNF(CXCL8); (e) ESR1; (f) BCL2L1; (g) CASP9; (h) MMP9; (i) PPARA; (j) NOS2A(NOS2); (k) PIK3CG; black line indicates low expression, and red line indicates high expression.

(target number 18), cellular responses to lipids (target number 18), negative regulation of intracellular signaling (target number 15), responses to lipopolysaccharides (target number 14), and responses to exogenous stimuli (target number 14) were significantly enriched in *Citrus aurantium* for the treatment of NSCLC, indicating that *Citrus aurantium* is able to treat NSCLC through multiple biological pathways. 140 pathways were obtained by KEGG enrichment analysis ($P < 0.01$), and 18 pathways with the highest correlation to NSCLC were obtained by screening (Figure 3(d)). The results showed the highest enrichment in tumor-related signaling pathway (target number 15), lipid and atherosclerosis signaling pathway (target number 10), PI3K-Akt signaling pathway (target number 10), and neurodegenerative signaling pathway (target number 10), indicating that *Citrus aurantium* can treat NSCLC through these pathways.
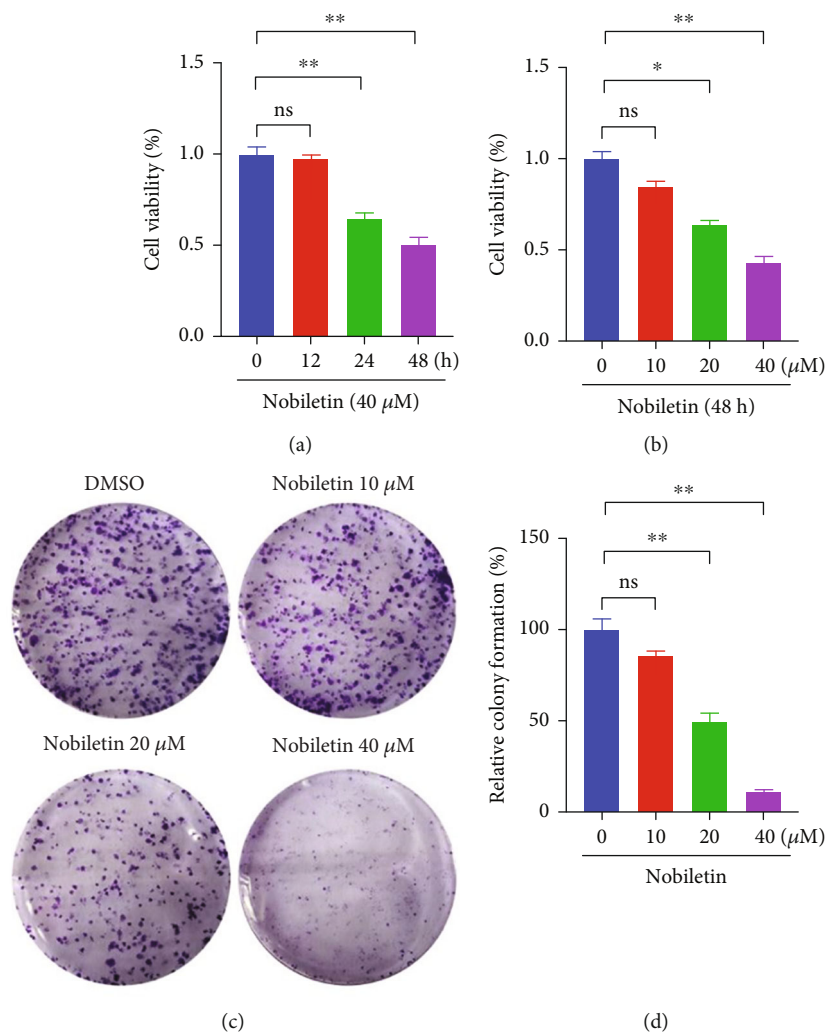
FIGURE 5: Effect of nobiletin on the proliferation of NSCLC cells. (a) NSCLC cells were treated with $40\,\mu$M nobiletin, and the effect of nobiletin on the proliferation of NSCLC cells at 0, 12, 24, and 48 h was examined by CCK-8 analysis. (b) NSCLC cells were treated with different concentrations of nobiletin for 48 h, and the effect of nobiletin on the proliferation of NSCLC cells was detected by CCK-8 analysis. (c, d) Cell proliferation was assessed by colony formation assay after treatment of NSCLC cells with different concentrations of nobiletin. $^{*}P < 0.05$ compared with the untreated group, $n = 5$.

3.5. Prognostic Value of Key Targets. Survival analysis was performed by the Kaplan-Meier plotter to evaluate the expression and prognosis of 12 key targets in NSCLC. As shown in Figure 4, TP53 (HR = 1.44 [1.27-1.64], logrank $P = 1.4e - 08$), CXCL8 (HR = 1.3 [1.15-1.47], logrank $P = 4.6e - 05$), BCL2L1 (HR = 1.38 [1.38-1.87], logrank $P = 7.1e - 10$), MMP9 (HR = 1.15 [1.01-1.3], logrank $P = 0.032$), and NOS2 (HR = 1.41 [1.21-1.63], logrank $P = 5.2e - 06$) high mRNA expressions were associated with significantly shorter OS in all NSCLC patients ($P < 0.05$); i.e., survival was lower in the high expression group than in the low expression group. In contrast, CAT (HR = 0.48 [0.41-0.56], logrank $P < 1e - 16$), ESR1 (HR = 0.75 [0.66-0.85], logrank $P = 1.2e - 05$), MAPK14 (HR = 0.63 [0.55-0.72], logrank $P = 2.9e - 11$), CASP9 (HR = 0.7 [0.62-0.8], logrank $P = 6.9e - 08$), PIK3CG (HR = 0.39 [0.31-0.48], logrank $P < 1e - 16$), and PPAR-α (HR = 0.57 [0.49-0.68], logrank $P = 2e - 11$) mRNA high expressions were associated with significantly improved OS in all NSCLC patients ($P < 0.05$); i.e., survival was higher in the high expression group than in the low expression group. In addition, CDK1 lacked relevant data.

3.6. Effect of Nobiletin on the Proliferation of NSCLC A549 Cells. To assess whether nobiletin could inhibit the growth of NSCLC cells, we treated NSCLC cells with different concentrations of nobiletin (0, 10, 20, and $40\,\mu$M) for 12, 24, and 48 h and then measured cell viability using the CCK8 assay. The results showed that nobiletin inhibited the proliferation of NSCLC cells in a dose-dependent manner (Figures 5(a) and 5(b)). In addition, clonogenesis assays confirmed that nobiletin inhibited the colony-forming ability of NSCLC cells in a dose-dependent manner compared to untreated cells (Figures 5(c) and 5(d)). The above results suggest that nobiletin inhibits the proliferation of NSCLC A549 cells.

TABLE 4: Primer sequences for qRT-PCR.

Primer	Sequences
P53	Forward:5′-GTTTCCGTCTGGGCTTCT-3′
	Reverse: 5′-CAACCTCCGTCATGTGCT-3′
CXCL8	Forward: 5′-ACATACTCCAAACCTTTCC-3′
	Reverse: 5′-AACTTCTCCACAACCCTC-3′
ESR1	Forward: 5′-AGGGAAGTATGGCTATGGAA-3′
	Reverse: 5′-ACTGGTTGGTGGCTGGAC-3′
PPARA	Forward: 5′-CATCGGCGAGGATAGTTC-3′
	Reverse: 5′-TGAAAGCGTGTCCGTGAT-3′
MMP9	Forward: 5′-TCCCTGGAGACCTGAGAACC-3′
	Reverse: 5′-GCCACCCGAGTGTAACCAT-3′
GAPDH	Forward: 5′-AGGAGTAAGAAACCCTGGAC-3′
	Reverse: 5′-CTGGGATGGAATTGTGAG-3′

3.7. Effect of Nobiletin on Key Targets in NSCLC. To demonstrate the effect of nobiletin on key targets in NSCLC, we treated A549 cells with different concentrations of nobiletin (0, 10, 20, and 40 μM) for 48 h and detected the mRNA expression of p53, ESR1, MMP9, CXCL8, and PARPA by real-time PCR (Table 4). The protein expression level of p53 was detected by Western blotting method. The results showed that nobiletin dose-dependently increased the mRNA and protein expression of P53 (Figures 6(a) and 6(b)). In addition, we also found that nobiletin was able to increase the mRNA expression of PPAR-α and inhibit the mRNA level of MMP9 (Figures 6(e) and 6(f)). Moreover, nobiletin had no significant effect on the expression of CXCL8 and ESR1 (Figures 6(c) and 6(d)).

4. Discussion

Lung cancer is one of the malignant tumors with the highest incidence and mortality rate worldwide, but the current clinical treatment is not satisfactory [3]. In this study, we explored the potential therapeutic targets and major molecular mechanisms of *Citrus aurantium* for the treatment of NSCLC based on network pharmacology analysis and bioinformatics. Cyberpharmacology combines system biology and pharmacology to analyze and explore the multichannel regulation of signaling pathways through high-throughput sequencing, genomics, and other technologies to find therapeutic targets and signaling pathways for diseases [23]. Based on network pharmacology, we collected 5 active ingredients, 80 targets, and 177 disease targets of *Citrus aurantium* and obtained 54 crossover genes in this study. The results of protein interaction network combined with enrichment analysis were used to obtain nobiletin, a key compound of *Citrus aurantium* for the treatment of NSCLC, and five key targets: TP53, CXCL8, ESR1, PPAR-α, and MMP9. GO bioprocess analysis showed that *Citrus aurantium* can treat NSCLC as long as the biological processes such as cellular response through organic cyclic compounds,

cellular response to lipids, and negative regulation of intracellular signal transduction. KEGG signaling pathway enrichment analysis showed that the main pathways of *Citrus aurantium* for the treatment of NSCLC were tumor-associated signaling pathway, lipid and atherosclerosis signaling pathway, PI3K-Akt signaling pathway, neurodegenerative signaling pathway, and MAPK signaling pathway.

The development and progression of NSCLC is synergistically regulated by multiple extracellular and intracellular signals. The TP53 gene is located on human chromosome 17 and is involved in the encoding of the p53 protein, which inhibits cancer formation by interacting with various related signaling pathways [24]. Activated p53 protein transcriptionally regulates hundreds of genes involved in multiple biological processes, including DNA repair, cell cycle arrest, cell growth, cell division, apoptosis, senescence, autophagy, and metabolism, thereby mediating cancer suppression [25–28]. NF-κB and Bax proteins are upstream and downstream targets of p53, respectively, and play important roles in cell growth. Guo et al. [29] showed that PAQR3 inhibits the development and progression of NSCLC through the NF-κB/p53/Bax signaling pathway. In addition, it was found that p53 expression levels positively correlated with apoptosis in NSCLC tissues and inhibited the proliferation of lung cancer cells by increasing apoptosis, thereby inhibiting tumor growth and delaying the development of NSCLC [30]. MMP9, a member of the matrix metalloproteinase family (MMPs), is located on human chromosome 20 and is one of the most important enzymes in the breakdown of the extracellular matrix, playing a key role in the invasion and metastasis of cancer [31]. Previous studies have shown that MMP9 expression can be downregulated by reducing AKT/mTOR levels that promote H3K27Ac and H3K56A on the MMP9 promoter region, thereby inhibiting the proliferation and metastasis of triple-negative breast cancer [32], and that MMP-9 can also promote the invasion and migration of gastric cancer cells through the ERK pathway [33]. In addition, a study by Zhang et al. [34] found that the expression level of MMP9 was significantly higher in lung cancer patients than in normal subjects, and the higher the expression of MMP9, the worse the survival status of lung cancer patients. In the present work, we found that nobiletin significantly increased the expression level of P53 and inhibited the expression of MMP9 in A549 cells, suggesting that P53 and MMP9 may be downstream targets of nobiletin in regulating NSCLC.

CXCL8 is a proinflammatory CXC chemokine, called interleukin-8 (IL-8), involved in tumor angiogenesis to promote tumorigenesis and metastasis [35]. The Kaplan-Meier survival analysis showed that high IL-8 expression was associated with a poorer prognosis in NSCLC patients ($P < 0.05$, Figure 4(b)). CXCL8 interacts with CXCL1 and CXCL2 to promote the secretion of multiple proinflammatory, angiogenic, and immunomodulatory factors (including MMP and VEGF) by neutrophils, thereby promoting tumor metastasis in patients with NSCLC [36, 37]. Yan et al. [38] showed that IL-8 is highly expressed in lung cancer and suggested that it could be a potential biomarker for lung cancer and has strong diagnostic properties for lung cancer. In another

(a)

(b)

(c)

(d)

(e)

(f)
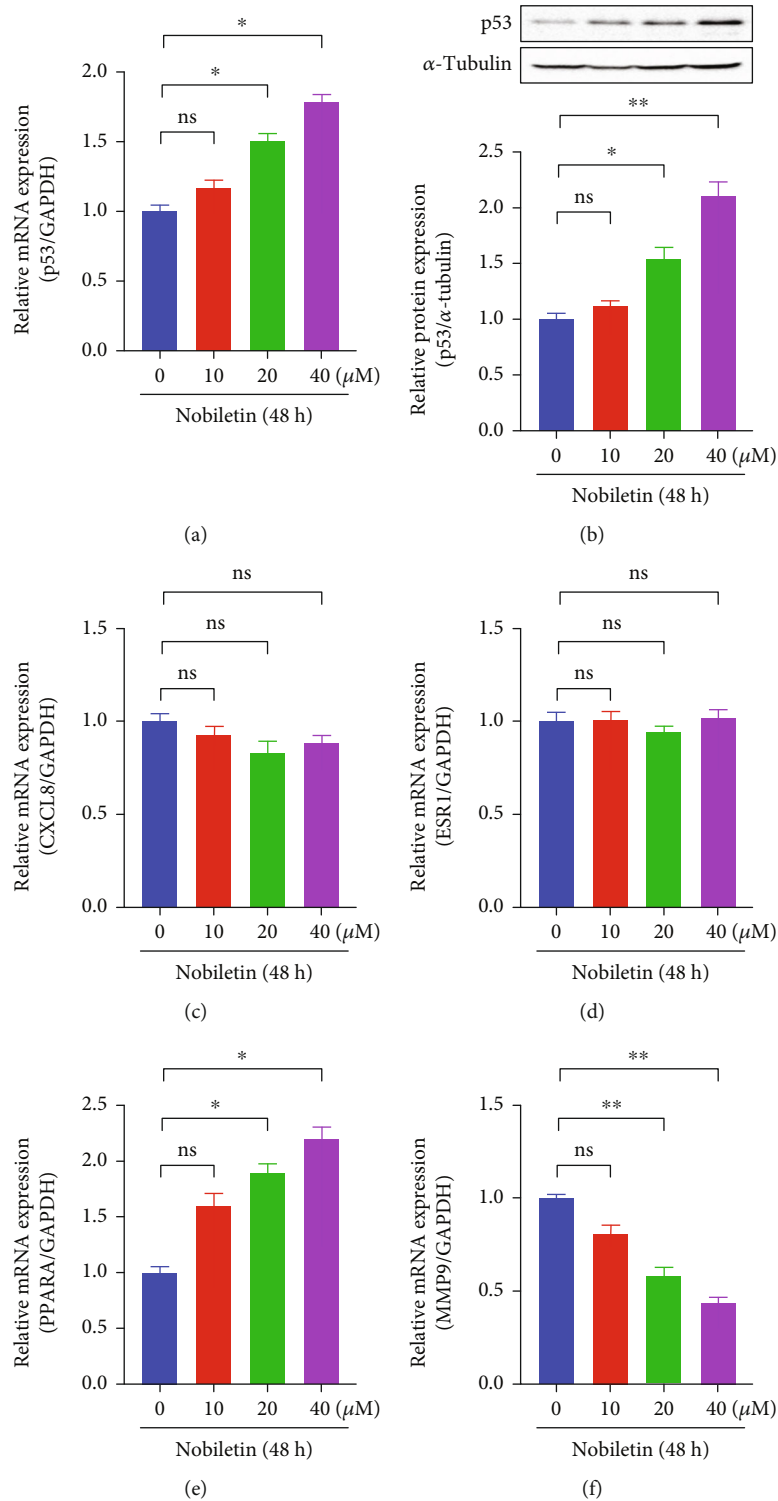
FIGURE 6: Effect of nobiletin on the expression of key target genes. NSCLC cells were treated with 0, 10, 20, and 40 μM nobiletin for 48 h. Real-time PCR was performed to detect the mRNA expression of (a) TP53, (c) CXCL8, (d) ESR1, (e) PPARA, and (f) MMP9. (b) Protein expression of TP53 was detected by protein immunoblotting. $^*P < 0.05$ compared with the untreated group, $n = 5$.

study, the methyltransferase SETD2 was found to inhibit tumor growth and metastasis through STAT1-IL-8 signaling-mediated epithelial-mesenchymal transition in lung adenocarcinoma [39]. ESR1 is localized on chromosome 6 and belongs to the transcriptional activator super-

family, whose protein product is a transcription factor primarily involved in encoding the estrogen receptor. It was shown that hypermethylation of ESR1 was detected only in lung tumors but not in adjacent normal lung tissue, suggesting that ESR1 hypermethylation may be associated with

the development of lung cancer. Assessment of p16 and ESR1 methylation in blood facilitates early diagnosis of lung cancer, and these methylation genes may be biomarkers for early lung cancer [40, 41]. It has been shown that ESR1 signaling plays a biological role in both epithelial and mesenchymal cells in the lung and that ESR1 may promote lung cancer by acting directly on precancerous or tumor cells or indirectly on lung fibroblasts [42]. However, in the present study, we did not find that nobiletin was able to affect the levels of ESR1 and CXCL8.

Peroxisome proliferator-activated receptor alpha (PPAR-α) is a ligand-activated nuclear receptor that regulates transcription of target genes associated with lipid homeostasis, differentiation, and inflammation in a variety of ways [43–45]. Luo et al. [46] showed that intestinal PPAR-α deficiency in mice increased azomethane- (AOM-) induced colon tumorigenesis and tumor growth. In addition, they demonstrated by IHC staining that the PPAR-α-DNMT1/PRMT6-p21/p27 regulatory pathway may also play a role in the early stages of human colorectal carcinogenesis. Previous studies found that apatinib exerts its antitumor effects through the induction of ketogenesis and demonstrated that this tumor-suppressive effect is PPAR-α-dependent [47]. In another study, fenofibrate, a PPAR-α agonist, was found to alleviate resistance to gefitinib in NSCLC cell lines by modulating the PPAR-α/AMPK/AKT/FoxO1 signaling pathway and demonstrated that the increased antiproliferative effect of fenofibrate was abolished when PPAR-α was silenced [48]. In addition, several studies have shown that activation of PPAR-α can inhibit lung cancer growth and metastasis by downregulating cytochrome P450 arachidonic acid cyclooxygenase (Cyp2c) [49, 50]. In the present study, we found that nobiletin significantly increased the expression of PPAR-α, suggesting that PPAR-α may also be involved in the regulatory role of nobiletin in NSCLC.

5. Conclusion

In conclusion, we found through our study that nobiletin in *Citrus aurantium* may be a key active ingredient in the treatment of NSCLC. In addition, further analysis showed that nobiletin inhibited the development of NSCLC through targets such as TP53, CXCL8, ESR1, PPAR-α, and MMP9 and related signaling pathways. Through pharmacological experiments, we verified that nobiletin inhibited the proliferation of NSCLC A549 cell line and affected the expression of P53, PPAR-α, and MMP9. In future experiments, we will further clarify the downstream targets of nobiletin that regulate the proliferation of NSCLC through gene overexpression and silencing. This study provides a reference for further research on the mechanism of action of *Citrus aurantium* in the treatment of NSCLC.

Data Availability

The data used to support the findings of this study are available from the corresponding authors upon reasonable request.

Conflicts of Interest

The authors have declared that no conflict of interest exists.

Acknowledgments

References

[1] H. Sung, J. Ferlay, R. L. Siegel et al., "Global cancer statistics 2020: GLOBOCAN estimates of incidence and mortality worldwide for 36 cancers in 185 countries," *CA: a Cancer Journal for Clinicians*, vol. 71, no. 3, pp. 209–249, 2021.

[2] K. Inamura, "Update on immunohistochemistry for the diagnosis of lung cancer," *Cancers*, vol. 10, no. 3, p. 72, 2018.

[3] F. Liu, T. Liu, and H. Li, "Aloperine inhibits the progression of non-small-cell lung cancer through the PI3K/Akt signaling pathway," *Cancer Cell International*, vol. 21, no. 1, p. 662, 2021.

[4] F. Palma, A. Affinito, S. Nuzzo et al., "miR-34c-3p targets CDK1 a synthetic lethality partner of KRAS in non-small cell lung cancer," *Cancer Gene Therapy*, vol. 28, no. 5, pp. 413–426, 2021.

[5] W. He, H. Zhang, Y. Wang et al., "CTHRC1 induces non-small cell lung cancer (NSCLC) invasion through upregulating MMP-7/MMP-9," *BMC Cancer*, vol. 18, no. 1, p. 400, 2018.

[6] S. H. Han, J. H. Han, W. J. Chun, S. S. Lee, H. S. Kim, and J. W. Lee, "Nobiletin inhibits non-small-cell lung cancer by inactivating WNT/beta-catenin signaling through downregulating miR-15-5p," *Evidence-Based Complementary and Alternative Medicine*, vol. 2021, Article ID 7782963, 9 pages, 2021.

[7] D. Rocco, V. Gregorc, L. Della Gravara, C. Lazzari, G. Palazzolo, and C. Gridelli, "New immunotherapeutic drugs in advanced non-small cell lung cancer (NSCLC): from preclinical to phase I clinical trials," *Expert Opinion on Investigational Drugs*, vol. 29, no. 9, pp. 1005–1023, 2020.

[8] A. Upadhya, K. S. Yadav, and A. Misra, "Targeted drug therapy in non-small cell lung cancer: clinical significance and possible solutions-part I," *Expert Opinion on Drug Delivery*, vol. 18, no. 1, pp. 73–102, 2021.

[9] J. Zheng, T. Xu, F. Chen, and Y. Zhang, "MiRNA-195-5p functions as a tumor suppressor and a predictive of poor prognosis in non-small cell lung cancer by directly targeting CIAPIN1," *Pathology Oncology Research*, vol. 25, no. 3, pp. 1181–1190, 2019.

[10] L. Zhu, Z. Chen, H. Zang et al., "Targeting c-Myc to overcome acquired resistance of EGFR mutant NSCLC cells to the third-generation EGFR tyrosine kinase inhibitor, osimertinib," *Cancer Research*, vol. 81, no. 18, pp. 4822–4834, 2021.

[11] Y. Pan, C. Deng, Z. Qiu, C. Cao, and F. Wu, "The resistance mechanisms and treatment strategies for ALK-rearranged non-small cell lung cancer," *Frontiers in Oncology*, vol. 11, article 713530, 2021.

[12] X. Zhang, Q. Guo, C. Li et al., "Immortal time bias-corrected effectiveness of traditional Chinese medicine in non-small cell lung cancer (C-EVID): a prospective cohort study," *Frontiers in Oncology*, vol. 12, article 845613, 2022.

[13] Y. Lu, C. Sun, L. Jiao, Y. Liu, Y. Gong, and L. Xu, "Chinese herbal medicine combined with first-generation EGFR-TKIs in treatment of advanced non-small cell lung cancer with EGFR sensitizing mutation: a systematic review and meta-analysis," *Frontiers in Pharmacology*, vol. 12, article 698371, 2021.

[14] J. Ni, Y. Guo, N. Chang et al., "Effect of _N_ -methyltyramine on the regulation of adrenergic receptors via enzymatic epinephrine synthesis for the treatment of gastrointestinal disorders," *Biomedicine & Pharmacotherapy*, vol. 111, pp. 1393–1398, 2019.

[15] X. Zhang, L. Han, J. Liu et al., "Pharmacokinetic study of 7 compounds following oral administration of Fructus Aurantii to depressive rats," *Frontiers in Pharmacology*, vol. 9, p. 131, 2018.

[16] M. Wu, H. Zhang, C. Zhou, H. Jia, Z. Ma, and Z. Zou, "Identification of the chemical constituents in aqueous extract of Zhi-Qiao and evaluation of its antidepressant effect," *Molecules*, vol. 20, no. 4, pp. 6925–6940, 2015.

[17] X. Li, Q. Liang, Y. Sun et al., "Potential mechanisms responsible for the antinephrolithic effects of an aqueous extract of Fructus Aurantii," *Evidence-Based Complementary and Alternative Medicine*, vol. 2015, Article ID 491409, 11 pages, 2015.

[18] J. Wu, G. Huang, Y. Li, and X. Li, "Flavonoids from Aurantii Fructus Immaturus and Aurantii Fructus: promising phytomedicines for the treatment of liver diseases," *Chinese Medicine*, vol. 15, no. 1, p. 89, 2020.

[19] Q. Jin, J. Lu, R. Gao, J. Xu, X. Pan, and L. Wang, "Systematically deciphering the pharmacological mechanism of Fructus Aurantii via network pharmacology," *Evidence-Based Complementary and Alternative Medicine*, vol. 2021, Article ID 6236135, 14 pages, 2021.

[20] Y. Bian, X. Chen, H. Cao et al., "A correlational study of Weifuchun and its clinical effect on intestinal flora in precancerous lesions of gastric cancer," *Chinese Medicine*, vol. 16, no. 1, p. 120, 2021.

[21] S. Jiang, C. Huang, S. Wang et al., "Network pharmacology-based strategy for predicting therapy targets of Citri Reticulatae Pericarpium on myocardial hypertrophy," *BioMed Research International*, vol. 2022, Article ID 4293265, 13 pages, 2022.

[22] A. Nagy, A. Lanczky, O. Menyhart, and B. Gyorffy, "Validation of miRNA prognostic power in hepatocellular carcinoma using expression data of independent datasets," *Scientific Reports*, vol. 8, no. 1, p. 9227, 2018.

[23] J. Muhammad, A. Khan, A. Ali et al., "Network pharmacology: exploring the resources and methodologies," *Current Topics in Medicinal Chemistry*, vol. 18, no. 12, pp. 949–964, 2018.

[24] H. E. Marei, A. Althani, N. Afifi et al., "p53 signaling in cancer progression and therapy," *Cancer Cell International*, vol. 21, no. 1, p. 703, 2021.

[25] A. Hafner, M. L. Bulyk, A. Jambhekar, and G. Lahav, "The multiple mechanisms that regulate p53 activity and cell fate," *Nature Reviews Molecular Cell Biology*, vol. 20, no. 4, pp. 199–210, 2019.

[26] O. Timofeev, "Editorial: mutant p53 in cancer progression and personalized therapeutic treatments," *Frontiers in Oncology*, vol. 11, article 740578, 2021.

[27] A. J. Levine, "The many faces of p53: something for everyone," *Journal of Molecular Cell Biology*, vol. 11, no. 7, pp. 524–530, 2019.

[28] A. Janic, L. J. Valente, M. J. Wakefield et al., "DNA repair processes are critical mediators of p53-dependent tumor suppression," *Nature Medicine*, vol. 24, no. 7, pp. 947–953, 2018.

[29] Q. Guo, X. X. Ke, S. X. Fang et al., "PAQR3 inhibits non-small cell lung cancer growth by regulating the NF-κB/p53/Bax axis," *Frontiers in Cell and Developmental Biology*, vol. 8, article 581919, 2020.

[30] T. Zhang, Y. Li, R. Zhu et al., "Transcription factor p53 suppresses tumor growth by prompting pyroptosis in non-small-cell lung cancer," *Oxidative Medicine and Cellular Longevity*, vol. 2019, Article ID 8746895, 9 pages, 2019.

[31] Y. Zeng, M. Gao, D. Lin, G. Du, and Y. Cai, "Prognostic and immunological roles of MMP-9 in pan-cancer," *Biomed Res Int*, vol. 2022, article 2592962, 32 pages, 2022.

[32] H. T. Wu, J. Lin, Y. E. Liu et al., "Luteolin suppresses androgen receptor-positive triple-negative breast cancer cell proliferation and metastasis by epigenetic regulation of MMP9 expression via the AKT/mTOR signaling pathway," *Phytomedicine*, vol. 81, article ???, 2021.

[33] H. Akter, M. Park, O. S. Kwon, E. J. Song, W. S. Park, and M. J. Kang, "Activation of matrix metalloproteinase-9 (MMP-9) by neurotensin promotes cell invasion and migration through ERK pathway in gastric cancer," *Tumour Biology*, vol. 36, no. 8, pp. 6053–6062, 2015.

[34] H. Zhang, B. Zhao, Z. G. Zhai, J. D. Zheng, Y. K. Wang, and Y. Y. Zhao, "Expression and clinical significance of MMP-9 and P53 in lung cancer," *European Review for Medical and Pharmacological Sciences*, vol. 25, no. 3, pp. 1358–1365, 2021.

[35] L. Gu, Y. Yao, and Z. Chen, "An inter-correlation among chemokine (C-X-C motif) ligand (CXCL) 1, CXCL2 and CXCL8, and their diversified potential as biomarkers for tumor features and survival profiles in non-small cell lung cancer patients," *Translational Cancer Research*, vol. 10, no. 2, pp. 748–758, 2021.

[36] R. Ogawa, T. Yamamoto, H. Hirai et al., "Loss of SMAD4 promotes colorectal cancer progression by recruiting tumor-associated neutrophils via the CXCL1/8-CXCR2 axis," *Clinical Cancer Research*, vol. 25, no. 9, pp. 2887–2899, 2019.

[37] Y. Yamamoto, K. Kuroda, T. Sera et al., "The clinicopathological significance of the CXCR2 ligands, CXCL1, CXCL2, CXCL3, CXCL5, CXCL6, CXCL7, and CXCL8 in gastric cancer," *Anticancer Research*, vol. 39, no. 12, pp. 6645–6652, 2019.

[38] X. Yan, L. Han, R. Zhao, S. Fatima, L. Zhao, and F. Gao, "Prognosis value of IL-6, IL-8, and IL-1β in serum of patients with lung cancer: A fresh look at interleukins as a biomarker," *Heliyon*, vol. 8, no. 8, article ???, 2022.

[39] X. Yang, R. Chen, Y. Chen et al., "Methyltransferase SETD2 inhibits tumor growth and metastasis via STAT1-IL-8 signaling-mediated epithelial-mesenchymal transition in lung adenocarcinoma," *Cancer Science*, vol. 113, no. 4, pp. 1195–1207, 2022.

[40] J. C. Lai, Y. W. Cheng, H. L. Chiou, M. F. Wu, C. Y. Chen, and H. Lee, "Gender difference in estrogen receptor alpha promoter hypermethylation and its prognostic value in non-small cell lung cancer," *International Journal of Cancer*, vol. 117, no. 6, pp. 974–980, 2005.

[41] Y. Suga, K. Miyajima, T. Oikawa et al., "Quantitative p16 and ESR1 methylation in the peripheral blood of patients with non-small cell lung cancer," *Oncology Reports*, vol. 20, no. 5, pp. 1137–1142, 2008.

[42] L. P. Stabile, A. L. Davis, C. T. Gubish et al., "Human non-small cell lung tumors and cells derived from normal lung express both estrogen receptor alpha and beta and show biological responses to estrogen," *Cancer Research*, vol. 62, no. 7, pp. 2141–2150, 2002.

[43] C. N. Brocker, D. Kim, T. Melia et al., "Long non-coding RNA Gm15441 attenuates hepatic inflammasome activation in response to PPARA agonism and fasting," *Nature Communications*, vol. 11, no. 1, p. 5847, 2020.

[44] S. Kamata, T. Oyama, K. Saito et al., "PPARα Ligand-Binding Domain Structures with Endogenous Fatty Acids and Fibrates," *iScience*, vol. 23, no. 11, article ???, 2020.

[45] V. Dubois, J. Eeckhoute, P. Lefebvre, and B. Staels, "Distinct but complementary contributions of PPAR isotypes to energy homeostasis," *The Journal of Clinical Investigation*, vol. 127, no. 4, pp. 1202–1214, 2017.

[46] Y. Luo, C. Xie, C. N. Brocker et al., "Intestinal PPARα Protects Against Colon Carcinogenesis via Regulation of Methyltransferases DNMT1 and PRMT6," *Gastroenterology*, vol. 157, no. 3, pp. 744–759.e4, 2019.

[47] S. Feng, H. Wang, Y. Wang et al., "Apatinib induces 3-hydroxybutyric acid production in the liver of mice by peroxisome proliferator-activated receptor α activation to aid its antitumor effect," *Cancer Science*, vol. 110, no. 10, pp. 3328–3339, 2019.

[48] M. S. Wang, Q. S. Han, Z. R. Jia et al., "PPARα agonist fenofibrate relieves acquired resistance to gefitinib in non- small cell lung cancer by promoting apoptosis via PPARα/AMPK/Akt/ FoxO1 pathway," *Acta Pharmacologica Sinica*, vol. 43, no. 1, pp. 167–176, 2022.

[49] L. Wu, W. Wang, M. Dai, H. Li, C. Chen, and D. Wang, "PPARα ligand, AVE8134, and cyclooxygenase inhibitor therapy synergistically suppress lung cancer growth and metastasis," *BMC Cancer*, vol. 19, no. 1, p. 1166, 2019.

[50] N. Skrypnyk, X. Chen, W. Hu et al., "PPARα activation can help prevent and treat non-small cell lung cancer," *Cancer Research*, vol. 74, no. 2, pp. 621–631, 2014.

Retraction

Retracted: Multifunctional Drug-Loaded Phase-Change Nanoparticles Inhibit the Epithelial-Mesenchymal Transition of Hepatocellular Carcinoma by Affecting the Activity of Activated Hepatic Stellate Cells

BioMed Research International

This article has been retracted by Hindawi following an investigation undertaken by the publisher [1]. This investigation has uncovered evidence of one or more of the following indicators of systematic manipulation of the publication process:

(1) Discrepancies in scope

(2) Discrepancies in the description of the research reported

(3) Discrepancies between the availability of data and the research described

(4) Inappropriate citations

(5) Incoherent, meaningless and/or irrelevant content included in the article

(6) Manipulated or compromised peer review

The presence of these indicators undermines our confidence in the integrity of the article's content and we cannot, therefore, vouch for its reliability. Please note that this notice is intended solely to alert readers that the content of this article is unreliable. We have not investigated whether authors were aware of or involved in the systematic manipulation of the publication process.

Wiley and Hindawi regrets that the usual quality checks did not identify these issues before publication and have since put additional measures in place to safeguard research integrity.

We wish to credit our own Research Integrity and Research Publishing teams and anonymous and named external researchers and research integrity experts for contributing to this investigation.

The corresponding author, as the representative of all authors, has been given the opportunity to register their agreement or disagreement to this retraction. We have kept a record of any response received.

References

[1] X. Zou, T. Li, Y. Mao et al., "Multifunctional Drug-Loaded Phase-Change Nanoparticles Inhibit the Epithelial-Mesenchymal Transition of Hepatocellular Carcinoma by Affecting the Activity of Activated Hepatic Stellate Cells," *BioMed Research International*, vol. 2022, Article ID 6441179, 18 pages, 2022.

Hindawi

Research Article

Multifunctional Drug-Loaded Phase-Change Nanoparticles Inhibit the Epithelial-Mesenchymal Transition of Hepatocellular Carcinoma by Affecting the Activity of Activated Hepatic Stellate Cells

Xiaomeng Zou, Tiantian Li, Yingxuan Mao, Mingwei Zhu, Xi Chen, Jiamei Niu, Tianxiu Dong, Jian Jiang, and Xiuhua Yang [ID]

Department of Abdominal Ultrasound, The First Affiliated Hospital of Harbin Medical University, Harbin 150001, China

Correspondence should be addressed to Xiuhua Yang; yangxiuhua@hrbmu.edu.cn

Objectives. Preparation of a multifunctional drug-loaded phase-change nanoparticle (NP), pirfenidone perfluoropentane liposome NPs (PPL NPs), and combined with low-intensity focused ultrasound (LIFU) to influence epithelial mesenchymal transition (EMT) for hepatocellular carcinoma (HCC) by inhibiting the activity of activated Hepatic Stellate Cells (a-HSCs*). Methods*. PPL NPs were prepared by the thin film dispersion method. The appearance, particle size, zeta potential, encapsulation efficiency, drug loading rate, drug release in vitro, and stability of PPL NPs were tested. The role of a-HSCs in HCC metastasis was studied by CCK-8, colony formation assay, apoptosis, cellular uptake assay, wound healing assay, and Transwell assay. Western blot was used to detect the related protein expression levels. In vitro and vivo, the acoustic droplet vaporization (ADV) of PPL NPs was tested at different times and LIFU intensities. Biosafety of the PPL NPs was assessed by measuring nude mouse body weight and hematoxylin and eosin (H&E) staining. *Results*. The results showed that the PPL NPs had good biosafety, with an average particle size of 346.6 ± 62.21 nm and an average zeta potential of -15.23 mV. When the LIFU power is 2.4 W/cm^2, it can improve the permeability of cells, further promote the uptake of drugs by cells, and improve the toxicity of drugs. In vitro experiments showed that PPL NPs could inhibit the proliferation of a-HSCs cells, thereby affecting the metastasis of HCC, and were related to the TGFβ-Smad2/3-Snail signaling pathway. Both in vivo and in vitro PPL NPs enhanced ultrasound imaging by LIFU-triggered ADV. *Conclusion*. The PPL NPs designed and prepared in this study combined with LIFU irradiation could significantly alter the EMT of HCC by inhibiting LX2. Clinically, PPL NPs will also be considered a promising contrast agent due to their ultrasound imaging capabilities.

1. Introduction

Primary liver cancer is the 4th leading cause of tumor death worldwide, of which HCC accounts for about 90% [1, 2]. Recent studies have shown that the tumor microenvironment is closely related to HCC progression, prognosis, and drug resistance. However, the most current therapeutic regimen targets only tumor cells, ignoring the important role of the tumor microenvironment, and this could be the reason why many patients experience recurrence and metastasis after treatment [3, 4].

Mesenchymal cells including fibroblasts, infiltrating immune cells, and angiogenic cells in the liver, their extracellular matrix (ECM) components, and cytokines together constitute the microenvironment that promotes the development of HCC. Among them, dense ECM is essential in the HCC microenvironment, and activated hepatic stellate cells (a-HSCs), as the main source of tumor-associated fibroblasts in HCC, are responsible for regulating the density of HCC; ECM can participate in the development of cancer cell transfer [5]. After being activated by matrix components, ECM components act on integrin-adhesive plaque complexes on

the surface of a-HSCs, resulting in the massive release of stored TGF-β, which in turn activates a-HSCs [6].

TGF-β is not only the most potent profibrotic cytokine but also a key component of extracellular matrix-induced EMT of tumor cells [7, 8]. Scientists have demonstrated that the extratumoral microenvironment provides the necessary transduction signals for EMT and determines the fate of disseminated cells at peripheral metastatic sites [9], that is, whether proliferating and reverting to a more epithelial phenotype or remaining dormant for extended periods of time [5]. Understanding the molecular mechanisms in EMT protocols which initiate tumor invasion and metastasis is key to improving therapeutic interventions. Su et al. have illustrated that the induction of EMT in pancreatic cancer cells by TGF-β through the TGF-β/Smad pathway is dependent on the activation of RAS responsive element binding protein 1 (RREB1) downstream of the RAS/MAPK pathway. MAPK-activated of which RREB1 recruits the TGF-β-activated Smad factor to downstream Snail, drives the expression of Snail and fibrogenic agents, and promotes pancreatic cancer stromal fibrosis and tumor growth [10]. TGF-β in the hepatocellular carcinoma microenvironment can also induce epithelial-mesenchymal transformation of hepatocellular carcinoma cells through the TGF-β/Smad pathway and is related to the activation of the MAPK signaling pathway [11, 12].

Pirfenidone (PFD) as a new drug authorized by the US Food and Drug Administration for the medical treatment of idiopathic pulmonary fibrosis [13, 14]. Studies have shown PFD can inhibit the activity of a-HSCs and downregulate the expression of TGF-β and fibrous matrix components, to alleviate liver fibrosis [15]. However, free small molecules of PFD are mostly cleared by metabolism during circulation in vivo, leading to low effective dose in HCC tissue. Also, oral PFD can cause serious gastrointestinal side effects, and treatment with PFD alone is ineffective. Therefore, there is an urgent need for a new drug delivery system to reduce its toxic side effects and improve its therapeutic efficiency for future applications.

Liposome, a kind of nanoparticles (NPs) with the size of 5-500 nm, are formed by self-assembly of amphiphilic lipid molecular layers with high biosafety and long blood circulation time [16]. It is a commonly used drug carrier in cancer treatment research [17, 18]. In addition, PEG was modified outside our liposomes to induce NP PEGylation. PEG is one of the most used polymer materials because it has the advantages of nontoxicity, no immunogenicity, no antigenicity, and good water solubility. A drug technique in which PEG covalently combined with a drug improves the pharmacokinetic, pharmacodynamic, and immunological properties of the drug, thereby enhancing its therapeutic effect. NPs modified with PEG can reduce administration times, increase efficacy, improve tolerability, and reduce severity and incidence of adverse events [19, 20]. So, liposome can be used as an anticancer drug carrier to penetrate the endothelial gaps of tumor blood vessels through the effect of penetration and retention (EPR), enhance the concentration of drugs concentrated at the tumor sites, and achieve the passive targeting of therapeutic drugs. Liquid fluorocarbon per-

fluoropentane (PFP) undergoes a liquid-gas phase transition to ultrasonic microbubbles upon external stimulus [21, 22]. Zhu and coworkers prepared NP containing PFP compounds that produce an ADV effect by LIFU. NPs encapsulated with PFP will be transformed into microbubbles (MBs) to enhance ultrasound imaging effect while increasing the irradiation power, and LIFU can trigger liposomes to drive drug release, thus enabling the integration of disease diagnosis and treatment [23].

Ultrasound has been widely used in clinical practice due to its outstanding advantages such as nonradiative, noninvasive, and cost-effective [24, 25]. Besides, the development of nanostructured materials in therapeutic perspective has further attracted attention to the combined application of both these fronts [26]. However, it has been found that it is difficult for either passively or actively targeted drug-laden NPs to penetrate tumor tissues due to high interstitial fluid pressure and dense extracellular matrix obstruction. Ultrasound-targeted microbubble destruction (UTMD), induced by LIFU, enhances the penetration depth of drug-loaded NPs and increases the antitumor efficacy of drugs through the cavitation effect generated by the instantaneous bursting of ultrasound microbubbles [27, 28]. More importantly, LIFU can also be used for ultrasonography imaging to localize the lesion and guide the timing of UTMD before triggering the ultrasound microbubble UTMD effect, enabling precise visualization of the treatment.

Based on the above results, instead of PFD alone, we propose to prepare PEGylated PFD/PFP/liposome nanoparticles (PPL NPs) combined with LIFU-triggered UTMD to inhibit the activity of a-HSCs and reduce the expression of TGF-β, which in turn inhibits the EMT of HCC. After coculturing a-HSCs with HCC cells, the release of TGF-β from a-HSCs is reduced, which in turn inhibits the TGF-β/Smad pathway in HCC cells, coordinates the expression of the downstream transcription factor Snail, and hinders EMT of fibroblast-derived HCC cells, thereby preventing HCC metastasis and improving patient prognosis.

The encapsulated PFP phase was transformed into microbubbles under the triggering of LIFU, which not only significantly enhanced the ultrasound imaging effect but also further amplified the blasting ability of LIFU on microbubbles and triggered the UTMD effect, thereby loosening the extracellular matrix. In addition, PFD could further drive into HCC tissues and inhibit the proliferation of a-HSCs cells and production of TGF-β, which could improve the microenvironment of the HCC extracellular matrix, thereby inhibiting the migration and invasion of HCC, enabling synergistic therapy, and achieving visual integration of therapy.

More importantly, our prepared PPL NPs are structurally stable, allowing stable drug delivery without damaging normal tissues or cells, and enabling relatively high drug encapsulation efficiency, by encapsulating the drug in liposomes, the systemic toxicity of PFD is significantly reduced and have good biocompatibility, which is important for reducing systemic toxicity in disease treatment [29]. In addition, this core-shell structure can well protect the contents, especially PFP, which can efficiently achieve ADV because of the presence of lipid structure and keep its morphology

temporarily undisturbed; due to the phase-transition properties of PFP, the simultaneous implementation of strategies for ultrasound imaging and optimization of drug delivery efficiency will greatly improve the therapeutic effect of the disease. Finally, the combination of LIFU with drug therapy has been shown by many studies to be a promising strategy to improve treatment efficiency compared with monotherapy.

In conclusion, this synergistic treatment strategy has a good therapeutic effect on EMT of HCC and its systemic metastases. Combine with its function of ultrasound imaging, the PPL NP visual drug loading platform is expected to be a therapeutic strategy for further clinical application.

2. Materials and Methods

2.1. Cells and Reagents. Human hepatic stellate cells line LX2 and human HCC cells line HCCLM3 were supplied by the Institute of Chinese Academy of Science, China. LX2 and HCCLM3 cells were cultured in Dulbecco's modified Eagle's medium (DMEM) supplemented with 10% and 15% fetal bovine serum, respectively, and 1% antibiotics. All these cells were cultured at 37°C in 5% CO_2. 1,2-Dipalmitoyl-sn-glycero-3-phosphatidylcholine (DPPC),1-palmitoyl-2-stearoyl-sn-glycero-3phosphocholine,1,2-distearoyl-sn-glycero-3-phosphoethanolamine-N-[amino (polyethylene glycol)-2000] (DSPE-PEG (2000)), 1,2-dipalmitoyl-sn-glycero-3-phospho-(1′-rac-glycerol) (DPPG), cholesterol, and Perfluoropentane (PFP) were obtained from Sigma–Aldrich (St. Louis, MO, USA). Pirfenidone (PFD) was obtained from Aladdin Chemistry, Co., Ltd. (Shanghai, China). Rhodamine B (RB) was provided from MCE (New Jersey, USA).

2.2. Preparation and Characterization of PPL NPs. PPL NPs were prepared using a simple thin-film hydration-sonication method. Specifically, a mixture of 10 mg of DPPC, 4 mg of DPPG, 4 mg of DPPE-PEG, 2 mg of cholesterol, and 2 mg of PFD was weighed and dissolved in 10 ml of chloroform, then transferred to a flask and evaporated by rotary vacuum (1 h, 50°C), and hydrated in 2 ml precooled PBS. The hydration fluid was placed in an ice box and emulsified with 200 μl of PFP using a sonicator at 100 W for 6 mins (10 s interval between switches) (Scheme 1). The mixtures were centrifuged at 8000 rpm for 5 minutes and kept at 4°C and then washed 3 times with ultrapure water to remove the PFD other than PPL NPs and then stored at 4°C until next use.

2.3. Drug Releasing. To evaluate the degree of release of PFD in PPL NPs, the cumulative release efficiency was tested using PBS solution. A dialysis bag containing 1 ml of a solution of PPL NPs was placed in a beaker containing 149 ml of PBS solution, keeping its volume at 150 ml throughout the experiment, and then, the beaker was placed in a rotary evaporator at 37°C. Collect 1 ml of each sample solution from the dialysis bag at different times (1, 2, 3, 4, 5, 6, 7, 8, 9, 10, 11, 12, 24, and 36 h) and make up an equal volume of PBS immediately back to the dialysis bag. Repeat 3 times per set. Finally, the concentration of PFD was measured at

240 nm by UV-Vis spectrophotometry (UH5300, Hitachi), and the drug release rate was calculated.

2.4. In Vitro ADV and Ultrasound Imaging. We evaluated the best parameters for LIFU (1.0 MHz, focal length 1.5 cm, duty cycle 50%, pulsed wave mode) to trigger ADV of PPL NPs in vitro, and we also explored time dependence (1-4 min). PPL NPs were stimulated with LIFU equipment (LMSC051 ACA; Institute of Ultrasound Imaging, Chongqing Medical Sciences, Chongqing, China) at the following intensities: 2, 2.4, and 2.8 W/cm^2 in vitro. The changes of PPL NPs were observed by optical microscope (Olympus DP70, Canada). Subsequently, 500 μl of PPL NPs was added with a pipette tip to an agar gel model (3% agar w/v in distilled water). Fill the coupling agent between the agarose gel model and the LIFU instrument to make sure that it can accurately irradiate the PPL NPs. And after that, images of PPL NPs could be sonicated in the agar gel model. Finally, B-mode and contrast-enhanced ultrasound (CEUS) was observed using a Philips iU Elite Ultrasound System (Philips Healthcare, Amsterdam, The Netherlands).

2.5. In Vitro Cellular Uptake Analysis. RB/PFP/liposomes NPs (RPL NPs) were prepared with RB fluorescent dye instead of PFD, and the binding of RPL NPs to LX2 cells was assayed in vitro using a flow cytometry instrument (FACSCalibur, BD Biosciences). LX2 ($4 × 10^5$ cells) were seeded in 6-well plates in complete DMEM and placed in a 37°C cell incubator containing overnight. After that, the old DMEM was replaced with fresh DMEM which contained RB, RPL NPs, and RPL NPs+LIFU in equal amounts of RB (5 μg/ml) for 24 h. The LIFU conditions were 1.0 MHz; 2.4 W/cm^2; duty cycle, 50%; focal length, 1.5 cm; and pulse wave mode; 4 min. After 24 h, LX2 were washed 3 times with prechilled PBS, collected by Trypsin, and then detected by flow cytometry for red fluorescence intensity.

2.6. Cell Proliferation Assay. The viability of cells was evaluated by Cell Counting Kit 8 (CCK-8) (Dojindo Molecular Technology, Japan) after treatment. Cells were firstly inoculated into 96-well plates (5000 cells/well) for 24 hours, each group was repeated 3 times. Then, cells were incubated with different concentrations of PFD and PPL NPs were prepared with various concentrations (1-4 mg/ml) of PFD and diluted with serum-free DMEM, with or without LIFU irradiation for 24 h. Various optical densities at 450 nm were measured with a microplate reader (Elx800, Bio-Tek, USA), and the percentage of cell viability in other groups was calculated according to the control group.

2.7. Plate Colony Formation Assay. LX2 cells were cultured in 6-well plates at a density of 1000 cells in 3 ml of complete DMEM each well. In the following day, the cells were treated in the assigned groups:(1) control (no treatment), (2) PFD(0.4 mg/ml), (3) PPL NPs (4 mg/ml solution only,200 μl), and (4) PPL NPs+LIFU (1.0 MHz; 2.4 W/cm^2; duty cycle, 50%; focal length, 1.5 cm; and pulse wave mode; 4 min) for 4 hours. After that, the medium containing the pharmaceutical was removed and fresh complete DMEM was used to replace it. Two weeks later, after removing the
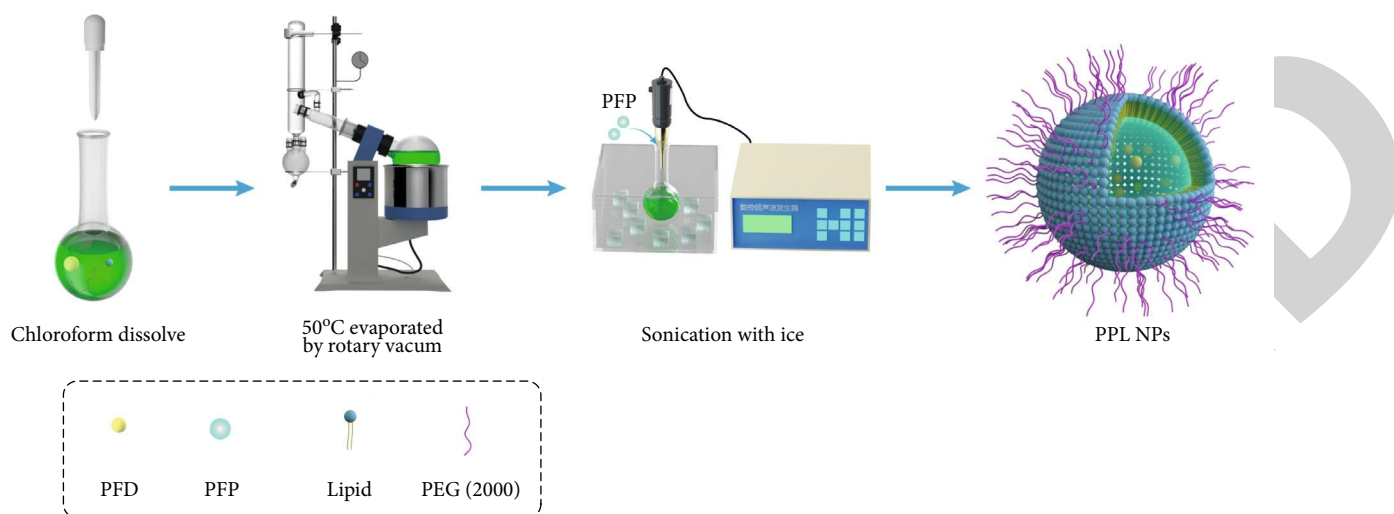
Scheme 1: Schematic illustration of preparation of PPL NPs.

old complete DMEM and washing by PBS for 3 times, the colonies were fixed with methanol and then stained with 0.5% crystal violet for 15 mins. Counting cells was done using light microscopy. Each group was repeated 3 times.

2.8. Apoptosis. Annexin V-FITC/PI Apoptosis Detection Kit (4A Biotech, Beijing, China) was used to analyze result of LX2 cell apoptosis. The cells were divided into the following four groups:(1) control, (2) PFD, (3) PPL NPs, and (4) PPL NPs+LIFU. 24 hours later, cells were digested with 0.25% no EDTA trypsin, deposited in centrifuge tube with low-speed, washed with PBS 3 times, then incubated with $5\,\mu$l Annexin V-FITC and $10\,\mu$l PI into $500\,\mu$l binding buffer 15 mins, and kept in dark at $37°$C. Analysis of apoptotic cells was done by the flow cytometry procedure (BD Biosciences, Franklin Lakes, NJ, USA).

2.9. Collection of Conditioned Medium and Coculture with HCCLM3. LX2 cells were cultured to a density of 80%, washed twice with PBS, then cultured in serum-free DMEM for 18 hours, then treated with PFD, PPL NPs, and PPL NPs +LIFU for 24 hours in vitro, and collected conditioned medium (CM) of LX2 including PFD-(CM), PPL NPs-(CM), and PPL NPs+LIFU-(CM). The collected CM was centrifuged at 1500 rpm for 5 mins to remove cell debris and then stored at -20°C with 0.5% FBS until next use. HCCLM3 cells were cultured in serum-free medium for 18 hours, and then, CM was added for coculture experiments.

2.10. Western Blotting. After LX2, HCCLM3, and HCCLM3 coculture with CM were treated, proteins were extracted in culture and coculture flasks. Then, it was lysed using RIPA buffer (Beyotime, Shanghai, China) and centrifuged at 12,000 g for 10 min keep 4°C, respectively. Bicinchoninic acid (BCA, Beyotime, Shanghai, China) method was used to detect the total protein content. 50 mg protein from each

group was transferred onto nitrocellulose (NC) membranes after through 10%-12% sodium dodecyl sulfate-polyacrylamide gel electrophoresis (SDS-PAGE, Beyotime, Shanghai, China). Membranes were blocked with 5% fat-free milk for 60 min and incubated continuously with the following primary antibodies overnight at 4°C: CD133, PCNA, TGF-β, Collagen1, Smad2, Smad3, Snail, E-cadherin, N-cadherin, and β-actin, purchased from Proteintech Group (Wuhan, China). Finally, they were incubated with secondary antibodies (LI-COR Biosciences, Nebraska, USA) and imaged with an Odyssey Fc imaging system (LI-COR Biosciences, Nebraska, USA).

2.11. Wound Healing and Transwell Assay. The migration of HCCLM3 cells exposed to CM was measured by wound healing assay. HCCLM3 cells were inoculated in 6-well plates until the cell density grow to about 80% confluency, and three parallel lines were drawn with a sterile $200\,\mu$l pipette tip to scratch the central of each well. HCCLM3 cells were washed by PBS and incubated with CM from different treatment groups, and images were obtained by light microscopy at 0 h and 48 h after scratching, and the scratching gap was calculated to compare the migration ability of HCCLM3 cells in each group.

Transwell chambers ($8\,\mu$m pore size, Corning, Tewksbury, USA) were used to establish the metastasis model as well. HCCLM3 cells were cultured in serum-free DMEM and in the Transwell chamber embedded into CM. 48 hours later, HCCLM3 cells were fixed and stained with crystal violet, and the cells on the upper surface of the upper chamber were carefully wiped off with a clean swab; the number of HCCLM3 cells penetrating to the lower surface of the chamber was observed under the light microscope to determine the influence of migration ability of CM to HCCLM3. The invasion ability of HCCLM3 cells can be measured by

(a)

(b)

(c)

(d)

(e)

(f)

1 day　　　　3 day　　　　5 day　　　　7 day

(g)

FIGURE 1: Continued.

(h)
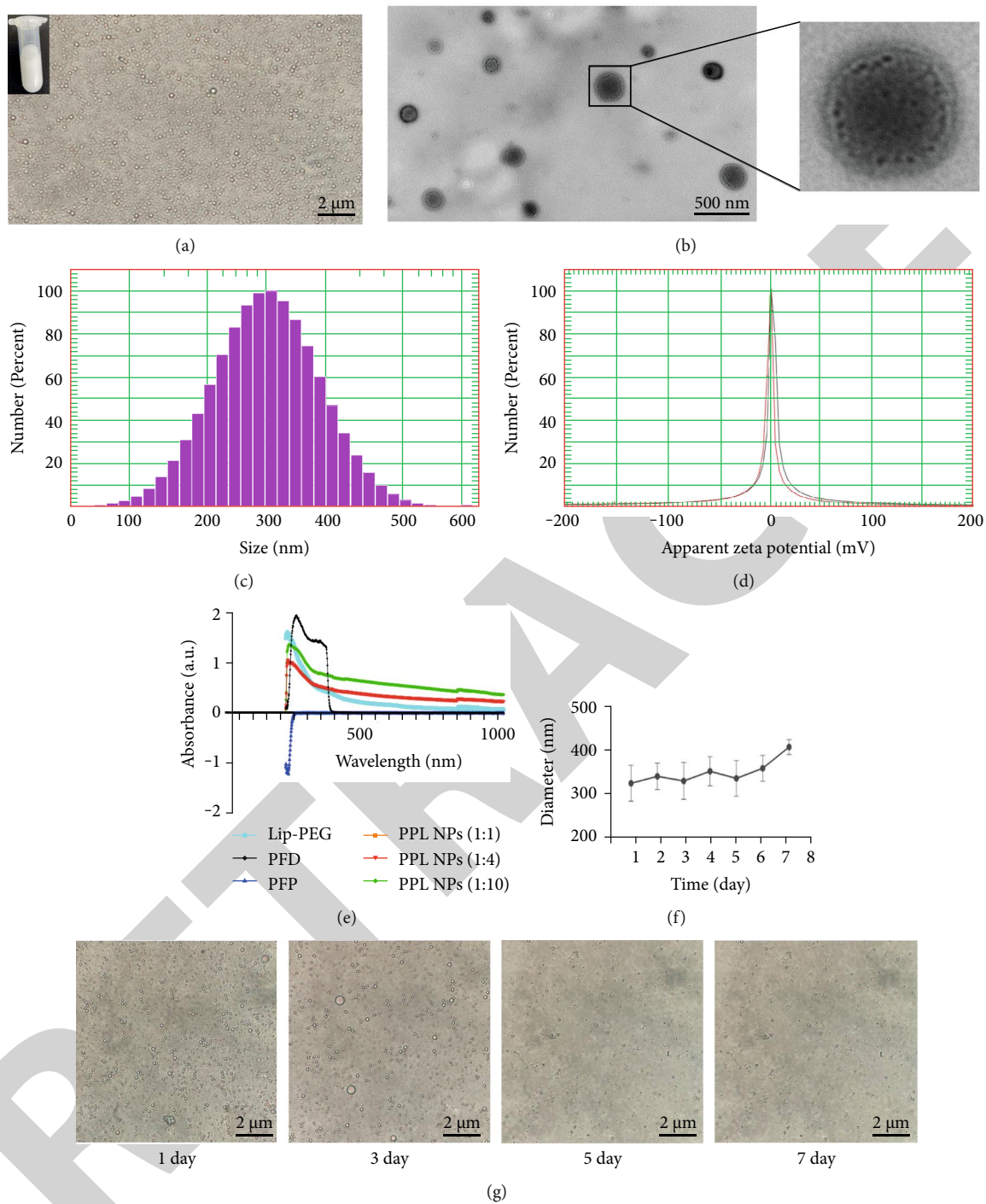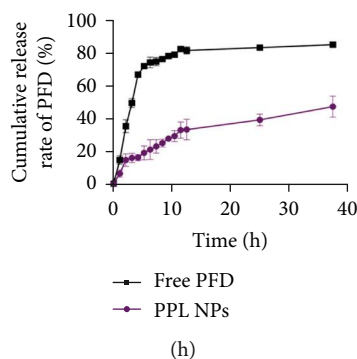
FIGURE 1: Characterization of PPL NPs. (a) Light microscope image of PPL NPs (scale bar: 2 μm). (b) TEM (scale bar: 500 nm). (c) Surface zeta potential of PPL NPs. (d) Size distribution. (e) The UV–Vis spectrum of PFP, PFD, Lip-PEG, and PPL NPs, respectively. (f) The size distribution of PPL NPs within 7 days. (g) Optical microscope of PPL NPs within 7 days (scale bar: 2 μm). (h) The releasing rate of PFD.

spreading Matrigel matrix gel in the chambers and performing the same procedure as above.

2.12. In Vivo ADV and Ultrasound Imaging. Female BALB/c nude health mice (4–5 weeks) were provided by Beijing Vital River Laboratory Animal Technology Co., Ltd. and housed in a pathogen-free rat house according to animal care guidelines. To establish tumor-bearing model, HCCLM3 cells (1×10^7/ml) were inoculated into the left upper limb of BALB/c mice. When tumor size had grown to approximately 70 mm^3, Balb/c nude mice were injected with PPL NPs (with or without LIFU). The LIFU parameter is set to 1.0 MHz; 3.2 W/cm^2; duty cycle, 50%; focal length, 1.5 cm; and pulse wave mode; 4 min. 6 hours before the ultrasound imaging, PPL NPs were injected through the tail vein using an insulin needle. Ultrasound linear array probe was used to scan the tumor site twice with and without LIFU irradiation, and the obtained ultrasound images were observed to evaluate the ultrasound-enhanced imaging effect of PPL NPs after LIFU irradiation. 2D and CEUS imaging were obtained with ultrasound diagnostic equipment.

2.13. In Vivo Biosafety of PPL NPs. To verify the biosecurity of PPL NPs, representative BALB/c mice ($n = 3$) were randomly divided 3 groups: the control group, PPL NPs (5 mg/kg) group, and PPL NPs (10 mg/kg) group. PPL NPs were injected through the tail vein of BALB/c mice, and the mice ad libitum obtain feed, mineral water, and no further injection. Mouse body weights were measured every 4 days with weighing scale. Mice were sacrificed after 7-8 weeks. The heart, liver, spleen, lung, and kidney were taken and fixed in 4% formaldehyde for 48 hours, cut into 4 mm thick paraffin-embedded sections, stained with hematoxylin-eosin (H&E), and observed under light microscope to assess the pathological changes.

2.14. Statistical Analysis. Data were presented as mean ± standard deviation. Statistical analysis was performed using SPSS 22.0. Student's *t*-test was performed for statistical assessment. $^*P < 0.05$, $^{**}P < 0.01$, and $^{***}P < 0.001$ were considered statistically significant.

3. Results

3.1. Characterization of PPL NPs and Drug Releasing Efficiency. The commonly used thin film hydration method was adopted to fabricate the PPL NPs. Lipid material was used as the carrier, encapsulating the phase change material PFP and the antifibrotic drug PFD inside, which would appear as a milky white solution when dispersed into PBS. The regular spherical shape and clear core-shell structure of PPL NPs can be observed both by light microscopy and transmission electron microscopy (Figures 1(a) and 1(b)).

The average diameter of PPL NPs was 346.6 ± 62.21 nm, and the surface zeta potential was -15.23 mV, respectively (Figures 1(c) and 1(d)). PPL NPs could passively accumulate to the tumor site through the EPR due to its appropriate size [30, 31]. However, the negative zeta potential of PPL NPs indicates the same charge can be mutually exclusive with each other, allowing a good dispersion and verifying their relative stability.

In terms of UV visibility, it is to be noted that the spectra of the successfully prepared PPL NPs exhibited similar peaks to the PFD, PFP, and liposomes-PEG, indicating the successful encapsulation of the various materials. According to the standard curve, we prepared different proportions of PPL NPs, and the encapsulation rate was the highest when the PFD drug mass ratio was 1 : 10 to other materials, with the encapsulation efficiency of 52.62% (Figure 1(e)). The particle size distribution remained between 329.5 and 428.1 nm over 7 days and record it under the light microscope (Figures 1(f) and 1(g)), showing the relatively stable of PPL NPs. In addition, to further evaluate the stability of PPL NPs, the efficiency of in vitro drug release was shown in Figure 1(h). The single-drug release efficiency of PFD, compared to PPL NPs dissolved in PBS, increased the release index of PFD by nearly 2-fold, which indicates that the successful PPL NPS exhibit excellent in vivo drug release stability and circulation time.

3.2. Cellular Uptake. The uptake of Rb within LX2 cells was assessed using flow cytometry studies with the assistance of LIFU. The results of the cellular ingestion process were compared using FACS. As shown in (Figures 2(a) and 2(b)), it

(a)

(b)
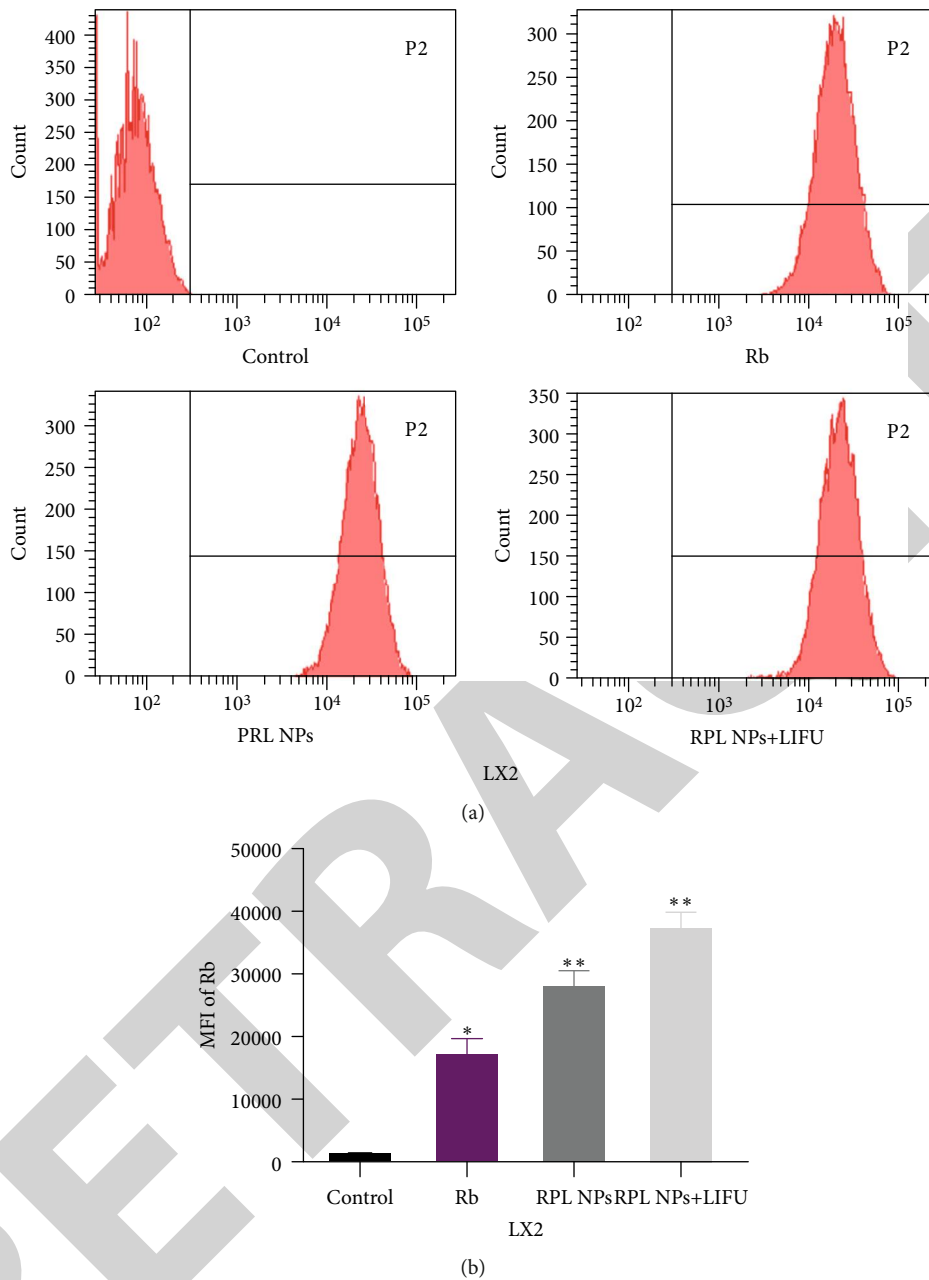
FIGURE 2: Cellular uptake of RB, RPL NPs, and RPL NPs+LIFU in 24 h. (a) Flow cytometry. (b) Corresponding mean fluorescence intensity of data represented in (a) ($^*P < 0.05$, $^{**}P < 0.01$, $n = 3$).

can be clearly seen that the uptake of RPL NPs in the presence of LIFU was significantly enhanced in LIFU-treated RPL NPs compared to that in free RB, no-LIFU case. The results showed that the cavitation effects [32] and sonoporation [33] due to the LIFU-triggered UTMD could lead to higher uptake of RPL NPs. In conclusion, these data demonstrated that the prepared NPs can be taken up by many cells and suggested that the LIFU-triggered UTMD effect can further enhance the total drug uptake.

3.3. PPL NPs Inhibits LX2 Cell Proliferation and Fibrillation. To demonstrate that PPL NPs combined with LIFU can effectively inhibit this aspect, we first treated LX2 and

HCCLM3 with different concentrations of PFD for the same time. Afterwards, the cell viability of the two cell lines was detected, respectively, and CCK-8 analysis showed that PFD could inhibit the cell viability of a-HSCs in a concentration-dependent manner but had no obvious impact on HCCLM3 cell viability (Figures 3(a) and 3(b)).

Based on the order, the appropriate concentration of PPL NPs was selected to treat LX2, and its cytotoxicity was tested. Different groups were designed at different concentrations of PPL NPs with or without LIFU irradiation. The results showed that in the absence of LIFU exposure, even at the highest concentration (4 mg/ml), PPL NPs had no significant effect on the viability of LX2 cells after coincubation

(a)

(b)

(c)

(d)

(e)
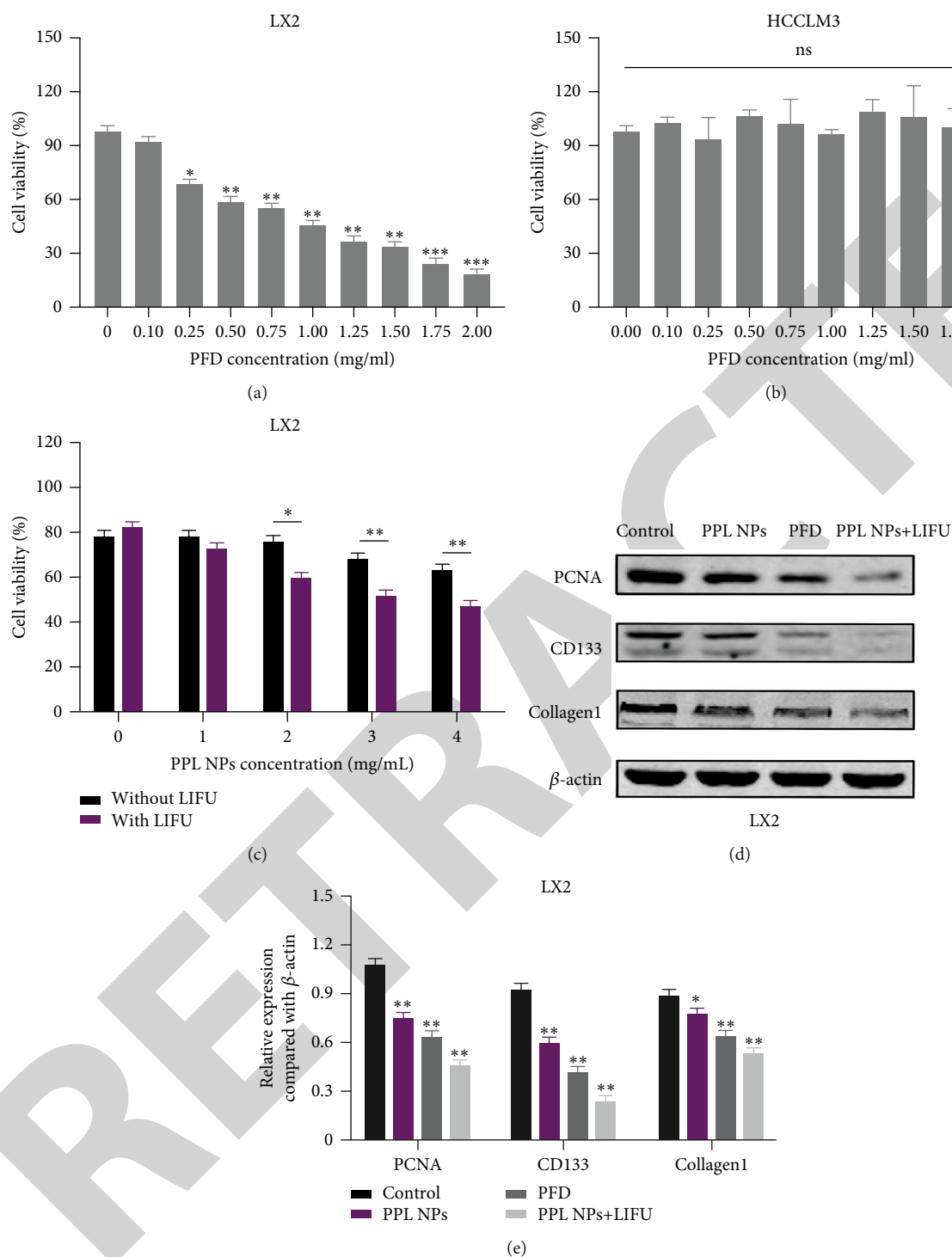
Figure 3: Cell viability for (a) LX2 and (b) HCCLM3 after treatment with PFD and (c) LX2 treated with different PPL NPs concentrations with or without LIFU irradiation. (d) Changes in the protein expression levels of PCNA, CD133, and Collagen1 in LX2 cells following treatment evaluated by Western blotting. (e) Statistical analysis of protein expression ($^{*}P < 0.05$, $^{**}P < 0.01$; $n = 3$).

for 24 h, indicating that PPL NPs have good in vitro stability. In contrast, the cell viability decreased significantly after LIFU irradiation, indicating that the combined effect of PPL NPs and LIFU could significantly enhance the toxicity of LX2 cells (Figure 3(c)).

Similarly, Western blot results also showed that the PPL NPs+LIFU group could maximally inhibit the expression of collagen indicator Collagen1 and proliferation indicators PCNA and CD133 in LX2 cell line in a concentration-dependent manner (Figures 3(d) and 3(e)).
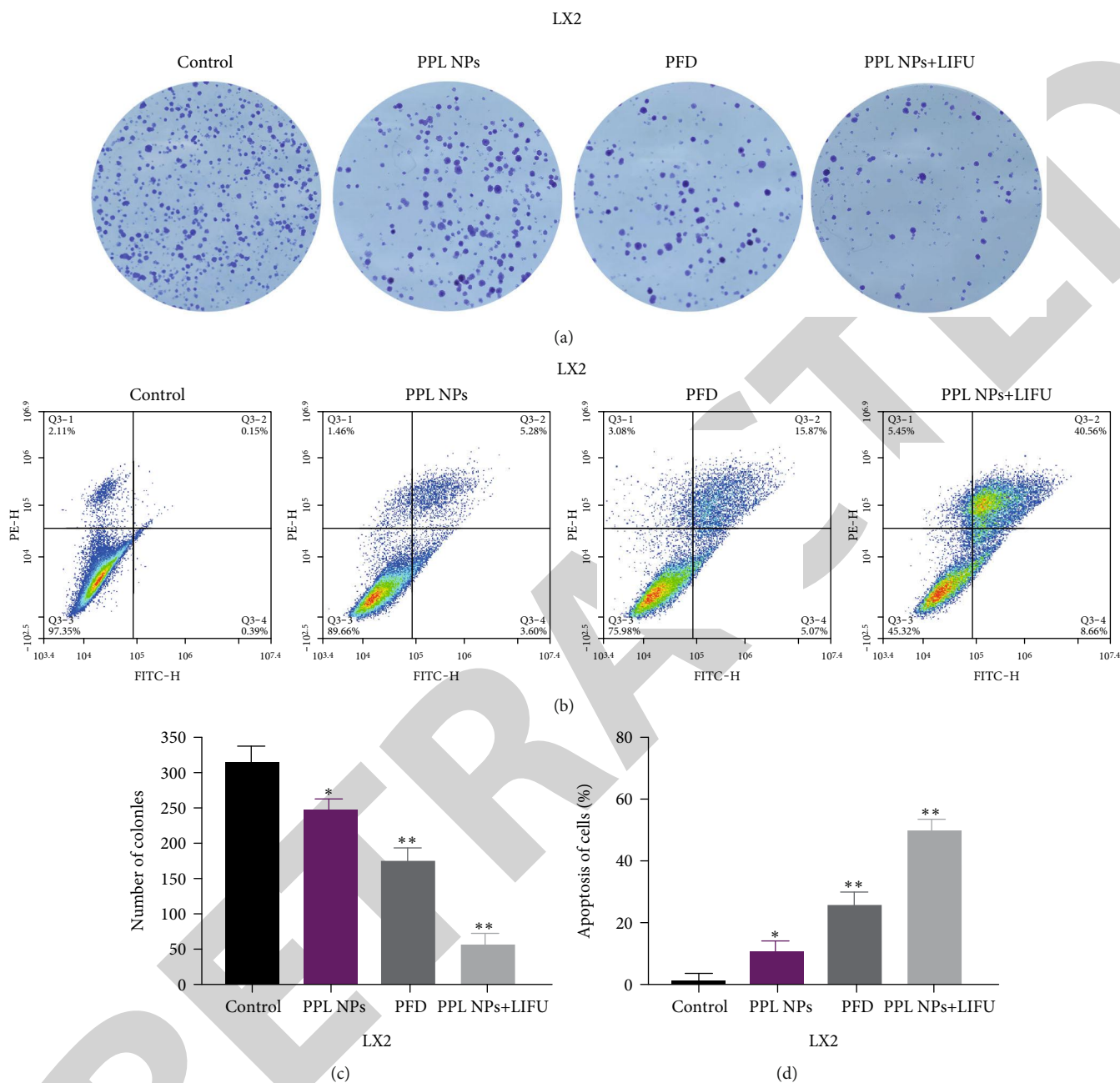
FIGURE 4: Proliferation and apoptosis of LX2 cells after treatment with different groups (control, PFD, PPL NPs, and PPL NPs+LIFU; 24 h). (a) Representative images of colony formation of LX2 cells following treatment with different group and (c) statistical analysis of the colony formation assay. (b) Apoptosis assays of LX2 cells following treatment with various groups and (d) statistical analysis of cell apoptosis ($^*P < 0.05$, $^{**}P < 0.01$; $n = 3$).

3.4. Cytotoxicity and Concerted Treatment Capability of PPL NPs In Vitro. After confirming that the PPL NPs could successfully inhibit the cell activity of LX2, we tested the in vitro cytotoxicity of PPL NPs using the colony formation assay as well. The results, as shown in (Figures 4(a) and 4(c)), indicated the LX2 viability of the LIFU-irradiated group was significantly decreased compared to that of the non-LIFU-exposed group after 24 h coincubation, which suggested that the combined action of PPL NPs and LIFU could remark-

ably inhibit the proliferation of LX2 cells as a synergistic effect of the drug and UTMD.

To further evaluate the efficacy of PPL NPs in inhibiting the LX2 cell line, the results of flow apoptosis cytometry showed that the PPL NPs + LIFU group had the highest cell apoptosis indices, and notably, the apoptosis rate in the PPL NPs+ LIFU group was 2-fold higher than that in the PFD alone group after 24 h, which in another way ensured the significant combined treatment, as shown in (Figures 4(b)
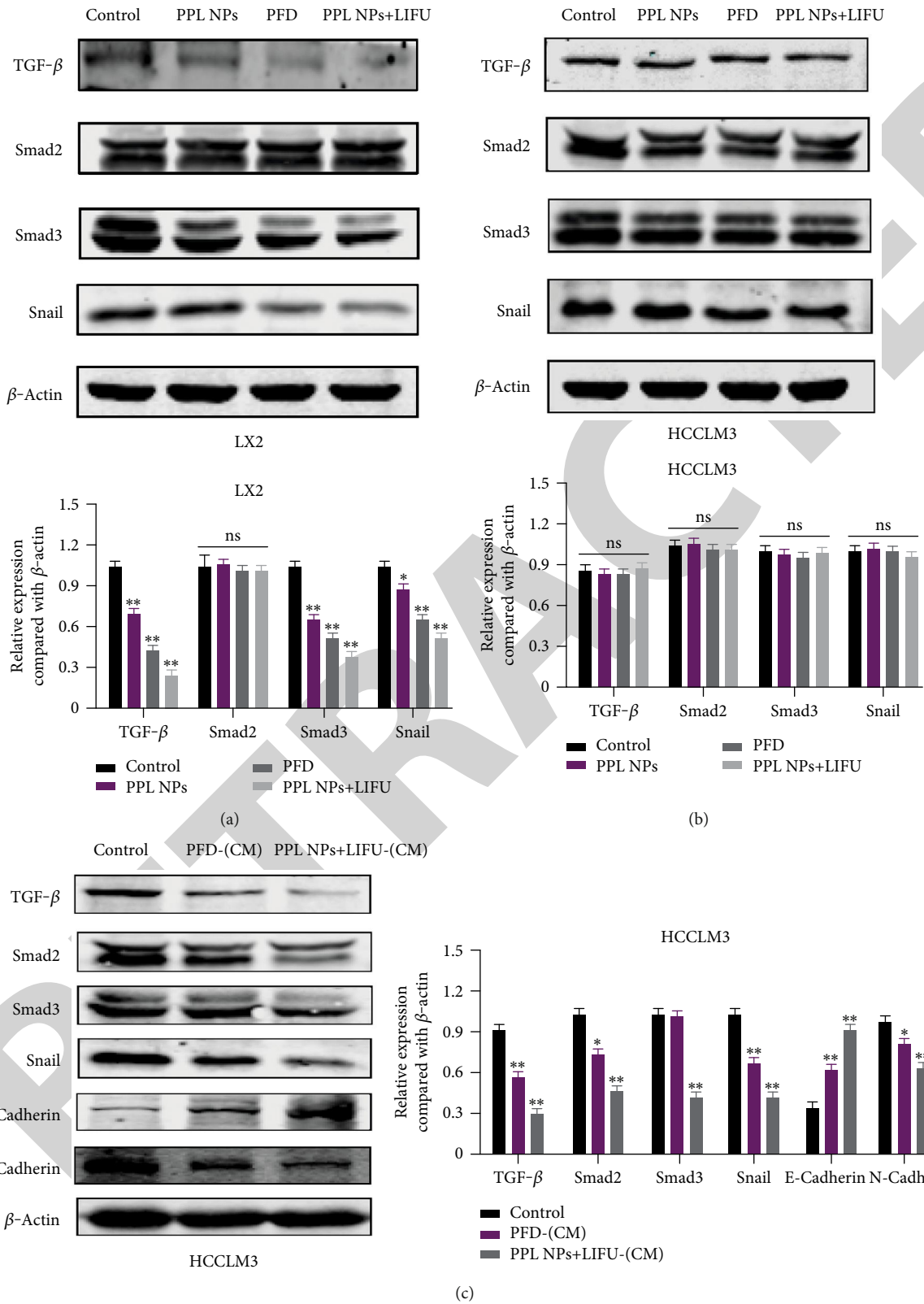
Figure 5: Expression of EMT regulatory factors and signaling pathway after treatment in LX2 and HCCLM3 cells. (a, b) The expression of TGF-β, Smad2, Smad3, and Snail of LX2 and HCCLM3 cells after treatment with different groups. (c) The expression of TGF-β, Smad2, Smad3, Snail, E-cadherin, and N-cadherin of HCCLM3 after treatment with CM ($^*P < 0.05$, $^{**}P < 0.01$; $n = 3$).

(a)

(b)

(c)
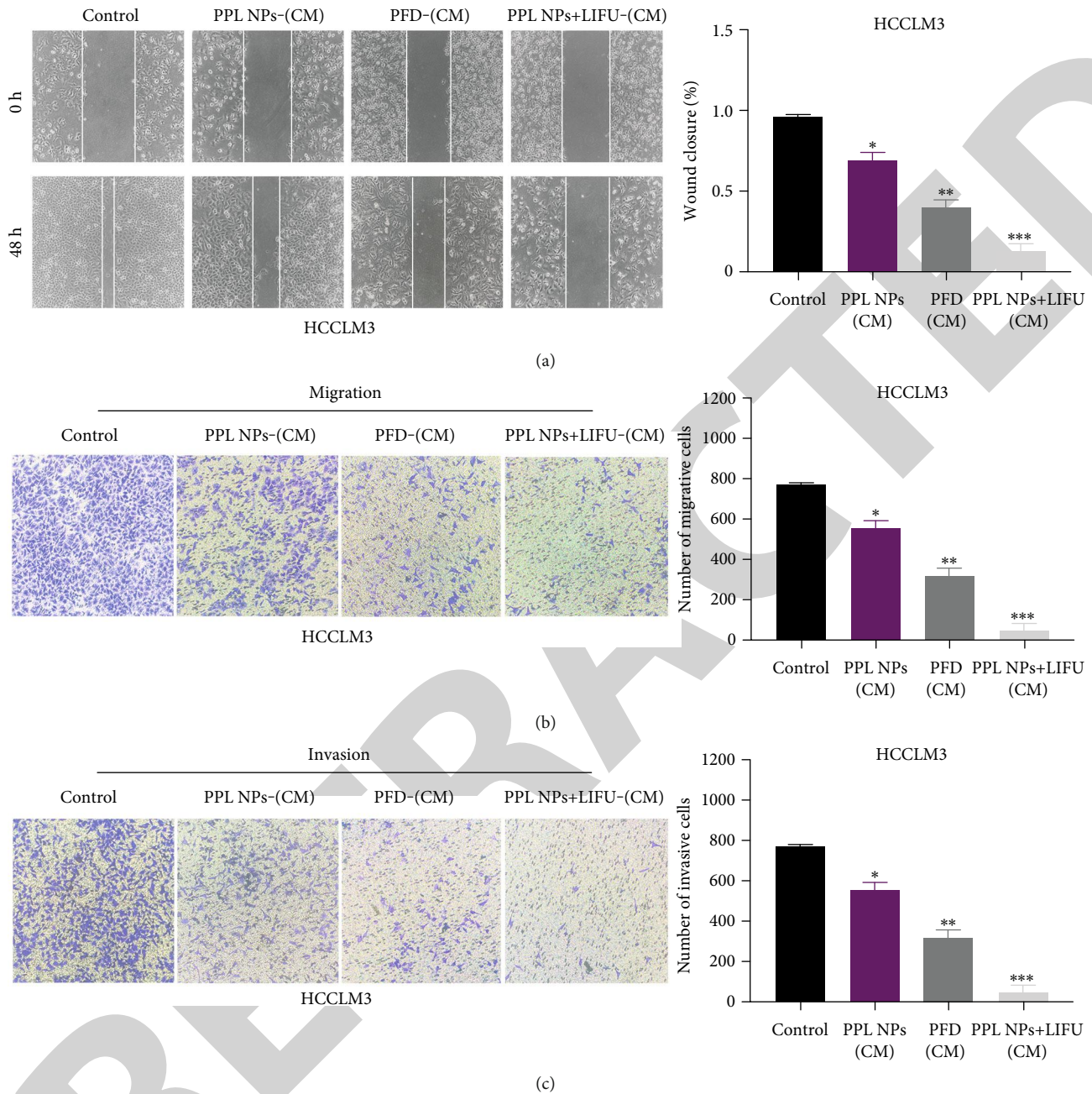
FIGURE 6: Migration and invasion of HCCLM3 cells after CM treatment. (a) Wound healing assay of GBM cells after treatment with various CMs. (b, c) Migration and invasion assay of HCCLM3 cells after treatment with various CMs ($^*P < 0.05$, $^{**}P < 0.01$, and $^{***}P < 0.001$; $n = 3$).

and 4(d)). The synergistic therapeutic effect of UTMD with PPL NPs in LX2 cell apoptosis was confirmed as well.

3.5. PPL NPs Inhibited the EMT of HCC by Reducing the Activation of TGF-β/Smad Signaling Pathway in HCCLM3 by Inhibiting LX2. In order to verify that TGF-β produced by LX2 cells can affect the TGF-β/Smad pathway in the HCC microenvironment, thereby regulating the EMT of HCC cells, we first treated the same groups of LX2 and HCCLM3 cells for 24 h and extracted cellular proteins for Western blotting analyze. The results are shown in

(Figures 5(a) and 5(b)): After grouping for 24 h, the expressions of TGF-β, Smad3, and Snail in LX2 cells decreased, but the expression of Smad2 did not change significantly. The TGF-β/Smad3 signaling pathway is an important mechanism for regulating the production of extracellular matrix components in LX2 cells, and the PPL NPs+LIFU group can significantly inhibit the activation of the TGF-β/Smad3 pathway. However, after the same group was treated with HCCLM3, there was no significant change in the same protein index, and the results were like our expectations, indicating that the drug did not directly inhibit the EMT

(a)

(b)

(c)
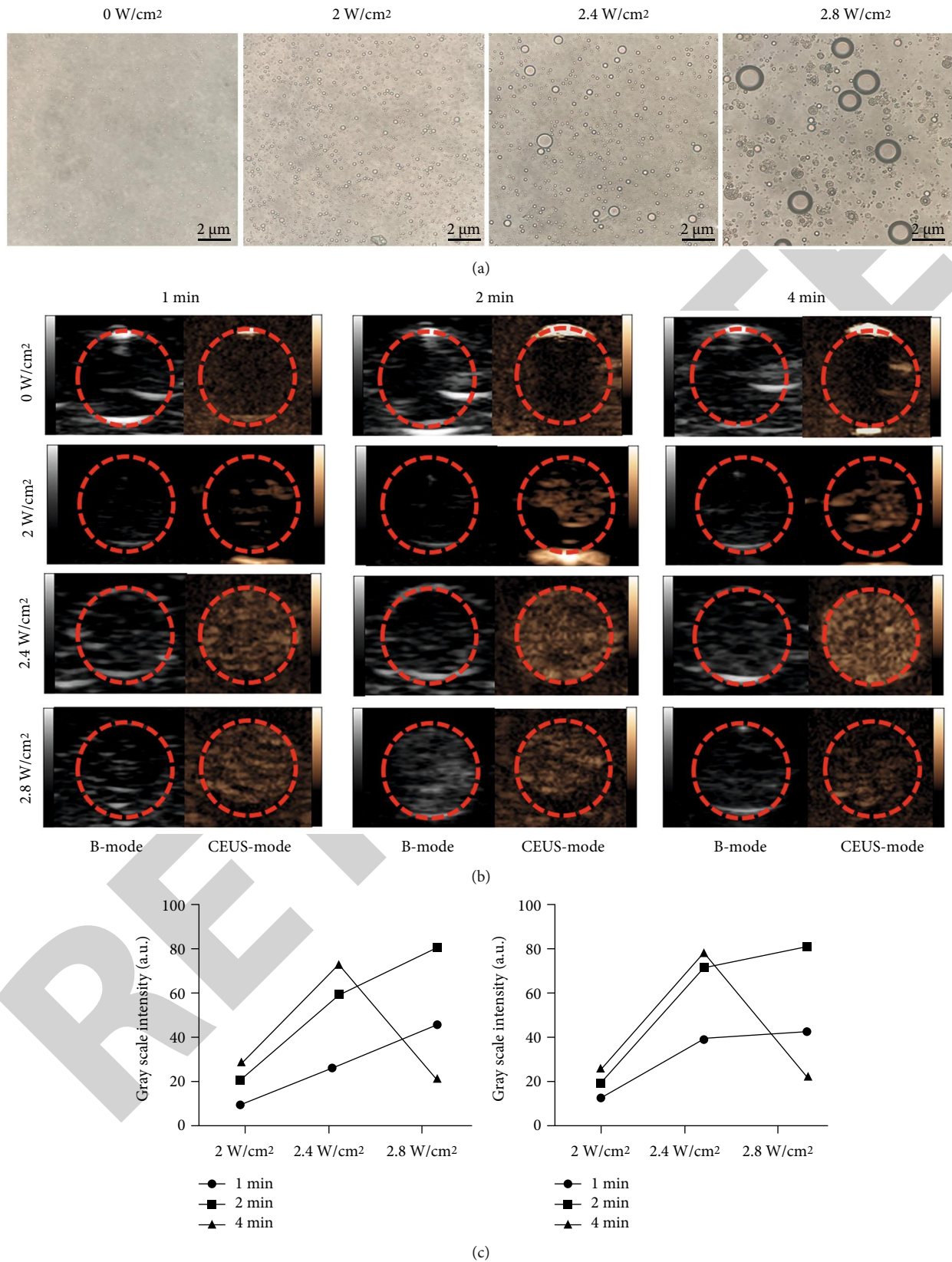
Figure 7: Phase-transformation imaging and enhanced ultrasound imaging of PPL NPs in vitro. (a) Light microscope images of phase transformation by LIFU irradiation. (b) Ultrasound images (B-mode and CEUS mode) of PPL NPs after being irradiated by LIFU under different conditions. (c) The corresponding grayscale intensity at different intensities and times of 2D imaging and CEUS imaging.
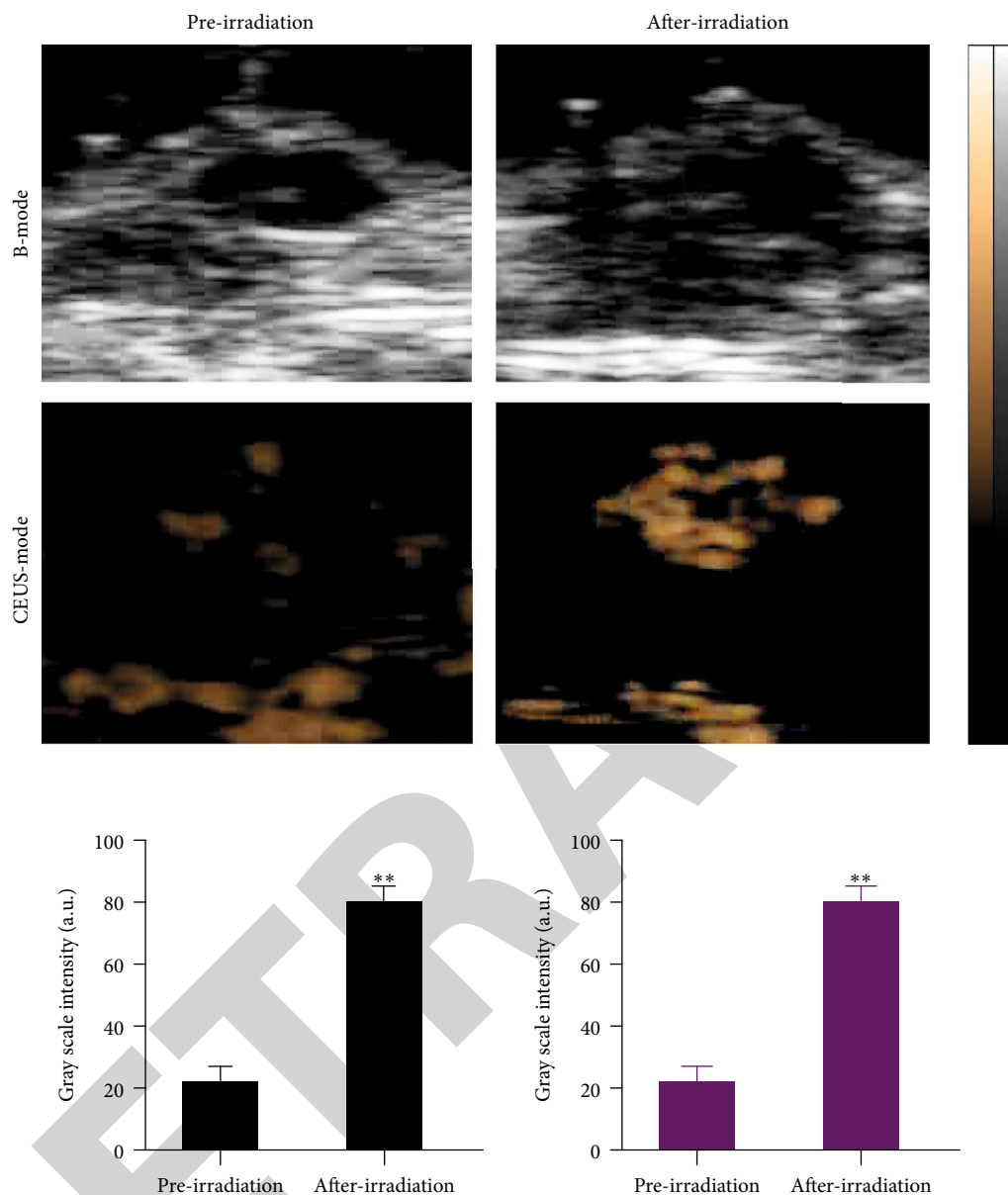
Figure 8: Enhanced ultrasound imaging of PPL NPs in vivo. 2D and CEUS images with and without LIFU irradiation and the corresponding grayscale intensity analysis measured by ImageJ ($^{**}P < 0.01$, $n = 3$).

pathways of the HCCLM3 cell line. At the same time, our results show that it is precisely because of UTMD that PPL NPs could maximally inhibit the production of LX2 extracellular matrix components and the expression of downstream-related molecules.

Then, we used the treated CM to intervene HCCLM3 cells again for 24 h and detected the protein expression of the above pathway-related indicators in HCCLM3 cells and compared them. The results are shown in (Figure 5(c)): different from the above treatment of HCCLM3 alone, in the case of coculture of CM and HCCLM3 cells, the expressions of TGF-β, Smad2, Smad3, and their downstream indicators Snail and N-cadherin were all decreased, while E-cadherin was elevated. Likewise, the PPL NPs combined with the LIFU group showed the most significant effect. The above results can preliminarily confirm that PFD can inhibit the

activity of LX2 cells and the expression of TGF-β, thereby reducing the activation level of the TGF-β/Smad2 signaling pathway in HCCLM3 cells, thereby inhibiting the occurrence of EMT in HCC. Similarly, our results also confirmed that the combination of our prepared PPL NPs with UTMD can more effectively strengthen this mechanism.

3.6. PPL NPs Inhibited Cell Metastasis In Vitro. The ability of tumor cells to invade and migrate is a decisive aspect of tumor metastasis development [34, 35]. As shown in (Figure 6(a)), CM treated with PPL NPs+LIFU group maximally inhibited the wound healing ability of HCCLM3 cells and weakened the migration ability of these cells. Likewise, Transwell analysis showed that the number of CM migrating and invading HCCLM3 cells affected by the PPL NPs+LIFU group was significantly reduced compared with other groups

(a)

(b)
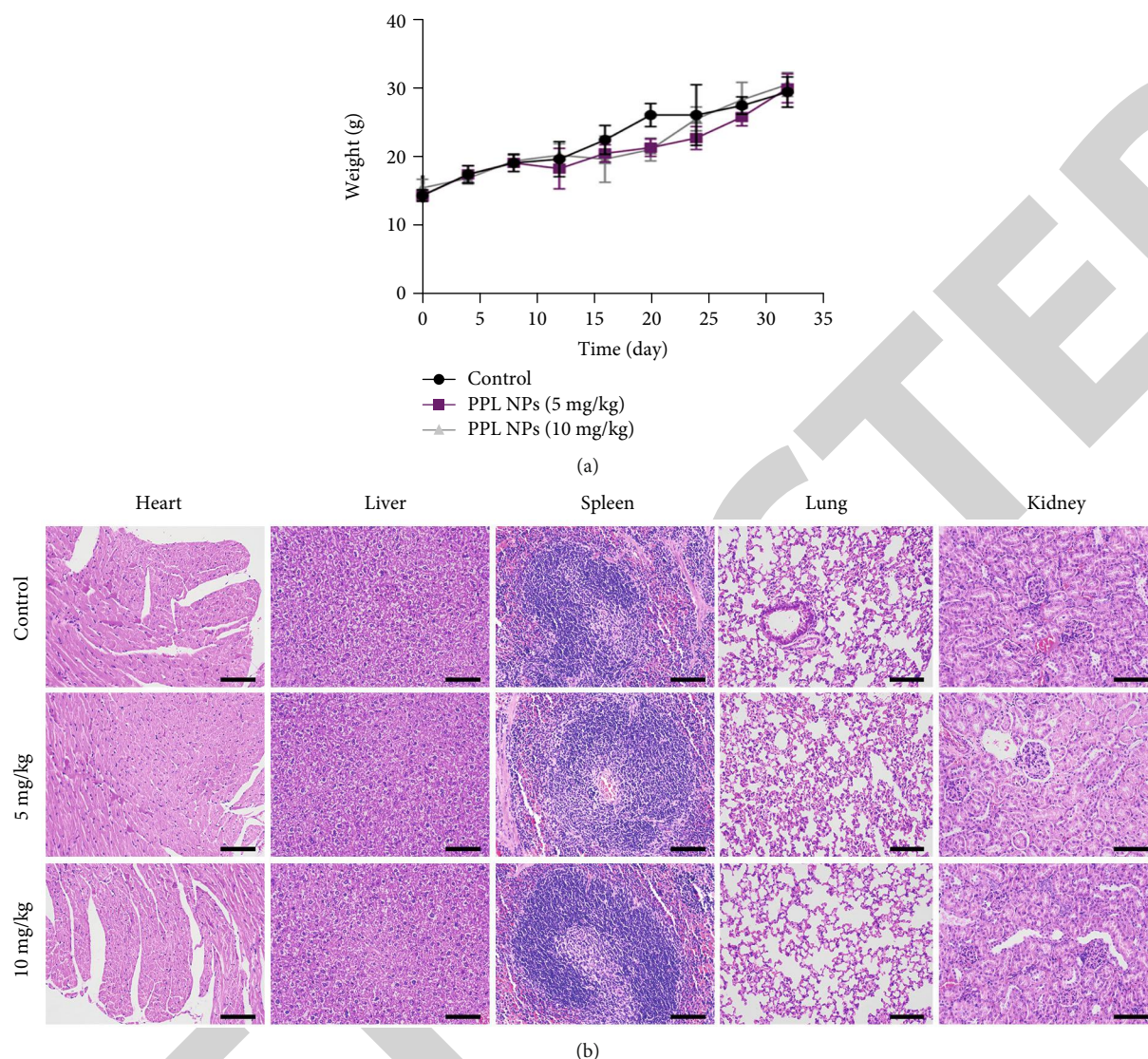
Figure 9: Biosafety of PPL NPs. (a) The weights of healthy mice under various concentrations of PPL NPs ($n = 3$). (b) H&E results of the heart, liver, spleen, lung, and kidney of mice (scale bar: 100 μm).

(Figures 6(b) and 6(c)), which further suggested that synergistic treatment has excellent antitransfer ability. Taken together, these data demonstrate that the combination of UTMD with PPL NPs can reduce LX2 cell viability through efficient ultrasonic cavitation, mechanical effects, and drug release, thereby inhibiting HCCLM3 cell migration and invasion in vitro.

3.7. Ultrasound Imaging In Vitro. First, we observed PPL NPs under an optical microscope, and the experiments proved that PPL NPs could be transformed into microbubbles after LIFU irradiation, which first provided the basis for their in vitro imaging (Figure 7(a)). Afterwards, in the agarose model, we observed that the PPL NPs had no obvious ultrasound enhancement before LIFU irradiation, but after LIFU, they improved the efficiency of ultrasound imaging due to the good phase transition ability of PFP; 2D and CEUS all showed a trend towards enhanced ultrasound

imaging. The results for 2D and CEUS were most significant when the LIFU intensity reached 2.4 W/cm^2 for 4 minutes. Unsurprisingly, if the LIFU irradiation time and intensity continued to increase, UTMD would be triggered and the microbubbles would burst, greatly reducing the imaging effect, as shown in (Figures 7(b) and 7(c)). The above results indicate that LIFU irradiation can be used as the trigger source of ADV for PFP [36], and at the same time, the successful encapsulation of PFP and PFD in PPL NPs can significantly improve the ultrasound imaging ability and trigger drug release, improving the therapeutic effect [37].

3.8. Ultrasound Imaging In Vivo. After validating the role of PPL NPs in in vitro imaging, we further evaluated their characteristic ultrasound imaging capabilities in vivo and validated their phase transition capabilities with vaccinated subcutaneous tumor-bearing mice. The subcutaneous ultrasound images of tumor-bearing mice are shown in

(Figure 8): When the PPL NPs reached the lesion site and LIFU trigger ADV, the tumor images were enhanced in both B-mode and CEUS-mode, indicating that after LIFU irradiation, The PPL NPs we prepared can phase-transform locally to appear strong echo signals, which can be effectively used for enhanced ultrasound imaging and disease treatment. It is worth noting that the irradiation intensity and irradiation temperature of LIFU used in this study are much lower than those of HIFU, which fully demonstrates the controllability and safety of LIFU [38].

3.9. Biosafety of PPL NPs In Vivo. In vivo biosafety is a top priority [39]. After demonstrating significant diagnostic and therapeutic efficacy of PPL NPs, we explored their safe distribution in vivo. No significant body weight loss was observed in any group of mice studied by body weight measurement, which tentatively suggested that PPL NPs have good biosafety (Figure 9(a)). In addition, the H&E staining of each organ did not change significantly (Figure 9(b)), which further indicated that the application of PPL NPs has excellent biosafety in vivo.

4. Discussion

It is well known that the promotion of tumor metastasis by EMT is one of the important reasons affecting the prognosis of HCC [40, 41]. Recent studies have shown that the tumor microenvironment is closely related to the progression, prognosis, and drug resistance of HCC. However, most current tumor treatment strategies only target tumor cells, ignoring the important role of the tumor microenvironment, so many patients will experience recurrence and metastasis after treatment [3, 42]. Admittedly, a single antifibrotic drug has certain limitations, and it may still be insufficient in further cancer microenvironment therapy. In recent years, the combination of NPs and medicine has been strongly developed, and NPs have obvious advantages such as low poison, noninvasive, and good biocompatibility. Applying this new drug-loading system, researchers can make better use of multifunctional therapeutic strategies to improve the efficiency of exploring anticancer [42, 43].

We constructed a multifunctional integrated nanodrug delivery system by encapsulating the phase-change material PFP and the antifibrotic drug PFD with lipid material as the outer structure, which further improved the efficiency of PFD drug action. PPL NPs achieve ideal aggregation mainly through EPR effect and activate UTMD effect through LIFU real-time dynamic observation, which opens broad prospects for integrated and precise diagnosis and treatment of PPL NPs. PPL NPs are ideal therapeutic approaches combined with ultrasound, and their efficient deep penetration capability and drug delivery system have been experimentally confirmed.

In this study, PPL NPs with uniform size and good dispersion were prepared by the well-established thin-film hydration method and acoustic vibration method [44]. Fine particles on the surface of the nanoparticles are clearly observed under transmission electron microscope, indicating that PFD have been successfully encapsulated. After the experiment, the best encapsulation efficiency of PFD was obtained, suggesting that PFD and PFP can be encapsulated in large quantities providing a theoretic basis for clinical use in tumor drug therapy.

The stability of PPL NPs was confirmed by 7-day particle size measurement and optical microscope observation, and the PFD was well protected by liposome encapsulation. In addition, the outer shell of the liposomes was also well protected against PFP, which was confirmed by the excellent in vitro imaging results. The results of in vivo ultrasound imaging in this study showed that after PPL NP injection, LIFU irradiated the tumor site of nude mice, and the ultrasound imaging effect was significantly enhanced. The ability of PPL NPs as ultrasound contrast agents to enhance image contrast and accumulate in tumor tissues suggests their potential applications in early diagnosis and treatment of tumors and confirms that PPL NPs can be used for real-time ultrasound monitoring of drug aggregation and targeted release to reduce drug effects on normal organs toxic side effects.

In in vitro drug release experiments, we proved that the release of PFD gradually increased with the extension of time and remained stable after 36 hours, confirming the good biological stability of PFD, which laid a solid foundation for its long-term circulation and sustained release in vivo [45]. The results of CCK-8, colony formation, and apoptosis confirmed the killing effect of PPL NPs on LX2 cells; we found that PPL NP treatment alone had the least toxicity to LX2 cells, while combined with LIFU, cytotoxicity and apoptosis were at the same concentration. Deaths also increased significantly. This result may be due to the increased drug distribution and cell permeability caused by fragmentation of PPL NPs by LIFU. It was further verified that the encapsulation of liposomes would not reduce the cytotoxic effect of PFD. On the contrary, the sustained release effect of liposomes could further help PFD to decrease LX2 cells activity.

In the present study, we provide new evidence for the link between TGF-β in LX2 and the TGF-β/Smad signaling pathway in HCC. The results showed that our prepared PPL NPs combined with UTMD could significantly reduce the cell proliferation and fibrosis generation capacity of LX2 through the TGF-β/Smad3 pathway. In addition, our results also verified by cell coculture experiments that PPL NPs combined with LIFU can maximize the inhibition of TGF-β produced by a-HSCs, thereby affecting the TGF-β/Smad2 pathway of HCC, leading to the downregulation of Snail and N-cadherin and upregulation of E-cadherin, thus inhibiting cell migration and invasion and inhibiting the production of EMT, thereby controlling cancer progression.

This experiment partially explains why the EMT of HCC may be affected by the mechanism by which LX2 inhibits proliferation and fibrosis development. However, in this experiment, we have not fully explored its mechanism. Also, in in vitro experiments, migration and invasion of HCCLM3 cells could be significantly inhibited in both scratch assay and Transwell assay due to the optimized therapeutic strategy due to LIFU stimulation. Next, we will primarily silence TGF-β in the LX2 cell line and then explore the effect of the

TGF-β/Smad pathway on HCC metastasis in the HCC microenvironment. Its impact should be further studied in the future.

Besides, ultrasound monitoring is crucial for the precise drug delivery [26, 46]. Ultrasound could not only excite the encapsulated PFD liposome to undergoe phase transition and therefore promote the targeted release of the drug but also monitor the aggregation of PPL NPs in the tumor in real time. The key of LIFU combined with PPL NPs is to trigger the UTMD effect, which influences the extracellular matrix while driving the drug further into the tumor tissue. However, the microbubbles generated by phase transition can be visualized near the tumor, and the cavitation after bursting can also make the cell membrane open instantly, which greatly enhances the therapeutic effect of the drug and inhibits cell proliferation, maximizing the efficiency of cancer treatment.

In this study, we designed a drug-loaded phase-change nanosystem to influence tumor progression by interfering with the tumor's extracellular microenvironment. Compared with chemotherapy drugs alone, this treatment effect is greatly improved [47]. Meanwhile, the combined LIFU stimulation treatment strategy has been shown to significantly improve the treatment efficiency. Notably, it is worth noting that because of this synergistic therapy that our developed PPL NPs enable "true" molecular aspect imaging and cellular physicochemical diagnosis and treatment. Therefore, PPL NPs combined with LIFU can be considered as a good system to prevent the poor prognosis of metastatic HCC.

5. Conclusion

We prepared PPL NPs successfully. First of all, the PPL NPs designed and prepared in this study combined with LIFU irradiation could significantly alter the EMT of HCC by inhibiting LX2. Second, PPL NPs can via ADV and then UTMD triggered by LIFU. This can maximize the integration of diagnosis and treatment. Finally, PPL NPs will also be considered a promising contrast agent due to their ultrasound imaging capabilities.

Data Availability

The data required to reproduce these findings cannot be shared at this time as the data also forms part of an ongoing study.

Conflicts of Interest

The authors declare that they have no conflicts of interest.

Acknowledgments

References

[1] J. M. Llovet, R. K. Kelley, A. Villanueva et al., "Hepatocellular carcinoma," *Nature Reviews Disease Primers*, vol. 7, no. 1, p. 6, 2021.

[2] A. L. Cheng, "Pursuing efficacious systemic therapy for hepatocellular carcinoma," *Nature Reviews. Gastroenterology & Hepatology*, vol. 18, no. 2, pp. 95-96, 2021.

[3] Y. Huang, T. Wang, J. Yang, X. Wu, W. Fan, and J. Chen, "Current strategies for the treatment of hepatocellular carcinoma by modulating the tumor microenvironment via nano-delivery systems: a review," *International Journal of Nanomedicine*, vol. Volume 17, pp. 2335–2352, 2022.

[4] Y. Du, D. Liu, and Y. Du, "Recent advances in hepatocellular carcinoma therapeutic strategies and imaging-guided treatment," *Journal of Drug Targeting*, vol. 30, no. 3, pp. 287–301, 2022.

[5] M. Song, J. He, Q. Z. Pan et al., "Cancer-associated fibroblast-mediated cellular crosstalk supports hepatocellular carcinoma progression," *Hepatology*, vol. 73, no. 5, pp. 1717–1735, 2021.

[6] M. C. Lampi and C. A. Reinhart-King, "Targeting extracellular matrix stiffness to attenuate disease: from molecular mechanisms to clinical trials," *Science Translational Medicine*, vol. 10, no. 422, 2018.

[7] D. Peng, M. Fu, M. Wang, Y. Wei, and X. Wei, "Targeting TGF-β signal transduction for fibrosis and cancer therapy," *Molecular Cancer*, vol. 21, no. 1, p. 104, 2022.

[8] J. Jiang, K. Wang, Y. Chen, H. Chen, E. C. Nice, and C. Huang, "Redox regulation in tumor cell epithelial-mesenchymal transition: molecular basis and therapeutic strategy," *Signal Transduction and Targeted Therapy*, vol. 2, no. 1, p. 17036, 2017.

[9] S. O. Imodoye, K. A. Adedokun, A. O. Muhammed et al., "Understanding the complex milieu of epithelial-mesenchymal transition in cancer metastasis: new insight into the roles of transcription factors," *Frontiers in Oncology*, vol. 11, article 762817, 2021.

[10] J. Su, S. M. Morgani, C. J. David et al., "Publisher correction: TGF-β orchestrates fibrogenic and developmental EMTs via the RAS effector RREB1," *Nature*, vol. 578, no. 7793, p. E11, 2020.

[11] J. Huang, M. Qiu, L. Wan et al., "TGF-β1 promotes hepatocellular carcinoma invasion and metastasis via ERK pathway-mediated FGFR4 expression," *Cellular Physiology and Biochemistry*, vol. 45, no. 4, pp. 1690–1699, 2018.

[12] L. Liu, N. Li, Q. Zhang, J. Zhou, L. Lin, and X. He, "Inhibition of ERK1/2 signaling impairs the promoting effects of TGF-β1 on hepatocellular carcinoma cell invasion and epithelial-mesenchymal transition," *Oncology Research*, vol. 25, no. 9, pp. 1607–1616, 2017.

[13] P. Spagnolo, J. A. Kropski, M. G. Jones et al., "Idiopathic pulmonary fibrosis: disease mechanisms and drug development," *Pharmacology & Therapeutics*, vol. 222, article 107798, 2021.

[14] P. Spagnolo, O. Distler, C. J. Ryerson et al., "Mechanisms of progressive fibrosis in connective tissue disease (CTD)-associated interstitial lung diseases (ILDs)," *Annals of the Rheumatic Diseases*, vol. 80, no. 2, pp. 143–150, 2021.

[15] A. Di Sario, E. Bendia, G. Svegliati Baroni et al., "Effect of pirfenidone on rat hepatic stellate cell proliferation and collagen production," *Journal of Hepatology*, vol. 37, no. 5, pp. 584–591, 2002.

[16] Y. Ding, L. Wang, H. Li et al., "Application of lipid nanovesicle drug delivery system in cancer immunotherapy," *Journal of Nanobiotechnology*, vol. 20, no. 1, p. 214, 2022.

[17] L. Yu, Z. Wang, Z. Mo et al., "Synergetic delivery of triptolide and Ce6 with light-activatable liposomes for efficient hepatocellular carcinoma therapy," *Acta Pharmaceutica Sinica B*, vol. 11, no. 7, pp. 2004–2015, 2021.

[18] C. Jia, F. Zhang, J. Lin et al., "Black phosphorus-Au-thiosugar nanosheets mediated photothermal induced anti-tumor effect enhancement by promoting infiltration of NK cells in hepatocellular carcinoma," *Journal of Nanobiotechnology*, vol. 20, no. 1, p. 90, 2022.

[19] Z. Li, Y. Yang, H. Wei et al., "Charge-reversal biodegradable MSNs for tumor synergetic chemo/photothermal and visualized therapy," *Journal of Controlled Release*, vol. 338, pp. 719–730, 2021.

[20] Z. Li, X. Shan, Z. Chen et al., "Applications of surface modification technologies in nanomedicine for deep tumor penetration," *Advanced Science*, vol. 8, no. 1, article 2002589, 2020.

[21] P. Tharkar, R. Varanasi, W. S. F. Wong, C. T. Jin, and W. Chrzanowski, "Nano-enhanced drug delivery and therapeutic ultrasound for cancer treatment and beyond," *Frontiers in Bioengineering and Biotechnology*, vol. 7, p. 324, 2019.

[22] S. K. Golombek, J. N. May, B. Theek et al., "Tumor targeting via EPR: strategies to enhance patient responses," *Advanced Drug Delivery Reviews*, vol. 130, pp. 17–38, 2018.

[23] L. Zhu, H. Zhao, Z. Zhou et al., "Peptide-functionalized phase-transformation nanoparticles for low intensity focused ultrasound-assisted tumor imaging and therapy," *Nano Letters*, vol. 18, no. 3, pp. 1831–1841, 2018.

[24] J. Ouyang, A. Xie, J. Zhou et al., "Minimally invasive nanomedicine: nanotechnology in photo-/ultrasound-/radiation-/magnetism-mediated therapy and imaging," *Chemical Society Reviews*, vol. 51, no. 12, pp. 4996–5041, 2022.

[25] A. G. Athanassiadis, Z. Ma, N. Moreno-Gomez et al., "Ultrasound-responsive systems as components for smart materials," *Chemical Reviews*, vol. 122, no. 5, pp. 5165–5208, 2022.

[26] H. Li, Y. Zhang, H. Shu, W. Lv, C. Su, and F. Nie, "Highlights in ultrasound-targeted microbubble destruction-mediated gene/drug delivery strategy for treatment of malignancies," *International Journal of Pharmaceutics*, vol. 613, article 121412, 2022.

[27] J. R. Eisenbrey, F. Forsberg, C. E. Wessner et al., "US-triggered microbubble destruction for augmenting hepatocellular carcinoma response to transarterial radioembolization: a randomized pilot clinical trial," *Radiology*, vol. 298, no. 2, pp. 450–457, 2021.

[28] J. C. Wischhusen, S. M. Chowdhury, T. Lee et al., "Ultrasound-mediated delivery of miRNA-122 and anti-miRNA-21 therapeutically immunomodulates murine hepatocellular carcinoma _in vivo_," *Journal of Controlled Release*, vol. 321, pp. 272–284, 2020.

[29] S. Sadat Akhavi and S. Moradi Dehaghi, "Drug delivery of amphotericin B through core-shell composite based on PLGA/Ag/Fe3O4: in vitro test," *Applied Biochemistry and Biotechnology*, vol. 191, no. 2, pp. 496–510, 2020.

[30] Y. Zi, K. Yang, J. He, Z. Wu, J. Liu, and W. Zhang, "Strategies to enhance drug delivery to solid tumors by harnessing the EPR effects and alternative targeting mechanisms," *Advanced Drug Delivery Reviews*, vol. 188, article 114449, 2022.

[31] M. Sharifi, W. C. Cho, A. Ansariesfahani et al., "An updated review on EPR-based solid tumor targeting nanocarriers for cancer treatment," *Cancers (Basel)*, vol. 14, no. 12, 2022.

[32] M. Li, Y. Zhu, C. Yang et al., "Acoustic triggered nanobomb for US imaging guided sonodynamic therapy and activating anti-tumor immunity," *Drug Delivery*, vol. 29, no. 1, pp. 2177–2189, 2022.

[33] J. Rich, Z. Tian, and T. J. Huang, "Sonoporation: past, present, and future," *Advanced Materials Technologies*, vol. 7, no. 1, p. 2100885, 2022.

[34] Z. Yin, K. Jiang, R. Li, C. Dong, and L. Wang, "Multipotent mesenchymal stromal cells play critical roles in hepatocellular carcinoma initiation, progression and therapy," *Molecular Cancer*, vol. 17, no. 1, p. 178, 2018.

[35] J. D. Yang, I. Nakamura, and L. R. Roberts, "The tumor microenvironment in hepatocellular carcinoma: current status and therapeutic targets," *Seminars in Cancer Biology*, vol. 21, no. 1, pp. 35–43, 2011.

[36] J. Liu, F. Xu, J. Huang et al., "Low-intensity focused ultrasound (LIFU)-activated nanodroplets as a theranostic agent for non-invasive cancer molecular imaging and drug delivery," *Biomaterials Science*, vol. 6, no. 11, pp. 2838–2849, 2018.

[37] M. Yang, N. Zhang, T. Zhang, X. Yin, and J. Shen, "Fabrication of doxorubicin-gated mesoporous polydopamine nanoplatforms for multimode imaging-guided synergistic chemophotothermal therapy of tumors," *Drug Delivery*, vol. 27, no. 1, pp. 367–377, 2020.

[38] L. de Los Ríos Cardenas, L. A. B. Varon, and W. C. de Albuquerque Pereira, "Parameter estimation in high-intensity focused ultrasound therapy," *International Journal for Numerical Methods in Biomedical Engineering*, vol. 38, no. 5, article e3591, 2022.

[39] L. Khalili, G. Dehghan, N. Sheibani, and A. Khataee, "Smart active-targeting of lipid-polymer hybrid nanoparticles for therapeutic applications: recent advances and challenges," *International Journal of Biological Macromolecules*, vol. 213, pp. 166–194, 2022.

[40] A. Jayachandran, B. Dhungel, and J. C. Steel, "Epithelial-to-mesenchymal plasticity of cancer stem cells: therapeutic targets in hepatocellular carcinoma," *Journal of hematology & oncology*, vol. 9, no. 1, p. 74, 2016.

[41] G. Giannelli, P. Koudelkova, F. Dituri, and W. Mikulits, "Role of epithelial to mesenchymal transition in hepatocellular carcinoma," *Journal of Hepatology*, vol. 65, no. 4, pp. 798–808, 2016.

[42] S. Han, S. Bi, T. Guo et al., "Nano co-delivery of Plumbagin and Dihydrotanshinone I reverses immunosuppressive TME of liver cancer," *Journal of Controlled Release*, vol. 348, pp. 250–263, 2022.

[43] A. R. Afshari, M. Sanati, H. Mollazadeh, P. Kesharwani, T. P. Johnston, and A. Sahebkar, "Nanoparticle-based drug delivery systems in cancer: a focus on inflammatory pathways," in *Seminars in Cancer Biology*, Academic Press, 2022.

[44] A. Ullah, G. Chen, Z. Yibang et al., "A new approach based on CXCR4-targeted combination liposomes for the treatment of liver fibrosis," *Biomaterials Science*, vol. 10, no. 10, pp. 2650–2664, 2022.

[45] P. Cruz-Nova, A. Ancira-Cortez, G. Ferro-Flores, B. Ocampo-García, and B. Gibbens-Bandala, "Controlled-release nanosystems with a dual function of targeted therapy and radiotherapy in colorectal cancer,," *Pharmaceutics*, vol. 14, no. 5, 2022.

Retraction

Retracted: PRP from Personal Blood Relieves Joint Fluid-Inducing Synovial Injury through NF-κB Pathway and Mitochondrial Apoptosis in Human Synovial Fibroblast Cells

BioMed Research International

This article has been retracted by Hindawi following an investigation undertaken by the publisher [1]. This investigation has uncovered evidence of one or more of the following indicators of systematic manipulation of the publication process:

(1) Discrepancies in scope

(2) Discrepancies in the description of the research reported

(3) Discrepancies between the availability of data and the research described

(4) Inappropriate citations

(5) Incoherent, meaningless and/or irrelevant content included in the article

(6) Peer-review manipulation

The presence of these indicators undermines our confidence in the integrity of the article's content and we cannot, therefore, vouch for its reliability. Please note that this notice is intended solely to alert readers that the content of this article is unreliable. We have not investigated whether authors were aware of or involved in the systematic manipulation of the publication process.

In addition, our investigation has also shown that one or more of the following human-subject reporting requirements has not been met in this article: ethical approval by an Institutional Review Board (IRB) committee or equivalent, patient/participant consent to participate, and/or agreement to publish patient/participant details (where relevant).

Wiley and Hindawi regrets that the usual quality checks did not identify these issues before publication and have since put additional measures in place to safeguard research integrity.

We wish to credit our own Research Integrity and Research Publishing teams and anonymous and named external researchers and research integrity experts for contributing to this investigation.

The corresponding author, as the representative of all authors, has been given the opportunity to register their agreement or disagreement to this retraction. We have kept a record of any response received.

References

[1] L. Xie, W. Lin, L. Zhu et al., "PRP from Personal Blood Relieves Joint Fluid-Inducing Synovial Injury through NF-κB Pathway and Mitochondrial Apoptosis in Human Synovial Fibroblast Cells," *BioMed Research International*, vol. 2022, Article ID 4496949, 10 pages, 2022.

Research Article

PRP from Personal Blood Relieves Joint Fluid-Inducing Synovial Injury through NF-κB Pathway and Mitochondrial Apoptosis in Human Synovial Fibroblast Cells

Li Xie ,[1,2,3] **Wanchang Lin** ,[4] **Lingqi Zhu** ,[1,2] **Liang Zhou** ,[1,2] **Dasheng Lin** ,[1,2] **Lianshui Huang** ,[1,2] **Wei Xie** ,[1,2] **and Wenliang Zhai** [1,2]

[1]*Orthopaedic Center of People's Liberation Army, Xiamen University Affiliated Southeast Hospital, Zhanghua Road 269, Zhangzhou 363000, China*
[2]*School of Medicine, Xiamen University, Xiamen University Xiang'an Campus, Xiang'an South Road, Xiamen 361102, China*
[3]*Affiliated Renhe Hospital of China Three Gorges University, Yiling Road 410, Yichang 443000, China*
[4]*The Second Hospital of Longyan, Shuangyang West Road 8, Longyan 364000, China*

Correspondence should be addressed to Wenliang Zhai; wlzhai1971@xmu.edu.cn

Background. Platelet-rich plasma (PRP) therapy is a new kind of biological therapy to retune the plasma concentrator into the patient's body for the treatment of osteoarthritis diseases. The present research aimsed to confirm the treatment effects of PRP against osteoarthritis injury and elucidate its potential mechanism via constructing a kind of cellular injury model of human synovial fibroblast cells (HSF cells) induced by synovial fluid from osteoarthritis patients. *Materials and Methods.* HSF cells wereas firstly treated with the different doses of synovial fluid from osteoarthritis patients, and evaluated for the cellular injury via cell morphology and MTT assay. And then, the protective effect of PRP against cellular injury were examined by cell morphology and MTT assay. Following, flow cytometry and western blot assay were employed to evaluate the effect of PRP on mitochondrial apoptosis. Finally, the effect of PRP on NF-κB pathway-associated inflammation wasere examined by Elisa ELISA assay and western blot. *Results.* The dilution ratio 1 : 5 of synovial fluid displayed an excellent injury effect against HSF cells and selected as the model condition. The data from cellular image and MTT assay showed that PRP with the doses 1 : 5 and 1 : 10 could alleviate the cellular mounts decrease in the damaged HSF cells. Flow cytometry, western blot, and Elisa ELISA assay displayed that PRP could relieve the cellular mitochondrial apoptosis and NF-κB pathway-associated inflammation in the damaged HSF cells. *Conclusion.* PRP might relieve HSF cells injury induced by synovial fluid from osteoarthritis patients through alleviating the mitochondrial apoptosis and NF-κB pathway-associated inflammation.

1. Introduction

Osteoarthritis, commonly occurring in the elderly patients, is recognized as a degenerative musculoskeletal disease characterized by osteoproliferation and the degeneration of cartilage articularis and synovium [1–3]. According to the statistics of Global Burden of Disease Study 2019 by Lancet, there is approximately 350 million incidences meeting with osteoarthritis around the earth [4], and the amount of osteoarthritis patients remain to be greatly rising with the growing aging population [5, 6]. The quietness of the early

symptoms and the lack of the effective early screening strategy in osteoarthritis make the delayed treatment and contribute to the osteoarthritis-associated cellular injury, which lead to the undesired disability incidence [7]. Recently, many strategies including surgery and pharmacological treatment such as nonsteroidal anti-inflammation drugs (NSAIDs) have been reported and used for treating osteoarthritis and relieving osteoarthritis-associated cellular injury [8, 9]. However, the effective treatment strategy for osteoarthritis-associated cellular injury and disability incidence was still facing a challenge clinically. Therefore, it is

an urgent issue to explore and understand the novel and effective treatment manner to fight against osteoarthritis.

Platelet-rich plasma (PRP) therapy is a new kind of biological therapy to retune the plasma concentrator into the patient's body for the treatment of diseases, which have been developed in the recent few years [10, 11]. Because it is an autologous biological agents prepared through extracting autologous blood, centrifuging at low speed and enriching high-concentration platelets, PRP exhibited a lower rejection and the side effect in body [12]. Currently, PRP therapy has been widely applied to the treatment of various diseases such as ophthalmology [13, 14], orthopedics, and dermatology [15, 16]. Our previous treatment in clinic found that autologous PRP therapy could effectively treat knee osteoarthritis of patients with level II and III according to Kellgren-Lawrence grading standard via accelerating the absorption of effusion of knee joint [17] and repairing the injury of synovial fibroblast cells. The accumulation of joint effusion and the injury of osteoarthritis-associated cells are two of the major symptoms of osteoarthritis. However, the mechanism of PRP therapy alleviating the two symptoms of osteoarthritis remains rarely reported up to now. Therefore, elucidating the mechanism of PRP therapy would be significant for understanding the effect of PRP and further developing PRP application in clinic.

Inflammation is considered as a common pathological event characterized by the symptoms of redden, swollen, hot, and painful, which occurs in nearly all of the acute and chronic diseases response to the physical injury and infection. For the response, the inflammation event initiates the expression of both proinflammation cytokines such as tumor necrosis factor α (TNFα), and in turn regulates, especially aggravate the localized tissue and cellular injury. Plenty of evidences have been confirmed that inflammation is an important indicator of osteoarthritis. Inflammation factors greatly aggregate in the joint effusion of patient with osteoarthritis and stimulate the tissues including synovium directly contacting joint effusion, which aggravate the damage of synovial tissue and fibroblast cells, consequently leading to the disability, and the loss of working capability for osteoarthritis patients. These implied that alleviating inflammation would be an effective strategy to treat the damage symptoms of osteoarthritis. However, it was rarely reported that whether PRP therapy alleviating damage of tissue and cells in osteoarthritis patients was associated with the inflammation. Therefore, elucidating the association of PRP therapy and inflammation would be a feasible significate for understanding the mechanism of PRP therapy alleviating osteoarthritis.

The present research aims to elucidate the roles of NF-κB-associated inflammation and mitochondrial apoptosis pathway in PRP therapy alleviating osteoarthritis. First, human synovial fibroblast cells (HSF cells) and synovial fluid were employed to construct the injury model of synovial fibroblast cells. The protective effect of PRP therapy was assessed by MTT assay. Second, the protective effect of apoptosis by PRP was examined by flow cytometry of dual-staining of FITC-Annexin V/PI, and the mitochondrial potential depolarization was detected via JC-1 staining. Following, the inflammation factors induced by synovial fluid and suppressed by PRP were assessed by ELISA and western blotting assays.

2. Materials and Methods

2.1. Chemicals and Reagents. Dulbecco's modified Eagle medium (DMEM) and RPMI-1640 medium were purchased from HyClone. Foetal bovine serum (FBS) was obtained from Gibco. The primary antibody of cleaved PARP, cleaved caspase3, caspase3, Bax, Bad, Bcl-2, COX2, iNOS, p-IKK, IKK, IκB, p-p65, and GAPDH were obtained from abcam (USA). Annexin V-FITC apoptosis kit was supplied from Becton and Dickinson Company (BD, USA). JC-1 dye was purchased from SolarBio (China).

2.2. Cell Culture. The human synovial fibroblast cells (HSF cells) were maintained in Dulbecco's modified Eagle medium (DMEM) containing 10% FBS in a 5% CO$_2$ atmosphere at 37°C. When the amounts of HSF cells in the logarithmic phase reached to 80-90% confluence in 10 cm cell culture plates, they were digested with 0.25% trypsin solution, resuspended into 5 mL EP tubes with PBS, and centrifuged at 1000 rpm for 5 minutes, following the precipitated cells were seeded into 6-wells plate and treated with synovial fluid, TNFα, and/or PRP as necessary. And then, the cells were collected and detected by the following experiments.

2.3. The Construction of Cellular Injury Model in HSF Cells. HSF cells were seeded into 96-wells cultured plate and maintained for 12 hours. And then, the seeded cells were treated with TNFα with different doses of 20, 40, and 60 ng/mL or synovial fluid with different dilution ratio of 1:5, 1:10, and 1:20 for 48 hours. After treating, the cellular morphology was imaged using microscope, and the cellular proliferation was detected by MTT assay. Finally, the condition under 1:5 dilution ratio of synovial fluid, displayed the abnormal morphology and the lower proliferation ratio in HSF cells, was chosen as the model condition for the research.

2.4. MTT Assay. HSF cells were seeded into the 96-wells plate and cultured for 12 hours. And then, the seeded cells were treated with synovial fluid, TNFα, and/or PRP at the response concentration for the specific time. After treating, the cells were added with 20 μL MTT (5 mg/mL), cultured for another 3 hours, diluted with 100 μL DMSO, and read the OD value using microplate reader (Peiqing, China). The proliferation rate was calculated using Microsoft Excel software following as:

$$\text{Proliferation Rate} = \frac{(\text{OD}_{\text{Sample}} - \text{OD}_{\text{Blank}})}{(\text{OD}_{\text{Control}} - \text{OD}_{\text{Blank}})} \times 100\%. \quad (1)$$

2.5. Flow Cytometry of Dual-Staining of FITC-Annexin V/PI Detecting the Cellular Apoptosis. The HSF cells treated by synovial fluid, TNFα and/or PRP were digested into single cells with 0.25% trypsin and transferred into 1.5 mL EP tubes. The digested cells were washed with precold PBS

Synovial fluid from patient's knee

Synovial fluid stored in-80°C

Medium with synovial fluid for cell culture

(a)

1 mL activating agent

9 mL original PRP

Mix and shock

Centrifuge at 1500 g for 10 min

Incubate at 4°C for 16 hours

Centrifuge at 3000 g for 20 min

Activated PRP

(b)
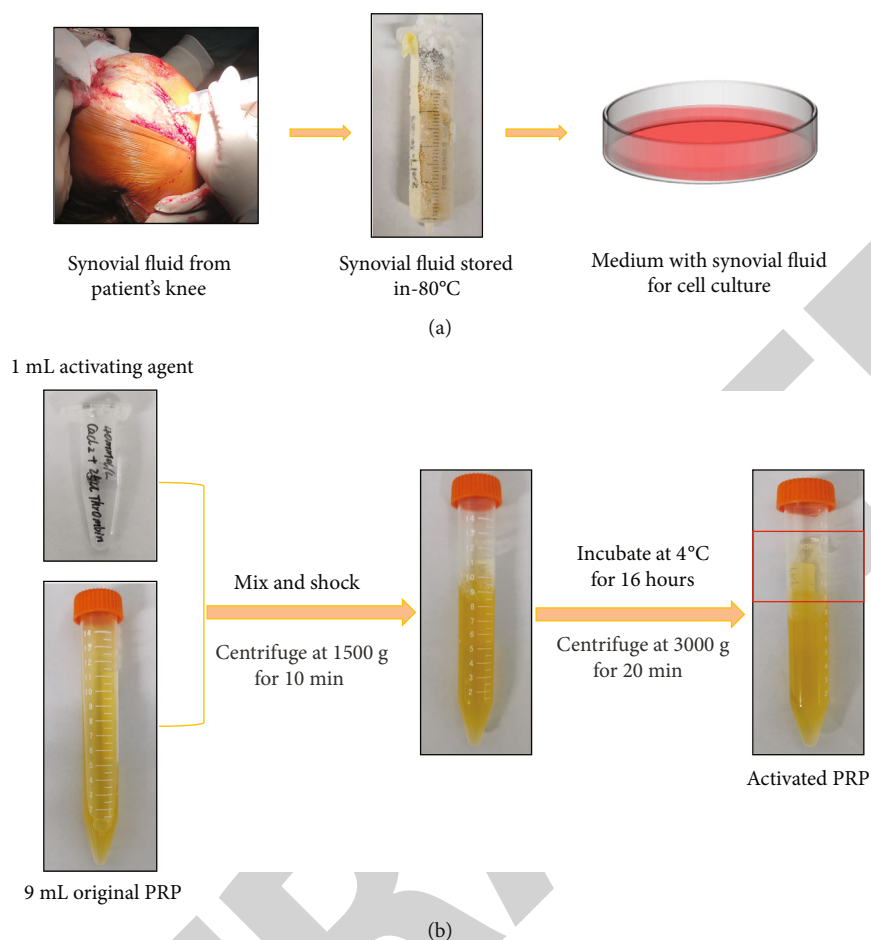
FIGURE 1: The preparation flow of synovial fluid (a) and platelet-rich plasma (b).

and centrifuged at 1500 rpm and 4°C for 5 minutes. The precipitate of cells was resuspended with 300 μL 1 × binding buffer, following 5 μL Annexin V-FITC was added to incubate at room temperature away from light for 15 minutes, and then 5 μL of PI was added to stain. At last, the stained cells were supplied with another 200 μL 1 × binding buffer and detected by the flow cytometry (Beckman, USA).

2.6. Western Blotting. The HSF cells treated by synovial fluid, TNFα and/or PRP were harvested and lysed with RIPA buffer. The total protein concentration of cell lysates was detected using BCA kit, and then was denatured with loading buffer under the condition of boiling. 30 μg of the total denatured proteins were loaded and subjected to the sodium dodecyl sulfate-polyacrylamide gel electrophoresis (SDS-PAGE) for protein separation. The separated proteins were transferred to PVDF membrane. After blocking with 5% skim milk in Tris-buffered saline with tween20 (TBST) for 1 hour, the PVDF membranes were incubated with the primary antibodies against cleaved PARP, cleaved caspase3, caspase3, Bax, bad, bcl-2, cox2, iNOS, p-IKK, IKK, IκB, p-p65 at 4°C overnight, and the antibody of GAPDH was employed as an internal reference. The PVDF membranes were washed with TBST three times and further incubated with the corresponding secondary antibody at room temper-

ature for 2 hours. Finally, the corresponding target on the PVDF membrane was probed using ECL reagent.

2.7. Flow Cytometry for Mitochondrial Potential by JC-1 Staining. HSF cells subjecting to with synovial fluid dilution, TNFα and/or PRP dilution were digested with 0.25% trypsin solution, washed with phosphate buffer solution, and then suspended with 1 mL fresh DMEM medium. The suspended cells were added with 1 mL JC-1 working solution and incubated at 37°C for 20 minutes. Following the incubated cells were centrifuged, washed twice using precold JC-1 washing buffer, and examined and analyzed using flow cytometry.

2.8. ELISA. HSF cells were seeded into 96-wells cultured plate and maintained for 12 hours. And then, the seeded cells were treated with synovial fluid of 1:5 dilution ratio for 24 hours and maintained with different doses of platelet-rich plasma for another 24 hours. After treatment, the cellular supernatant was collected, diluted with PBS for the corresponding proportion, and mixed with the buffer in ELISA kit according to 1:1. 100 μL of mixture solution, and the standard substance were added into the corresponding ELISA plate of IL-6, IL-1β, and TNFα, and incubation at 37°C for 30 minutes. The values were read using microreader, the standard curve was drawn, and the relative contents

(a)

(b)

(c)

(d)

(e)

(f)
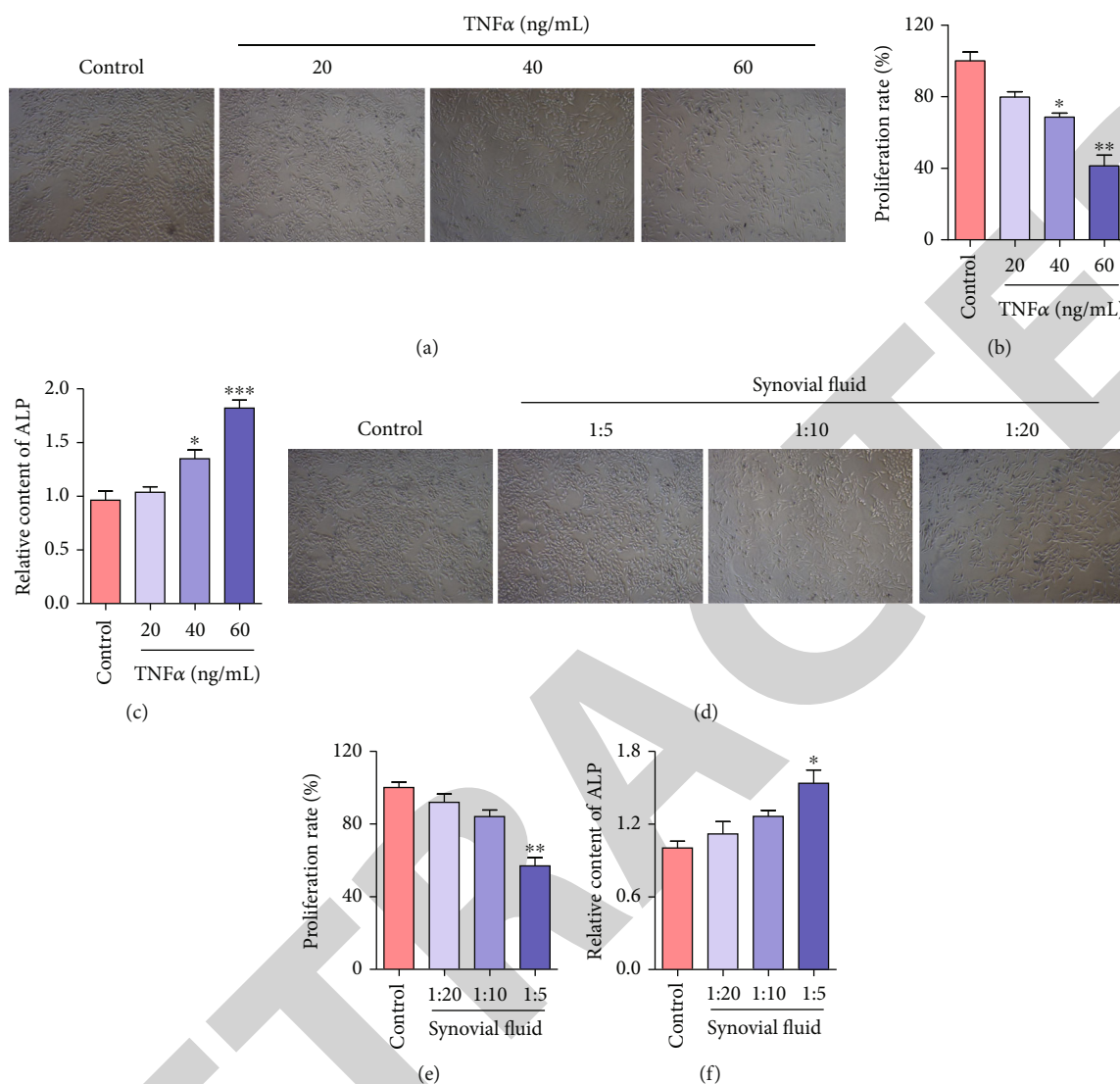
Figure 2: Establishment of synovial fluid-inducing cellular injury in human synovial fibroblast cells.

of the three inflammation factors were calculated according to the standard curve.

2.9. Statistical Analysis. SPSS software of version 19.0 (SPSS, USA) was employed for statistical analysis. The data were displayed as mean ± standard deviation (SD) and *t*-tests were used to compare the differences among the control, model, and synovial fluid/PRP groups. *P* < 0.05 represented significance of the statistical difference. The sign of * was for the comparison with the control group and the sign # was for the comparison with the model group.

3. Results

3.1. The Preparation Flow of Synovial Fluid and Platelet-Rich Plasma. The synovial fluid was drawn from the articular cavity of patients with level II and III knee osteoarthritis according to Kellgren-Lawrence grading standard and collected into the sterile tube stored at 20°C. When the cells were treated, the collected synovial fluid was diluted with the

DMEM medium with FBS by the ratio 1 : 4, 1 : 9, and 1 : 19, and replaced the normal DMEM medium to culture cells for the needed time (Figure 1(a)). The peripheral blood from individuals were harvested into the blood-collecting tube with anticoagulant and gently shake upside down for mixing uniformity, and centrifuged at 2500 rpm for 10 min. The supernatant serum was collected and transferred into another blood-collecting tube, secondly centrifuged at 3200 rpm for 8 min, and the supernatant was collected as the original PRP. Then, the original PRP was added with activating agent following the volume ratio of 9 : 1 for activation. The mixture was shocked and centrifuged at 1500 rpm for 10 min, incubated at 4°C for 16 hours, following centrifuged at 3000 rpm for another 20 min, and collected the supernatant to obtain the activated PRP (Figure 1(b)).

3.2. Synovial Fluid Induces the Cellular Injury in Human Synovial Fibroblast Cells. The number and morphology changes of cells subjecting to the inappropriate agents reflect the toxicity/injury effect of the agents on cells. The cellular

(a)

(b)

(c)
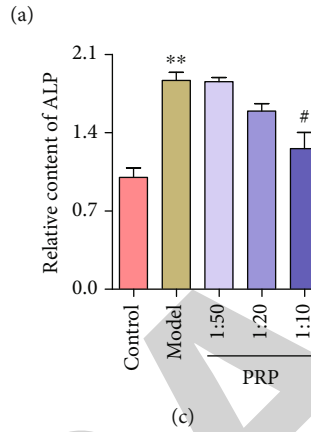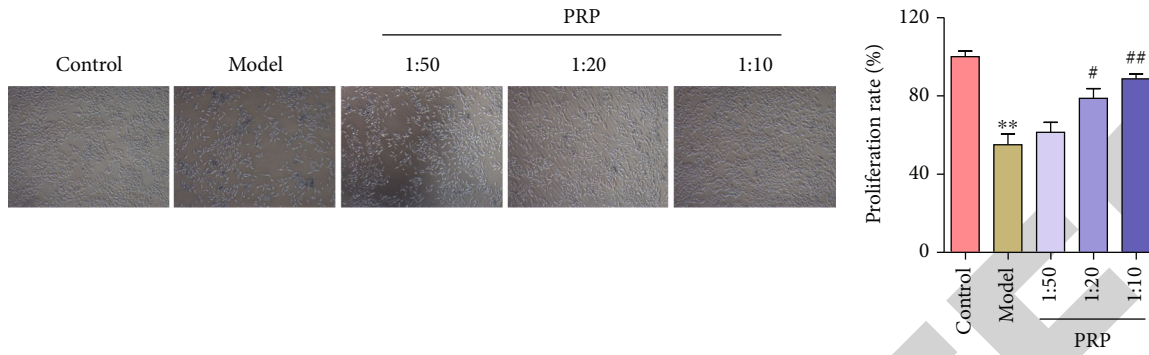
Figure 3: The protection effect of PRP on synovial fibroblast injury.

(a)

(b)
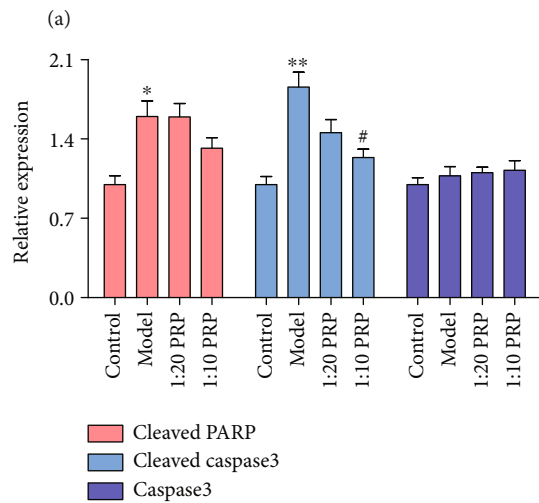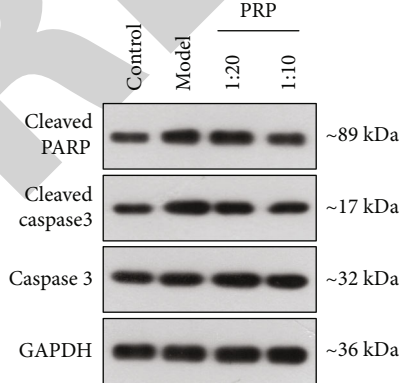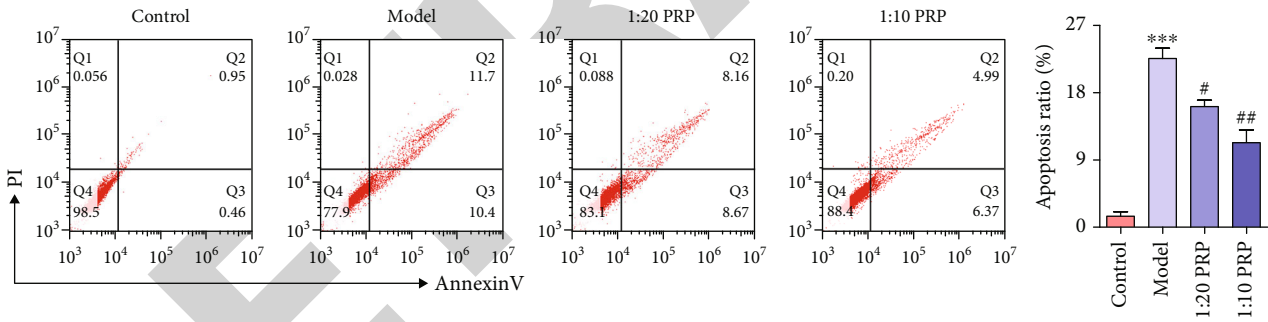
Figure 4: Effect of PRP on cellular apoptosis in the damaged HSFC.

(a)

(b)
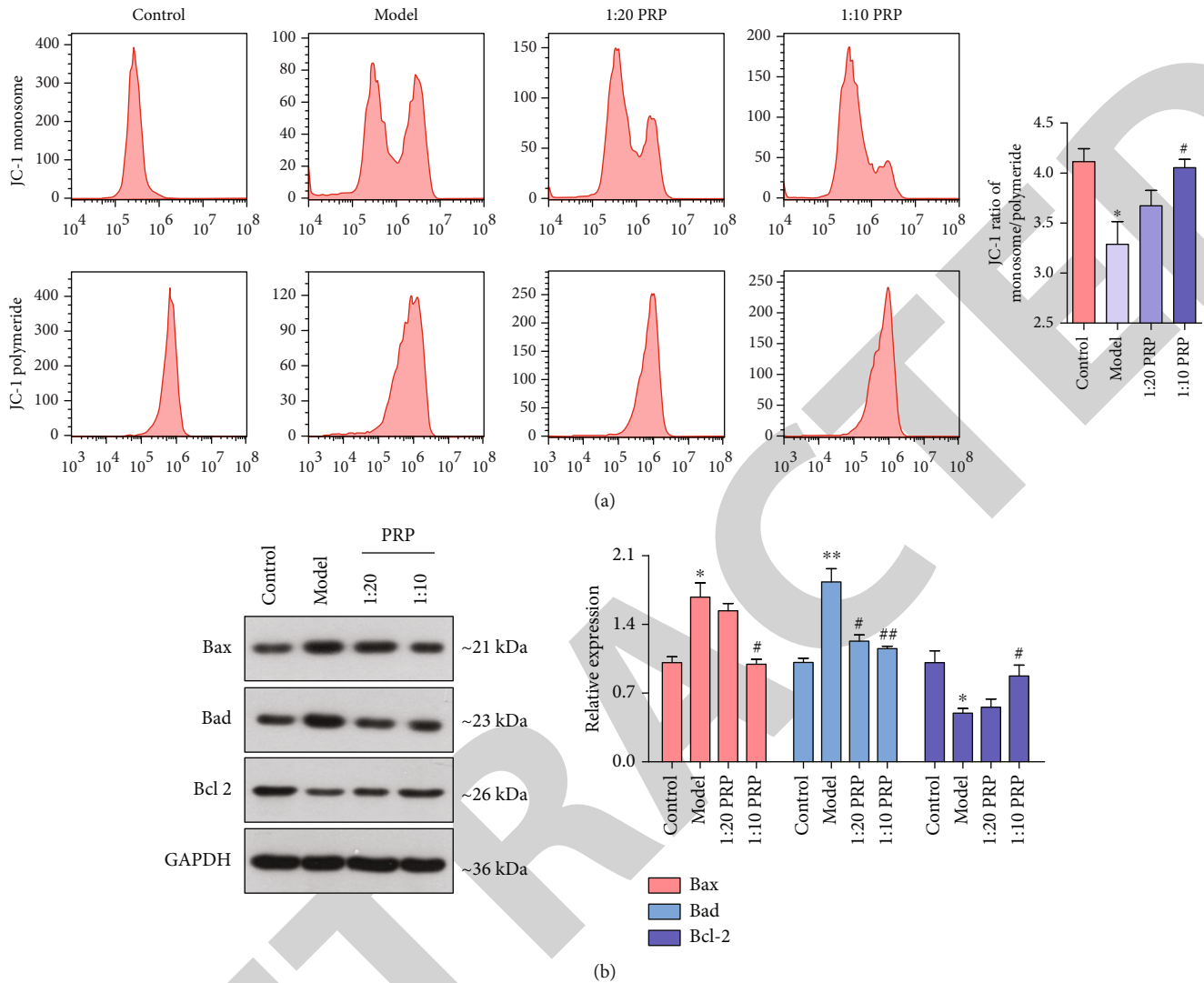
Figure 5: Effect of PRP on mitochondrial apoptosis in the damaged HSFC.

image (Figure 2(a)) showed that the outline of HSF cells subjecting to higher doses of 40 and 60 ng/mL TNFα displayed a dispersive and ambiguous state compared with that in control group, and the cellular amounts of higher doses TNFα were declined. MTT assay showed that HSF cells subjecting to the indicated concentrations of TNFα displayed a dose-dependent decrease of proliferation ratio (Figure 2(b)), reversely; the ALP level in HSF cells subjecting to the indicated concentrations of TNFα displayed an obvious increase (Figure 2(c)). Meanwhile, we employed the preprepared synovial fluid to treat HSF cells, and the cellular number and morphology was microscope imaged. Figure 2(d) shows that HSF cells treated with 1 : 10 and 1 : 20 diluent of synovial fluid displayed a dispersive state which was similar to the cells subjecting to TNFα. Furthermore, HSF cells subjecting to the indicated dilute ratio of synovial fluid displayed a dose-dependent decrease of proliferation ratio (Figure 2(e)) and increase of ALP level (Figure 2(f)). These results demonstrated that synovial fluid could induce the cellular injury in HSF cells similar with the effect of TNFα, and the condi-

tion of 1 : 5 dilution was used to construct the injury model of synovial fibroblast cells for the following research.

3.3. PRP Protects the Synovial Fluid-Inducing Cellular Injury in HSF Cells. In order to confirm the protection effect of PRP against synovial fibroblast cells injury, cell morphology was observed and the proliferation ratio was analyzed. Figure 3(a) shows that HSF cells in model group displayed a dispersive morphology and decreased amounts compared to that in control group, excitingly, PRP with the dilution ratio of 1 : 20 and 1 : 10 relieved the cellular injury induced by synovial fluid. MTT assay revealed that the low dose of PRP (1 : 50) slightly relieved synovial fluid-inducing the decrease of cellular proliferation ratio in HSF cells, and the middle and high doses of PRP obviously ease the decrease of cellular proliferation ratio induced by synovial fluid (Figure 3(b)). Furthermore, ALP level analysis showed that the middle and high doses of PRP inhibited the induction of ALP content by synovial fluid (Figure 3(c)). These results demonstrated that PRP could protect the synovial fluid-
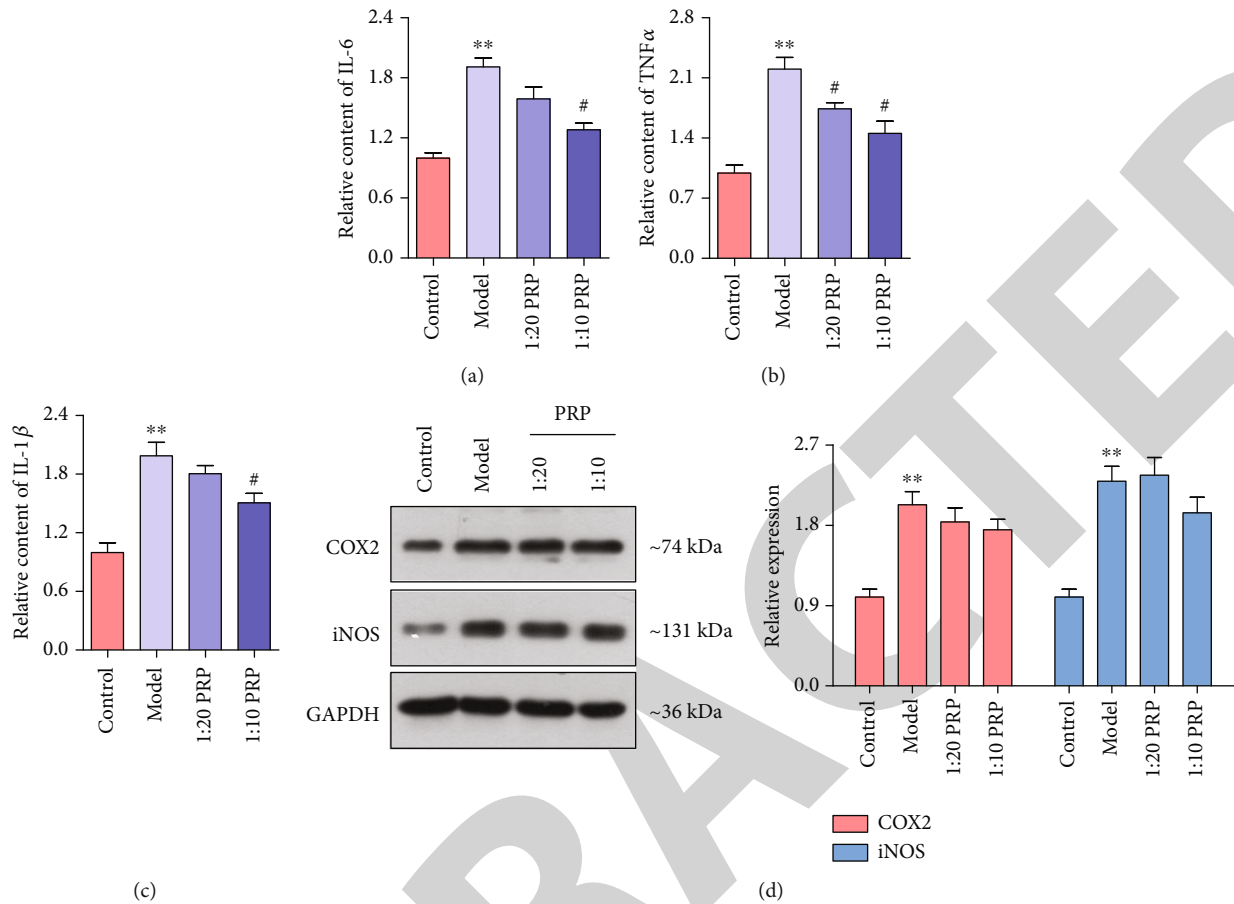
Figure 6: The inhibitory effect of PRP on inflammation in the damaged HSFC.

inducing cellular injury in HSF cells, which was consistent with the protective effect of PRP on damaged synovial tissues in patients with osteoarthritis.

3.4. PRP Relieves the Cellular Apoptosis in the Damaged HSF Cells. Cellular apoptosis is one of the common events for evaluating the normal cell injury. In order to further evaluate the protective effect of PRP against synovial fibroblast cells injury, dual-staining experiments of Annexin V-FITC and PI were performed, and the apoptosis proteins were detected by western blotting to evaluate the relieving effect of PRP on cell apoptosis. The scatter diagram of dual-staining experiments by flow cytometry showed that HSF cells in model group had an increase of apoptosis ratio from 1.41% to 22.1% compared to that in control group. Meanwhile, the damaged cells were treated with the higher dose of PRP (1 : 10) and had an obvious decrease of apoptosis ratio from 22.1% to 11.36% compared to that in model group, and the middle dose of PRP displayed a decrease of apoptosis ratio from 22.1% to 16.83% (Figure 4(a)). Furthermore, western blot assay showed that HSF cells in model group had an obvious cleavage induction of PARP and caspase 3. However, the higher dose of PRP (1 : 10) inhibited the cleavage induction of PARP and caspase 3 mediated by synovial fluid (Figure 4(b)). These results demonstrated that PRP could

relieve the cellular apoptosis in the damaged HSF cells induced by synovial fluid.

3.5. PRP Relieves the Mitochondrial Apoptosis in the Damaged HSF Cells. Mitochondrial was considered as a central organelle to mediate the respiratory chain for almost all of the cellular physiopathology, and exerted an important role in cellular apoptosis. In order to confirm whether mitochondrial was associated with the relieving effect of PRP on cellular apoptosis, mitochondrial membrane potential and related apoptosis proteins of Bax, Bcl-2, and Bad were studied. JC-1 staining data from flow cytometry analysis showed that the fluorescence ratio of aggregate/monomer in the HSF cells of model group was obviously increased compared to that in control group, and the treatment of PRP relieved the change trend of aggregate/monomer ratio (Figure 5(a)), demonstrating that synovial fluid induced the mitochondrial membrane potential depolarization and PRP reserved the depolarization induced by synovial fluid. Furthermore, western blot assay showed that HSF cells in model group had an obvious induction of Bax and Bad expression and inhibition of Bcl-2 expression. However, different doses of PRP relieved these change trends (Figure 5(b)). The results demonstrated that PRP could relieve the cellular apoptosis via
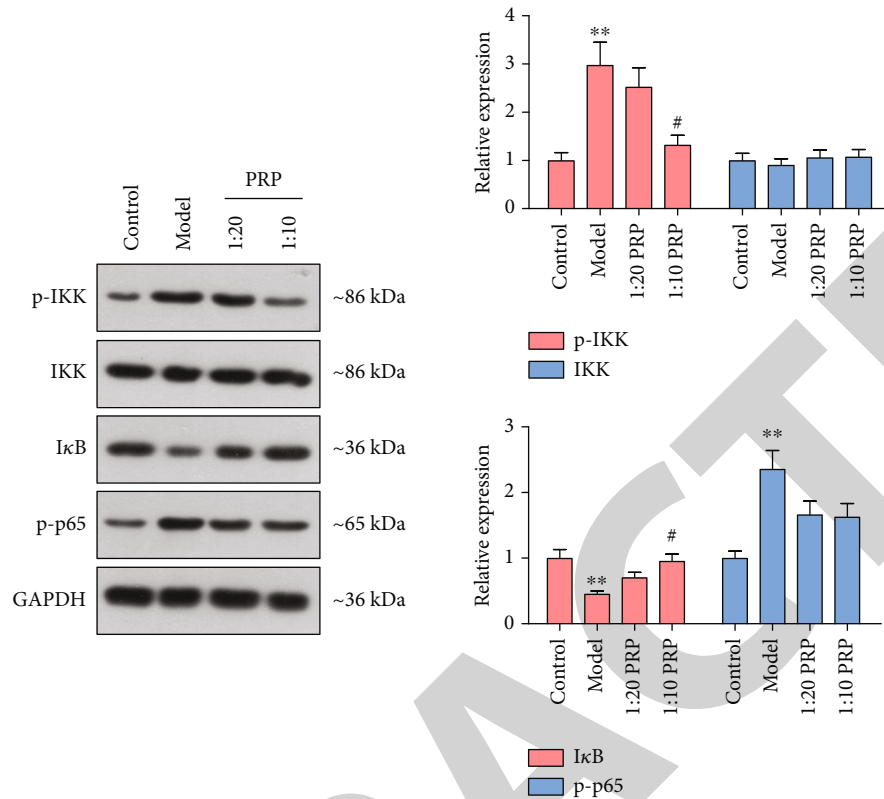
FIGURE 7: Effect of PRP on NF-κB pathway in the damaged HSFC.

mitochondrial pathway in the damaged HSF cells induced by synovial fluid.

3.6. PRP Inhibits the Inflammation in the Damaged HSF Cells. Inflammation is considered as one of the main causes for chronic disease such as cancer, diabetes, and degenerative disease of the joint, which mediates the physiological and pathological processes of the diseases. In order to confirm whether the inflammation was involved into the protective effect of PRP on cellular injury induced by synovial fluid, ELISA assay and western blot analysis were performed for detecting the inflammation factors TNFα, IL-1β, IL-6, COX2, and iNOS. Elisa assay revealed that HSF cells subjected to synovial fluid had a content increase of TNFα, IL-1β, and IL-6, and PRP inhibited the increases in a dose-dependent manner (Figures 6(a)–6(c)). Furthermore, western blot analysis showed that HSF cells in model group displayed the upregulation expression of COX2 and iNOS, and high-dose PRP inhibited the expression of COX2 and iNOS (Figure 6(d)). These results demonstrated that inflammation may take part in the cellular injury effect induced by synovial fluid and PRP could inhibit the inflammation in the damaged HSF cells.

3.7. PRP Inhibits the Activation of NF-κB Pathway Induced by Synovial Fluid in the HSF Cells. NF-κB (Nuclear Factor kappa-B) is an important pathway of inflammation, which is associated with cell proliferation, apoptosis, and injury. In order to further confirm the relationship between NF-κB pathway-related inflammation and the protection effect of PRP on cellular injury, the NF-κB pathway-related indicators were detected by western blot. Figure 7 shows that the phosphorylation level of IKK and p65 was obviously induced, and the IκB expression was inhibited during the inflammation induction by synovial fluid in HSF cells. However, HSF cells subjected to synovial fluid were treated with PRP, and then displayed the inhibition of IKK and p65 phosphorylation and the reversion of IκB expression inhibition. These results demonstrated that PRP could protect the cellular injury via clearing away the inflammation mediated by NF-κB pathway.

4. Discussion

PRP therapy has been widely applied to the treatment of various diseases such as ophthalmology, orthopedics, and dermatology. Our previous treatment in clinic found that PRP therapy could effectively alleviate knee osteoarthritis caused by exercise. However, the mechanism of PRP therapy alleviating osteoarthritis remains rarely reported up to now. Although it was in the vague understanding that how PRP therapy alleviating osteoarthritis, some shreds of evidence have shown that the inflammatory pathway of NF-κB is associated with the injury effect of osteoarthritis. Additionally, the mitochondrial apoptosis pathway plays a vital role in the cellular injury. In the present study, we found that PRP could alleviate the cellular apoptosis and mitochondrial depolarization during synovial fluid-inducing injury in HSF

cells, and regulate the mitochondrial-associated apoptosis protein expression. Furthermore, the inflammation factors and the NF-κB pathway-associated proteins p-IKK, IκB and p65 were also mediated by PRP treated. These results demonstrated that PRP therapy might relieve the synovial fluid-inducing injury via the mitochondrial apoptosis and NF-κB pathway-related inflammation.

Apoptosis is a kind of physiological process controlling the programmed cell death to maintain body homeostasis. It exerts essential roles throughout the life cycle including the differentiation, developments, growth, and aging. However, several pathological stimuli, such as inflammation factors, toxic substances, and physical events could also induce the abnormal cellular apoptosis leading to the tissue injury. Caspase 3, an important member of cysteinyl aspartate specific protease family, is commonly recognized as an executioner of apoptosis events. In the apoptosis process, caspase 3 is activated by other caspases initiators via its cleavage, induce the hydrolysis/cleavage of target proteins including poly ADP-ribose polymerase (PARP), and eventually lead to the cellular apoptosis and tissue injury. In the present research, we found that synovial fluid could induce the cellular apoptosis and trigger the cleavage of caspase 3 and PARP, meanwhile PRP treatment relieved the change trends of apoptotic. These results demonstrate that PRP could protect against synovial fluid-inducing cellular injury characterized by apoptosis.

It is commonly considered that apoptosis is divided into two pathways of intrinsic apoptosis and extrinsic apoptosis, and intrinsic pathway is the major manner. In the intrinsic apoptosis process, the mitochondria response to the apoptosis stimuli, cause the change of mitochondrial membrane potential, depolarization of mitochondrial, the expression changes of mitochondrial-associated protein Bax, Bad, and Bcl-2, and eventually lead to the cellular apoptosis [18]. In the present research, we found that synovial fluid could induce the change of mitochondrial membrane potential and depolarization of mitochondrial, which have been confirmed by JC-1 staining, furthermore, it had also been observed that synovial fluid could induce the expression of Bax and Bad, and inhibit the expression of Bcl-2. Reversely, PRP treatment relieved the change of mitochondrial membrane potential and the expression of mitochondrial-associated proteins Bax, Bad, and Bcl-2, demonstrating that PRP could protect against synovial fluid-inducing cellular injury via intrinsic apoptosis pathway.

Inflammation is a typical characteristic symptom of many chronic disease, which is not only the complication of disease, its occurrence would also aggravate the disease progress. Inflammation usually triggers the release of proinflammation including IL-6, TNFα, and IL-1β, and promotes the cellular apoptosis and tissue injury. The nuclear factor κB pathway (NF-κB pathway) is considered as an important inflammation pathway. In NF-κB pathway, IKK is initiatively phosphorylated response to the inflammation stimuli, following the degradation of IκB and phosphorylation of p65 are triggered, and then the proinflammation genes are activated. In the present research, we found the cells subjecting to synovial fluid displayed an obvious phosphorylation of IKK, degradation of IκB and phosphorylation of p65, meanwhile the cells treated with PRP had a reverse trend changes of the above NF-κB pathway indicators, demonstrating that PRP could protect against synovial fluid-inducing cellular injury via the NF-κB inflammation pathway.

Data Availability

The datasets used during the current study are available from the corresponding author on reasonable request.

Conflicts of Interest

The authors declare that there are no conflicts of interest.

Authors' Contributions

Li Xie and Wanchang Lin contributed equally to this research.

Acknowledgments

References

[1] M. A. Karsdal, M. Michaelis, C. Ladel et al., "Disease-modifying treatments for osteoarthritis (DMOADs) of the knee and hip: lessons learned from failures and opportunities for the future," *Osteoarthritis and Cartilage*, vol. 24, no. 12, pp. 2013–2021, 2016.

[2] T. L. Vincent, "Of mice and men: converging on a common molecular understanding of osteoarthritis," *The Lancet Rheumatology*, vol. 2, no. 10, pp. e633–e645, 2020.

[3] L. A. Mandl, "Osteoarthritis year in review 2018: clinical," *Osteoarthritis and Cartilage*, vol. 27, no. 3, pp. 359–364, 2019.

[4] T. Vos, S. S. Lim, C. Abbafati et al., "Global Burden of 369 Diseases and Injuries in 204 Countries and Territories, 1990–2019: A Systematic Analysis for the Global Burden of Disease Study 2019," *The Lancet*, vol. 396, no. 10258, pp. 1204–1222, 2020.

[5] P. K. Sacitharan, "Ageing and osteoarthritis," *Sub-Cellular Biochemistry*, vol. 91, pp. 123–159, 2019.

[6] S. Glyn-Jones, A. J. R. Palmer, R. Agricola et al., "Osteoarthritis," *Lancet*, vol. 386, no. 9991, pp. 376–387, 2015.

[7] B. Abramoff and F. E. Caldera, "Osteoarthritis: pathology, diagnosis, and treatment options," *The Medical Clinics of North America*, vol. 104, no. 2, pp. 293–311, 2020.

[8] H. S. Kan, P. K. Chan, K. Y. Chiu et al., "Non-surgical treatment of knee osteoarthritis," *Hong Kong Medical Journal*, vol. 25, no. 2, pp. 127–133, 2019.

[9] S. I. Macías-Hernández, J. D. Morones-Alba, A. Miranda-Duarte et al., "Glenohumeral osteoarthritis: overview, therapy, and rehabilitation," *Disability and Rehabilitation*, vol. 39, no. 16, pp. 1674–1682, 2017.

[10] P. Everts, K. Onishi, P. Jayaram, J. F. Lana, and K. Mautner, "Platelet-rich plasma: new performance understandings and

Research Article

Identification of Concomitant Inhibitors against Glutamine Synthetase and Isocitrate Lyase in *Mycobacterium tuberculosis* from Natural Sources

Anesha Chanda,[1] Sanjib Kalita,[2] Awdhesh Kumar Mishra,[3] Liza Changkakoti,[1] Janayita Biswa Sarma,[4] Kunal Biswas,[5] Debashree Kakati,[6] Yugal Kishore Mohanta ⓘ,[7] Bhaben Tanti,[2] Saurov Mahanta ⓘ,[1] and Muthupandian Saravanan ⓘ[8,9]

[1]*National Institute of Electronics and Information Technology, Guwahati, 781008 Assam, India*
[2]*Department of Botany, Gauhati University, Jalukbari, Guwahati, 781014 Assam, India*
[3]*Department of Biotechnology, Yeungnam University, Gyeongsan 38541, Republic of Korea*
[4]*Assam Science and Technology University, Jalukbari, Guwahati, 781014 Assam, India*
[5]*Centre for Nanoscience & Nanotechnology International Research Centre, Sathyabama Institute of Science and Technology, Jeppiaar Nagar, Rajiv Gandhi Salai, Chennai 600119, India*
[6]*Department of Botany, Mangaldai College, Mangaldai, 784125 Assam, India*
[7]*Department of Applied Biology, School of Biological Sciences, University of Science and Technology Meghalaya, 9th Mile, Techno city, Baridua, Ri-Bhoi, 793101 Meghalaya, India*
[8]*Department of Microbiology, Division of Biomedical Sciences, Mekelle University, Ethiopia*
[9]*AMR and Nanotherapeutics Laboratory, Department of Pharmacology, Saveetha Dental College, Saveetha Institute of Medical and Technical Sciences (SIMATS), Chennai 600077, India*

Correspondence should be addressed to Yugal Kishore Mohanta; ykmohanta@gmail.com,
Saurov Mahanta; saurov.mahanta@gmail.com, and Muthupandian Saravanan; bioinfosaran@gmail.com

Tuberculosis (T.B.) is a disease that occurs due to infection by the bacterium, *Mycobacterium tuberculosis* (Mtb), which is responsible for millions of deaths every year. Due to the emergence of multidrug and extensive drug-resistant Mtb strains, there is an urgent need to develop more powerful drugs for inclusion in the current tuberculosis treatment regime. In this study, 1778 molecules from four medicinal plants, *Azadirachta indica*, *Camellia sinensis*, *Adhatoda vasica,* and *Ginkgo biloba,* were selected and docked against two chosen drug targets, namely, Glutamine Synthetase (G.S.) and Isocitrate Lyase (I.C.L.). Molecular Docking was performed using the Glide module of the Schrödinger suite to identify the best-performing ligands; the complexes formed by the best-performing ligands were further investigated for their binding stability via Molecular Dynamics Simulation of 100 ns. The present study suggests that Azadiradione from *Azadirachta indica* possesses the potential to inhibit Glutamine Synthetase and Isocitrate Lyase of *M. tuberculosis* concomitantly. The excellent docking score of the ligand and the stability of receptor-ligand complexes, coupled with the complete pharmacokinetic profile of Azadiradione, support the proposal of the small molecule, Azadiradione as a novel antitubercular agent. Further, wet lab analysis of Azadiradione may lead to the possible discovery of a novel antitubercular drug.

1. Introduction

Tuberculosis is an air-borne disease affecting the lungs, presenting symptoms like severe cough, chest pain, and fever. Tuberculosis (T.B.) is a contagious bacterial infection resulting in 48.3 cases per 100,000 inhabitants per year [1]. As per periodic reports published by World Health Organization (WHO), every year 2-3 million people lose their lives due to active Tuberculosis, while billion others carry dormant T.B. throughout the world. In 1882, German Microbiologist Robert Koch revealed that *M. tuberculosis* is the disease-causing agent of T.B. [2]. Over the decades, different antibiotics have been introduced to treat T.B.; however, the emergence of the drug-resistant strains of *M. tuberculosis* has imposed hurdles in the treatment and control of T.B. Multidrug-Resistant (M.D.R.) strains have resistance to potent T.B. drugs, including Rifampin and Isoniazid; Extensive Drug-Resistant (XDR) T.B. strains exhibit resistance against Isoniazid, Rifampin, Amikacin, Kanamycin, and Capreomycin, while Total Drug-Resistant (TDR) T.B. has resistance to all first-line and second-line T.B. drugs [3, 4]. Tuberculosis caused by MDR/XDR strains requires long-term treatment spanning over 9-20 months or even more, with a success rate below 50% globally [3]. The principal reason behind the requirement of long-term treatment in MDR/XDR TB is the smaller subpopulations of nonreplicating cells, which are not affected by standard antibiotics used and hence, require particular drugs to combat the deadly disease [5, 6].

In comparison to developed countries, T.B. is much more prevalent in developing countries. About 10.5 million people were infected with T.B. in 2015, and more than 1.4 million T.B. patients died, with 95% of deaths occurring in developing countries [7]. Human Immunodeficiency Virus (H.I.V.) coinfection with T.B. and the development of strains resistant to the most effective, 1st line T.B. drugs are the two main factors responsible for the existing epidemic caused by T.B.

For the diagnosis and treatment of T.B., different strategies have been developed and are still being developed. In 1993, Directly Observed Treatment Short-Course (DOTS) was one of the most significant strategies among them. In 1998, DOTS plus was introduced to combat the multidrug-resistant (M.D.R.) strain [2, 7]. In the 1800s, "just sleep and eat nutritious food" was the advice given to T.B. patients [2]. In the beginning of the twentieth century, the *Bacillus* Calmette-Guerin (B.C.G.) vaccine was developed, saving many lives from this deadly disease. Until the discovery of Streptomycin in 1944, there was not even a single antitubercular drug [8]. But within a short period of time, Streptomycin also became ineffective in treating T.B., due to the emergence of Streptomycin-resistant strains. After that, different antitubercular drugs were introduced, including isoniazid (1952), pyrazinamide (1952), cysteine (1952), ethambutol (1962), rifampin (1957), and pyrazinamide (1957) [9]. However, due to the emergence of MDR-TB and XDR-TB strains, most commonly used antitubercular drugs became ineffective. Additionally, with the advancement of medical research in the last few years, scientists have obtained valuable insights into T.B. pathogenesis and treatment, yet further extensive research is required to decrease the incidence and subsequently eradicate T.B. successfully [2, 10]. Hence, there is an urgent need to identify new drug candidates in T.B. therapeutics [11].

According to the World Health Organization (WHO), "a medicinal plant" is any plant in which one or more of its organs contain substances that could be used for therapeutic purposes or as precursors for synthesizing suitable drugs. Plants are a repository of secondary metabolites which possess different medicinal properties. Plant secondary metabolites have caught much attention as drug candidates because of their less toxic nature [11]. Around 80% of the population in developing countries relies on traditional medicines derived from plants for their primary health care. In Ayurveda, different diseases, including Tuberculosis are treated using various plants based on the bioactive compounds available [12].

Microorganisms are usually controlled by blocking specific essential enzymes, thereby inhibiting the various biosynthetic pathways in them. Glutamine Synthetase (G.S.) and Isocitrate Lyase (I.C.L.) are two essential enzymes for >the growth of *M. tuberculosis*, and are effective drug targets [13, 14]. G.S. enzyme (E.C. 6.3.1.2) of *M. tuberculosis*, catalyses the ATP-dependent reaction between ammonium and glutamate, resulting in glutamine, A.D.P., phosphate, and a proton. Four G.S. homologues are found in *M. tuberculosis*, of which only one, encoded by the gene *glnA1*, is expressed highly for the survival of *M. tuberculosis* in both *in vitro* and *in vivo* conditions [15–17]. This enzyme can alter the ammonia concentration in the host cells where the infection is prevalent; it affects the pH of the phagosome resulting in the prevention of the phagosome fusion with the lysosome [18, 19].

In the Glyoxylate shunt, Isocitrate Lyase (I.C.L.) catalyses the conversion of Isocitrate to Succinate and Glyoxylate. Malate Synthetase condenses Glyoxylate with acetyl-CoA to form malate [20]. Two T.C.A. cycle steps involving decarboxylation are reportedly by-passed by I.C.L. and Malate Synthase, which is considered an essential phenomenon for fungal and bacterial pathogenesis [21]. ICL1 and ICL2, two forms of the enzyme Isocitrate Lyase encoded by genes *icl11* and *icl12*, respectively, are also crucial for the growth, survival, and virulence of *M. tuberculosis* [14].

TABLE 1: Docking results of Azadiradione with two enzymes GS and ICL.

Sl. No	Compound Name	Binding affinity of the ligands with glutamine synthetase				Binding affinity of the ligands with Isocitrate Lyase			
		Binding affinity (kcal/mol)	RMSD/UB	RMSD/LB	Number of H bonds formed (manually observed)	Binding affinity (kcal/mol)	RMSD/UB	RMSD/LB	Number of H-bonds observed
1	Azadiradione	-10.2	0	0	2	-8.5	0	0	2
2	7-Desacetyl-7-benzoylazadiradione	-10.1	0	0	2	-9	0	0	3
3	7-Desacetyl-7-benzoylgedunin	-9.1	0	0	2	-9.8	0	0	3
4	alpha-Amyrin	-8.8	10.503	6.395	2	-8	7.656	2.823	1
5	Gedunin	-8.7	0	0	2	-8.2	0	0	3

(a)

(b)

(c)

Charged (negative)
Charged (positive)
Glycine
Hydrophobic
Metal
Polar
Unspecified residue
Water
Hydration site
Hydration site (displaced)

Distance
H-bond
Halogen bond
Metal coordination
Pi-Pi stacking
Pi-cation
Salt bridge
Solvent exposure
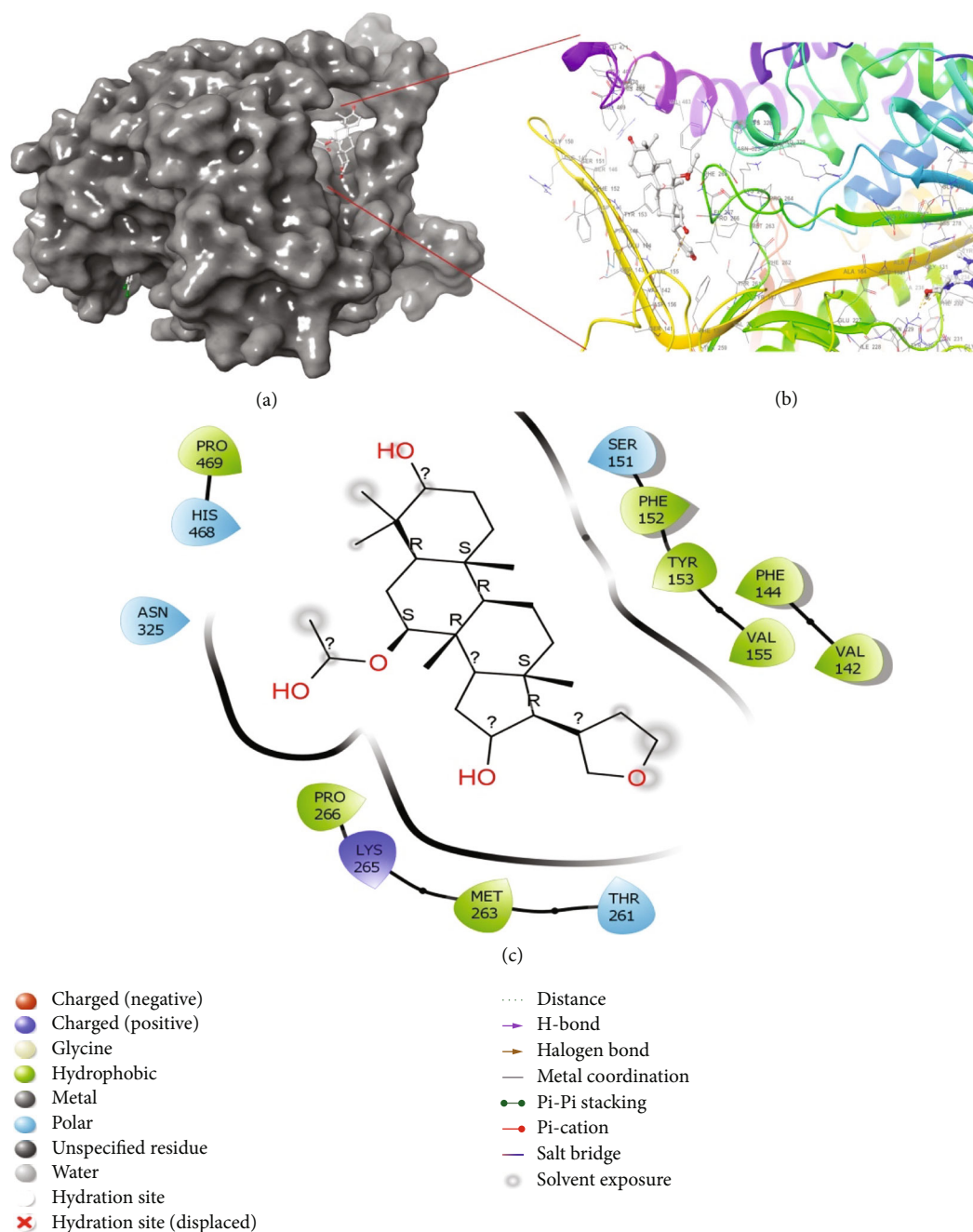
Figure 1: (a) Docking orientation of Azadiradione at the active site of 2WGS; (b) 3D-image of protein-ligand interaction generated using Maestro visualizer; (c) Docking pose and interaction of Azadiradione at the active site of 2WGS. The interaction diagram also illustrates the interactions at 0 ns of M.D. Simulation.

Based on their usage in traditional medicine and their documented antitubercular activity, four plant species, namely, *Azadirachta indica, Camellia sinensis, Adhatoda vasica,* and *Ginkgo biloba* were selected for the current study [21–25]. From the ligand database, that was prepared based on the selected medicinal plants, Computer-Aided Drug Discovery (CADD) protocols were used to identify compounds with inhibitory properties against the two targeted enzymes, Glutamine Synthetase and Isocitrate Lyase of *M. tuberculosis.*

2. Results and Discussions

2.1. Molecular Docking. The binding affinity of the ligands towards the two selected receptors, 2WGS and 1F61, was determined via the Molecular Docking study. The binding affinity was determined based on the docking score; the lower the docking score and the greater the affinity. It was observed that the bioactive compound Azadiradione showed the highest binding relationship towards 2WGS (binding affinity score -10.2) followed by 7-desacetyl-7-

(a)   (b)

(c)

Symbol	Meaning
● Charged (negative)	⋯ Distance
● Charged (positive)	→ H-bond
○ Glycine	→ Halogen bond
● Hydrophobic	— Metal coordination
● Metal	●—● Pi-Pi stacking
● Polar	●—● Pi-cation
● Unspecified residue	— Salt bridge
● Water	○ Solvent exposure
⌣ Hydration site	
✖ Hydration site (displaced)	
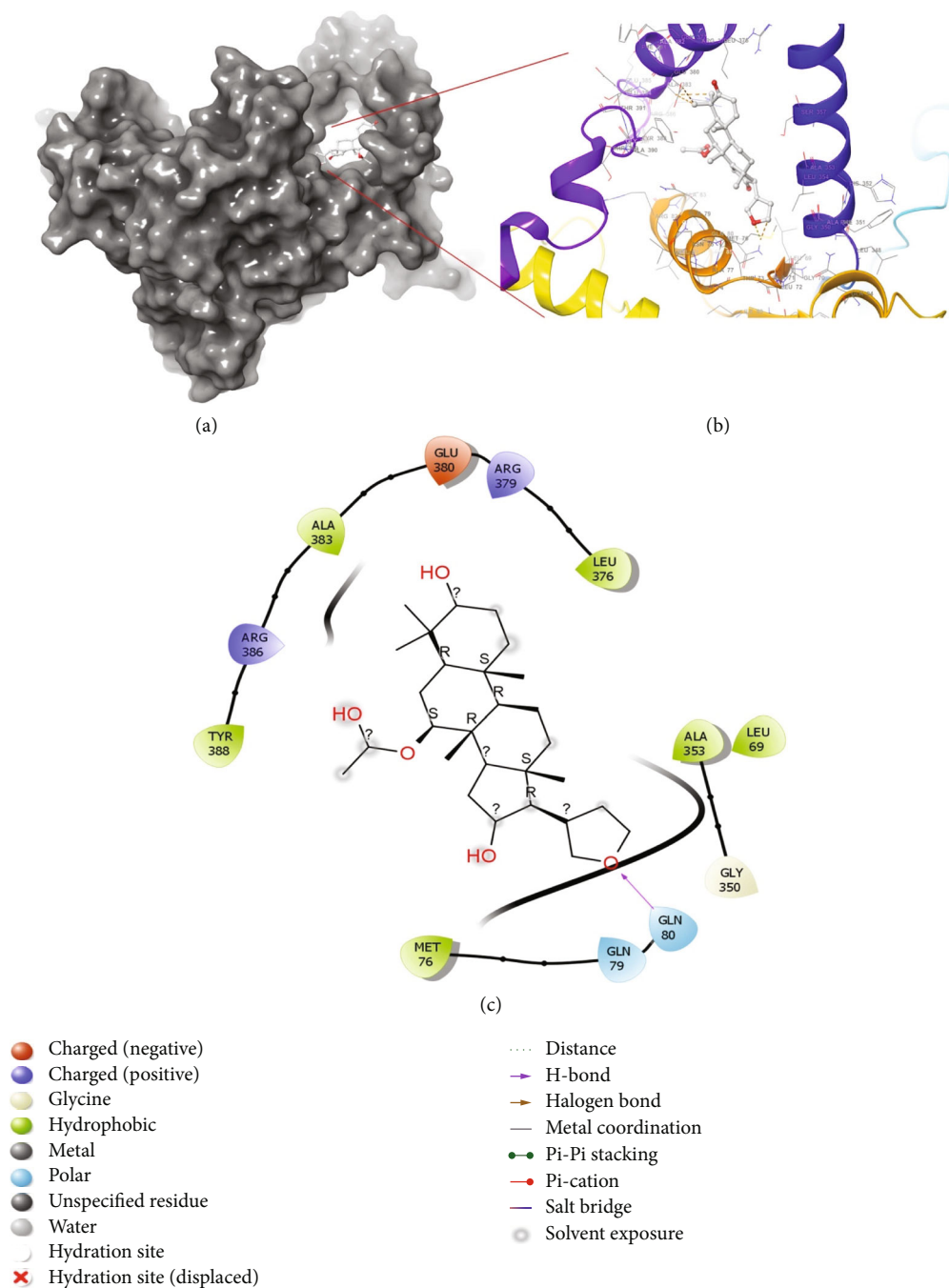
FIGURE 2: (a) Docking orientation of Azadiradione at the active site of 1F61; (b) 3D-image of protein-ligand interaction generated using Maestro visualizer; (c) Docking pose and interaction of Azadiradione at the active site of 1F61. The interaction diagram also illustrates the interactions at 0 ns of M.D. Simulation.

benzoylazadiradione, 7-desacetyl-7-benzoylgedunin, alpha-amyrin, and Gedunin with binding affinities, -10.1, -9.1, -8.8, and -8.7, respectively (Table 1). For the receptor 1F61, 7-desacetyl-7-benzoylazadiradione displayed the highest binding affinity (binding affinity score -9.8), followed by 7-desacetyl-7-benzoylazadiradione, Azadiradione, Gedunin, and alpha-amyrin with binding affinities, -9, -8.5, -8.2, and -8, respectively (Table 1). Based on the binding affinity and

the ability to effectively inhibit more than one receptor, the ligand, Azadiradione, was selected for further analysis.

2.2. Interaction of Azadiradione with the Active Sites of 2WGS and 1F61. The interaction of Azadiradione with the active sites of the two selected enzymes, 2WGS, and 1F61, was analyzed using Maestro Visualizer of Schrödinger Suite 2020-3. It was observed that no H-

(a)

(b)
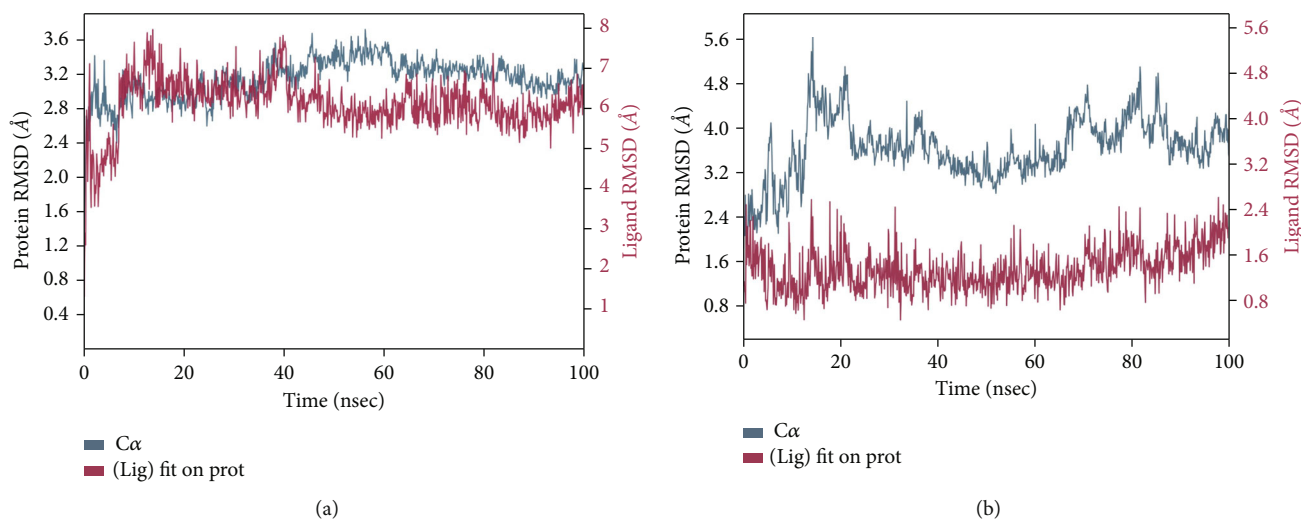
FIGURE 3: (a) R.M.S.D. plot of 2WGS and Azadiradione complex; (b) 1F61 and Azadiradione complex at 100 ns M.D. Simulation.

bonds were formed between Azadiradione and 2WGS (Figure 1(c)), while 3 H-bonds were formed between Azadiradione and the residue Gln 80 of 1F61, as shown in Figure 2(c).

2.3. Molecular Dynamics (M.D.) Simulation.

Molecular Dynamics Simulations were applied to the protein-ligand complexes to test the stability of the interactions between Azadiradione and the binding sites in the proteins. A simulation of 100 ns was run to check the stability of the ligand-protein complexes. Throughout the 100-ns simulation period, the backbone Root-Mean-Square Deviations (R.M.S.Ds) were analysed to measure the structural and dynamic properties of the protein-ligand complexes.

The R.M.S.D. plot for 2WGS and 2WGS bound to Azadiradione, presented in Figure 3(a), reveals the stability of the ligand-bound protein for the initial 10-40 ns of the M.D. Simulation; however, the structure displayed instability after 50 ns, followed by some stability around 100 ns. On the other hand, the R.M.S.D. plot for 1F61 and 1F61 bound to Azadiradione, presented in Figure 3(b), reveals the stability of both the protein and the ligand in the bound stage after 10 ns of M.D. Simulation.

The R.M.S.D. plots of Azadiradione-2WGS and Azadiradione-1F61 complexes during the 100 ns of Molecular Dynamic Simulation have been shown in Figures 3(a) and 3(b). Figures 4(a) and 4(b) represent the R.M.S.F. plots, which have been used to study R.M.S.F. of the residues present in the active sites of proteins 2WGS and 1F61. R.M.S.F. plot (Figure 5(a) indicates the steepest value range at 50 and 400 residual indices, which implies increased fluctuation of the protein residues at these regions, signifying a high entropy value. While the R.M.S.F. plot (Figure 5(b) shows no steep value at 50 and 400 residual indices, a higher value was observed at ~350 residual indices.

Out of the different types of protein-ligand interactions observed, hydrogen bonds, hydrophobic interactions, and water bridges were the most prominent ones which played vital roles in stabilizing the interactions.

As part of the M.D. Simulation, R.M.S.D., Radius of Gyration (rGyr), Molecule Surface Area (M.S.A.), Solvent Accessible Surface Area (S.A.S.A.), and Polar Surface Area (P.S.A.) of ligands concerning the reference conformation were also examined and are presented in Figures 4(a) and 4(b). Root-Mean-Square Fluctuations (R.M.S.F.) were measured and plotted to quantify the flexibility of residues in the ligand-protein complexes. The R.M.S.F. of the protein-ligand complexes showed significant fluctuation for all the complexes. It deviated at many points in the 100 ns simulation period in both complexes, as shown in Figures 4(a) and 4(b).

Additionally, the hydrogen bonds between Azadiradione, a bioactive compound, and residues of the active site of the proteins were examined throughout the simulation. In the complex formed by 2WGS and Azadiradione, H-bonds were observed between the ligand, Azadiradione, and the residues SER-146, SER-151, TRY-153, and PHE-262 of 2WGS (Figure 5(a)). In the complex formed by 1F61 and Azadiradione, H-bonds were observed between Azadiradione and the residues, GLN-80, ARG-379, and ARG-386 of 1F61 (Figure 5(b)).

From Figure 6(a), it was observed that among all the existing residues, Phe 144, Met 263, Pro 264, and Val 463, formed only hydrophobic bonds, and residues Tyr 153 and Val 324 predominantly formed hydrophobic bonds, along with other interactions. Residues Asp 145, Asn 149, Gly 150, Asn 458, Glu459, Arg 466, and His 468 formed only water bridges, and residues Ser 146, Ser 151, and Pro 462 predominantly formed water bridges, along with some other interactions. Residues Ser 146, Ser 151, Tyr 153, and Phe 262 formed H-bonds, along with some different types of interactions. Figure 6(b) shows
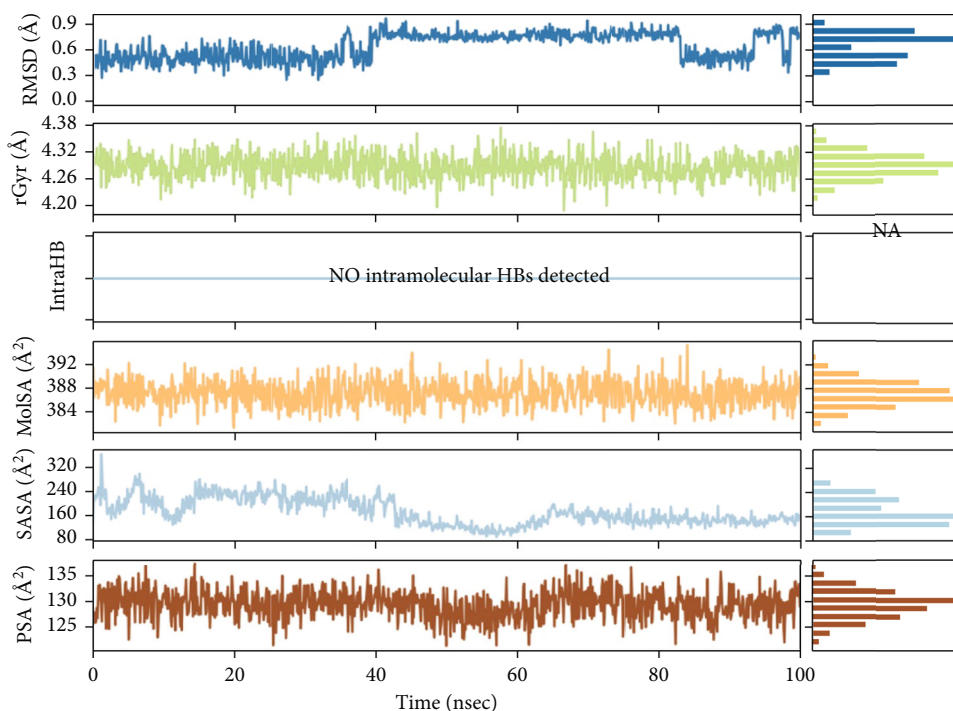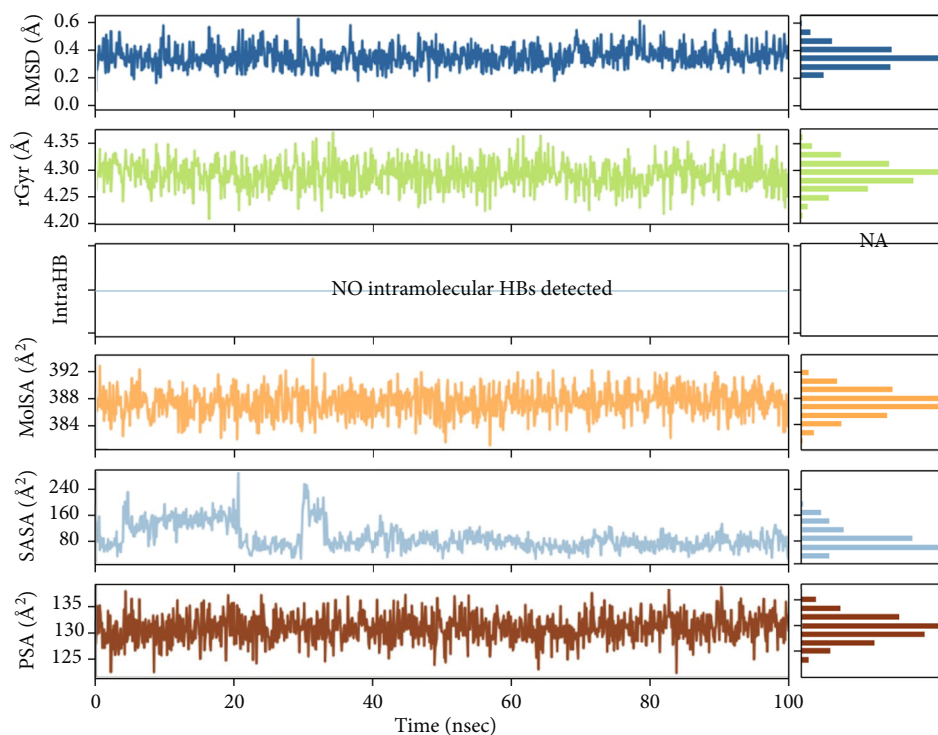
FIGURE 4: Ligand R.M.S.D.: Root-Mean-Square Deviation of ligands concerning the reference conformation. The radius of Gyration (rGyr): Representation of the "extendedness" of the ligands. Molecular Surface Area (M.S.A.): Molecular surface calculation with 1.4 Å probe radius. This value is reciprocal to a Van der Waals surface area. Solvent Accessible Surface Area (S.A.S.A.): The surface area of the respective ligands accessible by a water molecule is presented. Polar Surface Area (P.S.A.): Solvent accessible surface area in the ligands contributed only by oxygen and nitrogen atoms. (a) Azadiradione in complex with 2WGS. (b) Azadiradione in complex with 1F61.

(a)

(b)
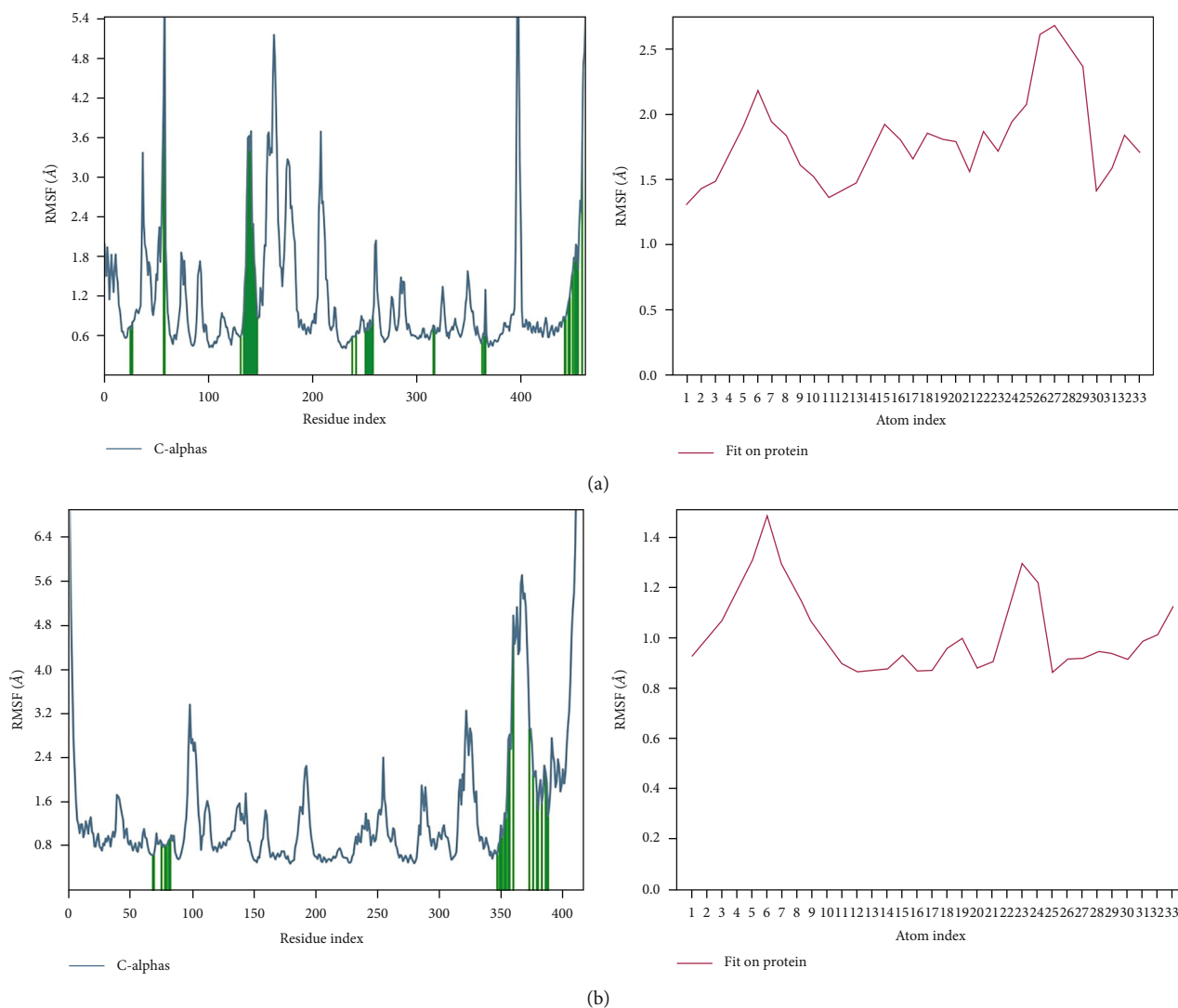
FIGURE 5: (a) R.M.S.F. plot of residues of the active site of 2WGS; (b) 1F61.

the formation of only a H-bond in Gln 80, and residues Arg 379 and Arg 386 formed H-bonds along with water bridges. Residues Leu 69, Met 76, Ala 349, and Ala 353 formed only hydrophobic bonds, and residue Gly 387 formed only water bridges. Predominant water bridges, along with H-bond, were formed in Arg 386.

2.4. ADME-Tox Study Using SWISS ADME. ADME-Tox study of Azadiradione exhibited noble drug-like properties [26–31]. ADME-Tox study results are presented in detail (Table 2).

The ADME-Tox analysis performed for the selected compound Azadiradione indicates that the compounds have an acceptable range of important physicochemical parameters such as Mw and Consensus Lipophilicity Score. In addition, it passed all the three major drug discovery rules: Lipinski, Ghose, and Veber rules. This ADME-Tox study revealed that the compound Azadiradione should not have any issue with becoming a

successful drug candidate from the biochemical point of view. The computational docking study of the selected plant-based ligand against the target enzymes G.S. and I.C.L., followed by Molecular Dynamics Simulation studies and ADME-Tox study, is sufficient to predict the antitubercular nature of Azadiradione. Azadiradione is a triterpenoid compound used traditionally in several diseases and has some reports against malaria, respiratory disorders, cancer, intestinal helminthiasis, leprosy, constipation, inflammation, blood morbidity, dermatological complications, rheumatism, and so on [32, 33], which also supports its existing acceptability as a drug molecule.

3. Conclusion

In view of the wide-spectrum resistance of the currently existing M.D.R. and XDR T.B. strains display against the presently used antitubercular drugs, the present study was designed to dock 1778 compounds from four
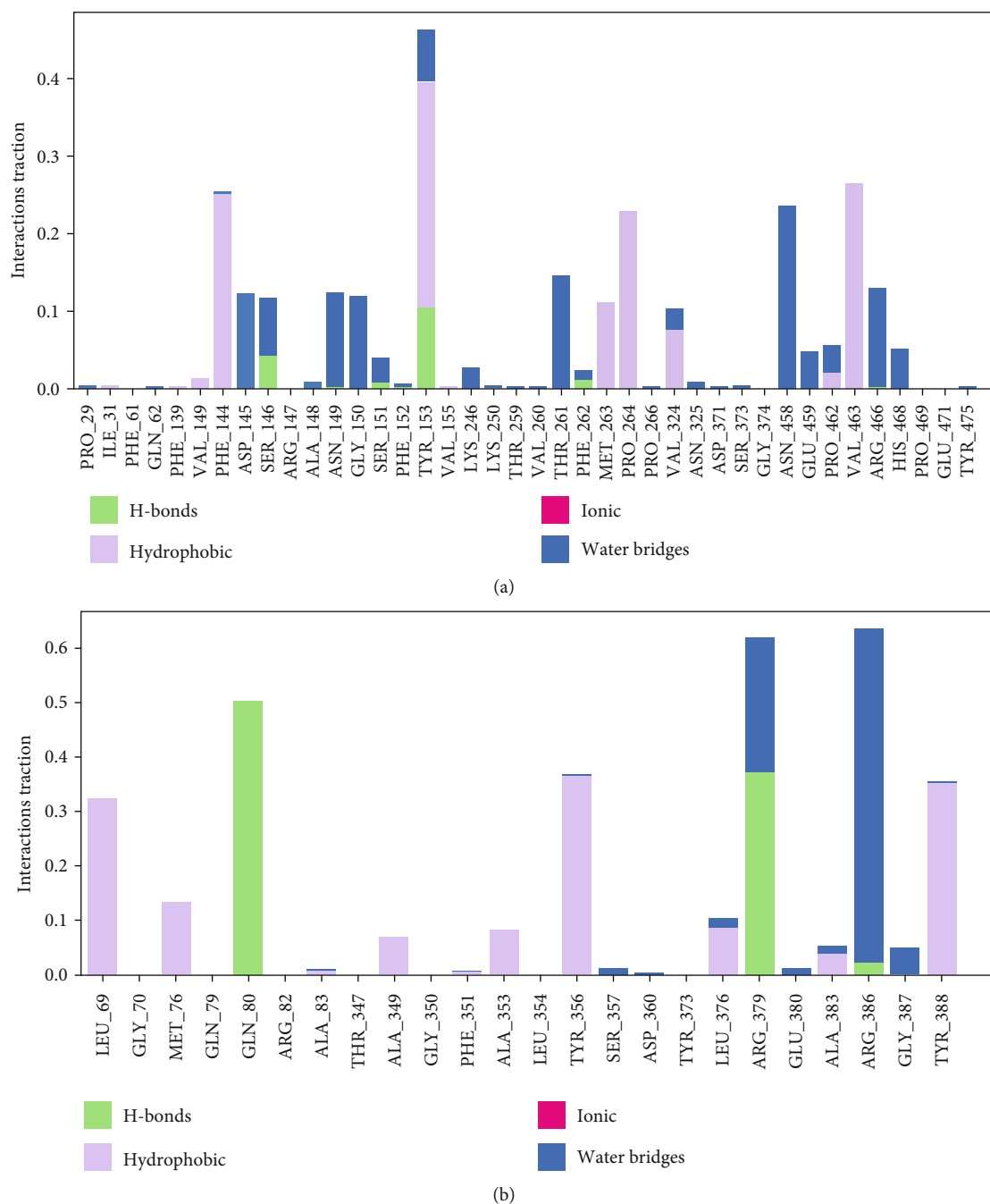
FIGURE 6: (a) Interaction diagram of 2WGS and Azadiradione during 100 ns M.D. Simulation. The green, blue, and purple colours represent H-bonding, water bridges, and hydrophobic interactions. (b) Interaction diagram of 1F61 and Azadiradione during 100 ns M.D. Simulation. The green, blue, and purple colours represent H-bonding, water bridges, and hydrophobic interactions.

medicinal plants. *Azadirachta indica*, *Camellia sinensis*, *Adhatoda vasica,* and *Ginkgo biloba* have been selected against two targeted enzymes: Glutamine Synthetase and Isocitrate Lyase, of *M. tuberculosis* to identify new antitubercular agent(s). The *in silico* study revealed the binding efficacy of a compound from *Azadirachta indica,* namely, Azadiradione, towards the targeted enzymes, Glutamine Synthetase and Isocitrate Lyase, suggesting its potential inhibitory property towards the targets. M.D. Simulation

study showed significant stability of the ligand-receptor complexes formed by Azadiradione (Table 3) with the two targeted enzymes.

Furthermore, the ADME-Tox study of Azadiradione exhibited noble drug-like properties of the ligand. The collective findings of the present *in silico* study, have been interpreted to propose that Azadiradione possesses significant potential as a candidate antitubercular molecule which is subject to future validation.

TABLE 2: Table of ADME-Tox study.

Compound	MW	Oral bioavailability						Pharmacokinetic properties	LogKp (skin permeation)	Water solubility	Lipinski/Ghose/Veber (pass(Y)/fail (N))
		cLogP	HBA	HBD	RB	TPSA (Å^2)	B-score				
Azadiaradione	450.57 g/mol	4.3	5	0	3	73.58	0.55	GI absorption high	-5.60 cm/s	Insoluble	Y/Y/Y
7-Desacetyl-7-benzoylazadiradione	512.64 g/mol	5.38	5	0	4	73.58	0.17	GI absorption low	-4.83 cm/s	Poorly soluble	N/N/Y
7-Desacetyl-7-benzoylgedunin	544.63 g/mol	4.86	7	0	4	95.34	0.55	GI absorption high	-5.45 cm/s	Poorly soluble	Y/N/Y
alpha-amyrin	426.72 g/mol	7.05	1	1	0	20.23	0.55	GI absorption low	-2.51 cm/s	Poorly soluble	Y/N/Y
Gedunin	482.57 g/mol	3.73	7	0	3	95.34	0.55	GI absorption High	-6.25 cm/s	Moderately soluble	Y/N/Y

MW: molecular weight; cLogP: consensus lipophilicity score; HBA: H-bond acceptor; HBD: H-bond donor; RB: no. of rotatable bonds; PSA: polar surface area; B-score: bioavailability score; Lipinski/Ghose/Veber: rules of drug discovery.

TABLE 3: 2D structure and properties of Azadiaradione.

2D structure of Azadiaradione	Properties as calculated by BIOVIA Draw
	PSA: 73.58
	ALogP: 4.0905
	Stereo center count: 7
	Hydrogen acceptor count: 4
	Hydrogen donor count: 0
	Composition: C: 74.6% H: 7.6% O: 17.8%
	Formula weight: 450.57
	Exact mass: 450.24
	Molecular formula: $C_{28}H_{34}O_5$

4. Materials and Methods

4.1. Hardware and Software Used. For the current study, a Lenovo computer unit with Linux and M.S. Windows operating systems, 1 T.B. S.S.D., 32 GB RAM supported by 8 GB graphics card was used. The software and tools used for different computational analyses were AutoDock Tools [34], AutoDock Vina version 1.1.2 [34–36], PyMol and Chimera Packages [37–40], Discovery Studio, and Schrödinger Suite version 2020-3. For Molecular Dynamics (M.D.) Simulation, the Desmond module provided by Schrödinger suite 2020-3 was used in a Linux platform supported by the above-mentioned hardware specifications. Other online resources used in the study have been mentioned in subsequent parts of the article.

4.2. Databases Used. Multiple databases were used at different stages of the study; one such significant database is the K.E.G.G. pathway, which includes the metabolic and regulatory pathways sections. Utilizing data from K.E.G.G. pathway database, the present study compared host metabolism with critical metabolic pathways of *M. tuberculosis*, and the necessary enzymes were identified [41]. Essential enzymes of the pathogen, *M. tuberculosis*, were also identified with the help of the Database of Essential Genes (D.E.G.). D.E.G. has reported 614 such essential genes [42].

3D structures of targeted proteins, that is, Glutamine Synthetase (Chain A, PDB ID: 2WGS) and Isocitrate Lyase (Chain A, PDB ID: 1F61) were retrieved from RCSB PDB database [14, 43–47]. Other databases like Drug Bank, PDB Bind, ZINC, and so on were also used in executing different steps of the research study, mainly to get the 2D and 3D information of the selected ligands.

4.3. Ligand Dataset Preparation. The active compounds from four different plants, *viz., Azadirachta indica, Camellia sinensis, Adhatoda vasica,* and *Ginkgo biloba* were collated to prepare a Ligand Library for the analysis. Databases like Drug Bank Database (https://go.drugbank.gov), ChEMBL, and PubChem (https://pubchem.ncbi.nlm.nih.gov) were used to obtain the structures of the small molecules for the preparation of the combinatorial library. A large number of previously reported phytochemicals in the four plants were also included in the library. 2D-structure trial and calculation of various chemical properties of the phytochemicals used in the present study were conducted in B.I.O.V.I.A. Draw of Dassault Systèms. T.O.R.S.D.O.F. utility in AutoDock Tools was used to set the ligands' default roots, rotatable bonds, and torsions.

4.4. Protein Structure Preparation. The three-dimensional structures of Glutamine Synthetase (PDB ID: 2WGS) and Isocitrate Lyase (RCSB PDB Identifier: 1F61) of *M. tuberculosis* were retrieved from R.C.S.B. Protein Data Bank and changed into P.D.B.Q.T. format. The protein structures were prepared by adding polar hydrogen bonds and removing hetero atoms, water molecules, and bound ligand(s) using AutoDock Tools utility. Only Chain A from 2WGS and 1F61 was selected for studying the docking interactions.

4.5. Molecular Docking Analysis. Protein-Ligand Docking study was carried out to understand the interaction of the two molecules with the ligands and determine the ligand(s) that would form complexes possessing minimal energy with the receptor. In docking analysis, a flexible receptor molecule has to be achieved. So by using the GRID module of Auto Dock v4.0, the flexible receptor molecule was achieved by setting a little residue. In contrast, AutoDock Vina with PyRx platform was used for calculating the affinity of small molecules against the targeted proteins Glutamine Synthetase and Isocitrate Lyase [48] (https://pyrx.sourceforge.io). The best protein-ligand complexes were then selected based on the energy conformation of the complexes. PyMOL software in PYTHON platform was used to analyse complex interactions, which illustrated hydrophobic interactions, ionic interactions, and hydrogen bonding between the receptors and the respective ligands.

4.6. Molecular Dynamics (M.D.) Simulation. The Desmond software module of Schrödinger suite 2020-3 was used for carrying out the M.D. Simulation. Simulations of 100 ns were performed to analyze the in silico stability of the complexes formed by 2WGS and 1F61 with G.S. and I.C.L. OPLS3 force field was used to study the 2WGS and 1F61 complexes in the explicit solvent system during M.D. Simulation. The atomic framework was solvated with crystallographic water (TIP3P) particles under orthorhombic intermittent limit conditions for 10 Å buffer region. In addition to the deletion of the overlapping water molecules, the entire structure of 34,255 atoms were neutralized by adding Na^+ as counter ions. An ensemble of a Nose-Hoover thermostat and barostat was utilized to maintain a constant temperature of 300 K and a constant pressure of 1 bar (N.P.T.) [26]. Hybrid energy minimization algorithms were used, consisting of 1000 steps of steepest descent followed by conjugate gradient algorithms. M.M.G.B.S.A. analysis was done for both the complexes to calculate ligand binding energies using the Prime module of Schrodinger Suite 2020-3.

4.7. In Silico ADME-Tox Study. ADMET-Tox plays a vital role in the field of drug testing and design. Servers and software are available that use data from previously reported drugs to predict the ADMET properties of ligand molecules. *In silico* ADME-Tox studies were performed using a Swiss ADME server to identify the best-performing ligands [27–30]. Various Lipinski parameters were used to evaluate ligand(s)' drug-likeness and ADMET properties.

Data Availability

The supporting data to the results reported in the article can be found with the corresponding authors, Dr. Saurov Mahanta and Dr. Saravanan Muthupandian.

Ethical Approval

Experimental research/field study on plants complies with relevant institutional, national, and international guidelines and legislation.

Conflicts of Interest

The authors declare that there are no conflicts of interest.

Authors' Contributions

SM and MS designed and supervised the manuscript. SM, AC, SK, AKM, LC, JBS, and DK curated the data and wrote the manuscript. SM, YKM, BT, and KB were responsible for software, visualization, and formal analysis and edited the manuscript. All the authors read and approved the final manuscript. Anesha Chanda, Sanjib Kalita, and Awdhesh Kumar Mishra contributed equally to this work.

References

[1] F. G. J. Cobelens, H. van Deutekom, I. W. E. Draayer-Jansen et al., "Risk of infection with *Mycobacterium tuberculosis* in travellers to areas of high tuberculosis endemicity," *Lancet*, vol. 356, no. 9228, pp. 461–465, 2000.

[2] S. Keshavjee and P. E. Farmer, "Tuberculosis, drug resistance, and the history of modern medicine," *The New England Journal of Medicine*, vol. 367, no. 10, pp. 931–936, 2012.

[3] World Health Organization, *Global tuberculosis report*, World Health Organization, 2015.

[4] C. R. Horsburgh, C. E. Barry, and C. Lange, "Treatment of tuberculosis," *The New England Journal of Medicine*, vol. 373, no. 22, pp. 2149–2160, 2015.

[5] W. McDermott, R. McCune Jr., and R. Tompsett, "Dynamics of antituberculous chemotherapy," *American Review of Tuberculosis and Pulmonary Diseases*, vol. 74, no. 2, pp. 100–108, 1956.

[6] Y. Hu, A. R. Coates, and D. A. Mitchison, "Sterilising action of pyrazinamide in models of dormant and rifampicin-tolerant Mycobacterium tuberculosis," *The International Journal of Tuberculosis and Lung Disease*, vol. 10, no. 3, pp. 317–322, 2006.

[7] I. Comas and S. Gagneux, "The past and future of tuberculosis research," *PLoS Pathogens*, vol. 5, no. 10, pp. 1–7, 2009.

[8] A. Schatz, E. Bugle, and S. A. Waksman, "Streptomycin, a substance exhibiting antibiotic activity against gram-positive and gram-negative bacteria∗," *Proceedings of the Society for Experimental Biology and Medicine*, vol. 55, no. 1, pp. 66–69, 1944.

[9] S. Chetty, M. Ramesh, A. Singh-Pillay, and M. E. S. Soliman, "Recent advancements in the development of antituberculosis drugs," *Bioorganic & Medicinal Chemistry Letters*, vol. 27, no. 3, pp. 370–386, 2017.

[10] L. Goldman and A. Schafer, "Tuberculosis: disease overview," in *Goldman's cecil medicine: expert consult premium edition*, Saunders Elsevier, St. Louis (MO), 24th edition, 2011.

[11] B. Singh, T. K. Bhat, and B. Singh, "Potential therapeutic applications of some antinutritional plant secondary metabolites," *Journal of Agricultural and Food Chemistry*, vol. 51, no. 19, pp. 5579–5597, 2003.

[12] S. Kumar, X. C. Sharma, S. R. Kaushik, A. Kulshreshtha, S. Chaturvedi, and V. P. Dwivedi, "The phytochemical bergenin as an adjunct immunotherapy for tuberculosis in mice," *The Journal of Biological Chemistry*, vol. 294, no. 21, pp. 8555–8563, 2019.

[13] N. Singh and M. I. Siddiqi, "Computational evaluation of glutamine synthetase as drug target against infectious diseases: molecular modeling, substrate-binding analysis, and molecular dynamics simulation studies," *Medicinal Chemistry Research*, vol. 26, no. 2, pp. 450–460, 2017.

[14] E. J. Muñoz-Elías and J. D. McKinney, "*Mycobacterium tuberculosis* isocitrate lyases 1 and 2 are jointly required for *in vivo*

growth and virulence," *Nature Medicine*, vol. 11, no. 6, pp. 638–644, 2005.

[15] G. Harth, D. L. Clemens, and M. A. Horwitz, "Glutamine synthetase of Mycobacterium tuberculosis: extracellular release and characterization of its enzymatic activity," *Proceedings of the National Academy of Sciences of the United States of America*, vol. 91, no. 20, pp. 9342–9346, 1994.

[16] L. Berlicki and P. Kafarski, "Computer-aided analysis of the interactions of glutamine synthetase with its inhibitors," *Bioorganic & Medicinal Chemistry*, vol. 14, no. 13, pp. 4578–4585, 2006.

[17] G. Harth and M. A. Horwitz, "Inhibition ofMycobacterium tuberculosisglutamine synthetase as a novel antibiotic strategy against tuberculosis: demonstration of efficacy in vivo," *Infection and Immunity*, vol. 71, no. 1, pp. 456–464, 2003.

[18] M. V. Tullius, G. Harth, and M. A. Horwitz, "High extracellular levels ofMycobacterium tuberculosisglutamine synthetase and superoxide dismutase in actively growing cultures are due to high expression and extracellular stability rather than to a protein-specific export mechanism," *Infection and Immunity*, vol. 69, no. 10, pp. 6348–6363, 2001.

[19] A. H. Gordon, P. D. Hart, and M. R. Young, "Ammonia inhibits phagosome-lysosome fusion in macrophages," *Nature*, vol. 286, no. 5768, pp. 79-80, 1980.

[20] P. Vanni, E. Giachetti, G. Pinzauti, and B. A. McFadden, "Comparative structure, function and regulation of isocitrate lyase, an important assimilatory enzyme," *Comparative Biochemistry and Physiology. B*, vol. 95, no. 3, pp. 431–458, 1990.

[21] M. F. Dunn, J. A. Ramírez-Trujillo, and I. Hernández-Lucas, "Major roles of isocitrate lyase and malate synthase in bacterial and fungal pathogenesis," *Microbiology*, vol. 155, no. 10, pp. 3166–3175, 2009.

[22] G. Brahmachari, "Neem—an omnipotent plant: a retrospection," *Chembiochem*, vol. 5, no. 4, pp. 408–421, 2004.

[23] U. P. Claeson, T. Malmfors, G. Wikman, and J. G. Bruhn, "*Adhatoda vasica* : a critical review of ethnopharmacological and toxicological data," *Journal of Ethnopharmacology*, vol. 72, no. 1–2, pp. 1–20, 2000.

[24] B. J. Diamond, S. C. Shiflett, N. Feiwel et al., "Ginkgo biloba extract: mechanisms and clinical indications," *Archives of Physical Medicine and Rehabilitation*, vol. 81, no. 5, pp. 668–678, 2000.

[25] J. M. Hamilton-Miller, "Antimicrobial properties of tea (Camellia sinensis L.)," *Antimicrobial Agents and Chemotherapy*, vol. 39, no. 11, pp. 2375–2377, 1995.

[26] G. J. Martyna, M. E. Tuckerman, D. J. Tobias, and M. L. Klein, "Explicit reversible integrators for extended systems dynamics," *Molecular Physics*, vol. 87, no. 5, pp. 1117–1157, 1996.

[27] F. Cheng, W. Li, Y. Zhou et al., "admetSAR: a comprehensive source and free tool for assessment of chemical ADMET properties," *Journal of Chemical Information and Modeling*, vol. 52, no. 11, pp. 3099–3105, 2012.

[28] A. Daina, O. Michielin, and V. Zoete, "SwissADME: a free web tool to evaluate pharmacokinetics, drug-likeness and medicinal chemistry friendliness of small molecules," *Scientific Reports*, vol. 7, no. 1, pp. 1–13, 2017.

[29] D. Lagorce, D. Douguet, M. A. Miteva, and B. O. Villoutreix, "Computational analysis of calculated physicochemical and ADMET properties of protein-protein interaction inhibitors," *Scientific Reports*, vol. 7, no. 1, article 46277, 2017.

[30] C. A. Lipinski, F. Lombardo, B. W. Dominy, and P. J. Feeney, "Experimental and computational approaches to estimate solubility and permeability in drug discovery and development settings," *Advanced Drug Delivery Reviews*, vol. 23, no. 1-3, pp. 3–25, 1997.

[31] A. Daina and V. Zoete, "A boiled-egg to predict gastrointestinal absorption and brain penetration of small molecules," *ChemMedChem*, vol. 11, no. 11, pp. 1117–1121, 2016.

[32] P. Kushwaha, V. Khedgikar, S. Haldar et al., "*Azadirachta indica* triterpenoids promote osteoblast differentiation and mineralization in vitro and in vivo," *Bioorganic & Medicinal Chemistry Letters*, vol. 26, no. 15, pp. 3719–3724, 2016.

[33] R. Singh, V. Mishra, S. Pandeti et al., "Cytoprotective and antisecretory effects of azadiradione isolated from the seeds of Azadirachta indica (neem) on gastric ulcers in rat models," *Phytotherapy Research*, vol. 29, no. 6, pp. 910–916, 2015.

[34] G. M. Morris, R. Huey, and A. J. Olson, "Using AutoDock for ligand-receptor docking," *Current Protocols in Bioinformatics*, vol. 24, no. 1, pp. 8–14, 2008.

[35] R. Quiroga and M. A. Villarreal, "Vinardo: a scoring function based on Autodock Vina improves scoring, docking, and virtual screening," *PLoS One*, vol. 11, no. 5, article e0155183, 2016.

[36] J. Biesiada, A. Porollo, P. Velayutham, M. Kouril, and J. Meller, "Survey of public domain software for docking simulations and virtual screening," *Human Genomics*, vol. 5, no. 5, pp. 497–505, 2011.

[37] A. Porollo and J. Meller, "POLYVIEW-MM: web-based platform for animation and analysis of molecular simulations," *Nucleic Acids Research*, vol. 38, Supplement_2, pp. W662–W666, 2010.

[38] D. Seeliger and B. L. de Groot, "Ligand docking and binding site analysis with PyMOL and Autodock/Vina," *Journal of Computer-Aided Molecular Design*, vol. 24, no. 5, pp. 417–422, 2010.

[39] S. Yuan, H. C. S. Chan, and Z. Hu, "Using PyMOL as a platform for computational drug design," *WIREs Computational Molecular Science*, vol. 7, no. 2, article e1298, 2017.

[40] E. F. Pettersen, T. D. Goddard, C. C. Huang et al., "UCSF Chimera?a visualization system for exploratory research and analysis," *Journal of Computational Chemistry*, vol. 25, no. 13, pp. 1605–1612, 2004.

[41] M. Kanehisa and S. Goto, "KEGG: Kyoto Encyclopedia of Genes and Genomes," *Nucleic Acids Research*, vol. 28, no. 1, pp. 27–30, 2000.

[42] R. Zhang and Y. Lin, "DEG 5.0, a database of essential genes in both prokaryotes and eukaryotes," *Nucleic Acids Research*, vol. 37, pp. D455–D458, 2009.

[43] M. T. Nilsson, W. W. Krajewski, S. Yellagunda et al., "Structural basis for the inhibition of *Mycobacterium tuberculosis* glutamine synthetase by novel ATP-competitive inhibitors," *Journal of Molecular Biology*, vol. 393, no. 2, pp. 504–513, 2009.

[44] S. Mahanta, P. Chowdhury, N. Gogoi et al., "Potential antiviral activity of approved repurposed drug against main protease of SARS-CoV-2: an in silico based approach," *Journal of Biomolecular Structure and Dynamics*, vol. 39, no. 10, pp. 3802–3811, 2021.

[45] S. L. Mowbray, M. K. Kathiravan, A. A. Pandey, and L. R. Odell, "Inhibition of glutamine synthetase: a potential drug target in Mycobacterium tuberculosis," *Molecules*, vol. 19, no. 9, pp. 13161–13176, 2014.

[46] Y.-V. Lee, H. A. Wahab, and Y. S. Choong, "Potential inhibitors for isocitrate lyase of Mycobacterium tuberculosis and non-M. tuberculosis: a summary," *BioMed Research International*, vol. 2015, Article ID 895453, 20 pages, 2015.

[47] V. Sharma, S. Sharma, K. H. zu Bentrup et al., "Structure of isocitrate lyase, a persistence factor of *Mycobacterium tuberculosis*," *Nature Structural Biology*, vol. 7, no. 8, pp. 663–668, 2000.

[48] S. Dallakyan and A. J. Olson, "Small-molecule library screening by docking with PyRx," in *Chemical biology*, J. Hempel, C. Williams, and C. Hong, Eds., vol. 1263 of Methods in Molecular Biology, pp. 243–250, Humana Press, New York, NY, 2015.

Retraction

Retracted: MSN@IL-4 Sustainingly Mediates Macrophagocyte M2 Polarization and Relieves Osteoblast Damage via NF-κB Pathway-Associated Apoptosis

BioMed Research International

This article has been retracted by Hindawi following an investigation undertaken by the publisher [1]. This investigation has uncovered evidence of one or more of the following indicators of systematic manipulation of the publication process:

(1) Discrepancies in scope

(2) Discrepancies in the description of the research reported

(3) Discrepancies between the availability of data and the research described

(4) Inappropriate citations

(5) Incoherent, meaningless and/or irrelevant content included in the article

(6) Manipulated or compromised peer review

The presence of these indicators undermines our confidence in the integrity of the article's content and we cannot, therefore, vouch for its reliability. Please note that this notice is intended solely to alert readers that the content of this article is unreliable. We have not investigated whether authors were aware of or involved in the systematic manipulation of the publication process.

Wiley and Hindawi regrets that the usual quality checks did not identify these issues before publication and have since put additional measures in place to safeguard research integrity.

We wish to credit our own Research Integrity and Research Publishing teams and anonymous and named external researchers and research integrity experts for contributing to this investigation.

The corresponding author, as the representative of all authors, has been given the opportunity to register their agreement or disagreement to this retraction. We have kept a record of any response received.

References

[1] C. Shi, F. Yuan, Z. Li et al., "MSN@IL-4 Sustainingly Mediates Macrophagocyte M2 Polarization and Relieves Osteoblast Damage via NF-κB Pathway-Associated Apoptosis," *BioMed Research International*, vol. 2022, Article ID 2898729, 10 pages, 2022.

Research Article

MSN@IL-4 Sustainingly Mediates Macrophagocyte M2 Polarization and Relieves Osteoblast Damage via NF-κB Pathway-Associated Apoptosis

Cheng Shi [ID],[1,2] **Fei Yuan** [ID],[1] **Zhilong Li** [ID],[1] **Zhenhua Zheng** [ID],[1] **Changliang Yuan** [ID],[1] **Ziyang Huang** [ID],[1] **Jianping Liu** [ID],[1] **Xuping Lin** [ID],[1] **Taoyi Cai** [ID],[1] **Guofeng Huang** [ID],[1,2] **and Zhenqi Ding** [ID][1]

[1]*Department of Orthopedics, Dongnan Hospital of Xiamen University, 269 Zhanghua Middle Road, Zhangzhou,*
363000 Fujian, China
[2]*School of Medicine, Xiamen University, 4221 Xiang'an South Road, Xiamen, 361102 Fujian, China*

Correspondence should be addressed to Guofeng Huang; huangguofeng@xmu.edu.cn and Zhenqi Ding; dingzhenqi175@163.com

Background. The microenvironment of bone defects displayed that M2 polarization of macrophagocyte could promote the osteoblast growth and benefit the wound healing. Bone scaffold transplantation is considered to be one of the most promising methods for repairing bone defects. The present research was aimed at constructing a kind of novel bone scaffold nanomaterial of MSN@IL-4 for treating bone defects responding to the wound microenvironment of bone defects and elucidating the mechanics of MSN@IL-4 treating bone defect via controlling release of IL-4, inducing M2 polarization and active factor release of macrophagocyte, and eventually relieving osteoblast injury. *Methods*. MSN@IL-4 was firstly fabricated and its release of IL-4 was assessed in vitro. Following, the effects of MSN@IL-4 nanocomplex on the release of active factors of macrophage were examined using Elisa assay and promoting M2 polarization of the macrophage by immunofluorescence staining. And then, the effects of active factors from macrophage supernatant induced by MSN@IL-4 on osteoblast growth were examined by CCK-8, flow cytometry, and western blot assay. *Results*. The release curve of IL-4 in vitro displayed that there was more than 80% release ratio for 30th day with a sustained manner in pH 5.5. Elisa assay data showed that MSN@IL-4 nanocomplex could constantly promote the release of proproliferative cytokine IL-10, SDF-1α, and BMP-2 in macrophagocyte compared to only IL-4 treatment, and immunofluorescent image showed that MSN@IL-4 could promote M2 polarization of macrophagocytes via inducing CD206 expression and suppressing CD86 expression. Osteoblast injury data showed that the supernatant from macrophagocyte treated by MSN@IL-4 could promote the osteoblast proliferation by MTT assay. Flow cytometry data showed that the supernatant from macrophagocyte treated by MSN@IL-4 could suppress the osteoblast apoptosis from 22.1% to 14.6%, and apoptosis-related protein expression data showed that the supernatant from macrophagocyte treated by MSN@IL-4 could suppress the expression of Bax, cleaved caspase 3, and cleaved caspase 8. Furthermore, the immunofluorescent image showed that the supernatant from macrophagocyte treated by MSN@IL-4 could inhibit nucleus location of p65, and western blot data showed that the supernatant from macrophagocyte treated by MSN@IL-4 could suppress the phosphorylation of IKK and induce the expression of IκB. *Conclusion*. MSN@IL-4 could control the sustaining release of IL-4, and it exerts the protective effect on osteoblast injury via inducing M2 polarization and proproliferative cytokine of macrophagocyte and following inhibiting the apoptosis and NF-κB pathway-associated inflammation of osteoblast.

1. Introduction

Bone defect is a kind of bone deficiency caused by trauma or surgery, which often causes bone nonunion, delayed healing or nonunion, and even local dysfunction [1, 2]. Tissue engineering bone transplantation, mainly composed of bone scaffold materials, seed cells, and cytokines, is considered to be one of the most promising methods for repairing bone

defects [3–6]. Although great progress has been made in the research of bone scaffold materials in the past 30 years, its clinical application has not made a breakthrough. The key reason is that the vascularization and osteogenic replacement of tissue-engineered bone scaffolds are slow after transplantation. Some researchers have improved the acceleration of bone regeneration by subcutaneous prevascularization of stents and achieved good results, but this is not feasible in clinical practice [6]. Our previous researches have constructed a series of deproteinized scaffolds which have played a role in the treatment of bone defects to some extent. However, there are still problems such as slow bone growth and poor sustainability. If the microenvironment on the surface of this bone scaffold can be adjusted to make it composite with other bioactive materials to reasonably promote osteogenesis, it will be more ideal and easier to be used in clinic. Therefore, we propose that modifying surface properties of bone scaffolds with bioactive materials may be a potential strategy to improve the healing efficiency of bone defects.

Bone immune response is a common inflammatory process response to bone defect, which runs through the whole process of bone healing and osteoblast growth [7–9]. Macrophages are an important immune regulatory cell of bone immune inflammatory response playing an essential role in phagocytosis of necrotic tissue, detection of bacterial products, and antigen presentation. Macrophages widely exist in periosteum and bone, affecting the maintenance of normal bone morphology and the process of fracture repair. It also exists and acts on multiple stages of fracture repair, producing prosynthetic growth factors at the fracture site and promoting more stable callus formation [10–13]. Macrophages possess many subtypes, and different subtypes can carry out different functions via the polarization transformation according to the changes of the cell environment. In acute inflammatory reaction, macrophages were stimulated by interleukin-2 (IL-2) or liposomes to polarize into M1 type (cd11c+ and ccr7+), which enhanced Th1 helper cells and promoted inflammatory reaction; when stimulated by IL-4, macrophages can polarize into M2 type (cd163+ and cd206 +), enhance Th2 helper cell function, reduce inflammation, and promote tissue repair [14, 15].

It has been reported that macrophages cultured on the modified bone scaffold can induce M2 polarization, produce many active bone factors, induce osteoblast proliferation, and eventually promote fracture healing [16]. Although macrophages indirectly participate in the process of bone regeneration, it promotes bone formation by inducing BMP-2 secretion. Many inflammatory cytokines such as IL-4 cannot also directly affect bone metabolism but promote osteoblast growth by inducing macrophage polarization. IL-4-modified tissue engineering bone scaffolds can effectively promote the polarization of macrophages in bone defects and the growth of osteoblasts to achieve the therapeutic effect of bone defects. However, IL-4-modified tissue engineering bone scaffold material still has the problem of one-time release of IL-4, which is difficult to continue to treat bone defects. Therefore, it is necessary to develop tissue engineering bone scaffolds that can control the slow and sustained release of IL-4.

Recently, drug-loaded nanoparticles with controlled release and regulation functions have been widely concerned in the research and development of targeted drugs for various diseases because of their good size and biocompatibility, which can effectively load drug molecules, change their biological distribution and drug metabolism, and control drug release. Among them, the mesoporous silicon nanocarrier (MSN) is a hollow spherical structure with thorns and holes on the surface, which has the characteristics of high specific surface area, good biocompatibility, easy modification, and so on. It is an ideal carrier material for disease treatment drugs. After modification, MSN nanoparticles that respond to low pH, redox reaction, photo enzyme, and other stimuli to control the release of drugs have been reported for many times. MSN nanomaterials can effectively adhere to the surface of deproteinized cancellous bone scaffolds because of their good spines on the surface. Meanwhile, a large number of hydroxyl groups exist on the surface of MSN nanomaterials and can be coupled with IL-4 to form MSN@IL-4 nanocomposites. In a slightly acidic environment, the nanocomposites can slowly release IL-4, so as to achieve the function of sustainable release of IL-4. Therefore, bone scaffold@MSN@IL-4 nanomaterials will be a potentially effective treatment for bone defects.

The present research was aimed at constructing a nanomaterial of bone scaffold@MSN@IL-4 and elucidating its mechanism of promoting fracture healing via the sustaining release of IL-4 to induce M2 polarization of the macrophage to produce many active bone factors causing osteoblast growth. Firstly, the MSN@IL-4 nanocomplex was fabricated and its release of IL-4 was assessed in vitro. Following, the effects of MSN@IL-4 nanocomplex on the release of active factors of macrophage were examined using Elisa assay and promoting M2 polarization of the macrophage by immunofluorescence staining. And then, the effects of active factors from macrophage supernatant induced by MSN@IL-4 on osteoblast growth were examined by CCK-8, flow cytometry, and western blot assay. Bone defect is a kind of bone deficiency caused by trauma or surgery, which often causes bone nonunion, delayed healing or nonunion, and even local dysfunction. Tissue engineering bone transplantation, mainly composed of bone scaffold materials, seed cells, and cytokines, is considered to be one of the most promising methods for repairing bone defects. Although great progress has been made in the research of bone scaffold materials in the past 30 years, its clinical application has not made a breakthrough. The key reason is that the vascularization and osteogenic replacement of tissue-engineered bone scaffolds are slow after transplantation. Some researchers have improved the acceleration of bone regeneration by subcutaneous prevascularization of stents and achieved good results, but this is not feasible in clinical practice. Our previous researches have constructed a series of deproteinized scaffolds which have played a role in the treatment of bone defects to some extent. However, there are still problems such as slow bone growth and poor sustainability. If the microenvironment on the surface of this bone scaffold can be adjusted to make it composite with other bioactive materials to reasonably promote osteogenesis, it will be more

ideal and easier to be used in clinic. Therefore, we propose that modifying surface properties of bone scaffolds with bioactive materials may be a potential strategy to improve the healing efficiency of bone defects.

2. Methods and Materials

2.1. Synthesis of MSN.
5 g cetyltrimethylammonium bromide (CTAB, Sigma, USA) was weighted and added into 100 mL of ultrapure water and stirred vigorously for 30 minutes at 90°C until CTAB was completely dissolved. 10 g triethanolamine (TTA, sigma, USA) was weighted and added into 30 mL of ultrapure water to obtain 0.3 mg/mL TTA solution. After that, 5 mL of TTA solution and an additional mixture solution of 30 mL cyclohexane (Sinopharm, China) and 8 mL ethyl orthosilicate (TEOS, Sinopharm, China) were added into the dissolved CTAB solution. The mixed solution reacted under the condition of the continuous stirring at 300 rpm and 90°C for 24 hours. After the reaction, the product of MSN was centrifuged at 1200 rpm for 20 minutes and washed with ethanol and sodium chloride solution for removing the excess raw materials of CTAB. Finally, the prepared MSN was incubated with IL-4 solution, and the product was characterized by scanning electron microscope (SEM).

2.2. Elisa Assay for Detecting the Controlled Release of IL-4 from MSN@lL-4.
The 100 mg MSN@IL-4 were, respectively, added into the indicated pH (pH 5.5, pH 7.2, and pH 8.8) of phosphate buffer. The buffer was stirred twice per day for 30 days, and the solution was collected at 10 time points of 3rd, 6th, 9th, 12th, 15th, 18th, 21st, 24th, 27th, and 30th day. After that, the collected buffer and the standard substrate were added into the coated wells from Elisa assay kit (R&D, USA) according to the instructions, and the coated plate was shocked and detected for OD value using microplate reader (Thermo, USA). The standard curve of IL-4 was drawn. The contents of IL-4 in buffer were calculated according to the standard curve, and the cumulative release curve of IL-4 was drawn.

2.3. Elisa Assay for Detecting the Secretion of Cytokines from Macrophagocyte.
The macrophage Raw 264.7 cells (ATCC, USA) were seeded into 12-well plate and cultured for 12 hours. And then, the seeded cells were treated with MSN@IL-4 or MSN for the specific time, and the cell supernatant was collected. After that, the collected supernatant and the standard substrate were added into the coated wells from Elisa assay kit (R&D, USA) according to the instructions, and the coated plate was shocked and detected for OD value using microplate reader (Thermo, USA). The standard curve of IL-10, SDF-1α, and BMP-2 was drawn, and their contents in cellular supernatant were calculated.

2.4. Immunofluorescent Assay for Detecting the Type of Macrophagocytes.
The macrophage Raw 264.7 cells (ATCC, USA) were seeded to the slices in a 24-well plate and cultured for 12 hours. And then, the seeded cells were treated with MSN@IL-4 or MSN for the specific time. After treating, the slices were fixed with 4% formaldehyde (Sinopharm,

China) at room temperature for 30 minutes, perforated with 1% triton X-100 solution (Solarbio, China) for 1 hour, blocked with 5% BSA (Aladdin, China) for 1 hour, incubated with primary antibody of CD206 (Abcam, USA) and CD86 (Abcam, USA) for 2 hours, following incubated with the rabbit secondary antibody (Lulong, China) at room temperature, and stained with DAPI (Solarbio, China) and sealed. At last, the slices were imaged by confocal microscope (Carl Zeiss AG, Germany).

2.5. MTT Assay for Detecting the Proliferation of Osteoblast.
The osteoblast cells were prepared from shin bone of mice and cultured in DMEM medium containing 10% fetal calf serum (FBS, Gibco, USA) for 3 days. And then, the cells were seeded into 96-well plate, cultured in incubator (ThermoFisher, USA) with 5% CO_2 for 12 hours, and treated with H_2O_2 and the secretion supernatant from macrophagocyte subjected to MSN@IL-4. After treating, the cells in wells were added with 20 μL MTT solution (Bio-Tek, China) with the final concentration of 0.5 mg/mL and incubated at 37°C for 2 hours. The precipitate of formazan in the incubated wells of 96-well plates was diluted with 100 μL DMSO (Sigma, USA) per well, and the absorbance at 490 nm was tested by microplate reader (ThermoFisher, USA). The proliferation ratio was calculated as

$$\text{Proliferation rate} = \frac{\text{OD}_{\text{sample}} - \text{OD}_{\text{blank}}}{\text{OD}_{\text{control}} - \text{OD}_{\text{blank}}} \times 100\%. \qquad (1)$$

2.6. Flow Cytometry of Dual Staining of FITC-Annexin V/PI for Detecting the Cellular Apoptosis in Osteoblast.
The prepared osteoblast cells treated by H_2O_2 and the secretion supernatant from macrophagocyte subjected to MSN@IL-4 were digested into single cells with 0.25% trypsin (Biosharp, China) and, following stopping the digestion with DMEM medium with FBS, washed and resuspended with PBS. The resuspended cells were stained via adding 5 μL Annexin V-FITC and PI to incubate at 25°C for 15 minutes according to the instruction from manufacturer (RD, Germany). Finally, the stained osteoblast was diluted with PBS to 1.0 mL and tested using the flow cytometry (BD, USA).

2.7. Western Blotting for Detecting the Apoptosis-Related Protein Expression in Osteoblast.
The osteoblast cells treated by H_2O_2 and the secretion supernatant from macrophagocyte subjected to MSN@IL-4 were collected and lysed with RIPA buffer, and the total protein was harvested and denatured. The denatured proteins were separated by SDS-PAGE and transferred to PVDF membrane (Millipore, USA). The PVDF membrane loading with the protein was blocked with 5% skim milk and incubated with the primary antibodies against Bcl-2 (CST, USA), Bax (CST, USA), caspase 3 (CST, USA), caspase 8 (Abcam, UK), and β-actin (CST, USA) at 4°C overnight, following the corresponding secondary antibody (CST, USA). Finally, the band from PVDF membrane was detected by enhanced chemiluminescence solution (ECL, Sigma, USA) and photographic film (Keda, USA).

2.8. Immunofluorescent Assay for Detecting the NF-κB Pathway-Related p65 Nuclear Location in Osteoblast. The prepared osteoblast cells were seeded to the slices in a 24-well plate and cultured for 12 hours. And then, the seeded cells were treated with H_2O_2 and the secretion supernatant from macrophagocyte subjected to MSN@IL-4 for the specific time. After treating, the slices were fixed with 4% formaldehyde (Sinopharm, China) at room temperature for 30 minutes, perforated with 1% triton X-100 solution (Solarbio, China) for 1 hour, blocked with 5% BSA (Aladdin, China) for 1 hour, incubated with primary antibody of CD206 (Abcam, USA) and CD86 (Abcam, USA) for 2 hours, following incubated with the rabbit secondary antibody (CST, USA) at room temperature, and stained with DAPI (Solarbio, China) and sealed. Finally, the slices were imaged by confocal microscope (Carl Zeiss AG, Germany).

2.9. Western Blotting for Detecting the NF-κB Pathway-Related Protein Expression in Osteoblast. The osteoblast cells treated by H_2O_2 and the secretion supernatant from macrophagocyte subjected to MSN@IL-4 were collected and lysed with RIPA buffer, and the total protein was harvested and denatured. The denatured proteins were separated by SDS-PAGE and transferred to PVDF membrane (Millipore, USA). The PVDF membrane loading with the protein was blocked with 5% skim milk and incubated with the primary antibodies against p-IKK (CST, USA), IKK (CST, USA), IκB (CST, USA), and β-actin (CST, USA) at 4°C overnight, following the corresponding secondary antibody (CST, USA). Finally, the band from PVDF membrane was detected by enhanced chemiluminescence solution (ECL, Sigma, USA) and photographic film (Keda, USA).

2.10. Statistical Analysis. By using the software of SPSS and GraphPad, all of the experimental data were presented as the mean ± standard deviation(S.D.). The statistical differences among the groups were compared using one-way ANOVA by SPSS of version 19.0 (SPSS, USA). $p < 0.05$ was considered to be statistically significant. The asterisk (∗) represented the comparison with the normal group, and the pound sign (#) was for the comparison with model group.

3. Results

3.1. Characteristics of MSN@IL-4 Scaffold and IL-4 Release Rate In Vitro. In order to obtain the controlled-release IL-4 system, MSN@IL-4 nanomaterial was fabricated via two-phase process, and in vitro IL-4 release response to pH was evaluated via Elisa assay. SEM photograph of MSN@IL-4 nanoparticle in Figure 1(a) showed that several black spherical particles adhere to the surface of the grey balls, demonstrating that IL-4 was conjugated to MSN. The release curve of IL-4 in vitro (Figure 1(b)) showed that there are 12% release rate for 3th day and more than 80% for 30th day with a sustained manner in pH 5.5, and the release is adequate during 30 days; however, the release rate is only 51% in pH 7.2 and lower than 20% in pH 8.8 for 30th day; even from 15th day, the release is extremely slow or standstill. These release data demonstrate that MSN@IL-4 nanosystem possesses the sustained and adequate IL-4 release potential response to the acid environment.

3.2. MSN@IL-4 Promote the Sustaining Secretion of Cytokines of IL-10, SDF-1α, and BMP-2 in Macrophagocyte. In order to confirm the effect of fabricated MSN@IL-4 nanomaterial on controlling pro-proliferative cytokine release, the secretion difference of IL-10, SDF-1α and BMP-2 in acrophagocyte subjecting to MSN@IL-4 nanocomplex or only IL-4 were detected by Elisa assay. The content curve in Figure 2(a) showed that the cells subjected to MSN@IL-4 nanocomplex treatment with the indicated time displayed a constantly linear increase of IL-10 secretion from 12 hours to 72 hours; however, the content of IL-10 in macrophagocyte subjected to only IL-4 displayed a rising for 24 hours compared to 12 hours and a constant decreasing from 24 hours to 72 hours. The change trends of SDF-1α secretion (Figure 2(b)) and BMP-2 secretion (Figure 2(c)) were similar in macrophagocyte subjected to MSN@IL-4 nanocomplex and only IL-4, which were that MSN@IL-4 promotes the constant and time-dependent increase of cytokines and only IL-4 was unsustainable. These results demonstrated that MSN@IL-4 nanocomplex could constantly promote proproliferative cytokine release in macrophagocyte compared to only IL-4 treatment.

3.3. MSN@IL-4 Promotes M2 Polarization in Macrophagocyte. To evaluate the promotive effect of MSN@IL-4 on M2 polarization, the M1/M2 indicator of CD86 and CD206 was detected via immunofluorescent experiments. The fluorescent images in Figure 3 showed that macrophagocyte in MSN@IL-4 group displayed a decrease of CD86 expression compared to that in control group ($0.01 < ∗p < 0.05$); oppositely, CD206 expression displayed an increasing trend in cells subjected to MSN@IL-4 nanomaterial compared to that in the control group ($0.001 < ∗∗p < 0.01$). Meanwhile, the cells in only MSN group displayed similar expressions of CD86 and CD206 with that in the control group. These results demonstrated that MSN@IL-4 nanocomplex could promote the M2 polarization of macrophagocyte, but only MSN has no the similar effect.

3.4. The Secretion Supernatant from Macrophagocyte Subjected to MSN@IL-4 Protects the Damaged Osteoblast. To confirm the protective effect of M2-polarizationed macrophagocyte on osteoblast, the secretion supernatant from macrophagocyte subjected to MSN@IL-4 was employed to treat the damaged osteoblast, the proliferation was examined via CCK-8 assay and apoptosis was evaluated by flow cytometer. CCK-8 data in Figure 4(a) showed that osteoblast subjected to H_2O_2 displayed a decrease of proliferation rate from 100% to 54.7% relative to cells in normal group ($0.001 < ∗∗p < 0.01$), and the osteoblast treated with H_2O_2 and the supernatant from macrophagocyte subjected to MSN@IL-4 displayed a reverse enhancement of proliferation rate from 54.7% to 84.2% compared to that in the model group ($0.01 < \#p < 0.05$). The scatter diagram of flow cytometer in Figure 4(b) showed that osteoblast subjected to H_2O_2 displayed an increase of apoptosis rate from 7.5% to 27.3% relative to cells in the normal group ($0.001 < ∗∗p < 0.01$), and the osteoblast treated with H_2O_2 and the supernatant from macrophagocyte subjected to MSN@IL-4 displayed a reverse

(a)

(b)
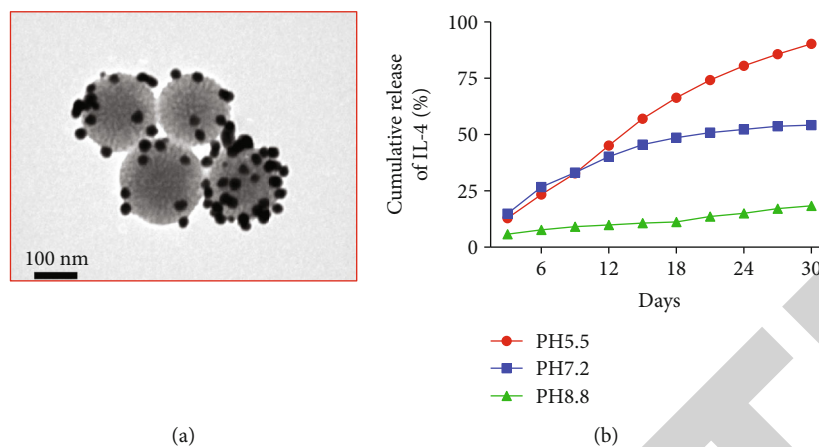
Figure 1: The scaffold of MSN@IL-4 and IL-4 release from MSN@IL-4 in vitro. (a) SEM image of MSN@IL-4 and (b) cumulative release of IL-4 response to pH.

(a)

(b)

(c)
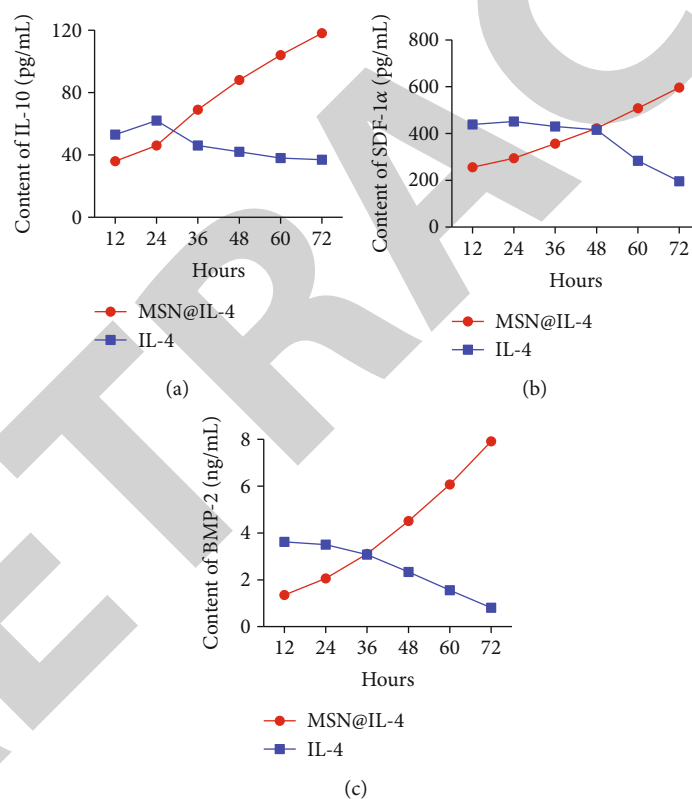
Figure 2: The effect of MSN@IL-4 nanomaterials for promoting the sustaining secretion of cytokines of IL-10, SDF-1α, and BMP-2 in macrophagocyte. Elisa assay for detecting the contents of IL-10 (a), SDF-1α (b), and BMP-2 (c) in the cellular supernatant.

decrease of apoptosis rate from 27.3% to 14.5% compared to that in the model group ($0.01 < \#p < 0.05$). These results demonstrated that the supernatant from the M2-polarizationed macrophagocyte induced by MSN@IL-4 could protect the osteoblast from H_2O_2-induced injury.

3.5. The Secretion Supernatant from Macrophagocyte Subjected to MSN@IL-4 Suppresses the Apoptosis-Related Protein Expression in Osteoblast. To further confirm the pro-

tective effect of M2-polarizationed macrophagocyte on the apoptosis during osteoblast injury, the apoptosis-associated proteins of bcl-2, bax, caspase 3, and caspase 9 were probed using western blotting. The band images in Figure 5 showed that osteoblast subjected to H_2O_2 displayed the expression increase of bax ($**p < 0.01$), cleaved caspase 3 ($**p < 0.01$), and cleaved caspase 8 ($**p < 0.01$) relative to cells in the normal group. Expectantly, the osteoblast treated with H_2O_2 and the supernatant from macrophagocyte subjected to MSN@IL-
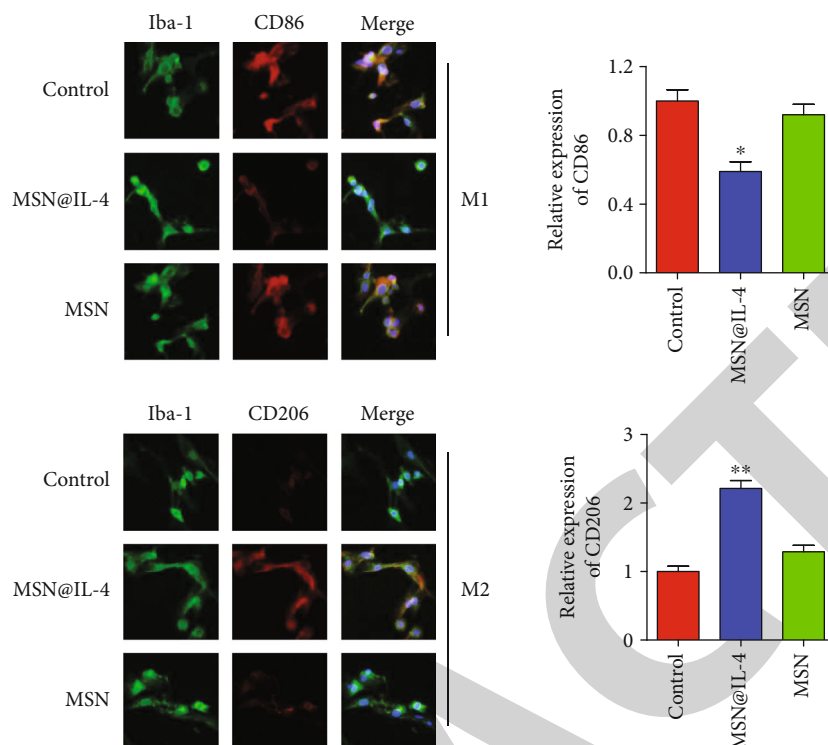
Figure 3: The promotive effect of MSN@IL-4 nanomaterials on M2 polarization in macrophagocyte. The representative fluorescent images of the stained CD86 and CD206 were displayed and relative expression were analyzed using GraphPad software. $*p < 0.05$ and $**p < 0.01$ vs. control group.

4 displayed a reverse regulation of protein expression that bax ($\#\#p < 0.01$), cleaved caspase 3 ($\#p < 0.05$), and cleaved caspase 8 ($\#p < 0.05$) were inhibited relative to cells in the model group. These results were consist with the apoptosis data from flow cytometry, demonstrating that the supernatant from the M2-polarizationed macrophagocyte induced by MSN@IL-4 could protect the osteoblast from H_2O_2-induced apoptosis.

3.6. The Secretion Supernatant from Macrophagocyte Subjected to MSN@IL-4 Suppresses the NF-κB Pathway-Related p65 Nuclear Location in Osteoblast. To evaluate the inhibitory effect of M2-polarizationed macrophagocyte on osteoblast inflammation, p65 nucleus location, a classical NF-κB pathway indicator, was probed via immunofluorescent experiments. The fluorescent images in Figure 6 showed the osteoblast treated with H_2O_2 and the supernatant from macrophagocyte subjected to MSN@IL-4 displayed a inhibitory effect of p65 nucleus location compared that in the model group and have the significant statistical difference of $0.01 < **p < 0.01$; however, the osteoblast treated with H_2O_2 and the supernatant from macrophagocyte subjected to MSN displayed a weak inhibitory of p65 nucleus location with no statistical difference compared that in the model group. The result demonstrated that the supernatant from the M2-polarizationed macrophagocyte induced by MSN@IL-4 could suppress the osteoblast inflammation via NF-κB p65 nuclear location.

3.7. The Secretion Supernatant from Macrophagocyte Subjected to MSN@IL-4 Suppresses the NF-κB Pathway-

Related Protein Expression in Osteoblast. To further confirm the suppressive effect of M2-polarizationed macrophagocyte on inflammation during osteoblast injury, the NF-κB pathway-associated proteins of p-IKK, IKK, and IκB were probed using western blotting. The band images in Figure 7 showed that osteoblast subjected to H_2O_2 displayed a evident decrease of IκB expression ($**p < 0.01$) and the phosphorylation increase of IKK ($**p < 0.01$) relative to cells in the normal group. Expectantly, the osteoblast treated with H_2O_2 and the supernatant from macrophagocyte subjected to MSN@IL-4 displayed a reverse regulation of protein expression that IκB expression in osteoblast cells of MSN@IL-4 group was induced ($\#\#p < 0.01$) and the protein phosphorylation of IKK was inhibited ($\#p < 0.05$) relative to cells in the model group. These results were consistent with the p65 nuclear location from immunofluorescent, demonstrating that the supernatant from the M2-polarizationed macrophagocyte induced by MSN@IL-4 could suppress NF-κB pathway-associated inflammation in osteoblast.

4. Discussion

It is commonly recognized that a large number of inflammatory cells infiltrated at the injury site of bone defect, and inflammatory cells under different conditions will have different subtypes exerting diametrically opposite regulatory effects on osteoblasts of wound [17–19]. M2-polarized macrophages can play an importantly role in wound healing by promoting the secretion of proosteocyte

(a)

(b)

(c)
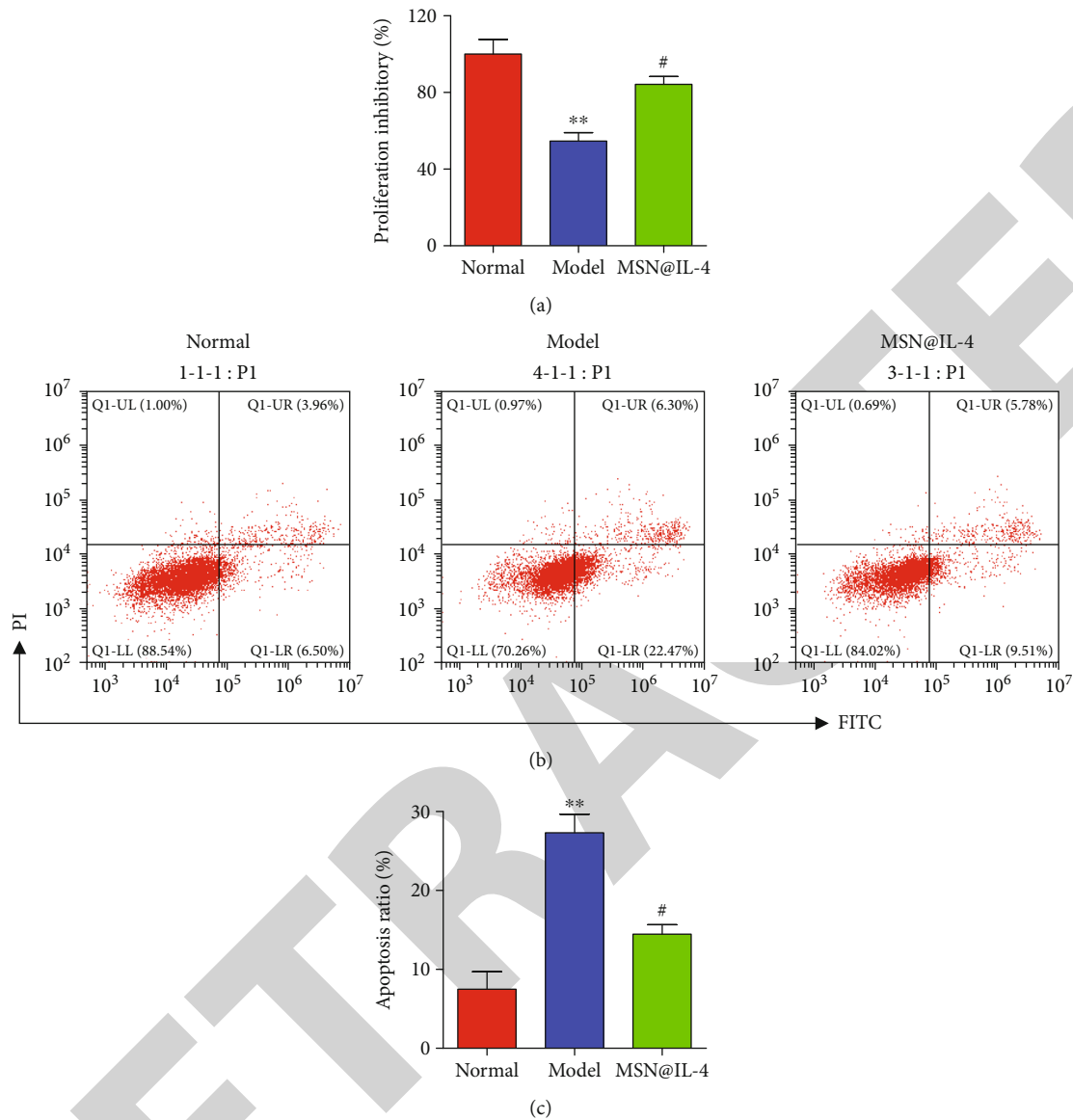
Figure 4: The protective effect of the secretion supernatant from macrophagocyte subjected to MSN@IL-4 nanomaterial against H_2O_2-induced osteoblast injury. (a) CCK-8 assay for detecting the cellular proliferation of the normal osteoblast (normal group), H_2O_2-treated osteoblast (model group), and the treated osteoblast with H_2O_2 and supernatant from macrophagocyte subjected to MSN@IL-4 nanomaterial (MSN@IL-4 group). (b) Flow cytometry analysis with dual staining of PI and FITC-annexin V for testing the cellular apoptosis rate. (c) The statistical analysis for the apoptosis rate using GraphPad software. $**p < 0.01$ and $***p < 0.001$ vs. normal group; $\#p < 0.05$ vs. model group.

growth factors [20, 21]. Therefore, the supplement of inducer of macrophage-M2-polarizaition such as IL-4 into the wound of bone defect would effectively promote wound healing. At present, the main treatment method for bone defects is bone transplantation. We have also reported the therapeutic effect of deproteinized bone scaffolds in the treatment of bone defects. However, the modified bone scaffolds added with macrophage M2 polarization inducers such as IL-4 have rarely been reported in the treatment of bone defects. Meanwhile, how to control the release of IL-4 in the modified bone scaffold to achieve sustained induction of macrophage

polarization is also a technical problem. In this project, we constructed a nanomaterial of MSN@IL-4 loaded on a deproteinized bone scaffold, which can continuously and slowly release IL-4 in response to a slightly acidic environment. We found that MSN@IL-4 could promote the sustaining secretion of cytokines of IL-10, SDF-1α, and BMP-2 compared to only IL-4 and induced M2 polarization in macrophagocyte. The supernatant from macrophagocyte treated with MSN@IL-4 was added into the damaged osteoblast by H_2O_2, the proliferation ratio of the damaged osteoblast increased, the apoptosis ratio decreased, and NF-κB-associated inflammation was
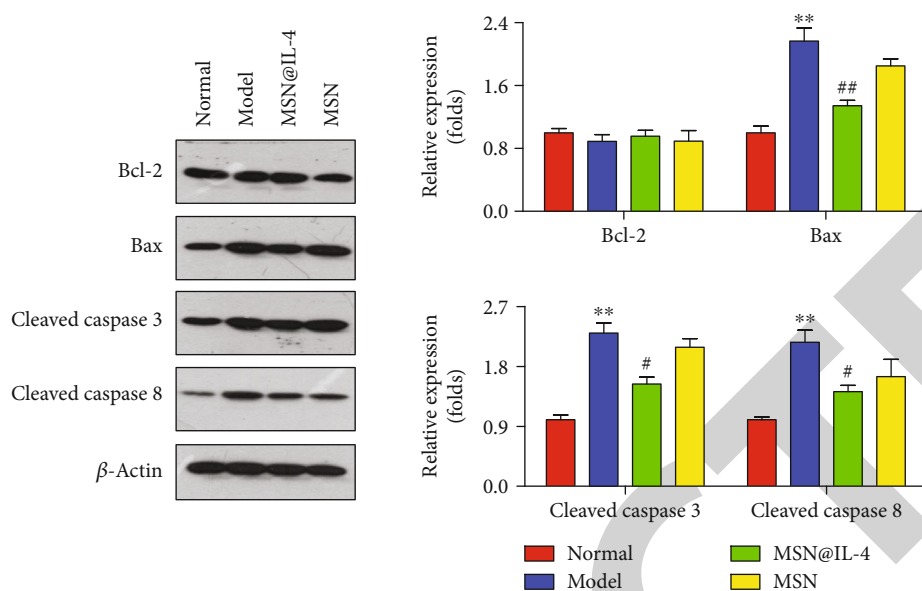
Figure 5: The regulatory effect of the secretion supernatant from macrophagocyte subjected to MSN@IL-4 nanomaterial on apoptosis-associated proteins of bcl-2, bax, cleaved caspase 3, and cleaved caspase 8. $**p < 0.01$ vs. normal group; $#p < 0.05$ and $##p < 0.01$ vs. model group.
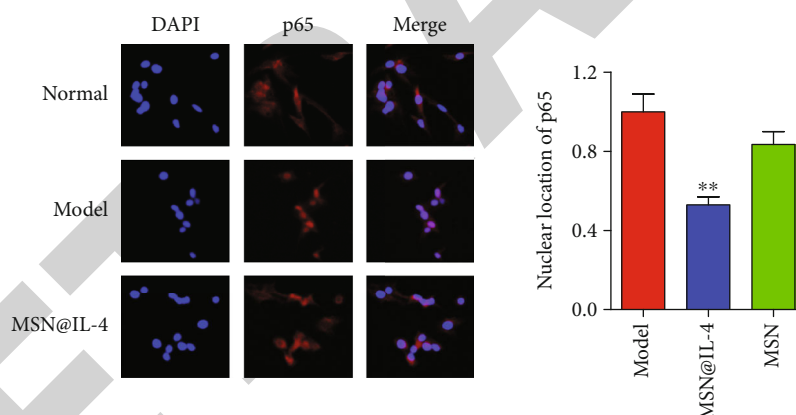
Figure 6: The inhibitive effect of the secretion supernatant from macrophagocyte subjected to MSN@IL-4 nanomaterial on the NF-κB pathway. The nucleus location of p65 in H_2O_2-treated osteoblast (model group) and the treated osteoblast with supernatant from macrophagocyte subjected to MSN@IL-4 nanomaterial (MSN@IL-4 group) or only MSN (MSN group). The statistical analysis of p65 nucleus location using GraphPad software. $**p < 0.01$ vs. model group.

inhibited. These results demonstrated that MSN@IL-4 could protect osteoblast against cell injury induced H_2O_2 via macrophagocyte M2 polarization and sustainingly promoted the release of active osteoblast factor.

Apoptosis is considered as a physiologically and pathologically programmed cell death process to clear off the redundant and malfunctional cells for keeping the cellular homeostasis [22]. Mitochondrial exerts the roles of the controlling center for cellular activities, which masters the oxidative phosphorylation and respiratory chain regulating almost all of the cellular physiopathology including apoptosis. During the apoptosis progression, apoptosis stimuli initiate the mitochondrial depolarization, induces/

inhibits the expression of apoptosis-associated proteins of bax, bad, and bcl-2 from mitochondrial, triggers the cysteinyl aspartate specific proteinase (caspase) of caspase 3, caspase 8, and caspase 9, and consequently activates the cleavage of poly ADP-ribose polymerase (PARP), cell death, and tissue damage [23]. In the present research, H_2O_2 initiate the osteoblast apoptosis via regulating bax and bcl-2 expression and evoking caspase activities. Oppositely, the supernatant from macrophagocyte treated by MSN@IL-4 relieved the apoptosis induced by H_2O_2. These data demonstrated that MSN@IL-4 could relieve osteoblast injury via inducing macrophagocyte release the active cellular factors.
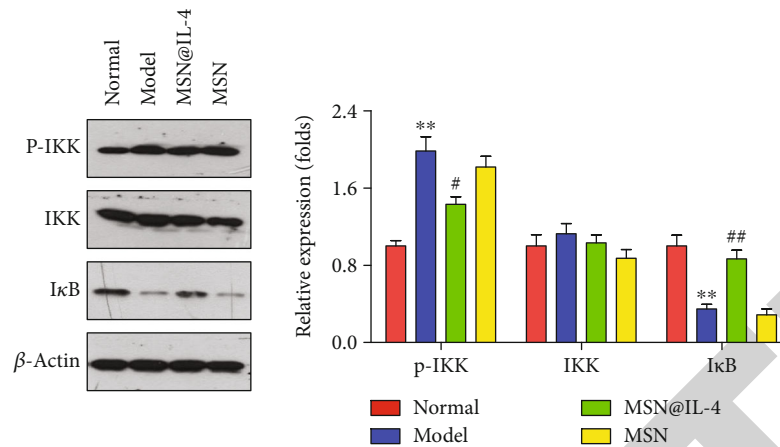
FIGURE 7: The regulatory effect of the secretion supernatant from macrophagocyte subjected to MSN@IL-4 nanomaterial on NF-κB pathway-associated proteins of p-IKK, IKK, and IκB. $*p < 0.01$ vs. normal group; $\#p < 0.05$ and $\#\#p < 0.01$ vs. model group.
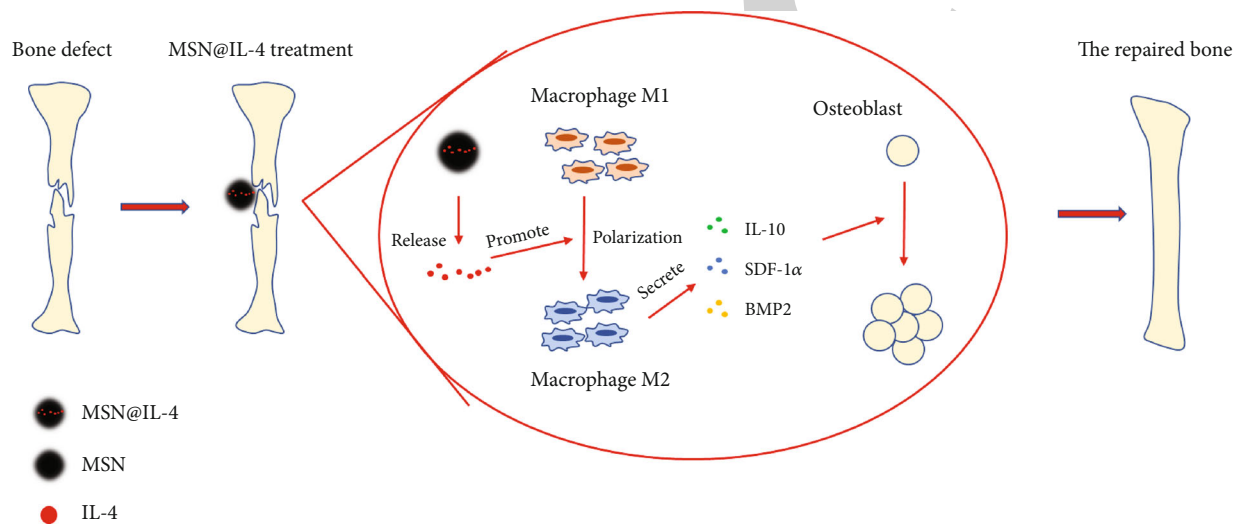
FIGURE 8: Scheme summarizing MSN@IL-4 relieving osteoblast damage via macrophagocyte M2 polarization.

The nuclear factor κB pathway (NF-κB pathway) has long been considered as a prototypical proinflammatory signaling pathway and controlled the expression of proinflammatory genes including cytokines, chemokines, and adhesion molecules [24]. NF-κB pathway was initiatively trigged with the phosphorylation of IKK response to inflammation factor, following the phosphorylation and degradation of IκB and then release the p65 protein from the complex of p65/p115/IκB, and induced its translocation from cytoplasm to nucleus for activating the gene expression of inflammatory factor such as TNFα, IL-1β, and IL-6, consequently causing the development of chronic diseases including cancer, diabetes, and osteoarthritis. In the present research, we found that the osteoblast damaged by H_2O_2 displayed an obvious phosphorylation of IKK, degradation of IκB, and phosphorylation of p65; meanwhile, the cells treated with the supernatant from macrophagocyte treated by MSN@IL-4 had a reverse trend change of the above NF-κB pathway indicators, demonstrating that MSN@IL-4 could protect against H_2O_2-inducing osteoblast injury via the induction of macrophagocyte release of the active cellular factors inhibiting the NF-κB inflammation pathway in osteoblast (Figure 8).

Data Availability

The data supporting the findings of this article will be available by the authors.

Conflicts of Interest

The authors declare that there are no conflicts of interest.

Hindawi

Research Article

Vaccinomics to Design a Multiepitope Vaccine against *Legionella pneumophila*

Ahitsham Umar,[1] Sadia Liaquat,[1] Israr Fatima,[1] Abdur Rehman,[1] Danish Rasool,[1] Abdulrahman Alshammari,[2] Metab Alharbi,[2] Muhammad Shahid Riaz Rajoka ⬮,[3] Mohsin Khurshid ⬮,[4] Usman Ali Ashfaq ⬮,[1] and Asma Haque ⬮[1]

[1]*Department of Bioinformatics and Biotechnology, Government College University Faisalabad, Faisalabad 38000, Pakistan*
[2]*Department of Pharmacology and Toxicology, College of Pharmacy, King Saud University, P.O. Box 2455, Riyadh 11451, Saudi Arabia*
[3]*Laboratory of Animal Food Function, Graduate School of Agricultural Science, Tohoku University, Sendai 980-8572, Japan*
[4]*Department of Microbiology, Government College University Faisalabad, Faisalabad 38000, Pakistan*

Correspondence should be addressed to Usman Ali Ashfaq; ashfaqua@gcuf.edu.pk and Asma Haque; asma@gcuf.edu.pk

Legionella pneumophila is found in the natural aquatic environment and can resist a wide range of environmental conditions. There are around fifty species of Legionella, at least twenty-four of which are directly linked to infections in humans. *L. pneumophila* is the cause of Legionnaires' disease, a potentially lethal form of pneumonia. By blocking phagosome-lysosome fusion, *L. pneumophila* lives and proliferates inside macrophages. For this disease, there is presently no authorized multiepitope vaccine available. For the multi-epitope-based vaccine (MEBV), the best antigenic candidates were identified using immunoinformatics and subtractive proteomic techniques. Several immunoinformatics methods were utilized to predict B and T cell epitopes from vaccine candidate proteins. To construct an *in silico* vaccine, epitopes (07 CTL, 03 HTL, and 07 LBL) were carefully selected and docked with MHC molecules (MHC-I and MHC-II) and human TLR4 molecules. To increase the immunological response, the vaccine was combined with a 50S ribosomal adjuvant. To maximize vaccine protein expression, MEBV was cloned and reverse-translated in *Escherichia coli*. To prove the MEBV's efficacy, more experimental validation is required. After its development, the resulting vaccine is greatly hoped to aid in the prevention of *L. pneumophila* infections.

1. Introduction

Legionnaires' disease is a severe form of pneumonia caused by *L. pneumophila*, aerobic Gram-negative, motile, and rod-shaped bacteria of the proteobacterial lineage. These bacteria are primarily found in artificial aquatic environments [1]. An episomal and chromosomal 45 kb pair region, selective expansions of key gene families, genes for unexpected metabolic pathways, and previously recognized putative virulence factors make up its genome. Intracellular pathogens exploit the iCM/dot type secretion system to deliver effector proteins to host cells, altering phagocytic vacuole destiny by inhibiting phagosome-lysosome fusion, vacuole acidification, and recruitment of vesicles with

endoplasmic reticulum-like characteristics [2–4]. Virulence levels of Legionella species have different ranges in nonpathogenic *L. pneumophila* [5, 6].

Lung infection is caused by inhaling microdroplets as well as aerosols from water infected through Legionella. Though these bacteria are common in natural water systems, the sickness is caused by higher populations in artificial water systems, which are more likely to produce aerosols that host the bacteria. Premise plumbing, misters, showers, and cooling towers are examples of aerosol-producing designed water systems [7]. Throughout the SARS-CoV2 pandemic, the situation has become even more severe, as massive worldwide "stay-at-home" orders have made a conducive atmosphere for the

growth of Legionella and propagation [8]. In reaction to the new coronavirus epidemic, the directives have resulted in the closure of buildings, institutions, and offices. Water usage and flow have been curtailed due to the widespread closures and "shut-downs," resulting in water stagnation [9]. In 1976, Philadelphia was the site of the first big outbreak of Legionnaires' disease (LD). Since then, many attacks and occasional cases have been documented, most linked to *Legionella pneumophila* bacteria [10]. According to the US National Academies of Sciences, Engineering, and Medicine (NASEM), Legionella is five times higher than its 20-year previous incidence [11]. The total number of cases in both the United States and Canada is thought to be significantly increased [1, 12].

For Legionella detection, two methods are utilized: ISO 2017 culture (AFNOR NF T90-431, ISO 11731) and qPCR (AFNOR NF T90-471, ISO/TS 12869) [13, 14]. The culture method is time-demanding, sensitive to sample selection, and prone to false-negative results because of interfering flora and viable but nonculturable (VBNC) cells [15]. The qPCR approach is more sensitive and rapid, but it risks overestimating Lp levels because it cannot differentiate live from nonviable bacteria [16]. It also necessitates additional processing and elimination processes to remove chemicals from complex matrices that could interfere with qPCR responses [16, 17]. The use of surface plasmon resonance imaging (SPRi) biosensors can solve several issues that contemporary technologies pose. Unlike present approaches, real-time detection could be carried out by using SPRI technology, allowing complex samples, and detecting surface regeneration, all of which would avoid several processing stages and ensure the system's convenient operation at a cheaper cost [18, 19].

There is presently no approved *L. pneumophila* medication vaccination available, while a few investigational medications are undergoing clinical studies. Vaccination is the most efficient way to avoid viral infections. The availability of genetic data, advanced software, and immunological data sets now make it much easier for researchers to find efficient active subunit vaccines that could be manufactured using epitopes of infection proteins [20–22].

Antigenic proteins that may be anticipated for T cells and B cells using their major histocompatibility complex (MHC) alleles were found in the proteome of *L. pneumophila*. Antigenicity, conservation, and worldwide coverage of expected epitopes have all been explored by linking the most promising and interacting epitopes, and by adding an adjuvant, a multi-epitope-based vaccine (MEBV) was constructed. Since MEBVs are more cost-effective than conventional single-epitope vaccines, they are also more stable specific and time-efficient. Due to the inclusion of both T cell and B cell epitopes, they are supposed to elicit large humoral and cellular immunological responses simultaneously [23]. Several *in silico* techniques were used to validate the antigenicity, allergenicity, immunogenicity, toxicity, structural stability/flexibility, and physicochemical properties of developed MEBVs. The usage of computational methods and molecular dynamic simulation was employed to evaluate the stability and interaction of MEBV with human receptors. Moreover, *in silico* cloning was performed to demonstrate expression profiling using MEBV codons optimized for *E. coli*.

There is currently no way to either cure the condition or prevent it via drugs or immunizations. This study used subtractive proteomics, reverse vaccinology, and immunoinformatics as the research tools to identify key targets of *L. pneumophila* that may be exploited in the development of vaccines to regulate humoral and cellular immune responses. These targets may be exploited in the development of vaccines. Because of this discovery, scientists now could perform research experiments toward the development of a vaccine that can protect against *L. pneumophila* as well as the many other viruses that are resistant to antibiotics. This approach has been used to predict various MEBVs for different viral infections.

2. Methodology

2.1. Retrieval of Proteome Analysis. The whole proteome of the *L. pneumophila* strain was extracted in FASTA format using UniProt [24]. The Geptop 2.0 server was used to find essential proteins [25]. Human proteins should not be used as vaccine candidates to prevent an autoimmune response. Nonhomologous proteins were predicted using BLASTp, and in this general sequence, identification and similarity search with different proteins was done [26]. The outer membrane proteins were chosen by cellular localization using PSORTb 3.0.3 [27]. Since immunogenicity is a measure of someone's capacity for quick response and generating an effective immune response to an antigen, peptide-based vaccines were created using more antigenic proteins. The Vaxijen 2.0 server was used to evaluate the antigenicity of all *L. pneumophila* proteins with a 0.5 threshold [28]. This server has a 70-89 percent accuracy when employing the autocross covariance transformation algorithm [28]. To predict the transmembrane helix, the TMHMM v-2.0 server was employed [29].

2.2. CTL Epitope Selection and Evaluation. Cytotoxic T cells are crucial in identifying specific antigens and the correct design of CTL epitopes, which are vital for vaccine development. Most importantly, compared to wet laboratory tests, it reduces the time and cost of predicting epitopes [30].CTL epitopes were determined using Immune Epitope Database's MHC-I binding tool (IEDB) [31]. Multiple options used to run the queries that have multiple tools that are linked within its resource options like MHC-I and MHC-II could be predicted by using the links given in the epitope analysis resource option box; B cell prediction tool links are given in the B cell prediction toolbox, same as population coverage could be predicted by epitope analysis tool options.

Because a lower percentile rank suggests better affinity, the percentile rank was set to 2. Highly antigenic, immunogenic, and nontoxic CTL epitopes were selected to develop vaccines. The IEDB database was used to calculate the immunogenicity of the epitopes [31]. Toxicity and antigenicity were determined using the Toxin Pred and Vaxijen servers [32, 33]. The Toxin Pred server uses a quantitative matrix and machine learning technique to analyze peptide

characteristics. In this tool, the SVM method by default E value cutoff value was used that was 10 to predict if the epitope is toxic or nontoxic. Allergenicity was determined with the help of AllergenFP, which has an accuracy of 88.9% [34].

2.3. Selection and Analysis of Helper T Lymphocyte (HTL) Epitopes.
HTL cells are the most important cells in the adaptive immune response because they turn on CTL cells, which kill pathogens, macrophages, which eat pathogens, and B cells, which make antibodies [35]. It is, therefore, crucial to involve helper T cell epitopes for a healthy immune response. HTL can produce interleukin-4 (IL-4) and IL-10 as well as interferon-gamma (IFN-γ), which causes immune cells including macrophages and cytotoxic T cells to become activated [36]. As a result, HTL epitopes that produce cytokines are crucial for vaccine development. The IEDB employed its MHC-II binding tool to predict HTL epitopes (15-mer) of target proteins [31]. This tool was used to predict IFN-gamma-inducing regions in the protein of interest. The SVM method is used, and positively scored epitopes were selected for further process.

In SOPMA, by applying motif scan and SVM approach, overlapping HTL sequence peptides were found against the query protein using the IFN-γ epitope server [37]. The interleukin-4 (IL-4) web server allows design, discovery, and peptide map to genuinely produce IL-4 with the threshold of 0.2, which is significant for subunit vaccines [38]. At a threshold value of 0.3, IL-10 Pred was also employed to predict the inducing qualities [39].

2.4. LBL Epitope Identification and Evaluation.
The surface receptor identified B cell epitopes, which create antigen-related immunoglobulins. As a result, developing a B cell epitope vaccination would be critical for adaptive immunity [40]. ABCPred, an internet-based server based on neural networks, identified LEPS B cells with the highest accuracy of 75 percent [41]. AllergenFP v1.0 was utilized to test the allergenicity of the query sequence. ToxinPred retrieved toxicity, and VaxiJen v2.0 servers retrieved antigenicity of anticipated B cell epitopes [28, 32, 34].

2.5. Population Coverage Analysis.
In different ethnic groups, distinct HLA alleles and their expression are distributed at varied frequencies. The distribution of HLA alleles around the globe is thus critical for the creation of multiepitope vaccines [42]. The primary objective of these population coverage studies determines if the candidates selected were suitable for a broad group of individuals [43]. Population coverage of the specified epitopes and their HLA alleles was determined using the IEDB's population coverage server [44].

2.6. Vaccine's Mapping.
The selected CTL, HTL, and LBL epitopes were linked and formed a fusion peptide using different linkers like AAY, KK, and GPGPG and 50S ribosomal protein L7/L12 as adjuvant. By connecting, coupling adjuvants to the sequence may enhance immunogenicity and long-lasting immune response. As a result, the EAAAK linker was used to attach the TLR4 against (RS-09; Sequence: APPHALS) adjuvant to the CTL epitope.

For each epitope to function properly, a linker must be employed to connect two epitopes.

2.7. Structural Analysis.
The vaccine was first examined using BLASTp to see if it was identical to the human proteome [45]. The vaccine construct's physiochemical features were assessed using the ProtParam web server [46]. The molecular weight, extension coefficient, isoelectric point, and half-life were all computed by ProtParam. The Vaxijen server was utilized to assess v antigenicity [31, 33]. Another crucial step was to use the AllerTOP service to calculate the vaccine design's allergenicity (allergen or nonallergen) [47]. The SOPMA tool, which is critical for predicting protein folding, predicts the vaccine's 2D structure. In this tool, the number of confirmational states was 4 (helix, sheet, turn, and coils); the similarity threshold was set to be default as 8. SOPMA's secondary structure prediction is 69.5 percent accurate, with a three-state structure (α-helix, β-sheet, and coil) description [48]. The ProtParam tool was used to evaluate the physiochemical properties of our vaccine. The SOLpro is a useful tool used for predicting vaccine solubility in the final stages of vaccine development, with a prediction accuracy of 74% and several runs of 10-fold cross-validation [49].

2.8. Prediction of Tertiary Structure, Confirmation, and Refinement.
The amino acid sequence can be used to construct a 3D protein model using computer techniques. The I-TASSER suit was used to model the MEBV in three dimensions (3D) [50]. It takes structural templates from the protein database through multiple threading approaches and then predicts the structure through iterative template-based fragment assembly simulation.

The vaccine model was refined using the GalaxyRefine web server after it was predicted [51]. The GalaxyRefine server reshapes the side chain before performing structural reassembling and overall structural assessment using molecular dynamics. As the CASP refinement category demonstrates, it is extremely helpful in increasing the quality of local structures. The Ramachandran plot was used to determine which phi and psi dihedral angle preferences of amino acid residues were energetically allowed or banned [52]. Furthermore, ProSA-web calculates special requirements to verify the 3D structures obtained from NMR spectroscopy, X-ray, and theoretical calculations [53]. The ERRAT program predicted the tertiary structure of the protein and assigned a quality factor based on nonbonded atomic interactions within the protein [54].

2.9. B Cell Epitope Screening.
The ABCpred server was used to identify conformational and linear B cell epitopes [41, 55]. The ABCpred server set the length and threshold of the MEBV amino acid sequence to 14 and 0.5, respectively. The MEBV's tertiary structure was also entered into the Elli-Pro program using the default parameters.

2.10. Docking of TLR4 Receptor with Constructed Vaccine Disulphide.
The constructed vaccine candidate ultimately interacts with host immune cells to elicit an efficient immune response. HADDOCK 2.2 is utilized to dock MEBV

Table 1: Top selected proteins with highest antigenic nature with extracellular location.

Sr. no.	Protein name	Accession no.	Antigenicity	Helices	Location
1	YARHG domain-containing protein	A0A127V420	0.51	0	Extracellular
2	TPR-region domain-containing protein	A0A140J7Y2	0.72	0	Extracellular
3	SPOR domain-containing protein	A0A140J8J4	0.69	0	Extracellular
4	Sel1 repeat protein	A0A127V446	0.54	0	Extracellular
5	Metalloprotease PmbA	A0A127V344	0.55	0	Extracellular
5	Peptide ABC transporter substrate-binding protein	A0A140J2V6	0.53	0	Extracellular

Table 2: Final CTL selected epitopes for the construction of vaccine against *L. pneumophila*.

Epitope	Protein	Alleles	Position	Antigenicity	Immunogenicity
CSEIDPKADY	YARHG domain-containing protein	HLA-A*01:01 HLA-A*30:02	4-35	1.4910	0.0202
FPPLATVNIH	YARHG domain-containing protein	HLA-B*53:01 HLA-B*35:01	3-38	1.1473	0.1723
FSFLFLFSTFTF	Uncharacterized protein	HLA-A*23:01 HLA-A*24:02 HLA-B*46:01 HLA-B*15:02 HLA-A*29:02 HLA-C*07:02 HLA-B*58:01 HLA-B*35:01 HLA-B*57:01	1-6	1.8775	0.24096
NVSGRTLRLDLW	Uncharacterized protein	HLA-B*58:01	1-49	2.4487	0.11
KPQWLLSLGYEY	SPOR domain-containing protein	HLA-A*29:02 HLA-A*30:02 HLA-B*35:01	6-27	1.1161	0.07907
GFSVDVRMGEVE	Metalloprotease PmbA	HLA-B*46:01 HLA-C*08:02 HLA-C*15:02	1-47	1.9821	0.06956
PFFAPVPWEADL	Peptide ABC transporter substrate-binding protein	HLA-B*35:03 HLA-C*03:03 HLA-C*07:02	5-10	1.0915	0.4519

Table 3: Final HTl epitopes for the construction of vaccine against Legionella pneumophila.

Epitope	Protein	Alleles	Position	Antigenicity	IFN-γ	IL-4	IL-10
YFWKTTFPPLATVNI	YARHG domain-containing protein	HLA-DPA1*02:01/DPB1*14:01	152-166	0.8325	Positive	Inducer	Negative
GIYYSHFFNMDINGQ	SPOR domain-containing protein	HLA-DRB1*04:05 HLA-DPA1*01:03/DPB1*04:01	161-175	1.1525	Positive	Inducer	Negative
VGIYYSHFFNMDING	SPOR domain-containing protein	HLA-DRB1*04:05 HLA-DPA1*01:03/DPB1*04:01 LA-DPA1*01:03/DPB1*02:01	160-174	1.0893	Positive	Inducer	Negative

with human Toll-like receptors (TLR4) and MHC molecules (MHC-I and MHC-II) [56]. HADDOCK is a high ambiguity docking program that may use data from the interface zone between molecular components and their orientations. C port values of both protein and residue have to paste in given boxes as well as structures of both have to attach there. In output, we received the docking score, cluster size, RMSD values, and Van-der-Waals energy values.

In contrast to other docking tools, the HADDOCK V2.2 step allows overall conformational changes involving the modifications in the backbone. Docking multimodel NMR structures and other Protein Data Bank (PDB) structures

TABLE 4: Final selected B cell epitopes for vaccine construction.

Epitope	Protein	Score	Position	Antigenicity	Immunogenicity
YHTIQNVSGRTLRLDL	Uncharacterized protein	0.85	44	1.5483	0.06924
GRTLRLDLWVDKIVAG	Uncharacterized protein	0.73	52	1.1531	0.30232
LFIITLNLHCINVAFS	SPOR domain-containing protein	0.73	13	1.6755	0.4296
SWDITPQQAIDLALKC	Metalloprotease PmbA	0.78	131	1.5251	0.02249
KNHPDLDLYHSWDITP	Metalloprotease PmbA	0.78	121	1.0760	0.25932
KMRIGHAQIFSWGWNA	Peptide ABC transporter substrate-binding protein	0.92	550	1.2577	0.65378
DLNIRATLYNRFQEKM	Peptide ABC transporter substrate-binding protein	0.62	536	1.2516	0.25128
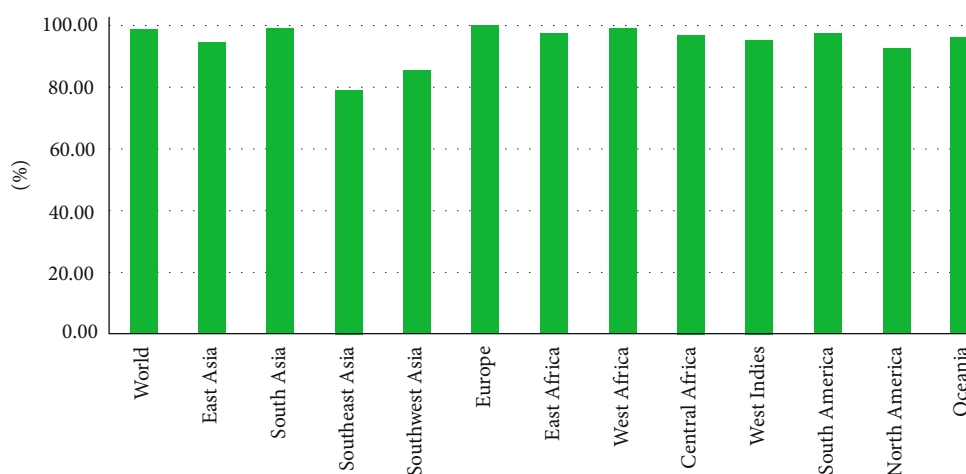
FIGURE 1: Worldwide population coverage analysis of selected epitopes.
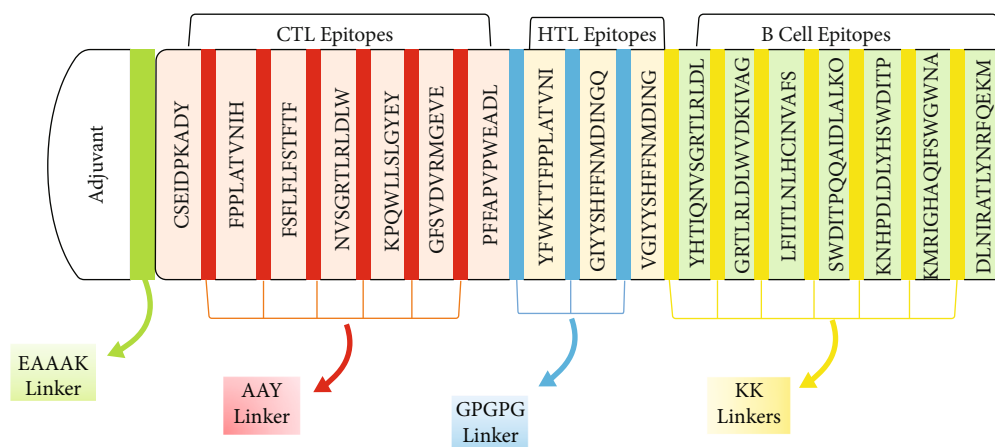
FIGURE 2: Constructed vaccine figure with adjuvants and linkers. Each color represents the specific linker.

are also possible with HADDOCK [57]. Crystal structures of TLR4 (ID: 4G8A), TLR2 (ID: 2Z7X), MHC-I (ID: 1I1Y), and MHC-II (ID: 1KG0) were retrieved from the Protein Data Bank (PDB) (ID: 1KG0) [58–61]. Analysis of docked complexes in the PDBsum database and imaging of the docked complexes with the PyMOL molecular visualization system leads to the discovery of interactions [62, 63]. PDBsum is an online web server that depicts a wide variety of information about a macromolecular structure in a PDB. This includes PROMOTIF structural analysis, images of the structure, PROCHECK results, and schematic illustrations of protein-DNA and protein-ligand interactions.

MAKLSTDELLDAFKEMTLLELSDFVKKFEETFEVTAAAPVAVAAAGAAPAGAAVEAAE
EQSEFDVILEAAGDKKIGVIKVVREIVSGLGLKEAKDLVDGAPKPLLEKVAKEAADEAK
AKLEAAGATVTVKEAAAKCSEIDPKADYAAYFPPLATVNIHAAYFSFLFLFSTFTFAAY
NVSGRTLRLDLWAAYKPQWLLSLGYEYAAYGFSVDVRMGEVEAAYPFFAPVPWEADL
GPGPGYFWKTTFPPLATVNIGPGPGGIYYSHFFNMDINGQGPGPGVGIYYSHFFNMDING
KKYHTIQNVSGRTLRLDLKKGRTLRLDLWVDKIVAGKKLFIITLNLHCINVAFSKKSWDI
TPQQAIDLALKCKKKNHPDLDLYHSWDITPKKKMRIGHAQIFSWGWNAKKDLNIRATL
YNRFQEKM
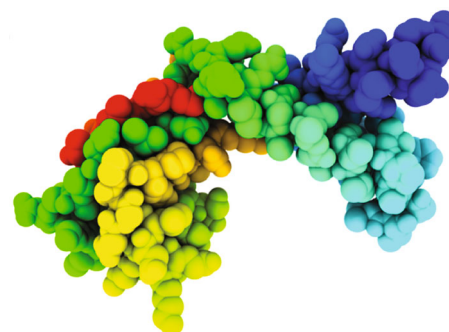
(a)

(b)
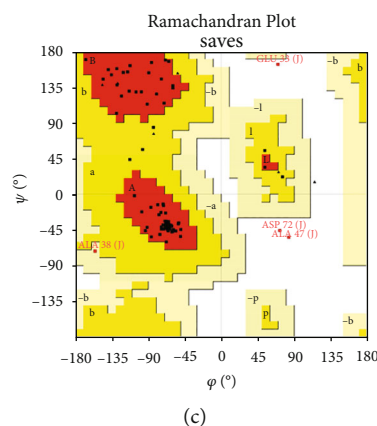
(c)

FIGURE 3: (a–c) Vaccine construct sequence along with predicted structure and structure evaluation analysis: (a) depicts the sequence of the vaccine after addition of different linkers and an adjuvant; (b) is the predicted structure of the vaccine using I-TASSER server; (c) describes the conformational analysis of the structure, and the red zones in that plot indicated the favored regions and the number of residues in it.

2.11. Molecular Dynamic Simulation. Molecular dynamics plays an important role in confirming and determining the stability of proteins and protein complexes in all *in silico* studies. Analyzing the modes of essential proteins can measure protein stability [64, 65]. The iMODs (internal coordinate normal mode analysis) server was utilized to describe joint-protein mobility in inner coordinates [66]. Internal complex movements were measured using this site. The value of the standard mode was determined by the stiffness of motion. When the eigenvalue is low, it aids in the deformation of structures that have a certain energy.

2.12. Immune Stimulation. The C-IMMSIM web server evaluated the immunological profile of the MEBV finalized candidate. The C-IMMSIM is a flexible tool that uses a position-specific scoring matrix (PSSM) to forecast the peptide interactions for immune response. The C-IMMSIM web server is commonly used in immune informatics investigations and provides accurate findings in terms of vaccination strategy [67–69]. The simulation was carried out in 1000 steps over four weeks, with two dosages administered.

2.13. In Silico Cloning and Optimization of Codons. A codon optimization technique can help the host increase the expression of foreign genes. Codon usage fluctuates from organism to organism, and this variation in codon usage may lead to a low foreign gene expression rate. The vaccine sequence was codon adapted using the JCat tool, ensuring

the codon usage per *E. coli* K12 strain [70]. Finally, an *E. coli* vector was used to clone the modified nucleotide sequence of pET30a (+) by employing Snap Gene v5.0.8 software [71]. The pET30a cloning vector was used in this project because it has similar restriction sites regarding MEBV, and it has a high expression level than pET28a. pET28a had no similar restriction sites according to the vaccine construct [72–74].

3. Results

3.1. Protein Selection. To identify the most promising candidates for *Legionella pneumophila* MEBV design, this study used a subtractive proteomic technique. It slowly gets rid of less desirable proteins from the complete proteome of *L. pneumophila.* "ATCC 33152/DSM 7513" is the name of the *L. pneumophila* strain that was downloaded from UniProt. It has 2889 proteins (Accession no.: UP000000609). The proteome was filtered using CD-HIT with a threshold of 80% (0.8). Nonparalogous proteins were removed from further analysis using the CD-HIT suite. The Geptop server was used to identify essential proteins. The essentiality score cutoff was set to be 0.24. Only 398 essential proteins were found, and their similarity with the human proteome was confirmed (Taxonomic id: 9606). To avoid an autoimmune reaction that attacks and destroys its cells after identifying them as alien particles, it is critical to get rid of human homologs. To avoid a situation like this, homologous proteins should be avoided. The CELLO server projected that
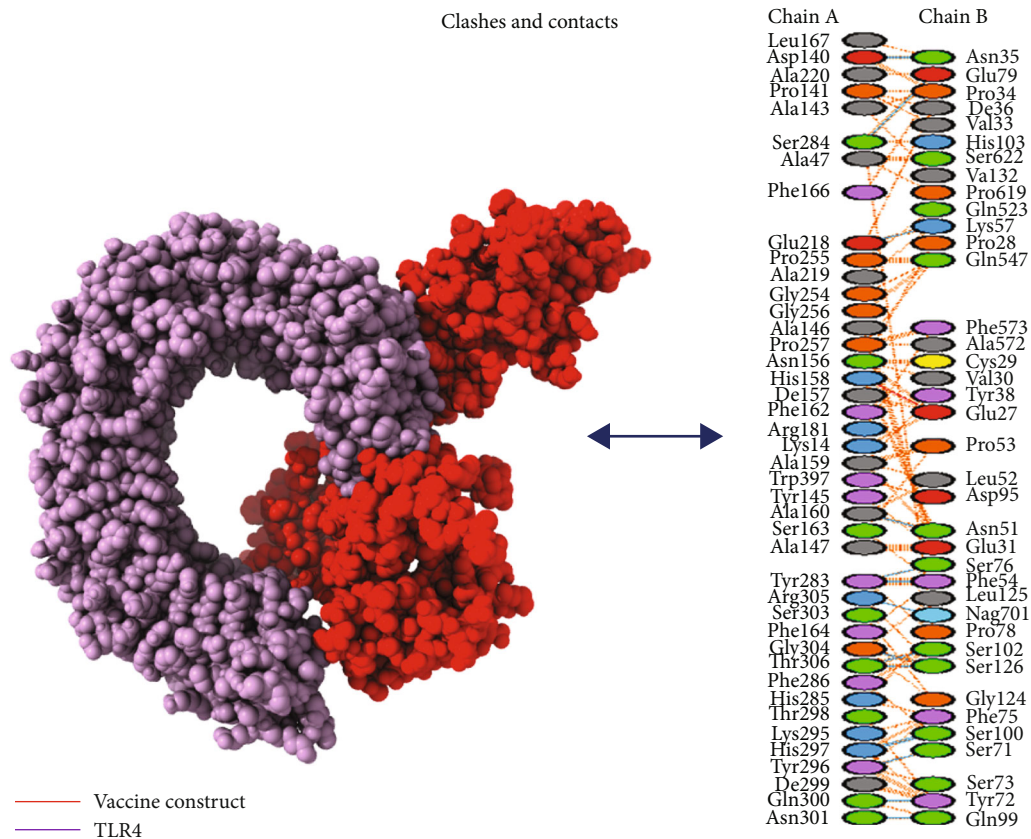
FIGURE 4: Docked complex of TLR4 construct with the vaccine construct indicating the interacting part along with the interacting residue. The red part is for the vaccine, and the purple is for theTLR4 in this docking.

those 379 essential proteins would be found in the cytoplasm, 11 in the outer membrane region and 8 in extracellular locations. For further study, the cytoplasmic proteins were eliminated, while the remaining proteins were selected. Six of the proteins were chosen for the epitope's prediction and further procedure (Table 1).

3.2. CTL Epitope Selection and Evaluation. From the L. pneumophila target protein, thirty-one CTL epitopes (12-mer) were identified (Table S1). With the help of this method, the top seven epitopes with the highest immunogenicity, antigenicity, and nonallergenicity as well as nontoxicity were discovered for vaccine development (Table 2). There was a total of 6 unique HTL epitopes chosen for vaccine construction (Table S2). The top 3 epitopes were finalized for vaccine construction based on their cytokine capacity, and only these 3 fulfill the following properties of antigenicity, allergenicity, and toxicity (Table 3). Similarly, after analyzing the allergenicity, toxicity, and immunogenicity of 35 LBL epitopes (Table S3), a total of 7 epitopes were selected for vaccine manufacture (Table 4).

3.3. Population Coverage. In the development of vaccines, population coverage is a critical aspect. The whole population coverage of selected MHC-I and MHC-II epitopes with corresponding HLA alleles was assessed in this study. The overall coverage of the selected epitopes was calculated to

be 87% of the world's population. North America was discovered to have the highest population coverage, at 99.99 percent. According to our research, the chosen epitopes are expected to be great vaccine candidates (Figure 1).

3.4. Construction of Vaccine. For vaccine construction, all the selected epitopes were utilized. All CTL, HTL, and LBL epitopes were attached using AAY, KK, and GPGPG linkers. These linkers were chosen because they aid in vaccination and epitope presentation while preventing junctional epitope formation [75, 76]. With the first CTL epitopes, the 50S ribosomal protein L7/L12 (124 residues) was employed as an adjuvant, along with the EAAAK linker. The EAAAK linker improves structural stability with effective division and reduces interaction with neighboring protein regions [77]. The final 419 amino acid vaccine design demonstrates how different epitopes and linkers were used to develop a successful vaccination (Figure 2).

3.5. Physiochemical and Immunogenic Profiling. The manufactured vaccine's immunogenicity and physicochemical properties are investigated further. When the similarity of the made vaccine to the human proteome was compared, it was found that no two human proteomes are the same. As a result of these analyses, our vaccine proved to be highly antigenic, nonallergenic, and nontoxic. ProtParam was used to evaluate the physicochemical properties of the

TABLE 5: Docking table indicating the docking scores along with different energy values of TLR4, MHC-I, and MHC-II with vaccine construct.

Parameters	Values
TLR4	
HADDOCK v.2.2 score	635.2 ± 9.3
Cluster size	18
RMSD from the overall lowest energy structure	21.3 ± 0.0
Van-der-Waals energy	-130.5 ± 14.2
Electrostatic energy	-352.4 ± 71.9
Desolvation energy	-51.1 ± 12.3
Restraint violation energy	3412.9 ± 178.99
Buried surface area	3918.1 ± 163.1
Z-score	-1.8
MHC-I receptor	
HADDOCK v.2.4 score	345.3 ± 27.1
Cluster size	11
RMSD from the overall lowest energy structure	16.7 ± 0.0
Van-der-Waals energy	-136.6 ± 10.0
Electrostatic energy	-324.3 ± 32.8
Desolvation energy	-43.3 ± 5.6
Restraint violation energy	3678.0 ± 162.5
Buried surface area	4565.7 ± 289.0
Z-score	-1.3
MHC-II receptor	
HADDOCK v.2.4 score	279.8 ± 31.5
Cluster size	9
RMSD from the overall lowest energy structure	17.3 ± 0.4
Van-der-Waals energy	-148.5 ± 15.4
Electrostatic energy	-289.3 ± 39.0
Desolvation energy	-67.6 ± 5.1
Restraint violation energy	3106.9 ± 165.4
Buried surface area	3781.5 ± 267.0
Z-score	-1.6

compounds. The final construct had 7.61pI 46284.37 kDa MW, respectively. The GRAVY was calculated to be -0.065 and has a half-life *in vitro* of thirty hours, in vivo of more than twenty hours (yeast), and in vivo of more than ten hours (*E. coli*). SOLpro results indicated soluble with probability of 0.937616. All these characteristics suggest that *L. pneumophila* is a suitable vaccine candidate.

3.6. Structural Evaluation. The following characteristics also support *L. pneumophila* as a promising vaccine candidate. The alpha-helix contains 155 amino acids, which account for 36.99 percent of the sequence, 110 amino acids in extended chains, which account for 26.25 percent, and 108 amino acids in coils, which account for 25.78 percent of the vaccine's construct.

3.7. Prediction of Tertiary Structure, Refinement, and Validation. 3D structure prediction of our vaccine was done through an online server I-TASSER. *C*-score was measured as -1.66 in the results. The structure was modified and refined by utilizing the GalaxyRefine web server. After that, analysis of the modeled structure was done through the Ramachandran plot, which indicated the best values of the favored region about 92.7 percent, 3.5 percent in the favored region, and 2.7 percent in the outer region. *Z*-score was calculated as 0.395, and ERRAT analysis exhibited a score of 95. These results proved our refined model to be excellent (Figures 3(a)–3(c)).

3.8. Selection of B Cell Epitopes. B lymphocytes generate antibodies, which result in humoral immunity [78]. Therefore,
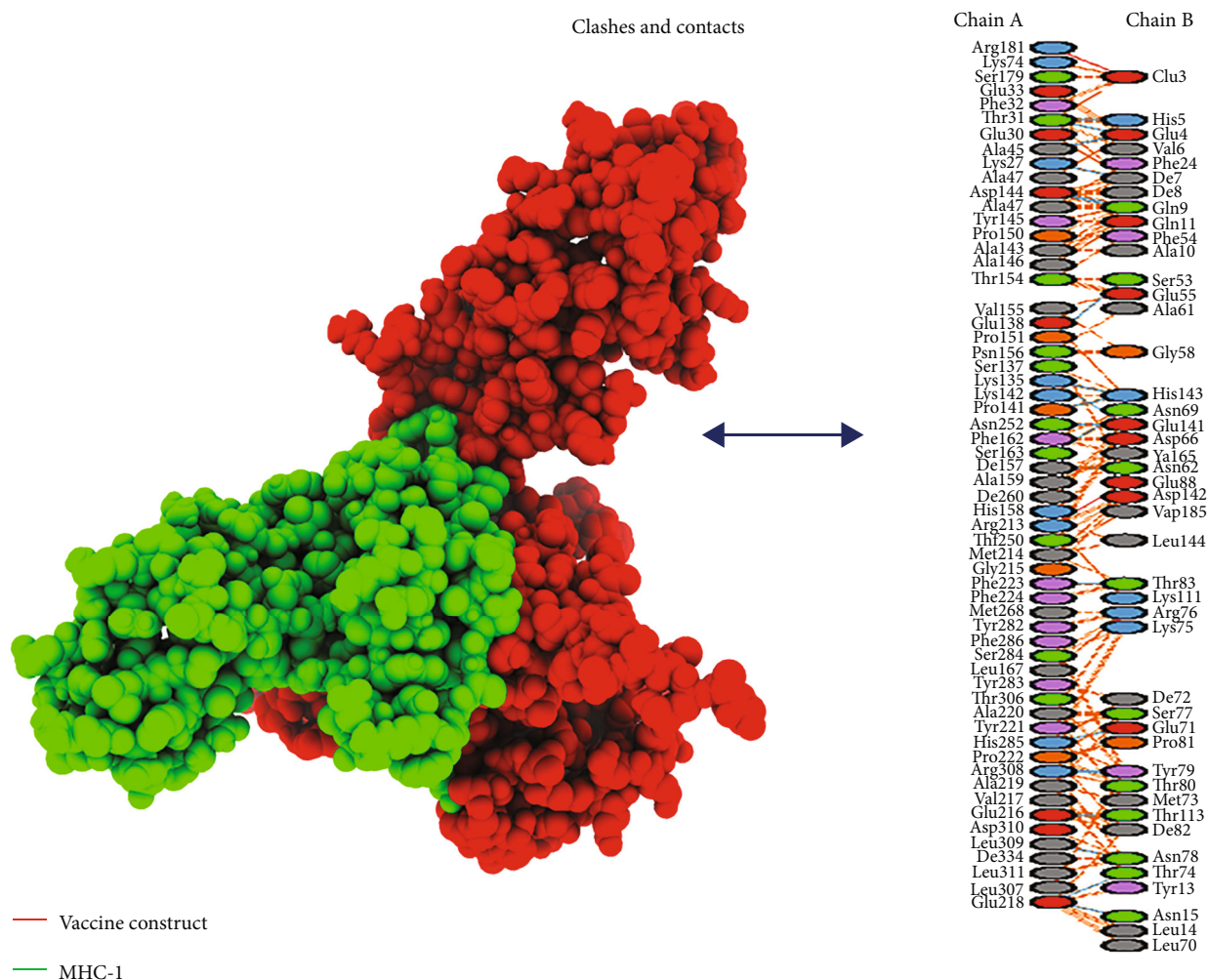
FIGURE 5: Interaction of vaccine construct with MHC-I construct. The red part is of the vaccine, and the green one is indicating the MHC-I construct; clashes and contacts are also given.

the vaccination must have excellent B cell epitope domains. Using default settings, it was utilized to predict 24 linear-continuous and 3 conformational-discontinuous vaccine constructs using ABCPred 2.0. The conformational B cell epitopes in the vaccine design were visualized using PyMOL v.1.3, a molecular graphic system.

3.9. Molecular Docking. An active immune response requires effective antigen-receptor interaction. Using HADDOCK v.2.4, the vaccine was docked with TLR4, MHC-I, and MHC-II receptors (immune receptors of humans). TLR4 facilitates an effective immune response to bacterial recognition. Vaccine and TLR4 show a substantial interaction, according to the docking data. The TLR4 vaccine binding score was calculated to be 635.2 kcal/mol. On the map, TLR4 was shown in cyan, whereas MEBSV was shown in green (Figure 4). It was discovered that TLR4 and vaccination had desolvation energy within a range of -51.1 kcal⁻¹. With the use of the HADDOCK v.2.4 software, the vaccine structure was also docked with the MHC-I and MHC-II receptors. HADDOCK scores of 345.4 and 279.8 were found, respectively, with desolvation energies of -43.3 kcal⁻¹ and

-67.6 kcal⁻¹. The docking results are displayed in Table 5. Eleven (11) hydrogen bond interactions were discovered in the docked complex of MHC-II and vaccine design. However, there were seven interacting residues in the MHC-I complex, as illustrated in Figures 5 and 6.

3.10. Normal Mode Analysis. The normal mode analysis (NMA) was utilized to explore the mobility and stability of proteins on a wide scale. The iMODS server was employed for it, which relied on the internal coordinates of the docked complex. Individual residue distortion determined the complex's deformability, as evidenced by the chain's hinges (Figure 7(b)). The value for the complex was calculated as $2.974921e - 05$ (Figure 7(a)). The eigenvalue was calculated by inverting the variance associated with each normal mode [79]. As a consequence of the normal mode analysis, the B-factor value was proportional to RMS (Figure 7(c)). A covariance matrix represents the pairings of residue pairs, with different colors representing associated, disassociated, or irrelevant movements, such as red, blue, and white (Figure 7(d)). The elastic map showed spring-connected joint atoms, with each point representing one spring and a
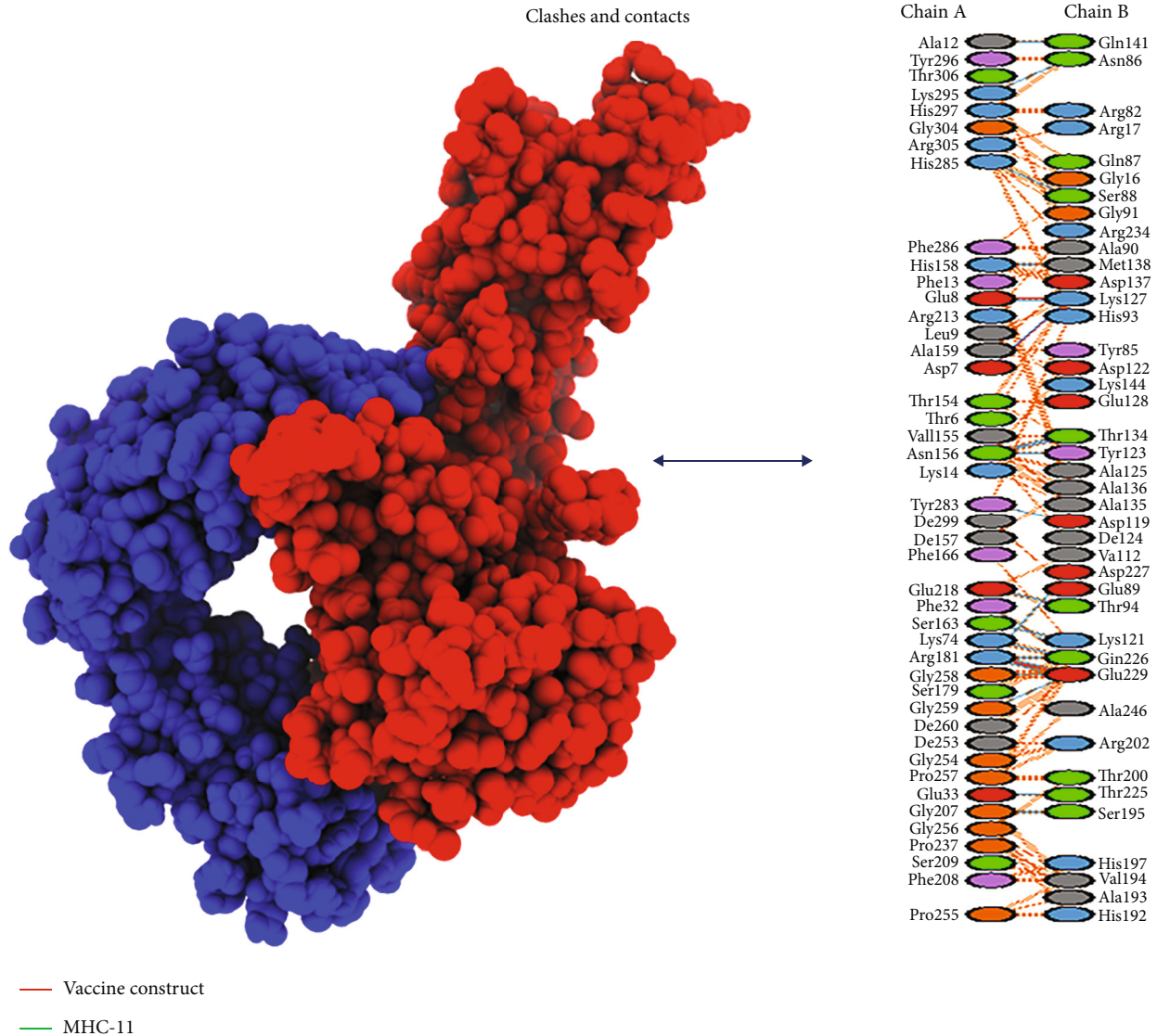
FIGURE 6: Interaction of vaccine construct with MHC-II construct. The blue part depicts the MHC-II and clashes, and contacts are given on the right side of the figure.

grey color indicating stiffer locations, with intensity proportional to stiffness (Figure 7(e)). These results have been evaluated for TLR4 because it is a universal human receptor to compare any results through it [80].

3.11. Immune Simulation. Every secondary and primary immune response contributes to distinct immunological responses to diseases. The host immune system responds to the antigen in silico as shown in Figure 8. The results of the simulations of the candidate vaccine were found to be very similar. Both the candidate vaccine and the control showed a significant drop in the number of antigens over time. After the second and third doses of the candidate vaccine, the levels of antibodies were much higher. There was a rise in IgG+IgM and a fall in antigen in the secondary and primary stages of the initial reaction, which was characterized by high levels of IgG+IgM and IgM. The effectiveness of interleukin and cytokine reactions has been discovered as indicated; there was an effective immunological response to the vaccine, as well as clearance after consecutive treatments (Figure 8).

3.12. In Silico Cloning. Codon optimization and in silico cloning were utilized to validate that the vaccine protein was successfully produced in the E. coli host system. The vaccine's codons are identical to the E. coli K12 codon of the potential host. First, the vaccine sequence was reversed and transcribed to make the cDNA of the vaccine, and then, some changes have been done if needed to enhance the GC contents of the sequence and CAI value. In enhanced DNA, the CAI value was 0.9, and the GC content value was 48.87 percent. The synthesized codon was inserted into the E. coli vector pET 30a (+) between Nco1 and restriction sites. Additionally, the clone was 6452 bp in length (Figure 9).

(a)

(b)

(c)

(d)

(e)
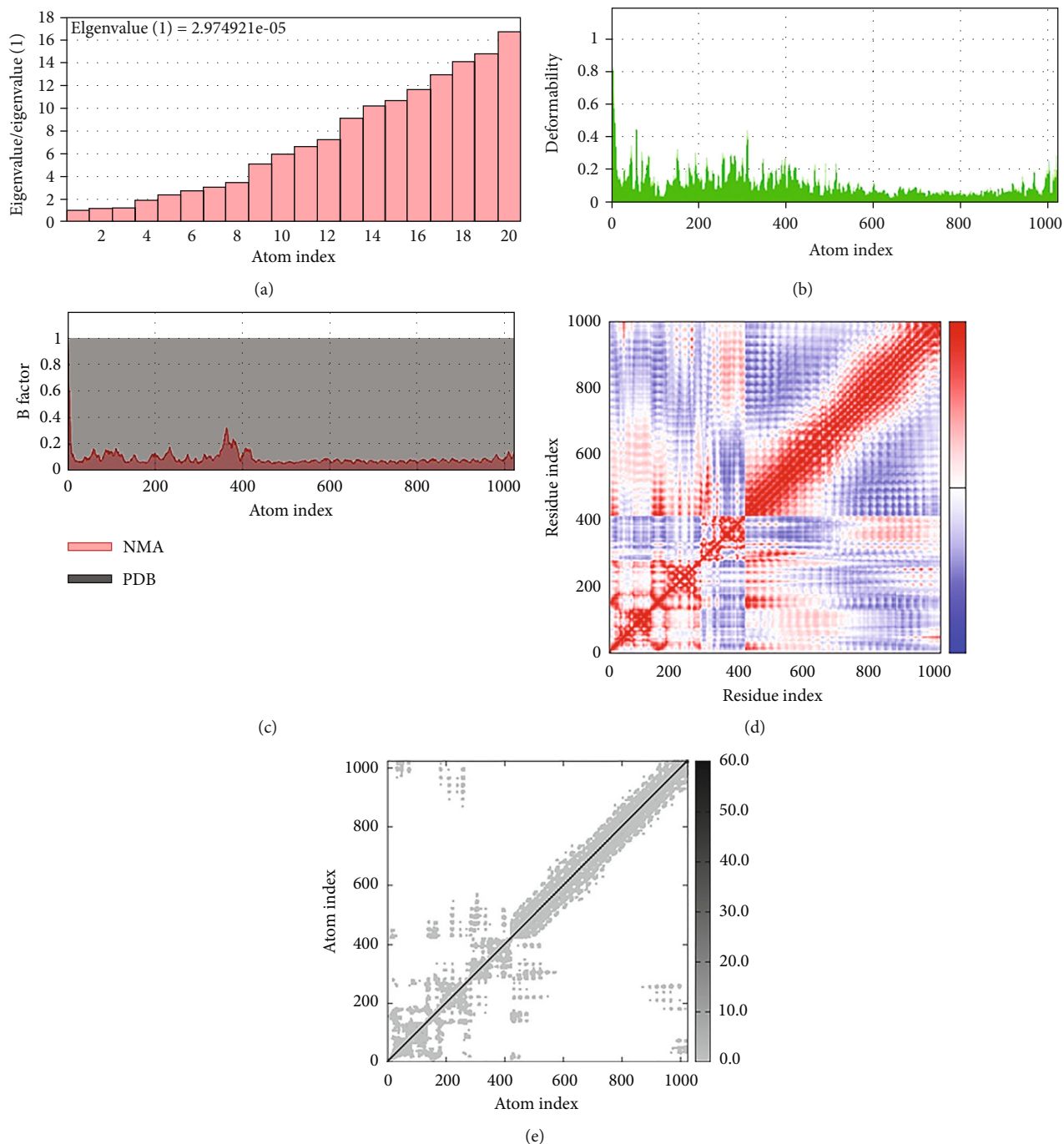
Figure 7: (a–e) Molecular dynamic simulation of the vaccine-TLR4 complex, showing (a) eigenvalue, (b) deformability, (c) B-factor, (d) covariance matrix, and (e) elastic network analysis.

4. Discussion

Despite advancements in the treatment of infectious diseases, pathogenic microorganisms continue to pose the greatest threat to public health, while conventional vaccines have largely been responsible for the treatment or eradication of some pathogens, the rapid emergence of infectious diseases necessitates new approaches to vaccine development [81]. Traditional vaccine production techniques require the cultivation of pathogenic microorganisms and

identifying their immunogenic components, which takes time and can only detect antigens that are highly produced and purified [82]. Protein abundance does not always imply immunogenicity, and antigens produced *in vivo* during pathogenesis cannot always be produced in *in vitro* conditions. Possible surface proteins were identified using a strategy that begins with the genome rather than the microbe and uses computational tools and pattern recognition to identify them [83]. As a result, in addition to finding all antigens that can be investigated using traditional approaches, this

(a)

(b)
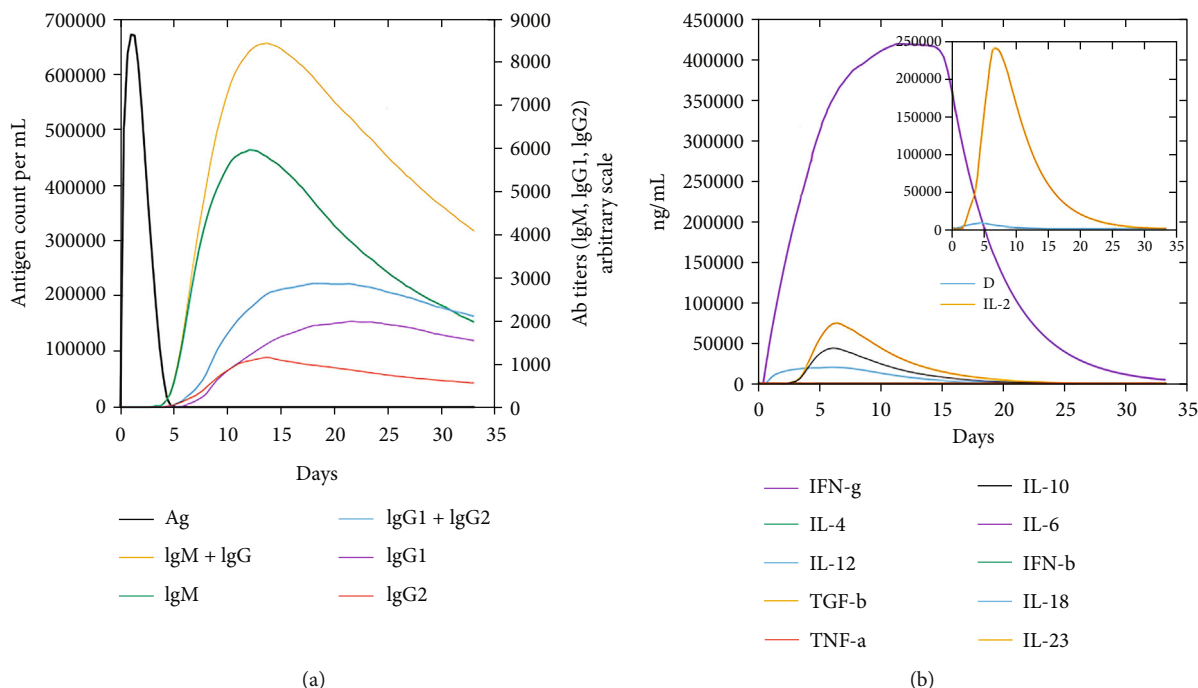
FIGURE 8: (a, b) In silico immune responses of vaccine as an antigen: (a) immunoglobulin generation and B cell isotypes following exposure in different states with the Simpson index to the antigen; (b) development of cytokine and interleukins.

method can also identify novel antigens critical to new vaccines' immunogenicity. By focusing on *in silico* investigations, vaccine design and manufacture can be completed in the quickest possible time [84]. In reality, this form of vaccine creation is a comprehensive and successful example of computer-aided biotechnology, which was originally utilized to overcome the limitations of traditional methods [85]. Based on these ideas, "immune informatics," a bioinformatics approach focusing on immunology and vaccination, has arisen. Immunoinformatics is currently regarded as a powerful example of applied bioinformatics in the field of immunology. A reverse vaccinology design demonstrates how immune informatics may help and validate biotechnological research [86].

The amino acid sequences of antigens were downloaded from NCBI for the first phase in the current investigation to build a multiepitope vaccine against *Legionella pneumophila.* Then, using an immune informatics technique, possible CTL, HTL, and LBL epitopes were predicted and examined. Multi T cell epitope subunit vaccinations are currently gaining popularity. Subunit epitope vaccines have several benefits, including low cost, high specificity, and safety. Some bioinformatics and immune informatics technologies have been created in recent years that are useful in vaccine design. Recognizing immunogenic epitopes from protective antigens is critical for developing epitope-based subunit vaccines. Immunoinformatics techniques can find random/indiscriminate immune-dominant epitopes from any protein, saving time and money while also assisting in identifying appropriate epitopes.

Epitopes of CTL, HTL, and B cell were predicted to develop the construct vaccine based on their immunogeni-city and antigenicity. Helper T cells that deliver cytokines including interleukin-4 (IL-4), interferon-gamma (IFN-γ), and interleukin-10 (IL-10) may minimize tissue damage by preventing proinflammatory responses. Cytotoxic T cells, B lymphocytes, the innate immune system, and other immune cells are all stimulated by helper T cells. As a result, during the selection of the fusion construct vaccine, the capacity of specific HTL epitopes to induce cytokine was also evaluated. GPGPG, AAY, and KK linkers were used to bind HTL, CTL, and B cell epitopes, respectively, to finish the vaccine assembly. In developing vaccine peptides, linkers can help in expression, stability, and folding. The vaccine we produced has a molecular weight of 46284.37 kDa in this research, which falls in the normal range of a multi-epitope-based vaccine's molecular weight. The solubility of overexpressed recombinant proteins within an *E. coli* host is crucial in functional and biochemical investigations [87]. By comparing these results with the previously published papers, we found that results of our research work were similar according to the standards [72, 88]. The produced vaccine protein's solubility was observed, indicating that it has simple access to the host. The theoretical pI value was determined to validate the vaccine's potential, exhibiting basic nature. Moreover, the stability index forecast in our study validates the protein's stability following expression, representing an increase in its usage capacity. The aliphatic index and GRAVY score, respectively, measure thermostability and hydrophilicity [89]. The 3D structure of a protein provides information on the protein's unique assembly and helps understand protein dynamics and protein-ligand interactions of other proteins. The vaccine's desired properties were significantly improved once it was refined.
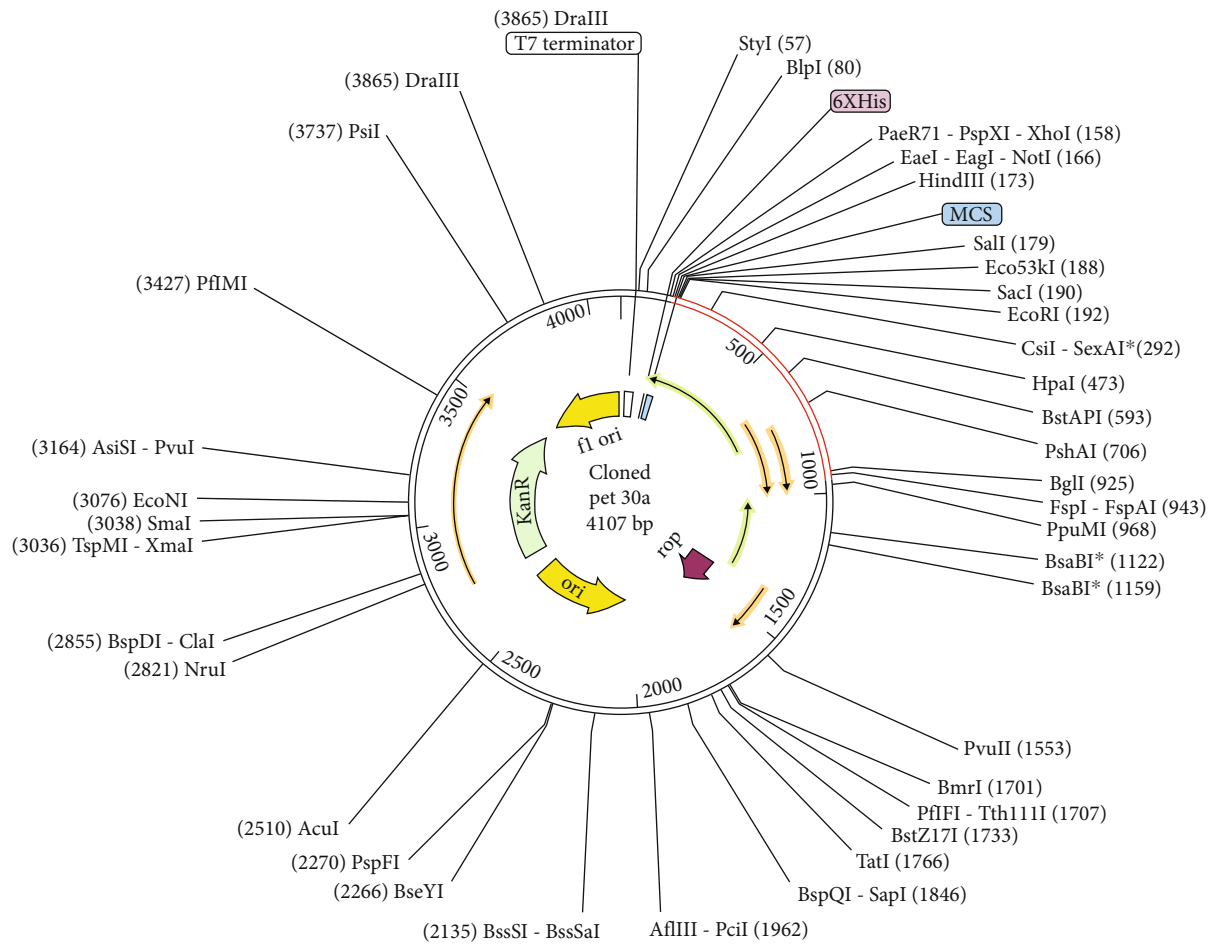
FIGURE 9: In silico cloning of codon-optimized vaccine into E. coli K12 expression system. The plasmid backbone is kept in black while the inserted DNA sequence is shown in red color.

Only a few residues were found in the prohibited zone by the Ramachandran plot, whereas the majority were found in preferred regions (92.9 percent). This further confirmed the entire model's adequacy in terms of quality. Additionally, energy minimization was used to minimize the system's potential energy and stabilize the entire structure of the multiepitope vaccine. Molecular dynamic simulation and ligand-receptor docking studies were used to assess the stability and potential immunological interaction between multiepitope vaccination and TLR4, MHC-I, and MHC-II as adjuvant. Serological testing of a vaccine's immunological function is one of the preliminary steps in its certification [90]. Immune simulation was performed to validate the immunity response of the body after injecting the constructed vaccine, and the results were compared to standards mentioned in previous publications [72]. A suitable host must be used to express the recombinant protein. To make recombinant proteins, E. coli expression methods were used. In this study, codon optimization was aimed at achieving high-level recombinant vaccine protein expression in E. coli K12. The obtained values for GC content (50.51 percent) and codon adaptation are supposed to predict protein expression in bacteria (0.97). Improving protein stability in many mechanical and biological applications is the primary goal. This research employed immune informatics to create a new multiepitope vaccination against L. pneumophila that potentially induces immunological responses mediated by cells and humoral immune responses.

5. Conclusions

L. pneumophila is a global health threat as medication or vaccinations are still ineffective in treating or preventing it. Antibacterial drugs have been studied, but none are efficient in avoiding its infection. Using subtractive genomics and immunoinformatics, the main goal of making a MEBS vaccine is to control the body's humoral and cellular immune responses. Using subtractive genomics, the therapeutic proteins needed for bacterial survival but not found in the host were found. The proposed MEBSV model, when combined with computer analyses and immune-information data, could lead to the development of a possible vaccine against L. pneumophila. Further research is needed to establish the MEBS vaccine model's efficiency and safety.

Data Availability

All available data are included in the manuscript.

Conflicts of Interest

The authors report no conflicts of interest for this work.

Authors' Contributions

Ahitsham Umar worked on conceptualization, methodology, software, and original draft preparation. Sadia Liaquat and Israr Fatima worked on data curation and writing—original draft preparation. Abdur Rehman and Danish Rasool worked on visualization, investigation, and software. Abdulrahman Alshammari and Metab Alharbi worked on software, validation, and original draft preparation. Muhammad Shahid Riaz Rajoka and Mohsin Khurshid worked on software, validation, and original draft preparation. Asma Haque and Usman Ali Ashfaq worked on project administration and writing—reviewing and editing.

Acknowledgments

Supplementary Materials

The data used to support the findings of this study are included within Supplementary Materials. Table S1: final MHC-I epitopes selected on the basis of different parameters. Table S2: final MHC-II epitopes selected on the basis of different parameters. Table S3: final B cell epitopes selected on the basis of different parameters. (*Supplementary Materials*)

References

[1] M. Saad, F. R. Castiello, S. P. Faucher, and M. Tabrizian, "Introducing an SPRi-based titration assay using aptamers for the detection of Legionella pneumophila," *Sensors and Actuators B: Chemical*, vol. 351, p. 130933, 2021.

[2] D. S. Zamboni, S. McGrath, M. Rabinovitch, and C. R. Roy, "Coxiella burnetii express type IV secretion system proteins that function similarly to components of the Legionella pneumophila Dot/Icm system," *Molecular Microbiology*, vol. 49, no. 4, pp. 965–976, 2003.

[3] T. Zusman, G. Yerushalmi, and G. Segal, "Functional similarities between the icm/dot pathogenesis systems of Coxiella burnetii and Legionella pneumophila," *Infection and Immunity*, vol. 71, no. 7, pp. 3714–3723, 2003.

[4] J. Chen, K. S. de Felipe, M. Clarke et al., "Legionella effectors that promote nonlytic release from protozoa," *Science*, vol. 303, no. 5662, pp. 1358–1361, 2004.

[5] D. W. Fraser, T. R. Tsai, W. Orenstein et al., "Legionnaires' disease," *New England Journal of Medicine*, vol. 297, no. 22, pp. 1189–1197, 1977.

[6] B. S. Fields, R. F. Benson, and R. E. Besser, "Legionella and Legionnaires disease: 25 years of investigation," *Clinical Microbiology Reviews*, vol. 15, no. 3, pp. 506–526, 2002.

[7] I. G. Gonçalves, L. C. Simões, and M. L. Simões, *Legionella pneumophila*, 2021.

[8] J. Shen, M. Kong, B. Dong, M. J. Birnkrant, and J. Zhang, "A systematic approach to estimating the effectiveness of multi-scale IAQ strategies for reducing the risk of airborne infection of SARS-CoV-2," *Building and Environment*, vol. 200, p. 107926, 2021.

[9] W. J. Rhoads and F. Hammes, "Growth of Legionella during COVID-19 lockdown stagnation," *Environmental Science: Water Research & Technology*, vol. 7, no. 1, pp. 10–15, 2021.

[10] M. Scaturro, M. C. Rota, M. G. Caporali et al., "A community-acquired Legionnaires' disease outbreak caused by Legionella pneumophila serogroup 2: an uncommon event, Italy, August to October 2018," *Eurosurveillance*, vol. 26, no. 25, p. 2001961, 2021.

[11] K. Cassell, J. L. Davis, and R. Berkelman, "Legionnaires' disease in the time of COVID-19," *Pneumonia*, vol. 13, no. 1, pp. 1–3, 2021.

[12] E. Portal, G. Descours, C. Ginevra et al., "Legionella antibiotic susceptibility testing: is it time for international standardization and evidence-based guidance?," *Journal of Antimicrobial Chemotherapy*, vol. 76, no. 5, pp. 1113–1116, 2021.

[13] D. Toplitsch, S. Platzer, R. Zehner, S. Maitz, F. Mascher, and C. Kittinger, "Comparison of updated methods for Legionella detection in environmental water samples," *International Journal of Environmental Research and Public Health*, vol. 18, no. 10, p. 5436, 2021.

[14] C. K. Huang, A. Weerasekara, P. L. Bond, K. D. Weynberg, and J. Guo, "Characterizing the premise plumbing microbiome in both water and biofilms of a 50-year-old building," *Science of the Total Environment*, vol. 798, p. 149225, 2021.

[15] L.-J. Alshae'R, M. Flood, and J. B. Rose, "Enumeration and characterization of five pathogenic legionella species from large research and educational buildings," *Environmental Science: Water Research & Technology*, vol. 7, no. 2, pp. 321–334, 2021.

[16] M. J. Taylor, R. H. Bentham, and K. E. Ross, "Limitations of using propidium monoazide with qPCR to discriminate between live and DeadLegionellain biofilm samples," *Microbiology insights*, vol. 7, p. MBI.S17723, 2014.

[17] J. Gentry-Shields, A. Wang, R. M. Cory, and J. R. Stewart, "Determination of specific types and relative levels of qPCR inhibitors in environmental water samples using excitation-emission matrix spectroscopy and PARAFAC," *Water Research*, vol. 47, no. 10, pp. 3467–3476, 2013.

[18] H. H. Nguyen, J. Park, S. Kang, and M. Kim, "Surface plasmon resonance: a versatile technique for biosensor applications," *Sensors*, vol. 15, no. 5, pp. 10481–10510, 2015.

[19] D. Wang, J. F. C. Loo, J. Chen et al., "Recent advances in surface plasmon resonance imaging sensors," *Sensors*, vol. 19, no. 6, p. 1266, 2019.

[20] E. De Gregorio and R. Rappuoli, "Vaccines for the future: learning from human immunology," *Microbial Biotechnology*, vol. 5, no. 2, pp. 149–155, 2012.

[21] A. Patronov and I. Doytchinova, "T-cell epitope vaccine design by immunoinformatics," *Open Biology*, vol. 3, no. 1, p. 120139, 2013.

[22] N. Gupta, H. Regar, V. K. Verma, D. Prusty, A. Mishra, and V. K. Prajapati, "Receptor-ligand based molecular interaction to discover adjuvant for immune cell TLRs to develop next-generation vaccine," *International Journal of Biological Macromolecules*, vol. 152, pp. 535–545, 2020.

[23] S. Ahmad, Y. Waheed, S. Ismail, S. W. Abbasi, and M. H. Najmi, "A computational study to disclose potential drugs and vaccine ensemble for COVID-19 conundrum," *Journal of Molecular Liquids*, vol. 324, p. 114734, 2021.

[24] U. Consortium, "UniProt: a hub for protein information," *Nucleic Acids Research*, vol. 43, no. D1, pp. D204–D212, 2015.

[25] Q.-F. Wen, S. Liu, C. Dong, H.-X. Guo, Y.-Z. Gao, and F.-B. Guo, "Geptop 2.0: an updated, more precise, and faster Geptop server for identification of prokaryotic essential genes," *Frontiers in Microbiology*, vol. 10, p. 1236, 2019.

[26] R. Lavigne, D. Seto, P. Mahadevan, H.-W. Ackermann, and A. M. Kropinski, "Unifying classical and molecular taxonomic classification: analysis of the _Podoviridae_ using BLASTP-based tools," *Research in Microbiology*, vol. 159, no. 5, pp. 406–414, 2008.

[27] M. Faria, N. Bordin, J. Kizina, J. Harder, D. Devos, and O. M. Lage, "_Planctomycetes_ attached to algal surfaces: insight into their genomes," *Genomics*, vol. 110, no. 5, pp. 231–238, 2018.

[28] I. A. Doytchinova and D. R. Flower, "VaxiJen: a server for prediction of protective antigens, tumour antigens and subunit vaccines," *BMC Bioinformatics*, vol. 8, no. 1, pp. 1–7, 2007.

[29] A. Krogh, B. Larsson, G. Von Heijne, and E. L. Sonnhammer, "Predicting transmembrane protein topology with a hidden markov model: application to complete genomes1," *Journal of Molecular Biology*, vol. 305, no. 3, pp. 567–580, 2001.

[30] B. Ahmad, U. A. Ashfaq, M.-u. Rahman, M. S. Masoud, and M. Z. Yousaf, "Conserved B and T cell epitopes prediction of ebola virus glycoprotein for vaccine development: an immuno-informatics approach," *Microbial Pathogenesis*, vol. 132, pp. 243–253, 2019.

[31] R. Vita, J. A. Overton, J. A. Greenbaum et al., "The immune epitope database (IEDB) 3.0," *Nucleic Acids Research*, vol. 43, no. D1, pp. D405–D412, 2015.

[32] S. Gupta, P. Kapoor, K. Chaudhary et al., "In silico approach for predicting toxicity of peptides and proteins," *PLoS One*, vol. 8, no. 9, p. e73957, 2013.

[33] N. Zaharieva, I. Dimitrov, D. R. Flower, and I. Doytchinova, "VaxiJen dataset of bacterial immunogens: an update," *Current Computer-Aided Drug Design*, vol. 15, no. 5, pp. 398–400, 2019.

[34] I. Dimitrov, L. Naneva, I. Doytchinova, and I. Bangov, "AllergenFP: allergenicity prediction by descriptor fingerprints," *Bioinformatics*, vol. 30, no. 6, pp. 846–851, 2014.

[35] J. Zhu and W. E. Paul, "CD4 T cells: fates, functions, and faults," *Blood*, vol. 112, no. 5, pp. 1557–1569, 2008.

[36] V. L. Rishi, Z. Rui, D. V. Asha, and X. Bing, "CD4+ T cells: differentiation and functions," *Clinical & Developmental Immunology*, vol. 2012, p. 925135, 2012.

[37] S. K. Dhanda, P. Vir, and G. P. Raghava, "Designing of interferon-gamma inducing MHC class-II binders," *Biology Direct*, vol. 8, no. 1, pp. 1–15, 2013.

[38] A. Karkhah, M. Saadi, and H. R. Nouri, "In silico analyses of heat shock protein 60 and calreticulin to designing a novel vaccine shifting immune response toward T helper 2 in atherosclerosis," *Computational Biology and Chemistry*, vol. 67, pp. 244–254, 2017.

[39] G. Nagpal, S. S. Usmani, S. K. Dhanda et al., "Computer-aided designing of immunosuppressive peptides based on IL-10 inducing potential," *Scientific Reports*, vol. 7, no. 1, pp. 1–10, 2017.

[40] M. D. Cooper, "The early history of B cells," *Nature Reviews Immunology*, vol. 15, no. 3, pp. 191–197, 2015.

[41] S. Saha and G. P. S. Raghava, "Prediction of continuous B-cell epitopes in an antigen using recurrent neural network," *Proteins: Structure, Function, and Bioinformatics*, vol. 65, no. 1, pp. 40–48, 2006.

[42] U. K. Adhikari and M. M. Rahman, "Overlapping CD8 \+ and CD4 \+ T-cell epitopes identification for the progression of epitope-based peptide vaccine from nucleocapsid and glycoprotein of emerging Rift Valley fever virus using immunoinformatics approach," *Genetics and Evolution*, vol. 56, pp. 75–91, 2017.

[43] Z. Nain, F. Abdulla, M. M. Rahman et al., "Proteome-wide screening for designing a multi-epitope vaccine against emerging pathogenElizabethkingia anophelisusing immunoinformatic approaches," *Journal of Biomolecular Structure and Dynamics*, vol. 38, no. 16, pp. 4850–4867, 2020.

[44] E. Ong, Y. He, and Z. Yang, "Epitope promiscuity and population coverage of _Mycobacterium tuberculosis_ protein antigens in current subunit vaccines under development," *Genetics and Evolution*, vol. 80, p. 104186, 2020.

[45] S. F. Altschul, W. Gish, W. Miller, E. W. Myers, and D. J. Lipman, "Basic local alignment search tool," *Journal of Molecular Biology*, vol. 215, no. 3, pp. 403–410, 1990.

[46] V. K. Garg, H. Avashthi, A. Tiwari et al., "MFPPI–multi FASTA ProtParam interface," *Bioinformation*, vol. 12, no. 2, pp. 74–77, 2016.

[47] I. Dimitrov, D. R. Flower, and I. Doytchinova, "AllerTOP-a server for in silico prediction of allergens," *BMC Bioinformatics*, vol. 14, no. S6, pp. 1–9, 2013.

[48] G. Deléage, "ALIGNSEC: viewing protein secondary structure predictions within large multiple sequence alignments," *Bioinformatics*, vol. 33, no. 24, pp. 3991-3992, 2017.

[49] C. N. Magnan, M. Zeller, M. A. Kayala et al., "High-throughput prediction of protein antigenicity using protein microarray data," *Bioinformatics*, vol. 26, no. 23, pp. 2936–2943, 2010.

[50] Y. Zhang, "I-TASSER server for protein 3D structure prediction," *BMC Bioinformatics*, vol. 9, no. 1, pp. 1–8, 2008.

[51] J. Ko, H. Park, L. Heo, and C. Seok, "GalaxyWEB server for protein structure prediction and refinement," *Nucleic Acids Research*, vol. 40, no. W1, pp. W294–W297, 2012.

[52] S. C. Lovell, I. W. Davis, W. B. Arendall et al., "Structure validation by Cα geometry: ϕ, ψ and Cβ deviation," *Proteins: Structure, Function, and Bioinformatics*, vol. 50, no. 3, pp. 437–450, 2003.

[53] M. Wiederstein and M. J. Sippl, "ProSA-web: interactive web service for the recognition of errors in three-dimensional structures of proteins," *Nucleic Acids Research*, vol. 35, no. Web Server, pp. W407–W410, 2007.

[54] M. Lengths and M. Angles, *Limitations of Structure Evaluation Tools Errat*, 2018.

[55] S. K. Dhanda, S. Mahajan, S. Paul et al., "IEDB-AR: immune epitope database—analysis resource in 2019," *Nucleic Acids Research*, vol. 47, no. W1, pp. W502–W506, 2019.

[56] G. Van Zundert, J. Rodrigues, M. Trellet et al., "The HADDOCK2.2 web server: user-friendly integrative modeling of biomolecular complexes," *Journal of Molecular Biology*, vol. 428, no. 4, pp. 720–725, 2016.

[57] S. J. De Vries, M. Van Dijk, and A. M. Bonvin, "The HADDOCK web server for data-driven biomolecular docking," *Nature Protocols*, vol. 5, no. 5, pp. 883–897, 2010.

[58] U. Ohto, N. Yamakawa, S. Akashi-Takamura, K. Miyake, and T. Shimizu, "Structural analyses of human toll-like receptor 4 polymorphisms D299G and T399I," *Journal of Biological Chemistry*, vol. 287, no. 48, pp. 40611–40617, 2012.

[59] M. S. Jin, S. E. Kim, J. Y. Heo et al., "Crystal structure of the TLR1-TLR2 heterodimer induced by binding of a tri-acylated lipopeptide," *Cell*, vol. 130, no. 6, pp. 1071–1082, 2007.

[60] T. J. Kirksey, R. R. Pogue-Caley, J. A. Frelinger, and E. J. Collins, "The structural basis for the increased immunogenicity of two HIV-reverse transcriptase peptide variant/class I major histocompatibility complexes," *Journal of Biological Chemistry*, vol. 274, no. 52, pp. 37259–37264, 1999.

[61] M. M. Mullen, K. M. Haan, R. Longnecker, and T. S. Jardetzky, "Structure of the Epstein-Barr virus gp42 protein bound to the MHC class II receptor HLA-DR1," *Molecular Cell*, vol. 9, no. 2, pp. 375–385, 2002.

[62] R. A. Laskowski, J. Jabłońska, L. Pravda, R. S. Vařeková, and J. M. Thornton, "PDBsum: structural summaries of PDB entries," *Protein Science*, vol. 27, no. 1, pp. 129–134, 2018.

[63] W. L. DeLano, "Pymol: an open-source molecular graphics tool," *CCP4 Newsletter on Protein Crystallography*, vol. 40, no. 1, pp. 82–92, 2002.

[64] D. M. Van Aalten, B. L. De Groot, J. B. Findlay, H. J. Berendsen, and A. Amadei, "A comparison of techniques for calculating protein essential dynamics," *Journal of Computational Chemistry*, vol. 18, no. 2, pp. 169–181, 1997.

[65] K. Wüthrich, G. Wagner, R. Richarz, and W. Braun, "Correlations between internal mobility and stability of globular proteins," *Biophysical Journal*, vol. 32, no. 1, pp. 549–560, 1980.

[66] J. R. López-Blanco, J. I. Aliaga, E. S. Quintana-Ortí, and P. Chacón, "iMODS: internal coordinates normal mode analysis server," *Nucleic Acids Research*, vol. 42, no. W1, pp. W271–W276, 2014.

[67] M. Pritam, G. Singh, S. Swaroop, A. K. Singh, B. Pandey, and S. P. Singh, "A cutting-edge immunoinformatics approach for design of multi-epitope oral vaccine against dreadful human malaria," *International Journal of Biological Macromolecules*, vol. 158, pp. 159–179, 2020.

[68] S. Banerjee, K. Majumder, G. J. Gutierrez, D. Gupta, and B. Mittal, *Immuno-Informatics Approach for Multi-Epitope Vaccine Designing against SARS-CoV-2*, 2020, BioRxiv.

[69] N. Rapin, O. Lund, and F. Castiglione, "Immune system simulation online," *Bioinformatics*, vol. 27, no. 14, pp. 2013-2014, 2011.

[70] A. Grote, K. Hiller, M. Scheer et al., "JCat: a novel tool to adapt codon usage of a target gene to its potential expression host," *Nucleic Acids Research*, vol. 33, no. Web Server, pp. W526–W531, 2005.

[71] A. Rehman, S. Ahmad, F. Shahid et al., "Integrated core proteomics, subtractive proteomics, and immunoinformatics investigation to unveil a potential multi-epitope vaccine against schistosomiasis," *Vaccine*, vol. 9, no. 6, p. 658, 2021.

[72] A. Safavi, A. Kefayat, E. Mahdevar, A. Abiri, and F. Ghahremani, "Exploring the out of sight antigens of SARS-CoV-2 to design a candidate multi- epitope vaccine by utilizing immunoinformatics approaches," *Vaccine*, vol. 38, no. 48, pp. 7612–7628, 2020.

[73] A. Safavi, A. Kefayat, A. Abiri, E. Mahdevar, A. H. Behnia, and F. Ghahremani, "_In silico_ analysis of transmembrane pro-

[74] A. Safavi, A. Kefayat, F. Sotoodehnejadnematalahi, M. Salehi, and M. H. Modarressi, "In silico analysis of synaptonemal complex protein 1 (SYCP1) and acrosin binding protein (ACRBP) antigens to design novel multiepitope peptide cancer vaccine against breast cancer," *International Journal of Peptide Research and Therapeutics*, vol. 25, no. 4, pp. 1343–1359, 2019.

[75] B. Livingston, C. Crimi, M. Newman et al., "A rational strategy to design multiepitope immunogens based on multiple Th lymphocyte epitopes," *The Journal of Immunology*, vol. 168, no. 11, pp. 5499–5506, 2002.

[76] N. Nezafat, Z. Karimi, M. Eslami, M. Mohkam, S. Zandian, and Y. Ghasemi, "Designing an efficient multi-epitope peptide vaccine against _Vibrio cholerae via_ combined immunoinformatics and protein interaction based approaches," *Computational Biology and Chemistry*, vol. 62, pp. 82–95, 2016.

[77] R. Arai, H. Ueda, A. Kitayama, N. Kamiya, and T. Nagamune, "Design of the linkers which effectively separate domains of a bifunctional fusion protein," *Protein Engineering*, vol. 14, no. 8, pp. 529–532, 2001.

[78] F. E. Lund, "Cytokine-producing B lymphocytes – key regulators of immunity," *Current Opinion in Immunology*, vol. 20, no. 3, pp. 332–338, 2008.

[79] J. A. Kovacs, P. Chacón, and R. Abagyan, "Predictions of protein flexibility: first-order measures," *Proteins: Structure, Function, and Bioinformatics*, vol. 56, no. 4, pp. 661–668, 2004.

[80] A. Umar, A. Haque, Y. S. Alghamdi et al., "Development of a candidate multi-epitope subunit vaccine against Klebsiella aerogenes: subtractive proteomics and immuno-informatics approach," *Vaccine*, vol. 9, no. 11, p. 1373, 2021.

[81] R. Arnon and T. Ben-Yedidia, "Old and new vaccine approaches," *International Immunopharmacology*, vol. 3, no. 8, pp. 1195–1204, 2003.

[82] B. Temizoz, E. Kuroda, and K. J. Ishii, "Vaccine adjuvants as potential cancer immunotherapeutics," *International Immunology*, vol. 28, no. 7, pp. 329–338, 2016.

[83] M. N. Davies and D. R. Flower, "Harnessing bioinformatics to discover new vaccines," *Drug Discovery Today*, vol. 12, no. 9-10, pp. 389–395, 2007.

[84] M. Negahdaripour, N. Nezafat, M. Eslami et al., "Structural vaccinology considerations for _in silico_ designing of a multi-epitope vaccine," *Genetics and Evolution*, vol. 58, pp. 96–109, 2018.

[85] D. Serruto, L. Serino, V. Masignani, and M. Pizza, "Genome-based approaches to develop vaccines against bacterial pathogens," *Vaccine*, vol. 27, no. 25-26, pp. 3245–3250, 2009.

[86] B. Korber, M. LaBute, and K. Yusim, "Immunoinformatics comes of age," *PLoS Computational Biology*, vol. 2, no. 6, p. e71, 2006.

[87] N. Khatoon, R. K. Pandey, and V. K. Prajapati, "Exploring Leishmania secretory proteins to design B and T cell multi-epitope subunit vaccine using immunoinformatics approach," *Scientific Reports*, vol. 7, no. 1, pp. 1–12, 2017.

[88] E. Mahdevar, A. Safavi, A. Abiri et al., "Exploring the cancer-testis antigen BORIS to design a novel multi-epitope vaccine against breast cancer based on immunoinformatics approaches," *Journal of Biomolecular Structure and Dynamics*, vol. 40, pp. 1–18, 2022.

[89] S. Vivona, J. L. Gardy, S. Ramachandran et al., "Computer-aided biotechnology: from immuno-informatics to reverse vaccinology," *Trends in Biotechnology*, vol. 26, no. 4, pp. 190–200, 2008.

[90] A. Gori, R. Longhi, C. Peri, and G. Colombo, "Peptides for immunological purposes: design, strategies and applications," *Amino Acids*, vol. 45, no. 2, pp. 257–268, 2013.

Retraction

Retracted: Network Pharmacology-Integrated Molecular Docking Reveals the Expected Anticancer Mechanism of *Picrorhizae Rhizoma* Extract

BioMed Research International

This article has been retracted by Hindawi following an investigation undertaken by the publisher [1]. This investigation has uncovered evidence of one or more of the following indicators of systematic manipulation of the publication process:

(1) Discrepancies in scope

(2) Discrepancies in the description of the research reported

(3) Discrepancies between the availability of data and the research described

(4) Inappropriate citations

(5) Incoherent, meaningless and/or irrelevant content included in the article

(6) Manipulated or compromised peer review

The presence of these indicators undermines our confidence in the integrity of the article's content and we cannot, therefore, vouch for its reliability. Please note that this notice is intended solely to alert readers that the content of this article is unreliable. We have not investigated whether authors were aware of or involved in the systematic manipulation of the publication process.

Wiley and Hindawi regrets that the usual quality checks did not identify these issues before publication and have since put additional measures in place to safeguard research integrity.

We wish to credit our own Research Integrity and Research Publishing teams and anonymous and named external researchers and research integrity experts for contributing to this investigation.

The corresponding author, as the representative of all authors, has been given the opportunity to register their agreement or disagreement to this retraction. We have kept a record of any response received.

References

[1] X. Hu, S. Zhao, Y. Cai et al., "Network Pharmacology-Integrated Molecular Docking Reveals the Expected Anticancer Mechanism of *Picrorhizae Rhizoma* Extract," *BioMed Research International*, vol. 2022, Article ID 3268773, 16 pages, 2022.

Research Article

Network Pharmacology-Integrated Molecular Docking Reveals the Expected Anticancer Mechanism of *Picrorhizae Rhizoma* Extract

Xiaomeng Hu,[1] **Shengchao Zhao,**[1,2] **Yi Cai** ⓘ**,**[3] **Shasank S. Swain** ⓘ**,**[4] **Liangliang Yao** ⓘ**,**[5] **Wei Liu** ⓘ**,**[1] **and Tingdong Yan** ⓘ[2]

[1]*University and College Key Lab of Natural Product Chemistry and Application in Xinjiang, School of Chemistry and Environmental Science, Yili Normal University, Yining 835000, China*

[2]*School of Life Sciences, Shanghai University, 99 Shangda Road, Shanghai 200444, China*

[3]*Guangzhou Municipal and Guangdong Provincial Key Laboratory of Molecular Target & Clinical Pharmacology, The NMPA and State Key Laboratory of Respiratory Disease, School of Pharmaceutical Sciences and the Fifth Affiliated Hospital, Guangzhou Medical University, Guangzhou 511436, China*

[4]*Division of Microbiology and NCDs, ICMR-Regional Medical Research Centre, Bhubaneswar, 751023 Odisha, India*

[5]*Affiliated Hospital of Jiangxi University of Chinese Medicine, Nanchang 330006, China*

Correspondence should be addressed to Wei Liu; nculiuwei@126.com and Tingdong Yan; yantdntu2018@163.com

This study sought to explore the anticancer mechanism of *Picrorhizae Rhizoma* (PR) extract based on network pharmacology and molecular docking. The potential chemicals of PR were screened through the Traditional Chinese Medicine Systems Pharmacology (TCMSP) database and relevant literatures. Corresponding targets of active ingredients were found with the help of the UniProtKB database, and therapeutic targets for cancer action were screened with the help of the GeneCards database. We used Cytoscape software to construct the compound-target-pathway network of PR extract. We utilized the STRING database to obtain the protein-protein interaction (PPI) network. We used DAVID database combining Gene Ontology (GO) analysis and Kyoto Encyclopedia of Genes and Genomes (KEGG) pathway enrichment analysis. Finally, molecular docking was employed for initial efficacy checking. We have identified 16 potential active components of PR through screening, involving 112 disease action targets. Utilizing the GeneCards database, 112 intersecting targets between PR extract and cancer were found, which mainly exerts anticancer effects by regulating tumor necrosis factor (TNF), recombinant caspase 3 (CASP3), c-Jun NH2-terminal kinase (JNK)/JUN, epidermal growth factor receptor (EGFR), and estrogen receptor-1 (ESR1) with some other target genes and pathways associated with cancer. The major anticancer species are prostate cancer, colorectal cancer, small cell lung cancer, etc. In the molecular docking study, herbactin had a strong affinity for TNF. Based on network pharmacology and molecular docking studies, PR and their compounds have demonstrated potential anticancer activities against several key targets. Our preliminary findings provide a strong foundation for further experiments with PR constituents.

1. Introduction

Picrorhizae Rhizoma (PR) is a perennial herb in the Scrophulariaceae family with a similar name to *Rhizoma Coptidis* (RC), and both are products of cold clearing heat and dampness, improving the removal of gastrointestinal dampness and treating dampness and dampness, which are the same herbal medicines for dampness and laxity and dysentery, distributed in Sichuan, Yunnan, Tibet, and Himalayas, with main birth in India. PR is mainly effective in clearing heat, etc. Modern pharmacology has shown that PR has antidiabetic [1], blood glucose and lipid regulation [2],
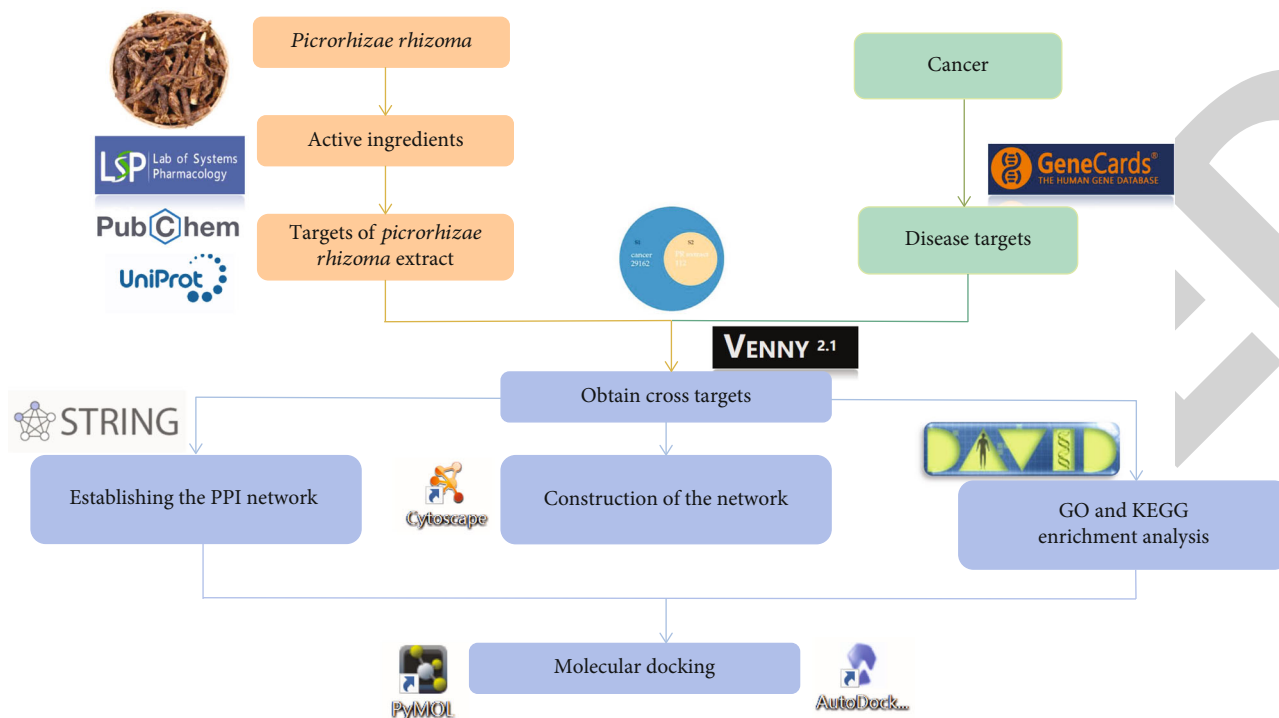
Figure 1: Study step flow diagram.

hepatoprotective and choleretic effects [3, 4], protective effects against neuronal cell injury [5], protective effects against myocardial apoptosis [6, 7], and immunomodulatory effects.

Simultaneously, PR extract has been found to have potential against a wide range of tumors and cancers such as renal cancer [8], esophageal cancer [9], breast cancer [10], and liver cancer [11] by targeting several cancer-regulated enzymes and pathways. Overall, it has shown promising anticancer properties and could be used as alternative anticancer remedies individually as well as synergistically with other mainstream drugs. At present, only articles have analyzed and studied the extracts of PR, such as the biological activity of tetracyclic triterpenes [12]; picroside II has various pharmacological effects, such as anti-inflammatory, antioxidative stress, antiapoptosis, antitumor, and antifibrosis [13], but there are no research reports on the mechanism of action of PR extract on cancer by using the method of network pharmacology; there are also few reports on its antitumor effective components, targets, pathways, and related molecular mechanisms of action.

In this study, the methods of network pharmacology and molecular docking were applied to predict the multitarget multipathway synergy of PR extract against cancer. Technically, the synergistic effects with multicomponents may target multipathways and multitargets as most of traditional Chinese medicine has been reported previously. And that artificial intelligence-based platforms such as network pharmacology and molecular docking offer new perspectives for studying and applying TCM in mainstream medicine within a limited amount of time and resources. This study comprehensively and systematically reveals their mechanism of action, which is of great significance for the development

Table 1: Database and software information used in the experiment.

Name	Website
TCMSP	https://old.tcmsp-e.com/tcmsp.php
UniProt	https://www.uniprot.org/
PubChem	https://pubchem.ncbi.nlm.nih.gov/
Swiss Target Prediction	http://www.swisstargetprediction.ch/
GeneCards	https://www.genecards.org/
Venny 2.1	https://bioinfogp.cnb.csic.es/tools/venny/
STRING	https://cn.string-db.org/
Cytoscape 3.8.2	https://cytoscape.org/release_notes_3_8_2.html
DAVID	https://david.ncifcrf.gov/
ImageGP	http://www.ehbio.com/ImageGP/
AutoDock 1.5.7	https://autodock.scripps.edu/
RCSB PDB	https://www.rcsb.org/
PyMOL	https://pymol.org/2/

and utilization of anticancer efficacy of PR, and provides reference for basic and clinical cancer research. The study step flow diagram is presented in Figure 1.

2. Materials and Methods

As per the hypothesis and objective of the study, we have used several bioinformatics software, tools, and reference databases during analyses (Table 1).

2.1. Screening of Drug Active Ingredients. The active components of PR were identified from the Traditional Chinese

TABLE 2: Potential active ingredient in *Picrorhizae Rhizoma*.

Name	OB (%)	MW	Molecular formula
Herbacetin	36.07	302.25	$C_{15}H_{10}O_7$
(5S)-5,9-Dihydroxy-4-(4-hydroxyphenyl)-5,6-dihydro-1-benzoxocin-2-one	44.34	298.31	$C_{17}H_{14}O_5$
Picroside I_qt	19.40	330.36	$C_{18}H_{18}O_6$
Hederagenin	36.91	472.7	$C_{30}H_{48}O_4$
β-Sitosterol	36.91	414.79	$C_{29}H_{50}O$
Scrophuloside A	33.3	536.58	$C_{26}H_{32}O_{12}$
Picroside I	21.73	492.52	$C_{24}H_{28}O_{11}$
Picroside IV	0.17	508.48	$C_{24}H_{28}O_{12}$
Scrophuloside A_QT	68.83	374.42	$C_{20}H_{22}O_7$
Picroside II_qt	22.45	350.35	$C_{17}H_{18}O_8$
Picroside III	30.45	552.58	$C_{26}H_{31}O_{13}$
Catalpol	5.07	362.37	$C_{15}H_{22}O_{10}$
Catapol_qt	44.69	200.21	$C_9H_{12}O_5$
Picroside II	29.19	512.51	$C_{23}H_{28}O_{13}$
6-Feruloylcatalpol	31.38	538.55	$C_{25}H_{30}O_{13}$
Aucubin	36.56	346.37	$C_{15}H_{22}O_9$
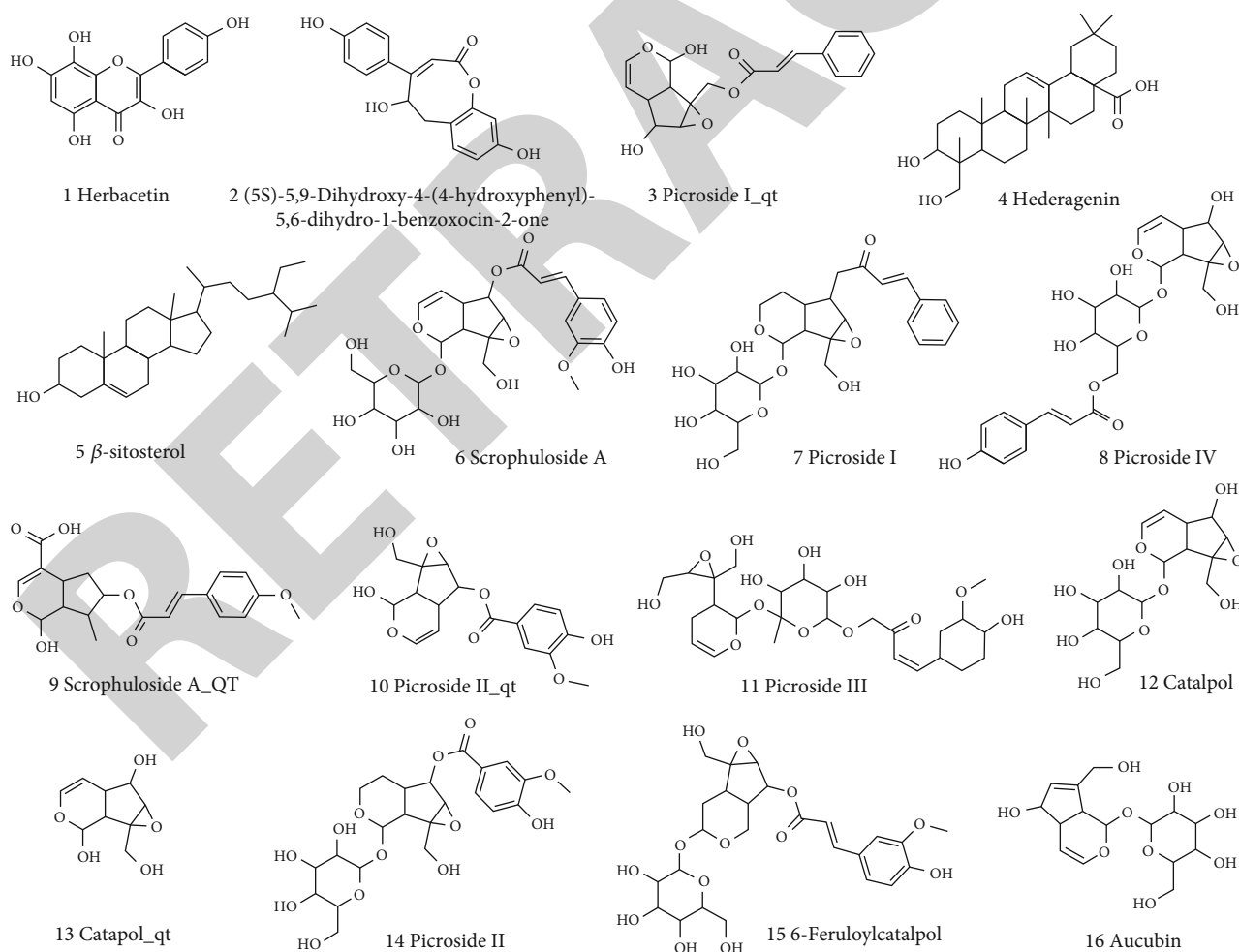
FIGURE 2: The chemical structures of 16 compounds.
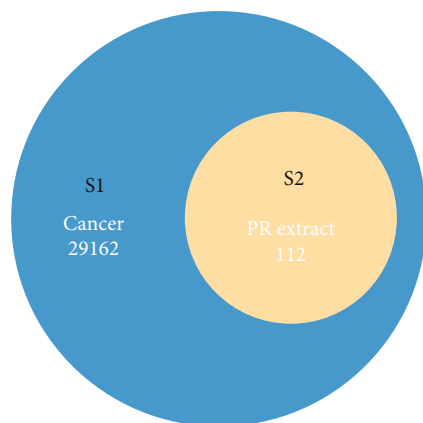
FIGURE 3: Venn diagram showed the intersection of PR extract and cancer-related genes.

Medicine Systems Pharmacology (TCMSP) database. The screening conditions were OB (oral availability) ≥ 30% and DL (similarity of patent medicine) ≥ 0.18. After screening combined with literature mining, the reported active ingredients were collected for supplementation.

2.2. Collection of Active Compound Targets of Action. TCMSP input into PR was used to search and curate compounds action targets. The targets of action of the active ingredient were imported into the UniProtKB database into corresponding gene names, and the human gene ("Homo sapiens") was screened. If no information can be found in UniProtKB, use PubChem database to check the simplified molecular-input line-entry system (SMILES) number to Swiss Target Prediction database to predict the possible target information. Further, targets with a likelihood greater than 0.1 were filtered and duplicates were removed.

2.3. Collection and Acquisition Disease Target. Find keywords "cancer," "neoplasm," and "tumor" from the Gene-Cards database. Delete duplicate genes. The active components and disease targets of drugs were matched. Further, Venny (version 2.1) software was used to draw a Venn diagram to determine the potential anticancer targets according to active ingredients of PR.

2.4. Establishing the Protein–Protein Interaction (PPI) Network. The obtained common anticancer targets were imported into STRING database in the form of gene symbols, the interactions between proteins were analyzed, and the protein-protein interaction (PPI) network diagram of PR extract core targets for the treatment of cancer was obtained. The species was selected as "Homo sapiens," and PPI with a minimum interaction value ("minimum required interaction score") > 0.4 were selected. Hide free dots, download PPI graphics, and save as "tsv." format.

2.5. Construction of the Network. Then, the Cytoscape software (version 3.8.2) was used to construct a network map of drug and disease targets to show the relationship between PR extract and various cancer targets, to explore the mechanism of the anticancer effect of PR extract.

2.6. GO and KEGG Enrichment Analysis of Common Targets of PR Extract and the Cancers. The GO functional enrichment analysis was performed to further analyze the roles of target proteins of TCM compounds in gene function with a rough understanding of their differential gene enrichment. Then, KEGG pathway enrichment analysis was performed to know the genes and their pathway, which help to understand the significantly changed metabolic pathways under the experimental conditions. Active ingredient corresponding targets and cancer-related common targets were entered into the DAVID database. GO enrichment analysis of target genes and KEGG pathway enrichment analysis were performed. Data were downloaded and ranked from small to large based on the corrected P values. Screening GOTERM_CC_DIRECT, GOTERM_BP_DIRECT, and GOTERM_MF_DIRECT, the top 15 for each of direct are summarized into a new table. KEGG pathway selects the top 20 data, all ordered in the order sample group, gene ratio, Q value, count, and description, where description is equivalent to term and Q value is equivalent to FDR. And output the results as a bubble plot in the ImageGP online sketch drawing software.

2.7. Molecular Docking. The 3D chemical structure of PR extract was downloaded from PubChem. The crystal structures of target proteins were obtained from the Protein Data Bank. The key active ingredients and core targets after screening were subjected to molecular docking validation. The protein receptor was optimized by PyMOL software to remove the attached ligands, heteroatoms, and water molecules before docking [14, 15]. The obtained molecular ligand and protein receptor were docked and visualized by Auto-Dock (version 1.5.7) software, and the individual docking scores of each component were recorded [14, 15] The only criteria for target selection for active ingredients are currently not well defined. Therefore, the lower binding scores for each component were recorded against specific cancer targets.

3. Results

3.1. Collection of Drug Active Ingredients. Through TCMSP, "*Picorrhizae Rhizoma*" compounds were retrieved, and 55 effective compounds were identified. A total of 10 active ingredients were screened based on OB ≥ 30% and DL ≥ 0.18. Six reported active ingredients were collected in combination with literature mining [16]. A total of 16 potential active ingredients of PR (Table 2) were obtained. Figure 2 shows all 2D chemical structures of 16 extracted compounds and sort there according to expected activity.

3.2. Target Collection of PR Extract. Through TCMSP data platform, UniProtKB database, and PubChem database, a total of 203 targets were collected from the 16 active ingredients of PR. After screening of human genes ("Homo sapiens"), there were 183 targets. The repeated targets in each compound were removed, and the gene names of 112 related targets were obtained.
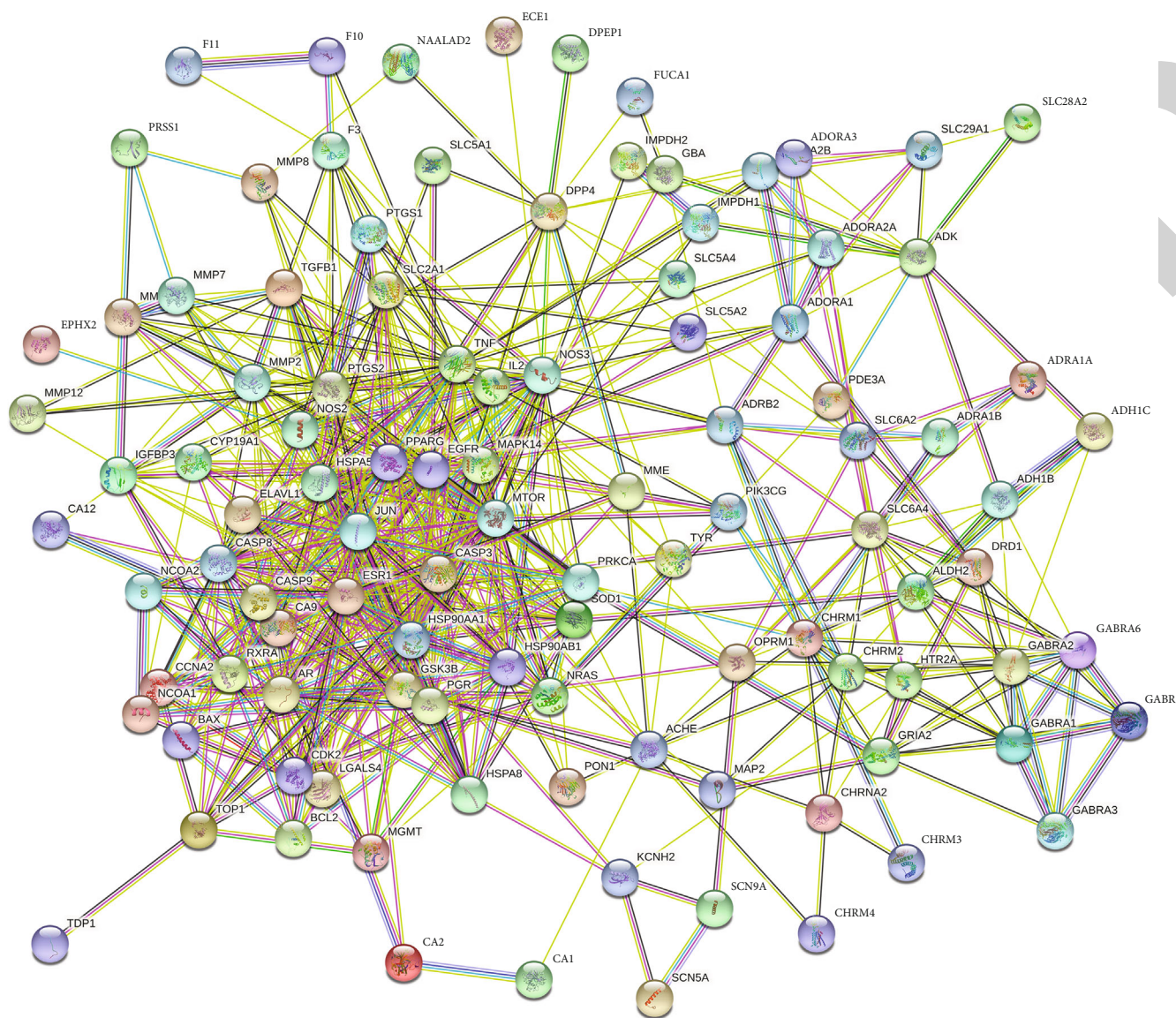
FIGURE 4: PPI interaction network of the intersecting targets.

3.3. Collection of Disease-Related Targets. By using the Gen-eCards database, 29162 cancer genes (Figure 3 S1) were found. The active ingredient targets of PR in treating diseases were matched to screen out the common targets, resulting in 112 common targets (Figure 3 S2). Then, 112 overlapped targets were obtained, and they were considered as the intersecting targets of PR extract and cancer (Figure 3).

3.4. Results of PPI Network Construction. The common targets of 112 PR extract cancer were entered into STRING database for analysis to obtain PPI. After concealing the free points, this network graph contained a total of 111 nodes with 628 edges. The average node degree value was 11.3, and the PPI enrichment P value is less than $1.0e - 16$. Among them, nodes represent proteins, and each edge indicates a protein-protein interaction relationship. The greater the number of lines, the stronger the association (Figure 4).

The tsv.dot (tsv.) file downloaded from string was processed to draw a bar graph according to the degree value (degree $\geq$ 50). The PPI core gene targets were obtained: TNF (degree = 86), EGFR (degree = 81), CASP3 (degree = 76), ESR1 (degree = 76), etc. (Figure 5), indicating the importance of the above targets in the anticancer effect of PR extract. It can be used as a key target to study the anti-tumor effect of PR extract.

3.5. Construction and Analysis of Drug-Active Ingredient-Target-Disease Network. PR and its 16 active ingredients, 112 PR extract, and cancer common targets were imported into Cytoscape 3.8.2 software to construct the drug-active ingredient-target-disease network diagram (Figure 6). Green triangles represent drug PR, pink hexagons represent active ingredients, cyan rectangles represent diseases cancer, and blue circles represent active ingredients corresponding action targets in the network diagram. After analyzing it
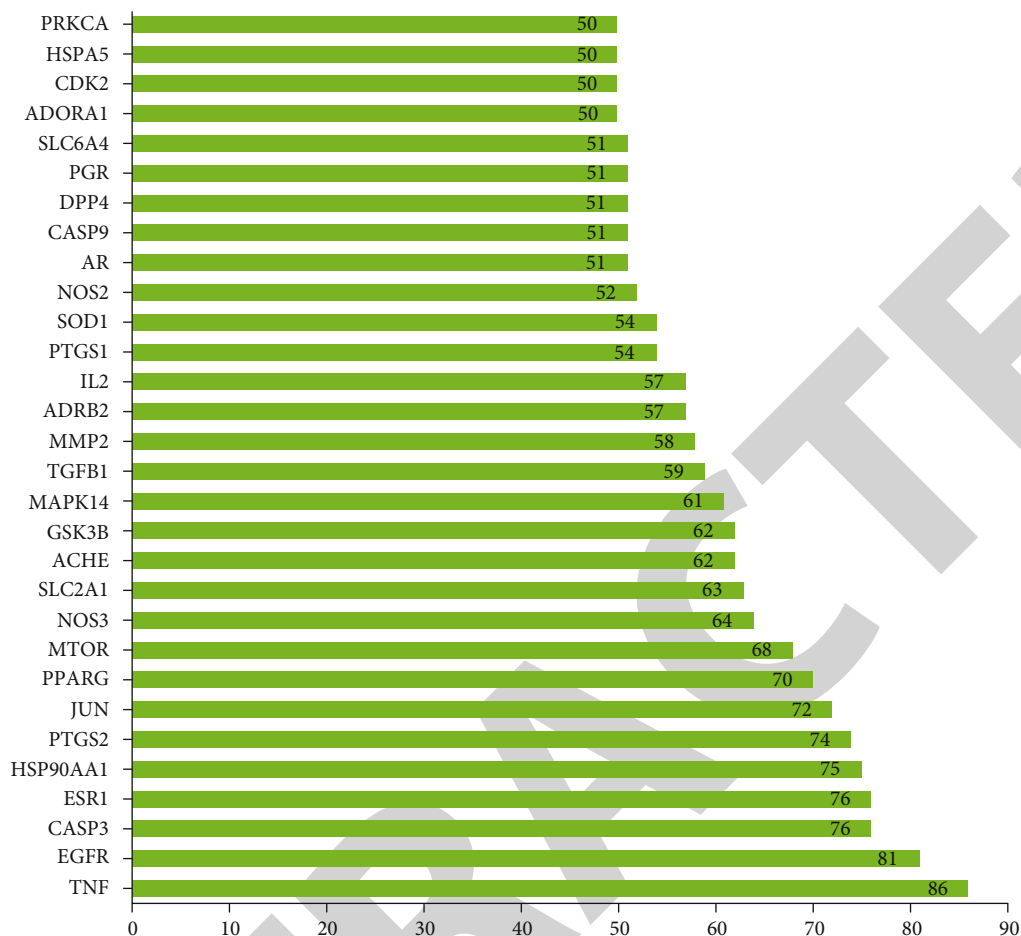
FIGURE 5: Core gene targets of PPI.

with Cytoscape 3.8.2 software, we found that picroside I had the most targets, which was 38, followed by β-sitosterol with 32 targets and hederagenin with 22 targets. Select the target with degree, closeness, and betweenness greater than the median to obtain the core target. From the analysis of the targets of action, the top six connections were TNF, CASP3, JUN, EGFR, ESR1, and HSP90AA1. The same active ingredient of surface PR extract can act on different targets, and the same target can in turn be affected by different active ingredients, which embodies the multicomponent, multitarget properties of PR extract anticancer.

3.6. GO Enrichment Analyses.
Go enrichment analysis of 112 potential anticancer and antitumor targets of PR extract in DAVID was performed to screen $P < 0.05$, and a total of 527 biological process entries were obtained, including 357 biological process (BP) items, 69 cellular component (CC) items, and 101 molecular function (MF) items. The top 15 items of each component were imported into ImageGP for visualization (see Figure 7). In this context, the P value is a measure of significance of enrichment, and the smaller the resulting P value, the more biased the color will be towards red and vice versa towards green. The abscissa represents the gene ratio with larger ratios indicating greater enrichment. The size of a

dot indicates the number of enriched targets in that pathway, and a larger dot indicates more enriched targets and so on. Molecular functions include neurotransmitter receptor activity and enzyme binding. Cell composition mainly involves plasma membrane, integral component of presynaptic membrane, and integral component of plasma membrane. As shown in the figure, the first three GO entries of enrichment factors are all about the binding of plasma membrane and enzymes. It showed that the anticancer effect of PR extract was closely related to the combination of cell plasma membrane and enzyme.

3.7. KEGG Pathway Enrichment Analyses.
There were 124 Kyoto Encyclopedia of Genes and Genomes (KEGG) signaling pathways. As shown in Figure 8, the top 30 KEGG signaling pathways of the intersecting targets were pathways in cancer. The pathways in cancer and neuroactive ligand-receptor interactions were significantly recorded. Secondly are lipid and atherosclerosis, estrogen signaling pathway, and activation. It can also be seen that PR extract may also have therapeutic effects on colorectal cancer, prostate cancer, and small cell lung cancer. The results showed that the active component of PR extract-cancer target was distributed in different pathways. It can play an anticancer role through the coordination of various pathways. At the same time,

FIGURE 6: Drug-active ingredient-target-disease network.

the key target genes of PR extract-cancer are enriched in a variety of cancer pathways. It can provide a theoretical basis for further study on the antitumor effect of PR extract.

3.8. Molecular Docking Results. The role of PR extract in treatment was further verified by molecular docking technology and further verified the results of network pharmacology. A total of 30 key targets were screened using PPI networking and analyzed by Cytoscape. The average shortest path, intermediate number, and degree of freedom in the network are calculated. TNF, CASP3, JUN, EGFR, ESR1, and HSP90AA1 which are the top six proteins with a large intermediate number, large degree value, and small average

shortest paths were chosen for molecular docking with the screened sixteen active components. Recorded docking scores indicated that all candidates displayed docking scores between 0.11 and -6.51 kcal/mol. According to AutoDock software, 0.11 kcal/mol displayed candidates have the lowest activity, where -6.51 kcal/mol displayed candidates which have the highest affinity for the specific target enzyme. When the binding energy of ligand and receptor is less than 0, it indicates that it can bind spontaneously. Table 3 shows the binding energy of docking between the target molecule and the compound molecule.

Then, select the best compound from each target and visualize it, as shown in Figure 9.

Figure 7: GO functional enrichment analysis results.
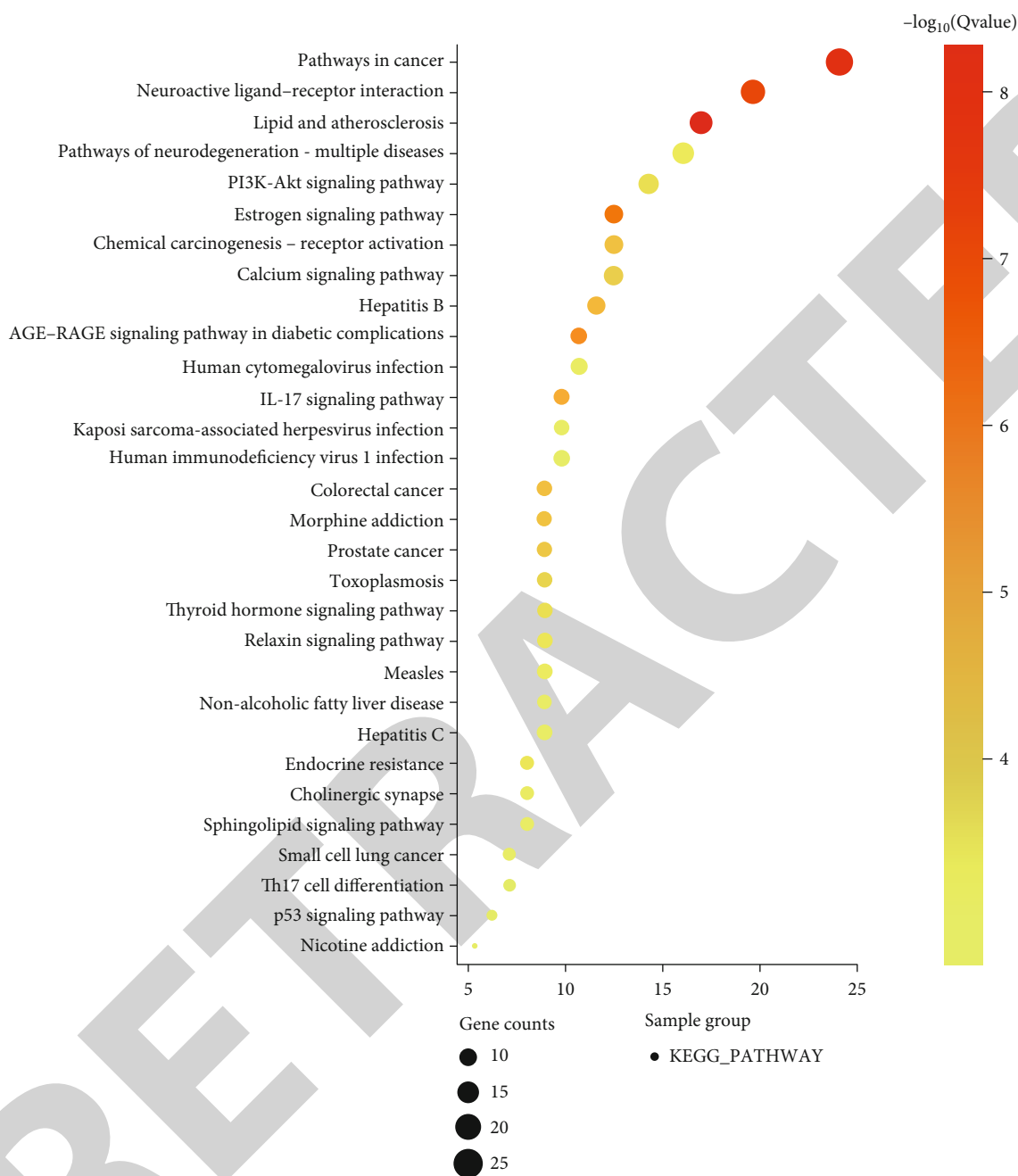
FIGURE 8: KEGG pathway analysis results.

The results suggest that the active ingredient herbacetin can form hydrogen bonds with the amino acid residues of TNF (GLU-116, GLN-149, PRO-113, SER-95, and TYR-119). (5S)-5,9-Dihydroxy-4-(4-hydroxyphenyl)-5,6-dihydro-1-benzoxo can form hydrogen bonds with the amino acid residues of CASP3 (ASP-107, LYS-105, ARG-147, and SER-104). Hederagenin can form hydrogen bonds with the amino acid residues of JUN (GLU-293), and ESR1 (LYS-416) and can bind well with the corresponding target proteins. β-Sitosterol can form hydrogen bonds with the amino acids of EGFR (MET-795), and HSP90AA1 (SER-72) residues combine to form hydrogen bonds. These interactions allow proteins to form stable compounds with compounds.

Table 4 shows the inhibition constants of the docking between the target and the compound molecules. A small inhibition constant is a good docking.

4. Discussion

In this study, the method of network pharmacology was used to explore the complex network of multicomponent, multitarget, and multichannel anticancer potency of PR extract. First, several compound target databases and disease target databases were searched; 16 main active components and 112 anticancer and antitumor targets of PR extract were identified. Based on the network pharmacology method,

Table 3: Binding energy of molecular docking (kcal/mol).

Compound	TNF	CASP3	JUN	EGFR	ESR1	HSP90AA1
Herbacetin	-6.51	-2.38	-2.75	-3.56	-3.12	-3.79
(5S)-5,9-Dihydroxy-4-(4-hydroxyphenyl)-5,6-dihydro-1-benzoxocin-2-one	-6.36	-4.20	-2.19	-3.05	-3.47	-4.16
Picroside I_qt	-6.19	-3.51	-3.00	-3.01	-2.59	-3.65
Hederagenin	-6.06	-3.25	-3.95	-4.96	-4.73	-4.83
β-Sitosterol	-5.52	-3.83	-3.47	-5.91	-4.16	-5.36
Scrophuloside A	-5.19	-2.66	-0.41	0.07	-0.73	-2.04
Picroside I	-5.06	-0.18	-0.73	-2.84	-1.47	-2.54
Picroside IV	-4.84	-0.32	-0.70	0.11	-2.62	-2.44
Scrophuloside A_QT	-4.73	-2.61	-1.16	-4.16	-2.91	-4.26
Picroside II_qt	-4.58	-2.49	-1.79	-1.88	-0.31	-2.97
Picroside III	-4.56	-1.88	-1.17	0.68	-0.36	-1.08
Catalpol	-4.22	-2.65	-2.23	-2.39	-2.62	-2.73
Catapol_qt	-3.95	-2.8	-1.87	-2.48	-2.46	-2.79
Picroside II	-3.80	-1.07	-0.45	-0.25	-1.79	-1.71
6-Feruloylcatalpol	-3.63	-1.29	-0.53	0.89	-0.4	-1.21
Aucubin	-2.94	-1.62	-0.81	-0.51	-2.04	-1.84

picroside I, β-sitosterol, hederagenin, picroside IV, scrophuloside A_QT, herbacetin, and other 16 anticancer active ingredients were confirmed. Among them, herbacetin belongs to flavonoids, which are widely distributed and have a variety of biological activities. It can induce apoptosis of HepG2 cells and play an anticancer role. Hederagenin belongs to triterpenoids, which have a wide range of physiological activities. Pharmacological properties have been shown to be anti-inflammatory and hepatoprotective from antitumor aspects. Hederagenin can inhibit gastric, cervical, and colon cancer cells [17–19]. β-Sitosterol belongs to tetracyclic triterpenes and is a natural small molecule with antitumor effects. Scrophuloside A is a phenolic glycoside, and phenolic glycosides can also prevent tumors. Picroside I, picroside IV, picroside III, picroside II, catalpol, 6-feruloylcatalpol, and aucubin all belong to iridoids, which are widely distributed in traditional Chinese medicine.

Thirty key targets such as TNF, EGFR, CASP3, and ESR1 were identified. The pathways in the cancer signal pathway are closely related to the anticancer effect of PR extract. The binding activity was simulated based on molecular docking, and the results showed that all of them had binding activity. Currently, molecular docking has been widely used by academicians, drug developers, and pharmaceutical companies to assess the potency of compounds against target enzymes associated with diseases or disorders with minimal resources and time [20, 21]. Nevertheless, all tools and software used for biological analyses are based on coding or programming and we need to be handy to select ideal tools as per the objective of the research, avoid errors, and obtain reliable outputs [14, 15, 20, 21].

It is interconnected with many disease targets in the anticancer and antitumor target network of active components of PR. It can be seen from this that picroside I, β-sitosterol, hederagenin, scrophuloside A_QT, picroside IV, and herbacetin have the highest correlation with the target path-

way. These ingredients can play multiple roles in the human body to achieve the effect of disease prevention and treatment. Through the visualization of PPI protein network analysis and Cytoscape software, we can see that the key targets of PR extract on cancer are TNF, CASP3, JUN, EGFR, ESR1, HSP90AA1, PPARG, PTGS2, MTOR, etc. TNF is a tumor necrosis factor, which is a cytokine that can directly kill tumor cells, but has no obvious toxic effect on normal cells. It is also one of the most potent bioactive factors to kill tumors. It is produced by activated macrophages, NK cells, and T lymphocytes and can inhibit osteoblasts and stimulate osteoclasts. It can be used as a cytokine for tumor biotherapy [22]. TNF is a relevant target of cervical cancer, colon cancer, and bladder cancer [22, 23]. CASP3 is a protease that can specifically cleave poly-ADP ribose polymerase (PARP1) and acetyl-devd-7-amino-4-methylcoumarin (ac-devd-amc), leading to DNA cleavage and promoting apoptosis. It is one of the most important enzymes in the apoptotic pathway and has an important relationship with the occurrence of cancer, aging, and cardiovascular diseases [24]. Similarly, EGFR is an epidermal growth factor receptor, which is a multifunctional glycoprotein widely distributed on the cell membrane of human tissues, and is one of HER/ERBB family members [25]. Loss of function of EGFR and other protein tyrosine kinases or abnormal activity or cell localization of key factors in their related signaling pathways can cause tumors, diabetes, immune deficiency, and cardiovascular diseases. EGFR is a target involved in non-small-cell, lung cancer, lung adenocarcinoma, and cholangiocarcinoma [26–28]. ESR1, an estrogen receptor, affects cell proliferation and differentiation in target tissues, participating in the pathological process including breast cancer, endometrial cancer, and osteoporosis [29, 30]. HSP90AA1 is a target associated with colorectal cancer, non-small-cell, lung cancer, gastric cancer, breast cancer, and hepatocellular carcinoma [31–36]. It not only affects the survival of tumor

(a)

(b)

(c)

FIGURE 9: Continued.

(d)

(e)

(f)
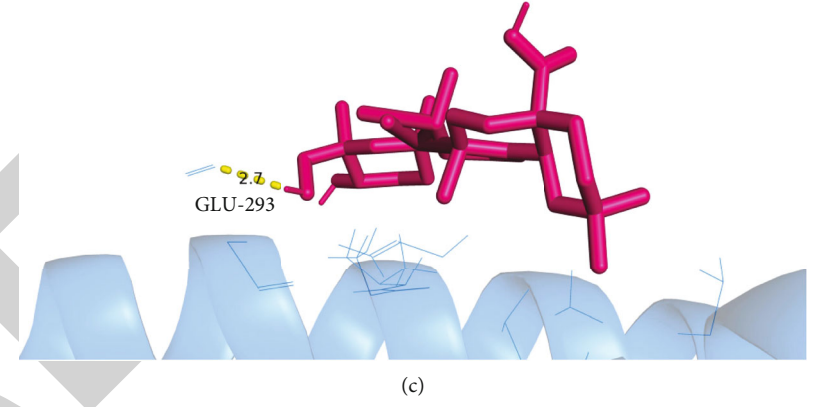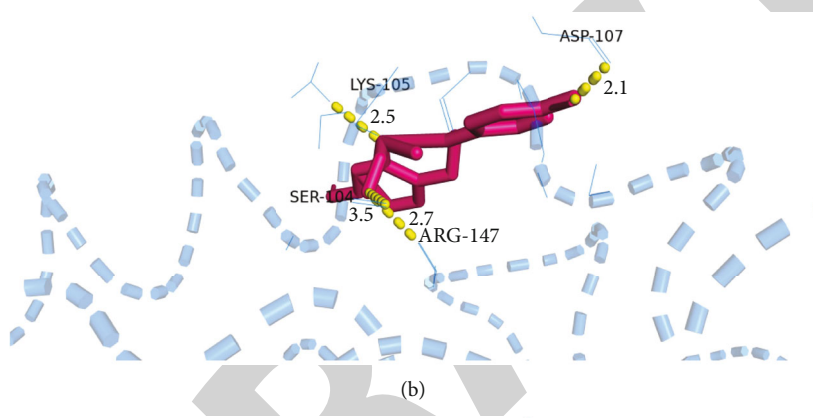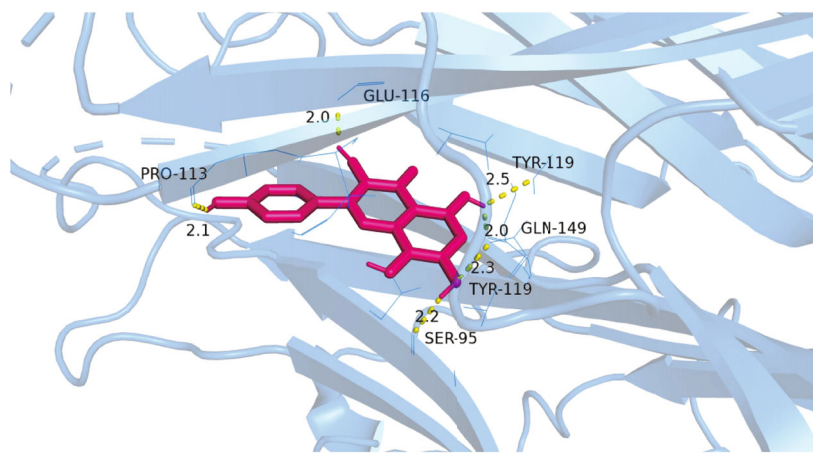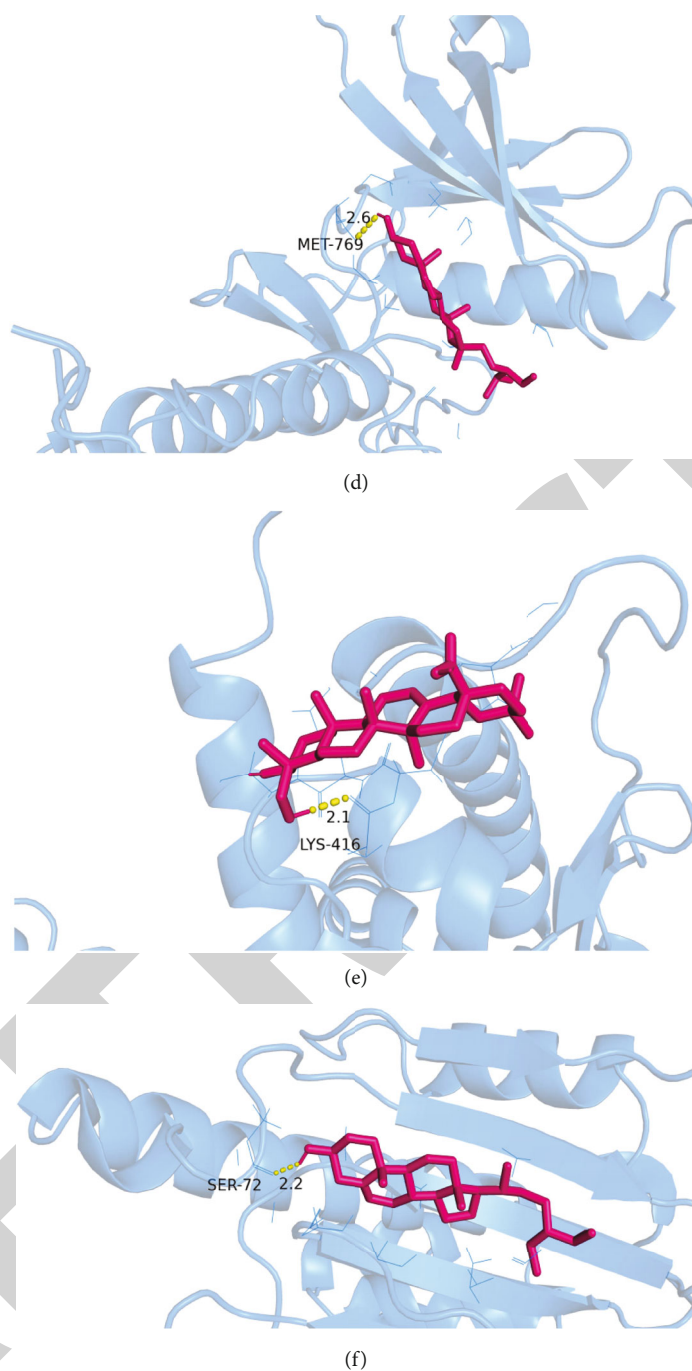
FIGURE 9: Visualization of protein-ligand interaction docking results. (a) The docking of herbacetin with TNF. (b) The docking of (5S)-5,9-dihydroxy-4-(4-hydroxyphenyl)-5,6-dihydro-1-benzoxocin-2-one with CASP3. (c, e) The docking of hederagenin with JUN and ESR1. (d, f) The docking of β-sitosterol with EGFR and HSP90AA1, respectively.

cells but also acts on the invasion and migration of cancer cells and is closely related to the poor prognosis of tumors [37]. PPARG is a target associated with breast cancer, lung cancer, hypopharyngeal squamous cell carcinoma, esophageal carcinoma, and lung squamous cell carcinoma [38–41]. PTGS2 is a target associated with cervical cancer, pancreatic ductal adenocarcinoma, nasopharyngeal carcinoma, and colorectal cancer [42–45]. MTOR [45–52] is a target associated with breast cancer, bladder cancer, hysteromyoma, laryngeal cancer, kidney cancer, liver cancer, thy-

roid cancer, epidermoid squamous cell carcinoma, and colorectal cancer.

Through GO enrichment analysis, it is known that the anticancer effect of PR of extract is related to the association of cytoplasmic membrane and enzymes. The cytoplasmic membrane is an extremely thin layer of membrane that surrounds the cell surface, mainly composed of membrane lipids and membrane proteins. The basic role of the cytoplasmic membrane is to maintain the relative stability of the intracellular microenvironment. It also participates in

TABLE 4: Inhibition constant of molecular docking.

Compound	TNF	CASP3	JUN	EGFR	ESR1	HSP90AA1
Herbacetin	16.84	18.10	9.70	2.47	5.17	1.68
(5S)-5,9-Dihydroxy-4-(4-hydroxyphenyl)-5,6-dihydro-1-benzoxocin-2-one	21.6	837.08	24.82	5.82	2.87	896.3
Picroside I_qt	28.88	2.67	6.35	6.24	12.71	2.12
Hederagenin	36.22	4.12	1.28	232.7	338.48	286.36
β-Sitosterol	90.63	1.55	2.85	46.49	895.72	116.96
Scrophuloside A	158.1	11.18	503.53	-4.11	290.48	32.09
Picroside I	195.04	736.69	289.56	8.34	84.09	13.77
Picroside IV	281.61	581.03	304.36	-4.07	11.94	16.18
Scrophuloside A_QT	343.25	12.19	140.89	885.98	7.36	750.19
Picroside II_qt	442.5	15.04	48.68	41.91	590	6.66
Picroside III	455.33	42.02	139.88	-3.80	546.83	160.51
Catalpol	805.01	11.40	23.30	17.63	12.04	9.99
Catapol_qt	1.27	8.84	42.63	15.22	15.67	8.95
Picroside II	1.64	164.71	469.11	656.96	48.44	55.32
6-Feruloylcatalpol	2.19	112.86	406.18	-3.58	512.52	129.33
Aucubin	6.97	64.75	252.97	425.51	31.81	45.08

the external environment for the exchange of materials, energy, and information and overall plays an active role in both the survival and differentiation of cells. Of the 112 targets that we screened, 68 all had effects on the cytoplasmic membrane. Of the top 30 targets in degree value, 20 all had an effect on the cytoplasmic membrane.

According to KEGG pathway analysis, 27 target genes are associated with cancer pathways contributing to the development and proliferation of metastatic cancer. Of these, 11 target genes are associated with colorectal cancer, 10 target genes with prostate cancer, and 10 target genes with small cell lung cancer. Through literature, it is known that estrogen plays a role in liver and breast cancer. Estrogen protects against liver cancer through genomic pathways, rapid transduction pathways, noncoding RNAs, tumor microenvironment, estrogen metabolites, and inhibition of hepatitis infection and replication [53]. The expression of RANKL and its receptor in T47D versus MCF-7 cell lines was regulated by estrogen. Estrogen has the potential to affect breast cancer cell bone metastasis through RANKL and its receptor [54]. The IL-17 signaling pathway has been shown to be effective in the treatment of colorectal cancer [55], breast cancer [56], gastric cancer [57], prostate cancer [58], and laryngeal squamous cell carcinoma [59]. The PI3K-Akt signaling pathway promotes liver cancer cell proliferation and metastasis [60]. In human cytomegalovirus infection, there is association of CCR5Δ32 deletion and human cytomegalovirus infection with colorectal cancer in Tunisia [61]. Kaposi sarcoma-associated herpesvirus infection regulates proliferation of glioma stem-like cells [62], relieves the Warburg effect through p53 activation, thereby inhibiting breast cancer cell growth [63], inhibits renal cancer cell growth by regulating the p53 signaling pathway [48], suppresses lung cancer growth by activating the p53 signaling pathway [64], promotes cholangiocarcinoma cell proliferation, migration, and invasion by decreasing p53

expression [65], and promotes pancreatic cancer growth and metastasis through the p53 transcriptional pathway [66]. In addition, th17 cells play a key role in autoimmunity and their cell differentiation contributes greatly to the treatment of cancer.

Based on molecular docking scores, herbacetin, (5S)-5,9-dihydroxy-4-(4-hydroxyphenyl)-5,6-dihydro-1-benzoxocin-2-one, picroside I_qt, and hederagenin comparatively exhibited strong binding affinity against TNF, and β-sitosterol has strong binding force with EGFR and HSP90AA1. Overall, flavonoid herbacetin exhibited the highest binding or docking score against TNF (-6.51 kcal/mol). Analyzing the interaction mode between proteins and ligands, it can be concluded that the extracts of PR can bind well to these selected targets and obtain lower binding energy mainly by forming multiple hydrogen bonds. In addition, molecular docking models provide evidence for how these compounds act on targets to inhibit cancer. It is preliminarily confirmed that many effective components of PR play a therapeutic role on cancer through key targets.

5. Conclusion

In this study, the therapeutic effects of PR extract on cancer and tumor were preliminarily analyzed by means of network pharmacology and molecular docking. The potential anticancer and antitumor targets, related signal pathways, and biological processes of PR extract were predicted. It is revealed that the anticancer and antitumor effects of PR are the result of the joint action of multiple components, multiple targets, and multiple pathways. Network pharmacology of traditional Chinese medicine is the development and integration of ancient Chinese medicine and modern medicine in the interdisciplinary fields of network, pharmacology, biology, and computer. In network visualization, the main active components, anticancer and antitumor targets,

and pathways of PR extract can be deduced from a large array of data integrations and calculations, which provides a theoretical basis for anticancer and antitumor research. This study provides a theoretical basis for the anticancer and antitumor mechanism of PR extract and its future experimental verification, in order to serve as a reference for later drug development and clinical application.

Data Availability

All data used to support the findings of this study are included in the paper.

Conflicts of Interest

The authors declare no conflict of interest.

Authors' Contributions

X. M. Hu and S. C. Zhao searched the literature and wrote the first draft; Y. Cai and L. L. Yao performed the statistical analysis and interpreted the data; S. S. Swain revised the manuscript; W. Liu and T. D. Yan designed the protocol of systematic review. All authors approved the final draft.

Acknowledgments

References

[1] S. Zahiruddin, W. Khan, R. Nehra et al., "Pharmacokinetics and comparative metabolic profiling of iridoid enriched fraction of Picrorhiza kurroa – an Ayurvedic herb," *Journal of Ethnopharmacology*, vol. 197, pp. 157–164, 2016.

[2] V. Patile, A. Bandivadekar, and D. D. Debjani, "Inhibition of Propionibacterium acnes lipase by extracts of Indian medicinal plants," *International Journal of Cosmetic Science*, vol. 34, no. 3, pp. 234–239, 2012.

[3] L. Wang, X. H. Liu, H. Chen et al., "Picroside II decreases the development of fibrosis induced by ischemia/reperfusion injury in rats," *Renal Failure*, vol. 36, no. 9, pp. 1443–1448, 2014.

[4] S. Madhavan, R. Johanna, and D. Jamuna, "Hepatoprotective activity of hepatoplus on isonaizid and rifampicin induced hepatotoxicity in rats," *Pakistan Journal of Pharmaceutical Sciences*, vol. 28, no. 3, pp. 983–990, 2015.

[5] D. Upadhyay, R. P. Dash, S. Anandjiwala, and M. Nivsarkar, "Comparative pharmacokinetic profiles of picrosides I and II from kutkin, Picrorhiza kurroa extract and its formulation in rats," *Fitoterapia*, vol. 85, pp. 76–83, 2013.

[6] M. F. Ji, J. S. Min, and Y. Bo, "Picroside II protects cardiomyocytes from hypoxia/reoxygenation-induced apoptosis by activating the PI3K/Akt and CREB pathways," *International Journal of Molecular Medicine*, vol. 30, no. 2, pp. 263–270, 2012.

[7] M. Nandave, S. K. Ojha, S. Kumari et al., "Cardioprotective effect of root extract of Picrorhiza kurroa (Royle Ex Benth)

against isoproterenol-induced cardiotoxicity in rats," *Indian Journal of Experimental Biology*, vol. 51, no. 9, pp. 694–701, 2013.

[8] Z. Lu and H. Ying, "Induction of apoptosis in renal cancer cells by mitochondrial pathway using Picroside II," *Journal of Clinical Nephrology*, vol. 20, no. 6, pp. 504–507, 2020.

[9] Y. Qian, Z. Jun, M. Y. Quan, and T. X. Min, "Mechanism of picroside II inhibiting proliferation. Invasionand metastasisof esophageal cancer cells through MEK / ERK pathway," *Evaluation and Analysis of Drug-Use in Hospitals of China*, vol. 21, no. 7, pp. 820–825, 2021.

[10] Y. Hong, Z. Jie, and Y. X. Qing, "Effect and mechanism of picroside II on autophagy in MCF-7 breast cancer cells," *Chinese Journal of Clinical Pharmacology and Therapeutics*, vol. 24, no. 5, pp. 535–540, 2019.

[11] Z. Miao, G. C. Yu, S. M. Yue, and Y. H. Jun, "Chrysaron and Kutkin I regulate hepcidin expression in hepatoma cell," *Journal of Shanxi University(Natural Science Edition)*, vol. 38, no. 4, pp. 715–720, 2015.

[12] J. H. Jie, H. S. Lan, L. Lin, W. S. Min, W. X. Xing, and T. X. Dong, "Research progress on cucurbitane-type tetracyclic triterpenes in Picrorhizae Rhizoma and their bioactivities," *Chinese Traditional and Herbal Drugs*, vol. 53, no. 15, pp. 4875–4881, 2022.

[13] C. Nan, L. X. Xuan, Z. L. Bin, C. N. Ning, X. X. Feng, and L. C. Xiao, "Research progress on pharmacological effects of picroside II," *Journal of Tianjin University of Traditional Chinese Medicine*, vol. 41, no. 1, pp. 124–130, 2022.

[14] A. Sahoo, S. Fuloria, S. S. Swain et al., "Potential of marine terpenoids against SARS-CoV-2: an in silico drug development approach," *Biomedicines*, vol. 9, no. 11, p. 1505, 2021.

[15] S. S. Swain, S. R. Singh, S. Alaka, P. P. Kumar, H. Tahziba, and P. Sanghamitra, "Integrated bioinformatics-cheminformatics approach toward locating pseudo-potential antiviral marine alkaloids againstSARS-CoV-2-Mpro," *Proteins*, vol. 90, no. 9, pp. 1617–1633, 2022.

[16] W. Y. Ping, M. Q. Na, C. X. Cao, and L. X. Bin, "Extraction of active components and pharmacological effects of Picrorhizae Rhizoma," *Journal of Yan'an University(Medical Science Edition)*, vol. 15, no. 2, pp. 70–73, 2017.

[17] Z. Fang, C. Cheng, G. Cheng, R. Qian, W. Y. Ping, and Y. J. Xi, "Anit-breast cancer effect of hederagenin and its mechanism in vitro," *Chinese Journal of Coal Industry Medicine*, vol. 23, no. 3, pp. 239–242, 2020.

[18] F. L. Wen, L. M. Ming, and C. L. Ling, "Hederagenin inhibits proliferation and promotes apoptosis of cervical cancer CaSki cells by blocking STAT3 pathway," *Chinese Journal of Cellular and Molecular Immunology*, vol. 35, no. 2, pp. 140–145, 2019.

[19] L. B. X. Zi, W. R. Ping, Z. Xi, and Z. J. Yong, "The effect of hederagenin on the proliferation, adhesion, invasionand migration of human colon cancer cells LoVo," *Journal of Nanjing University of Traditional Chinese Medicine*, vol. 29, no. 1, pp. 44–47, 2013.

[20] S. Alaka, S. S. Swain, P. Biswaranjan, and P. Maitreyee, "Combinatorial approach of vitamin C derivative and anti-HIV drug-darunavir against SARS-CoV-2," *Frontiers in Bioscience*, vol. 27, no. 1, p. 10, 2022.

[21] M. Yan, Z. X. Yan, Y. J. Cheng, J. Y. Ping, X. Ying, and Q. J. Ping, "Comprehensive molecular analyses of a TNF family-based gene signature as a potentially novel prognostic

biomarker for cervical cancer," *Frontiers in Oncology*, vol. 12, p. 854615, 2022.

[22] B. L. Salomon, M. Leclerc, J. Tosello, E. Ronin, E. Piaggio, and J. L. Cohen, "Tumor necrosis factor α and regulatory T cells in oncoimmunology," *Frontiers in Immunology*, vol. 9, p. 444, 2018.

[23] L. H. Huang, L. S. Yuan, L. C. Xuan, X. Z. Cheng, H. Jiao, and Z. Cheng, "TNF family–based signature predicts prognosis, tumor microenvironment, and molecular subtypes in bladder carcinoma," *Frontiers in Cell and Developmental Biology*, vol. 9, p. 800967, 2022.

[24] Z. Zheng, X. S. Ying, J. L. Hao, T. Zhuo, and W. J. Feng, "A systematic pan-cancer analysis of CASP3 as a potential target for immunotherapy," *Frontiers in Molecular Biosciences*, vol. 9, p. 776808, 2022.

[25] D. L. Wheeler, S. Huang, T. J. Kruser et al., "Mechanisms of acquired resistance to cetuximab: role of HER (ErbB) family members," *Oncogene*, vol. 27, no. 28, pp. 3944–3956, 2008.

[26] G. Yang, Y. Yang, R. Liu et al., "First-line immunotherapy or angiogenesis inhibitor combined with chemotherapy for advanced non-small cell lung cancer with EGFR exon 20 insertions: real-world evidence from China," *Cancer Medicine*, vol. 11, 2022.

[27] Y. Yang, J. F. Huang, B. Q. Hu et al., "B7-H3 is eligible for predicting clinical outcomes in lung adenocarcinoma patients treated with EGFR tyrosine kinase inhibitors," *World Journal of Surgical Oncology*, vol. 20, no. 1, p. 159, 2022.

[28] U. Thamrongwaranggoon, M. Detarya, W. Seubwai et al., "Lactic acidosis promotes aggressive features of cholangiocarcinoma cells via upregulating ALDH1A3 expression through EGFR axis," *Life Sciences*, vol. 302, p. 120648, 2022.

[29] D. J. Hosfield, S. Weber, N. S. Li et al., "Stereospecific lasofoxifene derivatives reveal the interplay between estrogen receptor alpha stability and antagonistic activity in ESR1 mutant breast cancer cells," *Elief*, vol. 11, p. e72512, 2022.

[30] K. Dessources, K. M. Miller, E. Kertowidjojo et al., "ESR1 hotspot mutations in endometrial stromal sarcoma with high-grade transformation and endocrine treatment," *Modern Pathology*, vol. 35, no. 7, pp. 972–978, 2022.

[31] M. Zhang, Y. Peng, Z. Yang et al., "DAB2IP down-regulates HSP90AA1 to inhibit the malignant biological behaviors of colorectal cancer," *BMC Cancer*, vol. 22, no. 1, p. 561, 2022.

[32] N. Bhattacharyya, S. Gupta, S. Sharma et al., "CDK1 and HSP90AA1 appear as the novel regulatory genes in non-small cell lung cancer: a bioinformatics approach," *Journal of Personalized Medicine*, vol. 12, no. 3, p. 393, 2022.

[33] B. M. Chen, B. Zheng, G. Y. Feng, L. K. Peng, W. Y. Bing, and T. Y. Nuo, "Knockdown of lncRNA ZNRD1-AS1 suppresses gastric cancer cell proliferation and metastasis by targeting the miR-9-5p/HSP90AA1 axis," *Aging (Albany NY)*, vol. 13, pp. 17285–17301, 2021.

[34] H. Liu, Z. Zhang, Y. Huang et al., "Plasma HSP90AA1 predicts the risk of breast cancer onset and distant metastasis," *FrontiersI in Cell and Developmental Biology*, vol. 9, p. 639596, 2021.

[35] W. Shi, L. Feng, S. Dong et al., "FBXL6 governs c-MYC to promote hepatocellular carcinoma through ubiquitination and stabilization of HSP90AA1," *Cell Communication and Signaling*, vol. 18, no. 1, p. 100, 2020.

[36] X. Xiao, W. Wang, Y. Li et al., "HSP90AA1-mediated autophagy promotes drug resistance in osteosarcoma," *Journal of Experimental & Clinical Cancer Research*, vol. 37, no. 1, p. 201, 2018.

[37] L. Lin, X. Y. Yi, W. Nan, Z. M. Zhi, and G. Y. Ting, "Breast cancer stem cells-derived extracellular vesicles affect PPARG expression by delivering microRNA-197 in breast cancer cells," *Clinical Breast Cancer*, vol. 22, no. 5, pp. 478–490, 2022.

[38] M. Lian, Y. Tao, J. Chen et al., "Variation of PPARG expression in chemotherapy-sensitive patients of hypopharyngeal squamous cell carcinoma," *PPAR Research*, vol. 2021, Article ID 5525091, 7 pages, 2021.

[39] S. S. Bin, Y. G. Ping, H. Bin, M. Y. Dong, K. Yan, and S. J. Pia, "PPARG could work as a valid therapeutic strategy for the treatment of lung squamous cell carcinoma," *PPAR Research*, vol. 2020, Article ID 2510951, 9 pages, 2020.

[40] Z. Chang, X. F. Fang, S. J. Cheng, and X. S. Hua, "Identification of a ferroptosis-related prognostic gene PTGS2 based on risk modeling and immune microenvironment of early-stage cervical cancer," *Journal of Oncology*, vol. 2022, Article ID 3997562, 32 pages, 2022.

[41] S. Ma, B. Zhou, Q. Yang et al., "A transcriptional regulatory loop of master regulator transcription factors, PPARG, and fatty acid synthesis promotes esophageal adenocarcinoma," *Cancer Research*, vol. 81, no. 5, pp. 1216–1229, 2021.

[42] Y. Liu, X. Wang, Y. Zhu et al., "The CTCF/LncRNA-PACERR complex recruits E1A binding protein p300 to induce pro-tumour macrophages in pancreatic ductal adenocarcinoma via directly regulating PTGS2 expression," *Clinical and Translational Medicine*, vol. 12, no. 2, p. e654, 2022.

[43] C. B. Lin, Q. Xiu, K. Dan, and L. Yi, "miR-26a-5p suppresses nasopharyngeal carcinoma progression by inhibiting PTGS2 expression," *Cell Cycle*, vol. 21, no. 6, pp. 618–629, 2022.

[44] G. Souvik, S. F. Mehrabi, L. M. Mehdawi, S. S. Ranjan, and S. Anita, "Identification of a novel five-gene signature as a prognostic and diagnostic biomarker in colorectal cancers," *International Journal of Molecular Sciences*, vol. 23, no. 2, p. 793, 2022.

[45] M. N. Ilozumba, S. Yao, A. A. Llanos et al., "mTOR pathway gene expression in association with race and clinicopathological characteristics in Black and White breast cancer patients," *Discover Oncology*, vol. 13, no. 1, p. 34, 2022.

[46] Z. Shen, D. Xue, K. Wang et al., "Metformin exerts an antitumor effect by inhibiting bladder cancer cell migration and growth, and promoting apoptosis through the PI3K/AKT/mTOR pathway," *Journal of Computer Virology and Hacking Techniques*, vol. 22, no. 1, p. 79, 2022.

[47] W. C. Cui, S. Yuan, C. Shuo, and Z. F. Yue, "Insulin-like growth factor-1 promotes human uterine leiomyoma cells proliferation via PI3K/AKT/mTOR pathway," *Cells Tissues Organs*, vol. 85, 2022.

[48] Y. Wu, Y. Wu, C. Xu et al., "CHMP1A suppresses the growth of renal cell carcinoma cells via regulation of the PI3K/mTOR/p53 signaling pathway," *Genes & Genomics*, vol. 44, no. 7, pp. 823–832, 2022.

[49] Z. Pu, D. G. Duda, Y. Zhu et al., "VCP interaction with HMGB1 promotes hepatocellular carcinoma progression by activating the PI3K/AKT/mTOR pathway," *Journal of Translational Medicine*, vol. 20, no. 1, p. 212, 2022.

[50] G. H. Ji, W. W. Ge, and L. Q. Qu, "GANT61 suppresses cell survival, invasion and epithelial-mesenchymal transition through inactivating AKT/mTOR and JAK/STAT3 pathways in anaplastic thyroid carcinoma," *Cancer Biology & Therapy*, vol. 23, no. 1, pp. 369–377, 2022.

Research Article

Network Pharmacology and Molecular Docking-Based Mechanism Study to Reveal Antihypertensive Effect of Gedan Jiangya Decoction

Hanxing Liu,[1] **Shadi A. D. Mohammed** ,[1] **Fang Lu,**[2] **Pingping Chen,**[2] **Yu Wang,**[2] **and Shumin Liu** [2]

[1]*Graduate School of Heilongjiang University of Chinese Medicine, Harbin, 150040 Heilongjiang, China*
[2]*Institute of Traditional Chinese Medicine, Heilongjiang University of Chinese Medicine, Harbin, 150040 Heilongjiang, China*

Correspondence should be addressed to Shumin Liu; keji-liu@163.com

Primary hypertension is understood as a disease with diverse etiology, a complicated pathological mechanism, and progressive changes. Gedan Jiangya Decoction (GJD), with the patent publication number CN114246896A, was designed to treat primary hypertension. It contains six botanical drugs; however, the underlying mechanism is uncertain. We utilized network pharmacology to predict the active components, targets, and signaling pathways of GJD in the treatment of primary hypertension. We also investigated the potential molecular mechanism using molecular docking and animal experiments. The Traditional Chinese Medicine System Pharmacology Database and Analysis Platform (TCMSP), the Protein Database (UniProt), and a literature review were used to identify the active components and related targets of GJD's pharmacological effects. The GeneCards, Online Mendelian Inheritance in Man (OMIM), Therapeutic Target Database (TTD), and DrugBank databases were utilized to identify hypertension-related targets. Based on a Venn diagram of designed intersection targets, 214 intersection targets were obtained and 35 key targets for the treatment of hypertension were determined using the STRING data platform and Cytoscape software. The Kyoto Encyclopedia of Genes and Genomes (KEGG) enrichment analysis of key targets revealed that the relevant molecular action pathways of GJD in the treatment of hypertension include the Toll-like receptor, MAPK, PI3K-Akt, and renin-angiotensin signaling pathways. A GJD active ingredient-key target-pathway connection diagram was created using Cytoscape software, and 11 essential active components were selected. Molecular docking was then used to verify the binding activity of key targets and key active ingredients in GJD to treat primary hypertension. The results of this study indicate that AGTR1, AKT1 with puerarin, EDNRA with tanshinone IIA, MAPK14 with daidzein, MAPK8 with ursolic acid, and CHRM2 with cryptotanshinone had high binding activity to the targets with active components, whereas AGTR1 was selected as target genes verified by our experiment. HPLC was utilized to identify the five active ingredients. Experiments in high-salt rats demonstrated that GJD might decrease the expression of AGTR1 in the kidney and thoracic aorta while increasing the expression of eNOS by preventing the activation of the renin-angiotensin pathway, thereby reducing lowering systolic and diastolic blood pressure.

1. Introduction

Hypertension is well-defined as a high systemic arterial blood pressure induced by the environment, polygenic heredity, and several risk factors. It has a great influence on the structure and function of blood vessels and often leads to brain, renal, and heart complications. It is also a major risk factor for cardiovascular diseases such as coronary heart disease, left ventricular hypertrophy, and arrhythmia [1]. Hypertension is classified into two major groups, which are primary and secondary hypertension, with primary hypertension responsible for 90% of hypertension patients [2]. The occurrence of hypertension in China increases yearly due to the changes in the environment and

their social lifestyle. A recent study [3] revealed that 44.7% of Chinese people within the age range of 35 to 75 are reported to have high blood pressure, with over 260 million hypertensive people having uncontrolled blood pressure and less than one-third getting treatment. As such, the treatment and prevention of high blood pressure are important priorities.

Traditional Chinese medicine (TCM) is a combination of a complex herbal formula that has been used for thousands of years to treat countless diseases and increase life expectancy in various parts of the world. The complex interaction of several bioactive components in herbal preparations or medicine results in the synergistic therapeutic effect of TCM [4]. When treating hypertension, TCM has the advantages of stability, multiefficacy, prospective, multitarget, improved cardiovascular remodeling, synergistic blood pressure reduction, improving vascular endothelial function, reducing toxicity, protecting target organs, and increasing efficiency [5–7]. TCM has been mostly used at the grassroots level in China to treat and prevent hypertension. It stresses the concept of therapy and differentiation from a general perspective, which is highly satisfactory in controlling various risk factors of hypertension and decreasing the overall cardiovascular risk [8]. However, establishing its efficiency through scientific experiments and analyzing its molecular mechanism remain a great challenge.

In recent years, network pharmacology, based on bioinformatics and systems biology, has been widely used in TCM research to clarify the TCM treatment of complex ailments from a multicomponent, multitarget, multipathway approach [9]. The primary molecular mechanism of network pharmacology is expected to become an essential direction in TCM research. This method represents the interaction of drug components, targets, and diseases in a network form, revealing the molecular mechanism of different active ingredients and providing new methods and ideas for understanding the processes or pathways of disease medication treatment [10]. The molecular docking technique simulates ligand-receptor docking to predict the affinity and binding mechanism between therapeutic and target molecules. Molecular docking is utilized to understand the relation between ligands and receptors and the manufacturing and design of new medications [11, 12]. Currently, the joint use of network pharmacology and molecular docking has been efficiently applied to the study of TCM and its compound prescriptions [13–15].

Gedan Jiangya Decoction (GJD; patent publication number: CN114246896A) includes six botanical drugs: Uncaria rhynchophylla (Miq.) Miq. ex Havil. (Gouteng), Salvia miltiorrhiza Bunge (Danshen), Pueraria lobata (Willd.) Ohwi. (Gegen), Eucommia ulmoides Oliv. (Duzhong), Prunella vulgaris L. (Xiakucao), and Achyranthes bidentata Blume (Niuxi). Previous studies have revealed that isorhynchophylline and rhynchophylline in Uncaria rhynchophylla can reflexively and directly inhibit the vasomotor center, dilating peripheral blood vessels as exertion antihypertensive effects by inhibiting the influx of extracellular Ca^{2+} [16, 17]. Studies have also revealed that both Salvia miltiorrhiza and Pueraria lobata have a wide variety of pharmacological effects on the cardiovascular system, including anti-inflam-

matory, endothelial cell function protection, antioxidant, vasodilation, and myocardial protection [18–21]. Prunella vulgaris, Achyranthes bidentata, and Eucommia ulmoides also have therapeutic benefits for cardiovascular diseases such as hypertension [22–24].

Previous studies have mostly concentrated on a single medication or ingredient, making it challenging to precisely represent the mechanism of GJD's multichannel, multitarget, and multicomponent compound. Therefore, this research seeks to use the study methods of molecular docking and network pharmacology to produce the GJD active ingredient-key target-pathway, analyze the molecular mechanism of GJD in treating hypertension, and provide a reference for future medical clinical experiments and theoretical research.

2. Materials and Method

2.1. Network Pharmacology Analysis

2.1.1. GJD Active Ingredients, Screening, and Target Prediction. The TCMSP database (https://old.tcmsp-e.com/index.php) [25] was used to collect the active components of Uncaria rhynchophylla, Salvia miltiorrhiza, Pueraria lobata, Eucommia ulmoides, Prunella vulgaris, and Achyranthes bidentata, and the active components were preliminarily evaluated based on the two ADME properties of oral bioavailability (OB) ≥ 30% and drug-likeness (DL) ≥ 0.18. Simultaneously, the screened components were complemented using published literature to obtain the GJD active ingredients. The TCMSP database is used to predict the target of active ingredients. The UniProt database (https://www.uniprot.org/) [26] is then utilized to standardize protein target information and screen the targets with "Reviewed" and "Human" as screening conditions and complete the transformation from protein name to gene name to obtain the relevant target of GJD.

2.1.2. Prediction of Primary Hypertension Targets. We used the GeneCards database (https://www.genecards.org/), the OMIM database (https://omim.org/), the TTD database (http://db.idrblab.net/ttd/) [27], and the DrugBank database (https://go.drugbank.com/) [28] to collect potential primary hypertension targets with "primary hypertension" as the keyword. The higher the score value in the GeneCards database, the more closely connected the target is to the disease. To obtain the potential primary hypertension target, first, we select the target with a score value more than the median and then select the remaining target with a higher score than the median. Then, combine the primary hypertension-related targets from the four disease databases mentioned above and remove duplicates to get the primary hypertension-related targets.

2.1.3. Protein-Protein Interaction Network. The GJD-related and primary hypertension-related targets were imported into the R language, and the intersection of the targets was drawn as a Venn diagram. Then, import the intersection targets into the STRING 11.0 data platform [29], setting the biological species to "Homo sapiens" and the minimum interaction score to "highest confidence" (>0.9), and hide

the free isolates node to build a protein-protein interaction (PPI) network model. After that, use the Cytoscape 3.8.0 [30] tool to calculate and screen the degree value, and choose the intersection target with a degree value greater than twice the median as the key target for primary hypertension treatment.

2.1.4. GO and KEGG Pathway Enrichment Analyses.
We import key targets into the Metascape data platform (https://metascape.org) [31], select "H. sapiens" for "Input as species" and "Analysis as species" conditions, and then select "custom analysis" with $P < 0.01$ as the screening condition; GO function analysis and KEGG pathway enrichment analysis are performed for key targets; and the enrichment results are drawn into a bubble plot in the R language.

2.1.5. Network Construction and Analysis of Target Pathway.
The active components corresponding to the key targets were screened out, and the drugs, key targets, and KEGG pathways were transferred into Cytoscape program for analysis, and the network diagram of the GJD active ingredient-key target-pathway was obtained. Use the "Analyze Network" of the Cytoscape toolbar to calculate it, and select the active ingredients with a degree value greater than 2 times the median as the key ingredients in treating primary hypertension.

2.2. Molecular Docking (Key Ingredients to Key Targets).
Using the PDB database (http://www.rcsb.org/) [32] to download the three-dimensional protein structure of key targets, select the species source as "Homo sapiens," and the resolution is high (resolution < 3.0 Å) and the protein with the crystal structure of the original complex ligand, and save it as a PDB format file; use Discovery Studio to preprocess it, including deleting water molecules, hydrogenation, charge distribution, and other operations to the original ligand, focusing on the spatial structure of the original ligand; create the active docking pocket using PyMOL's GetBox plugin; record the spatial location and radius of the active pocket; and then import it into AutoDockTools [33] and export it in PDBQT format. Then, get the core component SDF format file and convert it via the PubChem database (https://pubchem.ncbi.nlm.nih.gov/) [34]; save it in PDB format, input it into AutoDockTools, and output it as PDBQT format. Finally, AutoDock Vina [35] was used for molecular docking, while PyMOL and Discovery Studio were used for mapping.

2.3. Experiment

2.3.1. Preparation of GJD.
GJD's composition is as follows: Uncaria rhynchophylla (Miq.) Miq. ex Havil. (Gouteng), 10 g; Salvia miltiorrhiza Bunge (Danshen), 25 g; Pueraria lobata (Willd.) Ohwi (Gegen), 30 g; Eucommia ulmoides Oliv. (Duzhong), 15 g; Prunella vulgaris L. (Xiakucao), 15 g; and Achyranthes bidentata Blume (Niuxi), 20 g. The botanical drugs described above were purchased from Heilongjiang Xiushengtang Pharmaceutical Co., Ltd. First, mix the botanical drugs (Salvia miltiorrhiza, Pueraria lobata, Eucom-

Table 1: Primer's list for RT-qPCR.

Gene	Sequences of primers
AGTR1	Forward: 5′-AATATTTGGAAACAGCTTGGT-3′
	Reverse: 5′-ATGATGATGCAGGTGACTTTG-3′
ACE	Forward: 5′-CCAACAAGACTGCCACCTG-3′
	Reverse: 5′-GTACTGGTGACATCGAGGTTG-3′
eNOS	Forward: 5′-GGATTCTGGCAAGACCGATTAC-3′
	Reverse: 5′-GGTGAGGACTTGTCCAAACACT-3′
GAPDH	Forward: 5′-TGCACCACCAACTGCTTAG-3′
	Reverse: 5′-GATGCAGGGATGATGTTC-3′

mia ulmoides, Prunella vulgaris, and Achyranthes bidentata) with 60% aqueous ethanol solution in a material liquid ratio of 1 g : 10 ml, soak for 0.5 hour, heat and reflux the soaking solution for 1.5 hours (keep the solution slightly boiling during the reflux process), and filter with six layers of degreasing gauze; after that, in the same way, reheat and reflux with 10 times the amount of 60% aqueous ethanol solution for 1.5 hours and filter; then, to get extracts of Salvia miltiorrhiza, Pueraria lobata, Eucommia ulmoides, Prunella vulgaris, and Achyranthes bidentata, combine two filtrates, distill ethanol under reduced pressure using a rotary evaporator, and then dry under reduced pressure and vacuum. Second, soak Uncaria rhynchophylla in a 70% aqueous ethanol solution in a 1 g : 10 ml ratio for 0.5 hour, then heat it to 65~75°C, and soak it for 2 hours. Filter it through six layers of degreasing gauze, then soak it in 10 times amount of 70% aqueous ethanol solution for 2 hours, filter it, then use the above method to get the extract of Uncaria rhynchophylla. Finally, combine the two extracts to make GJD.

2.3.2. HPLC Analysis of GJD.
This analysis was performed using the Waters Alliance e2695, Waters 2998 PDA Detector, and Diamonsil® C18 column (250×4.6 mm, 5μm). Puerarin (Lot No. 110752-201816, Purity: 95.4%), tanshinone IIA (Lot No. 110766-202022, Purity: 98.9%), daidzein (Lot No. 111502-202003, 99.3%), ursolic acid (Lot No. 110742-201823, Purity: 99.9%), and cryptotanshinone (Lot no. 110852-201807, Purity: 99.0%) were purchased from National Institutes for Food and Drug Control. Take a dosage of puerarin, tanshinone IIA, daidzein, ursolic acid, and cryptotanshinone, and dissolve it in methanol. Standard solutions with concentrations of 0.3, 0.25, 0.5, 0.5, and 0.3 mg/ml were prepared. Before HPLC analysis, 1 g of GJD extract powder is mixed with 10 ml of methanol and filtered through a 0.22 μm filter. The mobile phase was acetonitrile (A) -0.1% aqueous phosphoric acid solution (B). The following is the gradient elution program: 0-14 min, 30-37% A; 14-17 min, 37-55% A; 17-29 min, 55-67% A; 29-40 min, 67-89% A; 40-48 min, 89-97% A; and, 48-54 min, 97-100% A; column temperature: 30°C; flow rate: 1.0 ml/min. The wavelength of detection was 210 nm. The injection volume was 10 μl.
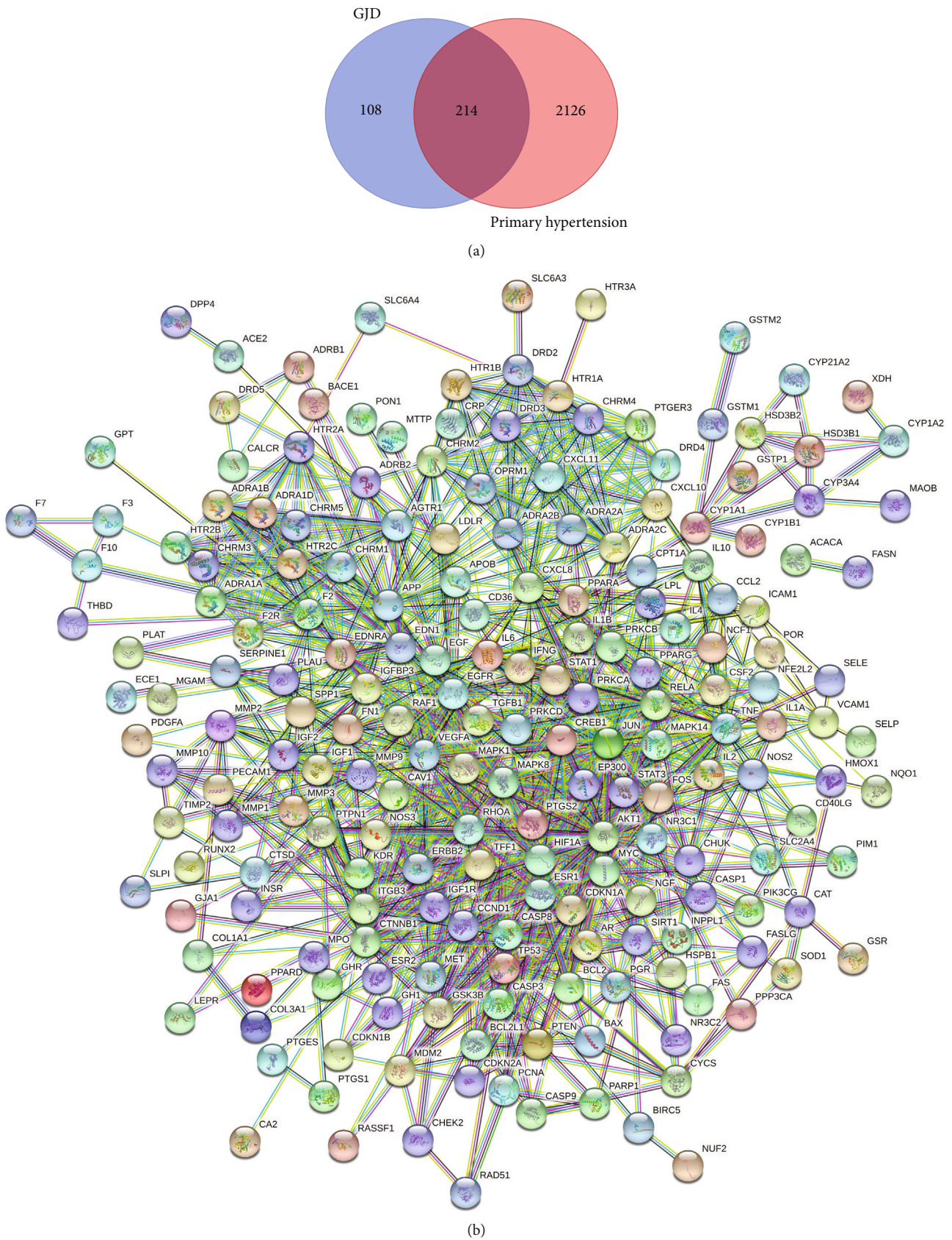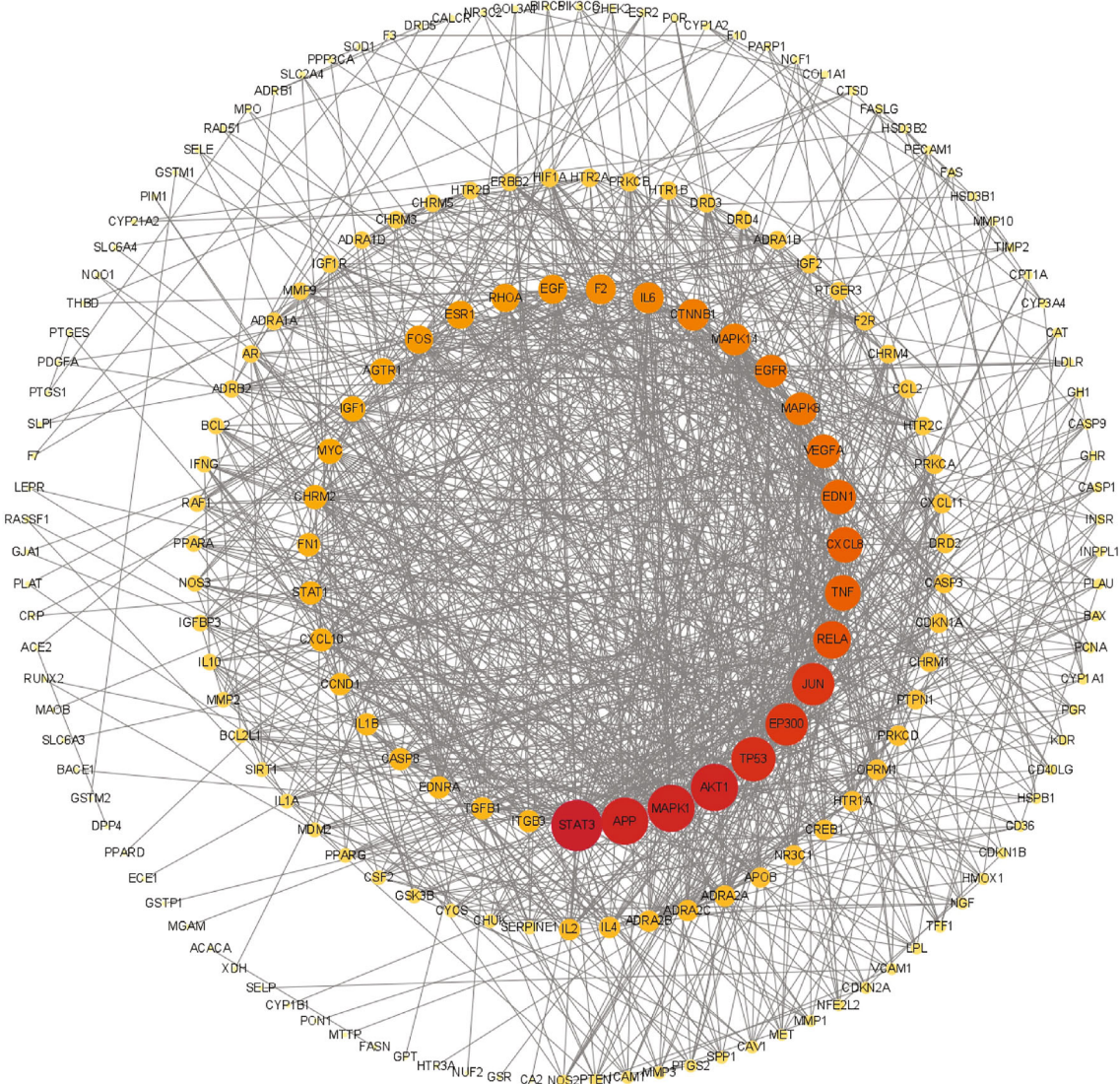
(a)

(b)

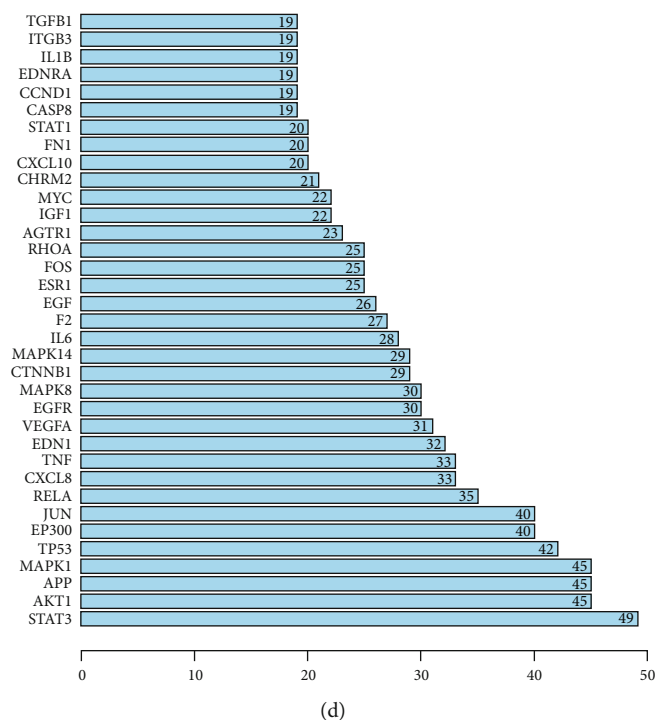Figure 1: Continued.

(c)

Figure 1: Continued.

(d)

Figure 1: (a) According to a Venn diagram, GJD and primary hypertension have 214 common targets that might be utilized as therapeutic targets. (b) Target protein interaction network (PPI). (c) Target protein interaction network analysis in Cytoscape software. (d) The top 35 potential targets of PPI. As the degree value increases from small to large, the node's color changes from yellow to red, and the node's size changes from small to large.

2.3.3. *Animals.* Twenty-one male SD (Sprague Dawley) rats (body weight 170 ± 10 g) were acquired from Liaoning Changsheng Biotechnology Co., Ltd. (license number SYXK (Hei) 2018-007) and maintained at a constant temperature ($22 \pm 2°C$), humidity ($55 \pm 5\%$), and lighting ($12:12$ hr light-dark cycle). One week before the experiment, rats were given unrestricted access to food and water to acclimatize to their surroundings. All experimental protocols were approved by the Animal Ethics Committee of Heilongjiang University of Chinese Medicine, with approval number 2020031203.

2.3.4. *Construction of High-Salt Diet-Induced Hypertension Model.* The SD rats were randomly divided into 3 groups, 7 rats in the control group, 7 rats in the model group, and 7 rats in the GJD group. The rats in the control group were fed with standard chow. In contrast, the rats in the other groups were fed with 8% NaCl high-salt feed (7.5%NaCl + 92.5%common feed, purchased from Guangdong Provincial Medical Laboratory Animal Center, license number Guangdong Feed Certificate (2019) 05073) for 8 weeks with free access to water. The body weight of the rats in each group was recorded every two weeks. The systolic blood pressure (SBP) and diastolic blood pressure (DBP), as well as heart rate (HR), were monitored every two weeks by the noninvasive blood pressure measurement system ALC-NIBP (Shanghai Alcott Biotechnology Co., Ltd.) using the tail-cuff method. Each rat was measured three times, and the average value was recorded. A long-term 8% high-salt

diet for 8 weeks caused hypertension in rats [36]; rats with SBP of ≥ 160 mmHg were considered to have successfully established a hypertension model. All rats in the model and GJD groups were modeled successfully.

2.3.5. *Drug Treatment and Blood Pressure Measurement.* For four weeks, each rat in the GJD group received 1.5 ml of GJD extract 1.07 g/kg/d by gavage, whereas the other groups received the same amount of 0.9% normal saline by gavage. The body weight of the rats in each group was recorded every two weeks. Rats' SBP, DBP, and HR were recorded every two weeks using the noninvasive blood pressure measurement system (ALC-NIBP). Each rat was measured three times, and the average value was recorded.

2.3.6. *Sample Preparation.* All rats were anesthetized with an intraperitoneal injection of 3% sodium pentobarbital (45 mg/kg), and blood samples were obtained from the abdominal aorta and put in disposable blood collection tubes. Centrifuge at 3500 rpm for 15 minutes at 4°C, then extract serum and put it in a centrifuge tube. Hearts were removed and washed in cold saline. The heart's left ventricle is obtained by resecting the atrial free wall, major arteries, and right ventricle along the atrioventricular junction. Left ventricular mass index (LVMI) is calculated by the following formula: LVMI = left ventricular weight (mg)/ body weight (g). At the same time, thoracic aorta and kidney tissues were taken and frozen at -80°C for detection using RT-qPCR, Western blot, and kits.
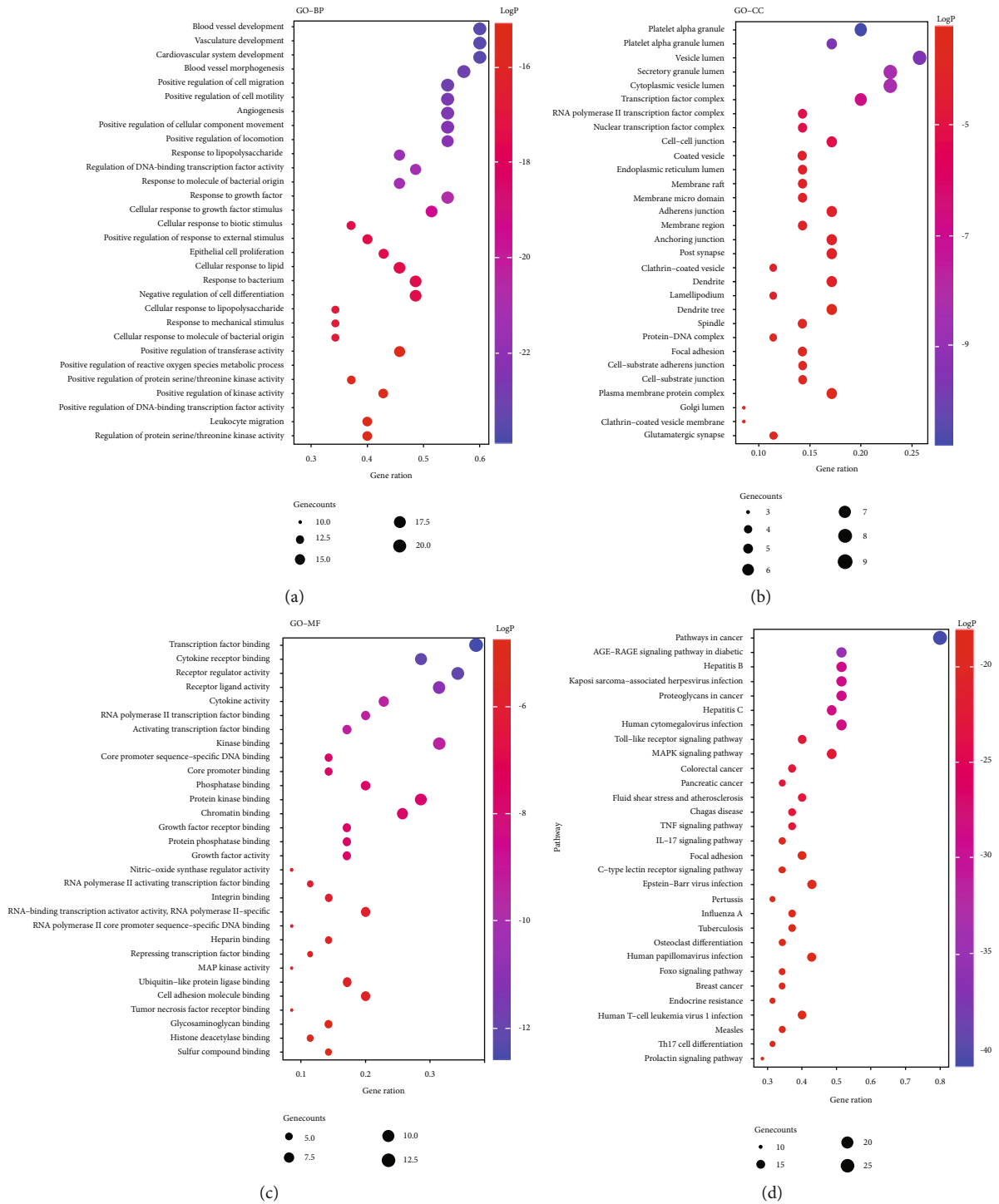
FIGURE 2: (a) The top 30 biological processes. (b) The top 30 cellular components. (c) The top 30 molecular functions. (d) The top 30 KEGG pathways.

2.3.7. ELISA Kit Index Determination. The ELISA Kit was used to measure the expression levels of renin, Ang II, ALD, and NO in serum and Ang II in renal tissue (Ang II kit was purchased from Jiangsu Jingmei Biotechnology Co., Ltd., and ALD, renin, and NO (nitrate reductase method) kit was purchased from Nanjing Jiancheng Bioengineering Institute). The procedure was carried out in strict accordance with the kit's instructions.

2.3.8. RT-qPCR. The total RNA was extracted from kidney and thoracic aorta tissues using Trizol reagent (Takara), reverse transcribed into cDNA using PrimeScript RT Kit
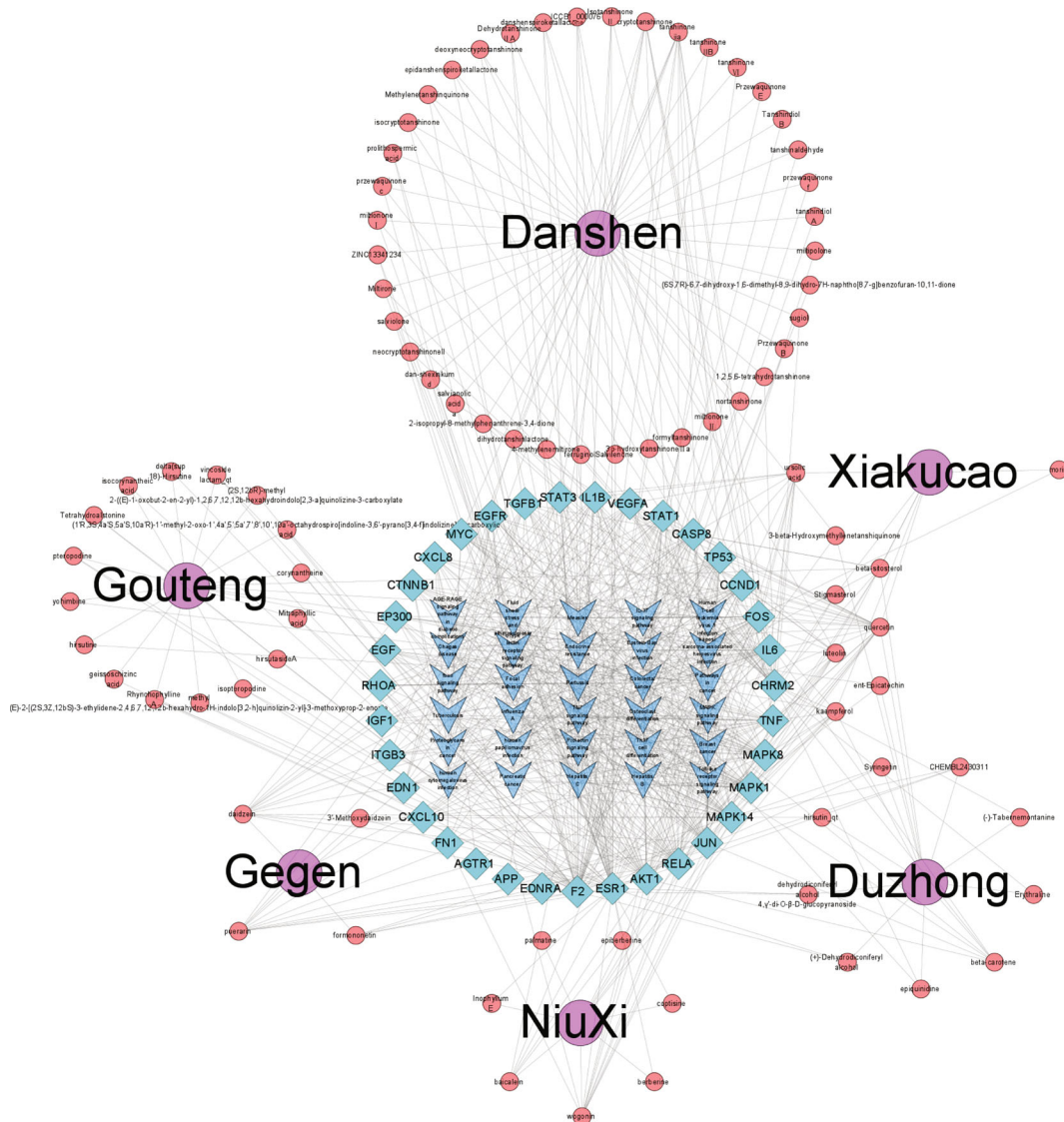
Figure 3: Using Cytoscape, construct the GJD active ingredient-key target-pathway network. 11 key ingredients were screened for potential treatment of primary hypertension. The purple circles in the outer circle represent the 6 Chinese herbal medicines in GJD, the red circles in the outer circle represent the active components of each Chinese herbal medicine, the blue diamonds in the inner circle represent the core targets, and the blue arrows in the inner circle represent the KEGG pathway.

(Takara), and then subjected to real-time PCR reaction using TB Green® Premix Ex Taq™ II (Tli RNaseH Plus) (Takara), and the gene expression level was quantified using QuantStudio™3 Real-Time PCR system. The $2^{-\Delta\Delta CT}$ method was used to calculate and analyze the data, with GAPDH acting as an internal control. The following primers were used for PCR amplification Table 1.

2.3.9. Western Blot Analysis. The total protein was obtained from the kidney and thoracic aorta using RIPA lysis buffer with PMSF and phosphatase inhibitor (Servicebio, China), and protein concentration was measured using a BCA protein detection kit (Servicebio, China). SDS-PAGE was used to separate the whole protein, which was subsequently transferred to $0.45\,\mu$m on the PVDF membrane (Servicebio, China). The membrane was sealed with 5% nonfat milk at

room temperature for 1 hour before incubating with primary antibody overnight at 4°C. The membrane was washed three times with TBST and incubated with a secondary antibody at room temperature for 1 hour, and the protein was identified using an ECL reagent (Servicebio, China). Primary antibodies include AGTR1 (1:1,000, Boster, China), eNOS (1:1,000, Servicebio, China), and β-actin (1:2,000, Servicebio, China).

2.3.10. Statistical Analysis. All data in this experiment were statistically analyzed using the SPSS 26.0 software; measurement data were represented as mean ± standard deviation (mean ± SD), and one-way analysis of variance (ANOVA) was used to compare multiple groups. For variance homogeneity of pairwise comparisons between groups, the LSD test was employed, and Tamhane's T2 (M) test was used for

	Quercetin	Daizein	Ursolic acid	Wogonin	Luteolin	TanshinoneIIA	Puerarin	Kaempferol	Cryptotanshinone	Beta-carotene	Baicalein
F2	−8.7	0	0	0	0	−7.9	0	−8.5	0	0	0
ESR1	0	−8.6	0	−9.1	0	0	−7.4	0	0	0	0
TNF	−7.2	−6.5	−7.2	−6.6	−6.5	0	−7.3	−6.6	−7	0	0
CTNB1	0	0	0	0	0	0	0	0	0	−3	0
EGFR	−8	0	0	0	−8.2	0	0	0	0	0	0
MAPK14	0	−9.8	0	−8.6	0	0	0	0	0	0	0
MAPK8	0	0	8	0	0	0	0	−8.5	0	0	0
IL 1B	0.4	0	−8.8	0	0	0	0	0	0	0	0
CXLB	6	0	0	−6.2	0	0	0	0	0	0	0
EP300	0	−8.1	0	0	0	0	0	0	0	0	0
VEGFA	−5.7	−6.1	−7	0	−6	0	−5.7	0	0	−6.3	−5.6
RHOA	0	−6.7	0	0	0	0	0	0	0	0	0
MAPK1	−8	0	0	0	−8.3	0	0	0	0	0	0
TP53	−5.4	−5.1	−6.2	−5.6	−5.6	−5.8	0	0	0	0	−5.5
AKT1	−10	0	0	−9.7	10.2	0	−10.6	−9.8	0	−9.8	−10
STAT3	0	0	−6.4	0	0	0	−5.5	0	−6	0	0
CASP8	−6.7	0	−7.3	0	0	0	−7.4	0	0	−6.9	0
CCND1	−7.8	0	−7.3	−6.9	−6.6	0	0	0	−7.3	0	0
CCND1	0	0	0	0	0	0	−9.2	0	0	0	0
FN1	0	0	0	−5.7	0	0	0	0	0	0	0
APP	0	0	0	0	−6.8	0	0	0	−6.7	0	0
MYC	−5.9	0	0	0	0	−6.4	0	0	0	−7.6	0
EDN1	0	0	0	0	0	−6.3	0	0	0	0	0
ITGB3	0	0	0	0	0	−7.9	0	0	0	0	0
CHRM2	0	0	0	0	0	−6.6	0	−7.4	−8.6	0	0
IGF1	0	−6.2	0	0	0	0	0	0	0	0	0
EDNRA	0	0	0	0	0	−8.1	0	0	0	0	0
JUN	−5.3	−5.1	−6.1	−5	−5.4	−5.7	−5.3	−5.3	0	−6.5	0
IL6	−7.2	−7	−7	−6.5	−7	0	0	0	0	0	0
TGFB1	−6.7	0	0	0	0	0	0	0	0	0	0
STAT1	−6.7	−6.4	0	0	0	0	0	−6.5	0	0	0
EGF	−6.2	0	0	0	0	0	0	0	0	0	0
CXCL10	−6	0	0	0	0	0	0	0	0	0	0
RELA	−7.2	−7.2	−7.8	−6.9	−7.2	−7.7	−7.5	−7.2	−7.9	0	−7.5
FOS	−5.1	−5.3	−6.2	0	0	−5.9	−5.2	0	0	0	−5.4

FIGURE 4: Heatmap of docking scores for 35 target proteins with 11 active ingredient molecules. The darker the color, the stronger the binding activity. The score of 0 means they are not molecularly docked.

variance heterogeneity. $P < 0.05$ was regarded as statistically significant. The statistical analysis findings were created using the GraphPad Prism 7.0 program.

3. Results

3.1. Network Pharmacology Analysis

3.1.1. GJD Target Prediction Results in Primary Hypertension Treatment.
We obtained 32 active ingredients of Uncaria rhynchophylla, 59 active ingredients of Salvia miltiorrhiza, 4 active ingredients of Pueraria lobata, 26 active ingredients of Eucommia ulmoides, 11 active ingredients of Prunella vulgaris, and 17 active ingredients of Achyranthes bidentata through ADME screening and the TCMSP database, and according to the literature review, there is one active ingredient of Salvia miltiorrhiza [37, 38], two active ingredients of Pueraria lobata [39, 40], and two active ingredients of Prunella vulgaris [23, 41]. Finally, 154 GJD active ingredients were obtained, and 322 predicted targets for GJD

TABLE 2: PDB ID of the target proteins.

| Target	PDB ID	Target	PDB ID	Target	PDB ID	Target	PDB ID
F2	8KME	EP300	6V8K	AGTR1	6OS2	JUN	5FV8
ESR1	7KCA	VEGFA	6V7K	FN1	6MSV	IL6	5FUC
TNF	7JRA	RHOA	6V6U	APP	6GFI	TGFB1	5FFO
CTNNB1	7AFW	MAPK1	6SLG	MYC	6G6K	STAT1	3WWT
EGFR	7A2A	TP53	6SL6	EDN1	6DK5	EGF	3NJP
MAPK14	6ZWP	AKT1	6S9W	ITGB3	6BXJ	CXCL10	1O7Y
MAPK8	6ZR5	STAT3	6QHD	CHRM2	5ZKC	RELA	1NFI
IL1B	6Y8M	CASP8	6PX9	IGF1	5U8Q	FOS	1A02
CXCL8	6WZM	CCND1	6P8E	EDNRA	5GLH		
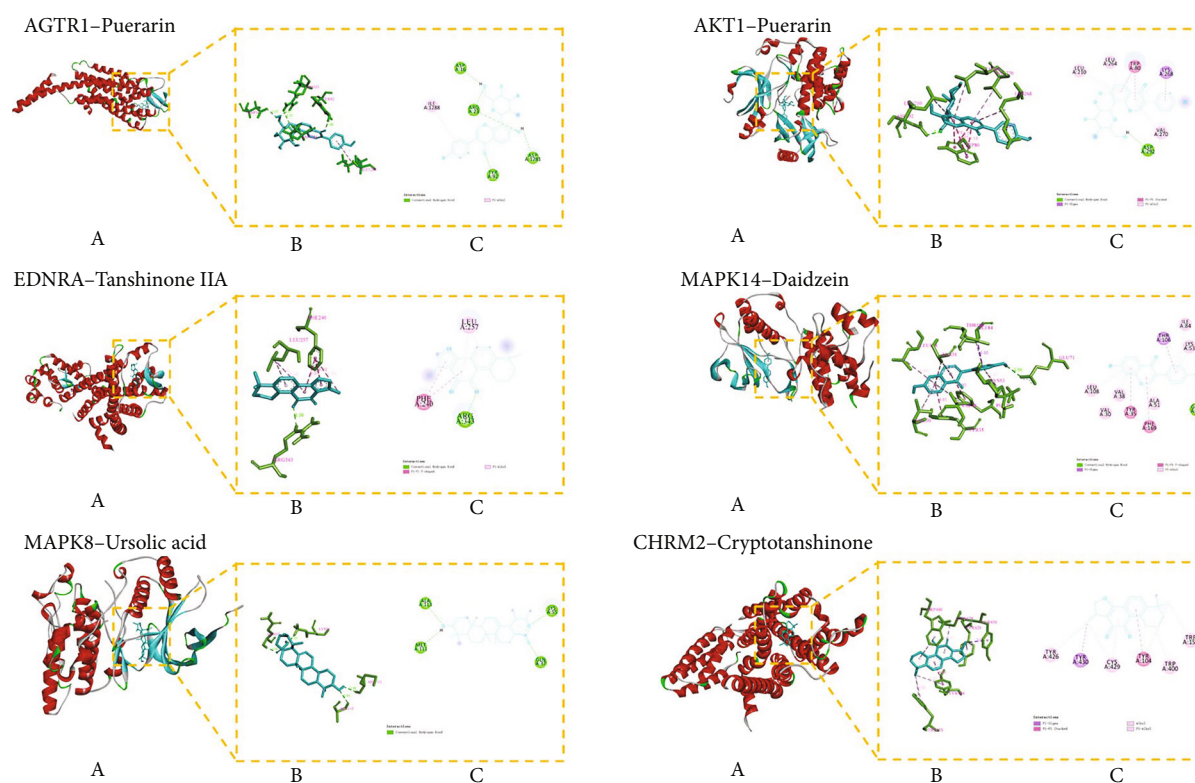
FIGURE 5: The molecular docking pattern. Each target protein with its active ingredient molecular docking pattern diagram is divided into three little figures (a), (b), and (c). (a) Represents the overall binding position of small molecule compounds (sticks model) on related proteins (cartoon model). (b) Shows the interaction of small molecule compounds (blue) with important residues (green) on related proteins. (c) Displays a two-dimensional plan, which is convenient for observing the hydrogen bonding and hydrophobic interactions between small molecule compounds and protein residues.

active ingredients were collected using the TCMSP database. We obtained 2236 hypertension-related targets from the GeneCards database, 126 from the OMIM database, 107 from the TTD database, and 43 from the DrugBank database. The primary hypertension-related targets collected from the four databases mentioned above were merged together, and duplicate targets were removed, yielding 2340 potential primary hypertension targets. Using the R language, 322 GJD-related targets and 2340 primary hypertension-related targets were intersected, and a Venn diagram was drawn, giving 214 intersected targets, as shown in Figure 1(a).

3.1.2. Constructing of PPI Network and Acquiring Key Targets.
As shown in Figure 1(b), the GJD target protein-protein interaction (PPI) network for treating primary hypertension was created by importing the intersection target into the STRING data platform. Cytoscape was used to visualize it (see Figure 1(c)), and there are 199 nodes and
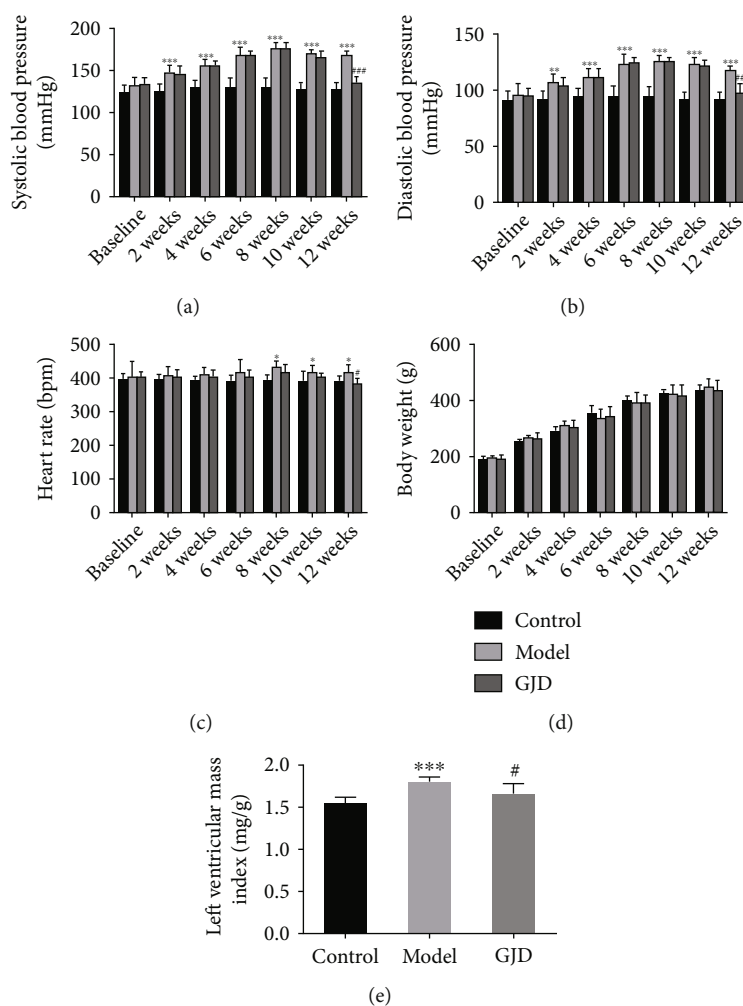
(a)

(b)

(c)

(d)

(e)

Figure 6: SBP, DBP, HR, and body weight indexes of SD rats ($n = 7$) before high-salt modeling, 8-week high-salt modeling, and 4 weeks of GJD treatment and LVMI after 4 weeks of GJD treatment. (a) Systolic blood pressure. (b) Diastolic blood pressure. (c) Heart rate. (d) Body weight. (e) Left ventricular mass index. $^*P < 0.05$, $^{**}P < 0.01$, and $^{***}P < 0.001$ as compared to the control group; $^#P < 0.05$, $^{##}P < 0.01$, and $^{###}P < 0.001$ as compared to the model group.

1145 edges in total. Thirty-five key targets with a degree value greater than 18 (2 times the median) were obtained, which may be the targets for GJD to play an essential role in primary hypertension treatment (see Figure 1(d)).

3.1.3. GO and KEGG Analysis Results. The key targets were imported into the Metascape data platform, and the results of the GO enrichment function analysis showed that the targets were mainly involved in biological processes such as blood vessel development, vasculature development, cardiovascular system development, blood vessel morphogenesis, and angiogenesis; the main related molecular functions are transcription factor binding, cytokine receptor binding, receptor regulator activity, receptor-ligand activity, cytokine activity, and nitric-oxide synthase regulator activity.

A total of 149 pathways were obtained from the KEGG pathway enrichment analysis. Among them are the Toll-like receptor signaling pathway, PI3K-Akt signaling pathway, MAPK signaling pathway, TNF signaling pathway, NOD-like receptor signaling pathway, NF-κB pathway, and

renin-angiotensin pathway which are strongly correlated with hypertension. According to the enrichment analysis results, according to the Log$P$ value from small to large, the top 30 items of GO-BP, GO-CC, GO-MF, and KEGG were selected, respectively, and visualized by using the R language, as shown in Figure 2.

3.1.4. Network Construction of Target Pathway and Key Ingredient Acquisition. The GJD active ingredient-key target-pathway network diagram was constructed using Cytoscape (see Figure 3), and through the "Analyze Network" tool of Cytoscape, 11 key ingredients of GJD in treating primary hypertension are screened, as shown in Supplementary Material (2).

3.2. Molecular Docking Result. The target protein's and active ingredient molecules' docking results are shown in Figure 4, and these target proteins' PDB ID are shown in Table 2. The results showed that binding energies below -5.0 kcal·mol^{-1} represented 98% of the targets, indicating that
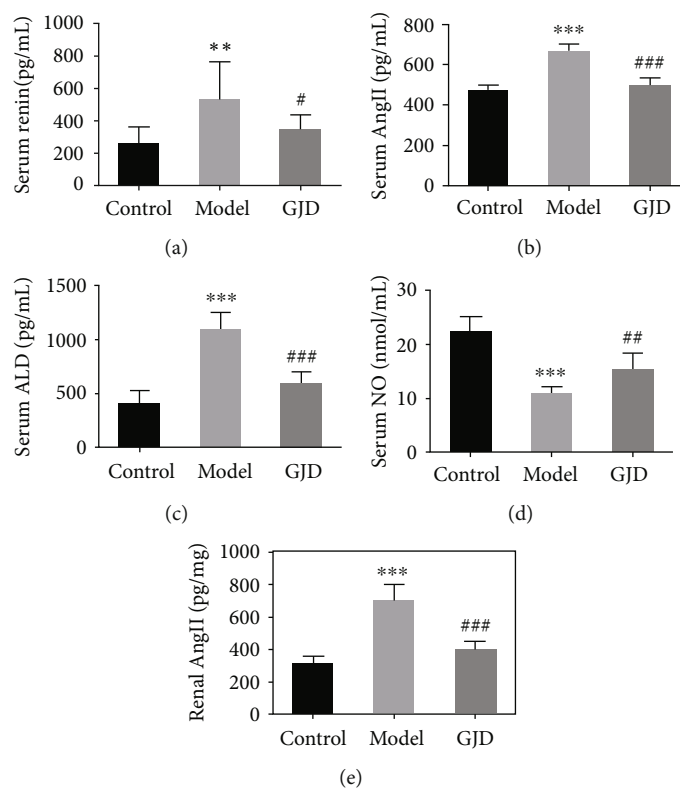
(a)

(b)

(c)

(d)

(e)

Figure 7: Effects of GJD on renin, Ang II, ALD, and NO expression in serum and Ang II in kidney tissue of high-salt induced hypertensive rats ($n = 7$). (a) Serum renin level. (b) Serum Ang II level. (c) Serum ALD level. (d) Serum NO level. (e) Kidney tissue Ang II level. $^{*}P < 0.05$, $^{**}P < 0.01$, and $^{***}P < 0.001$ compared to the control group; $^{#}P < 0.05$, $^{##}P < 0.01$, and $^{###}P < 0.001$ compared to the model group.

most of the targets had strong binding activity to the active ingredients, demonstrating the reliability of the network pharmacology prediction results. Among them, AGTR1, AKT1 with puerarin, EDNRA with tanshinone IIA, MAPK14 with daidzein, MAPK8 with ursolic acid, and CHRM2 with cryptotanshinone all have a strong correlation with GJD in the treatment of primary hypertension. Figure 5 illustrates their docking pattern. The molecular docking results indicated that the active ingredients of GJD, puerarin, have significant binding activity with the primary hypertension targets AGTR1. However, further experiments are needed to verify their strong interaction.

3.3. Result of HPLC Analysis. HPLC detected five key active ingredients of GJD, including puerarin, tanshinone IIA, daidzein, ursolic acid, and cryptotanshinone. Supplementary Material (1) shows the findings of HPLC analysis of these five active ingredients.

3.4. Experiment Verification

3.4.1. Effect of GJD on Blood Pressure and Heart Rate (HR). Elevated blood pressure is the main clinical manifestation of hypertension, and elevated heart rate is a common feature of individuals with hypertension [42, 43]. Therefore, we evaluated the effect of GJD on primary hypertension by measuring SBP, DBP, and HR in rats. As shown in Figures 6(a)–6(d), SD rats were fed 8% high-salt diet for 8

weeks, the SBP was 176.68 mmHg, the DBP was 125.62 mmHg in the model group, and the SBP was 176.86 mmHg in the GJD group, and the DBP was 125.28 mmHg, indicating that the hypertension model established is successful. After 4 weeks of treatment, the SBP was 168.95 mmHg, the DBP was 118.08 mmHg in the model group, the SBP was 135.31 mmHg, and the DBP was 97.69 mmHg in the GJD group. The SBP and DBP were significantly reduced in the GJD group ($P < 0.001$), indicating that GJD has a significant antihypertensive effect. In addition, the HR of the rats in the GJD group was also lower than that in the model group. ($P < 0.05$). By calculating the left ventricular mass/body weight of the rats in each group, after 4 weeks of treatment, the LVMI in the model group was significantly higher than that in the control group ($P < 0.001$), Figure 6(e), while that in the GJD group was decreased compared with the model group ($P < 0.05$). We also observed no difference in the body weight of rats between the groups during the same period (Figure 6(d)).

3.4.2. Effect of GJD on RAAS and Serum NO. The renin-angiotensin-aldosterone system plays an extremely important in the pathogenesis of primary hypertension, and NO is an important vasodilator factor in the body, and their expression changes in serum can reflect the development trend of primary hypertension. As shown in Figure 7, the expressions of renin, Ang II, and ALD in the model group's
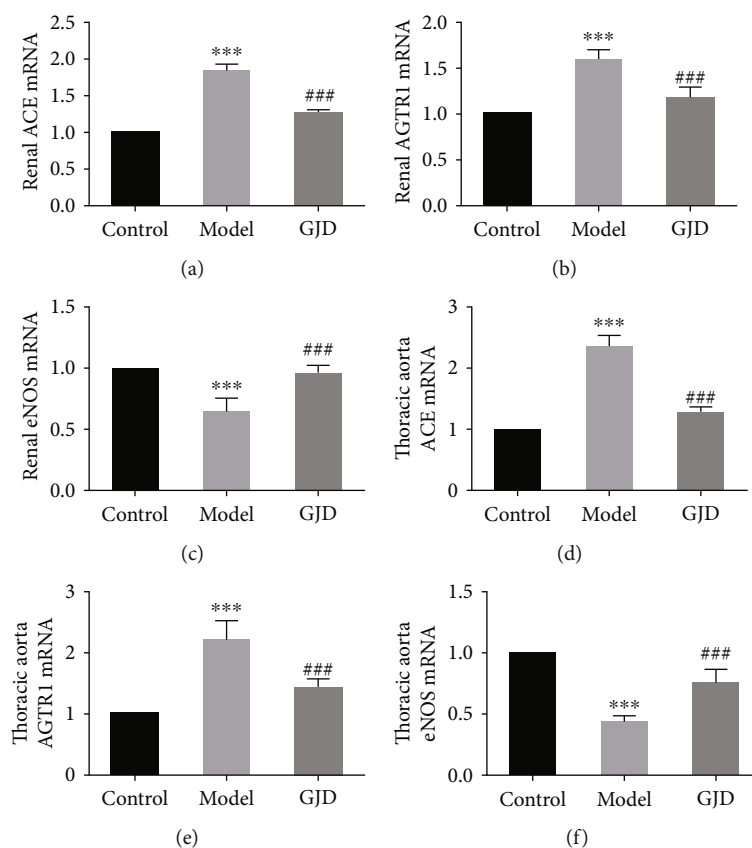
FIGURE 8: Effects of GJD on the expression of ACE (a, d), AGTR1 (b, e), and eNOS (c, f) mRNA in kidney and thoracic aorta of hypertensive rats ($n = 7$) induced by high-salt based on RT-qPCR. $*P < 0.05$, $**P < 0.01$, and $***P < 0.001$ compared with the control group; [#]$P < 0.05$, [##]$P < 0.01$, and [###]$P < 0.001$ compared with the model group.

serum were increased significantly ($P < 0.01, 0.001$, and 0.001) in comparison to the control group, and the expression of NO was significantly decreased ($P < 0.001$). Compared with the model group, the expressions of renin, Ang II, and ALD in the serum of the GJD group were significantly decreased ($P < 0.05, 0.001$, and 0.001), and the expression of NO was significantly increased ($P < 0.01$). The expression of Ang II in kidney tissue of rats in the group was also significantly decreased ($P < 0.001$). The results indicate that GJD may reduce blood pressure by inhibiting the activation of the renin-angiotensin-aldosterone system and upregulating NO expression.

3.4.3. Effect of GJD on the Expression of AGTR1 and eNOS. After preliminary verification based on network pharmacology analysis and molecular docking, this study found that AGTR1 and eNOS play key roles in GJD's antihypertension. The results of RT-qPCR revealed that the expression of ACE and AGTR1 mRNA in the GJD group's thoracic aorta and kidney was inhibited. In contrast, the expression of eNOS mRNA was increased. Western blot investigations showed that the GJD group's expression of AGTR1 protein in the thoracic aorta and kidney was significantly lower than that of the model group, whereas eNOS expression was significantly higher. The result is shown in Figures 8 and 9.

4. Discussion

Network pharmacological analysis of Chinese medicines is becoming a research tool for studying the influence of Chinese medicines on diseases, intending to reveal complicated components and unexplored targets [44–46]. The GJD was developed to treat primary hypertension; however, the underlying mechanism remains unknown. The active components, targets, and signaling pathways of GJD in treating primary hypertension were predicted using network pharmacology, and the putative molecular mechanism was examined using molecular docking and animal experiments.

In this study, the network pharmacology results showed that 214 possible GJD targets for the treatment of hypertension were identified. Moreover, 35 hub targets were also uncovered in the PPI network diagram of potential targets, including STAT3, AKT1, APP, MAPK1, TP53, EP300, JUN, RELA, CXCL8, TNF, and EDN1. Based on the diagram of the GJD active ingredient-key target-pathway network, 11 components that were identified as active (quercetin, daidzein, ursolic acid, wogonin, luteolin, tanshinone IIA, puerarin, kaempferol, cryptotanshinone, beta carotene, and baicalein) are correlated with major targets of GJD in the treatment of hypertension, and it can be utilized as major components that play a pivotal role.
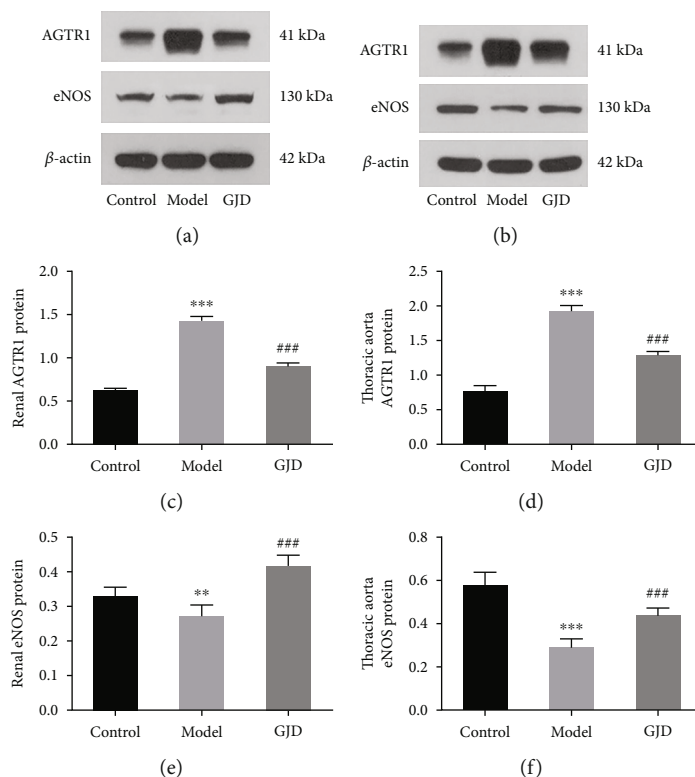
FIGURE 9: Effects of GJD on the expression of AGTR1 (a–d) and eNOS (a, b, e, and f) protein in the kidney (a) and thoracic aorta (b) of hypertensive rats induced by high-salt based on western blot analysis. $*P < 0.05$, $**P < 0.01$, and $***P < 0.001$ compared with the control group; $^{\#}P < 0.05$, $^{\#\#}P < 0.01$, and $^{\#\#\#}P < 0.001$ compared with the model group.

According to the KEGG analysis, the Toll-like receptor, MAPK, PI3K-Akt, TNF, NOD-like, NF-κB, and renin-angiotensin signaling pathways are major targets of GJD in the treatment of hypertension. Ang II is the most powerful vasoconstrictor molecule in RAAS, and it causes hypertension through oxidative activation and inflammatory response. Ang II may also change myocardial and blood vessels through controlling ALD production [47]. In this regard, the abnormal activation of the RAAS system would lead to hypertension and a wide range of cardiovascular diseases.

A molecular docking verification was conducted on 35 key targets and 11 active ingredients. The results indicate the AGTR1, AKT1 with puerarin, EDNRA with tanshinone IIA, MAPK14 with daidzein, MAPK8 with ursolic acid, and CHRM2 with cryptotanshinone had a high binding activity to targets with active ingredients. The smaller the binding energy, the more stable the ligand-receptor binding conformation, and the greater the possibility of interaction [35]. In our study, the binding of AGTR1 to puerarin is mainly through five hydrogen bond interactions with ASP16, ARG23, TYR92, ASP1281, and hydrophobic binding ILE1288, and its binding energy reaches $-9.2\,\text{kcal·mol}^{-1}$, indicating the binding of AGTR1 to puerarin is very active. Therefore, we performed experimental validation of the AGTR1 target.

When it comes to hypertensive individuals, antihypertensive medication is likely to lower the occurrence and death from disorders such as cardiovascular and cerebrovascular. Many clinical studies have pointed out that lowering the systolic blood pressure (SBP) by 10 mmHg or the diastolic blood pressure (DBP) at least by 5 mmHg may reduce the risk of mortality by 10%-15%, resulting in a 35% of reduced risk of stroke, 20% of lower risk of coronary heart disease, and 40% of lower risk of heart failure [48]. There are many variables that impact the incidence of critical hypertension; for instance, the excessive intake of salt is the most prevalent cause of hypertension, especially among Chinese citizens [49]. Excessive salt intake raises blood pressure, increasing the risk of hypertension and many other cardiovascular complications [49]. In this study, the SBP and DBP were significantly reduced in the GJD group, indicating that GJD has a significant antihypertensive effect. In addition, the LVMI of the rats in the GJD group was also lower than that in the model group, so GJD may also improve left ventricular hypertrophy, a complication of hypertension.

Many studies have been carried out recently to examine the association between excessive salt intake and elevated blood pressure; how increased salt consumption causes hypertension is not yet exclusively understood. Several studies have confirmed that high-salt foods damage the heart, renal, and vascular tissue and change the function of the renin-angiotensin system mechanism, thereby changing the levels of Ang II, ALD, renin, and AGTR1 in high-salt rats [36, 50, 51]. AGTR1 is regarded as an angiotensin II type 1 receptor, and the major active substance of the renin-angiotensin-aldosterone system (RAAS) is Ang II. Ang II

influences the development of vasoconstriction and aldosterone production in the adrenal cortex and causes hypertension via oxidative activation and inflammatory reactions [52]. A high-salt diet may influence the activation of the renal RAAS system and up the production of Ang II, leading to hypertension and renal damage in rats [53]. Puerarin is often used to treat various diseases, including hypertension, cardiac hypertrophy, atherosclerosis, diabetes-related cardiovascular complications, and stroke. Many experimental studies have indicated that puerarin can cause a reduction of AGTR1 expression in hypertension animal models. Puerarin can also boost cardiovascular function through increasing the eNOS expression and serum NO content via the PI3K/Akt pathway [20]. Vascular endothelial dysfunction can lead to various cardiovascular diseases, including hypertension, atherosclerosis, and thrombosis. Tanshinone IIA can decrease blood pressure and enhance endothelial-dependent vasodilation by quashing ET-1 expression induced by oxidative stress and increasing NO [19]. In addition, tanshinone IIA may inhibit the expression of EDNRA, upsurge the expression of EDNRB and eNOS, and guard against the endothelial function of the rat aorta [54]. GJD was observed to reduce the expression of AGTR1 mRNA and protein in the kidney and thoracic aorta of high-salt hypertension model rats while increasing the expression of eNOS mRNA and protein in the kidney and thoracic aorta.

The current study acknowledges that the GJD reduces the SBP, DBP, heart rate, and LVMI in high-salt hypertensive model rats and alters blood pressure-related biomarkers in rat serum. Renin, Ang II, and ALD expressions in the GJD group are also considerably reduced, but NO expression is highly increased. The results of RT-qPCR and WB indicate that GJD could lower the expression of AGTR1 mRNA and protein in the kidney and thoracic aorta of high-salt hypertension model rats, whereas it enhances the expression of eNOS mRNA and protein in the kidney and thoracic aorta, which concurs with the results of network pharmacology and a molecular docking prediction. Hence, this study confirms a few key targets and particular pathways.

5. Conclusion

As such, it can be concluded that the network pharmacology and molecular docking methods were utilized to investigate the intervention mechanism of GJD in primary hypertension. The research uncovered that the key active ingredients of GJD in managing primary hypertension are puerarin, tanshinone IIA, daidzein, ursolic acid, and cryptotanshinone, which are mainly expected to contain a regulatory function in conjunction with AGTR1, AKT1, EDNRA, MAPK14, MAPK8, and CHRM2. We identified these 5 key active ingredients in GJD by HPLC. Based on the results, the high-salt rat model experiment confirmed that GJD has an obvious antihypertensive effect by significantly reducing systolic and diastolic blood pressure, constrains the overactivation of the renin-angiotensin pathway, reduces the expression of AGTR1 in the kidney and thoracic aorta, and enhances the expression of eNOS. The current study discovered that GJD could be a potential therapeutic drug for primary hyperten-

sion, establishing a new strategy for the investigation and mechanism research of traditional Chinese medicine in treating hypertension.

Abbreviations

ADME: Absorption, distribution, metabolism, and excretion
AGTR1: Angiotensin II receptor type 1
DBP: Diastolic blood pressure
eNOS: Nitric oxide synthase 3
GJD: Gedan Jiangya Decoction
GO: Gene Ontology
HR: Heart rate
HPLC: High-performance liquid chromatography
KEGG: Kyoto Encyclopedia of Genes and Genomes
LVMI: Left ventricular mass index
SBP: Systolic blood pressure
STRING: Search Tool for the Retrieval of Interacting Genes/Proteins
TCM: Traditional Chinese medicine
TCMSP: Traditional Chinese Medicine Systems Pharmacology Database and Analysis Platform.

Data Availability

The data used to support the findings of this study are included within Supplementary Material (1) and Supplementary Material (2).

Conflicts of Interest

The authors declare that there are no conflicts of interest.

Authors' Contributions

The experiments were created and developed by Hanxing Liu, Shadi A.D. Mohammed, Fang Lu, and Shumin Liu. Hanxing Liu and Shadi A.D. Mohammed conducted the animal studies, analyzed the data, and wrote the manuscript. Pingping Chen and Yu Wang provided valuable suggestions for the research. All the authors have read and approved the final manuscript.

Supplementary Materials

Supplementary Material (1): all the experiment data. Supplementary Material (2): network pharmacology analysis. (Supplementary Materials)

References

[1] S. E. Kjeldsen, "Hypertension and cardiovascular risk: general aspects," *Pharmacological Research*, vol. 129, pp. 95–99, 2018.

[2] T. Verma, M. S. Tarawanti, N. Bansal, S. R. Yadav, K. Shah, and N. S. Chauhan, "Plants used as antihypertensive," *Natural products and bioprospecting*, vol. 11, no. 2, pp. 155–184, 2021.

[3] J. Lu, Y. Lu, X. Wang et al., "Prevalence, awareness, treatment, and control of hypertension in China: data from 1·7 million adults in a population-based screening study (China PEACE

Million Persons Project)," *Lancet*, vol. 390, no. 10112, pp. 2549–2558, 2017.

[4] X. Zhou, S. W. Seto, D. Chang et al., "Synergistic effects of Chinese herbal medicine: a comprehensive review of methodology and current research," *Frontiers in Pharmacology*, vol. 7, p. 201, 2016.

[5] M. Yang and L. Lao, "Emerging applications of metabolomics in traditional Chinese medicine treating hypertension: biomarkers," *Frontiers in Pharmacology*, vol. 10, p. 158, 2019.

[6] T. Liu and T. Zhang, "Review on the mechanism and advantages of traditional Chinese medicine in preventing and treating hypertension," *Journal of Traditional Chinese Medicine*, vol. 56, no. 1, pp. 77–82, 2015.

[7] X. Xiong, X. Yang, Y. Liu, Y. Zhang, P. Wang, and J. Wang, "Chinese herbal formulas for treating hypertension in traditional Chinese medicine: perspective of modern science," *Hypertension Research*, vol. 36, no. 7, pp. 570–579, 2013.

[8] National Center for Cardiovascular Diseases and T N E P H S P O f M o H i P H C N C o H M i P H C, "National clinical practice guidelines on the management of hypertension in primary health care in China (2020)Chinese," *Circulation Journal*, vol. 36, no. 3, pp. 209–220, 2021.

[9] T. T. Luo, Y. Lu, S. K. Yan, X. Xiao, X. L. Rong, and J. Guo, "Network pharmacology in research of Chinese medicine formula: methodology, application and prospective," *Chinese Journal of Integrative Medicine*, vol. 26, no. 1, pp. 72–80, 2020.

[10] S. Li and B. Zhang, "Traditional Chinese medicine network pharmacology: theory, methodology and application," *Chinese Journal of Natural Medicines*, vol. 11, no. 2, pp. 110–120, 2013.

[11] S. Saikia and M. Bordoloi, "Molecular docking: challenges, advances and its use in drug discovery perspective," *Current Drug Targets*, vol. 20, no. 5, pp. 501–521, 2019.

[12] X. Y. Meng, H. X. Zhang, M. Mezei, and M. Cui, "Molecular docking: a powerful approach for structure-based drug discovery," *Current Computer-Aided Drug Design*, vol. 7, no. 2, pp. 146–157, 2011.

[13] X. Shou, Y. Wang, X. S. Zhang et al., "Network pharmacology and molecular docking analysis on molecular mechanism of Qingzi Zhitong decoction in the treatment of ulcerative colitis," *Frontiers in Pharmacology*, vol. 13, p. 727608, 2022.

[14] Y. Wang, Y. W. Sun, Y. M. Wang, Y. Ju, and D. L. Meng, "Virtual screening of active compounds from Artemisia argyi and potential targets against gastric ulcer based on network pharmacology," *Bioorganic Chemistry*, vol. 88, p. 102924, 2019.

[15] G. Jia, X. Jiang, Z. Li et al., "Decoding the mechanism of Shen Qi Sha Bai decoction in treating acute myeloid leukemia based on network pharmacology and molecular docking," *Frontiers in Cell and Development Biology*, vol. 9, article 796757, 2021.

[16] Q. Zhang, J. J. Zhao, J. Xu, F. Feng, and W. Qu, "Medicinal uses, phytochemistry and pharmacology of the genus Uncaria," *Journal of Ethnopharmacology*, vol. 173, pp. 48–80, 2015.

[17] J. Zhou and S. Zhou, "Antihypertensive and neuroprotective activities of rhynchophylline: the role of rhynchophylline in neurotransmission and ion channel activity," *Journal of Ethnopharmacology*, vol. 132, no. 1, pp. 15–27, 2010.

[18] J. Ren, L. Fu, S. H. Nile, J. Zhang, and G. Kai, "Salvia miltiorrhiza in treating cardiovascular diseases: a review on its pharmacological and clinical applications," *Frontiers in Pharmacology*, vol. 10, p. 753, 2019.

[19] M. A. Ansari, F. B. Khan, H. A. Safdari et al., "Prospective therapeutic potential of Tanshinone IIA: an updated overview," *Pharmacological Research*, vol. 164, p. 105364, 2021.

[20] Y. X. Zhou, H. Zhang, and C. Peng, "Effects of puerarin on the prevention and treatment of cardiovascular diseases," *Frontiers in Pharmacology*, vol. 12, article 771793, 2021.

[21] Y. X. Zhou, H. Zhang, and C. Peng, "Puerarin: a review of pharmacological effects," *Phytotherapy Research*, vol. 28, no. 7, pp. 961–975, 2014.

[22] L. Huang, Q. Lyu, W. Zheng, Q. Yang, and G. Cao, "Traditional application and modern pharmacological research of Eucommia ulmoides Oliv," *Chinese Medicine*, vol. 16, no. 1, p. 73, 2021.

[23] Y. Bai, B. Xia, W. Xie et al., "Phytochemistry and pharmacological activities of the genus Prunella," *Food Chemistry*, vol. 204, pp. 483–496, 2016.

[24] J. Wang, B. Zhang, and F. A. Masoudi, "Effects of Achyranthes saponins on stroke-type spontaneously hypertensive rats," *China Journal of Chinese Materia Medica*, vol. 36, no. 9, pp. 1239–1241, 2011.

[25] J. Ru, P. Li, J. Wang et al., "TCMSP: a database of systems pharmacology for drug discovery from herbal medicines," *Journal of Cheminformatics*, vol. 6, p. 13, 2014.

[26] Consortium, U, "UniProt: the universal protein knowledgebase in 2021," *Nucleic Acids Research*, vol. 49, no. 1, pp. D480–D489, 2021.

[27] Y. Wang, S. Zhang, F. Li et al., "Therapeutic target database 2020: enriched resource for facilitating research and early development of targeted therapeutics," *Nucleic Acids Research*, vol. 48, no. 1, pp. D1031–D1041, 2020.

[28] D. S. Wishart, Y. D. Feunang, A. C. Guo et al., "DrugBank 5.0: a major update to the DrugBank database for 2018," *Nucleic Acids Research*, vol. 46, no. 1, pp. D1074–D1082, 2018.

[29] D. Szklarczyk, A. L. Gable, D. Lyon et al., "STRING v11: protein-protein association networks with increased coverage, supporting functional discovery in genome-wide experimental datasets," *Nucleic Acids Research*, vol. 47, no. 1, pp. D607–D613, 2019.

[30] P. Shannon, A. Markiel, O. Ozier et al., "Cytoscape: a software environment for integrated models of biomolecular interaction networks," *Genome Research*, vol. 13, no. 11, pp. 2498–2504, 2003.

[31] Y. Zhou, B. Zhou, L. Pache et al., "Metascape provides a biologist-oriented resource for the analysis of systems-level datasets," *Nature Communications*, vol. 10, no. 1, p. 1523, 2019.

[32] H. M. Berman, J. Westbrook, Z. Feng et al., "The Protein Data Bank," *Nucleic Acids Research*, vol. 28, no. 1, pp. 235–242, 2000.

[33] M. F. Sanner, "Python: a programming language for software integration and development," *Journal of Molecular Graphics & Modelling*, vol. 17, no. 1, pp. 57–61, 1999.

[34] S. Kim, J. Chen, T. Cheng et al., "PubChem in 2021: new data content and improved web interfaces," *Nucleic Acids Research*, vol. 49, no. 1, pp. D1388–D1395, 2021.

[35] O. Trott and A. J. Olson, "AutoDock Vina: improving the speed and accuracy of docking with a new scoring function, efficient optimization, and multithreading," *Journal of Computational Chemistry*, vol. 31, no. 2, pp. 455–461, 2010.

[36] J. W. Gu, A. P. Bailey, W. Tan, M. Shparago, and E. Young, "Long-term high salt diet causes hypertension and decreases

renal expression of vascular endothelial growth factor in Sprague-Dawley rats," *Journal of the American Society of Hypertension*, vol. 2, no. 4, pp. 275–285, 2008.

[37] X. Jiang and L. Shi, "Research progress on active constituents and pharmacological effects of Salvia miltiorrhiza," *Journal of Pharmaceutical Research*, vol. 36, no. 3, pp. 166–169, 2017.

[38] J. Zhang, S. J. An, J. Q. Fu et al., "Mixed aqueous extract of Salvia miltiorrhiza reduces blood pressure through inhibition of vascular remodelling and oxidative stress in spontaneously hypertensive rats," *Cellular Physiology and Biochemistry*, vol. 40, no. 1-2, pp. 347–360, 2016.

[39] Z. Zhang, T. N. Lam, and Z. Zuo, "Radix Puerariae: an overview of its chemistry, pharmacology, pharmacokinetics, and clinical use," *Journal of Clinical Pharmacology*, vol. 53, no. 8, pp. 787–811, 2013.

[40] J. M. Chu, M. Sy, and L. Hf, "Progress in effective components and pharmacological effects of Puerariae Lobatae Radix," *Food and Drug*, vol. 17, no. 2, pp. 142–146, 2015.

[41] J. H. Zhang, "Research progress on chemical constituents and pharmacological effects of Prunella vulgaris," *Chinese Traditional and Herbal Drugs*, vol. 49, no. 14, pp. 3432–3440, 2018.

[42] P. Palatini, "Role of elevated heart rate in the development of cardiovascular disease in hypertension," *Hypertension*, vol. 58, no. 5, pp. 745–750, 2011.

[43] Z. W. Shi, Y. Q. Feng, J. X. Lin et al., "Chinese expert consensus on heart rate management in hypertensive patients," *Chinese Journal of the Frontiers of Medical Science(Electronic Version)*, vol. 9, no. 8, pp. 29–36, 2017.

[44] X. Liang, H. Li, and S. Li, "A novel network pharmacology approach to analyse traditional herbal formulae: the Liu-Wei-Di-Huang pill as a case study," *Molecular BioSystems*, vol. 10, no. 5, pp. 1014–1022, 2014.

[45] T. Huang, Z. Ning, D. Hu et al., "Uncovering the mechanisms of Chinese herbal medicine (MaZiRenWan) for functional constipation by focused network pharmacology approach," *Frontiers in Pharmacology*, vol. 9, p. 270, 2018.

[46] M. Zhao, Y. Chen, C. Wang et al., "Systems pharmacology dissection of multi-scale mechanisms of action of Huo-Xiang-Zheng-Qi formula for the treatment of gastrointestinal diseases," *Frontiers in Pharmacology*, vol. 9, p. 1448, 2018.

[47] M. K. Ames, C. E. Atkins, and B. Pitt, "The renin-angiotensin-aldosterone system and its suppression," *Journal of Veterinary Internal Medicine*, vol. 33, no. 2, pp. 363–382, 2019.

[48] B. Williams, G. Mancia, W. Spiering et al., "2018 ESC/ESH guidelines for the management of arterial hypertension," *European Heart Journal*, vol. 39, no. 33, pp. 3021–3104, 2018.

[49] A. Grillo, L. Salvi, P. Coruzzi, P. Salvi, and G. Parati, "Sodium intake and hypertension," *Nutrients*, vol. 11, p. 9, 2019.

[50] E. Polychronopoulou, P. Braconnier, and M. Burnier, "New insights on the role of sodium in the physiological regulation of blood pressure and development of hypertension," *Frontiers in Cardiovascular Medicine*, vol. 6, p. 136, 2019.

[51] I. Drenjančević-Perić, B. Jelaković, J. H. Lombard, M. P. Kunert, A. Kibel, and M. Gros, "High-salt diet and hypertension: focus on the renin-angiotensin system," *Kidney & Blood Pressure Research*, vol. 34, no. 1, pp. 1–11, 2011.

[52] C. H. Fu, H. Yan, Y. G. Lu, X. G. Chen, and J. Z. Huang, "The correlation between essential hypertension and renin-angiotensin-aldosterone system," *Progress in modern Biomedicine*, vol. 12, no. 5, pp. 948–950+957, 2012.

[53] H. Wu, Y. X. Liang, Q. Bai, Z. Zhuang, D. X. Zheng, and Y. Wang, "Up-regulation of intrarenal renin-angiotensin system contributes to renal damage in high-salt induced hypertension rats," *Kidney & Blood Pressure Research*, vol. 39, no. 6, pp. 526–535, 2014.

[54] L. Chen, Q. H. Guo, Y. Chang, Y. S. Zhao, A. Y. Li, and E. S. Ji, "Tanshinone IIA ameliorated endothelial dysfunction in rats with chronic intermittent hypoxia," *Cardiovascular Pathology*, vol. 31, pp. 47–53, 2017.